N71-22414

Akademiya Nauk SSSR

PROCEEDINGS OF THE SIXTH WINTER SCHOOL ON SPACE PHYSICS

(Apatity, 18 March - 1 April 1969)

Part I

Edited by S.N. Vernov and G.E. Kocharov

CASE FILE COPY

TRANSLATED FROM RUSSIAN

Published for the National Aeronautics and Space Administration
and the National Science Foundation, Washington, D.C.
by the Israel Program for Scientific Translations

AKADEMIYA NAUK SSSR · NAUCHNYI SOVET PO KOMPLEKSNOI PROBLEME
"KOSMICHESKIE LUCHI"·KOL'SKII FILIAL IM. S. M. KIROVA
POLYARNYI GEOFIZICHESKII INSTITUT

Academy of Sciences of the USSR·Scientific Council on Cosmic Rays
Kola Branch im. S. M. Kirov·Polar Geophysical Institute

PROCEEDINGS OF THE SIXTH WINTER SCHOOL ON SPACE PHYSICS

(Trudy Shestoi Vsesoyuznoi ezhegodnoi zimnei shkoly po kosmofizike)

(Apatity, 18 March — 1 April 1969)

Part I

Edited by S.N. Vernov and G.E. Kocharov

Translated from Russian

Israel Program for Scientific Translations
Jerusalem 1971

TT 70-50079
NASA TT F-629

Published Pursuant to an Agreement with
THE NATIONAL AERONAUTICS AND SPACE ADMINISTRATION
and
THE NATIONAL SCIENCE FOUNDATION, WASHINGTON, D.C.

Copyright 1971
Israel Program for Scientific Translations Ltd.
IPST Cat. No. 5771

Translated by IPST staff

Printed in Jerusalem by Keter Press
Binding: Wiener Bindery Ltd., Jerusalem

Available from the
U.S. DEPARTMENT OF COMMERCE
National Technical Information Service
Springfield, Va. 22151

XII/16/3

Table of Contents

G. E. Kocharov. The first Apatity stage in the history of the Winter School on Space Physics 1

Section 1. THE UNIVERSE, GALAXIES AND STARS

V. A. Ruban and A. D. Chernin. Isotropization of inhomogeneous centrally symmetric cosmological models 13

A. G. Doroshkevich. Formation of galaxies in an expanding Universe . . 26

L. E. Gurevich and A. D. Chernin. The separation of galaxies into the halo and the disk subsystem 34

A. D. Chernin. Clusters of galaxies and the cosmological expansion 37

A. M. Finkel'shtein. Experimental verification of the gravitation theory in cosmology 44

G. S. Bisnovatyi-Kogan. Ejection of gas from stars in the late stages of evolution 49

Yu. V. Vandakurov. Low-frequency oscillations of a magnetic rotating neutron star 54

E. M. Drobyshevskii. Field generation in magnetic stars 62

R. A. Syunyaev. The spectrum of the extragalactic background radiation . 65

A. F. Nikiforov and B. V. Uvarov. Computation of the opacity of stars with allowance for line absorption 73

N. A. Vlasov. Charge symmetry of the Universe 77

B. P. Konstantinov, R. L. Aptekar', M. M. Bredov, S. V. Golenetskii, Yu. A. Gur'yan, V. N. Il'inskii, E. P. Mazets, and V. N. Panov. Gamma-ray measurements from KOSMOS-135 satellite with a view to possible detection of antimatter meteor streams 82

E. A. Bogomolov, V. K. Karakad'ko, N. D. Lubyanaya, V. A. Romanov, M. G. Totubalina, and M. A. Yamshchikov. Determination of the antiproton flux in primary cosmic rays 98

V. V. Cherdyntsev. Geochemical features of the composition of the Universe and the origin of atomic nuclei 102

E. E. Berlovich. The properties of nuclei far from the beta-stability strip 108

Section II. X RAYS, GAMMA RAYS, ELECTRONS AND NEUTRINO

S. I. Syrovatskii. Cosmic gamma and X rays 111

A. M. Romanov. Low-energy gamma rays (0.1—10 MeV) in the atmosphere and in outer space 128

M. M. Anisimov, L. S. Bratolyubova-Tsulukidze, N. L. Grigorov, L. F. Kalinkin, A. S. Melioranskii, E. A. Pryakhin, I. A. Savenko, and V. Ya. Yufarkin. X-ray and gamma-ray observations from artificial earth satellites 143

A. M. Gal'per and B. I. Luchkov. Variations of the electron cosmic-ray component with energies between 100 and 1500 MeV in the upper atmosphere 152

G. E. Kocharov. The neutrino emission of the Sun 158

S. S. Mandrykin and Yu. N. Starbunov. Differential rotation and nonsphericity of the Sun's surface 177

V. S. Kaftanov. Neutrino experiments on accelerators 186

Section III. PHYSICS OF THE SOLAR ACTIVITY AND DYNAMIC PROCESSES IN THE INTERPLANETARY SPACE AND IN THE EARTH'S MAGNETOSPHERE

S. N. Vernov, G. P. Lyubimov, and N. V. Pereslegina. Structure of the interplanetary space from observations of low-energy cosmic rays in 1965 — 1967 201

S. N. Vernov, E. V. Gorchakov, and G. A. Timofeev. Propagation of 1.5 MeV solar protons in the interplanetary space 211

M. M. Bredov, A. A. Kolchin, V. V. Lebedev, and G. P. Skrebtsov. Investigation of proton fluxes in the 1.50—50 MeV range with ZOND-4 and ZOND-5 automatic interplanetary stations 216

D. A. Varshalovich. Dynamic alignment of atomic and molecular spins as a new method of determination of the interplanetary magnetic field 220

Yu. N. Gnedin and A. Z. Dolginov. Radiation transfer in space physics 228

I. M. Podgornyi. Space-physical investigations in the laboratory 240

D. Kh. Morozov. The trapping of charged particles by the magnetic field with allowance for ionization losses 249

M. E. Kats and A. K. Yukhimuk. A contribution to the theory of particle acceleration in interplanetary plasma 253

M. V. Konyukov. A mechanism of acceleration of the solar wind plasma 254

V. M. Fadeev. Quasiequilibrium structures in the ionized atmospheres of stars and planets 256

I. M. Gordon. Radar astronomy of the Sun 264

L. L. Lazutin. Penetration of auroral particles into the Earth's atmosphere 269

B. E. Bryunelli. Magnetospheric electric fields and the rotation of the Earth 287

M. I. Pudovkin, S. I. Isaev, and S. A. Zaitseva. Magnetic storm development in the Earth's magnetosphere 299

V. O. Naidenov. Application of the methods of measurement of small and ultrasmall quantities of various isotopes to astrophysical research 310

B. B. Kadomtsev. Plasma containment in adiabatic traps 319

Yu. I. Gubar' and V. P. Shabanskii. Distribution of the outer belt protons in the μ, L space 321

M. A. Gintsburg. Self-similar flow in rarefied plasma 323

M. A. Gintsburg. Particle acceleration in a plasma in outer space . . . 325

A. B. Malyshev, P. M. Svidskii, V. A. Burov, I. G. Kleimenova, and V. A. Troitskaya. Comparison of the variations of high-energy electrons and ultra-low-frequency radiation 326

I. I. Alekseev, A. P. Kropotkin, and A. R. Shister. The effect of solar wind velocity inhomogeneities on the structure of the interplanetary field 327

I. I. Alekseev and A. P. Kropotkin. Interaction of high-energy particles with the neutral layer of the magnetosphere tail 328

V. P. Nefed'ev. Localization of active solar regions responsible for the generation of the geoeffective agent 330

T. Ya. Ryabova and K. A. Trukhanov. Application of electrical fields in interplanetary space as radiation shielding against protons and electrons 331

THE FIRST APATITY STAGE IN THE HISTORY OF THE WINTER SCHOOL ON SPACE PHYSICS

G. E. Kocharov

The 20th century will always be remembered as the era of great revolutions in human society. The guns of Aurora proclaimed a new era — the era of socialism and communism — and also played a revolutionary role in the progress of science and technology. It was not by accident that the first artificial Earth satellite was launched in the Soviet Union. The great advances in satellite technology opened new wide horizons for the study of the properties of outer space. New scientific disciplines developed: space physics, space medicine, etc. The scope of space research is steadily growing, and new methods and fields constantly arise. The flow of information in space science has become so vast that even the combined efforts of scientific research teams are insufficient to "digest" all the incoming data and to draw the relevant practical conclusions.

The principal aim of the School on Space Physics is clearly to familiarize the "students" with the state of the art and with the future perspectives of space physics, as well as to describe the interrelationship between the different directions of modern research. The latter aspect is particularly important, since only an all-sided, broad-minded approach to the solution of topical problems is sure to produce successful results. It is hard to envisage any progress in the study of cosmic ray variations or in neutrino astrophysics without complete grasp of the intricacies of pulsars, quasars, the background remnant radiation in space, etc. The name "School" is used advisedly: it is intended to distinguish the present gathering from symposia and conferences, whose principal aim is to provide a comprehensive and detailed discussion of a relatively narrow sector of science. In preparing the curriculum of the Fifth and Sixth Winter Schools on Space Physics, the steering committee, headed by Acad. S.N. Vernov, were aware of the urgent need of discussing the state of the art and the most promising directions of research in space physics. At the same time, sufficient emphasis was placed on detailed discussions of more restricted topics, which were considered to be of special interest. Before delving into a description of the exact aims of the Sixth Winter School, we will briefly describe the achievements of the previous sessions.

The First Winter School on Space Physics took place in Alma Ata between 22 January and 7 February 1964. It was initiated by a group of enthusiasts, headed by L.I. Dorman. Fifty scientists from 16 research institutes all over the Soviet Union participated in the sessions. Seventeen papers were read and discussed, which covered a wide range of topics: cosmology,

interior stellar structure and stellar evolution, the origin of cosmic rays, processes on the Sun and in the interplanetary medium, cosmic-ray variations, etc. The basic aim of the school from its very inception was thus to acquaint the "students" with the whole gamut of topics treated in space physics. The Second School was also organized by the Kazakh State University (the steering committee was headed by Z. Zakarin, the rector of this University). It took place between 23 January and 6 February 1965. The number of papers increased to 37, and the number of participants to 70. The curriculum remained essentially the same (see figure). E.V. Kolomeets greatly contributed to the success of the First and the Second Schools.

The Third School on Space Physics took place in Bakuriani between 15 and 26 February 1966, under the auspices of the Institute of Geophysics of the Georgian Academy of Sciences. Eighty participants attended the School. The number of papers was 39. The next School was also organized in Bakuriani, between 20 February and 4 March 1967 (100 participants, 70 papers). The success of the Third and the Fourth Schools was entirely due to the great organizing work done by the steering committee under S.N. Vernov. The exceptional contribution of V.K. Koiava and L.Kh. Shatashvili to the preparation and the routine work of these two Schools should be especially acknowledged.

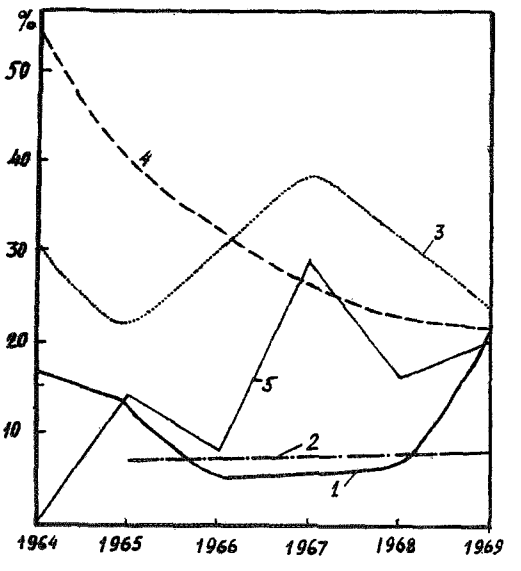

The proportions of the different directions in space physics in the 1964—1969 Schools:

1) the Universe, galaxies, stars; 2) X-ray and gamma-ray radiation, electrons, neutrinos; 3) physics of the Sun, interplanetary space; 4) cosmic rays; 5) methodology.

In accordance with the resolution of the Presidium of the USSR Academy of Sciences, the next two Schools took place in Apatity: the Fifth School

between 21 March and 5 April 1968 and the Sixth School between 18 March and 1 April 1969. One hundred and fifty participants attended the Fifth School, and three hundred participated in the Sixth School. The total number of papers approved for presentation was 57 in the Fifth School and 116 in the Sixth School. The relative proportions of the different research directions in space physics are shown in the figure.

The main emphasis in the Sixth School, as we see from the figure, was placed on four sections: the Universe, galaxies, and stars; physics of the solar activity and dynamic processes in interplanetary space and in the Earth's magnetosphere; generation, energy spectrum, variation, and propagation of cosmic rays; methodology. A significant feature is the steady decrease of the fourth section (cosmic rays) from 1964 to 1969, and the increase of the first and the fourth sections. In our opinion, the curriculum constantly improved from one school to the next.

Let us now consider in more detail some specific features of the Fifth and the Sixth Schools, which were organized with the direct participation of the present author. It is hoped that the organizers of the next schools will profit by this discussion.

Curriculum. Long before the scheduled beginning, the steering committee prepared a rough draft of the curriculum and approached scientists of repute with requests to contribute to the sessions of the School. Invitations to participate were sent to all the likely institutions. Having analyzed the various responses, the committee prepared a definitive curriculum, which was published and distributed before the opening of the School. This pre-publication of the curriculum naturally required large preparatory work and involved a certain risk — we were in danger of not meeting our obligations. No major catastrophes befell us, however: only 10% of the originally scheduled papers failed to materialize and had to be replaced by backups. Another difficulty encountered in the planning of the Sixth School was the great number of proposed papers: some of them absolutely had to be cut out. This tremendous active interest is the best proof of the excellent reputation that the School enjoys. This reputation was definitely enhanced by the considerable success of the previous schools and particularly by the speedy publication of the Proceedings of the Fifth School (the publications of the first four schools were never published) in record time: the Proceedings were published less than 4 months after the concluding session. In preparing the curriculum of the Sixth School, the steering committee were forced to give preference to review papers. At the same time, all the participants were given ample chance to take part in discussions. Following the suggestions of some participants, special discussion groups were organized on the following subjects:

1. Anisotropy of cosmic rays in interplanetary space (group leader, E. V. Kolomeets).
2. Methods of investigation of cosmic-ray variations (G. F. Krymskii).
3. Solar cosmic rays (L. I. Miroshnichenko).
4. Solar wind (L. Kh. Shatashvili).
5. Earth's magnetosphere (B. E. Bryunelli).
6. Methodology of solar cosmic rays (Ya. L. Blokh).

The concensus of opinion was that the discussions proved a success and were highly profitable. In future, discussions of special topics should be allotted a separate place in the general curriculum and the program

should be coordinated with the respective group leaders. This approach will enhance the impact of the discussion groups and, moreover, papers of narrow appeal presented to the steering committee will naturally be included in the respective discussion groups.

Publication of the Proceedings. As we have mentioned before, the Proceedings of the Fifth School were the first to be published. There is no need to dwell on the great importance of the publication of the Proceedings. One point should be borne in mind however: given the present rate of information acquisition, the Proceedings should be published either in a very short time or not published at all. The main value of the Proceedings is that they enable wide circles of scientists to familiarize themselves with the current state of the art in the various fields of science, and not with the state of the art as it was a year or two ago. And yet, the publication of the Proceedings in a very short time presents enormous problems. Each paper needs scientific and style editing and careful checking. Whenever necessary, the figures should be redrawn, the tables rearranged, the text typed, and formulas written in. The finished product should be proofread and checked and finally printed. All these stages are consecutive, and if there is only one stylist (this is highly desirable if the Proceedings are to be published in a uniform style) and the entire work is handled by a single person, the publications of the Proceedings may take at least 8—10 months. By organizing the work in parallel teams, on the other hand, the publication data can be brought forward to 2 months. An excellent example of this kind of crash program is the publication of the Proceedings of the Fifth School: the deadline for contributions was the end of May 1968, and the Proceedings were published in early August. Note that in order to speed up the publication, it is absolutely essential to reduce to a minimum (and if possible to eliminate altogether) the time gap between the last session and the deadline for the contributions to the Proceedings.

The editorial and printing work were very efficiently organized at the Kola Branch of the USSR Academy of Sciences. This was unquestionably due to the great efforts of Yu. A. Shashmurin, Scientific Secretary of the Kola Branch, A.N. Voronkov, Deputy Chairman of the Presidium of the Kola Branch, S.I. Isaev, Director of the Polar Geophysical Institute, and Yu. A. Volkov, Scientific Secretary of the Institute. N. Ya. Zamotkin, who headed the editorial and publishing team, also made an obvious contribution to the success of the project. The styling of the Proceedings of the Fifth and Sixth Schools was done with great competence and devotion by E. M. Aleksandrova. The printers A. A. Tolokontsev, V. A. Ganichev, and others worked overtime in order to meet the dates.

The contribution of V. A. Dergachev to the preparation and publication of the Proceedings was literally enormous. The present author is convinced that the energy, persistence, and single-minded devotion of V. A. Dergachev played the decisive role in the publication of the Proceedings in such a short time.

Accommodation and entertainment. In large cities, such as Moscow or Leningrad, nobody meets the participants on arrival. Moreover, no hotel accommodations are booked for unregistered and unexpected arrivals. The participants are supposed to make use of public transport and to find

suitable accommodation on their own. In small towns, however, all the participants have to be accommodated, whether with or without previous registration, since otherwise they stand the risk of "being left out in the cold" (literally). This year, more than 50 unregistered "students" arrived at Apatity, without any prior notification to the steering committee. The organizers found themselves in a very tight situation, and yet all the 300 participants were given accommodation. This was largely due to the efforts of the local Party Secretary, N.F. Vladimirov. Long before the scheduled opening of the School, N.F. Vladimirov obtained permission from the Municipality to accommodate the participants in a newly finished building, which at that time was still unoccupied. V.D. Degtyarev and P.S. Lobynichev were responsible for the physical accommodation in the various flats.

Between the sessions of the Fifth and Sixth Schools, excursions were organized to Monchegorsk, where the participants visited the "Severonikel" complex, the "Apatit" complex, the apatite-nepheline factory ANOF-2, the Botanical Gardens and the Geological Museum of the Kola Branch of the USSR Academy of Sciences. Excursions to Kirovsk, Murmansk, and other towns also took place. A number of participants agreed to give lectures to workers in Apatity and Kirovsk.

* * *

Because of the large volume of the Proceedings, the steering committee of the Sixth Winter School on Space Physics decided to publish in full only review papers of relatively general interest. Papers of restricted appeal were included in the form of brief summaries.

The curriculum was very extensive, with a tight time schedule. No paper, however detailed, can cover all the problems discussed in the school sessions. In terms of distances, the entire known range of wavelengths was covered. The topics ranged from discussions of the characteristics of quasars — objects at the very limit of the observable part of the Universe — to elementary particles with dimensions of the order of 10^{-13} cm. Considerable attention was devoted to one of the principal directions in the modern natural science — cosmology, the science of the general laws governing the structure and the evolution of the Universe. Cosmological topics were mainly dealt with in papers read by the students of Acad. Ya.B. Zel'dovich and Prof. L.F. Gurevich.

The paper of V.A. Ruban and A.D. Chernin presents a further development of the theory of expansion of the Universe. It is shown that the high symmetry of the Metagalaxy does not automatically imply isotropy and homogeneity in the distant past. It is suggested that the high symmetry evolved during the expansion of the Universe from an essentially inhomogeneous and anisotropic initial state of lower symmetry.

The formation of galaxies in an expanding Universe is discussed by A.G. Doroshkevich. Fridman's model is currently the cosmological model which has been developed in maximum detail so far. Certain difficulties are encountered, however, in reconciling Fridman's model with the existence of galaxies and clusters of galaxies. Two approaches are currently being considered to the problem of the formation of galaxies. Some authors are of the opinion that Fridman's model cannot be applied to the early stages of expansion, whereas others proceed from the

fluctuation hypothesis which postulates the existence of small deviations from the homogeneous and isotropic distribution and motion of matter. The main emphasis in A.G. Doroshkevich's paper is placed on the problem of the formation of galaxies in Fridman's model within the framework of the fluctuation hypothesis. Both the advances in this direction and the still unsolved problems are reviewed.

N.A. Lotova's paper on pulsars was particularly well received. The first pulsar was discovered in 1967 by Jacqueline Bell, a young assistant of the British radio astronomer A. Hewish. The behavior of pulsars is highly unusual and puzzling, so that the results remained a well-guarded secret for a relatively long time (half a year). A suggestion was made that the detected signals were of artificial origin, being transmitted by extraterrestrial civilizations. The entire problem was examined impassionately in a proper perspective, and the pulsar research now follows a standard groove. Extensive experimental material was accumulated in a relatively brief time. More than 20 pulsars are known at present with pulsation periods ranging between 35 msec and 1.96 sec. Quite recently the pulsar NP 0532 (in the Crab Nebula) was found to pulsate in the optical and the X-ray spectrum, as well as in the radio spectrum. The observational data seem to indicate that the pulsar NP 0532 is a neutron star. If the pulsar is treated as a rotating star with a strong magnetic field (10^{12} gauss), particles can be accelerated up to 10^{20} eV.

G.S. Komberg's review deals with quasars. Quasars are powerful energy sources: the luminosity of a single quasar is comparable with the luminosity of the entire Galaxy, which contains 100 billion stars. Various hypotheses were advanced in order to account for the tremendous energy output of quasars: a spontaneous explosion of a billion stars, matter—antimatter annihilation, gravitational collapse of a single star with a mass equal to 100 million solar masses. Each of these hypotheses encounters certain specific difficulties. The concensus of opinion now favors the suggestion that the quasar energy is of gravitational origin.

One of the fundamental problems of physics — the charge symmetry of the Universe— was dealt with in a separate session. N.A. Vlasov prepared a critical review of the various theoretical and experimental data on the charge symmetry of the Universe and the equivalence of matter and antimatter. He noted that contrary to the prevailing opinion, there is no definite proof of the absence of antimatter in our Galaxy, not to say in the whole Universe in general. Vlasov also considered the possibilities of experimental detection of antimatter in the Universe. In particular, he stressed the importance of the radioactive spots on the lunar surface as a possible source for the detection of annihilation products produced by antimeteors impacting on the Moon. M.M. Bredov, E.P. Mazets, and V.A. Romanov described the experimental work carried out at the Ioffe Physics Institute of the USSR Academy of Sciences in connection with the problem of the charge symmetry of the Universe. The results of experiments carried out over a number of years by analyzing the correlation between the intensities of the hard gamma quanta and neutrons at altitudes of 12—18 km, on the one hand, and the entries of individual meteorites into the atmosphere, on the other, seem to support Acad. B.P. Konstantinov's hypothesis which states that comets are made of antimatter. Experiments carried out with the KOSMOS-135

satellite reveal an enhanced intensity of the electron—positron annihilation radiation during the Geminid and Ursid meteor streams. If antimatter constitution is assumed for the meteor streams, the observed effect may be accounted for by a flux of 5—10 mg of antimatter penetrating daily into the atmosphere. This figure is consistent with the results obtained from the correlation experiments at altitudes of 12—18 km.

Interesting experimental results were presented by V.A. Romanov. Balloon measurements of the intensity of protons (p) and antiprotons ($\tilde{p}$) were carried out on the basis of the east—west cosmic-ray asymmetry. Between 1.9 and 2.6 BeV, the results give $\tilde{p}/p = 0.24 \pm 0.05$, which is much higher than the theoretical figures ($10^{-3} - 10^{-5}$) obtained under the assumption that the only source of antiprotons in cosmic rays are the nuclear reactions of cosmic rays with the interstellar gas.

The second section of the Proceedings begins with S. I. Syrovatskii's paper which describes mainly the various experimental data on gamma-ray and X-ray radiation from outer space. In conclusion it is noted that no common opinion has been formed regarding the origin of gamma-ray and X-ray radiation from outer space. A.M. Romanov described experimental measurements of the spatial and spectral distribution of low-energy gamma rays from space (0.1—10 MeV).

V.S. Kaftanov's review deals with neutrino experiments on accelerators. The first part describes the existing experiments and the corresponding results. The second part surveys the plans for the future neutrino experiments. Five institutes are scheduled to launch experiments on inelastic interaction of neutrino with matter in accelerators: Serpukhovo (USSR), CERN (Geneva, Switzerland), Argonne, Brookhaven, and Batavia (USA). Kaftanov stressed the importance of the experimental search for the W-meson, the study of lepton pair production in the Coulomb field of a nucleus without a W-meson, etc.

The third section of the Proceedings includes a considerable number of papers. S.N. Vernov, G.P. Lyubimov, and N.V. Pereslegina generalize the results of low-energy cosmic-ray measurements on ZOND-3, VENUS-2, VENUS-3, and VENUS-4 satellites. Low-energy cosmic rays carry valuable information on large-scale magnetic fields and solar plasma. It is noted that the magnetic fields issuing from the active regions on the Sun and rotating with the Sun display quasihelical structure. Shock waves from solar flares distort these fields and affect the velocity of propagation of solar cosmic rays. The observed slowing-down of shock waves from solar waves eliminates the Forbush decrease and this leads to an accumulation of solar cosmic rays at distances of 2 to 5 a.u. from the Sun. Large gradients of cosmic rays are set up at these distances. The data presented in the paper show that the variations of the galactic cosmic rays are determined by the dynamics of the active solar regions.

D.A. Varshalovich proposed a new method for the determination of the interplanetary magnetic field. Various astrophysical objects — interstellar and interplanetary gas, nebulae, upper layers of stellar and planetary atmospheres, comets, etc. — display dynamic alignment of atomic and molecular spins as a result of resonance scattering of isotropic non-polarized radiation fluxes. The magnetic level occupancies depend on the direction of the magnetic field. Therefore, measurements

of the relative line intensities and line polarizations make it possible to determine the direction of the magnetic field. Thus, by measuring the intensity ratio of the NaI lines D_1 ($\lambda = 5896$ Å) and D_2 ($\lambda = 5890$ Å) in the spectra of comets and the polarization of the D_2 line, we can find the direction of the magnetic field in the region of space occupied by the comet head at the particular time. The obvious advantage of the method is that it is applicable to very weak fields also, when other optical methods do not apply. Also note that artificial Earth satellites are capable of performing measurements in a relatively restricted region near the Earth's orbit, whereas comets constitute very cheap and simple probes for investigating the magnetic field geometry at distances from 0.03 to 3 – 5 a. u. from the Sun. These natural probes are effective not only in the plane of the ecliptic, but also off this plane.

I. M. Podgornyi considered in detail laboratory simulation of a number of effects associated with the interaction between the solar wind and the Earth's magnetic field. The results of laboratory experiments fit the satellite data. The simulation experiments are particularly advantageous in correlation measurements at different points in space. Application of the correlation technique to the results of microfluctuation measurements provided the first firm indication of the space scale of microfluctuations.

The participants showed considerable interest in the paper read by Yu. N. Gnedin, who discussed the theory of radiative transfer in space physics.

The physics of comets is now attracting considerable attention, as it became clear that comets can be used as deep space probes. We recall that the very existence of the solar wind and interplanetary magnetic fields was predicted as a result of the observations of comets. There is no consistent theory of comets, however, and the observational data therefore could not be interpreted to determine the characteristics of interplanetary space and the solar wind. A. Z. Dolginov noted that considerable progress in the theory of comets has been accomplished in recent years. The theory of cometary phenomena, however, is still far from being complete even for the case of a quiet, undisturbed interplanetary medium. Further advances in the theory are impossible without detailed examination of the individual molecular and atomic spectra of all the appearing comets, the line shapes, and the polarization of cometary light. Simulated model experiments should be carried out both in laboratory and in space.

V. I. Sharkov describes the results of laboratory simulation of cometary phenomena. Systematic studies of the behavior of water ice and frozen aqueous electrolyte solutions in vacuum at various temperatures revealed a number of highly important conclusions for the understanding of physical processes in comets. It was clearly demonstrated that significant results can be obtained at low cost without complicated equipment.

An important place in the general schedule was devoted to the discussion of the various aspects of acceleration and propagation of solar cosmic rays. L. I. Miroshnichenko presented a state-of-art review and noted, in particular, that the currently available observation results are adequate for quantitative analysis of the energy spectra of the solar cosmic rays near the Earth and in the source. There is thus a possibility of quantitatively verifying the numerous models of acceleration and propagation of solar particles of various energies.

T. N. Charakhch'yan read two papers. One paper dealt with the energy spectrum of cosmic rays in interplanetary space. Careful analysis of the extensive experimental material collected between 1957 and 1964 by 11,000 radiosonde measurements in the stratosphere showed that the energy spectrum of the galactic cosmic rays near the Earth in the epoch of maximum of the 11-year solar cycle is virtually identical to the extrapolated spectrum at zero solar activity. According to Charakhch'yan, the low-energy part of the spectrum of the galactic cosmic rays can hardly be attributed to solar modulation. It is probably determined by the spectrum of particles arriving from interstellar space. The second paper dealt with the diffusion of cosmic rays.

The 27-day variations of cosmic rays which emerge from ground and stratospheric data were considered by L. Kh. Shatashvili and V. P. Okhlopkov. Detailed analysis of the experimental data carried out by L. Kh. Shatashvili showed that the upward phase of the 20th solar activity cycle reveals distinct 27-day variations both in the sunspot number and in all the measured cosmic-ray components. He noted that these variations are associated with long-lived active formations on the Sun. V. P. Okhlopkov indicated that the cosmic-ray variations show a lag of 60 — 70 days relative to solar activity variations.

The variation of cosmic-ray anisotropy during the solar cycle was described by K. K. Fedchenko. The starting data for his analysis came from the neutron component records for the years 1958 and 1968, provided by two high-latitude Soviet stations, Apatity and Kheis Island. The true anisotropy beyond the atmosphere and the geomagnetic field is largely sensitive to the conditions prevailing in the interplanetary medium. Moreover, 27-day modulation of the cosmic-ray anisotropy was noted both in epochs of maximum and minimum.

As we have noted before, the proportion of the papers dealing with methodological aspects was fairly high, about 25%. In our opinion, this is a healthy situation. After all, representatives from cosmic-ray stations scattered in different and widely separated parts of the Soviet Union participated in the Winter School. A common meeting place for exchange of opinion and experience is absolutely essential for normal and continuous operation of the solar cosmic-ray stations. It is also important to familiarize the cosmic-ray specialists with the tremendous experience accumulated in elementary particle and nuclear physics with regard to the development of new radiation detectors.

A separate section of methodological papers was therefore organized. Various topics pertaining to solar cosmic rays were discussed by Ya. L. Blokh, Yu. A. Egorov, I. N. Kapustin, M. A. Kovalenko, N. G. Seregina, V. S. Smirnov, and others. The properties of the new instruments used in nuclear and elementary particle physics, such as spark and bubble chambers, Cherenkov and scintillation counters, etc., were described by L. V. Bakanov, E. A. Damaskinskii, E. M. Kruglov, V. S. Chukin, and others.

A number of lectures on mathematical statistics were read by Yu. I. Serebrennikov. The concensus of opinion is that Serebrennikov's lectures were extremely valuable and profitable for experimental physicists. An interesting paper was read by O. B. Vasil'ev on the subject of latent periodicities and statistical forecasting.

The Scientific Council on the Problem of Cosmic Rays convened on the last day of the School. Various topics relating to the sessions of the Sixth School on Space Physics and the publication of the Proceedings were discussed. The participants were of the opinion that in future review papers on a wide range of problems in space physics should again be combined with two-hour discussion groups on special topics.

The Scientific Council expressed general appreciation to the steering committee. A committee with the participation of S. N. Vernov, L. I. Dorman, G. E. Kocharov and E. V. Kolomeets was appointed for taking charge of the preparations for the next Winter School.

The title of this introductory paper, "The First Apatity Stage...", was chosen advisedly. I am deeply convinced that space physicists will again convene in Apatity after some time. This is not only because of the exceptional success of the staff of the Kola Branch of the USSR Academy of Sciences, headed by E. K. Kozlov, in the organization of large events of this kind, but also because here, north of the Polar Circle, we find ourselves in a live natural laboratory of space physics. Here we can witness with our own eyes the polar aurorae, those gigantic repercussions of the processes which take place on the Sun and in the interplanetary space. The Polar Geophysical Institute is equipped with excellent laboratories engaged in an extensive research program covering the ionosphere, the polar aurorae, the geomagnetic field, and cosmic rays. Here instruments are launched several times daily into the stratosphere. The close contact between the "students" and the activities of the Polar Geophysical Institute will certainly have far-reaching effects in the development of space physics.

Section I

THE UNIVERSE, GALAXIES AND STARS

Edited by G. E. Kocharov and V. A. Dergachev

ISOTROPIZATION OF INHOMOGENEOUS CENTRALLY SYMMETRIC COSMOLOGICAL MODELS

V. A. Ruban and A. D. Chernin

The observational results of extragalactic astronomy /1, 2/ indicate that large-scale distribution of matter in regions greater than 100 Mpc, which contain numerous clusters of galaxies, is on the average homogeneous, nonstationary, and is characterized by Hubble's expansion law. It therefore seems that Fridman's cosmological models /3, 4/ on the whole provide an adequate description of the "smoothed" structure and the dynamics of the Metagalaxy in the present epoch and in the near past.

The maximum symmetry of the homogeneous isotropic distribution of gravitating matter in general relativity indicates that a priori Fridman's model, because of its exceptional features, may be expected to describe even the earlier stages of evolution of the expanding Universe. However, the assumption of maximum symmetry of the Universe constitutes a far-reaching idealization even for the observable part — the Metagalaxy — and at its best it is satisfied only approximately. Moreover, unlimited interpolation of the homogeneity and isotropy of the Universe into the past all the way to the singular state constitutes an arbitrary hypothesis, and there is definitely room for a diametrically opposite point of view, according to which the observed high symmetry of the Metagalaxy is not an "inborn" feature but rather has been acquired as a result of evolution from an essentially inhomogeneous and anisotropic state of lower symmetry. This idea is supported by the absolute instability of Fridman's contracting models under small perturbations changing their homogeneity and isotropy /5/. Moreover, qualitative analysis of the dynamics of relativistic cosmological models with arbitrary distribution and motion of matter also shows that overall expansion in the co-moving frame of reference should be accompanied by inevitable reduction of anisotropy (or at least of some of the anisotropic features) /6/, so that the absence of marked anisotropy and inhomogeneity in the Metagalaxy does not justify our ignoring the possibility of pronounced and significant anisotropy and inhomogeneity in the early stages of expansion of the Universe. A vivid illustration and direct confirmation of this alternative description of the initial low-symmetry singular state are provided by special cases of cosmological solutions of Einstein's equations /4, 7 — 10/ which constitute a wider family of homogeneous anisotropic models significantly deviating from Fridman's models in the early stages of evolution, near the singular state, when the various directions in space are nonequivalent, and then gradually approaching Fridman's models in the course of expansion and eventually acquiring the appropriate isotropy characteristic of the Metagalaxy.

In this paper, we intend to analyze a simple and well-known case of centrally symmetric cosmological models /3, 4, 11, 12/ in order to illustrate the fundamental feasibility of an isotropic and homogeneous Metagalaxy evolving from a globally inhomogeneous and anisotropic singular state with infinite density and velocity gradients of matter. The spherically symmetric case is of particular interest in cosmology, since all Fridman's isotropic models are spherically symmetric and the hypothesis of centrally symmetric distribution and motion of the gravitating matter in the past constitutes a natural generalization, especially if the Metagalaxy is considered as a bounded finite giant system with a strong relativistic gravitation field. We will only analyze the idealized version of the cosmological models of a dust sphere with zero pressure, for which an exact analytical solution of the gravitation equations can be obtained /3, 4/ and the conditions of isotropization in the course of expansion, when the sphere evolves toward Fridman's models, can be elucidated.

The high isotropy of the cosmic radiation background ($\frac{\Delta T}{T} \approx 0.5\%$, $T \approx$ $\approx 3°K$) /13/, if considered within the framework of the "hot" model, indicates that the expansion of the Metagalaxy did not display pronounced anisotropy and inhomogeneity in the past, all the way to red shifts of $z = \frac{\lambda - \lambda_0}{\lambda_0} = 10$ /4/. Since the effect of radiation becomes negligible and the nonrelativistic matter assumes the dominant role in field sources at earlier times with $z \approx 1000 - 100$, inhomogeneous models in principle may isotropize in the later stages of expansion, when matter is in a state of free motion in its own gravitation field and the effect of pressure and pressure gradients on the dynamics is ignorable (which is true for such a massive object as the Metagalaxy). Our group of isotropizing inhomogeneous dust sphere models with anisotropy and inhomogeneity rapidly diminishing with expansion therefore does not clash with the observed data and may be used as a point of departure for the analysis of more realistic inhomogeneous models of the early stages of Metagalactic evolution.

NEWTONIAN COSMOLOGY

Consider centrally symmetric models of distribution and homologous motion of a gravitating dust-like medium with zero pressure. We will first analyze the dynamics within the framework of Newtonian cosmology /6, 7/. The Metagalaxy is a priori known to be a relativistic object with a strong gravitation field ($\varphi / c^2 \sim 1$, $v \approx HR \sim C$), and if it is a bounded finite system, its present-day boundary should lie inside Schwartzschild's sphere in the "expanding" T region /4/. However, because of far-reaching similarity in the local properties of relativistic and classical models, which is attributable to the characteristic features of spherical symmetry /11, 14/, the main results for the density and radial velocity distribution of the "dust" in a general-relativistic sphere (as in Fridman's homogeneous and isotropic models) /4, 15/ can be obtained in a simple way by combining Newtonian gravitation with the equations of classical hydrodynamics in Lagrange's form:

$$\frac{\partial^2 R}{\partial t^2} = -\frac{GM}{R^2}, \quad M = 4\pi\int_0^R \rho R^2 dR, \tag{1}$$

where $M(\chi)$ is the current total rest mass of the "dust" contained inside a "fluid" sphere of Euler radius $R(t, \chi)$, ρ is the density of the "dust," t is the absolute time, G is Newtonian gravitational constant. If mixing of different layers and departure from continuity conditions are ignored, the gravitating mass $M(\chi)$ impelling the dust particles of a given spherical layer χ will remain constant in this case of homologous motion of "dust" and it may be used as a convenient radial Lagrangian coordinate.

The first integral of the equation of motion (1) is the conserved total energy per unit "dust" mass:

$$E(M) = \frac{1}{2}\left(\frac{\partial R}{\partial t}\right)^2 - \frac{GM}{R} \tag{2}$$

and its sign differentiates between hyperbolic ($E>0$) and elliptical ($E<0$) types of motion of the layer. The law of motion of the "dust" in an arbitrary gravitating sphere may be derived in closed form by integrating (2). For the special case of parabolic motion ($E=0$), the integration can be carried out in explicit form:

$$R(t,M) = \left\{\frac{3}{2}\sqrt{2GM}\left[t - t_0(M)\right]\right\}^{\frac{2}{3}}, \tag{3}$$

whereas for $E(M) \neq 0$ it is expressed by implicit relations of the form

$$\begin{gathered} R(t,M) = |E(M)|^{\frac{1}{2}} a(t,M), \quad \frac{1}{2}\left(\frac{\partial a}{\partial t}\right)^2 = \frac{a_0(M)}{a} + \epsilon, \quad \epsilon = \pm 1, \\ \sqrt{2}\left[t - t_0(M)\right] = \int_0^a \left(\frac{a_0}{u} + \epsilon\right)^{-\frac{1}{2}} du, \quad a_0(M) = \frac{GM}{|E|^{\frac{3}{2}}}, \end{gathered} \tag{4}$$

or parametrically using a convenient dimensionless time $\eta = \int_0^t \frac{dt}{a(t,M)}$

Ideal spherical symmetry of "dust" motion produces focusing and accumulation of particles at a point. Therefore, a singular state is assumed to exist at the center of the sphere $R(t_0, M) = 0$, which is characterized by infinite density and infinite radial velocity of matter. It can be treated as an idealization of the superdense initial state, the Metagalactic "protonucleus," and the integration constant $t_0(M)$ then can be interpreted as the time at which a particle of a given layer left this central nucleus.

In the hyperbolic case, when $E(M)>0$,

$$a = \frac{a_0}{2}(ch\,\eta - 1), \quad \sqrt{2}(t - t_0) = \frac{a_0}{2}(sh\,\eta - \eta), \tag{5}$$

the only type of particle motion is unbounded recession from the central singularity ($0<\eta<\infty$).

In the elliptical case, when $E(M)<0$,

$$a = \frac{a_0}{2}(1 - \cos\eta), \quad \sqrt{2}(t - t_0) = \frac{a_0}{2}(\eta - \sin\eta), \tag{6}$$

the phase of outward motion ($0<\eta<\pi$) also originates in the singularity, but at a finite distance $R_{max} = \frac{GM}{|E|}$ from the center the direction of motion is reversed and the particles fall back to the center. The lifetime of the center is thus limited by the pulsation period $\Delta = \frac{\pi a_0}{\sqrt{2}}$. The corresponding distribution of the "dust" density and radial velocity in a nonstationary sphere is expressed by the relations

$$V(t,M) = |E|^{\frac{1}{2}}\left(\frac{a_0}{a}+\epsilon\right)^{\frac{1}{2}}, \quad \rho(t,M) = \frac{1}{4\pi R^2}\cdot\frac{\partial R}{\partial M},$$

where for $E(M) \neq 0$

$$\frac{1}{|E|^{\frac{1}{2}}}\frac{\partial R}{\partial M} = \frac{d\ln|E|^{\frac{1}{2}}}{dM}a + \left(\frac{a_0}{a}+\epsilon\right)^{\frac{1}{2}}\left(\frac{da_0}{dM}I_0 - \sqrt{2}\frac{dt_0}{dM}\right) - \frac{da_0}{dM};$$
$$I_0 = \begin{cases} \operatorname{Arcsh}\sqrt{\frac{a}{a_0}} \\ \arcsin\sqrt{\frac{a}{a_0}} \end{cases}; \quad \epsilon = \begin{cases} +1 \\ -1 \end{cases}. \tag{7}$$

The parabolic case $E=0$ is obtained directly from (3) by taking the limit $a \to 0$:

$$\rho = \frac{1}{6\pi G(t-t_0)^2}\left[1 - \frac{2M}{t-t_0}\frac{dt_0}{dM}\right]^{-1}. \tag{8}$$

The general solution of the Newtonian problem of centrally symmetric motion of "dust" in its own gravitation field depends on two essentially arbitrary functions of the radial Lagrangian coordinate: the distribution of the specific energy $E(M)$ or, more precisely, of a combination of the form $a_0(M) = GM/|E|^{3/2}$, and the time of collapse of particles of a given layer $t_0(M)$. These functions account for all the possible initial distributions of the "dust" density and radial velocity in an arbitrary inhomogeneous sphere; they are restricted only by the most general requirements ensuring homologous motion. For the particular cases

$$a_0 = \frac{GM}{|E|^{3/2}} = \text{const}, \quad t_0 = \text{const}; \quad E = 0, \quad t_0 = \text{const} \tag{9}$$

the above solution reduces to analogs of Fridman's cosmological models, which represent homogeneous spheres with isotropic Hubble velocity field of "dust" $\vec{V} = H(t)\vec{R}$. *In this exceptional case, there is no particular point* of the medium which may be regarded as the center $R = 0$ and this coordinate can be assigned to any element of the medium /4, 15/. The condition of isotropy of the radial velocity field $V = H(t)R$ or the equivalent requirement of homogeneous "dust" distribution $\rho(t) = \frac{3M}{4\pi R^3}$ (these two conditions are interrelated in a sphere) unambiguously isolate these special Milne-MacCrea solutions with separable variables, $R(t, M) = \varphi(M)a(t)$.

The law of total energy conservation of a homogeneous gravitating sphere for the case of parabolic "dust" motion ($E=0$) leads to the definition of

critical density $\rho_k = \frac{3H^2}{8\pi G}$, a well-known condition of quasi-Euclidean geometry of the Fridman universe, and the cases of elliptical ($E < 0$) and hyperbolic ($E > 0$) isotropic expansion of a homogeneous dust sphere correspond to a closed ($\rho > \rho_k$) and an open ($\rho < \rho_k$) Fridman models, and moreover present a complete classical analog of their local properties. Near the central singularity ($R(t_0, M) = 0$ for $t \to t_0(M)$), the energy integral $E(M)$ does not affect the dynamics and in fact drops out from the leading term of the expansion of the general solution (4) for $R \ll \frac{GM}{|E|}$, so that it coincides with the degenerate parabolic case (3) with $E = 0$. The distribution and the motion of "dust" in an arbitrary sphere at the early stages of expansion is essentially determined by one arbitrary function $t_0(M)$. Therefore the simultaneous collapse of the entire sphere to the center ($t_0 = \text{const}$) in accordance with (9) constitutes a case of quasi-isotropic motion with an asymptotic velocity field $V = H(t)R$, $H = 2/3(t - t_0)$, and in the limit $\rho \to \infty$ it leads to a homogeneous distribution of "dust", whose density goes to infinity as $\rho \approx 1/6\pi G(t - t_0)^2$, just like in the Milne—MacCrea model.

If different layers do not collapse simultaneously ($t_0(M) \neq \text{const}$), the motion of "dust" near the center is essentially anisotropic, and its density goes to infinity according to a different law:

$$\rho \approx \frac{1}{12\pi G} \frac{dt_0}{dM} (t - t_0)^{-1} \tag{10}$$

In accordance with this picture of successive collapse of the individual spherical layers, their longitudinal dimension in the direction of the radius is stretched because of the increase in the relative acceleration of the particles in the gravitation field (a characteristic "tidal effect") and the amplitude of the inhomogeneity, expressed in terms of the density gradient, increases indefinitely. In particular, its behavior in the parabolic case ($E = 0$)

$$\frac{\partial \ln \rho}{2\partial M} = \frac{2\frac{dt_0}{dM} + M\frac{d^2 t_0}{dM^2}}{\left(t - t_0 - 2M\frac{dt_0}{dM}\right)} - \frac{M\left(\frac{dt_0}{dM}\right)^2}{(t - t_0)\left(t - t_0 - 2M\frac{dt_0}{dM}\right)} \tag{11}$$

shows that in general the inhomogeneity near the center $R(t_0, M) = 0$ varies as

$$\frac{\partial \ln \rho}{\partial M} \sim \frac{dt_0/dM}{t - t_0} \sim R^{-\frac{3}{2}} \to \infty.$$

The expansion of the sphere may be treated as a simple reversal in time of its collapse, and the density and velocity distribution in the explosive phase repeats in reverse order the variation of these parameters during collapse.

In case of simultaneous ejection of all the particles from the center ($t_0 = \text{const}$, a "single explosion" of the protonucleus), the expansion begins with a homogeneous singular state and should involve a gradual growth of deviations from isotropy if $a_0(M) = \text{const}$:

$$R \approx \tilde{R}\left(1 + \frac{\tilde{R}}{5R_0}\right), \quad \tilde{R} = \left\{\frac{3}{2}\sqrt{2GM}(t - t_0)\right\}^{\frac{2}{3}}.$$

The correction term in the expansion may be interpreted as spontaneous creation and growth of inhomogeneity, together with the associated anisotropy of "dust" motion, as a result of the gravitational instability of the homogeneous isotropically expanding sphere under spherically symmetric fragmentation in the parabolic stage of expansion with $R \ll R_0 = GM/|E|$:

$$\frac{\delta\rho}{\rho} = \frac{\tilde{R}}{5R_0}\left(1 + \frac{d\ln E^3}{d\ln M}\right) \backsim \tilde{a} \backsim t^{\frac{2}{3}}; \quad \frac{\delta V}{V} \approx \frac{2}{5}\frac{\tilde{R}}{R_0} \backsim \tilde{a}. \tag{12}$$

The behavior of the general solution (4)—(7) in the late stages of expansion, when $t \gg t_0(M)$, is determined primarily by the total energy $E(M)$ of the "dust" and is relatively insensitive to the form of the function $t_0(M)$. Differences in ejection times of the successive envelopes from the "protonucleus" thus become insignificant at large distances from the center and do not affect the asymptotic behavior of hyperbolic motion. We thus conclude that the special class of solutions corresponding to the initial values

$$a_0 = \frac{GM}{|E|^{\frac{3}{2}}} = const, \; t_0(M) \neq const; \quad E = 0, \; t_0(M) \neq const, \tag{13}$$

represents all the possible isotropizing models of a dust sphere, which evolve into homogeneous isotropic models in the course of expansion from an essentially inhomogeneous singular state. In the parabolic case ($E=0$, $t_0(M) \neq$ const), the inhomogeneity amplitude (11) decreases as $a^{-3/2}$ during expansion, and if $t \gg t_0(M)$, the motion is isotropized and solution (3), (8) reduces to a homogeneous plane model with damped small perturbations of the form

$$\rho = \frac{1}{6\pi G t^2}, \quad \frac{\delta\rho}{\rho} = \frac{2}{t}\frac{dt_0}{d\ln M} \ll 1. \tag{14}$$

For hyperbolic expansion of the sphere with $E > 0$, $a_0 = \text{const}$, the "dust" distribution is also homogenized, and small deviations from the homogeneous isotropic background decay first according to (14) as $a^{-3/2}$ and then, for $a \gg a_0$, as $a^{-1} \sim 1/t$, although the two time dependences are identical:

$$\rho = \rho_0\left(\frac{a_0}{a}\right)^3, \; \rho_0 = \frac{3}{4\pi G a_0^2}, \quad \frac{\delta\rho}{\rho} \approx \frac{2}{a}\frac{dt_0}{d\ln E} \ll 1. \tag{15}$$

In the asymptotic limit $a \sim t \to \infty$, for vanishingly low density and constant inertial outward motion of the "dust" with $E > 0$, these initially inhomogeneous models of a sphere reduce to Milne's open kinematic model /4/. In the case of negative total energy $E(M) < 0$, the phase of overall expansion is of finite duration, of the order of $a_0(M)$, and perfect isotropization is unattainable, although inhomogeneous models with $t_0(M) \ll a_0 = \text{const}$ in the late stages of expansion ($t \gg t_0(M)$) may approach arbitrarily close to a "closed" homogeneous isotropic model.

For special classes of inhomogeneous spherical models, which contain a single arbitrary functions $a_0(M)$, or $t_0(M)$, and correspondingly isotropize during the collapse around a singular point or during the infinite expansion state, the dynamics may be treated as the case of nonlinear evolution of the

ascending and the declining branch of arbitrary spherically symmetric perturbations of "dust" distribution due to gravitational instability in the homogeneous isotropically expanding medium. We can thus readily investigate the behavior of any density and radial velocity perturbations in a sphere and, in particular, derive the classical results of the growth of Jeans instability in isotropic models /4, 5, 16/ from the exact solution, provided the variations in the initial values $\delta a_0(M)$ and $\delta t_0(M)$ are such that the deviations in density and velocity over a finite length of time from the original Fridman state are small, i.e., $\delta\rho/\rho \ll 1$, $\delta V/V \ll 1$, where

$$\frac{\delta\rho}{\rho} \approx Aa + Ba^{-\frac{3}{2}}, \quad \frac{\delta V}{V} \approx A'a + B'a^{-\frac{3}{2}} \tag{16}$$

In the linear approximation, the inhomogeneity amplitude contains a growing ($a_0(M) \neq$ const) and a decreasing ($t_0(M) \neq$ const) term; it increases only during the parabolic stage of expansion and goes to a constant limit for hyperbolic inertial outward motion of the "dust", when its gravitational interaction is negligible. Unlimited expansion of the sphere has a stabilizing effect on the growth of perturbations, whereas its collapse introduces substantial instability in the model and leads to a faster infinite growth of inhomogeneity and small velocity perturbations (including nonradial perturbations). The nonradial perturbations may become comparable with radial perturbations, thus increasing the nonsphericity and the instability of the ellipsoid figure under eccentricity-increasing forces and transforming it into a disk /17, 4/.

In the general case of hyperbolic expansion of a sphere with arbitrary initial "dust" distribution ($a_0(M) \neq$ const, $t_0(M) =$ const), the strong "inborn" inhomogeneity rapidly decays and the expansion reveals a tendency to isotropization, although the slowly growing Jeans branch (which is "frozen" in the inertial stage) prevents complete homogenization of the distribution of matter. In the asymptotic region ($a \sim t \to \infty$), where the "dust" particles move by inertia, hyperbolic expansion of any sphere becomes isotropic, and a slight residual density inhomogeneity is retained:

$$R \approx E^{\frac{1}{2}}(M)t, \quad \rho \approx \frac{1}{2\pi E^{\frac{1}{2}}} \frac{dE}{dM} t^{-3}. \tag{17}$$

Because of the relationship between isotropization and dynamic instability in collapsing spherical models, the results of linear analysis /17/ similarly indicate that the hypothesis of spherical symmetry of density and velocity distribution in the early stages of expansion is not unavoidable and there may be a more general initial inhomogeneous state, in particular a disk-shaped distribution /4/, which is also isotropized both in the Newtonian and in the relativistic theory.

RELATIVISTIC THEORY

The local similarity of relativistic and Newtonian spherical models does not extend to the global structure of these models; the classical concepts of absolute time and Euclidean space are clearly inapplicable to the

Metagalaxy, and we therefore have to repeat our analysis within the framework of the general relativity theory, additionally taking into consideration the possible existence of a nonzero cosmological constant $\Lambda \neq 0$ /18/.

Spherically symmetrical inhomogeneous models of dust matter constituted the subject of numerous studies and were analyzed from different points of view both in astrophysics (a bounded sphere) and in cosmology (an infinite medium) /11, 12, 19—23/ in connection with the problems of collapse, singularities, and formation of galaxies in the expanding Universe. As we know /3, 4, 11, 12/, Einstein's field equations in the co-moving (and synchronous) frame of reference of the "dust" with the metric

$$ds^2 = d\tau^2 - e^{\omega(\chi,\tau)} d\chi^2 - R^2(\chi,\tau)[d\vartheta^2 + \sin^2\vartheta\, d\varphi^2], \tag{18}$$

where τ is the intrinsic time,* χ is the radial Lagrangian coordinate of the particles in the spherical layer, have an exact solution which was derived by Tolman /21/:

$$e^{\omega} = \frac{R'^2}{1+f}, \quad \dot{R}^2 = f + \frac{2\mathfrak{m}}{R} + \frac{\Lambda R^2}{3}, \quad \rho = \frac{\mathfrak{m}'}{4\pi R^2 R'}. \tag{19}$$

The first integrals are $-1 < f(\chi) < \infty$, $\mathfrak{m}(\chi) \geq 0$ are arbitrary functions which define the distribution of the relativistic specific energy of the "dust" $W(\chi) = \sqrt{1+f}$ and the active gravitational mass of the sphere—the equivalent of its total energy; prime and dot denote partial differentiation with respect to χ and t.

The law of "dust" motion $R(\tau, \chi)$ is defined as the integral of the dynamic equation in (19):

$$\tau - \tau_0(\chi) = \int_{R_0(\chi)}^{R} \left(f + \frac{2\mathfrak{m}}{u} + \frac{\Lambda u^2}{3}\right)^{-\frac{1}{2}} du; \tag{20}$$

in the general case $\Lambda \neq 0$ it is expressed in terms of elliptical functions /12, 19/, and for $\Lambda = 0$ it is expressed by well known formulas in explicit or parametric form /3/ similar to (3)—(6) if we take $R = |f(\chi)|^{1/2} a(\tau, \chi)$ and set $R_0(\chi) = 0$, assuming $\tau_0(\chi)$ to be the time of collapse of the particles of a given spherical layer at the singular "center" $R(\chi, \tau_0) = 0$. The Tolman—Bondi—Lemaitre solution (19)—(20) actually depends only on two physically significant functions $a_0(\chi) = 2M / |f|^{3/2}$ and $\tau_0(\chi)$, since in view of the arbitrary choice of the radial Lagrangian coordinate, the function $f(\chi)$ may be expressed in a canonical form, which only depends on its sign

$$f(\chi) = \epsilon S^2(\chi), \quad S(\chi) = \begin{cases} \sin\chi, & \epsilon = -1 \\ \operatorname{sh}\chi, & \epsilon = +1 \end{cases}, \quad \mathfrak{m}(\chi) = \frac{a_0(\chi)}{2} S^3(\chi), \tag{21}$$

thus expressing the metric and the distribution of matter in the TBL models in terms of this irreducible set of initial values for the gravitaging "dust" sphere, $a_0(\chi)$ and $\tau_0(\chi)$:

$$\begin{gathered} R(\chi,\tau) = S(\chi)\, a(\tau,\chi), \quad e^{\frac{\omega}{2}} = a\left(1 + \frac{\partial \ln a}{\partial \ln S}\right), \\ \dot{a}^2 = \frac{a_0}{a} + \frac{\Lambda a^2}{3} + \epsilon, \quad \varkappa\rho = \frac{3a_0}{a^3} \frac{\left(1 + \frac{d\ln a_0}{d\ln S^3}\right)}{\left(1 + \frac{\partial \ln a}{\partial \ln S}\right)}. \end{gathered} \tag{22}$$

* The velocity of light and the Newtonian constant $c = G = 1$. Einstein's constant $\varkappa = 8\pi$.

Degenerate quasi-Euclidean models with $f=0$ correspond in (22) to $a_0=$ const, $S(\chi)=\chi$, $\mathcal{M}(\chi)=\frac{a_0}{2}\chi^3$, and they contain only one essentially arbitrary function, $\tau_0(\chi)$:

$$a=\left(\frac{3a_0}{\Lambda}\right)^{\frac{1}{3}} sh^{\frac{2}{3}}\frac{\sqrt{3\Lambda}}{2}\left[\tau-\tau_0(\chi)\right],\ \Lambda>0\ ;$$
$$a=\left(\frac{3a_0}{|\Lambda|}\right)^{\frac{1}{3}} sin^{\frac{2}{3}}\frac{\sqrt{3|\Lambda|}}{2}\left[\tau-\tau_0(\chi)\right],\ \Lambda<0 \qquad (23)$$

The radius of a fixed spherical "dust" layer satisfies a Fridman-type equation, and the basic results of the analysis of the dynamics of Fridman's models for $\Lambda\neq 0$ /18, 24/ and, in particular, their classification according to Robertson /25/ are directly applicable to the case of "dust" motion in inhomogeneous spherical models. These inhomogeneous models also can be classified according to the general features of expansion: oscillatory O_1, monotonic M_1, M_2, and asymptotic A_1, A_2, all of which approach Einstein's static model with $\Lambda=\varkappa\rho/2$ in the course of expansion or, respectively, collapse. The time dependence $a(\tau,\chi)$ precisely coincides with the behavior of the scale factor in the corresponding Fridman models, and for $\Lambda=0$ it can be expressed in parametric form in terms of Weierstrass's elliptical functions $\wp(z)$, $\zeta(z)$ and $\sigma(z)$ with the invariants $g_2=1/12$, $g_3=1/216-\Lambda a_0^2/48$:

$$a=\frac{a_0}{4}\left\{\wp(\eta)-\wp(\eta_0)\right\}^{-1},\ \tau-\tau_0=\frac{1}{\wp(\eta_0)}\left[2\eta\zeta(\eta_0)+\log\frac{\sigma(\eta-\eta_0)}{\sigma(\eta+\eta_0)}\right], \qquad (24)$$

where $\wp(\eta_0)=-1/12$, $\dot{\wp}=d\wp/d\eta$.

The TBL solution includes as a particular case the metric of homogeneous isotropic Fridman models

$$dS^2=d\tau^2-a^2(\tau)\left\{d\chi^2+S^2(\chi)\left[d\vartheta^2+sin^2\vartheta\, d\varphi^2\right]\right\},$$
$$\dot{a}^2=\frac{a_0}{a}+\frac{\Lambda a^2}{3}-k,\quad \varkappa\rho=\frac{3a_0}{a^3}\geqslant 0,\ k=\pm 1,0, \qquad (25)$$

which correspond to a special choice of the initial conditions for the "dust" in the general-relativistic sphere:

$$a_0=\frac{2\mathcal{M}}{|f|^{\frac{3}{2}}}=const,\ \tau=const\ ;\qquad f=0\ .\ \tau_0=const \qquad (26)$$

and, correspondingly,

$$R(\chi.\tau)=a(\tau)S(\chi),\quad \mathcal{M}(\chi)=\frac{a_0}{2}S^3(\chi),\ f=\epsilon S^2(\chi) \qquad (27)$$

Here, the function $S(\chi)$ differentiates between an open, a plane, and a closed model with spaces V_3 of constant negative, zero, and positive curvature $K=k/a^2$ according as $\epsilon=\pm 1$, 0. The homogeneous distribution of matter in the TBL models ($\rho=\rho(\tau)$, $\mathcal{M}(\chi)=\frac{4\pi}{3}\rho R^3$) automatically ensures separation of variables $R(\chi,\tau)=S(\chi)\,a(\tau)$ and it therefore invariably presupposes isotropy of the Hubble tensor of deformation rates (i.e., constant ratio of the circumferential distance R to the intrinsic radial distance $L(\chi)=\int_0^{\chi}e^{\omega/2}d\chi=\int_0^{R}\frac{dl}{\sqrt{1-f}}$ in the physical space V_3 of the co-moving frame of reference of the "dust") and also isotropy of the local curvature of V_3, which should be a space of constant curvature, although in general it has a non-Euclidean anisotropic

and inhomogeneous geometry /11/. Thus, in the centrally symmetric case, the spatial inhomogeneity, the isotropy of expansion, and the curvature of V_3 are all interdependent, although certain aspects of the anisotropy of models are nevertheless compatible with their homogeneity /6, 7/.

Einstein's equations in the co-moving frame of reference of the "dust" and their solution for the spherically symmetric case reveal a far-reaching similarity to the Newtonian dynamics of an arbitrary sphere in Lagrangian form /11, 7/, and the TBL models admit of a quasiclassical treatment, provided we modify the interpretation of the constants in the dynamic equation (19), which is regarded as the equivalent of the Newtonian energy integral in the presence of an additional cosmological force $\vec{F} = \frac{1}{3}\Lambda\vec{R}$ with the potential $\frac{\Lambda R^2}{6}$.

The main difference between the relativistic and the Newtonian models of a sphere is associated with the equivalence principle: in the general relativity theory, the active gravitational mass of the sphere $\mathcal{M}(\chi) = 4\pi\int_0^\chi \rho R^2 R' d\chi$ is represented by its total energy, which for $f \neq 0$ is different from the overall rest mass of the "dust" $M(\chi) = 4\pi\int_0^\chi \rho R^2 e^{\omega/2} d\chi$. It may include the intrinsic gravitational binding energy for $f<0$ (a negative mass defect $\mathcal{M} < M$), or a positive excess of the kinetic energy of the "dust" for $f>0$, when $\mathcal{M} > M$. These nonlinear effects — the mass defect and the gravitation of the excess kinetic energy of the "dust" — characteristically emerge through the non-Euclidean character of the co-moving space V_3, since the relativistic specific energy $W^2 = 1 + f$ which characterizes the ratio of the active to the intrinsic mass of the spherical layer ($\mathcal{M}' = WM'$) also determines the geometry of the space sections $\tau = \text{const}$ /11/. In particular, the sign of the quasi-Newtonian energy $f = 2E$, which for $\Lambda = 0$ differentiates between the different types of motion of the layer, is minus the sign of the local scalar curvature of V_3.

In strong gravitation gields, when the potential binding energy or the kinetic energy of the "dust" are comparable with the rest mass, the non-linearity of the general relativity theory becomes quite significant and leads to fundamental distinctions between the relativistic and the Newtonian model. These differences primarily affect the global properties, since the classical theory is locally applicable. In this respect, an instructive example is provided by the case of "semiclosed" and closed Fridman models /4, 12/,

$$R(\chi,\tau) = \sin\chi\, a(\tau),\quad \mathcal{M}(\chi) = \frac{a_0}{2}\sin^3\chi,\quad W = \cos\chi,$$

where the mass defect of a layer may exceed its rest mass ($\pi/2 < \chi < \pi$), thus leading to a non-Euclidean topology of V_3. Note that in Fridman's open model (25), the contribution from the excess kinetic energy of the outward motion of the "dust" to the active mass $\mathcal{M}(\chi) = \frac{a_0}{2}\mathrm{sh}^3\chi$ for $\chi \gg 1$ is greater than the total rest mass of the observed matter $M(\chi) = \frac{3}{4}a_0(\frac{\mathrm{sh}2\chi}{2} \chi)$ and accounts for the bulk of the total mass — energy of the sphere:

$$\Delta T(\chi) = \frac{3}{4}a_0\left(\frac{2}{3}\mathrm{sh}^3\chi - \frac{\mathrm{sh}2\chi}{2} + \chi\right). \tag{28}$$

If we ignore the non-Euclidean geometry of the co-moving space and identify the active mass with the intrinsic mass, the local properties of the relativistic and Newtonian models of the dust sphere completely coincide; moreover, the density and radial velocity distributions of the "dust" in these models coincide even for anisotropic collapse of the TBL models with $\tau_0(\chi) \neq$ const, when because of the non-Euclidean geometry of V_3 all the radial distances go to infinity and all circumferential distances shrink to zero, so that a "sphere" contracts to a line /3/. It should be emphasized, however, that the classical picture of spherical focusing of the particles from individual spherical envelopes at the center of the sphere is not entirely equivalent to the relativistic collapse, when the particles reach the singular state $\rho \to \infty$ on the space-like hypersurface $R(\chi, \tau_0) = 0$, i.e., almost always simultaneously in an appropriate frame of reference. Because of the global asymmetry of the "contracting" and "expanding" T-regions for $R(\chi, \tau) < 2\mathfrak{M}(\chi)$, where all the causal phenomena propagate in one direction only (i.e., toward the "central" singularity or away from it, in the outward direction), the anticollapse of the sphere cannot be treated as a simple time-reversal of its collapse /4, 21/.

Because of the analogy in the local properties of relativistic and classical models of a sphere, the results of the Newtonian analysis remain valid and are directly generalized to the general relativity theory.* It is readily seen that a special class of TBL solutions (19) – (24) with the particular initial conditions $a_0 =$ const, $\tau_0(\chi) \neq$ const corresponds to inhomogeneous models of a sphere which are isotropized in the course of expansion from a singular state with infinite matter density gradients and asymptotically approach in all their observed properties to Fridman's homogeneous isotropic models. For $\Lambda \geqslant 0$, hyperbolic expansions M_1, M_2, and A_2 of arbitrary inhomogeneous models of a sphere ($a_0(\chi) \neq$ const, $\tau_0(\chi) \neq$ const) also lead to asymptotic isotropy of deformations and curvature of V_3 in the presence of a slight "frozen" inhomogeneity. At the late stages of expansion, when the cosmological repulsion becomes dominant, these models reduce to de Sitter's universe /7/. In our model of the evolution of the Metagalaxy from a centrally symmetric inhomogeneous singular state, this general case has certain advantages, as it is improbable that the distribution of matter established at the end of the pressure-dominated phase ($P \neq 0$) will have the particular form needed for the perfectly isotropizing outward motion of the "dust."

Lifshits's approximate solution /4, 5/ for weakly perturbed Fridman models in the early superdense and "hot" stages with $P = \varepsilon/3$, which displays only one branch of long-wave Jeans density and velocity perturbations slowly growing with expansion ($\delta\varepsilon/\varepsilon \sim a^{4/3} \sim t^{2/3}$) and reveals absolute instability of the isotropic homogeneous collapse under small perturbations in the distribution of matter and the free gravitation field, indicates that for $P \neq 0$ and in the case without spherical symmetry, there should also exist a sufficiently wide class of inhomogeneous and anisotropic models which isotropize in the process of expansion.

The spherically symmetrical models considered this paper are applicable to the expanding Universe with a globally inhomogeneous

* It is shown in /14/ that the TBL solution is not general and in the general relativity theory there is a special class of T-models of a sphere without classical analog.

singular state and also to the Metagalaxy, when treated as a bounded realtivistic object which expands as a result of the "big bang" from a superdense singular state — the "protonucleus" — whose very inhomogeneity in principle allows conversion of the internal energy released by the hypothetical "explosion" into the kinetic energy of expansion. In accordance with the existing general concepts of cosmogonic evolution — both the traditional /4/ and that developed by V.A. Ambartsumyan /26/ — we can propose two schematic models of the "big bang": 1) continuous relativistic outflow of matter, which in the process of overall expansion is homogenized on a large scale while collecting into small condensations (galaxies and clusters of galaxies) as a result of gravitational instability; 2) ejection of D-bodies (mainly), which in the course of their cosmological outward motion become distributed fairly uniformly and provide the basis for the evolution of Metagalactic structure.

In conclusion note that if the hypothesis of the essentially inhomogeneous initial state of the Metagalaxy is applicable and isotropization indeed occurred at fairly late stages with $z \leqslant 10-100$, observations of distant regions with sufficiently large z should reveal large-scale inhomogeneity and anisotropy /27/. The authors are grateful to L.E. Gurevich, A.G. Doroshkevich, and Ya.B. Zel'dovich for the discussion of results and critical comments.

Bibliography

1. Observational Foundations of Cosmology.— Moscow, IL. 1965. [Russian translation.]
2. Davidson, W. and I.V. Narlicar.— Report Progr. Phys., London Phys. Soc., **29**:539. 1966.
3. Landau, L.D. and E.M. Lifshits. Teoriya polya (Theory of Fields).— Moskva, Izdatel'stvo "Nauka." 1967.
4. Zel'dovich, Ya.B. and I.D. Novikov. Relyativistskaya astrofizika (Relative Astrophysics).— Moskva, Izdatel'stvo "Nauka." 1967.
5. Lifshits, E.M. and I.M. Khalatnikov.— UFN, **80**:391. 1963.
6. Zel'manov, A.L.— Trudy 6-go soveshchaniya po voprosam kosmologii, p.144, Moskva, Izdatel'stvo AN SSSR. 1959.
7. Heckman, O. and E.M. Schüking.— XI Conseil de Physique Solvays, p.149, Bruxelles. 1958; Gravitation, p.438, New York, Acad. Press. 1962.
8. Misner, C.W.— Astrophys. J., **151**:431. 1968.
9. Hawking, S.W.— Monthly Not. RAS, **107**:129. 1969.
10. Grishchuk, L.P., A.G. Doroshkevich, and I.D. Novikov.— ZhETF, **55**:2281. 1968.
11. Bondi, H.— Monthly Not. RAS, **142**:410. 1947.
12. Lemaitre, G.— Rev. Mod. Phys., **21**:357. 1949.
13. Partridge, R.B. and D.T. Wilkinson.— Phys. Rev. Lett., **18**:557. 1967; Conklin, E.K. and R.N. Bracewell.— Phys. Rev. Lett., **18**:614. 1967.
14. Ruban, V.A.— ZhETF, **56**(6). 1969; ZhETF Letters, **8**:669. 1968.

15. McVittie, G.C. General Relativity and Cosmology, 2nd ed. — Univ. of Illinois Press, Urbana, Ill. 1965.
16. Bonnor, W.B.— Monthly Not. RAS, **117**:104. 1957.
17. Lin, C.C., L. Mestel, and F. H. Schu.— Astroph. J., **142**:1431. 1965; Lynden-Bell, D.— Proc. Cambridge Phil. Soc., **58**:709. 1962.
18. Zel'dovich, Ya.B.— UFN, **95**:209. 1968.
19. Tolman, R.C.— Proc. Nat. Acad. Sci., **20**:169. 1934.
20. Omer, G.C.— Proc. Nat. Acad. Sci., **53**(1). 1965.
21. Novikov, I.D.— Astronom. Zh., **41**:1075. 1964.
22. Bonnor, W.B.— Zs. F. Astrophys., **35**:10. 1954.
23. Peebles, P.— Astrophys. J., **147**:859, 1967.
24. Bondi, H. Cosmology.— Cambridge. 1960.
25. Robertson, H.P.— Rev. Mod. Phys., **5**:62. 1933.
26. Ambartsumyan, V.A.— In: "Voprosy Kosmogonii," **8**:3, Moskva, Izd. AN SSSR. 1962.
27. Wilkinson, D.T. and R.B. Partridge.— Nature, **215**:719. 1967; Rees, I. and D.W. Sciama.— Nature, **217**:511. 1968; Nature, **213**:374. 1967.

FORMATION OF GALAXIES IN AN EXPANDING UNIVERSE

A. G. Doroshkevich

One of the striking features of the observable part of the Universe is the highly isotropic expansion and the homogeneous distribution of matter over large scales. On a small scale, however, the distribution of matter is distinctly inhomogeneous: stars cluster in galaxies (mean density $\rho_g \sim 10^{-24} - 10^{-25}$ g/cm^3, mass $M_g \sim 10^8 - 10^{11} M_\odot$), galaxies in their turn form clusters of galaxies (mean density $\rho_c \sim 10^{-27}$ g/cm^3, mass $M_c \sim 10^{11} - 10^{14} M_\odot$). The existence of the next higher stage in this hierarchy — superclusters with masses $M_s \sim 10^{14} - 10^{17} M_\odot$ — is doubtful, however /1, 2/. Observations show that starting on a scale of 50 — 100 Mpc, the distribution of observable matter in the Universe is roughly homogeneous /3/.

The isotropic expansion and the homogeneous distribution of matter in the Universe are also evidenced by intensity (or temperature) observations of the relict background radiation. Isotropic radiation with temperature T = 2.7°K was discovered in 1965 by Pensias and Wilson /4/. The interaction of this radiation with matter is very weak (the only interaction channels are Compton scattering and gravitation), so that it provides information about the large-scale distribution and motion of matter at distances beyond the range of modern optical astronomy.

The red shift of the light emitted by an object $z = \frac{\lambda - \lambda_0}{\lambda_0}$, where λ is the wavelength of the incoming light and λ_0 is the wavelength of the emitted light, provides an adequate characteristic of the distance to far objects. The value of z is determined directly from observations of spectral lines. Once z has been found, we can determine the distance of the object (within the framework of the accepted cosmological model), the exact time of light emission, the mean density at the time of emission, etc. Thus, for example, $\rho_z = \rho_0 (1+z)^3$ (ρ_0 is the mean density at present). The brightest galaxies are observed up to $z \sim 0.2 - 0.3$; quasars are observed up to z = 2.2 (i.e., up to $\rho \approx 33 \rho_0$). With regard to relict radiation, the Universe is transparent at least up to $z = z^* \geqslant 8$,* i.e., to densities a factor of 730 as great as the present-day mean density!

According to the observations of Partridge and Wilkinson /5/, the temperature anisotropy of the relict radiation is $\frac{\Delta T}{T} \sim \pm(3 \pm 1) \cdot 10^{-3}$ for angular

* z^* depends on the mean density of the Universe at present and increases with diminishing density. $z^* = 8$ for the mean present-day density $\bar{\rho}_0 = 2 \cdot 10^{-29}$ g/cm^3, which corresponds to the critical density $\bar{\rho}_c = 3H_0^2/8\pi G$ (H_0 is Hubble's constant).

resolution of about 15°. The observations of the small-scale anisotropy of the relict radiation carried out by Conclin and Brasewell /6/ and by Pariiskii and Petunina /7/ give $\frac{\Delta T}{T} \lesssim 2 \cdot 10^{-3}$. These data point to excellent isotropy of motion and distribution of matter on a large scale in the Universe. A detailed analysis of the experiments intended to detect a possible anisotropy of the cosmological expansion was given in /8/. The estimates of the possible degree of inhomogeneity in the distribution of matter in the Universe according to these results are given in /9, 10/.

The assumption of homogeneous distribution of matter in the Universe and isotropic expansion leads to Fridman's cosmological model. This model, advanced by A.A. Fridman in 1922—1924 /11/, has been developed in greatest detail among the various currently available cosmological models and it reveals adequate consistency with all the known observations. There is one fundamental difficulty, however, and it is how to make Fridman's model consistent with the existence of galaxies and clusters of galaxies.

Fridman's model is a non-steady-state model. Within its framework, the expansion began at a certain point in a state of infinite density (which is used as the zero point on the time scale). Near this singular point, the classical theory of relativity is evidently inapplicable: quantum effects are not ignorable, and there may be other factors which are unknown under the standard present-day conditions. Dimensionality considerations indicate the probable limits of application of the general relativity theory: distance $l=(Gh/c^3)^{1/2} \simeq 10^{-33}$ cm, time $t = l/c \simeq 0.6 \cdot 10^{-43}$ sec, density $\rho = c^5/G^2h \simeq 10^{93}$ g/cm^3. When Fridman's model is extrapolated into the past of the Universe to $t = 0.6 \cdot 10^{-43}$ sec, the isotropic expansion and the homogeneous distribution of matter near the singularity should be retained on a scale comparable with the horizon $l_H = ct$, i.e., on a scale $l \gtrsim 10^{-33}$ cm. A natural solution to the problem of formation of galaxies under these conditions is provided by the fluctuation hypothesis, based on the assumption of small deviations of the distribution and expansion of matter from homogeneous and isotropic.

A number of studies have been published recently which treated the problem of formation of galaxies assuming a breakdown of the Fridman theory in the early stages of expansion. These models remove some of the characteristic restrictions of the Fridman model, and open new possibilities for explaining the origin of galaxies and clusters of galaxies. However, the breakdown of the Fridman model in the early stages of expansion involves a number of basic difficulties. The main thing is to ensure that the early models have the Fridman model as their limit and that they lead to a sufficiently low anisotropy of the relict radiation in accordance with observations /5, 6, 7/. This is a significant point, since not any model will go to Fridman's model with time. The second point is that the alternative models should ensure a sufficiently low content of helium (less than 30% by weight) and the heavy elements in the Universe. This requirement also restricts the permissible deviations of the cosmological model from Fridman's model, since according to Thorne /12/ anisotropic models may lead to an entirely different chemical composition of the protostellar matter (with helium accounting for more than 50% by weight). Finally, we should prevent the formation of objects liable to collapse in the early stages of expansion and large-mass

objects with densities much higher than the mean density of galaxies ($\rho_g \sim 10^{-24} - 10^{-25}$ g/cm^3). No such objects are observed at present and their existence (in numbers) would involve considerable difficulties.

These restrictions severely limit the gamut of the permissible cosmological models. At present, very few simple cosmological models differing from Fridman's model are known /8, 13/. These models are based on the assumption of homogeneous distribution of matter and they do not consider the formation of galaxies.

In this paper, the main emphasis is placed on the formation of galaxies in Fridman's model within the framework of the fluctuation hypothesis. Suppose that in the initial phase of expansion (e.g., for $t \sim 10^{-43}$ sec), the distribution of matter slightly deviates from the homogeneous distribution. Tracing the evolution of this perturbed Fridman's model into the future, we can try to account for the formation of galaxies and clusters of galaxies as a result of these small perturbations of Fridman's model. The problem thus falls into three interrelated parts:

1) the origin of the initial perturbations in the early stages of expansion;
2) the evolution of perturbations in the course of expansion;
3) the formation of galaxies and clusters of galaxies.

At this stage, only the solution of the second problem is available. The evolution of perturbations against the background of Fridman's homogeneous model was considered by Lifshits in 1946 /14/. Specific features arising as a result of the application of the general to Fridman's "hot" model were discussed later by various authors /8, 15, 16/.

In Fridman's "hot" model, four types of perturbations are possible:

1. Adiabatic perturbations of density, velocity, and metric.
2. Entropy perturbations of density, velocity, and metric.
3. Rotational perturbations of velocity and metric.
4. Metric perturbations of the type of gravitational waves.

In an expanding Universe, gravitational waves are evanescent. Rotational perturbations also decay during expansion. Perturbations of these types cannot affect the formation of galaxies in Fridman's model. The attempt to use rotational perturbations as the mechanism of formation of galaxies involved rejection of Fridman's model in the early stages of expansion /17/.

Entropy perturbations are associated with perturbations in the distribution of baryons against the homogeneous background of radiation. These perturbations are "frozen" at the stage $\varepsilon_\gamma \gg \varepsilon_m$ (ε_γ is the radiation energy density, ε_m is the matter energy density) and begin developing only after the stage of hydrogen recombination, where the interaction of radiation with matter has become weak.

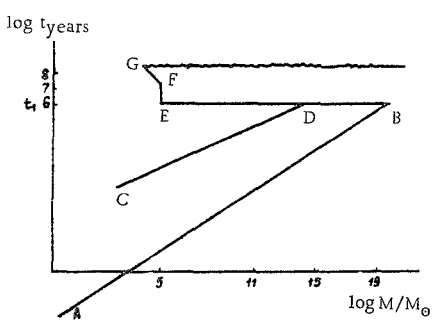

The growth of perturbations in Fridman's "hot" model.

The development of the adiabatic perturbations of density, velocity, and metric in the course of expansion depends on the scale of the perturbation. The evolution of entropy and adiabatic perturbations is illustrated by the figure.

The scale of perturbation is characterized by the combined rest mass of

the baryons encompassed by the perturbation. This is the variable laid off the horizontal axis. The vertical axis gives the time reckoned from the singularity instant. The time $t = t_1$ corresponds to the recombination of hydrogen (the same time approximately corresponds to the condition $\varepsilon_\gamma \sim \varepsilon_m$).

The line ABEFG corresponds to the Jeans wavelength — the boundary separating the instability region (to the right of this line) from the stability region. To the right of the line AB, the adiabatic density perturbations grow in proportion to time $\delta\rho/\rho \sim t$ (on constant scale), whereas to the left of the line AB acoustic oscillations of constant amplitude occur. The line CD limits the range of dissipative processes associated with Compton scattering of photons by electrons. To the right of the line CD, the dissipative processes are insignificant, whereas to the left of this line density perturbations decay exponentially with time.

After recombination, the radiation pressure can be ignored, and the Jeans wavelength therefore falls steeply. For $t > t_1$, there is no obvious difference between entropy and adiabatic perturbations. All density perturbations grow in proportion to $t^{2/3}$ to the right of the line EFG and decay as $t^{-1/6}$ to the left of this line.

In the early stages of expansion, the growth of perturbations was affected by the neutrino viscosity and other processes. These processes, however, were significant on a very small scale, and apparently they could not affect the formation of galaxies in Fridman's model.

Given the laws governing the growth of perturbations in Fridman's model, we can relate the perturbations occurring near the singular point to the third, nonlinear stage of formation of galaxies — the phase when the perturbation becomes comparable with 1 and the perturbation theory does not apply.

However, before proceeding with a discussion of the nonlinear phase of formation of galaxies, let us examine what we know about the origin of perturbations and their amplitudes near the singular point.

One of the possible points of view associates the perturbations with a hypothetical compression phase which possibly preceded the expansion phase. According to this conception, the inhomogeneities arose in the compression phase, remained intact during the transition through the singular point, and subsequently proceeded evolving according to the laws discussed above. The transition through the singular point has been the subject of numerous studies in recent years, but no great success has been achieved so far in this direction. The status of this theory is therefore still highly uncertain.

Another point of view calls for the construction of initial perturbations without resorting to an earlier compression phase. We may assume, for instance, that the homogeneity is only a statistical phenomenon. This will automatically lead to density perturbations $\delta N/N \sim 1\sqrt{N}$, where δN is the perturbation in the number of particles in a volume containing N particles. Lifshits /14/ noted that for a mean density $\bar{\rho} \sim 10^{14}$ g/cm^3 (which corresponds to the nuclear density), these perturbations are insufficient for the formation of galaxies. It is readily seen, however, that if such perturbations are postulated for $t \sim 10^{-43}$ sec, $\bar{\rho} \sim 10^{93}$ g/cm^3, they will be excessively large and will lead to formation of separate objects with masses $M \sim 10^{57} M_\odot$!

There is still another approach possible to the problem of initial perturbations. A perfectly homogeneous distribution of matter can be assumed

to start with, but there are random velocities associated with the temperature. This will naturally lead quite soon to density perturbations, but they will be insufficient for the formation of individualized galaxies. Incidentally, note that all the requirements imposed on the shape and the amplitude of the initial perturbations are borrowed from among the properties of quantum fluctuations of a degenerate Fermi gas, whereas there is no reason whatsoever to assume that such fluctuations indeed arise in Fridman's "hot" model.

There is thus no satisfactory theory of initial fluctuations at this stage. The parameters of the initial perturbations are arbitrary to a considerable extent and they have to be fixed so as to ensure the best fit of the final results of the theory with the current outlook on the Universe.

The third part of the problem of the formation of galaxies and clusters of galaxies in Fridman's model is highly complex, as it involves nonlinear effects. The treatment is generally confined to qualitative analysis of the various phenomena and order of magnitude estimates of the final results /16, 17, 19/. In particular, this is due to the large uncertainty in our information concerning the clusters of galaxies and the intergalactic medium.

The theory of the evolution of perturbations in Fridman's model yields three Jeans wavelengths λ (see figure): λ_1 before recombination corresponds to masses $M \simeq 10^{17} - 10^{19}\ M_\odot$, λ_2 in the dissipation range corresponds to masses $M \simeq 10^{11} - 10^{13}\ M_\odot$, and finally λ_3 after recombination corresponds to $M \simeq 10^5\ M_\odot$. No other wavelengths exist in the hydrodynamic theory for $t > t_1$. Let us relate the masses corresponding to $\lambda_1, \lambda_2, \lambda_3$ with the observed mass distribution of galaxies and clusters of galaxies.

The mass $M \simeq 10^5\ M_\odot$ is significant for entropy perturbations only, since adiabatic perturbations are small on the corresponding scale because of dissipative effects. The origin of galaxies in Fridman's model was prescribed to these perturbations in /16, 19/; a similar attempt was made by Harrison in connection with the theory of charge-symmetrical Universe /20/. These attempts meet with a number of objections in view of the latest estimates of the probable density and temperature of the intergalactic gas /21/. According to Harrison's theory, the perturbations are close to unity at the time of hydrogen recombination /22/, at variance with observations. A further attempt to apply the entropy perturbations was recently made by Peebles, who associated the mass $M \simeq 10^5 M_\odot$ with globular clusters in galaxies. The validity of these attempts is not clear at this stage.

The adiabatic perturbations in Fridman's model are associated with two characteristic masses, $10^{11} - 10^{13}\ M_\odot$ and $10^{17} - 10^{19} M_\odot$. The larger of these masses may be possibly related to the hypothetical superclusters of galaxies. The smaller mass is in good agreement with the estimates of the mass of large galaxies and small clusters of galaxies. It is therefore worthwhile to try and construct a theory of formation of galaxies and clusters of galaxies using this particular mass. The development of this theory meets with certain difficulties. The formation of galaxies and clusters of galaxies from a homogeneous metagalaxy poses a number of questions.

One of the main questions is to determine the exact proportion of matter in the Universe which is observed in the form of galaxies. The observed mean density of matter concentrated in galaxies is close to $\rho_2 \sim 5 \cdot 10^{-31}\ g/cm^3$.

The mean density of the intergalactic field has not been determined so far. The last estimates give an upper limit of $\bar{\rho} \sim (2-6) \cdot 10^{-30}$ g/cm^3 for this density. In other words, the galaxies should contain no less than 10 — 20% of the total mass of the Universe. This is quite a substantial proportion from the point of view of the theory which prescribes the formation of galaxies to small density perturbations. There is a possibility, however, that future observations will yield a lower density estimate for the intergalactic gas.

The second question is how we are to determine the mass distribution of galaxies and clusters of galaxies. The use of the characteristic mass $M \sim 10^{11} - 10^{13}$ $M_\odot$ in the theory gives some hope of finding a successive answer to this question.

The third question of the theory demands that we account for the observed rotation of galaxies and, possibly, clusters of galaxies. In the theory under discussion, no eddy velocities are observed in the early stages of evolution and all the random velocities are potential. This, however, is quite consistent with the rotation of galaxies and clusters of galaxies. This problem was considered in /23/, where it was shown that the rotation of galaxies may be partly related to the "embryonic" rotation which develops when a cloud condenses from a medium with random potential velocities and partly to the existence of a quadrupole moment in galaxies, which makes the galaxies spin through gravitational interaction with other galaxies. These suggestions should be further explored, but nevertheless they appear quite promising.

Still another problem arises in connection with the magnetic fields of galaxies and clusters of galaxies. So far, there is no theory which could account for the observed magnetic fields as a byproduct of the formation of galaxies. As a result, the existence of an "embryonic" magnetic field in the Universe had to be suggested. Cosmological models with a homogeneous magnetic field were constructed and the compatibility of the cosmological magnetic field with Fridman's model was proved /24/. It is by no means clear, however, that this approach is without alternative. Theoretical predictions are still difficult to compare with observations, because the latter are distorted by secondary effects — various ejection processes, explosions, etc. Powerful explosive processes are observed in the immediate vicinity of quasars and radio galaxies. There is some evidence that the significance of these processes was even greater in the past /25/. These processes may largely be responsible for the observed properties of galaxies and clusters of galaxies /24/. Observations of the distant quasars, for example, point to a vanishingly small density of neutral intergalactic hydrogen $\rho_H \lesssim 10^{-35}$ g/cm^3. On the other hand, according to the fluctuation theory of the formation of galaxies in Fridman's model, the mean density of intergalactic gas may hardly fall below the mean density of the galaxies, i.e., $\rho \sim 10^{-31}$ g/cm^3. The gas therefore should be very hot ($T = 10^6$ °K), Powerful energy production processes are needed to achieve this heating of the intergalactic gas.

Secondary explosive processes are probably also responsible for the currently observed expansion of the peripheral regions in clusters of galaxies. The observed velocity variance of the galaxies in clusters is of the order of 1000 km/sec, the clusters measuring 1 — 3 Mpc across.

If the clusters are maintained under steady-state conditions, their mass should be several times greater than the observed mass of the constituent galaxies /1, 26/. The expansion of clusters cannot be described as residual cosmological expansion, either, since the clusters expand at a much faster rate than the Universe as a whole. This expansion of clusters is possibly associated with powerful energy release processes at the center of the clusters.

In conclusion we should emphasize that although certain advances have been accomplished in the theory of formation of galaxies in an expanding Universe, there are still many unanswered questions. Further theoretical and observational work is needed.

Bibliography

1. Abell, G.O.— Annual Rev. Astronomy and Astrophysics, 3:1. 1965.
2. Zwicky, F. Morphological Astronomy, p.165.— Berlin, Springer-Verlag. 1957.
3. Zwicky, F. and K. Pudnicki.— Astrophys. J., 137:707. 1963.
4. Pensias, A.A. and R.W. Wilson.— Astrophys. J., 142:419. 1965.
5. Wilkinson, D.T. and R.B. Partridge.— Nature, 215:719. 1967.
6. Conclin, E.K. and R.V. Brasewell.— Phys. Rev. Lett., 18:614. 1967.
7. Pariiskii, Yu.N. and N.V. Petunina.— Konferentsiya po radio-astronomii. Riga. 1968.
8. Zel'dovich, Ya.B. and I.D. Novikov. Relyativistskaya astro-fizika (Relativistic Astrophysics).— Moskva, Izdatel'stvo "Nauka." 1967.
9. Zel'dovich, Ya.B. and R.A. Sunyaev.— Astrophys. and Space Science. (In press).
10. Ozernoi, L.M. and Chibisov.— Astronomicheskii Zhurnal. (In press).
11. Fridman, A.M.— UFN, 84:505. 1964.
12. Thorne, K.S.— Astrophys. J., 148:51. 1967.
13. Grishchuk, L.P., A.G. Doroshkevich, and I.D. Novikov.— ZhETF, 54:2281. 1968.
14. Lifshits, E.M.— ZhETF, 16:587. 1946.
15. Silk, J.— Astrophys. J., 151:459. 1968.
16. Doroshkevich, A.G., Ya.B. Zel'dovich, and I.D. Novikov.— Astronom. Zh., 44:295. 1967.
17. Ozernoi, L.M. and A.D. Chernin.— Astronom. Zh., 44:1131. 1967.
18. Zel'dovich, Ya.B.— Astronom. Zh., 1969 (in print); Harrison, E.R.— Preprint, Goddard Space Flight Center, Greenbelt, Md. 1968.
19. Peebles, P.J.E. and R.H. Dicke.— Astrophys. J., 154:898. 1968.
20. Harrison, E.R.— Phys. Rev., 167:1170. 1968.
21. Sunyaev, R.A.— Astrophys. Lett. 1969. (In press).
22. Field, G.B.— Preprint, Princeton University Observatory. 1968.

23. Peebles, P.J.E.— Astrophys. J., 155:393. 1969.
24. Zel'dovich, Ya.B.— Astronomicheskii Zhurnal. 1969. (In press).
25. Longair, M.S.— Monthly Notices RAS, 133:421. 1966.
26. Karachentsev, I.D.— Astrofizika, 1:303. 1965.

THE SEPARATION OF GALAXIES INTO THE HALO AND THE DISK SUBSYSTEM

L. E. Gurevich and A. D. Chernin

As is known, our Galaxy is one of the extensive class of spiral galaxies and it comprises a slowly rotating halo subsystem and a rapidly rotating disk subsystem. Theoretical interpretation of the formation of these subsystems from the original protogalactic cloud meets with serious difficulties. The disk and the halo are of comparable sizes, and this is hardly compatible with the assumption that in view of the different shape and rotation velocity of these subsystems, they originated as a result of different degrees of compression of the original clouds. On the other hand, the assumption that the protogalactic cloud "from the start" contained two components rotating with different velocities is unacceptable because in a gas such differential velocities will rapidly level out. The suggested solution of the problem presented in this paper is based on the concept of elastic and inelastic evolutionary processes in concentrated gravitational systems.

In a gravitational system consisting of numerous particles, collision processes of two types are possible: direct (or, as we say, contact) collisions and gravitational interaction between particles as a result of close encounter.

A system with prevalent gravitational interaction as a result of close encounter will evolve in a characteristic manner which, according to /1 – 3/, is specified by the following processes.

1. The constituent particles gradually evaporate from the system. The characteristic evaporation time if approximately two orders of magnitude the mean time between encounters.

2. Simultaneously with particle evaporation, the system undergoes compression, so that its dimensions decrease in proportion to the square of the number of particles.

3. If the system rotates, the evaporating particles carry off a certain angular momentum, which exceeds the mean angular momentum of the system particles. As a result, the rotation velocity diminishes, and the system becomes progressively more spherical as a result of evaporation. Evolution of this type will be called elastic (in reference to the relevant particle interactions, which are elastic collisions), or evaporational.

A system in which contact collisions predominate undergoes so-called inelastic evolution. Contact collisions are of necessity inelastic, and the kinetic energy of the colliding particles is expended in irreversible processes, in particular, separation of gas which falls to the center of the system or to the equatorial plane. In this inelastic evolution, no evaporation

is possible, and the total angular momentum is thus conserved. The compression of the system in this case does not produce a more spherical shape.

Evolutionary processes of both types occur in concentrated star systems and also in systems consisting of stars and gas clouds. Note that these processes may have played an important role in the formation of the halo and the disk subsystems of our Galaxy.

We will start our examination of the evolution of a protogalaxy from the stage when it was separated into gas clouds of different masses, ranging in all probability from $10^4 - 10^6$ to 10^{10} solar masses. Suppose that the mass of the protogalaxy in this stage was somewhat higher than the mass of a standard galaxy, and the specific (per unit mass) angular momentum of the protogalaxy was close to the specific angular momentum of the disk subsystem. The density of the protogalaxy was $^1/_{10} - ^1/_{30}$ of the standard present-day density. Further suppose that the combined mass of the small clouds was roughly one half of the mass of the entire protogalaxy, and that the large clouds (with masses of up to $10^{10} M_O$) occupied about 10% of the volume of the protogalaxy.

The origin of the mass spectrum of the gas clouds is an independent problem whose analysis clearly falls beyond the scope of the present paper. We will only point to some factors which could produce this mass spectrum: 1) initial turbulence in the protogalaxy, 2) differences in the differential rotation velocity of the protogalaxy in different parts, 3) unequal rate of gravitational condensation in different parts of the galaxy, possibly due, e.g., to differences in the rate of cooling or to differences in the magnetic field strength.

Small clouds, regardless of their origin, would fairly rapidly develop into star clusters, which would then break up into individual stars. The high rate of star formation in the small clouds may be due, in particular, to their high transparency to radiation and the smaller significance of differential rotation in small-sized objects. At the same time, the large clouds would retain their gaseous structure. Their compression and separation into stars would apparently be a much slower process, since their opacity and differential rotation would interfere with gravitational condensation.

The subsequent evolution of the protogalaxy was governed by two processes: elastic interaction of stars and star clusters with large gas clouds in close encounters and inelastic interaction of colliding gas clouds.

The elastic interaction process predominated in the initial stages of evolution. It led to evaporation of some stars and clusters and produced a certain loss of angular momentum in the star subsystem. This system compressed and became progressively more spherical, as it follows from the general theory /3/.

In the subsystem of gas clouds, contact collisions markedly prevailed over the gravitational interaction in encounters. Since the large gas clouds compressed relatively slowly, the inelastic collisions persisted for a long time and led to the separation of large masses of gas from the clouds. The total angular momentum of the entire gas did not change, however.

The separating gas, in addition to its regular rotational velocity, also had random velocities directed toward the axis. The decay of these random velocities, according to the common point of view /4/, leads to the precipitation of the separating gas onto the equatorial plane of the protogalaxy. In addition to gas separation, the dissipation of the kinetic energy of the clouds led to the compression of the entire gas subsystem. This process took place simultaneously with the previously considered compression of the star subsystem.

As the gas clouds deteriorated, their contribution to the elastic evolution of the star subsystem gradually diminished, and eventually this evolution virtually stopped. In the gas subsystem, a substantial fraction of the total mass precipitated to the plane of symmetry and a disk was thus formed. The fraction of the mass of the gas clouds which managed to condense into stars before falling to the plane of symmetry and which underwent partial evaporational evolution lost some of its angular momentum and formed the intermediate subsystems.

The model of the evolution of a protogalaxy explains its separation into subsystems not only qualitatively, but also quantitatively (to orders of magnitude). In particular, it is seen that the compression of the star subsystem and the star clusters to one half the original diameter will halve the rotational velocity, whereas the compression of the gas subsystem by the same factor will increase its rotation velocity — roughly by a factor of 2. The difference in the rotation velocities in the process of contraction of the protogalaxy should markedly increase, and by the time the system reaches the present-day standard density, the disk would spin at 4 — 5 times the velocity of the halo. These are in fact the differences in rotation velocities observed in our Galaxy.

Elastic and inelastic evolution processes in a system consisting of stars and gas clouds probably played an important role in the formation of galaxies of various morphological types, whose origin is attributable to the variety of conditions (specific angular momentum, particular inhomogeneities, etc.) prevailing in the initial protogalactic clouds. For example, for specific angular momenta substantially less than the angular momentum of our Galaxy, the relevant processes would apparently lead to the formation of an elliptical, and not spiral, galaxy.

Bibliography

1. Ambartsumyan, V.A.— Zapiski LGU, 22:19. 1938.
2. Spitzer, H.— Monthly Not. Roy. Astron. Soc., 100:396. 1940.
3. Gurevich, L.E.— Astronomicheskii Zhurnal. (In press).
4. Kaplan, S.A. and S.B. Pikel'ner. Mezhzvezdnaya sreda (Interplanetary Medium).— Moskva, Fizmatgiz. 1963.

CLUSTERS OF GALAXIES AND THE COSMOLOGICAL EXPANSION

A. D. Chernin

Clusters of galaxies are giant cosmic formations consisting of tens, hundreds, and sometimes thousands of galaxies similar to our Galaxy. A substantial number of such objects are known; they are dispersed at large distances from us and recede with velocities proportional to their distance. Some of these clusters have been studied in some detail, and the observation data permit making definite conclusions regarding their characteristic properties.

A fundamental property of clusters is probably their non-steady-state character. Unlike stars and galaxies, clusters have a positive energy and are in a state of expansion. Ambartsumyan /1/ (and later other authors /2/) reached this conclusion by analyzing the relationship between the virial mass M and the luminosity of the clusters.

The virial mass of a gravitational system is the mass that can be computed from the mean velocity v of the constituent particles and the radius R of the system:

$$M_V = \frac{2v^2R}{G},$$

where G is the gravitational constant.

For steady-state gravitationally bound systems, the virial mass is equal to the true mass. This constitutes the basis of the method for determining the mass of a galaxy from measured velocities of the stars and its size.

Taking the ratio of the virial mass to the luminosity for the individual galaxies in the cluster f_g and for the cluster as a whole $f_c = \frac{M_V}{L}$, we find that f_c is never less than f_g, and in most cases it is actually much higher than f_g. To understand the significance of this rule, consider a simple example. Let a cluster consist of N identical galaxies with the same f_g. Since the total luminosity of the cluster L is N times the luminosity of an individual galaxy, and the true mass of the cluster M is N times the mass of an individual galaxy, f_g is evidently equal to the ratio M/L. Now, since $f_c = \frac{M_V}{L}$ is greater than f_g, M_V clearly does not coincide with the true mass of the cluster, which is evidently less than M_V. Hence it follows that the kinetic energy of the cluster $E_k \simeq Mv^2 \simeq M\frac{GM_V}{R}$ is greater

in absolute magnitude than the gravitational potential energy $E_G \simeq -\frac{GM^2}{R}$. The ratio of the two energy components is $\frac{E_k}{|E_G|} \simeq \frac{M_V}{M} \simeq \frac{f_c}{f_g} > 1$. The same result (with f_g replaced by its mean value) clearly can be obtained if we extend our example to the case of a real cluster consisting of different galaxies.

For the largest clusters, f_c is of the order of 500 or even 700 $M_\odot/L_\odot$ ($M_\odot$ and $L_\odot$ are the mass and the luminosity of the Sun); f_g in its turn is different for galaxies of different morphological types, ranging from a few units to several tens. It would therefore seem that the kinetic energy of the largest clusters is roughly a factor of ten greater than the absolute value of the potential energy: $E_x \sim 10|E_G|$.

The unusually high value of the ratio $f_c = \frac{M_V}{L}$ for clusters thus leads to the conclusion that their total energy $E = E_k + E_G$ is positive. Note that in principle it could be inferred that the clusters of galaxies contain some nonluminous mass. However, its presence in the large quantities required to satisfy the relation $M_V = M$ cannot remain undetected /3, 4/.

A certain correlation is observed between f_c and the number of galaxies in the cluster: f_c steadily increases from small groups, where it is close to f_g, to rich clusters, where it reaches maximum values /5, 6/. According to the above, this signifies that the non-steady-state behavior of the clusters becomes more pronounced (on the average) as their mass increases.

What is the origin of the tremendous kinetic energy of the clusters? This is an obvious question, and without first finding a clear answer to it we will not be able to comprehend other, finer properties of clusters (a detailed review of these properties will be found in /7/).

EXPLOSION OR CONDENSATION?

There are two common approaches to the problem of clusters of galaxies. According to Ambartsumyan /1/, the origin of clusters is attributable to a number of explosions of superdense protostellar objects (D-bodies) which prior to the explosion had remained in a dormant frozen state. Each explosion event leads to a fragmentation of the D-body into a number of fragments, which then scatter, propelled by their initial velocities. Each fragment then develops into a galaxy, undergoing in its turn an active fission process with ejection of smaller fragments. According to this conception, clusters of galaxies are in a state of decay: a strongly bound system — the superdense object — is being converted into a free system.

Another more popular point of view considers the clusters of galaxies to have formed by compression under the gravitational forces of a rarefied cloud of appropriate mass, with a density substantially lower than the observed mean density of the clusters. The compression of the protocluster is accompanied by its breakup, for reasons of thermal or gravitational instability, into individual fragments which gradually develop into galaxies through further compression.

Thus the formation of clusters, according to one model, is associated with outward motions, whereas, according to the other model, it is associated with inward motions. If the evolution indeed proceeds through compression, there are no forces capable of reversing the compression and converting it into expansion. It is moreover clear that initial compression is feasible only if the total energy of the protocluster is negative. There is apparently no evidence suggesting that the sign of the total energy has changed for some reason, e.g., due to nuclear reactions. A cluster which formed by compression of a rarefied gas cloud will either continue shrinking or will develop to steady-state conditions. In the latter case, it should have a regular spherical or elliptical shape.

This picture of evolution is inconsistent with some empirical data about clusters and primarily with two basic facts: the positive energy of the clusters (which has been firmly established by now) and the conspicuously nonspherical shape of most clusters. With regard to these two aspects, the explosion hypothesis has distinct advantages compared to the hypothesis of gravitational condensation. The explosion hypothesis is obviously consistent with the above facts; the only additional assumption required is that the energy of the explosion is sufficiently high to ensure an excess of the kinetic energy of the fragments above the overall potential gravitational energy. In terms of morphology, irregular systems of ejections and jets are more likely in the case of explosion than a regular spherically symmetric motion.

Note that the concept of D-bodies formulated more than ten years ago in connection with the problem of clusters has been extended since to a number of other non-steady-state effects in cosmic systems, such as the activity of galactic nuclei and the outward motion of stars in associations. However, although covering a wider ground than originally, the concept met with a number of serious difficulties in its development in depth. The exact nature of the D-bodies still remains uncertain; we do not know what forces maintain them in a superdense state; what are the factors triggering their fragmentation and what are the sources of the explosion energy. No solution to the difficult problem of the angular momentum has been found. Pikel'ner /8/ has noted that the angular momentum of spiral galaxies is somewhat higher than the angular momentum of a compact fragment of the same mass and momentum which cannot exist as a bound system with a substantially smaller radius (the centrifugal forces would tear it apart in this case).

THE KINETIC ENERGY OF CLUSTERS AND COSMOLOGICAL EXPANSION

The contradictions of the traditional condensation approach, the difficulties encountered in the D-body hypothesis, and the understandable desire to check all the alternative possibilities encouraged the search for new ideas, not necessarily related to explosion and condensation. One of the alternative approaches is suggested by a comparative analysis of three cosmic objects: a galaxy, a cluster of galaxies, and the Metagalaxy — the largest formation in the Universe, which incorporates all the observed galaxies, clusters, and any other matter enclosed in this volume. Galaxies, as we know, are stationary (steady-state) bound

systems. Clusters, on the other hand, are nonbound expanding systems. The Metagalaxy is evidently a non-steady-state object in a state of expansion, as is evidenced by the famous cosmological red shift. This comparison hints at a possible genetic relation between the expansion of the clusters and the expansion of the Metagalaxy. We can trace an apparently meaningful smooth transition from an individual stationary galaxy and an almost stationary group of several galaxies through the markedly non-steady-state clusters of medium scale to the highly non-steady-state large clusters and, finally, the expanding Metagalaxy. Recently, the existence of this smooth transition was further accentuated by the work of I.D. Karachentsev /6, 9/, who analyzed a large volume of observation material. What is the "linkage mechanism" between the clusters and the Metagalaxy? To answer this question, we have to consider, at least in general outline, the evolution of the metagalactic medium from distant past to the present epoch.

It has been firmly established /10/ that the earliest phases of the expansion of the Metagalaxy were characterized by high temperature, high mass density, and high radiation density. Stars and star systems in their present form naturally could not exist under these conditions. All matter was thoroughly intermixed, and this state of affairs persisted apparently until the temperature has dropped sufficiently because of expansion, and the mass density has reached a level corresponding to the present-day density of galaxies ($10^{-23} - 10^{-24}$ g/cm^3). One must not believe, however, that prior to that time the metagalactic medium was completely homogeneous and isotropic, apart from statistical fluctuations. As we know from the classical results of Lifshits /11/, the metagalactic medium must have had a definite structure quite early in its evolution as a result of certain deviations from isotropy and/or homogeneity. This structure changed with the variation in the physical characteristics of the Metagalaxy as a whole and, finally, it reached the present level. The elements of the metagalactic structure in the present epoch are the density inhomogeneities — galaxies, clusters — with their proper motions.

The evolution of metagalactic structure is one of the fundamental and hitherto unsolved problems of theoretical astrophysics /12, 13/. However, even before the construction of a comprehensive theory, we can advance some simple general considerations unrelated to special assumptions and models.

One possible line of reasoning is the following. The development of pregalactic structure could have disengaged at a certain stage those objects destined to evolve into the steady-state galaxies from the overall cosmological expansion. Within these objects, the cosmological expansion would be switched off for some reason or other. We do not know how this could happen, but the mechanism turning off the cosmological expansion need not have been restricted to galactic masses: it could operate on a larger scale, encompassing masses of the order of a cluster mass. On this scale, however, the cosmological expansion is more significant (it increases in proportion to the scale) and the particular mechanism would not be able to extinguish the expansion completely, only reducing the corresponding velocities.

If the formation of clusters is indeed associated with the slowing-down of the overall cosmological expansion on an appropriate scale, the clusters expanding at a slower rate than the Metagalaxy as a whole will grow progressively more isolated and their density should progressively deviate from the density of the Metagalaxy. This implies that the clusters, although expanding, are not in a process of decay and actually continue forming. This hypothesis naturally explains why the clusters of large mass retain a more pronounced non-steady-state character.

The expansion of the clusters thus may be regarded as a residual cosmological expansion. The same conclusion also emerges from a more detailed analysis, assuming the existence of turbulent motion of matter and radiation in the pre-galactic stage /14, 12/. The cosmological velocity is damped down in this model by hydrodynamic instabilities.

According to the above assumption, the kinetic energy of a cluster is essentially identical with the energy of the cosmological expansion. We do not know what the exact reasons are for the expansion of the Metagalaxy, what caused the initial acceleration, and where the energy came from. There is no doubt, however, that the expansion is a significant, real effect which can be observed with our instruments. If we were to establish a relationship between the clusters and the Metagalaxy, observations of the properties of clusters would shed light on the properties of the Metagalaxy as a whole.

The non-steady-state character of the clusters was originally deduced from the fact that the ratio of the virial mass to luminosity for clusters significantly exceeded the ratio expected for a steady-state system. The kinetic energy of a cluster E_k is substantially larger than the absolute value of the potential energy E_G. A system with such kinetic energy is not bound and it inevitably expands. Let us compare this conclusion with the preceding discussion. According to our assumption, the expansion of clusters is associated with cosmological factors and therefore does not require any particular relationship between the kinetic and the potential energy. The main contribution to the kinetic energy derives from the residual cosmological expansion. The relation of these expansion velocities to mass (and hence to potential energy) may be quite different in different non-steady-state cosmological models. For this reason, the excess of the kinetic energy above the absolute value of the potential energy is by no means an automatic consequence of expansion. In principle, there may exist non-steady-state expanding clusters even if $E_k < |E_G|$. (This naturally would be a very elusive effect.) The positive energy of the cluster indicates that the kinetic energy of cosmological expansion of the particular mass from which the cluster formed originally exceeded the absolute value of the gravitational potential energy. This is possible only in an open cosmological model with hyperbolic expansion.

If we adopt this particular model, we can evaluate the mean density of matter ρ in the Metagalaxy. Indeed, in the open model, for any sphere consisting of given particles, the ratio of the kinetic energy to the absolute value of the potential energy is equal to the density ratio ρ_c/ρ, which is independent of the radius of the sphere ($\rho_c = \frac{3H^2}{8\pi G} \simeq 10^{-29}$ g/cm^3 is the critical density, H is Hubble's constant). This ratio should not be less

than the ratio $E_k/|E_G|$ in the rich clusters. For the largest clusters (see above) $E_k \sim 10\,|E_G|$, and this gives for the density

$$\rho < \frac{|E_G|}{|E_K|}\rho_c \sim 10^{-30}\ \mathrm{g/cm^3}.$$

This estimate is fairly uncertain because of inaccuracies in the determination of the mass/luminosity ratio. Nevertheless, a positive total energy of a cluster — under the above assumptions — definitely supports the open cosmological model with a density close to the density of all luminous matter spread throughout the Universe. This result is consistent with some theoretical arguments /15/ and also with new empirical estimates of the density of the intergalactic medium /16/. It is noteworthy that the cosmological model with this particular density has a number of properties which make it stand out (also for other reasons unrelated to clusters) among the great variety of Fridman models with various values of the parameters /17, 18/.

The above estimate of the mean metagalactic density apparently can be regarded as a positive result of the assumption of the cosmological origin of the expansion of clusters.

This assumption will probably yield answers to a number of other questions relating to the internal structure of clusters. This primarily refers to the correlation between cluster type and morphological constitution: why is it that irregular and spiral galaxies prevail in irregular clusters, and elliptical galaxies in regular clusters? Since the formation of galaxies and clusters is attributable, according to the above, to a common factor — e.g., hydrodynamic instability — this correlation seems to be fairly understandable. Turbulent hydrodynamic motions will preferentially result in systems with considerable inhomogeneities and internal motions, rather than regular formations. This corresponds to the observed prevalence of irregular clusters consisting of irregular and spiral galaxies. The existence of a certain number of regular clusters requires a separate interpretation, which apparently can be devised only within the framework of a more detailed and comprehensive system.

No such theory exists at this stage: there are only general qualitative considerations based either on the explosion hypothesis, or on the gravitational condensation model, or finally on the above assumption of the cosmological origin of the expansion of clusters. Each of the three approaches is essentially concerned with different particular aspects of the real clusters, and therefore they possibly supplement one another, without being mutually exclusive. Indeed, the hypothesis of gravitational acceleration accounts for the existence of systems of galaxies with negative total energies (along with the positive-energy expanding clusters), which could have evolved along the lines described for a condensing gravitationally bound gas cloud. The proportion of these systems is apparently not small among low-population clusters. On the other hand, we are familar with well-known cases of powerful explosions in galaxies, which are accompanied by the ejection of large masses and sometimes even compact blobs of matter, presumably reminiscent of dwarf galaxies. There is no need to prescribe these explosions to hypothetical D-bodies, but these effects show that some expanding clusters containing few galaxies could have

formed in principle as a result of active processes in the nucleus of the parent galaxy. Finally, the dynamics of the largest clusters (and also of superclusters, whose possible existence is supported by observational evidence) are not unlike the dynamics of the Metagalaxy, and the kinetic energy of these systems apparently may be regarded as the residual energy of the cosmological "bang." It would also seem that the mean density of the largest clusters and superclusters is markedly less than the critical cosmological density, as is proper for systems with a positive total energy which expand as a result of cosmological factors.

I would like to acknowledge the help of A. G. Doroshkevich, I. D. Karachentsev, I. D. Novikov, and L. M. Ozernoi, who discussed the problem and offered a number of critical comments.

Bibliography

1. Ambartsumyan, V.A.— Izvestiya Armyanskoi SSR, Seriya Fiziko-Matematicheskikh Nauk, 2:9. 1958; Voprosy Kosmologii, 8:3. 1962.
2. Burbidge, G.R. and E.M. Burbidge.— Astrophys. J., 130:629. 1959.
3. Pskovskii, Yu.P. and G.B. Sholomitskii.— In: "Nablyudatel'nye osnovy kosmologii," p.5, Moskva, Izdatel'stvo AN SSSR. 1965.
4. Karachentsev, I.D.— Astrofizika, 3:89. 1967.
5. Poveda, A.— Astrophys. J., 134:910. 1961.
6. Karachentsev, I.D.— Astrofizika, 2:81. 1966.
7. Abel, J.O.— In: "Nablyudatel'nye osnovy kosmologii," p.153, Moskva, Izdatel'stvo AN SSSR. 1965.
8. Pikel'ner, S.B.— Voprosy Kosmogonii, 9:60. 1963.
9. Karachentsev, I.D.— Thesis. Byurakan. 1967.
10. Zel'dovich, Ya.B. and I.D. Novikov. Relyativistskaya astrofizika (Relativistic Astrophysics).— Moskva, Izdatel'stvo "Nauka." 1967.
11. Lifshits, E.M.— ZhETF, 16:587. 1966.
12. Chernin, A.D.— Trudy V Vsesoyuznoi ezhegodnoi zimnei shkoly po kosmofizike, p.29, Apatity, Izd. Kol'skogo filiala AN SSSR. 1968.
13. Doroshkevich, A.G. Present collection, p. 26.
14. Ozernom, L.M. and A.D. Chernin.— Astronomicheskii Zhurnal, 44:1131. 1967; 45:1137. 1968; ZhETF Letters, 7:436. 1968.
15. Chiu, H.Y.— Ann. Phys., 43:1. 1967.
16. Syunyaev, R.A. Present collection, p. 65.
17. Chernin, A.D.—Nature, 220:250. 1968.
18. Chernin, A.D.— ZhETF Letters, 8:633. 1968.

EXPERIMENTAL VERIFICATION OF THE GRAVITATION THEORY IN COSMOLOGY

A. M. Finkel'shtein

There are currently a number of gravitation theories which predict the four known effects of general relativity. This circumstance discloses still another aspect of cosmology as a suitable tool for the verification of the various competing gravitation theories. For gravitation theories which are conceptually independent of general relativity, cosmology is only one of several checking alternatives, whereas for theories which in a sense constitute a generalization of the general relativity theory, cosmology provides the only ground for detecting possible differences between locally indistinguishable theories. However, the construction of a cosmological scheme which would yield results amenable to experimental verification (primarily in the field of extragalactic astronomy) requires a number of general assumptions regarding the structure of the Universe which extend beyond the framework of the particular gravitation theories. In short, some general cosmological principle is needed.

Robertson and Walker /1/ showed that the metric which admits as the isometry group the six-parametric Lie group of continuous transformations with space-like three-dimensional paths may be written in particular in the form

$$ds^2 = dx^{\circ 2} - \frac{R^2(t)}{\left(1 + \frac{kr^2}{4}\right)^2} d\sigma^2, \qquad (1)$$

where $d\sigma^2 = dr^2 + r^2 (\sin^2\theta\, d\varphi^2 + d\theta^2)$, $R(t)$ and $k = \pm 1, 0$ determine the sign and the scale of the Gaussian curvature of the space-like simultaneity hypersurface $x = \text{const}$, and $x^\circ = ct$ is the world time. A universe (the space-time continuum) described by a linear element (1) has a homogeneous and isotropic spatial part at any instant of the world time x° (the restricted cosmological principle), and the simultaneity hypersurfaces are geodesically parallel. Note that the conception of an isotropic Universe as it is defined by the restricted cosmological principle does not coincide with the conception of a homogeneous and isotropic Metagalaxy as formulated in extragalactic astronomy, since the latter only uses observations covering the section of the surface of the past light cone corresponding to the world line of the Earth-bound observer, i.e., the simultaneity hypersurface. The cosmological postulate thus should be considered as an independent principle, and all the consequences of the postulate may be regarded as potential verifications of the principle.

Robertson and Hoyle and Sandage /2/ proposed a method which made it possible to derive expressions for some observational relations of extragalactic astronomy in the form of expansions in powers of a small parameter, without using any field equations or resorting to any hypotheses concerning the present-day state of matter: the only starting point was the expression for the linear element (1). The same approach, though a much simpler technique, can be used to construct a scheme for the derivation of the observational relations in the form of expansions which are subsequently linked up with various gravitation theories, without integrating the corresponding field equations.

Let L be the bolometric luminosity of a point source at the time of emission. Then the observed bolometric luminosity will be

$$\ell_{bol} = \mathcal{L}\cdot(1+z)^{-2}\, Sn^{-2}\ell\, R_0^{-2}\,(4\pi)^{-1}, \qquad (2)$$

where $Sn\,l = \sin\sqrt{kl}/\sqrt{k}$, $l = \int_R^{R_0} dR/R\dot{R}$ is the world angular distance, $\dot{R} = dR/dx^0$, and the subscript 0 here and in what follows indicates that the corresponding parameters refer to the present epoch. We expand $R_0 Sn\,l$ in powers of the small parameter $R - R_0$, assuming $R(t)$ to be an analytical function near x_0^0. Retaining terms of the order $(R-R_0)^3 \sim z^3$ and introducing as the main parameters to be determined Hubble's constant $H_0 = \dot{R}_0/R_0$, the retardation parameter $q_0 = -\ddot{R}_0 R_0/\dot{R}_0^2$, the factor characterizing the sign and the scale of curvature of the surface $x^0 = \text{const} - k/R_0^2$, and the parameter $\tau_0 = \dddot{R}_0/R_0$, we obtain

$$R_0 Sn\,l = H_0^{-1} z\left[1 - \tfrac{1}{2}(1+q_0)z - \tfrac{1}{6} z^2 (k R_0^{-2} H_0^{-2} + \tau_0 H_0^{-3} - 3q_0^2 - 4q_0 - 2)\right]. \qquad (3)$$

Inserting (3) in (2), changing over to stellar magnitudes, and writing out the appropriate expansions, we obtain an expression for the observed dependence of the apparent stellar magnitude on the red shift (designated $[m_{bol}, z]$):

$$m_{bol} = M + 5\log_{10} H_0^{-1} z + 1.086\left[(1-q_0)z + \tfrac{z^2}{4}(3q_0^2 + \tfrac{10}{3}q_0 - \tfrac{7}{3} - \tfrac{4}{3}k R_0^{-2} H_0^{-2} - \tfrac{4}{3}\tau_0 H_0^{-3})\right], \qquad (4)$$

where $M = -2.5\log_{10} 4\pi L$ is the absolute stellar magnitude.

The terms in (4) proportional to z and z^2 constitute small corrections to Hubble's linear law $z = H_0 D = \bar{D}$, where $D = 10^{0.2(m_{bol} - M)}$. Hubble's law, regarded as a representation of the red shift phenomenon, is a direct consequence of the form of the linear element, being independent of any other factor. To terms of the order of z, relation (4) coincides with Robertson's formula /2/. The latter formula is independent of the sign of the curvature of the space part of the model and, like Hubble's law, it is of pure kinematic origin, being independent of and unrelated to any field equations. The term in (4) which is proportional to z^2 and contains the parameters k/R_0^2 and τ_0 determines the corrections to Hubble's law may be fixed by choosing a particular gravitation theory and a particular hypothesis regarding the equation of state of matter in the present epoch. It is this term which will probably enable us in some cases to distinguish between the competing gravitation theories.

A similar procedure leads to "kinematic" expressions for other famous relations of extragalactic astronomy: 1) the dependence of the number of sources vs. the red shift, [N, z]

$$N = \frac{4\pi}{3}\frac{\rho_{eff}}{Q} H_0^{-3} z^3 \left[1 \; \frac{3}{2}(1+q_0)z + z^2\left(\frac{5}{2} + 5q_0 + 3q_0^2 - \frac{1}{2}k R_0^{-2} H_0^{-2} - \frac{1}{2}\tau_0 H_0^{-3}\right)\right] \tag{5}$$

where ρ_{eff} is the number of sources per unit volume, and Q is the number of degrees squares on the observation sphere, and 2) the dependence of the apparent angular parameter vs. the red shift [θ_0, z],

$$\theta_0 = \zeta H_0 z^{-1}\left[1 + \frac{3+q_0}{2} z + \frac{1}{6}\left(k H_0^{-2} R_0^{-2} + \tau_0 H_0^{-3} + \frac{5}{2} + 2q_0 - \frac{3}{2} q_0^2\right) z^2\right], \tag{6}$$

where ζ is the linear size of the sources in the local system of coordinates.

Since galaxies are still observed when the red shift is no longer measurable, it is advisable to replace the z in (5) and (6) with the bolometric distance. Since $D = \frac{R_0^2}{R}$ Snl and

$$D = H_0^{-1} z\left[1 + \frac{1-q_0}{2} z - \frac{1}{6} z^2\left(k H_0^{-2} R_0^{-2} + \tau_0 H_0^{-3} - 3q_0^2 - q_0 + 1\right)\right], \tag{7}$$

we can invert (7) and eliminate z between (5) and (6) to obtain an expression for the observed number of sources vs. bolometric distance dependence [N, D]:

$$N = \frac{4\pi}{3}\frac{\rho_{eff}}{Q} H_0^{-3} \bar{D}^3 \left[1 - \frac{3}{2}(1+q_0)\bar{D} + \left(\frac{13}{4} + 5q_0^2 + \frac{9}{4} q_0^2 - \frac{1}{2} k R_0^{-2} H_0^{-2} - \frac{1}{2}\tau_0 H_0^{-3}\right)\bar{D}^2\right] \tag{8}$$

and for the angular source diameter vs. bolometric distance dependence [θ_0, D],

$$\theta_0 = \zeta H_0 \bar{D}^{-1}\left[1 + \frac{3+q_0}{2}\bar{D} + \frac{1}{6}\left(k H_0^{-2} R_0^{-2} + \tau_0 H_0^{-3} - 2 + 5q_0\right)\bar{D}^2\right]. \tag{9}$$

Before proceeding with particular theories of gravitation, or more specifically with those of Einstein and Hoyle, we have to make one basic remark. The region of small z, where the approximate relations apply, evidently does not cover all the possibilities of observational cosmology. Moreover, for objects with large z, the cosmological effects are the most pronounced. In this case, however, the "kinematic scheme" for the derivation of the observational relations is no longer applicable and rigorous integration of the field equations is needed, which in most cases constitutes a highly complex problem. The simple approximate expressions, which can be derived without integration of the field equation, may nevertheless be used for choosing between the different conceptions of gravitation. For Einstein's field equations with a cosmological term and a hydrodynamic energy — momentum tensor, the equation of state of matter + radiation has the form

$$\tau_0 H_0^{-3} = 4q_0 - 1 + 2\Lambda H_0^{-2} - k R_0^{-2} H_0^{-2}. \tag{10}$$

Using (10) to eliminate the parameter $\tau_0 H_0^{-3}$ from (4)—(6), we obtain $[m_{bol}, z]$:

$$m_{bol} = M + 5\log_{10} H_0^{-1} z + 1.086[(1-q_0)z + (3q_0^2 - 2q_0 - 1 - \tfrac{8}{3}\Lambda H_0^{-2})\tfrac{z^2}{4}]; \qquad (11)$$

$[N, z]$:

$$N = \frac{4\pi}{3}\frac{\rho_{eff}}{Q} H_0^{-3} z^3 [1 - \tfrac{3}{2}(1+q_0)z + z^2(3 + 3q_0^2 + 3q_0 - \Lambda H_0^{-2})]; \qquad (12)$$

$[\theta_0, z]$:

$$\theta_0 = L H_0 z^{-1} [1 + \tfrac{3+q_0}{2} z + (\tfrac{1}{2} + 2q_0 - \tfrac{1}{2}q_0^2 + \tfrac{2}{3}\Lambda H_0^{-2})\tfrac{z^2}{2}] \qquad (13)$$

A similar procedure can be applied to relations using the bolometric distance.

We wish to emphasize two points regarding these relations (including the relations expressed in terms of D). First, these relations do not contain the parameter k/R_0^2 and, second, these relations contain only two parameters (in addition to Λ) which have to be determined, whereas the known exact relations obtained for $\Lambda = 0$ contain three fundamental parameters /3/ and the resulting accuracy of estimates is much lower.

For the two limiting cases $W^* = 0$ (a model with matter without pressure) and $M^* = 0$ (a model with radiation) we have

$$\frac{k}{R_0^2} = \begin{cases} 2q_0 H_0^2 - H_0^2 + \Lambda \\ q_0 H_0^2 - H_0^2 + \frac{2}{3}\Lambda \end{cases}, \quad \frac{\tau_0}{H_0^3} = \begin{cases} 1 + \frac{k}{R_0^2} H_0^{-2} \text{ for } W^* = 0 \\ 3q_0 + \frac{4}{3}\Lambda H_0^{-2} \text{ for } M^* = 0 \end{cases} \qquad (14)$$

which leads to expressions for the observational relations which are entirely analogous to (11)—(13). The latter point signifies that observations associated with these relations cannot indicate which of the two components—matter or radiation (or both) — plays the leading role in the Universe in the present epoch. Clearly this conclusion is exactly applicable only to observations related to relatively near sources. Relations (11)—(13) are thus valuable because in principle they enable us to find the values of q_0 and Λ without imposing particularly restrictive assumptions on the equation of state of matter in the present epoch.

Hoyle /4/ proposed gravitation equations which in a sense constitute a generalization of Einstein's field equations (they were supplemented with a creative tensor, defined by the field of unit vectors orthogonal to the congruence characteristic of geodesics). We know that for the case $k = 0$ and $p = 0$ Hoyle's equations have a particular integral $R = \exp\left\{\frac{Btc}{3}\right\}$, where $B = 3H_0$, which defines the metric of the Bondi—Gold steady-state Universe /5/. Since for a steady-state Universe $q_0 = -1$, this conception hardly fits the observations (especially if selection effects are ignorable). However, this possibility nevertheless exists in more general models corresponding to the solutions of Hoyle's equations for $k \neq 0$. Indeed, in this case for $p = 0$

$$k R_0^{-2} H_0^{-2} = 2 + 2q_0 \ , \quad \tau_0 H_0^{-3} = \tfrac{3}{2} + \tfrac{1}{2} q_0 \qquad (15)$$

we may also have a solution with $q_0 > 0$ ($\inf q_0 = -3/2$). Inserting (15) in (4), we obtain, in particular, an expression for the observational relation $[m_{bol}, z]$:

$$m_{bol} = M + 5 \log_{10} H_0^{-1} z + 1.086 \left[(1 - q_0) z + (3 q_0^2 - 7) \frac{z^2}{4} \right]. \qquad (16)$$

For $q_0 = 1.0 - 1.5$, there is a definite possibility of making the brightness data (at least for the nearest sources) consistent with Hoyle's theory. The term $m_c^x - m_c^x = (q_0 - 3 + \frac{4}{3} \Lambda H_0^{-2})$ which characterizes the difference between the relations $[m_{bol}, z]$ in Hoyle's and Fridman's theories may prove to be relatively large for certain q_0 and Λ, so that starting with $z > 0.2 - 0.3$ the detailed differences between the two theories may be detected with the 200-in. telescope /6/.

A similar method can be applied to determine the observational relations for Hoyle's theory containing a generalizing Λ-term and expressed in a general covariant form. This procedure also can be applied to the theories of Dicke and Jordan /7/. The general conclusions regarding the possibilities of observational verification of these theories remain unaffected.

Bibliography

1. Robertson, H.— Astrophys. J., 82:284. 1935; Walker, A.G.— Proc. Lond. Math. Soc., 42:90, part 2. 1936.
2. Robertson, H.— PASP, 67:82. 1955; Hoyle, F. and A.Sandage.— PASP, 68:301. 1956.
3. Sapar, A.A.— Publ. TAO AN EstSSR, 34:223. 1966; 35:368. 1966; McIntosh, C.— Monthly Notices Roy. Astron. Soc., 138:423. 1968; Finkel'shtein, A.M.— Astronomicheskii Zhurnal. 1969. (In press).
4. Hoyle, F.— Monthly Notices Roy. Astron. Soc., 108:372. 1948; 109:365. 1949.
5. Bondi, H. and T. Gold.— Monthly Notices Roy. Astron. Soc., 108:252. 1948.
6. Sandage, A.— Astrophys. J., 133:353. 1961.
7. Finkel'shtein, A.M.— Byulleten' ITA AN SSSR, 12(6). 1969.

EJECTION OF GAS FROM STARS IN THE LATE STAGES OF EVOLUTION

G. S. Bisnovatyi-Kogan

Stars lose some of their mass apparently in all stages of evolution. Observations reveal an efflux of mass from the Sun (the solar wind) /1/, from hot O and B stars /2/, from red and yellow giants and supergiants /3/, i.e., mass is ejected both from young stars (the first two categories) and from stars in the late stages of evolution (the red giants). An example of objects which lose mass at a high rate is provided by planetary nebulae, which are currently regarded as stars far advanced in their evolution, and destined to evolve into white dwarfs.

The importance of mass ejection in stellar evolution depends on whether or not the star loses a significant portion of its mass during its lifetime. Observations yield certain estimates for the rates of mass loss. The rate of mass loss for the solar wind is $10^{11} - 10^{12}$ g/sec /1/, which is equal to $10^{-15} - 10^{-14}$ $M_\odot$/years (where $M_\odot$ is the solar mass). Since the evolutionary scale of the Sun is of the order of 10^9 years, solar-wind ejection is evidently of no importance in its evolution. The hot stars, according to Morton /2/, lose up to $10^{-8} - 10^{-6}$ $M_\odot$/year, which is more significant; the lifetime of these stars, which have masses of about 30 $M_\odot$, generally does not exceed $10^6 - 10^7$ years. Of the greatest evolutionary importance in this category is the loss of mass by the red giants, which may reach, according to /4/, $10^{-5} - 10^{-3}$ $M_\odot$/year, and by the planetary nebulae.

In addition to direct observations, there are indirect theoretical considerations which establish the great evolutionary impact of mass ejection. It seems that after the nuclear fuel has burnt up, the star will quietly cool down and terminate its evolution as a cold star. We know from the modern theory of cold stars /5/ that their mass does not exceed 1.2 $M_\odot$ (for white dwarfs) and 1.6 $M_\odot$ (for neutron stars). Large-mass stars collapse into frozen stars with a radius close to the gravitational radius for the corresponding mass. The evolution into a neutron or a frozen star is accompanied by an eminently nonstationary process of the type of supernova explosion. The masses of observable stars reach up to 100 $M_\odot$, and the frequency of supernova explosions is therefore expected to be such as to account for the last stages in the evolution of the sufficiently massive stars. And yet the statistics of supernova explosions reveals a distinct shortage of these phenomena: their frequency is approximately $1/30 - 1/300$ of the number predicted from evolutionary considerations /3/. This discrepancy can be eliminated either by assuming a "silent" nonstationary process, which does not produce any immediately observable

effects, which is not very likely, or assuming that the loss of mass in the course of evolution is effective to such an extent that most massive stars eventually evolve into white dwarfs.

GENERAL PROPERTIES OF HYDRODYNAMIC EJECTION

We will only consider the loss of mass during the quasi-stationary stage of evolution, without dealing with explosive mass loss processes.

Mass ejection during the quiet stage of evolution is caused by processes which occur in the outer envelopes of stars. Whereas the bulk of the stellar mass (some 97 – 99%) is in a state of static equilibrium, the outer envelope is in a state of outward hydrodynamic flow. The solar corona, for example, is produced by this hydrodynamic outflow of solar matter; the coronal mass, however, is so negligible that it can be ignored in terms of evolution. In a red giant, on the other hand, up to 3% of its mass may be tied up in hydrodynamic ejection processes. The mass losses in this case are highly significant for evolution, which should be considered in terms of a model with a static core and a hydrodynamic envelope /6, 7/. In this, as in the totally static case, an unambiguous model can be constructed. The general equations describing the outflow of stellar matter are the equations of hydrodynamics. They are valid since in all the known cases the particle path length l is less than the system dimensions L. The ejected matter escapes to infinity. The process of ejection may be regarded as steady-state, since the ratio of the partial derivative $\partial/\partial t$ to the convective derivative $u\,\partial/\partial r$ is equal to the inverse of the ratio of the evolution time t_{ev} to the time it takes the flowing matter to cover the characteristic size of the star R/u, which is clearly much less than unity /8/. The density and the temperature of the ejected matter monotonically decrease with the distance from the star and vanish at infinity. Steady-state flow with monotonic variation of the parameters is feasible only if the solution of the equations of hydrodynamics passes through a singular point where the flow velocity is equal to the adiabatic velocity of sound $u_a^2 = (\partial p/\partial \rho)_s$ /1/. Near the singular point (Figure 1) the solution behaves in such a manner that a saddle point is obtained. A physical solution is that with a monotonically increasing velocity, ab. Note that in this case the solution is necessarily passed through the point where the flow velocity is equal to the isothermal velocity of sound $u_T^2 = (\partial p/\partial \rho)_T$. In fact, the following situation is obtained: if we consider hydrodynamics without transport processes, the singular point is that where $u^2 = (\partial p/\partial \rho)_s$ is equal to the adiabatic velocity of sound. If heat conduction is taken into consideration, the properties of the

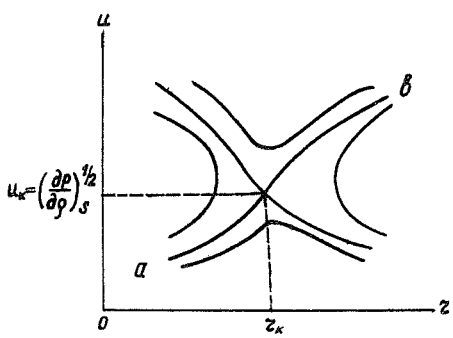

FIGURE 1. The integral curves of the equations of hydrodynamics describing gas outflow.

equations change discontinuously, and two singular points are obtained, one where $u^2 = (\partial P/\partial \rho)_T$ is equal to the isothermal velocity of sound and the other for $r = \infty$, $T = 0$, $\rho = 0$. If we further allow for viscosity, we are naturally left with a single singular point, the one at infinity. Although the properties of the equations change markedly when dissipative processes are introduced, the solution passing through the singular point and satisfying the boundary conditions is a continuous function of the parameter /9/. Ejection from stars of various types is characterized by different processes of interaction with radiation and different ejection mechanisms.

EJECTION FROM STARS NEAR THE MAIN SEQUENCE

The mean optical density τ of the solar wind and of the ejection from early-type stars is close to zero, although in individual lines it may approach unity. In this case, the equations of hydrodynamics are used with transport terms — viscosity and heat conduction. In a completely ionized gas. the contribution from viscosity is small compared to the contribution from heat conduction. Radiation is not in thermodynamic equilibrium with matter. It leads to local cooling of the ejected gas, thus accelerating the supersonic flow and decelerating the subsonic flow /3, 10/. Radiation also produces a certain acceleration of the gas flow due to pressure in spectra lines /11/. The factor responsible for the outflow of matter is the non-thermodynamic heating of the base of the corona.

MASS LOSSES OF STARS IN LATE STAGES OF EVOLUTION

The matter ejected from red giants and planetary nebulae is in equilibrium with radiation ($\tau \gg 1$) throughout the main ejection region, the critical point included. Therefore the properties of ejection and its very existence are significantly dependent on the opacity of matter. In this case, matter is in thermodynamic equilibrium with radiation, and an important contribution is due to the radiant heat conduction, whereas the effect of viscosity is negligible /7, 9/.

A star may be in a state of static equilibrium only if its luminosity /5/ is less than some critical luminosity (Eddington's condition) $L < L_c = \frac{4\pi c G M}{\varkappa}$, where $\varkappa$ is the opacity. If we draw a qualitative plot of opacity as a function of the star's radius, we obtain for stars with $M \approx 30\, M_\odot$ the curve shown in Figure 2 /1, 2/.

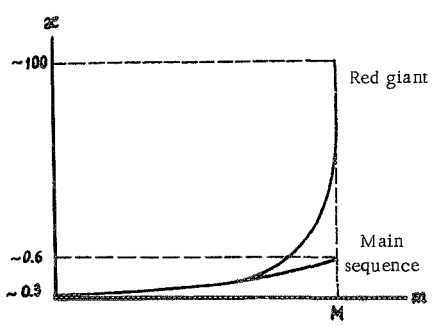

FIGURE 2. A qualitative curve of the opacity of a star in the late stages of evolution.

It is clear from Figure 2 that while on the main sequence $\varkappa$ is always relatively small, so that $L < L_c$, the opacity in the red giant stage steeply increases because of the significant cooling of the star's envelope, which produces a zone of incompletely ionized hydrogen. Moreover, the luminosity also increases by a considerable factor, and hydrodynamic ejection begins /7/. Note that convection effectively lowers the transparency and suppresses ejection, but in the outer layers the convection is highly nonadiabatic and may transport only a small fraction of the heat flux /7/. The larger the mass, the smaller is the density of the surface layers and the less effective is the convection. For $M \simeq 30\,M_\odot$, it does not prevent ejection after helium has begun burning. For $M \simeq 9\,M_\odot$, the convection does prevent ejection at this stage and the static evolution continues. The larger the mass, the less important is the external convection.

We see from the expression for L_c that the onset of ejection, in addition to $\varkappa$, also depends on the ratio L/M. It follows from the theory that on the main sequence $L \sim M^3$ or even $\sim M^4$ for small masses, and therefore the ratio L/M increases with increasing mass in this range. On the main sequence it is equal to $\sim 5 \cdot 10^{-5}\varkappa$ for $1\,M_\odot$ and reaches $0.3\varkappa$ for $30\,M_\odot$ /7, 13/. Thus, the larger the mass, the smaller is the increase in opacity and luminosity needed to initiate ejection. For small masses, on the other hand, the hydrodynamic ejection of the relevant type will begin at substantially later stages of evolution.

Computations of the static evolution of stars also lead to ejection. If the velocity is formally ignored in the equations and the envelope is considered as static even for $L > L_c$, we arrive at glaring contradictions: a strong inverse density gradient develops in the envelope, the expansion velocity obtained from a comparison of two static models increases and approaches the velocity of sound, and finally the solution with a static envelope breaks down completely. This occurs at the following stages of stellar evolution: for stars with $M > \sim 15\,M_\odot$ /12, 14/, when helium begins burning; for $\sim 5\,M_\odot < M < 15\,M_\odot$ /15 – 17/ when carbon begins burning; and for low-mass stars $\sim 1.3\,M_\odot$ /18/, ejection of this type occurs in the planetary nebula stage, when the star is evolving into a white dwarf. This ejection is evolutionarily significant: estimates for $30\,M_\odot$ give /7/ a mass loss of the order of $3 \cdot 10^{28}$ g/year, or about $10^{-5}\,M_\odot$/year.

To find the exact rates of mass loss, the evolution should be computed using instantaneous self-consistent models with a static nucleus and a hydrodynamic envelope. Such models can be constructed unambiguously /6, 7/ using the same techniques as for models with a static envelope. The static envelope is fully characterized by two parameters, e.g., L and the radius R. The conditions of matching with the nucleus lead to a unique model in each case. Although a hydrodynamic model contains one further variable – the velocity – and one more parameter – the rate of mass loss μ – the solution is constrained to pass through a singular point and to satisfy certain conditions at infinity, so that the hydrodynamic envelope is completely described by only two variables, e.g., L and the critical density ρ_k, which is also uniquely determined from the matching conditions. The rate of mass loss is a function of the state of the star.

Bibliography

1. Parker, E.N. Interplanetary Dynamic Processes. — New York, Wiley. 1963.
2. Morton, D.— Astrophys. J., 147:1017. 1967; 150:535. 1967.
3. Weyman, R.— Ann. Rev. Astron. and Astrophys., 1:97. 1963.
4. Rublev, S.V.— Kosmogonii, 10:119. 1964.
5. Zel'dovich, Ya.B. and I.D. Novikov. Relyativistskaya astrofizika (Relativistic Astrophysics).— Moskva, Izdatel'stvo "Nauka." 1968.
6. Bisnovatyi-Kogan, G.S. and D.I. Nadezhdin.— Nauchnye Informatsii Astronomicheskogo Soveta AN SSSR, 2:28. 1969.
7. Bisnovatyi-Kogan, G.S. and Ya.B. Zel'dovich.— Astronomicheskii Zhurnal, 45:241. 1968.
8. Bisnovatyi-Kogan, G.S. and Ya.B. Zel'dovich.— Astronomicheskii Zhurnal, 43:1200. 1966.
9. Bisnovatyi-Kogan, G.S.— Prikladnye Metody Mekhaniki, 31:762. 1967.
10. Bisnovatyi-Kogan, G.S.— Mekhanika Zhidkosti i Gaza, 4:182. 1968.
11. Lucy, L. and P. Solomon.— Astron. J., 72:310. 1967.
12. Nadezhdin, D.K.— Nauchnye Informatsii Astronomicheskogo Soveta AN SSSR, 4:37. 1966.
13. Haselgrove, C. and F. Hoyle.— Monthly Notices Roy. Astron. Soc., 119:112. 1959.
14. Kotok, E.V.— Astronomicheskii Zhurnal, 43:316. 1966.
15. Hofmeister, E., R. Kippenhahn, and A. Weigert. Stellar Evolution, p.263.— New York, Plenum Press. 1966.
16. Hofmeister, E.— Zeitschrift Astrophys., 65:164. 1967.
17. Weigert, A.— Colloq. Late-Type Stars, Proc., p.388. Trieste. 1966.
18. Savedoff, M., et al.— Astrophys. and Space Sci., No.1. 1969.

LOW-FREQUENCY OSCILLATIONS OF A MAGNETIC ROTATING NEUTRON STAR

Yu. V. Vandakurov

A neutron star with an internal magnetic field may undergo unstable nonradial low-frequency oscillations of convective character if the field falls off sufficiently fast away from the center /1/. In the present paper, we intend to analyze the equations of oscillations for an ideally conducting rotating configuration with a toroidal field. The rotation and the field are treated as small perturbations, and general relativity effects are ignored. The results bear out the possible existence of instability, although the self-sustained oscillations asymmetric relative to the spin axis are in no way related to convective oscillations (in particular, the instability region is much wider).

Introductory remarks

The instability of low-frequency nonradial oscillations of a star leads to convection. In a normal star the instability develops when the temperature gradient exceeds a certain limit value. In the presence of a magnetic field, a different instability criterion applies to the adiabatic nonradial oscillations, but when the ratio of the magnetic to gravitational force is low the corrections are not large.

Consider a superdense cold object in which the pressure p is a function of density ρ alone; the form of the function $p(\rho)$ is assumed to be independent of whether the object oscillates or not. This condition is observed for the case of a neutron star or a structurally homogeneous white dwarf. The case when the rate of nuclear reactions plays a significant role in the process of oscillation was discussed in /2/.

If $p = p(\rho)$, the Lagrangian components of the pressure and density perturbations (δp and $\delta\rho$) in the oscillating state are related by the equality

$$\frac{\rho\delta p}{p\delta\rho} = \frac{\rho dp}{p d\rho}. \qquad (1)$$

For adiabatic motions, the left-hand side of (1) is equal to the adiabatic index γ. Inserting (1) into the Schwartzschild criterion, we find that the neutron star is neutrally stable relative to convective perturbations. This result was derived in /1/.

A neutron star with a magnetic field may be convectively unstable /1/. The stability criterion is considered below in some detail. We should

stress, however, that because of the neutral stability of an unperturbed neutron star, the smallest field may cause instability. This situation is cardinally different from what we observe in normal stars. Because of the definite damping produced by the emission of gravitational waves and other processes, the field strength causing instability has a finite, and not infinitesimal, magnitude.

The equilibrium state

The equilibrium equations of an ideally conducting gas sphere with a general magnetic field distribution $\vec{H}(r,\vartheta)$ and a general angular rotation velocity $\Omega(r,\vartheta)$ were analyzed in /3/. Expressing the field $\vec{H}$ in terms of two scalar functions U and W, we find

$$\xi \vec{H} = \sqrt{4\pi}\,(-\vec{e}_\varphi \times \nabla U + \vec{e}_\varphi W), \quad \vec{v} = \vec{e}_\varphi\, \Omega \xi, \quad |\vec{e}_\varphi| = 1, \tag{2}$$

$$\frac{\nabla p}{\rho} + \nabla \Phi = \frac{1}{2}\Omega^2 \nabla \xi^2 - \frac{1}{2\rho\xi^2}\left\{\nabla W^2 + 2\xi(\vec{e}_\varphi \operatorname{rot}[\tfrac{1}{\xi}\vec{e}_\varphi \times \nabla U])\nabla U\right\}, \quad \xi = r\sin\vartheta. \tag{3}$$

Here r, ϑ, φ are the spherical coordinates.

In a neutron star, $p = p(\rho)$ and the rotor [curl] of the right-hand side of (3) should vanish. Since the rotation and the magnetic field are treated as perturbations, the right-hand side of (3) is a small quantity and we may therefore replace ρ with $\rho_0 = (\rho)_{\Omega=0, \vec{H}=0}$.

Without a poloidal field (U = 0), we have a solution $\Omega = \Omega(\xi)$, $W = W(\rho\xi^2)$. Let us further consider a solution in which the expansion in Legendre polynomials $P_n(\cos\vartheta)$ of the difference $\rho - \rho_0$ contains terms with P_0 and P_2 only. Then

$$\Omega = \Omega(r) \text{ and } U = 0, \quad W = \xi^{-} f(r), \quad (\Omega^2) = \rho_0 (f^2/\rho_0^2)', \tag{4}$$

where prime denotes differentiation. Choosing some $f(r)$, we obtain a certain law of differential rotation. On the stellar surface, ff'/ρ_0 should be bounded.

In the presence of a poloidal field, the condition of frozen fields and the absence of rotational forces impose more exacting restrictions on the field and rotation velocity distribution. In this case $\Omega = \Omega(U)$ (or Ω = const), $W = W(U)$. Suppose that the series for $\rho - \rho_0$ contains the polynomials P_0 and P_2 only. Then Ω = const,

$$\begin{cases} U = \xi^2 q(r), \quad W = EU, \quad E = \text{const} \\ rq'' + 4q' + E^2 rq = -Dr\rho, \quad D = \text{const} \end{cases} \tag{5}$$

The solution differs from (4) in that the field at the center is of the same order of magnitude as on the surface. For example, taking $\rho = \rho_c(1 - r^2/R^2)$, E = 0, ρ_c = const, we find $q = q_c - \frac{D\rho_c r^2}{10}\left(1 - \frac{5r^2}{14R^2}\right)$.

The equations of low-frequency oscillations

Let a small perturbation be applied to the equilibrium state, which is described by equations (2), (3) together with the equation of state and the

Poisson equation. Because of the perturbation, the field, the density, and other variables take on the perturbed values $\rho \to \rho^*, \vec{H} \to \vec{H}^*$, etc. The dependence of the perturbations $\rho^*, \vec{H}^*, \ldots$ on φ and t is taken in the form $\exp i(m\varphi + \omega t)$.

We will only consider low-frequency oscillations, when ω is either of the order of Ω or of the order of $H/\sqrt{4\pi\rho_c R^2}$, where $\rho_c = (\rho)_{r=0}$, R is the radius of the star. This means that $|\omega| \ll \sqrt{\pi G \rho_c}$. Corrections of the order $\omega^2/\pi G \rho_c$ are dropped. Note that in this approximation the difference $\rho - \rho_0 = \rho - (\rho)_{\Omega=0, \vec{H}=0}$ is small.

Equation (1) remains valid if the Lagrange variables $\delta p, \delta\rho$ are replaced by Euler variables p^*, ρ^*. The linearized equation of motion may be written in the form

$$i\omega\vec{v}^* + (\vec{v}\cdot\nabla)\vec{v}^* + (\vec{v}^*\cdot\nabla)\vec{v} + \nabla\Pi - \\ - \frac{1}{4\pi\rho_0}\left\{(\vec{H}\cdot\nabla)\vec{H}^* + (\vec{H}^*\nabla)\vec{H}\right\} + \frac{\nabla\rho_0}{4\pi\rho_0^2}\vec{H}\cdot\vec{H}^* = 0, \tag{6}$$

where

$$i\omega\vec{H}^* = \mathrm{rot}\,(\vec{v}\times\vec{H}^* + \vec{v}^*\times\vec{H}). \tag{7}$$

$\Pi = \Phi^* + p^*/\rho + \vec{H}\cdot\vec{H}^*/4\pi\rho$. In equation (6), the terms $\rho^*(\vec{H}\times\mathrm{rot}\,\vec{H})/4\pi\rho^2$, $(\rho-\rho_0)(\vec{H}^*\times\mathrm{rot}\,\vec{H})/4\pi\rho^2$, etc., have been dropped, since they constitute small corrections to the term $\nabla(p^*/\rho)$. The order of magnitude estimate for ρ^* which follows from (6) and (1) has the form $\rho^* \sim R\omega\rho_c^2 v^*/p_c$, and the equation of continuity in our approximation therefore takes the form

$$\mathrm{div}\,\rho_0\vec{v}^* = 0. \tag{8}$$

Equations (6) through (8) constitute a complete system for the unknowns $\vec{v}^*$ and $\vec{H}^*$. Note that the coefficients of this system depend only on the unperturbed density distribution $\rho_0(r)$.

Low-frequency oscillations of an infinite gravitating cylinder

A convenient model for investigating the general spectrum of frequencies of oscillating gravitating objects is provided by the cylindrical configuration. For a homogeneous density distribution, the analogy between the oscillations of a cylinder (in a plane perpendicular to its axis) and the oscillations of a sphere was emphasized in /4/.

Let the cylindrical coordinates be ξ, φ, z ($\xi = r\sin\vartheta$). Suppose that in the equilibrium state the cylinder rotates with a uniform angular velocity Ω, and the magnetic field is $\vec{H} = \sqrt{4\pi}\,[\vec{e}_\varphi \xi f(\xi) + \vec{e}_z h(\xi)]$ inside the cylinder and $\vec{H} = 0$ outside the cylinder (for $r \geq R$). For perturbations which are independent of z, we find from equations (7), (6) (the factor $\exp i(m\varphi + \omega t)$ and the index 0 of ρ_0 are omitted)

$$\omega_* \vec{H}^* = \sqrt{4\pi}\left\{mf\vec{v}^* + i\rho v_z^*\left[\xi\left(\frac{f}{\rho}\right)'\vec{e}_\varphi + \left(\frac{h}{\rho}\right)'\vec{e}_z\right]\right\}, \\ \omega_* \Pi' + i(a+d)v_\xi^* - c v_\varphi^* = 0, \quad m\omega_* \Pi = \xi(ic v_\xi^* - a v_\varphi^*); \tag{9}$$

$$a = \omega_*^2 - \frac{m^2 f^2}{\rho}, \quad c = 2\omega_* \Omega - \frac{m f^2}{\xi \rho^2}(\xi^2 \rho)', \quad \omega_* = \omega + m\Omega,$$
$$g = \frac{1}{2}(\xi^2 \rho)'\left(\frac{f^2}{\rho^2}\right)' + \frac{1}{2}\rho'\left(\frac{h^2}{\rho^2}\right)' - \frac{1}{a}\left(\frac{m f h \rho'}{\rho^2}\right)^2. \tag{10}$$

Using equation (8), we replace the initial system with a single equation for $X = \xi v_\xi^*$:

$$\xi \frac{d}{d\xi}\left(\frac{a\xi}{\rho}\frac{d\rho X}{d\xi}\right) - \left\{\xi\rho\left(\frac{c}{\rho}\right)' + m(a+g)\right\} mX = 0. \tag{11}$$

Without a field ($f = 0$, $h = 0$), taking $\rho = \rho_c (1-y)^w$, $y = (r/R)^\nu$, w, ν = const, we can express the solution of (11) in terms of the hypergeometric function $X = (1-y)\, F(\alpha, \beta, \alpha+\beta-1-w, y)$, $\alpha + \beta = 2 + w + 2m/\nu$, $\alpha\beta = 1 + w + \frac{m}{\nu}\left(2 + w + \frac{2\Omega w}{\omega_*}\right)$. The condition of boundedness of X for $\xi = R$, $y = 1$ gives $\alpha = -\kappa$, where $\kappa = 0, 1, 2, \ldots$ Thus

$$\frac{\omega}{m\Omega} + 1 = -\frac{2w}{\nu\left\{\kappa(\kappa + 2 + w + 2m/\nu) + 1 + w + \frac{m}{\nu}(2+w)\right\}}. \tag{12}$$

For a rotating cylinder with longitudinal magnetic field only ($f=0$, $h\neq 0$), a and c are constant and there are always solutions of equation (11) with small ω_* (ω_* is the frequency in the coordinate system rotating with the cylinder). For these frequencies, using the method of /5/, we obtain the following asymptotic expression:

$$\omega + m\Omega = \pm \frac{2i}{\pi(2j+d)} \int \frac{\sqrt{m^2 g}}{r}\, dr, \tag{13}$$

where j is a large positive number, d is some constant ($|d| \ll j$), and integration is carried out over the regions where $g > 0$ (it was assumed in the derivation that such regions exist).

A convective instability arises if in some regions the field falls off faster than the density. The reason for the development of instability is clearly understood from simple qualitative considerations /1/. Consider interchangeability of individual magnetic force tubes, together with the particles enclosed in these tubes. If there are regions with a rapidly diminishing field, the outward displacement of such a tube substitutes hydrostatic pressure for field pressure in the interior regions while substituting field pressure for hydrostatic pressure in the outer layers. This process produces an instability of the same type that is observed in a high-density liquid supported from below by a low-density liquid.

A more interesting model is the one with a toroidal field ($h=0$, $f\neq 0$), since the oscillations of such a system constitute to a certain extent a two-dimensional analog of the oscillations of a sphere. This model was analyzed by means of numerical integration of equation (11). In the equilibrium state, we took

$$p = p_c \theta^{n+1}, \quad \rho = \rho_c \theta^n, \quad f = f_c \theta^{n\beta}, \quad n = 1.5,$$
$$\frac{d^2\theta}{d\xi^2} + \frac{1}{\xi}\frac{d\theta}{d\xi} + \theta^n = 0, \quad \xi = \frac{\xi}{R_E}, \quad R_E^2 = \frac{(n+1)p_c}{4\pi G \rho_c^2}, \tag{14}$$

where β = const $> \frac{5}{6}$. The radius and the mass per unit cylinder length are $2.6\, R_E$ and $6.5 \rho_c R_E^2$.

The calculations were carried out as follows. For some complex ω_*, the solution of (11) was obtained first by integration from the center $\xi = 0$ and then by integration from the surface $\xi = R$. The condition of matching of the two solutions at an intermediate point ξ_f requires that the complex determinant Δ be equal to zero. If for the particular ω_* chosen $\Delta \neq 0$, a new ξ_f is chosen from the condition that $|\Delta|$ should decrease at the fastest rate. No provision was made in the program, however, for encircling the regular singular point $a = 0$, and therefore for $f_c \neq 0$ the roots ω_* with a very small imaginary part could not be computed.

For $f_c = 0$, by analogy with (12), there are numerous solutions ω_*. For example, if $m = 2$, the largest root is $\omega_* = -0.62\,\Omega$.

For $m = 2$, $\beta = 1.5$, $f_c^2 \rho_c = 200\,\Omega^2$, we obtained the root $\omega_* = (-0.066 \pm i\,0.12)\Omega$, but all attempts to determine the second root failed. Irrespective of the initial ω_*, the computations yielded the same root. All the other solutions are apparently real. The root is highly sensitive to changes in m: if $m = 1$ we have $\omega_* = (-0.18 \pm i\,1.4)\,\Omega$, and there are again apparently no other complex roots. No complex roots could be found for $m = 3$ and the same β and $f_c^2 \rho_c$.

For $\beta = 1$ and $f_c^2/\rho_c = 10\,\Omega^2$ (the ratio of the magnetic energy to rotational energy $\varkappa$ is around 4), the following roots were obtained:

$$m=1 \quad \omega_* = (-0.147 \pm i\,0.54)\,\Omega,$$
$$m=2 \quad \omega_* = (-0.153 \pm i\,0.63)\,\Omega.$$

In this case, the dependence on m is different from that observed for $\beta = 1.5$. The figure plots the real and the imaginary parts Re ω_* and $[\mathrm{Im}\,\omega_*]$ as a function of the parameter β. The curve $\varkappa(\beta)$ is also drawn approximately.

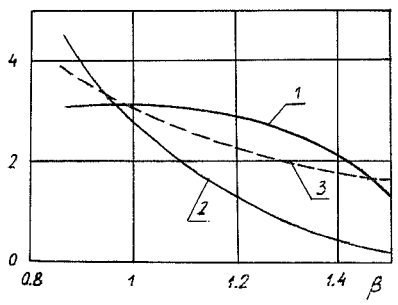

Oscillation frequency ω vs. β characterizing the rate of field decrease:

1) $\left[-\frac{Re(\omega + m\Omega)}{\Omega}\cdot 20\right]$; 2) $\left[\frac{|Im(\omega + m\Omega)|}{\Omega}\right]$

3) approximate ratio of magnetic energy to rotational energy divided by 25.

The existence of instability for $\beta \leq 1$ is an unexpected result, since an analysis of the interchangeability of individual force tubes leads to the conclusion that for the distribution corresponding to the stability limit, f is proportional to ρ or $\beta = 1$. It is clear, however, that this remark is valid only for axisymmetric perturbations $m = 0$. Indeed, if we assume that the dependence of the perturbation on φ and z is expressed by $\exp ikz$, we find for $h = 0$, $f \neq 0$ instead of (11)

$$\xi \frac{d}{d\xi}\left(\frac{1}{\xi\rho}\frac{d\rho X}{d\xi}\right) - \left(1 + \frac{g}{\omega^2}\right)k^2 X = 0, \tag{15}$$

where g is expressed by (10) with $h = 0$. We thus see that instability develops if there exist regions with $g > 0$.

The stability of a star with a toroidal field

Let the equilibrium state of a rotating neutron star with a toroidal magnetic field be described by equations (2), (4). From the equations

of oscillations (7) and (6) we have

$$\begin{aligned}
&\omega_* \vec{H}^* = \sqrt{4\pi}\left\{ m f \vec{v}^* + i\xi \vec{e}_\varphi \left[f \operatorname{div} \vec{v}^* + \omega_* \vec{v}^* \cdot \nabla\left(\frac{f}{\omega_*}\right)\right]\right\} \\
&i a \vec{v}^* + \omega_* \nabla \Pi - 2\Omega\omega_* v_\varphi^* \nabla \xi + \frac{f \nabla(\xi^2 \rho)}{\xi \rho^2}\left[m f v_\varphi^* + \right. \\
&\left. + i\xi\rho\omega_* \vec{v}^* \nabla\left(\frac{f}{\omega_* \rho}\right)\right] + \frac{\omega_*}{\xi} \vec{e}_\varphi \left\{ \vec{v}^* \nabla(\xi^3 \Omega) - \frac{m f^2}{\omega_* \rho^2} \vec{v}^* \cdot \nabla(\rho \omega_* \xi^2)\right\} = 0,
\end{aligned} \tag{16}$$

where ω_* and a represent the same combinations as in (10). Since m only enters as $m\Omega$ and m^2, we may take $m \geq 0$.

We seek a solution in the form of a series in associate Legendre polynomials $P_k^m(\cos\vartheta)$:

$$\begin{cases}
v_r^* = i\omega_* \sum_k X_k P_k^m, \quad \Pi = r \sum_k W_k P_k^m, \quad b = \omega_* \Omega - \frac{m f^2}{\rho}, \\
v_\varphi^* = \frac{\omega_*}{\sin\vartheta} \sum_k \left[Z_k - \frac{r \omega_* f \sin^2\vartheta}{b} \left(\frac{f}{\rho\omega_*}\right)' X_k \right] P_k^m .
\end{cases} \tag{17}$$

The additional term in the expression for v_φ^* is chosen so that (16) gives the simplest possible expression for v_ϑ^*:

$$v_\vartheta^* = \frac{i\omega_*}{a} \sum_k \left(W_k \frac{\partial P_k^m}{\partial \vartheta} - \frac{2 b \cos\vartheta}{\sin\vartheta} Z_k P_k^m \right).$$

Multiplying equation (8) by $\sin^3\vartheta\, P_\ell^m$ and the first and the third components of (16) by $\sin\vartheta\, P_\ell^m$ and $\sin^2\vartheta\, P_\ell^m$, respectively, we obtain after integration over ϑ from 0 to π

$$\begin{cases}
\sum_k \left\{ \left(m a Z_k + m^2 W_k \right) \delta_{k\ell} + \left[\frac{a(r^2 \rho X_k)'}{r\rho} + 2 b Z_k - k(k+1) W_k \right] J_{k\ell}^0 - \right. \\
\left. - 2 b Z_k J_{k\ell}^1 \right\} = 0, \\
\sum_k \left\{ \left[a X_k + c Z_k - (r W_k)' \right] \delta_{k\ell} + \frac{r^2 f f'}{\rho} \left(\frac{f}{\rho}\right)' X_k J_{k\ell}^0 \right\} = 0, \\
\sum_k \left\{ \left[\left(a - \frac{4b^2}{a}\right) Z_k + m W_k \right] \delta_{k\ell} + \left(c X_k + \frac{4b^2}{a} Z_k\right) J_{k\ell}^0 + \frac{2b}{a} W_k J_{k\ell}^1 \right\} = 0, \\
c = 2\omega_* \Omega - \frac{m f^2 (r^2 \rho)'}{r \rho^2}
\end{cases} \tag{18}$$

Here

$$\begin{aligned}
&J_{k\ell}^0 = \frac{1}{I_\ell} \int_0^\pi P_k^m P_\ell^m \sin^3\vartheta\, d\vartheta = -\mathcal{K}_\ell^{(-)} \delta_{k+2,\ell} + \mathcal{K}_\ell \delta_{k\ell} - \mathcal{K}_\ell^{(+)} \delta_{k-2,\ell}; \\
&J_{k\ell}^1 = \frac{1}{I_\ell} \int_0^\pi \frac{\partial P_k^m}{\partial \vartheta} P_\ell^m \sin^2\vartheta \cos\vartheta\, d\vartheta = (\ell-2) \mathcal{K}_\ell^{(-)} \delta_{k+2,\ell} + \left(\tfrac{3}{2}\mathcal{K}_\ell - 1\right) \delta_{k\ell} - (\ell+3) \mathcal{K}_\ell^{(+)} \delta_{k-2,\ell}; \\
&I_\ell = \frac{2}{2\ell+1} \frac{(\ell+m)!}{(\ell-m)!}; \quad \mathcal{K}_\ell = \frac{2[\ell(\ell+1)+m^2-1]}{(2\ell-1)(2\ell+3)}; \quad \mathcal{K}_\ell^{(\pm)} = \frac{(\ell \pm m \pm 1)(\ell+1 \pm m \pm 1)}{(2\ell \pm 3)(2\ell+2 \pm 3)}.
\end{aligned}$$

$\delta_{k\ell} = 1$ for $k = \ell$, $\delta_{k\ell} = 0$ for $k \neq \ell$.

The integrals are readily evaluated if $\sin^2\vartheta\, P_k^m$, etc., are expressed with the aid of known recursive relations /6/ in terms of the three polynomials P_k^m and $P_{k\pm2}^m$. The problem of oscillations thus reduces to finding the eigenvalues ω of a system of coupled equations (18).

Consider an approximate method of solution of this system. Let ℓ be equal either to m or to $m+1$, when $\mathcal{K}_\ell^{(-)} = 0$. If we omit the terms containing $\mathcal{K}_\ell^{(+)}$, we obtain a system of two first-order differential equations for X_ℓ and W_ℓ. We will refer to this as the first approximation. In the second approximation, we obtain a system X_ℓ, $X_{\ell+2}$, W_ℓ, $W_{\ell+2}$, etc.

The convergence of this process for a system similar to (18) is considered for one particular numerical example in /8/, where the nonradial oscillations of a nonmagnetic rotating normal star are investigated to a certain approximation. The first approximation ensures an accuracy of about 4%, and the second approximation 0.2%.

If we restrict the analysis to the first approximation only, we obtain a system which has some features in common with equations (8)—(9) for a cylinder. The principal properties of the unstable oscillations of a sphere are in all probability qualitatively similar to the unstable oscillations investigated in the previous example. Numerical integration of equations (18) will be carried out in the nearest future.

The above analysis leads to the conclusion that two types of instabilities are apparently possible in a neutron star with a toroidal magnetic field. The first type is symmetrical about the spin axis ($m = 0, \ell \neq 0$). This is a convective instability, and a criterion of its existence can be derived by simple qualitative considerations based on considerations of interchangeability of magnetic force tubes. For the distribution corresponding to the stability limit, the field H_φ is proportional to $\rho r \sin\vartheta$.

By analogy with the oscillations of a cylinder, we can expect that the conditions of the excitation of the second type of instability ($m \neq 0, \ell \geq |m|$) are much more favorable. In this case, the self-sustained oscillation modes are isolated and their number increases with the increase in the ratio of the magnetic energy to the rotational energy. If, moreover, the field falls off sufficiently fast away from the center, the effect of the field on oscillation modes which have numerous nodes along the radius or in the azimuthal direction is markedly suppressed. It therefore seems that there exist configurations with only one unstable harmonic $\ell = 1$, $m = 1$.

For both types of instability, the density, the pressure, and the gravitational potential experience characteristically small perturbations during the oscillations. On the surface of the star, the particles are displaced almost horizontally (to orders of magnitude, the vertical component is less than the horizontal component by a factor of $H_\varphi^2/G\rho_c^2 R^2$). For $m \neq 0$, the instability is oscillatory with a frequency $\mathrm{Re}\,\omega$ which mainly depends on the rotation velocity and with an increment $|\mathrm{Im}\,\omega|$ which is mainly determined by the magnetic field strength.

Let us now consider the hypothesis /1/ according to which the recently discovered pulsating radio sources /8/ are in fact magnetic rotating neutron stars with instabilities of the type described above.

If a star of the Sun's mass with an internal magnetic field of the order of 10^3 Oe is converted into a neutron star with a radius $R \sim 10^6$ cm, the field on the average increases to 10^{13} Oe, and the magnetic energy in the final state will be $E_m \sim 10^{43} - 10^{44}$ erg. The strength of the poloidal field of the neutron star near the surface will markedly increase, since this field has the same order of magnitude in the outer and the inner layers of the star. In all probability, it will be ejected from the star in the earlier stage of gravitational collapse.

The magnetic energy in the form of a toroidal field may have any degree of concentration toward the center. Both types of instabilities will probably be excited in such a star $m = 0$ and $m \neq 0$). Convection will intermix the various layers until a convectionally stable state is formed. The amplitude of the unstable oscillation modes with $m \neq 0$ (or of one such mode) will be

determined by nonlinear effects and probably by processes involving ejection of lumps of matter with frozen-in field. The latter instability apparently may exist until the field is reduced below some limit value which depends on the oscillation damping factors. An estimate of the instability lifetime τ is obtained if we divide the magnetic energy E_m by the luminosity L. For $E_m \sim 10^{44}$ erg and $L \sim 10^{30}$ erg/sec, we find $\tau \sim 3 \cdot 10^6$ years.

The recurrence frequency of the pulses will be comparable with the angular rotation velocity, since $\omega + m\Omega$ is generally small. Rotation periods from 0.03 to a few seconds are quite likely for neutron stars. A more detailed comparison with experimental data requires further development of the theory.

Bibliography

1. Vandakurov, Yu.B.— ZhETF Letters, 9:133. 1969.
2. Meltzer, D.W. and K.S. Thorne.— Astrophys. J., 145:514. 1966.
3. Vandakurov, Yu. V. —Astronomicheskii Zhurnal, 45:103. 1968.
4. Vandakurov, Yu.V. and E.N. Kolesnikova.— Astronomicheskii Zhurnal, 43:99. 1966.
5. Vandakurov, Yu.V. —Astronomicheskii Zhurnal, 44:786. 1967.
6. Lebedev, N.N. Spetsial'nye funktsii i ikh prilozheniya (Special Functions and Applications).— Moskva, Fizmatgiz. 1963.
7. Durney, B. and A. Skumanich.— Astrophys. J., 152:255. 1968.
8. Hewish, A., S.J. Bell, J.D.H. Pilkington, P.F. Scott, and R.A. Collins.— Nature, 217:709. 1968.

FIELD GENERATION IN MAGNETIC STARS

E. M. Drobyshevskii

There are about a hundred stars with magnetic fields /1/. These are mainly peculiar stars of F2 – B8 types. Their magnetic fields reach a few thousand oersteds. The magnitude and even the direction of the field vary with periods of ~4 – 10 days. These stars possess a thin convective envelope, which disappears for stars of later types /2/. The degree of ionization in the convective zone is high enough to treat the gas as completely ionized.

Plasma acceleration almost invariably involves the development of a certain inertial emf /3/:

$$\vec{E}^{i} = \frac{m_e - f_{ei} m_i}{1 + f_{ei}} \frac{1}{e} \frac{d\vec{V}}{dt}. \tag{1}$$

Here $f_{ei} = \frac{F_e}{F_i}$, where $\vec{F}_{e,i}$ are forces of an arbitrary nature, except electric and friction forces between plasma components, which act on the average on every particle of the particular component (we take $\vec{F}_i \parallel \vec{F}_e$); m_e and m_i are the particle masses.

In the convective zone of stars, the gas is accelerated in various directions. However, only the Coriolis acceleration in the longitudinal direction in rotating stars is capable of producing large-scale effects: because of the temperature difference of the gas in the ascending and descending convective fluxes, the inertial emf's do not fully cancel one another. A certain resultant eddy emf remains.

Convection in stars is characterized by zero total mass flow through a surface of any radius:

$$\xi \rho_1 V_1 + (1 - \xi) \rho_2 V_2 = 0 . \tag{2}$$

Here the subscript 1 refers to ascending gas streams (with relative volume ξ), and 2 to descending gas streams ($p_1 = p_2 = p$, $T_1 - T_2 \ll T_1 + T_2$). The energy flux transferred by convective streams is

$$\pi F_{\kappa} = \xi C_p \rho_1 T_1 V_1 + (1 - \xi) C_p \rho_2 T_2 V_2 = C_p \xi \rho_1 V_1 (T_1 - T_2), \tag{3}$$

where ρ is the gas density, C_p is the heat capacity of the gas.

The current density in a binary mixture of components with different conductivities σ, in the presence of oppositely directed emf's in the two components, falls between the two extreme cases of differently oriented (relative to emf) layer models with the same volume content of the components /4/. The current densities in the layer models are

$$j_{equator} = \xi \sigma_1 E_1 + (1 - \xi) \sigma_2 E_2 , \tag{4}$$

$$j_{\text{merid}} = [\varepsilon E_1 + (1-\varepsilon) E_2] \frac{\sigma_1 \sigma_2}{\sigma_1 + \sigma_2}. \tag{5}$$

Assuming a constant rotation velocity Ω within the convective zone ($dV/dt = 2\Omega V \cos\vartheta$, ϑ is the latitude), and using (1), (2), and (3), we find

$$j_{\text{equator}} = -2\Omega\pi F_k \frac{m_i}{e} \frac{1}{c_0} \frac{a}{dT} \left(\frac{\sigma}{\rho}\right)_p \cos\vartheta. \tag{6}$$

We assumed $1 \leq f_{ei} < \infty$, which corresponds to the case of gas-magnetic or electromagnetic interaction of convective elements with one another. If $\sigma \sim T^{3/2}$, we have $_{\text{equator}} = 2.5 j_{\text{merid}}$. Integration for the case of spherical symmetry gives for the poloidal magnetic field $H \sim \Omega R \pi F_k$.

The data of /2, 5/ were applied to compute the polar magnetic field H_p for the main-sequence stars (see figure).

An adequate fit is observed. Indeed, 1) the computed fields are of the same order of magnitude as the observed fields, 2) the field gradually increases from F0 to A0 stars, 3) the field markedly diminishes from A0 to B9 stars, this being due to the immersion of the outer boundary of the convective zone in the region of the second ionization of helium.

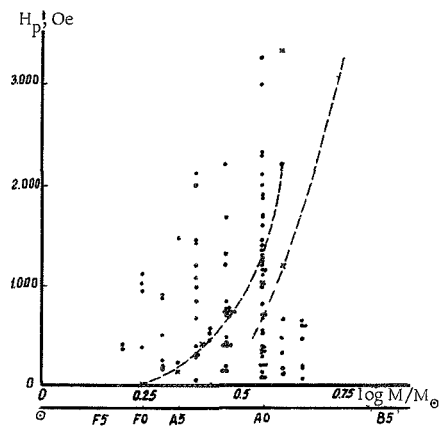

Computed magnetic fields H_p for the pole of main-sequence stars (crosses, dashed lines) and the magnetic fields measured by Babcock /6/ (dots).

Our previous analysis ignored the transient time of the magnetic field. It is generally assumed /7/ that the transient time is comparable to or greater than the lifetime of the star. This is true for stars without mixing. In our case, the main part of the field-generating current is confined to a very thin ($\ell \sim 10^7 - 10^8$ cm) surface skin layer. The time to establish a nearly steady-state current distribution in this thin layer is small ($\tau \approx \frac{\sigma \ell^2}{c^2}$), and most of the time is required to allow the magnetic field to penetrate through the remaining volume of the star. If the stellar matter is in a state of vigorous mixing, the magnetic field is transported together with the mixed matter into the stellar interior. A particularly favorable case in this respect is observed when the convective envelope occupies a large part of the star volume (late-type stars, including the Sun). In double stars (the peculiar stars are probably double stars /8/) vigorous mixing occurs, so that despite the small thickness of the convective envelope in F0 — B8 stars, the magnetic field reaches steady-state conditions in a fairly short time. Finally, mixing may be excited in stars by the magnetic field itself if its configuration is far removed from the configuration corresponding to the steady-state current distribution /9/.

Bibliography

1. Severnyi, A.B.— UFN, 88:3. 1966.
2. Gorbatskii, V.G. and A.K. Kolesov.— Astrofizika, 2:273. 1966.
3. Drobyshevskii, E.M.— ZhTF, 38:1609. 1968.
4. Bursian, V.R. Teoriya elektromagnitnykh polei, primenyaemykh v elektrorazvedke (Theory of Electromagnetic Field in Electrical Prospecting), Part 1.— GTTI, Moskva-Leningrad. 1933.
5. Allen, C.W. Astrophysical Quantities, 2nd edition. London. 1963.
6. Babcock, H.W.— In: "Stellar Atmospheres," ed. J.L. Greenstein, Univ. of Chicago Press. 1960.
7. Cowling, T.G.— M.N., 105:166. 1945.
8. Heuvel, E.P.J. van den.— B. A. N., 19:326. 1968.
9. Kipper, A.Ya.— Trudy IV soveshchaniya po voprosam kosmogonii, p.1425. Moskva, Izd. AN SSSR. 1955.

THE SPECTRUM OF THE EXTRAGALACTIC BACKGROUND RADIATION

R. A. Syunyaev

The observations of optical sources through giant telescopes at the beginning of this century led to the discovery of the red shift in the spectral lines of the distant galaxies and provided a proof of the expansion of the Universe. The next fundamental result which shed some light on the properties of the Universe as a whole was only obtained in 1965: this was the discovery of the relict radiation in the radio spectrum — the remnant radiation of the primeval fireball, carrying information about the early stages of evolution of the Universe. The relict radiation is not associated with individually resolvable sources — this is background radiation. In this paper, we will describe the entire spectrum of the background electromagnetic radiation of the Universe — from radio frequencies to gamma rays (Figure 1), discussing its sources and properties.

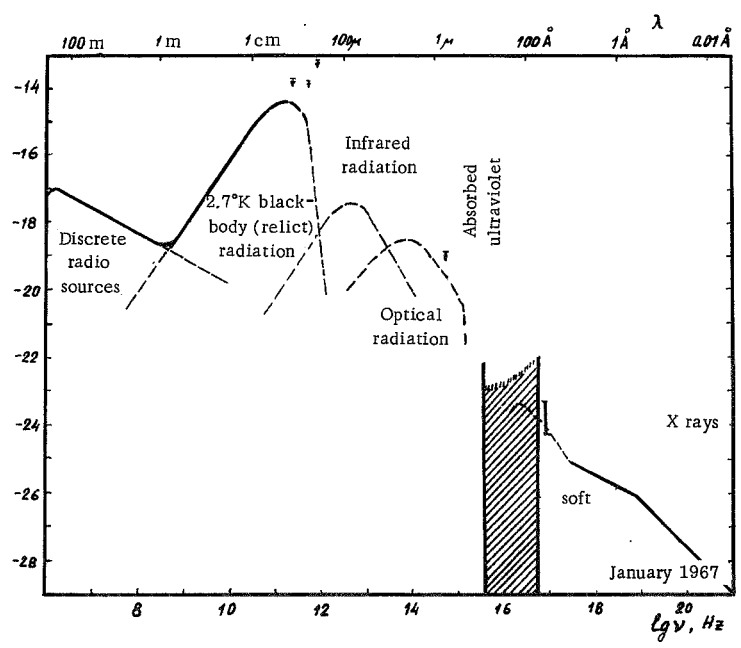

FIGURE 1. The spectrum of the background radiation of the Universe.

The comprehensive description became possible only following the tremendous advances in experimental astrophysics (both in radio astronomy and in the so-called extra-atmospheric — namely ultraviolet, X-ray, gamma-ray, and partly infrared and optical — astronomy).

RADIO FREQUENCIES

The radio spectrum is generally divided into two regions, the long-wave region associated with the total emission of low-power discrete radio sources, and the short-wave region, where relict radiation predominates.

50 cm $< \lambda <$ 300 m, $10^6 < \nu < 6 \cdot 10^8$ Hz

The metagalactic background radiation is very difficult to isolate in this region, since the radio telescopes receive both the true background radiation and the synchrotron radiation of the relativistic electrons in our Galaxy, which apparently accounts for between 60 to almost 100 percent (depending on direction) of the total signal at 1.7 m wavelength. The separation of the extragalactic component was facilitated by the discovery that its spectrum $I_\nu \sim \nu^{-\alpha}$ differs from the radio spectrum of the Galaxy at meter wavelengths. The British radio astronomers /1/ carried out careful measurements at various wavelengths in several directions close to the galactic pole, where the radiation of the Galaxy is minimum. As a result, they succeeded in determining both the spectrum and the intensity of the background radio emission, which at 1.7 m corresponds to a brightness temperature of $T_e = \frac{I_\nu \lambda^2}{2k} = 30 \pm 7°K$. The background is readily accounted for by the radiation from distant discrete radio sources, especially as its spectral index α is 0.75, being equal to the spectral index of most radio galaxies and quasars at these wavelengths. However, the spatial density of galaxies and radio galaxies and their power proved insufficient to ensure the observed background intensity. The situation clarified only after a careful computation of the number of weak (and apparently distant) radio sources carried out by the British radio astronomers. They obtained a curve plotting the number of radio sources with a flux greater than a given value N(s) as a function of the incoming flux s. This curve provided evidence of evolution of the number or the power of radio sources in the past. The density of the powerful radio sources in unit moving volume (moving together with the expanding Universe) or their mean power should be much higher than the present-day figures /2/. At present, we can count weak sources with received fluxes exceeding $s = 10^{-28}$ W/m$^2 \cdot$Hz at 1.7 m; these counts require radio telescopes of tremendous sensitivity, and the number of these sources over the entire sky is over a million, while each (a radio galaxy or a quasar) has an enormous power output. The shape of the curve N(s) is such that the main contribution to the background radiation comes from the weakest sources. This is due to the rapid increase in the number of sources with the decrease in their flux. A dependence of this kind is a clear sign of

evolution. The growth of the N(s) is somewhat slowed down at very low s. This feature is also predicted by the background intensity, which is only slightly higher than the total flux from all the known radio sources.

We have mentioned above that the spectrum of our Galaxy ($\alpha \sim 0.4$) at meter wavelengths differs from the background spectrum ($\alpha \sim 0.75$), so that at longer wavelengths the contribution of the extragalactic component received by the Earth radio telescopes is larger. Measurements at 150 m revealed a surprisingly low intensity, which apparently could not be related to strong absorption in the Galaxy /3/. This effect is probably due to self-absorption in the sources. We can apply it to our purposes to compute the spatial density of radio quanta in the Universe: such a computation would have been unfeasible had the number of quanta continued increasing with wavelength. The density of radio quanta and the energy density of the background radio emission are listed in the table for comparison with other spectral regions.

Density of quanta and energy density of background radiation in various frequency ranges

Frequency range	Energy density, eV/cm^3	Density of quanta, cm^{-3}
Discrete radio source	10^{-7}	1
Relict radiation	0.25	400
Infrared sources	10^{-2}	1
Optical spectrum	$3 \cdot 10^{-3}$	10^{-3}
Soft X-ray spectrum	10^{-4}—10^{-5}	$3 \cdot (10^{-7}$—$10^{-8})$
Hard X-ray spectrum	10^{-4}	$3 \cdot 10^{-9}$

$3 \cdot 10^{-2}$ cm $< \lambda <$ 50 cm, $6 \cdot 10^{8} < \nu < 10^{12}$ Hz

The main contribution to the observed background comes from the relict radiation, whose discovery in 1965 confirmed the validity of the hot model of the Universe /4, 5/. The temperature of the relict radiation is currently known with a 5% accuracy. According to Princeton measurements at wavelengths of 0.86, 1.58, and 3.2 cm, $T = 2.68^{+0.09}_{-0.14}$ °K /6/. Measurements carried out by the same group at 0.33 cm /7/ and indirect determination of the temperature of the relict radiation from the population of the levels of the interstellar CN molecules ($\lambda = 0.264$ cm) /8/ show that the background spectrum at these wavelengths deviates from the straight line and develops a Planckian shoulder. The sensational report /9/ of the discovery of a tremendous radiation flux between $4 \cdot 10^{-2}$ cm and 0.13 cm — almost double the expected flux for the Planckian spectrum (brightness temperature $T_b \sim 8$°K) — was disproved by observations of the level populations of the interstellar molecules CN, CH, CH^+ ($\lambda = 0.132$, 0.0559, 0.0359 cm) /8/. The true intensity and the true spectrum in the Wien region have not been established so far. And yet these measurements are of the highest importance. The spectrum of the relict radiation in the Wien region should be distorted by the interaction of this radiation component with hot intergalactic gas: Compton scattering of the relict

quanta by thermal electrons with temperatures $T_e \gg T_r$ increases the mean energy of the quantum and alters the radiation spectrum /10, 11/. The amount of distortion provides an indication of the time when the secondary, nonequilibrium ($T_e \gg T_r$) heating of the metagalactic plasma occurred. Modern experimental data confirm that the recombination of hydrogen in the Universe ($t \sim 10^{13}$ sec, red shift $z \sim 1500$) was followed by a period of neutral hydrogen and that the metagalactic gas was not always ionized.

Relict radiation also carries information about the earlier stages of the evolution of the Universe ($t \ll 10^{13}$ sec). The point is that even before the recombination of hydrogen in the Universe, the primary plasma and radiation were not maintained in a perfect thermodynamic equilibrium: radiation and matter had the same temperature, the electrons showed a Maxwellian velocity distribution, but the characteristic time of the slowing-down process exceeded the cosmological time for the relevant period. Therefore, if a large quantity of energy were to be released for some reason at that time, the radiation spectrum would be distorted. The radiation energy would increase in such a case, whereas the number of quanta would remain the same because of the slow slowing-down processes. In other words, no Planckian distribution would be obtained. Compton scattering of quanta by electrons establishes a Bose-Einstein distribution $I_{B-E} \sim x^3/(e^{x+\mu}-1)$ rather than the Planckian distribution $I_P \sim x^3/(e^x - 1)$, where $x = h\nu/kT$. For $x < \mu < kT$, these distortions become significant, $I_{P-E} \sim x^3$, whereas the Rayleigh–Jeans law gives $I_P \sim x^2$. The absence of pronounced distortions of the relict radiation spectrum in the Rayleigh–Jeans region imposes definite restrictions on the velocities of turbulent motion in the Universe, precludes the existence of antimatter regions in the Universe, and provides a powerful argument in favor of charge asymmetry of the Universe /12/. Possible deviations from the Planckian curve are shown in Figure 2.

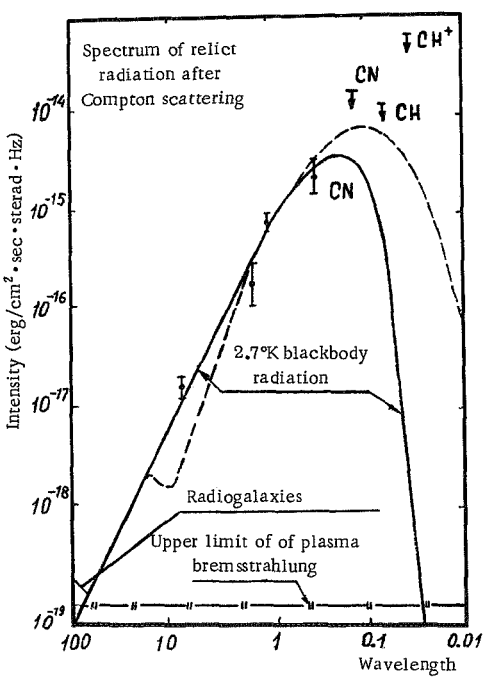

FIGURE 2. Possible distortions of the relict radiation spectrum (dashed curve).

INFRARED RADIATION

In this region ($3\mu < \lambda < 300\mu$, $10^{12} < \nu < 10^{14}$ Hz), no direct measurements of the background radiation are available, but a wide class of objects

are known with a maximum at the infrared. These are both galactic sources, such as the Crab Nebula and the galactic center region, and extragalactic sources, including normal galaxies, Soifert galaxies, and N-galaxies, as well as quasars. No accurate estimate of the background from these sources can be obtained at present, since neither the number nor the luminosity function is known. Order of magnitude estimates were made by Low and Tucker /13/; their results are shown in Figure 1 and in the table.

OPTICAL RADIATION

For this region ($3000\,\text{Å} < \lambda < 3 \cdot 10^4\,\text{Å}$, $10^{14} < \nu < 10^{15}$ Hz), observers only give the upper limit of the background radiation intensity $I_\nu < 1.3 \cdot 10^{-19}$ erg/cm^2 · sec · sterad · Hz at 5560 Å /14/. The extragalactic component is very difficult to isolate against the background of the Earth's atmospheric radiation, zodiacal light (solar light scattered by interplanetary dust), and the light of the stars in our Galaxy, which produce a flux 100 times as high as the expected luminous flux from the normal galaxies and almost one order of magnitude higher than the above upper limit figure. The upper limit was derived by eliminating the atmospheric contribution, which is a function of the angle and the time of observation, and making measurements at wavelengths corresponding to Fraunhofer absorption lines in the solar spectrum and in the spectrum of the zodiacal light, so as to reduce the interplanetary intensity. The main contribution to the background radiation of the Universe in the optical spectrum is apparently due to the normal galaxies. The expected spectrum /14/ is shown in Figure 1. Improved data for the background radiation at these wavelengths would enable us to fix significant constraints for the evolution of galaxies and their luminosities in the past.

ULTRAVIOLET RADIATION

This spectral region can be divided into two parts: the right-hand part is accessible only to observations from satellites and rockets outside the atmosphere, and the left-hand part which cannot be observed from inside the solar system.

$912\,\text{Å} < \lambda < 3000\,\text{Å}$, $10^{15} < \nu < 3.3 \cdot 10^{15}$ Hz

The only experimental measurements are the data of Kurt /15/ based on the material collected by the VENUS spacecraft:

$$I_\nu < 10^{-21}\ \text{erg/cm}^2 \cdot \text{sec} \cdot \text{sterad} \cdot \text{Hz at } \lambda = 1300\,\text{Å}.$$

These measurements also provide an estimate of the integrated luminosity of stars in our Galaxy, $L \sim 10^{40}$ erg/sec for $1225\,\text{Å} < \lambda < 1340\,\text{Å}$ /16/ and establish an upper limit for the energy density ($W < 10^{-3}$ eV/cm^3) of subcosmic particles with energies of the order of 100 keV in the interstellar medium.*

Only the hot stars emit in this region, and the expected background from the normal galaxies is therefore several orders of magnitude lower than the above upper limit. The main contribution is apparently from the emission of the hot intergalactic gas.

$50\,\text{Å} < \lambda < 912\,\text{Å}$, $3.3 \cdot 10^{15} < \nu < 6 \cdot 10^{16}$ Hz

This region of the background radiation spectrum of the Universe is fundamentally inaccessible to direct observations from inside the solar system because of the absorption of the ultraviolet quanta by the interstellar neutral hydrogen. When absorbed, the background radiation creates ionization zones around galaxies, not unlike the Stromgren zones near hot stars. The available observations of galaxies at 21 cm reveal the presence of neutral hydrogen far beyond the optical limits of galaxies. The density of hydrogen and the number of atoms along the line of sight in the peripheral regions of galaxies are exceedingly low, and this hydrogen is fully ionized for background radiation intensities exceeding $I_\nu = 10^{-23}$ erg/cm^2 sec · sterad near 912 Å (this corresponds to 10,000 ionizing quanta for each cm^2 of the surface of galaxies each second) /18/. An estimate of the density of the intergalactic gas based on this result is given below.

X-RAY RADIATION

The observed spectrum of the hard X-ray background radiation may be fitted with two power functions, $I_\nu \sim \nu^{-\alpha}$, with $\alpha = 0.7$ between 1.5 and 40 keV and with $\alpha = 1.2$ for $E > 40$ keV. The latter slope does not change up to around 1 MeV. For $E < 1.5$ keV, only measurements at 40 – 70 Å are available /19, 20/ (the effective energy corresponding to these wavelengths is $E_{ef} \sim 270$ eV). The exact flux value in this region is not known because of the uncertainty in the absorption corrections in the Galaxy. However, even without correcting for absorption, the soft X-ray flux is seen to be higher than the value expected on the basis of extrapolation from the hard region.

Measurements of the X-ray background provided fundamentally new information about the properties of the hot intergalactic gas (observations at 21 cm and the conspicuous absence of the absorption band corresponding to the L_α line in the spectra of distant quasars show that the intergalactic gas should be highly ionized and have a high temperature).

* Nonresonant charge exchange between a subcosmic proton and the atoms of neutral hydrogen in the interstellar medium produces a fast excited atom, which emits L_α quanta of Doppler-shifted frequency. The estimates of /17/ impose certain restrictions on the intensity of this radiation, and there is thus a way to determine the upper limit of the density of subcosmic particles.

The transparency of the intergalactic gas for 270 eV quanta indicates that the helium in this gas (the content of helium in the primordial matter in the "hot" model of the Universe is fixed at 30 wt.%) is completely ionized, which is possible only at temperatures $T > 10^5$ °K. At the same time, if the density of the intergalactic gas is of the order of the critical density $\rho_{crit} = \frac{3H_0^2}{8\pi G} = 2 \cdot 10^{-29}$ g/cm^3, its temperature may not exceed 10^6 °K, since otherwise the emission of the intergalactic gas in the X-ray region would exceed the observed background radiation. This is quite clear, since the bremsstrahlung intensity of an optically thin gas layer is proportional to $T^{-1/2} e^{-h\nu/kT} \rho^2$ rapidly decreasing with the increase in the ratio $h\nu/kT$. A gas heated to $10^5 - 10^6$ °K will mainly lose energy in the form of quanta with $h\nu \sim kT$, i.e., in the ultraviolet range. The above restriction on the intensity of the ultraviolet background radiation in the Universe sets an upper limit on the emission of the intergalactic gas, and as it is proportional to the square of the gas density, we obtain an upper limit value for the density of the intergalactic gas $\rho < 1/3 \rho_{crit}$ /18/. It follows in particular, that the intergalactic gas is definitely not the source of the observed soft X-ray background radiation.

Since the hard X-ray radiation is described by a power spectrum, the radiation is generally assumed to originate in extragalactic objects or in the intergalactic space as a result of energy redistribution between low-energy quanta and relativistic electrons with a power spectrum formed by Compton scattering. Radio galaxies hardly can be regarded as the main source of relativistic electrons. If this were so, only one thousandth of the energy released by radio galaxies would fall in the radio spectrum. As we see from the table, the energy density of the X-ray background quanta is 1000 times the energy density in the long-wave part of the radio spectrum, associated with radio sources. Moreover, this mechanism would not produce the observed break in the X-ray spectrum.

Longair and the author proposed a model which explains the principal features of the X-ray background radiation in the soft and the hard region. This model associates the sources of relativistic electrons with the nuclei of extragalactic objects, which are sources of infrared radiation. Compton scattering of the infrared radiation by relativistic electrons is responsible for the generation of the hard part of the X-ray background spectrum. The break in the spectrum occurs when the high-energy electrons lose their entire energy on being scattered by the infrared quanta (in this process $\frac{dE_e}{dt} \sim E_e^2$) and change their spectrum, whereas the lower-energy electrons escape into the intergalactic space having lost only part of their energy and without changing the spectrum. Then these electrons scatter quanta of the relict radiation, whose mean energy is one order of magnitude lower than the energy of the infrared quanta, and soft X-ray quanta are produced in this way. We see from the table that to ensure the observed intensity of the X-ray background, only 1% of the energy converted in the nuclei of galaxies into infrared radiation should be released in the form of relativistic electrons. So far, no reliable measurements have been made of the background radiation in the gamma-ray spectrum ($E \gg 1$ MeV). This range probably carries valuable information about metagalactic cosmic rays.

Bibliography

1. Bridle, A.N.— Monthly Notices Roy. Astron. Soc., 136:219. 1967.
2. Longair, M.S.— Monthly Notices Roy. Astron. Soc., 133:421. 1966.
3. Bridle, A.N.— Nature, 219:136. 1968.
4. Zel'dovich, Ya.B.— UFN, 89:647. 1966.
5. Zel'dovich, Ya.B. and I.D. Novikov. Relyativistskaya astrofizika (Relativistic Astrophysics).— Moskva, Izdatel'stvo "Nauka." 1967.
6. Wilkinson, D.T.— Phys. Rev. Lett., 19:1195. 1967.
7. Broynton, P.E., R.A. Stokes, and D.T. Wilkinson.— Phys. Rev. Lett., 21:462. 1968.
8. Bortolot, V., J.F. Clauser, and P. Thaddeus.— Preprint. 1968.
9. Shivanandan, K., J.R. Houck, and M.O. Harvit.— Phys. Rev. Lett., 21:1460. 1968.
10. Weymann, R.— Astrophys. J., 145:560. 1966.
11. Zel'dovich, Ya.B. and R.A. Syunyaev.— Preprint, IMP. 1968.
12. Zel'dovich, Ya.B. and R.A. Syunyaev.— Preprint, IMP. 1969.
13. Low, S.J. and W.N. Tucker.— Phys. Rev. Lett., 21:1538. 1960.
14. Peebles, P.J.E. and R.B. Partridge.— Astrophys. J., 148:713. 1967.
15. Kurt, V.G. and R.A. Syunyaev.— Kosmicheskie Issledovaniya, 5:573. 1967.
16. Kurt, V.G. and R.A. Syunyaev.— Astronomicheskii Zhurnal, 44:1157. 1967.
17. Kurt, V.G. and R.A. Syunyaev.— ZhETF Letters. 1968.
18. Syunyaev, R.A.— Astronomicheskii Zhurnal. (In press); Astrophys. Lett., 3:33. 1969.
19. Bowyer, C.S., G.B. Field, and J.E. Mack.— Nature, 217:32. 1968.
20. Henry, R.C., G. Fritz, J.E. Meekins, H. Friedman, and E.T. Byram.— Astrophys. J., 153:L11. 1968.

COMPUTATION OF THE OPACITY OF STARS WITH ALLOWANCE FOR LINE ABSORPTION

A. F. Nikiforov and B. V. Uvarov

The opacity of stellar matter has a significant effect on the structure of stars, since the main mechanism of energy transfer in stars is in the form of radiant energy. In the stellar interior, where the diffusive approximation is applicable to the equation of radiative transfer, the radiant energy flux is expressed in terms of the Rosseland photon mean free path.

At a given temperature and density, the Rosseland free path is obtained by averaging, with a certain weight, the free paths $l(\omega)$ computed for fixed photon frequencies ω. The free path $l(\omega)$ is determined by the effective scattering and absorption cross sections of electrons for the respective photons. The most significant factors are Compton scattering, line absorption, photoionization, and bremsstrahlung absorption. Until recently, stellar opacity computations were made using photoionization and bremsstrahlung absorption only. Keller and Meyerott's tables computed in this approximation for a number of mixtures in a wide range of temperatures and densities have found extensive uses in astrophysics. Although the frequency-integrated absorption cross sections of lines are comparable with the photoionization cross sections, the discrete-discrete transitions were ignored. However, the very first computations of opacity with allowance for line absorption indicated that in the astrophysically relevant range of temperatures and densities, the Rosseland mean free path may decrease to $1/3 - 1/5$ of the earlier value as a result of line absorption. These computations were carried out in the USA by A. Cox and co-workers /1 – 2/ and very recently by T. Carson et al. in England /3 – 4/.

The effect of discrete-discrete transitions on the opacity of stellar matter is attributable to the presence of relatively heavy elements in stars, whose atoms at high temperatures have a large number of states with various degrees of ionization and excitation. As a result, the spectrum shows thousands of lines at different frequencies. Moreover, ions with a given electron occupancy of the levels have different systems of lines depending on the position of the nearby ions and the resulting Stark splitting. Other factors may also cause line broadening. They include various processes which reduce the lifetime of an ion in a given state of excitation: collisions of the ion with free electrons, interaction of the ion with the electromagnetic radiation field, Auger effect. Frequency shift associated with the thermal motion of ions leads to Doppler broadening.

Since the results obtained by Cox and Carson for the Rosseland mean free path are markedly divergent (by a factor of 2 – 3), we will try to analyze in some detail each of the computation methods. The physical approach to the problem and the allowance for the various effects influencing the stellar opacity are nearly the same in the work of Cox and that of

Carson. The main difference is in the particular methods used for the determination of the electron wave functions of the continuous and the discrete spectrum, the electron energy levels, and the chemical potential of the electrons.

Cox used a model with constant density of free electrons, and the wave functions were those of the hydrogen-like atom, determined with the aid of Slater's semiempirical screening constants. One of the principal shortcomings of Cox's procedure is that the occupancies of the electron shells are highly sensitive to the choice of the screening constant, which on the other hand cannot be determined with sufficient reliability. Moreover, in computing the electron energies, Cox ignored external screening created by bound electrons, which in some cases may be quite significant.

Carson's recent study /3/ using the Thomas—Fermi self-consistent potential /5/ is free from these shortcomings. Carson /4/ therefore considers his results as the first serious attempt to overcome the shortcomings of the hydrogen-like model in opacity computations. Carson's results, however, are adversely affected by a number of significant errors in the physical formulation of the problem, which are associated with improper application of the Thomas—Fermi model. One of the basic errors is the clearly wrong choice of the conditions of thermodynamic equilibrium for the various mixture components in the computation of the Thomas—Fermi potential of each atom in the stellar mixture. In thermodynamic equilibrium, the chemical potentials of the electrons for each component should be constant, and at the boundaries of atomic cells /5/, where the electrons are not affected by Coulomb forces, the free electron density in case of equal chemical potentials will be the same for each mixture component, as is physically proper. Carson, on the other hand, described thermodynamic equilibrium in terms of equal total pressures of electrons and atoms of each element at the boundaries of the atomic cell. As a result of this definition, the free electron density is discontinuous at the atomic cell boundaries in Carson's model. Another reason why the total pressure at the cell boundaries may not be equal is that thermodynamic equilibrium of electrons, because of their high velocities compared to the velocities of the nuclei, is established over a length of time during which the nuclei remain virtually stationary, so that in fact we may speak of the thermodynamic equilibrium of electrons for fixed nuclei.

We carried out some opacity computations illustrating the importance of this effect. Even without line absorption, our results sometimes differ from Carson's figures by as much as a factor of 2, and on the whole are closer to the results of Cox, although in individual instances there is a difference of about 50% between the two sets of data. The computations were carried out for a mixture of the following composition (mixture 1 in /3/):

Element	z	m_i
H	1	0.7440
He	2	0.2360
C	6	0.0007
N	7	0.0029
O	8	0.0057
Ne	10	0.0070
Al	13	0.0015
Si	14	0.0013
Fe	26	0.0009

(m_i is the weight fraction of the element).

The following results were obtained:

T	ρ	k	k_1	k_2
0.1	0.2017	63	106	54
0.3162	0.0627	1.37	2.66	1.54
0.3162	0.629	6.44	8.00	6.43

Here T is the temperature of the mixture, keV; ρ is the density, g/cm^3; k, k_1, k_2 are the opacities, in cm^2/g, computed by the present authors, by Carson /3/, and by Cox /1/, respectively. Note that /3–4/ also contain a number of other errors. For example, the Fermi–Dirac statistics is improperly used in the case of strong degeneracy of matter.

Let us briefly describe the procedure used in our computations. To compute the effective photon absorption and scattering cross sections, we require 1) the electron wave functions of the continuous and the discrete spectrum and the energy levels of the bound electrons; 2) the mean occupancies of the electron states and the mean degree of ionization of matter; 3) the probability distribution of various occupancies of the electron states; 4) the probability distribution for various electric field strengths set up by the ions; 5) the shape and the position of the spectral lines.

Since the Thomas–Fermi statistical model for given temperature and density is sufficiently accurate and convenient at high temperatures, we computed the electron wave functions in the first approximation using the Schroedinger equation with the Thomas–Fermi potential. The Thomas–Fermi potential was found using the procedure described in /6/. The electron states within an atomic cell can be classified, depending on the electron energy, into the states of the discrete and the continuous spectrum or intermediate states. An analysis has shown that the electrons of the intermediate group are relatively few under the relevant conditions, and they may be lumped with the electrons of the continuous spectrum. An approximate method, which may be called the test potential method, has been proposed for the determination of the discrete energy levels and the corresponding wave functions $R_{nl}(r)$ /7/. Using this method, we analyzed the applicability of the hydrogen-like wave function. The method was tested on a large number of problems and the results proved to be inadequate agreement with those obtained by a direct solution of the Schroedinger equation by the phase method /8/. The wave functions of the continuous spectrum were also found without numerical integration of the Schroedinger equation. An improved WKB approximation /9/ was found to ensure adequate accuracy, the vicinity of turning points included. The Coulomb wave functions proved to be a poor approximation for the continuous spectrum.

The mean occupancies for the discrete-spectrum electrons were determined according to the Fermi–Dirac statistics. Note that the application of the Fermi–Dirac statistics to the atomic electrons is by no means trivial, since we are dealing with a system of interacting particles, and not with an ideal gas in an external field. It can be shown that the Fermi–Dirac statistics is applicable to the atomic electrons.

A binomial distribution was used for the occupancies /3/. This distribution is derived from the Gibbs distribution for subsystems with a

variable number of particles when the deviations of the occupancies from the mean values are small.

The position of the spectral lines was determined with allowance for relativistic effects and line shift due to fluctuations of the electron occupancies. Effects associated with deviations of the self-consistent field from central symmetry were ignored, as in /1 – 4/.

The effective photon absorption cross sections were computed in the nonrelativistic dipole approximation. Since the photoionization formulas can be obtained in the limit from expressions for the line absorption cross sections, discrete-discrete transitions were effectively taken into consideration for overlapping lines using the corresponding expressions for the photoionization cross sections. Therefore, in some cases, the discrete-discrete transitions could be taken into consideration for small values of the principal quantum number n only. Since the Stark splitting markedly diminishes with the decrease in n, the Stark effect could be ignored in some cases. Since the effect of line shape on opacity is not very pronounced, Lorenzian line contours were used, as in / 1 – 4/ . The line widths were computed using the electron wave functions.

In conclusion, we would like to acknowledge the help of A.A. Samarskii, who actively participated in discussions, and Yu.N. Babaev and E.S. Fradkin, who suggested the original problem.

Bibliography

1. Cox, A.N. Stellar Structure (ed. G. Kuiper), p. 195. Chicago, London. 1965.
2. Cox, A.N., J.N. Stewart, and D.D. Eilers.– Astrophys. J., Suppl., 11(94):1. 1965.
3. Carson, T.R., D.F. Mayers, and D.W.N. Stibbs.– Monthly Notices, Roy. Astron. Soc., 140:483. 1968.
4. Carson, T.R. and H.M. Hollingsworth.– Monthly Notices, Roy. Astron. Soc., 141:77. 1968.
5. Feyman, R., N. Metropolis, and E. Teller.– Phys. Rev., 75:1561. 1949.
6. Nikiforov, A.F. and V.B. Uvarov.– ZhVM i MF, 9. 1969. (In press).
7. Nikiforov, A.F. and V.B. Uvarov.–ZhVM i MF, 1:177. 1959.
8. Uvarov, V.B. and V.I. Aldonyasov.– ZhVM i MF, 7:436. 1967.
9. Schiff, L. Quantum Mechanics. – New York, McGraw-Hill. 1955.

CHARGE SYMMETRY OF THE UNIVERSE

N. A. Vlasov

Dirac's theory and the discovery of antiparticles established the existence of charge symmetry in nature. A universe consisting of protons and electrons is definitely asymmetric, since the positive charge is associated with a heavy particle, whereas the negative charge is associated with a light particle. The discovery of the positron and the antiproton proved the existence of charge-conjugate antiparticles: both the positive and the negative charges are associated with particles of equal mass. Every charged particle has an oppositely charged antiparticle. The charge conjugation operation, moving a particle into its antiparticle, is universal, and the fundamental laws of nature governing the transformations of elementary particles are therefore charge independent, or in other words they possess charge symmetry.

Particles and antiparticles are created and annihilated in pairs, and matter consisting of particles of a finite rest mass could be created some time in the past by the process of pair production. As a result charge symmetry may be characteristic of the Universe as a whole. Charge symmetry of the Universe would indicate that on the whole it is neutral: the total charge of particles and antiparticles in the Universe is zero. This charge neutrality of the Universe does not follow from the charge symmetry of the elementary reactions: it should be proved separately, or adopted as an independent starting hypothesis.

Neutrality of electric charge is essential in a homogeneous and isotropic Universe. If the total electric charge of matter were different from zero, an electric field would result which would violate the isotropy of space. The exact equality of the proton and the electron charge (in absolute value) was considered in connection with the problem of the electric neutrality of the Universe. If the proton charge e_p is not quite equal to the electron charge e_e, i.e.,

$$e_p = -(1+y)\, e_e, \text{ for } y \neq 0,$$

the resultant charge of a system containing protons and electrons in equal number is no longer zero and Coulomb repulsion arises between the individual elements. For $y = 0.9 \cdot 10^{-18}$, the gravitational attraction of the hydrogen atoms will be fully compensated by the Coulomb repulsion. The value of y can be estimated from certain astrophysical observations, e.g., from the magnetic moments of rotating celestial bodies. The magnetic moment of the Earth gives $y \leqslant 2 \cdot 10^{-19}$. Laboratory measurements of y in experiments

passing beams of neutral atoms and molecules through strong transverse electric fields yielded even lower upper limits. The neutron charge, which should be $|ye|$ if the charge conservation in the reaction $n \rightarrow p + e$ is exact, was found to be $|e_n| < 3 \cdot 10^{-20} e$ /2/. The non-deflection of a beam of SF_6 molecules yields $y < 2 \cdot 10^{-22}$. Thus, if we assume that the Universe is isotropic and homogeneous and the electric charge is conserved, we are inevitably led to the conclusion that the Universe is electrically neutral.

No such conclusion can be reached regarding the baryon charge, however. No long-range forces with a potential of the form $u \sim 1/r$ are known for the baryon charge. Therefore, neutrality with regard to the baryon charge does not clash with the isotropy of the Universe. If the hot model is valid, the Universe in a state of high density and temperature ($kT \simeq M_p c^2$) was very close to neutrality or was simply neutral with regard to the baryon charge. In this state, the bulk of matter was represented by baryon — antibaryon pairs in a state of thermodynamic equilibrium with radiation. As the Universe expanded, these pairs annihilated. The residual matter in the present-day Universe comprises $10^{-8} - 10^{-9}$ of the annihilated matter in the hot Universe. Even if the residual matter displays baryon charge asymmetry, i.e., there is no antimatter in the present-day Universe, the asymmetry of the hot Universe, for $kT \simeq M_p c^2$, was truly negligible, the relative excess of baryons over antibaryons having been of the order of $10^{-8} - 10^{-9}$. The assumption of perfect symmetry under the hot Universe conditions is naturally more attractive, although it is not indispensible. Thus Zel'dovich and Novikov /3/ assume that there is in fact an excess of baryons over antibaryons in the hot state, so that further evolution gives a Universe with distinct matter asymmetry.

The assumption of charge neutrality in the hot Universe admits of different evolutionary alternatives in the course of expansion. Sakharov covered this topic in his paper at the GAISh* seminar in January 1969 in Moscow and in /4/. To derive the present-day asymmetric Universe from the charge-neutral hot state, Sakharov postulates that at the stage of quark-to-baryon conversion, there occur certain reactions which are asymmetric with regard to the baryon charge, in the same sense that the following decays are asymmetric:

$$K_2^0 \begin{cases} \pi^- \mu^+ \nu \\ \pi^+ \mu^- \bar{\nu} \end{cases} \quad \text{and} \quad K_2^0 \begin{cases} \pi^- e^+ \nu \\ \pi^+ e^- \bar{\nu} \end{cases} .$$

Both decay modes are relatively unlikely compared to the fundamental decay $K_2^0 \rightarrow 3\pi$. The two branches of each of these decay modes are charge-conjugate and should have the same probability if the combined CP parity is conserved. In fact, however, the first branches (with μ^+ and e^+) are about 0.5% more probable than the second branches (with μ^- and e^-) /5, 6/.

The asymmetry of these decays incidentally points to a fundamental difference between matter and antimatter. If radio astronomers were to establish communication with a distant civilization, this asymmetry would enable them to identify whether the planet of our counterparts consists of matter or antimatter. To this end, it suffices to inquire what electrons are more numerous in their atoms — those which are more numerous in K_2^0 decay or those which are fewer in this decay.

* [GAISh — The Shternberg State Astrophysical Institute.]

If the answer is that the former is true, our counterparts exist in an antimatter world.

The above examples of CP-asymmetric decays, however, have no bearing on the subject of the baryon charge: for all the particles taking part in these decays, the baryon charge is zero. Therefore, the non-conservation of CP-parity in K_2^0 decay is not sufficient to indicate the existence of reactions which are asymmetric relative to the baryon charge. This evidence only spurs us to examine this possibility. There is always a possibility that the interaction is CP-noninvariant in K_2^0 decays or that another similar interaction is responsible for the asymmetry of quark-to-baryon conversions. Assuming a certain type of such asymmetric reactions, Sakharov derived in the final state a Universe in which all the visible matter carried positive baryon charge, whereas the negative baryon charge was confined to the invisible electrically neutral antiquarks. The total baryon charge was zero. In the first version, Sakharov assumed compensation of the baryon charge of matter by the muon charge of the muonic neutrino, but this variant proved to be inconsistent with baryon charge conservation, which had been established with very high accuracy. It is a known fact that nucleon decays forbidden for reasons of baryon charge conservation are characterized by times greater than 10^{28} years /7/. The second version of Sakharov's hypothesis does not contradict the baryon charge conservation, but it leads to a mass of unobservable antiquarks which is markedly greater than the mass of visible matter (approximately by a factor of 40). There are three antiquarks for each nucleon, and their mass is approximately one order of magnitude higher than the nucleon mass. It is hard to visualize how this tremendous invisible mass can be fitted into the Universe.

Sakharov's hypotheses constitute an interesting exercise the purpose of which is to reconcile the charge neutrality of the hot Universe with the present state in which antimatter (in the form of aggregations of antinucleons) is assumed to be absent. Both Sakharov's hypothesis of the asymmetry of quark-to-baryon conversions and Zel'dovich's hypothesis of the aboriginal charge asymmetry of the Universe are motivated by the assumption that the present-day Universe contains no antimatter objects (antigalaxies, antistars, etc.).

If we assume charge symmetry of the present-day Universe, its total charge will be zero, so that matter and antimatter objects on the average will be equiprobable, though definitely separated in space. We will then have, first, to find suitable mechanisms for separation of matter from antimatter and, second, to explain the total lack of observational evidence pointing to the existence of antimatter.

The separation of matter and antimatter constitutes an unsolved problem within the framework of the hot model and should be further investigated. Some separation mechanisms, however, have been proposed already. Konstantinov /8/ suggests that the existence of magnetic fields in the symmetric plasma is a basic premise for separation of matter and antimatter. In an inhomogeneous magnetic field, charged particles wind onto the magnetic lines of force and also "drift" in the transversal direction. This drift occurs in opposite directions for particles and antiparticles, as it is determined by the electric charge sign.

Separation in combined gravitational and electromagnetic fields was discussed by Alfvén /9/. The gravitational field exerts a different force on the heavy (protons and antiprotons) and the light (electrons and positrons) components of the symmetrical plasma. If the plasma is in thermodynamic equilibrium, a homogeneous gravitational field produces an exponential variation of density "with altitude." The exponential argument for the heavy component is a factor of 1836 higher than for the light component, as it is proportional to the particle mass. The heavy component is therefore concentrated "at the bottom," and in a certain region of space a transition is observed from a predominantly heavy plasma to a predominantly light plasma. If there is moreover an electrical field with a component normal to the interface of the two regions, it will displace the electrons and protons (or the positrons and antiprotons, depending on the field direction) one toward the other. The electrical field may be generated by a nonstationary magnetic field. Thus an excess of matter or antimatter will arise near the interface; in other words, separation of a symmetrical plasma has occurred.

Neither of these separation mechanisms can be immediately related to the conditions of the very dense plasma in the hot Universe. In this ultra-dense plasma, however, it suffices to ensure separation of a very small fraction ($\sim 10^{-8} - 10^{-9}$) of matter and antimatter in order to form the present-day Universe with equal numbers of galaxies and antigalaxies, or stars and antistars. If there is a mechanism capable of achieving this separation, the present-day Universe need not be regarded as asymmetric, and our task is to establish the exact manifestation of symmetry: are there galaxies and antigalaxies, or are the galaxies themselves symmetric and there are stars and antistars in equal numbers.

With regard to observations which are interpreted as evidence against the existence of antimatter, we would like to call attention to a common inconsistency which probably leads to the excessively pessimistic outlook. For example, the intensity of gamma rays accompanying particle-antiparticle annihilation may give the averaged product of proton and antiproton densities $\overline{p^+p^-}$ along the line of sight. The result obtained for this product is divided by the known value of p^+, and the quotient is regarded as the average density of p^-. This approach ignores the space separation. If the separation of matter and antimatter is complete, we have $\overline{p^+p^-} = 0$ for all p^+ and p^-. Despite the prevailing opinion, there are actually no firm data which prove the absence of antimatter even in our Galaxy, let alone in other galaxies. Among observations which are consistent with the possible existence of antimatter in the Galaxy, we should mention the observation of Clark et al. /10/ who discovered a gamma-ray flux with energies greater than 100 MeV from the plane of the Galaxy, and especially from its center. If the Galaxy has charge symmetry, matter—antimatter collisions leading to annihilation and emission of gamma quanta in pion decay are most probable in its center!

Bibliography

1. Hughes, V. W.—In: "Gravitation and Relativity", H.-Y. Chiu and W. F. Hoffman, editors.—N. Y., W. Benjamin. 1964.

2. Shull, C.G., K.W. Biliman, and F.A. Wedgwood.— Phys. Rev., 153:1415. 1967.
3. Zel'dovich, Ya.B. and I.D. Novikov. Relyativistskaya astrofizika (Relativistic Astrophysics).— Moskva, Izdatel'stvo "Nauka." 1967.
4. Sakharov, A.D.— ZhETF Letters. 1969. (In press).
5. Dorfan, D., J. Enstrom, D. Raymond, M. Schwartz, S. Wojcicki, D.N. Miller, and M. Paciotti.— Phys. Rev. Lett., 19:987. 1967.
6. Bennet, S., D. Nygren, H. Saal, J. Stenberger, and J. Sunderland.— Phys. Rev. Lett., 19:993. 1967.
7. Gurr, H.S., W.R. Kropp, F. Reines, and B. Meyer.— Phys. Rev., 158:1321. 1967.
8. Konstantinov, B.P., M.M. Bredov, A.I. Belyaevskii, and I.A. Sokolov.— *Kosmicheskie Issledovaniya*, 4:66. 1966.
9. Alfven, H.— Arkiv Fys., 23:187. 1963.
10. Clark, G.W., G. Garmier, and W.L. Kraushaar.— Astrophys. J., 153:L203. 1968.

GAMMA-RAY MEASUREMENTS FROM KOSMOS-135 SATELLITE WITH A VIEW TO POSSIBLE DETECTION OF ANTIMATTER METEOR STREAMS

B.P. Konstantinov, R.L. Aptekar', M.M. Bredov, S.V. Golenetskii, Yu.A. Gur'yan, V.N. Il'inskii, E.P. Mazets, and V.N. Panov

The possible existence of antimatter in the Universe has been repeatedly discussed in the literature in various forms over a number of years. A hypothesis of the antimatter constitution of comets and the associated meteor streams was advanced, among other things. Experiments intended to check this hypothesis were described in /1, 2/. These experiments measured the correlation between the intensity of the hard gamma quanta and neutrons at altitudes of 12 – 18 km in conjunction with the entry of individual meteors into the atmosphere. The results obtained seem to point in favor of the antimatter hypothesis.

To substantiate the hypothesis, we naturally need more than one independent piece of evidence. One of the possible ways of verifying the antimatter hypothesis is by observing the integrated fluxes of annihilation radiation which may arise in the upper atmosphere under the impact of antimeteors. Measurements of the intensity of the electron-positron annihilation radiation in the epochs of the Geminids, Ursids, and Quadrantids were carried out from KOSMOS-135 as part of the general study of the gamma-ray spectra and intensities in the Earth space.

EQUIPMENT AND MEASUREMENT TECHNIQUE

The KOSMOS-135 satellite was launched on 12 December 1966 into an orbit with the following parameters: apogee height 662 km, perigee height 259 km, orbit inclination 48.5°, orbital period 93.5 min. The satellite was equipped with a scintillation gamma spectrometer (Figure 1) and a 64-channel pulse amplitude analyzer which measured the spectra of gamma quanta between 0.3 and 2.5 MeV. The spectrometer also carried out integrated measurements of the gamma-ray counting rates at 0.4 – 0.6 MeV and 0.6 – 2.5 MeV and measured the counting rate of charged particles (electrons with $E_e \geqslant 1.5$ MeV and protons with $E_p \geqslant 27$ MeV).

The "phoswich" scintillation detector of the spectrometer consisted of a 40×40 mm NaI(Tl) crystal surrounded by a shielding plastic scintillator. The spectrometer also incorporated a pulse shape discriminator

circuit, which separated between gamma quanta and charged particles, a 64-channel pulse amplitude analyzer, a two-channel differential analyzer for measuring the counting rates of gamma quanta in a wide energy interval, and other electronic devices essential for automatic functioning of the equipment /3/. Detector shielding does not exceed 0.8 g/cm^2 Al in a solid angle equal to 80% of 4π. The spectrometer resolution is 13% for the 661 keV line.

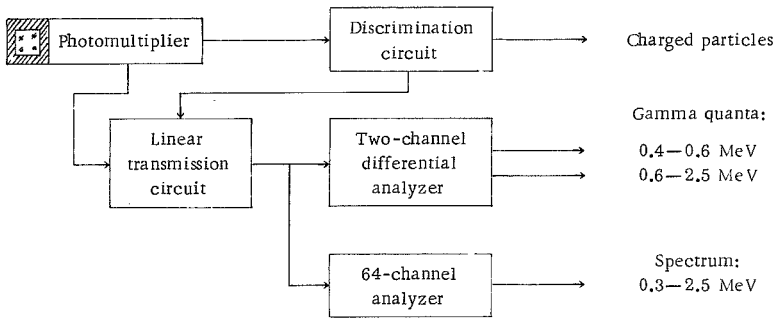

FIGURE 1. Block diagram of the gamma spectrometer.

Gamma spectrum measurements with the multichannel analyzer were carried out at fixed intervals of 10 min; the duration of each measurement was 2 min. The gamma quanta in wide energy intervals and the charged particles were counted every 2 min.

Figure 2 gives a specimen recording to the counting rate of charged particles (top) and 0.6 – 2.5 MeV gamma quanta (bottom) for successive orbital circuits of the satellite. The intensities of both charged particles and gamma rays depend on the geomagnetic latitude. The minimum counting rates correspond to the geomagnetic equator.

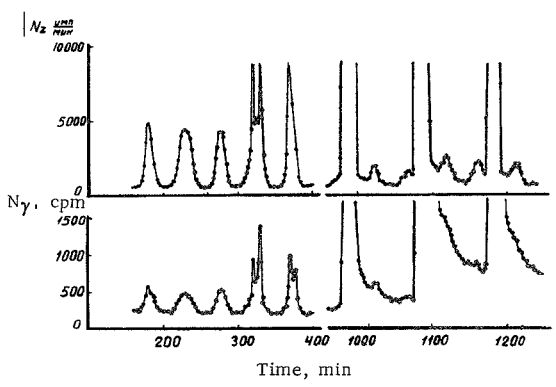

FIGURE 2. Variation of the counting rate of gamma quanta and charged particles with the satellite moving in the geomagnetic field.

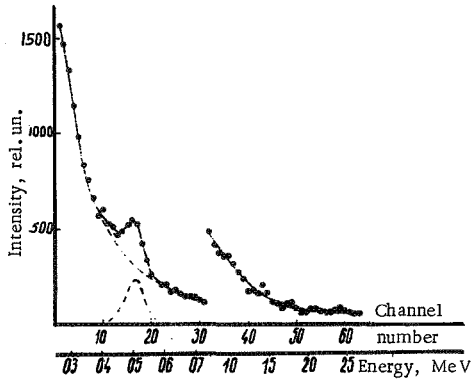

FIGURE 3. The total gamma spectrum from measurements of 13 Dec. 1966.

The counting rate increases at higher geomagnetic latitudes. Electron bremsstrahlung is picked up at latitudes where the satellite touches the radiation belts (320 and 350 min). At 1000, 1100, and 1200 min the satellite passed over the radiation zone in the area of the South Brazilian Anomaly. The detector and the satellite were then exposed to a high-intensity flux of protons.

The total spectrum of gamma quanta from measurements during the first day in orbit is shown in Figure 3. The strong line in the spectrum corresponding to channels 16 — 17 represents positron annihilation radiation.

BACKGROUND EFFECTS

The recording of weak gamma-ray fluxes in orbit is difficult because of the considerable secondary radiation background produced in the detector and satellite material by cosmic rays and protons from the radiation belts. Analysis of the experimental data shows that in low orbits, the main source of background radiation is provided by the activation of the scintillation detector material by the protons of the South Brazilian Anomaly. The nuclear reactions with the participation of the principal components of the NaI crystal (mainly iodine) produce a number of radioactive isotopes with half-lives ranging from a few minutes to several days. It is highly significant that, as these isotopes are produced in the detector, their radiation cannot be recorded in the form of discrete lines: the beta spectrum is inherently continuous. The results of measurements of the residual counting rate for 0.6 — 2.5 MeV gamma quanta after the emergence from the radiation zone are given in Figure 4. This is a typical decay curve of induced radioactivity and it may be used to derive the necessary corrections.

The experimental data (Figure 5) also show — and this is further confirmed by an analysis of the possible nuclear reactions with the material surrounding the detector — that the source of the background radiation comprises exclusively the short-lived components. These are the β^+-active isotopes C^{11} and F^{18} with half-lives of 21 and 110 min, respectively. The isotope C^{11} is produced by the (p, pn) reaction with the carbon of the plastic scintillator. F^{18} may be produced by the (p, pn) reaction from F^{19}, which is present in small quantities in the detector, and also by the reaction (p, 5p5n) from aluminum.

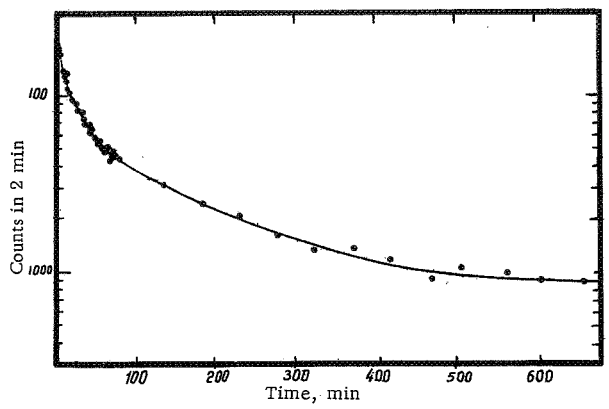

FIGURE 4. The excess counting rate of gamma quanta, associated with induced radioactivity.

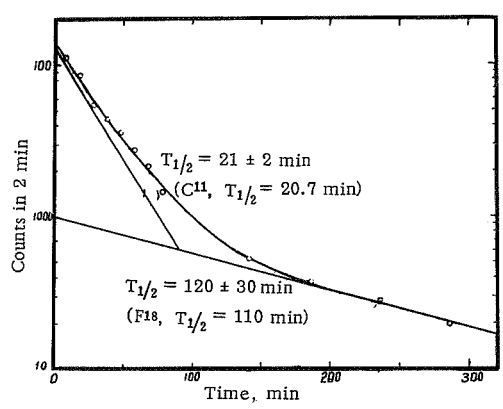

FIGURE 5. The decay of the induced β^+ activity.

The detailed data on the induced radioactivity may be applied to determine the background correction. In practice, however, in order to reduce the various errors in studying the intensity variations of the annihilation line, the measurements used for processing are those made 4—5 hrs after re-emergence from the radiation zone. The corrections for the short-lived background components to the line and to the entire spectrum are then quite negligible. The corrections for the long-lived background components to the integrated gamma-ray fluxes were determined daily from the observed variation of the counting rate near the geomagnetic equator. The corresponding curve for December 1966, January and February 1967 is shown in Figure 6 (curve 1). The variation of the correction in the initial period is associated with the buildup of the long-lived component, whereas its variation in the subsequent period is due to changes in the conditions of exposure in the anomaly zone because of a change in the flight altitude of the satellite in this area. Curve 2 gives in relative units the integrated

proton fluxes in the area of the anomaly, determined from the intensity of the short-lived components of the induced radioactivity. On the average, the corrections for the background of the long-lived gamma activity between 0.4 and 2.5 MeV reached about 50% near the geomagnetic equator and about 20% at high latitudes.

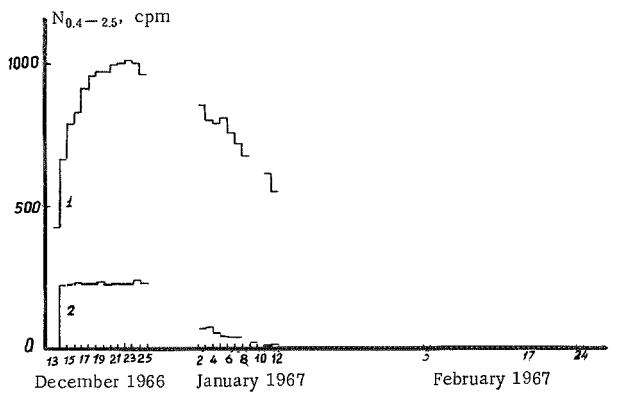

FIGURE 6. Gamma-ray counting rate near the geomagnetic equator (1) and the relative variation of the proton flux in the anomaly zone (2).

INTEGRATED MEASUREMENTS OF GAMMA QUANTA AND CHARGED PARTICLES

The flux measurements of charged particles and gamma quanta are shown in Figure 7. Curve 1 plots the charge-particle flux as a function of the threshold rigidity at altitudes of 250 – 350 km. Since the intensity of the primary cosmic-ray component is reliably known in the entire rigidity range, we can estimate the intensity of the Earth's albedo particles at the altitudes of the satellite orbit.

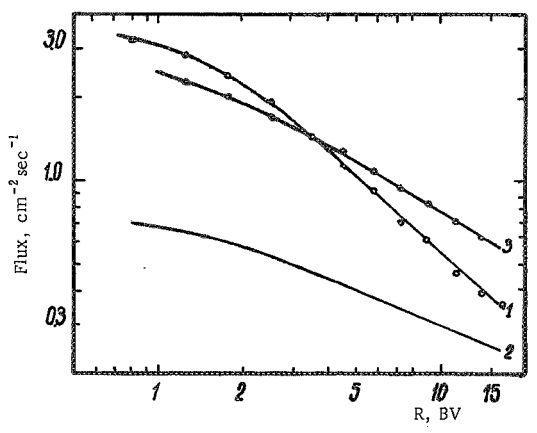

FIGURE 7. Fluxes of the charged component (1), albedo (2), and gamma quanta (3).

Curve 2 gives the albedo at the same altitudes as a function of rigidity. These particles include electrons with energies over 1.5 MeV and protons with energies over 27 MeV. Curve 3 plots the averaged dependence of the flux of 0.4 – 2.5 MeV gamma quanta (minus the flux of annihilation gamma quanta) on rigidity. Figure 8 shows the averaged dependence of the gamma-ray flux on the geomagnetic threshold rigidity on a linear scale for the observation period from 13 to 18 December 1966. The experimental points closely fit a smooth curve. The errors marked on the graph include statistical scatter, the scatter of measurements in the rigidity range over which averaging is performed, and the scatter of data over altitude. The subsequent gamma-ray measurements in December, January, and February are consistent with this dependence within the margin of error shown (3 – 7%).

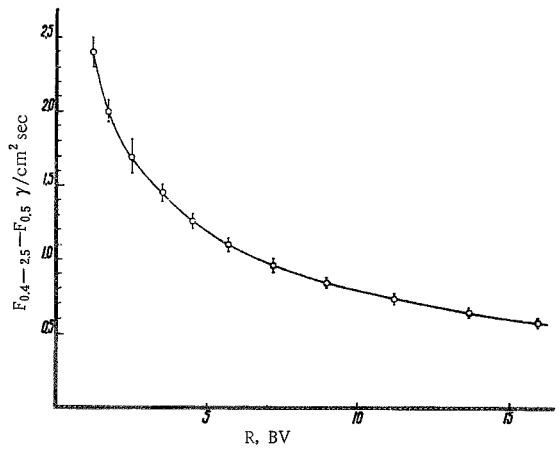

FIGURE 8. Gamma-ray flux between 0.4 and 2.5 MeV.

Using similar data on charged-particle intensities, we conclude that no statistically significant time variations were observed between 13 December 1966 and 25 February 1967 in the intensity of charged particles and 0.4 – 2.5 MeV gamma rays forming continuous spectra.

MEASUREMENTS OF THE FLUXES OF 0.511 MeV ANNIHILATION GAMMA RAYS

The experimental values of the flux of the 0.511 MeV annihilation gamma quanta also may be plotted as a function of the rigidity R. Figure 9 shows the measured results for 13 – 22 December 1966. On the average, the intensity of the annihilation radiation increases with decreasing rigidity. The scatter of points on the whole is consistent with the accuracy of

individual measurements, but in some measurements the deviations are markedly larger than the permissible statistical fluctuations.

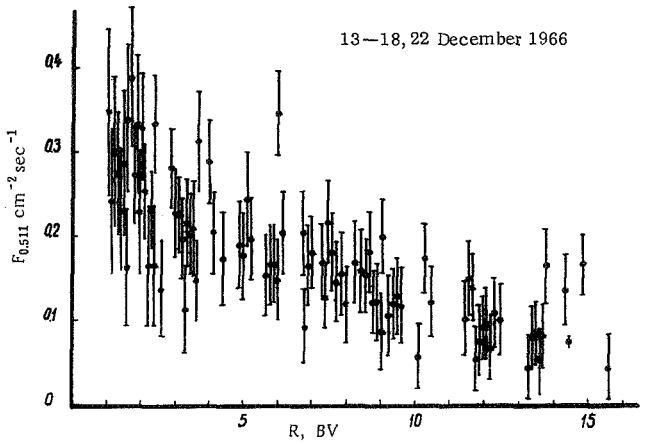

FIGURE 9. Gamma-ray fluxes at 0.511 MeV.

Balloon measurements of the gamma-ray intensity in the upper atmosphere were carried out in /4, 5/. The gamma-ray fluxes extrapolated to the boundary of the atmosphere are on the whole consistent with our data for the corresponding threshold rigidities R.

The statistical accuracy of the individual measurements of the annihilation radiation fluxes is on the average 20 — 30%. In principle, the error should be reduced by summing the spectra over a sufficient length of time. As we have noted, the spectra were measured at fixed intervals of 10 min. The observation conditions in the course of the orbital motion of the satellite are continuously variable, and close rigidities therefore occur seldom, even during long spans of time.

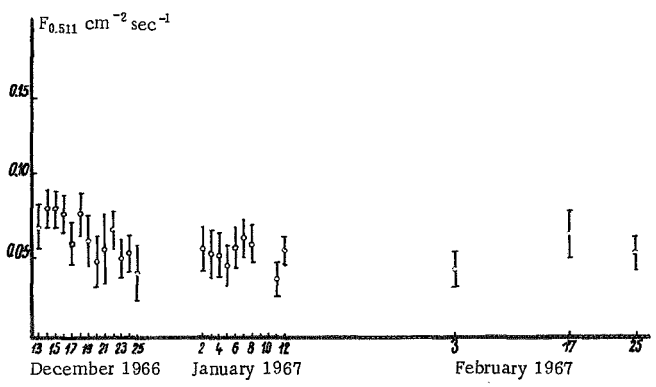

FIGURE 10. Daily average fluxes of 0.511 MeV gamma rays in the equatorial region.

The averaging is best carried out for the geomagnetic equator, where the cosmic-ray intensity and hence the intensity of the resulting secondary radiation varies relatively slowly. Figure 10 gives the daily average equatorial fluxes of the 0.511 MeV annihilation radiation for mean rigidity of about 14 GV. In each case, the averaging was carried out over 5 – 15 spectra.

The plot shows that the intensity of the annihilation gamma rays near the geomagnetic equator is apparently subjected to time variations which is a characteristic – from the standpoint of our hypothesis – trend. A more detailed analysis of the space and time distribution of the gamma-ray fluxes is indicated, using the data obtained for higher geomagnetic latitudes.

STATISTICAL ANALYSIS OF MEASUREMENT RESULTS

The discrete measurements of the gamma-ray spectra do not provide sufficient data for the straight-line approach, which calls for a comparison of spectra successively taken in the same parts of the geomagnetic fields. The total number of the individual spectra taken in the region of space free from strong fluxes of trapped radiation is about 600 for the period of December through February. These measurements are fairly uniformly distributed over the various geomagnetic coordinates and on the average they correspond to points with a considerable separation in space. Moreover, the statistical accuracy of the individual measurements is not high (20 – 30%). On the other hand, the dependence of the radiation intensity of the geomagnetic coordinates is fairly steep. Therefore methods employing integrated distributions and average values had to be used.

The above data show that the intensity of the annihilation radiation, like the intensity of gamma rays in a wide energy range, increases at higher geomagnetic latitudes. The relative variation of these intensities was compared for every day of observations. Figure 11 plots the intensity of the annihilation line as a function of the total gamma-ray intensity between 0.4 and 2.5 MeV on 14 December 1966. $N_{\gamma 0.511}$ on the plot is the counting rate of the 0.511 MeV gamma quanta, and $N_{\gamma\, 0.4-2.5}$ is the counting rate of the gamma quanta between 0.4 and 2.5 MeV. The lines were drawn by the least squares method. In view of the given statistical accuracy of the individual measurements and their volume, the regression curve contains two terms. This is a straight line passing very near the origin. Figure 11 shows the exact characteristics of the distribution of errors for the coefficients of the regression line and the small (40%) and the large (85%) confidence regions for the sought correlation.

A similar analysis was carried out for every day of observation, and the $N_{\gamma 0.511} = f(N_{\gamma 0.4-2.5})$ lines were found to fall into two groups: 1) the observations in the second ten-day period in December (13 – 18 and 22 December) and 2) the observations in the third ten-day period in December (19 – 21 and 23 – 25 December) and in January and February.

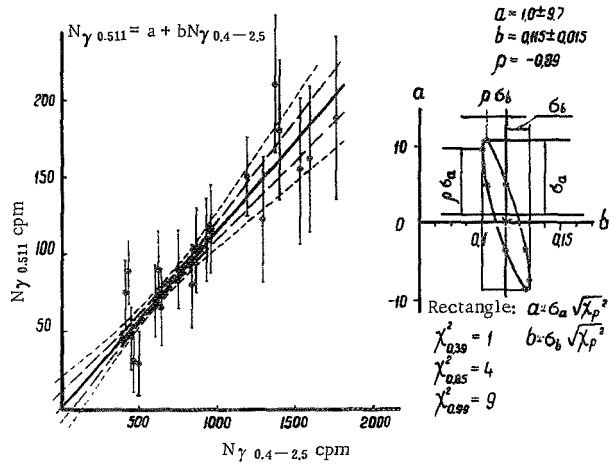

FIGURE 11. The dependence of the intensity of the annihilation line on the total intensity of the gamma spectrum between 0.2 and 2.5 MeV (measurements of 14 December 1966).

The averaged lines for the first and the second period of observation are shown in Figure 12. The dashed lines are the 99% confidence limits for the corresponding solid lines. Application of statistical tests to the comparison of regression lines shows that the observed difference between the two groups has virtually a 100% significance.

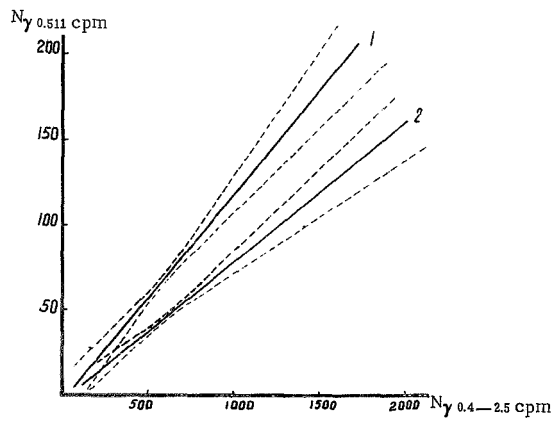

FIGURE 12. The dependence of the 0.511 MeV line on the total intensity of the gamma spectrum for two observation periods:

1) 13—18 and 21 December 1966; 2) 19—21, 23—25 December 1966, January and February 1967.

Let us now consider the distribution of the variable y, which corresponds to the ratio of the annihilation radiation in the entire gamma spectrum, $y = N_{\gamma 0.511}/N_{\gamma 0.4-2.5}$. These distributions for the two observation periods are shown in Figure 13. Statistical samples containing approximately the same number of individual spectra n were used. Each group contains about 85 readings. Figure 13 gives the mean values and the errors for the two groups. We see that the mean fraction of the annihilation radiation in the gamma spectrum reaches 0.130 for the firts group and 0.083 for the second group. In the second group, there are four spectra which markedly deviate from the general distribution. These cases were mentioned before, when we noted that in isolated cases anomalously large annihilation fluxes are observed (see Figure 9).

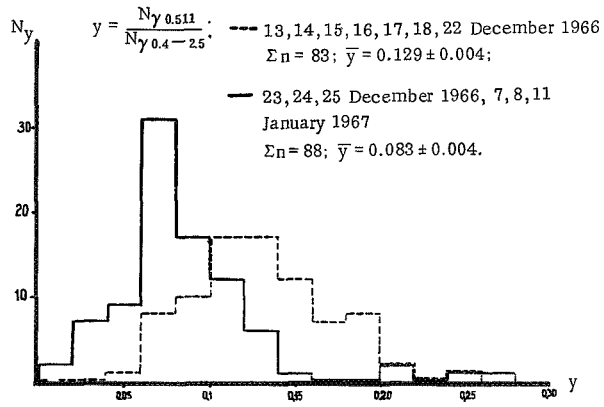

FIGURE 13. Distribution of the relative contribution of the annihilation gamma rays.

The distribution of y was investigated. Figure 14 shows the distribution of the experimental cumulative frequency in coordinates corresponding to the normal distribution of the probability P. For the first group, the experimental points closely follow a straight line, which implies that the distribution is indeed normal. For the second group, in the region of large y, the experimental dependence markedly deviates from a straight line. This deviation is traceable to the four anomalous spectra mentioned above. When they are eliminated from the sample, all the experimental points are seen to follow closely a straight line. This fact signifies that the observation of anomalously large fluxes of 0.511 MeV gamma rays at intervals of less than 10 min is by no means a result of statistical fluctuations.

Figure 14 shows some estimates of the distribution parameters. The observed frequency of occurrence of spectra with $y \geqslant 0.24$, equal to $^2/_{88}$, is a factor of 10^3 higher than the corresponding probability. We conclude that in the Earth space there are cases when the intensity of the annihilation radiation exceeds for a brief time the normal level by as much as a factor of 3 – 4, whereas the intensity in other spectral regions remains unaffected.

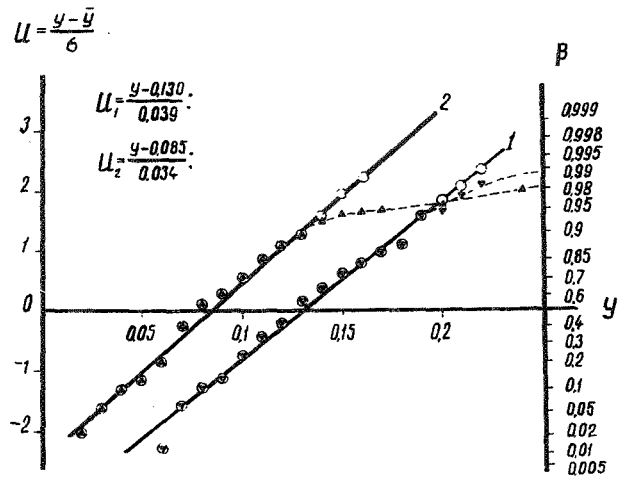

FIGURE 14. A check of the normal distribution.

More accurate estimates of the distribution parameters — the mean, the error of a single measurement, and the error of the mean — are given below:

	n	$\bar{y}$	σ	$\sigma/\sqrt{n}$
Group I	83	0.129	0.038	0.004
Group II	88	0.083	0.040	0.004

Comparison of these figures shows that the intensity of the annihilation radiation fluxes for the first group of observations if a factor of 1.5 higher than for the second group of observations, and the difference between the two groups is greater than 7.5 standard errors. Application of Student's test shows that the observed difference is virtually 100% significant. This conclusion bears out the result obtained from a comparison of the regression lines.

TIME VARIATION OF THE INTENSITY OF THE ANNIHILATION GAMMA RAYS

One day was chosen as the averaging unit for investigating the time variation of the gamma-ray intensity. The intensity of the annihilation line in the overall spectrum summed over one day of observations can be determined with adequate statistical accuracy. However, the relative value $y = \bar{N}_{\gamma 0.511}/\bar{N}_{\gamma 0.4-2.5}$ may characterize observations irrespective of geomagnetic coordinates, the number of spectra in the sample, and the duration of measurements. Special analysis has established that the ratio y determined from the overall spectrum is consistent with the figure obtained from the regression line for the corresponding days. This result confirms the validity of our summation and averaging procedure.

The time variation of the daily average fluxes of the annihilation gamma rays is plotted in Figure 15. The figure shows that, in accordance with the preceding analysis, the annihilation fluxes for the first group of observations (13 – 16 and 22 December 1966) are 1.5 times higher than for the other observations. The data reproduced in Figure 15 include the measurements near the geomagnetic equator (see Figure 10). Note that by extending the analysis to higher geomagnetic latitudes, we confirmed and increased the reliability of the observed time dependence of the intensity of the annihilation gamma rays.

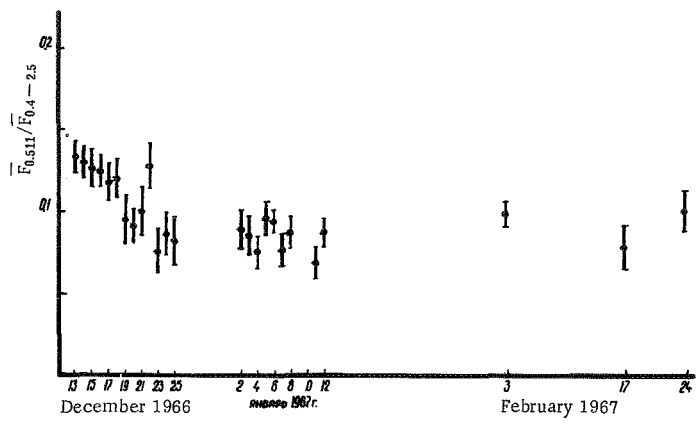

FIGURE 15. The time variation of the relative intensity of the annihilation gamma rays.

We have so far mainly spoken in terms of the relative fraction of the annihilation radiation in the overall gamma-ray spectrum, rather than in terms of the absolute intensities. This approach served a useful intermediate purpose, since the variation of the gamma-ray intensity as a function of the geomagnetic coordinates or as a function of the rigidity R is not linear. In view of the low statistical accuracy of the individual measurements and the limited volume of observations, manipulation of the absolute fluxes would lead to unnecessary complications. However, once the effect has been reliably established in terms of the relative fluxes and the principal features of the time variation have been identified, we may return to the absolute gamma-ray fluxes.

Figure 16 shows the distribution of the annihilation line intensity as a function of the cutoff rigidity R on the Earth's surface for observations in January 1967. The experimental data are based on an analysis of many tens and hundreds of spectra. The relevant rigidity range is divided into 11 intervals. The figure gives the average intensities of the annihilation line for all spectra corresponding to a given interval.

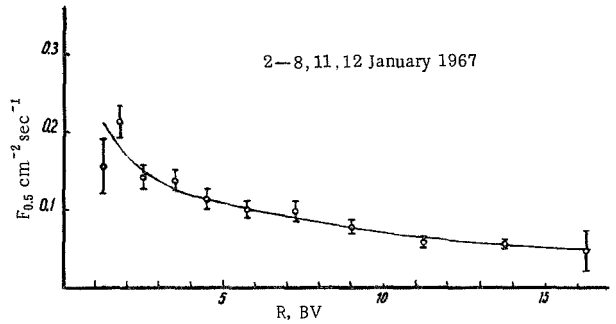

FIGURE 16. The intensity of the 0.511 MeV gamma rays in January 1967.

Similar results for observations from 13 to 18 December 1966 are shown in Figure 17. For comparison, the same plot gives the dependence (dashed line) of the intensity on rigidity for measurements in January 1967. We see that the absolute gamma-ray fluxes at 0.511 MeV for 13—18 December 1966 are on the average 1.5—2 times higher than the values obtained for 2—8 and 11—12 January 1967. The statistical significance of the observed differences is fairly high. The average dependences obtained in fact represent the 1.2 regression lines for the first and the second observation periods recalculated for new coordinates (see Figure 12).

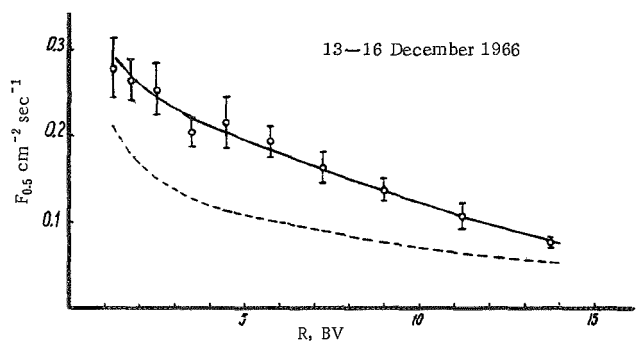

FIGURE 17. The intensity of the 0.511 MeV gamma rays in mid-December 1967.

Unlike the intensity of the gamma-ray line, the intensity of the remaining part of the spectrum from 0.4 to 2.5 MeV does not reveal significant time variation. Figure 18 shows the gamma-ray flux at 0.4—2.5 MeV minus the line flux as a function of the threshold geomagnetic rigidity for three observation periods: 13—18 December 1966, 19—25 December 1966, 2—8 and 11—12 January 1967.

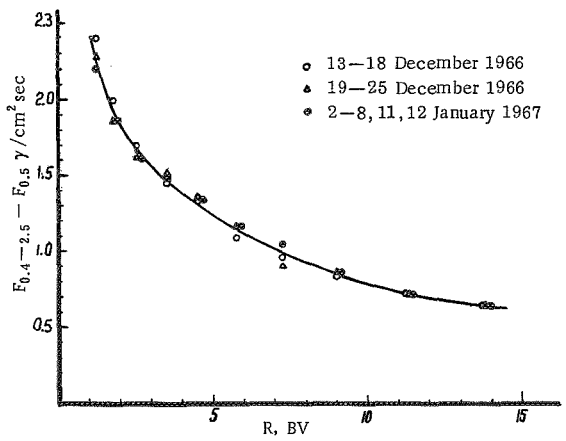

FIGURE 18. The gamma-ray intensity between 0.4 and 2.5 MeV for three observation periods.

The different sets of data closely coincide. No significant time variation in the intensity of charged particles F_Z is observed, either (Figure 19). Note that the scatter of points around the mean curve in the region of low rigidities is a reflection of the variation of the charged-particle intensity with altitude, since the high and the low altitudes are represented in different proportions for different measurement periods. Analogous curves plotted for measurements in smaller altitude ranges reveal a substantially smaller scatter.

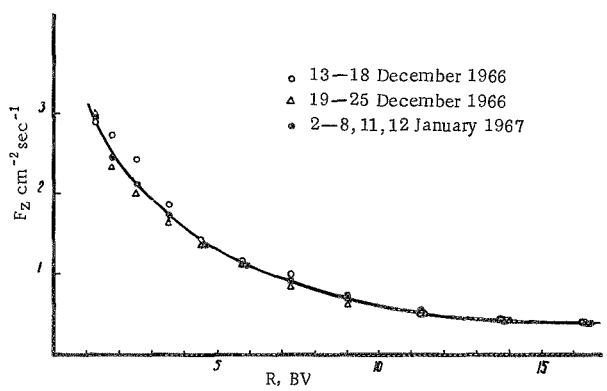

FIGURE 19. Charged-particle intensity for three observation periods.

We have thus established that the intensity of the electron—positron annihilation radiation displays a definite variation in time. The effect reaches about 50—70%. It does not extend to gamma rays of other energies between 0.4 and 2.5 MeV, nor to the fluxes of charged particles

(electrons with $E_e \geqslant 1.5$ MeV and protons with $E_p \geqslant 27$ MeV). The increased line intensity was observed between 13 and 18 December and on 22 December 1966. Figure 15 shows that the intensity of the annihilation radiation according to measurements on various days in February 1967 corresponds to the mean level at the end of December 1966 and in January 1967. Various sources of biased errors were analyzed and all proved to be insignificant.

ANALYSIS OF SOLAR AND METEOR ACTIVITY DURING THE OBSERVATION PERIOD

It is interesting to compare the gamma-ray observation results with observations of solar activity, geomagnetic activity, and cosmic rays in the relevant period. Figure 20 plots the sunspot number R_z, the planetary geomagnetic index A_p, and the readings of neutron monitors in Apatity and in Moscow for December 1966 and January 1967 /6/. We see from the graphs that the observation period was characterized by moderate solar activity, with numerous active regions moving across the solar disk, geomagnetic field disturbances and geomagnetic storms on individual occasions, and instances of a Forbush effect in cosmic rays. It is clear that the periods between 10 and 20 December 1966 and between 1 and 15 January 1967, which markedly differ with regard to the observed intensity of the 0.511 MeV gamma-ray intensity, are characterized by virtually the same solar and geomagnetic activity. Thus, we can hardly speak of any direct correlation between the observed effect and solar activity. The enhanced intensity of the annihilation radiation is observed at all the geomagnetic latitudes, and yet it is not accompanied by changes in the recorded flux of charged particles and is slowly variable in time. As we have seen, the sudden burst of the annihilation line in individual spectra, its intensity rising to 3 — 4 times the mean level, is an exceptional event (see Figure 14).

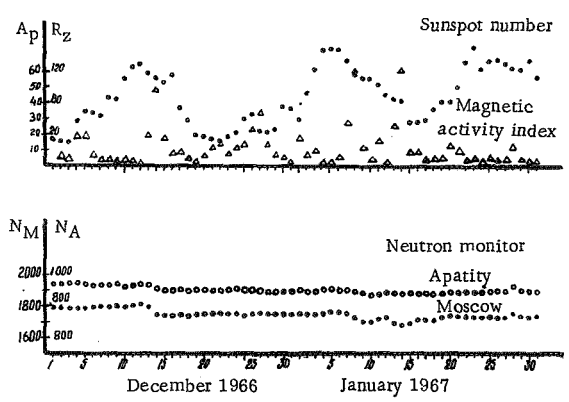

FIGURE 20. Characteristics of solar and geomagnetic activity.

The characteristic features that we have described apparently rule out any possibility of a relation between the observed effect and the injection of trapped radiation into the atmosphere, since the radiation injection is much stronger at high geomagnetic latitudes, and the flux of charged particles varies by several orders of magnitude /7/.

Let us now consider the distribution of meteor activity in the relevant period. In December and January, the Earth crosses the orbits of three annual meteor streams. The maxima according to optical and radar data are observed for Geminids on 13—14 December, for Ursids on 22 December, and for Quadrantids on 2—3 January. The last two streams are active only for a brief period of time. The main Ursid maximum is observed for one day, and that of Quadrantids for a few hours only /8/. The characteristics of these streams in winter 1966/67 did not differ significantly from the many-year averages.

Figures 10 and 15 show that the increase in the intensity of the annihilation radiation coincides with the activity of the Geminids and Ursids, but is not observed for the epoch of the Quadrantids. If we start with the assumption of the antimatter constitution of the meteor streams, the magnitude of the observed effect can be accounted for if 5—10 mg of antimatter are injected into the Earth's atmosphere daily. Note that the data of /1/ also enable us to estimate the range of possible values of the antimatter flux. This estimate gives 100—1 mg of antimatter per day, which is consistent to orders of magnitude with the above figure. In our opinion, the results of the KOSMOS measurements improve the chances of the antimatter hypothesis and require further detailed experimental observations.

Bibliography

1. Konstantinov, B.P., M.M. Bredov, A.I. Belyaevskii, and I.A. Sokolov.— Kosmicheskie Issledovaniya, 4:66. 1966.
2. Konstantinov, B.P., M.M. Bredov, L.P. Pakhomov, V.K. Bocharkin, L.F. Alekseev, N.I. Orlov, and V.I. Chesnokov.— ZhTF, 37:743. 1967.
3. Golenetskii, S.V., V.N. Il'inskii, R.L. Aptekar', Yu.A. Gur'yan, E.P. Mazets, V.N. Panov, T.V.Kharitonova.— PTE. 1969. (In press); Golenetskii, S.V., V.N. Il'inskii, R.L. Aptekar', Yu.A. Gur'yan, E.P. Mazets, V.N. Panov, and T.V. Kharitonova. Present Collection, Part 2, p. 178.
4. Peterson, L.E.— J. Geophys. Res., 68:979. 1963.
5. Chupp, E.L., A.A. Sarkady, and H.P. Gilman.— Planet Space Science, 15:881. 1967.
6. Kosmicheskie Dannye.— Mesyachnye Obzory, No. 12(130), December 1966 and No. 1(131), January 1967. Moskva, Izdatel'stvo "Nauka." 1967; Lincoln, J. Virginia—J. Geophys. Res., 72:2467. 1967; Lincoln, J. Virginia—J. Geophys. Res., 72:2984. 1967.
7. O'Brien, B. J.—J. Geophys. Res., 69:1964. 1964.
8. Lovell, B.—Meteor Astronomy.—Oxford, Clarendon Press. 1954.

DETERMINATION OF THE ANTIPROTON FLUX IN PRIMARY COSMIC RAYS

E.A. Bogomolov, V.K. Karakad'ko, N.D. Lubyanaya, V.A. Romanov, M.G. Totubalina, and M.A. Yamshchikov

Positively charged particles constitute the main component of the primary cosmic rays. Theoretical estimates made under the assumption that the only source of antiprotons in cosmic rays are nuclear reactions of the cosmic-ray particles with the interstellar gas set an upper limit of $\tilde{p}/p \sim 10^{-3} - 10^{-7}$ for the antiproton-to-proton flux ratio /1 – 5/. Experimental estimates of the fraction of antiprotons in primary cosmic rays were mainly obtained from measurements of east – west asymmetry /6 – 15/. Most of these measurements were carried out in the early 1950s. Recent reports describe results obtained by other methods /16 – 18/.

Apparao /16/ searched for antiproton tracks in emulsions exposed in Churchill, Canada, at residual pressures of 4.2 g/cm^2. For energies between 100 and 150 MeV, Apparao obtained an upper limit of $\tilde{p}/p \sim 3 \cdot 10^{-4}$. Brooke and Wolfendall /17/ obtained $\tilde{p}/p \sim 5 \cdot 10^{-2}$ for particles with energies around 1000 BeV from measurements of the charge composition of particles with energies 30 BeV at sea level. Another estimate of the upper limit of the relative content of antiprotons can be derived from the results of /18/, which give the electron spectrum in the range of 0.50 – 8.4 BV measured from a balloon with a telescope consisting of spark chambers and a deflecting magnet. The angular distribution of particles which passed through the magnet gap and did not interact in the shower spark chamber gives an upper limit of $\tilde{p}/p \sim 4 \cdot 10^{-2}$ for energies between 2 and 5 BeV.

Measurements of the east – west asymmetry between 3 and 20 BeV were carried out from balloons and rockets using Geiger counter telescopes /6 – 13/ and telescopes of directional Cherenkov counters /14, 15/. The experimental asymmetries were compared with the figures computed under the assumption that the primary cosmic rays consist of protons only and the geomagnetic field is a dipole field. The experimental asymmetry was invariably less than the theoretical figure. This divergence, according to the estimates of /1, 19/ may be accounted for by the presence of about 10% of antiprotons in cosmic rays. (The antiproton spectrum is assumed to be similar to the spectrum of protons.) It seems that the sum total of the experimental data does not rule out a substantial content of antiprotons in primary cosmic rays.

We tried to establish a better estimate for the upper limit of the ratio $\tilde{p}/p$ obtained in east – west asymmetry experiments. We planned to measure

with a balloon the differential spectra of singly charged particles in the east and west directions in the region of the geomagnetic thresholds with suitable correction for the albedo and the particles produced in the residual atmosphere. On the other hand, in order to improve the theoretically computed asymmetry, we meant to determine the geomagnetic thresholds with allowance for the non-dipole terms in the geomagnetic field expression.

A telescope consisting of two scintillation counters, a directional Cherenkov counter with a Plexiglas radiator, and a gas Cherenkov counter was built /20, 21/. The directional Cherenkov counter eliminated the albedo particles and isolated the singly charged particles. The gas Cherenkov counters working in the anticoincidence mode generated the particle spectrum at energies between 1.7 and 5 BeV (for protons), i.e., in the region of middle-latitude geomagnetic thresholds. The upper energy threshold of the instrument was adjusted in flight by letting out the gas in portions from the gas counters. The spectrum of the secondary particles between 0.6 and 1.7 BeV was determined by means of pulse amplitude analysis using the directional Cherenkov counter. The measurements were carried out at a zenith angle of 60°. The telescope was alternately pointed east and west. The instrument was oriented relative to the geomagnetic field. The figure shows the spectra of singly charged particles obtained in August 1967 at geomagnetic latitude $\lambda_m = 47°$ and residual pressure of about 10 g/cm^2 (from the results of four flights). The background of secondary particles produced in the residual atmosphere was computed as follows. The background spectrum between 0.6 and 1.9 BeV was determined from the data collected over the flight section with 1.9 BeV gas counter threshold and the analysis of the directional counter pulses. The resulting spectrum was then extrapolated to high energies. Absorption and ionization losses of the primary particles in the residual atmosphere were taken into consideration. These two corrections are significant only for the derivation of the absolute particle fluxes. They are not particularly important for the determination of the relative fluxes $\tilde{p}/p$, since their contribution is virtually identical for protons and antiprotons.

The dashed lines in the figure represent the proton spectra generated by a computer. The penetrability of the region of geomagnetic thresholds was determined by numerical integration of the equations of particle motion in the geomagnetic field /22/. The Earth's magnetic field was represented by six spherical harmonics, and the Gaussian coefficients g_n^m and h_n^m for the epoch 1960 were used /23/. The theoretical spectrum was computed using $\gamma = 2.3$ for the index of the differential energy spectrum of the primary protons /24/.

There are significant differences between the experimental spectra and the spectra computed for protons alone. The computation of penetrability with the coefficients g_n^m and h_n^m for 1967 /25/ has shown that this parameter hardly changed between 1960 and 1967. For energies between 1.9 and 2.6 BeV, the ratio $\tilde{p}/p$ is equal to $N_{east}(1.9 - 2.6\ \text{BeV})/N_{west}(1.9 - 2.6\ \text{BeV})$. The small fraction of protons entering this interval from the east can be subtracted by using its computed value. Averaging over the four flights gives $\tilde{p}/p = 0.24 \pm 0.05$.

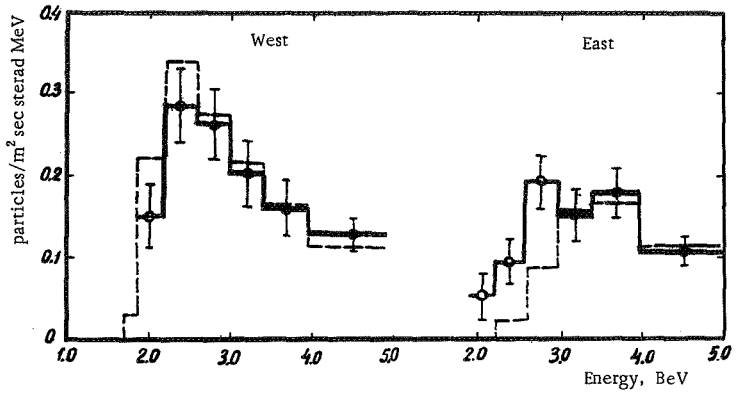

Spectra of singly charged particles in east and west directions at geomagnetic latitude $\lambda_m = 47°$. Zenith angle 60°.

Solid line, experimental; dashed line, computed.

The observed differences in the spectra cannot be attributed to any short-lived magnetospheric disturbances, since the measurements were continued for one month and the ratio $\tilde{p}/p$ was constant for all flights within the margin of error. Moreover, comparison of the proton intensities at $E > 30$ MeV measured at the same time by VENUS-4 /26/ beyond the limits of the magnetosphere with the data of Earth measurements /27/ reveals a total absence of strong magnetospheric disturbances in the relevant period.

There is a possibility, of course, still undecided, that the differences in spectra are associated with geomagnetic field irregularities (deformation of the magnetosphere by solar wind, ring current, etc.). Further experiments should be carried out in order to establish whether the relative content of antiprotons in the primary cosmic rays actually exceeds the theoretically expected figure. With regard to measurements of the east—west asymmetry, the computation of geomagnetic effects clearly should be based on all the currently available data concerning the Earth's magnetosphere and low-latitude experiments should be performed in the nearest future.

Bibliography

1. Fradkin, M.I.— ZhETF, 29:147. 1955.
2. Milford, S.N. and S. Rosen.— Nature, 205:582. 1965.
3. Rosen, S.— Phys. Rev., 158:1227. 1967.
4. Shen, C.S. and G.B. Berkley.— Phys. Rev., 171:1344. 1968.
5. Wayland, J.R. and T. Bowen.— Phys. Rev., 171:1376. 1968.
6. Johnson, T. and J. Barry.— Phys. Rev., 56:219. 1939.
7. Vernov, S.N., N.L. Grigorov, N.A. Dobrotin, S.I. Sokolov, F.D. Savin, and A.I. Kurakin.— DAN SSSR, 68:253. 1949.
8. Vernov, S.N., A.M. Kulikov, and A.N. Charakhch'yan.— DAN SSSR, 85:525. 1952.

9. Winckler, J.R., T. Stix, K. Dwight, and R. Sabin.— Phys. Rev., 79:656. 1950.
10. Winckler, J.R.— Phys. Rev., 85:1054. 1952.
11. Allen, J.A. van and A.V. Gangnes.— Phys. Rev., 79:51. 1950.
12. Singer, S.F.— Phys. Rev., 80:47. 1950.
13. Shafer, Yu.G., V.D. Sokolov, N.G. Skryabin, S.K. Dergeim, and R.B. Selimzibarov.— Kosmicheskie Issledovaniya, 2:933. 1964.
14. Winckler, J.R. and K. Anderson.— Phys. Rev., 93:596. 1954.
15. Agrawal, P.C., S.V. Damle, G.S. Gokhale, C. Joseph, P.K. Kunte, M.G.K. Menon, and R. Sunderrajam.— Proc. Ninth Intern. Conf. on Cosmic Rays, 1:457. 1965.
16. Apparao, M.V.K.— Nature, 215:727. 1967.
17. Brooke, G. and A.W. Wolfendall.— Nature, 202:480. 1964.
18. Fanselow, I.L.— Astrophys. J., 152:783. 1968.
19. Bhowmic, B.— Phys. Rev., 89:327. 1953.
20. Bogomolov, E.A., V.K. Karakad'ko, N.D. Lubyanaya, V.A. Romanov, M.G. Totubalina, and M.A. Jamshchikov.— In: "Kosmicheskie luchi," No. 10. 1969.
21. Bogomolov, E.A., V.K. Karakadko, N.D. Lubjanaja, V.A. Romanov, M.G. Totubalina, and M.A. Jamshchikov.— Can. J. Phys., 46:S805. 1968.
22. Belous, L.G., E.A. Bogomolov, V.K. Karakad'ko, N.D. Lubyanaya, V.A. Romanov, V.S. Smirnov, M.G. Totubalina, and M.A. Jamshchikov. — Materialy Vsesoyuznoi Konferentsii po fizike Kosmicheskikh luchei v Tashkente. 1968. (In press).
23. Adam, N.V., N.I. Osipov, L.O. Tyurlina, and A.P. Shlyakhtina.— Geomagnetizm i Aeronomiya, 4:1130. 1964.
24. Freier, P.S. and C. J. Waddington. — J. Geophys. Res., 73:4261. 1968.
25. IGRF coefficients adopted by the Third IAGA Committee. Washington. 1968.
26. Vernov, S.N., A.E. Chudakov, P.V. Vakulov, E.V. Gorchakov, N.N. Kontor, S.N. Kuznetsov, Yu.I. Logachev, G.P. Lyubimov, A.G. Nikolaev, N.V. Pereslegina, and B.A. Tverskoi.— Trudy V Vsesoyuznoi ezhegodnoi zimnei shkoly po kosmofizike, Apatity, Izd. Kol'skogo filiala AN SSSR, No. 5. 1968.
27. Kosmicheskie Dannye (Space Data).— Moskva, Izdatel'stvo "Nauka." 1967.

GEOCHEMICAL FEATURES OF THE COMPOSITION OF THE UNIVERSE AND THE ORIGIN OF ATOMIC NUCLEI

V. V. Cherdyntsev

REGULAR FEATURES IN THE ABUNDANCE OF ATOMIC NUCLEI

The principal features in the abundance of isotopes and elements are known for a number of systems (Earth's crust, meteorites, the outer envelope of the Sun and of most main-sequence stars; interstellar matter and cosmic rays have been studied to a lesser extent). These features /1/ correspond to the "standard" composition of matter in the Universe, irrespective of the particular astrophysical characteristics and the age of the various objects.

1. The curve of the nuclide abundance q as a function of the mass number A, in the form log q = f(A), falls off rapidly in the region of light nuclei, dropping by about 10 orders of magnitude from hydrogen (Z = 1) to gallium (Z = 30). As A increases further, the curve levels out, but there is a minimum in the region of medium mass numbers (A = 140 – 160). This minimum is particularly distinct for the isotopes of one element which have the same parity. The heaviest nuclides exceed the minimum level approximately by one order of magnitude.

2. The abundance of even isotopes (q_S) is higher than the abundance of odd isotopes (q_A) – the Oddo – Harkins rule.

3. The ratio q_S/q_A is a function of the mass number. This ratio reaches 500 for oxygen isotopes, is equal on the average to 10 for the light nuclides, and drops approximately to 2 for the heavy nuclides.

4. Among the even isobars, the low-charge isobars (q_{Z-2}) are more abundant than the high-charge isobars (q_Z, q_{Z+2} – the protected isobars). There is a distinct dependence on the position of the energy levels of the isobars, but even for virtually identical energy states the abundance of the low-charge isobars is higher by a certain factor.

5. The ratio q_{Z-2}/q_Z markedly increases with the increase in the atomic number of the even isobars and varies by two orders of magnitude on passing from the light isobars ($Z < 30$) to the last isobars of the stable elements.

6. The abundance of the low-charge odd isobars is also higher than the abundance of the corresponding high-charge isobars, although among the known cases of radioactive transitions between these isobars, it is the low-charge isobar that is invariably unstable.

The above regular features of abundance cannot be explained by the energy properties of the atomic nuclei. The curve $\log q = f(A)$ does not fit the binding energy curve. The energy difference between the even and the odd isotopes diminishes for the heavy nuclides, and yet a distinct prevalence of the even isotopes is observed in this range. Even isobars with approximately identical energy levels show a distinct excess of the low-charge states. The ligher states of the odd isobars are more abundant, although many of them are unstable, i.e., occupy higher energy states.

7. The deviation of the curve $\log q = f(A)$ from the level trend is in general considerable, but there are regions of particularly high abundance of nuclides, corresponding to filled neutron shells ($A - Z = 50, 82, 126$). The high-abundance isotopes Sr^{88} and Zr^{90} occur for $A - Z = 50$, and Ba^{138} and Ce^{140} correspond to $A - Z = 82$. A distinct iron peak is observed. The cosmic abundance of Fe^{56} and Ni^{58} is approximately the same as that of Ar^{36} and Ca^{40}, whereas the abundance of the intermediate even nuclei is $1 - 2$ orders of magnitude lower. A reverse anomaly — a very low abundance of Sc^{45} — is observed in all the known systems in the Universe /1/. Particularly low abundance is characteristic of high-spin nuclides, whether odd (e.g., Sc^{45}, $j = 7/2$) or particularly even (K^{40}, V^{50}, Lu^{176}, etc.).

8. There are secondary deviations of the nuclide abundance curve, namely the gap in the region of the light metals ($Z = 3 - 5$) which burn in the thermonuclear reactions in the stellar interior and the gaps beyond the region of isotopes which are not subject to spontaneous decay ($Z > 83$), where only the regions with the isotopes $Z = 90$, 92, and probably also $Z \approx 108$ stand out as isolated stability islands.

The isotopic ratio of lithium and boron is markedly different from that of other elements at the beginning of the Periodic Table (the odd and the heavy isotopes prevail). This probably points to a different mechanism of formation of the isotopic composition of these elements.

The above features cover the entire range of atomic nuclei, and no significant gaps or discontinuities are observed. This suggests that nucleogenesis took place in a single system and that the conditions of nucleogenesis did not markedly differ between different parts of the Universe. It is also significant that this primary process produced all the atomic nuclei up to the heaviest radioactive nuclides, unlike the secondary processes (thermonuclear reactions, nuclear reactions triggered by cosmic rays) which are known to be highly selective.

THE DEVELOPMENT OF THE CONCEPTS OF NUCLEOGENESIS

Pokrovskii /2/ was the first to show that the common features governing the chemical composition of virtually all the isotopes in nature are of necessity an indication of the fact that all the atomic nuclei were produced in a medium close to the state of thermodynamic equilibrium. The density of such a system, as is readily seen, should be subnuclear, and its temperature should be close to the nuclear temperature ($kT = n$ MeV). The particular isotopic ratio which developed in the system was fixed to perpetuity because the system apparently "froze," i.e., rapidly moved to the conditions

of relatively low densities and energies commonly characteristic of the Universe as a whole. Nucleogenesis, according to Pokrovskii, thus occurred during the explosion of an ultradense star and, according to the modern terminology, it can be classified as an r-process. The main shortcoming of this theory was that a thermodynamic equilibrium of atomic nuclei for any choice of system parameters led to an abundance curve which greatly differed from the real curve: the theoretical abundance of the heavy elements worked out to be much lower than the actual abundance. Other authors (Weizsäcker developed the most detailed model /3/) failed to overcome this "heavy nuclei difficulty." The attempts to describe the nucleogenesis of the light and the heavy isotopes as two separate processes /4/ did not constitute a significant advance. So far no break or seam has been detected on the abundance curve enabling to separate between the groups of nuclei which allegedly formed under different conditions.

The main difficulty encountered in nucleogenesis is the synthesis of the heavy nuclei from A = 209 (Bi) to A = 232 (Th), which have very short half-lives. Following the discovery of the far transuranide with the probable values $Z \approx 108$ and $A \approx 290$, we were faced with the need of bridging over an even wider range of short-lived isotopes.

In the mid-1930s, Baade and Zwicky /5/ discovered the supernovae and advanced the suggestion — not easily accepted by other astrophysicists — that the supernova explosions produced a neutron phase. In the same period, theoretical physicists, and primarily S. Chandrasekhar /6/, L. Landau /7/, and H. Bethe /8/, proved the possible existence of ultradense stars and established the relative enrichment of neutrons in the course of evolution of stellar matter. In 1940, the synthesis of atomic nuclei in a medium consisting almost entirely of neutrons and maintained in thermodynamic equilibrium was described in /9/. These conditions fitted the conditions of supernova eruptions. The neutron fragments undergo beta decay and produce the common atomic nuclei. Among the even isobars, the low-charge isobars are preferably formed. The high-charge even isobars are produced by secondary reactions in the post-explosion stage under conditions far from thermodynamic equilibrium. This conception led to a quantitative description of the various features of the abundance curve and explained the dependence of the abundance on parity. It also provided a qualitative explanation of the observed abundance of the isobars. It was shown that the evolution of stars with masses below some critical value is terminated with the formation of neutron stars — the "vacuum cleaners" of the Universe which actively trap all disperse matter in their ultrastrong gravitational field. These theoretical conceptions have meanwhile received partial experimental corroboration in astrophysics.

The range of pressure-unstable atomic nuclei extends to $A = (1-3) \cdot 10^4$ /9/. The recent computations of Swiatecki /10/ give an upper limit of $A = 1.3 \cdot 10^4$. If such ultraheavy atomic nuclei actually exist in nature, they are probably concentrated in stellar interiors. Their presence in cosmic rays following ejection into space during supernova explosions has not been proved so far.

A more detailed description of nucleogenesis was advanced by G. and E. Burbidge, Fowler, Hoyle, and Christy in 1956—1957 /11, 12/. In

addition to nuclide formation in an exploding neutron system (a fast r-process according to their terminology), they also considered a number of slow processes initiated by neutrons and protons in stars in the late stages of their evolution, and also in the diffuse matter in space.

The bulk of the evidence seems to indicate at this stage that the main process responsible for the formation of the "standard" chemical composition which constitutes the basis of the observed composition of matter in the solar system and in cosmic rays is the extremely fast process of nucleogenesis in a neutron medium. The fine features of the abundance of the atomic nuclei are very difficult to compute, since the energy parameters of the initial neutron fragments cannot be accurately extrapolated. It is clear, however, that the primary nuclei of these neutron fragments are radically different from the stable atomic nuclei of the existing systems. This is obvious from the very ease with which they bridge over the gap at $A = 210 - 230$ or $250 - 290$, where the ordinary atomic nuclei are highly unstable. In addition to "standard"-composition matter, the Universe also contains stars in the late stages of evolution where nuclear processes with the participation of alpha particles and neutrons, as well as protons, actively take place. The character of these slow processes was first discussed in /11, 12/ Stars are known where the proton energy source have been depleted to such an extent that their spectra show no hydrogen lines, and the lines of helium, carbon, and neon predominate. Certain groups of stars are enriched in C^{13}, the C^{12}/C^{13} ratio reaching $3 - 4$, i.e., one magnitude higher than the Earth enrichment of this isotope. Various types of stars in the late stages of evolution reveal a distinct enrichment of the heavy elements of the lanthanide group, zirconium, and lead. Of the greatest interest are the S stars, whose spectrum shows technetium lines. The most long-lived isotope of this element has a half-life of $2.1 \cdot 10^5$ years (Tc^{99}), so that the presence of technetium distinctly points to the presence of active nuclear reactions which encompass the region of the heavy elements /13/.

Further analysis and systematic classification of the relevant material are highly important. These stars, however, hardly inject "non-standard" matter into the Universe. The evolution of the anomalous-composition stars either terminates in a supernova explosion, which restores the "standard" chemical composition of the star, or in the formation of a neutron star.

THE HISTORY OF THE HEAVY ISOTOPES

While the first efforts in the theory of nucleogenesis could not overcome the "heavy nuclei difficulty" — the marked deficit in the computed abundance of the heavy nuclei compared to the actual abundance of these nuclei in the Universe — we are currently faced with an opposite difficulty. The heavy nuclei in the radioactive region are produced in comparable quantities with the neighboring nuclei ($Z < 83$, $Z = 90, 92$), which are either stable or are conserved during nucleogenesis. We will not consider the fate of nuclides with $A > 300$. There is a possibility that the matter of a collapsing star had not become fully converted into a neutron phase before it exploded as a supernova. A certain number of protons in this medium, i.e., a small charge of neutron nuclei, prevents their interaction with

the surrounding matter during the brief explosion phase, so that the conditions of thermodynamic equilibrium are not quite exact. Let us now consider the lighter nuclei.

For nuclei with $A > 250$, spontaneous fission is the predominant mode of decay (except for individual nuclides in the stability region around $Z = 108$). The fission products gravitate mainly to regions of filled shells, $A - Z = 50, 82$, and their buildup, as was first noted by Frenkel' and Selinov /14/, may account for the maxima on the abundance curve in these regions. The fision products in meteorites — rare gas isotopes — actually point to two different spontaneously fissile isotopes, U^{238} and some heavy isotope, possibly Pu^{244}. The difference in the fission spectrum of the heavy and the light transuranides may probably account for the buildup of isotopes around $A - Z = 50, 82$. The protected isobars only constitute a minority among the elements corresponding to these maxima. Zirconium has no such isotopes, and their content for Sr, Xe, Ba, and Ce is 10.4, 6.2, 10.4, and 0.4%, respectively. They are definitely not fission products of heavy nuclei, but their abundance does not exceed the normal abundance of the isotopes with given A.

A significant fraction of the atomic nuclei around $A = 236 - 250$ decay into the long-lived isotopes Th^{232}, U^{235}, and U^{238}. U^{236} and Pu^{244}, which are the product isotopes of the Th^{232} decay, possibly existed in the early stage of the solar system. The nuclides of this region with mass number of the form $A = 4n + 1$ rapidly decay to the final stable product Bi^{209}. The atomic nuclei around $A = 210 - 234$ are the decay products of natural radioactive elements formed in nucleogenesis; they apparently decayed rapidly, enriching the isotopes of lead and bismuth. Of these isotopes, U^{234} is probably the only survivor from the pre-solar-system times.

The decay of atomic nuclei with $A \geqslant 210$ thus enriches, on the one hand, the regions of atomic nuclei with filled neutron shells and, on the other hand, results in a buildup of Pb, Bi and also Th and U. The content of the lead isotopes Pb^{206}, Pb^{207}, Pb^{208} may probably increase, although hardly more than by one order of magnitude, compared to the original abundance in the nucleogenesis system. Thsi is evident from the isotopic composition of lead in iron meteorites, which is probably virtually undistorted by radiogenic lead impurities during the entire previous history of the meteorites. The content of the protected isobar Pb^{204} in meteorites is about 2% (compared to the current content of about 1.3% in the lead ores of the Earth's crust).

The quantitative increment of the heavy radioelements due to the decay of the primary transuranides is a big unknown. The enrichment of U^{235} by the decay products of the element $Z \approx 108$ probably reached about 10% of the original content of U^{235} during the last 3.5 billion years of the Earth's history /15/. The lead—bismuth system was probably enriched with decay products of the nucleogenesis alpha emitters to a greater extent that the uranium—thorium system. As a result, the filled shell region at $A = 126$ acquired a maximum on the abundance curve, not unlike the maxima in the region of medium mass number isotopes.

Bibliography

1. Cherdyntsev, V.V. Rasprostranennost' khimicheskikh elementov (Abundance of Chemical Elements).— ONTI, Moskva. 1956.
2. Pokrovskii, G.I.— Phys. Zeitschr., **32**:374. 1931.
3. Weizsäcker, C.— Phys. Zeitschr., **39**:633. 1938.
4. Chandrasekhar, S. and L. Heinrich.— Astrophys. J., **95**:288. 1942.
5. Baade, W. and F. Zwicky.— Nat. Ac. Sc. (Wash.), **20**:254. 1934.
6. Chandrasekhar, S. Introduction to the Study of Stellar Structures.— Chicago, Univ. of Chicago Press. 1939.
7. Landau, L.D.— DAN SSSR, **17**:301. 1937.
8. Bethe, H.— In: "Astrofizicheskii sbornik," Moskva, IL. 1949. [Russian translation.]
9. Cherdyntsev, V.V.— Astronomicheskii Zhurnal, **17**:1. 1940; **18**:1. 1941.
10. Swiatecki, W.— Science News, **94**:593. 1968.
11. Burbidge, G., F. Hoyle, E. Burbidge, K. Christy, and W. Fowler.— Phys. Rev., **103**:1145. 1956.
12. Burbidge, G., E. Burbidge, W. Fowler, and F. Hoyle.— Rev. Mod. Phys., **29**:549. 1957.
13. Aller, L. The Abundance of the Elements. New York. 1961.
14. Selinov, I.P.— In: Ya.I. Frenkel'. Printsipy teorii atomnykh yader (Principles of Nuclear Theory), p.273. Moskva, Izdatel'stvo AN SSSR. 1950.
15. Naidenov, B.M. and V.V. Cherdyntsev.— DAN SSSR, **172**:688. 1967.

THE PROPERTIES OF NUCLEI FAR FROM THE BETA-STABILITY STRIP

E. E. Berlovich

The number of nuclides between the limits of nucleon stability is several times higher than the number of nuclides near the beta-stability strip, which were the only ones available for actual experimental work until recently. However, these nuclides are being continuously synthesized in various processes in celestial objects (rapid neutron capture in supernova explosions, spallation reactions and fission reactions initiated by high-energy protons, etc.) and play an important role in the evolution of matter in the Universe. As a result, the study of their properties is highly significant for the solution of the fundamental problems of astrophysics. On the other hand, information on the properties of these nuclei is needed for the construction of an adequate theory of the nucleus. These nuclei differ from the nuclei lying near the beta-stability strip on the following counts: a) the neutron-to-proton ratio, b) the ratio of Coulomb to nuclear forces, c) the ratio of the binding energies of the two types of nucleons, d) possibly different distribution radii of nucleons of the two types, e) large beta-decay energies.

Studies of the properties of these nuclei are significant for solving a number of fundamental problems of nuclear physics, such as the determination of the limits of nucleon stability (which are currently estimated mainly by rough semiempirical mass formulas) and, in particular, the problem of the existence of neutron nuclei. The region of nuclei far from the beta-stability strip shows a large variety of interesting physical phenomena: a) alpha decay in new regions, p and 2 p decays; b) beta decay and a quasi-continuous spectrum; c) delayed p, n, α, He^3, H^3 decays from excited states and, possibly, decays of nucleon pairs and more complex formations; d) delayed fission of nuclei from excited states, which is a highly significant effect for heavy-nuclei nucleogenesis; e) double beta decay which (if it exists) should have a substantially higher probability near the limits of nucleon stability; f) deformation of nuclei in new regions.

The properties of these nuclides, which are characterized by short beta-decay half-lives, may be studied using systems with targets placed directly in the beam of particles initiating the relevant nuclear reactions.

Section II

X RAYS, GAMMA RAYS, ELECTRONS AND NEUTRINO

Edited by G. E. Kocharov and V. A. Dergachev

COSMIC GAMMA AND X RAYS

S. I. Syrovatskii

The region of X rays and gamma rays occupies a special position in the wide spectrum of electromagnetic radiation reaching the Earth from outer space. The high energy of the corresponding photons provides a direct indication of the high energy of the originating particles. These energies are such that only the region of soft X rays with photons of less than about 10 keV can be associated with high-temperature regions of the Universe. All the other parts of the X-ray and gamma-ray spectrum are definitely attributable to nonthermal particles accelerated to high energies, which include, in particular, the omnipresent cosmic rays. Another significant factor is that X rays and gamma rays, unlike charged particles, are not deflected by the magnetic fields in outer space, whereas scattering and absorption in the interstellar and the intergalactic medium affects only the very soft X rays. Cosmic gamma and X rays thus constitute direct evidence of special physical conditions in certain parts of the Universe and primarily provide an indication of the existence of high-energy particles. The main emphasis in this paper is placed on experimental and observational data which were available at the beginning of 1969. Theoretical interpretation of these data is still fairly uncertain, and we will therefore only point to the principal trends of theoretical analysis, briefly listing the various emission mechanisms in the relevant range of frequencies. The boundary between X rays and gamma rays is placed fairly arbitrarily at photon energies $E_\gamma = 1000\,\text{keV} = 1\,\text{MeV}$. Another radiation characteristic, besides the energy E_γ, is the wavelength λ and the frequency ν of radiation. These quantities are related by simple standard relations:

$$\lambda = \frac{c}{\nu} = \frac{12.4}{E_\gamma}\ \text{Å}, \tag{1}$$

$$\nu = \frac{E_\gamma}{h} = 2.42 \cdot 10^{17}\ E_\gamma\ \text{sec}^{-1}, \tag{2}$$

where in numerical expressions the photon energy E_γ should be expressed in keV.

The first advances of X-ray astronomy are traceable to the observations of the Sun, which began in the late 1940s with various rocket observations, and later orbital observations from satellites. These measurements, besides the soft X-ray emission of the quiet Sun corresponding to coronal temperatures of a few million degrees, also detected marked enhancements of X-ray intensity associated with active regions and solar flares; these enhancements were particularly prominent in the hard X-ray region. In a number of cases,

photons with energies of a few hundred keV were observed. A characteristic feature of the transient emission of solar flares, as we know now, is the nonthermal origin of the radiation during the growth phase of the intensity curve and its thermal origin during the decline phase /1/. An intensity curve of this kind is obtained if the flare generates nonthermal particles (electrons), which are soon thermalized and create hot regions with temperatures reaching a few tens of millions of degrees.

Observations of solar X rays constitute an extensive and entirely independent field of research. These observations are particularly promising because of the wealth of experimental data, the easy comparison with other phenomena observed on the Sun, and the relatively high current level of solar physics as a whole. They evidently provide a deeper insight into the various processes occurring on the Sun and primarily into the mechanism of solar activity, and they may possibly shed some light on the mechanism of X-ray emission in other parts of the Universe. In this paper we only consider X rays and gamma rays whose origin is not related to the Sun or the solar system. Some parameters characterizing the X-ray activity of the Sun are given for comparison purposes only.

Depending on the activity level near the Earth, the energy flux of solar X rays at wavelengths $\lambda < 8$ Å ($E_\gamma > 1.5$ keV) falls between the limits

$$F(\lambda < 8\text{Å}) = 10^{-3} - 3 \cdot 10^{-1}\ \text{erg/cm}^2 \cdot \text{sec}, \qquad (3)$$

where the largest figure corresponds to strong chromospheric flares /2/. This value corresponds to the following X-ray power of the Sun:

$$P(\lambda < 8\text{Å}) = 4\pi R^2 F(\lambda < 8\text{Å}) \approx 10^{27}\ \text{erg/sec}, \qquad (4)$$

where $R = 1.5 \cdot 10^{13}$ cm is the Earth—Sun distance. Strong flares, however, are infrequent, and the mean power of the Sun in this range is therefore approximately 1/100 of the figure in (4), i.e., it is close to 10^{25} erg/sec. If all the stars in the Galaxy have the same power on the average, the radiation intensity in the direction to the galactic center, over a path length $L = 20$ kpc $\simeq 6 \cdot 10^{22}$ cm, will not exceed

$$I(\lambda < 8\text{Å}) = \frac{L}{4\pi} \frac{P(\lambda < 8\text{Å})}{V_s} \simeq 5 \cdot 10^{-10} \frac{\text{erg}}{\text{cm}^2 \cdot \text{sec} \cdot \text{sterad}} \approx 0.2 \frac{\text{photons}}{\text{cm}^2 \cdot \text{sec} \cdot \text{sterad}}, \qquad (5)$$

where $V_s \approx 10^{56}$ cm^3 is the mean volume per star in the Galactic disk. We will see in what follows that the observed fluxes are significantly larger.

OBSERVATION DATA

The strong atmospheric absorption effectively screens the Earth's surface from gamma rays and X rays. The only exception are gamma rays of very high energies $E_\gamma > 10^{11} - 10^{12}$ eV, which produce electron-photon showers in the atmosphere. These showers are observed with the aid of their Cherenkov emission and by other methods of the physics of high-energy cosmic rays. The observational gamma-ray and X-ray astronomy is therefore closely

linked with the launching of high-altitude rockets and artificial satellites, which in fact provided the main impetus for the development of this extensive field of science.

The principal observational characteristics are the energy spectrum and the spatial distribution of radiation. For discrete sources, these are supplemented by the time-variation of the source intensity and the exact source coordinates, which are needed for identifying the X-ray sources with known optical or radio objects. The degree of polarization of X-ray emission, although highly important for elucidating the emission mechanism,, has not been measured so far.

Discrete X-ray sources. The first galactic X-ray source was discovered in Scorpius in 1962; it is designated Sco XR-1 /3/. This is not only the first, but also the most powerful of all the known X-ray sources: its flux at the Earth is

$$F(\lambda<8\text{Å}) \simeq 40\,\frac{\text{photons}}{\text{cm}^2\cdot\text{sec}} \simeq 2\cdot 10^{-7}\,\frac{\text{erg}}{\text{cm}^2\cdot\text{sec}}. \qquad (6)$$

Some 30 discrete X-ray sources are currently known /4/. This number is largely limited by the sensitivity and the angular resolution of our detectors, since at this stage sources with fluxes $F < 0.1$ photons/cm$^2\cdot$sec are difficult to detect reliably against the background of diffuse X-ray emission. A special satellite, X-RAY EXPLORER, is scheduled to be launched in 1970 for extrasolar X-ray measurements. This satellite will probably achieve a sensitivity higher by a factor of 60 /5/.

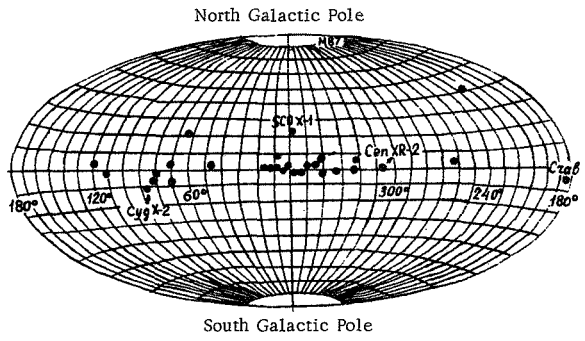

FIGURE 1. The distribution of X-ray sources over the sky in galactic coordinates.

The great majority of the discrete sources are concentrated in the galactic disk, as we see from Figure 1 /4, 5, 6/, i.e., these sources are definitely objects of galactic origin. The distribution of sources in galactic longitude is nonuniform. Some of them cluster in Cygnus—Cassiopeia and are possibly associated with the Orion spiral arm stretching in this direction (the Sun is also part of this galactic arm). Most of the other sources cluster in the centerward direction with a mean deviation of ±3.5° from the galactic plane. This mean deviation corresponds to mean distances of about 3 kpc, i.e., the distance to the Sagittarius spiral arm, if we assume that the latitudinal

distribution of the X-ray sources follows the same pattern as the distribution of most stars in the Galaxy /6/. However, the distribution in galactic longitude is significantly different, and it seems that the objects indeed cluster near the galactic center /7/.

The known spectra of X-ray sources can be reliably divided into two groups. The first group contains sources with distinctly nonthermal spectrum, which may be fitted with a power function of the photon energy in a wide range of energies, $dN/dE_\gamma \sim E_\gamma^{-\beta}$. A typical representative of sources of this kind is Tau XR-1, which has been firmly identified with the Crab Nebula, a remnant of Supernova 1054. Its angular dimension is about 100", and virtually coincides with the apparent diameter of the nebula. For energies $10\,\text{keV} < E_\gamma < 100\,\text{keV}$, the spectrum has the form /8/

$$\frac{dN}{dE_\gamma} = 3.5 \cdot E_\gamma^{-1.9 \pm 0.1} \frac{\text{photons}}{\text{cm}^2 \cdot \text{sec} \cdot \text{keV}} \qquad (7)$$

According to other data /4/, the spectral index in a wide range of energies ($1\,\text{keV} < E_\gamma < 500\,\text{keV}$) is somewhat higher: $\beta = 2.3 \pm 0.2$ (Figure 2). Taking 1400 pc for the distance of the Crab Nebula, we can estimate the total power emitted in the X-ray region,

$$P(E_\gamma > 1\ \text{keV}) \approx 2 \cdot 10^{37}\ \text{erg/sec}, \qquad (8)$$

which is much higher than the power emitted by the nebula in the optical (about 10^{36} erg/sec) and the radio (about 10^{34} erg/sec) spectra. Another source /8/, which has not been identified so far with any known object, is characterized virtually by the same intensity (7). The lack of identification may be due to the low surface luminance of the corresponding optical object and the high optical absorption in the particular direction. In the radio spectrum, however, this object should be at least 500 times weaker than the Crab Nebula; there are some, hitherto unconfirmed, indications of possible variability of the source. Because of its hard spectrum, this source is brighter than Sco XR-1 for $E_\gamma > 50\,\text{keV}$. A nonthermal spectrum is also displayed by the source Lup XR-1 ($\beta \simeq 2.5$ /9/) and a number of sources near the galactic center ($\beta \simeq 2$ /10, 11/).

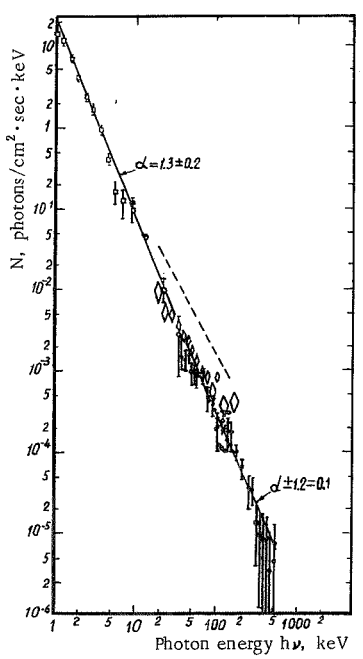

FIGURE 2. The X-ray spectrum of Tau XR-1 /4/ according to various authors, $\beta = \alpha + 1$.

In view of the strong X-ray emission of the Crab Nebula, other known radio sources identifiable with supernova envelopes should be examined for possible X-ray activity. In /12/, the X-ray source Cas XR-1 is identified with the radio source Cassiopeia A, which is the brightest known radio source in the sky and is known to be related to the envelope of Supernova 1702. Its X-ray power is $P(1\text{–}10\,\text{Å}) \simeq 6 \cdot 10^{36}$ erg/sec,

whereas the radio power is $P_r \simeq 3 \cdot 10^{35}$ erg/sec. The weak source Cep XR-1, according to /6/, is probably related to the envelope of Tycho Brahe's Supernova of 1572. The X-ray power of this source is $P(1-10\,\text{Å}) \simeq 3 \cdot 10^{36}$ erg/sec, whereas the radio power is $P_r \simeq 10^{34}$ erg/sec. Unfortunately, these identifications are still highly tentative. In any case, there is no one-to-one correspondence between X-ray sources and supernovae. Numerous sources, including Sco XR-1, Cyg XR-1, Sgr XR-1, and others, have no relation to known radio sources; on the other hand, Kepler's Supernova shows no traces of X-ray emission.

The second group includes X-ray sources which show an exponential dependence of intensity on energy, at least for moderate photon energies: this dependence is characteristic of the thermal emission of hot gas. The best known representative of this class is Sco XR-1. This is a source of small angular size (less than 20'' /13/) which has been identified with a peculiar optical object of 13th magnitude with a high luminosity excess in the ultraviolet spectrum and a continuous spectrum with weak emission lines /14/. This object turned out to be variable both in the optical spectrum, where its light changes by as much as 1 stellar magnitude in a few hours /14/ (a change of 1 stellar magnitude corresponds to a change in brightness by a factor of 2.5), and in the X-ray spectrum /15/. An X-ray flare was observed between 20 and 30 keV in /16/: the intensity of this source increased four-fold in 10 min, and then declined to the original level in 20 min. Measurements in the radio spectrum, at $\lambda = 6$ cm, also revealed strong intensity variations: by as much as a factor of 8 in 1 hr /17/. Sco XR-1 is thus characterized by flaring activity in all the regions of the observed electromagnetic spectrum.

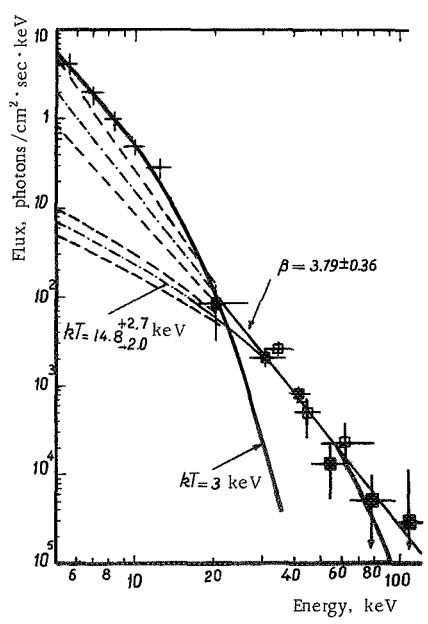

FIGURE 3. The X-ray spectrum of Sco XR-1 according to different sources:

+ – /25/; ✚, ✚ – /10/.

The spectrum of Sco XR-1 between 1 and 20 keV is adequately fitted with the function $dN/dE_\gamma \sim e^{-E_\gamma/kT} dE_\gamma/E_\gamma$, which corresponds to thermal emission of optically thin plasma. Extrapolation of this spectrum into the optical region gives adequate results for the brightness of the optical object; hence it is clear, in particular, that the X-ray power of Sco XR-1 is approximately 1000 times as high as its optical power. A characteristic temperature is $T = 6 \cdot 10^7$ °K, but the temperature is variable and it may change by as much as a factor of 2 from one observation to the next /18/. For $E_\gamma > 20-30$ keV, the emission spectrum markedly deviates from the thermal spectrum /19/: it may be represented by a function with $\beta \simeq 4$ /10/ (Figure 3).

Sco XR-1 is apparently a relatively near source, located at a distance not exceeding 200 pc. This is evident from its large angular distance from the galactic center and the conspicuous lack of absorption of the soft components of the spectrum at $E_\gamma \simeq 0.25$ keV /56/. Among other thermal sources, we should mention Cyg XR-2, which is tentatively identified with a variable blue object of 15th mag, whose properties are highly similar to the properties of the optical object in Sco XR-1, and the source Cen XR-2, which is variable in the soft region of the spectrum /20/ (between 4 April and 18 May 1967, the intensity was halved, and the temperature accordingly dropped from 3.7 to 1.5 keV). Cen XR-2 also shows a nonthermal hard X-ray tail for $E_\gamma > 20$ keV /21/. This fact, combined with the analogous behavior of the spectrum of Sco XR-1 at high energies, indicates that the classification of X-ray sources into a separate group with thermal spectra is valid only for the soft-energy components. The nonthermal spectrum is probably characteristic on the whole of all the X-ray sources, and it is associated with a specific dissipation mechanism which produces nonthermal accelerated particles /22/. Nevertheless, the division into thermal and nonthermal sources is convenient in that it correlates with some other known properties (association with peculiar stellar objects, variation) and clearly provides a reflection of the physical conditions in the relevant region of space. Cyg XR-3 and Crux XR-1 are also sources with thermal spectra. The spectrum of Cyg XR-3 shows absorption around $E_\gamma \lesssim 2.5$ keV, which may provide an indication of its great distance from the Earth ($\gtrsim 3$ kpc) /23/.

Extragalactic radio sources are of great interest. A source in the direction of the radio galaxy M 87 (Virgo A) has been reliably observed /12, 24/; its flux

$$F(1.5 < E_\gamma < 6 \text{ keV}) = 5 \cdot 10^{-10} \frac{\text{erg}}{\text{cm}^2 \cdot \text{sec}} \tag{9}$$

is approximately 1/300 of the flux of Sco XR-1 in the same energy interval. If this source is indeed associated with the radio galaxy Virgo A (distant $\simeq 11$ Mpc $= 3.3 \cdot 10^{25}$ cm), its power is

$$P \simeq 7 \cdot 10^{42} \text{ erg/sec}, \tag{10}$$

which is approximately 20 times the radio power ($3 \cdot 10^{41}$ erg/sec) and 1/10 of the optical power ($\sim 10^{44}$ erg/sec) of the corresponding object. However, if we only concentrate on the jet of Virgo A, which is regarded as a source of radio and optical synchrotron emission ($\sim 10^{42}-10^{43}$ erg/sec), the entire spectrum from radio to X-ray frequencies can be fitted with a single power

function with the index

$$\alpha = \beta - 1 \simeq 0.75 \ /24, 25/ .$$

The flux of the powerful radio galaxy Cygnus A has the upper bound value $F(2-5\,\text{keV}) < 0.03$ photons/cm$^2 \cdot$ sec /26/, but even this maximum value corresponds to a power $P < 7 \cdot 10^{43}$ erg/sec, which is less than the radio ($\sim 4 \cdot 10^{44}$ erg/sec) and the optical ($\sim 10^{44}$ erg/sec) power of the object. The upper limit $F(1.5-6\,\text{keV}) < 4 \cdot 10^{-10}$ erg/cm$^2 \cdot$ sec has also been found for the quasar 3C 273 /24/. The comparative characteristics of various X-ray sources are summarized in the table. The distances of most X-ray sources are unavailable, and the parenthetical figures therefore give the tentative values for which the power has been computed.

X-ray sources in the Universe

Source	Distance	Flux ($E_\gamma > 1.5$ keV), erg/cm$^2 \cdot$ sec	Emitted power, erg/sec		
			X-ray $E_\gamma > 1.5$ keV	optical $\nu = \Delta\nu = 10^{14}$	radio $10^7 < \nu < 10^{10}$
Quiet Sun	$1.5 \cdot 10^{13}$ cm	10^{-3}	10^{25}	$4 \cdot 10^{33}$	
Solar flares		0.3	10^{27}	$2 \cdot 10^{28}$	10^{22}
Crab Nebula	1.4 kpc	$3 \cdot 10^{-8}$	10^{37}	10^{36}	10^{34}
Cassiopeia A	3.4 kpc	$3 \cdot 10^{-9}$	$6 \cdot 10^{36}$	—	$3 \cdot 10^{35}$
Tycho Brahe	5 kpc	$\leqslant 10^{-9}$	$\leqslant 3 \cdot 10^{36}$	—	10^{34}
Cyg XR-1	(1 kpc)	$3 \cdot 10^{-8}$	$3 \cdot 10^{36}$	—	—
Sco XR-1	(200 pc)	$2 \cdot 10^{-7}$	10^{36}	$\sim 10^{28}$	10^{33}
Cyg XR-2	(1 kpc)	10^{-8}	10^{36}	—	—
Galaxy			$\sim 10^{40}$	$4 \cdot 10^{44}$	10^{39}
Virgo A	11 Mpc	$5 \cdot 10^{-10}$	10^{43}	10^{44}	$3 \cdot 10^{41}$
Cygnus A	220 Mpc	$< 10^{-10}$	$< 10^{44}$	10^{44}	$4 \cdot 10^{44}$
Quasar 3C 273	500 Mpc	$< 4 \cdot 10^{-10}$	$< 10^{46}$	10^{46}	$3 \cdot 10^{43}$

Diffuse X-ray emission. Simultaneously with the discovery of the first discrete X-ray source, the diffuse X-ray emission was discovered, which creates an isotropic X-ray background /3/. The extraterrestrial origin of this radiation has been established with fair certainty /27/. Moreover, the high isotropy of this component (when the sky is divided into 30-deg sectors, the differences in intensity do not exceed 8% /28/) points to its Metagalactic origin, i.e., it is associated with the Metagalaxy as a whole or with a significant part of its volume.

The spectrum composition of the diffuse radiation has been studied in fairly great detail, especially between 1 and 60 keV. At these energies, the spectrum can be fitted with a function

$$\frac{dN}{dE_\gamma} = 12.4\, E_\gamma^{-1.7\pm0.2} \ \frac{\text{photons}}{\text{cm}^2 \cdot \text{sec} \cdot \text{sterad} \cdot \text{keV}} . \qquad (11)$$

For $E_\gamma < 1$ keV, no adequate data are available. The results of /29/, and especially of /30/, for $E_\gamma \simeq 0.28$ keV lie above the spectrum (11) when extended to this energy. However, in /29/, the divergence amounts to no

more than twice the measurement error, whereas in /30/ the observations were made in a small part of the sky so in principle they could contain a contribution of various local sources. The evidence is thus inadequate to establish the existence of a break in the spectrum, although this possibility should not be ruled out. 125

For $E_\gamma > 60$ keV, the diffuse spectrum becomes softer, i.e., its slope increases. Thus, according to /27/, the average intensity for $10\,\text{keV} < E_\gamma < 180\,\text{keV}$ is characterized by the dependence $E^{-2.4\pm0.2}$. On the other hand, according to /28/, in a wide energy range from 60 keV to gamma energies of $E \gtrsim 100$ MeV /31/, the spectrum is adequately fitted by a function of the form E^{-2}. It should be stressed, however, that in /31/, strictly speaking, the upper limit of the flux value was obtained, $\varphi(E \gtrsim 100\,\text{MeV}) = 1.1 \pm 0.2 \cdot 10^{-4}$ photons/cm^2 · sec · sterad; moreover, because of the lack of data for energies between 1 and 100 MeV, it is not clear whether the spectrum for $E \gtrsim 100$ MeV is a smooth continuation of the X-ray spectrum or not. Measurements for $E = 1$—100 MeV should be carried out with the greatest urgency, together with more detailed measurements for $E > 100$ MeV. Proceeding from the results of /27, 28/, the following intensity function should be adopted for $E > 60$ keV:

$$\frac{dN}{dE} = 60\, E^{-2.2\pm0.2}\, \frac{\text{photons}}{\text{cm}^2 \cdot \text{sec} \cdot \text{sterad} \cdot \text{keV}}. \qquad (12)$$

Cosmic gamma rays. The measurements in this part of the spectrum are complicated because of the small fluxes of hard photons with $E_\gamma > 1$ MeV and the strong background associated with cosmic rays and the atmospheric albedo. The first positive result for energies $E_\gamma \gtrsim 100$ MeV was obtained in /31/ from measurements with the OSO-3 orbiting station. A gamma-ray flux was detected, which was found to diminish rapidly with the distance from the galactic plane, reaching a maximum in the centerward direction (Figure 4). This provided a virtually unambiguous proof of the galactic origin of the gamma rays.*

The low angular resolution of the telescope ($\sim 30°$) makes it impossible to determine the true intensity of this radiation, and it is therefore characterized by the so-called "line" intensity, integrated along one of the directions, e.g., over the galactic latitude and thus depending on the galactic longitude only. This "line" intensity has a peak in the centerward direction and is equal to

$$I_e (\gtrsim 100\ \text{MeV}) = 5 \cdot 10^{-4}\, \frac{\text{photons}}{\text{cm}^2 \cdot \text{sec} \cdot \text{rad}}. \qquad (13)$$

The intensity is a nonmonotonic function of longitude, and it displays a prominent secondary maximum in the direction of the anticenter ($\sim 3 \cdot 10^{-4}$ 1/cm^2 · sec · rad). The isolation of the isotropic component (the background) is less reliable than of the galactic component, and the numerical result

$$I (\gtrsim 100\ \text{MeV}) = 1.1 \pm 0.2 \cdot 10^{-4}\, \frac{\text{photons}}{\text{cm}^2 \cdot \text{sec} \cdot \text{sterad}}, \qquad (14)$$

* A similar result obtained with the PROTON-2 satellite was reported at the All-Union Conference on Cosmic-Ray Physics (Tashkent, 1968) by L. S. Bratolyubov-Tsulukidze, N. L. Grigorov, L. F. Kalinkin, A. S. Melioranskii, E. A. Pryakhin, and I. A. Savenko.

strictly speaking, should only be considered as an upper limit, although some experimental indications seem to suggest that this figure is not far from the truth /31/. All other results in gamma-ray astronomy are so far confined to upper bound values of the possible fluxes. Balloon observations with photographic emulsions limit the primary fluxes to /32/

$$I(E_\gamma > 10^{11}\ \text{eV}) < 4 \cdot 10^{-7}\ \frac{\text{photons}}{\text{cm}^2 \cdot \text{sec} \cdot \text{sterad}},$$
$$I(E_\gamma > 10^{12}\ \text{eV}) < 5 \cdot 10^{-9}\ \frac{\text{photons}}{\text{cm}^2 \cdot \text{sec} \cdot \text{sterad}}, \tag{15}$$

and, by /33/,

$$I(E_\gamma > 4.7 \cdot 10^{11}\ \text{eV}) < 10^{-7}\ \frac{\text{photons}}{\text{cm}^2 \cdot \text{sec} \cdot \text{sterad}}, \tag{16}$$

which is less than 0.1% of all the cosmic rays of the same energy.

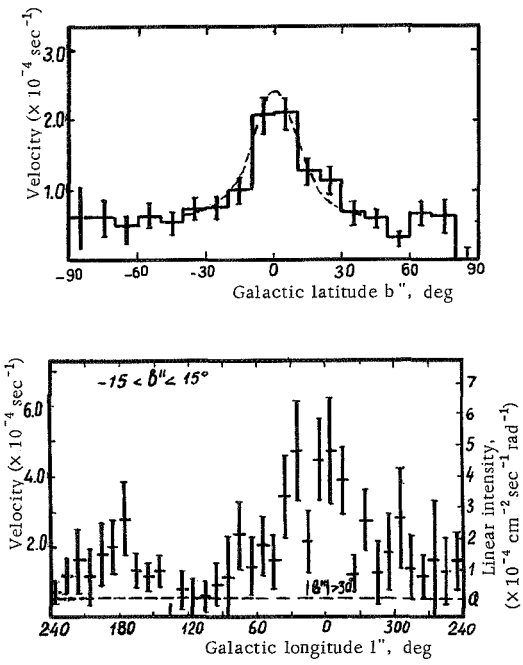

FIGURE 4. The flux of hard gamma rays ($E_\gamma \gtrsim 100$ MeV) vs. galactic latitude (top) and galactic longitude (bottom).

At very high energies $E_\gamma \approx 10^{15}$–10^{16} eV, the upper bound value of the gamma-ray flux may be established by an analysis of the μ-meson content of the wide showers (showers triggered by primary photons should contain an anomalously low count of μ-mesons). Thus, in /34/, the proportion of primary photons among all cosmic rays producing showers with $E > 10^{15}$ eV is estimated at 10^{-3}. According to /35/, between 10^{15} and 10^{16} eV, $I_\gamma(E) = 2 \cdot 10^{-4} I_{cr}(E)$, where $I_{cr}(E)$ is the intensity of all cosmic rays of given energy. For $E > 10^{16}$ eV, the proportion of these showers is apparently even

less. No such showers were detected in /35/, and in /36/ the upper bound intensity value is given as

$$I_\gamma (E_\gamma > 10^{16}\ \text{eV}) < 2 \cdot 10^{-4}\ I_{cr} (E > 10^{16}\ \text{eV}). \qquad (17)$$

The relationship of the muon-poor wide atmospheric showers with high-energy primary photons will be confirmed by the discovery of an anisotropy in the originating direction of these showers (high-energy photons in all probability form in the galactic disk). Some indications of this anisotropy are provided by /35/, but there is no statistical justification of these results.

Finally, there are some measurements of the upper bound value of the gamma-ray flux for some discrete sources. A spark chamber launched on a balloon /37/ helped to establish the following upper bound value for the Crab Nebula, Cygnus A, Sco XR-1, and a number of quasars:

$$F (30 < E_\gamma < 500\ \text{MeV}) \leqslant 10^{-4} \frac{\text{photons}}{\text{cm}^2 \cdot \text{sec}} \qquad (18)$$

Repeat measurements /38/ gave $F(E_\gamma > 75\ \text{MeV}) < 10^{-5}\ 1/\text{cm}^2\text{sec}$ for Cygnus A; for the quasar 3C 273 and the radio galaxy M 87, the results are $F(E_\gamma > 50\ \text{MeV}) < 1.1 \cdot 10^{-5}$ and $0.5 \cdot 10^{-5}\ 1/\text{cm}^2 \cdot \text{sec}$, respectively. For very high energy photons, $E_\gamma > 5 \cdot 10^{12}$ eV, the upper bound flux value for a number of objects is given in /39, 40/; a typical flux value (Crab Nebula, quasar 3C 273) is about 10^{-11} photons/cm$^2 \cdot$ sec. A summary of the experimental results for the upper bound values of the gamma-ray fluxes from a number of discrete sources will be found in /41/.

THE MECHANISMS OF X-RAY AND GAMMA-RAY EMISSION

Before proceeding with an analysis of particular hypotheses regarding the nature of the hard cosmic radiation, we will briefly consider the fundamental physical processes responsible for the emission of hard photons. These processes have been studied in considerable detail, and our discussion is therefore based on a firm theoretical foundation. The fundamental processes include synchroton radiation, Compton emission (sometimes called an inverse Compton effect), and the bremsstrahlung of electrons; for gamma energies $E_\gamma > 50$ MeV, some contribution is also due to creation and decay of neutral mesons in nuclear collisions of high-energy nucleons. There are also a number of other, mainly secondary processes. They include gamma rays emitted in transitions of excited nuclei, in electron-positron annihilation, in the decay of neutral pions produced by creation and decay of hyperons, and also directly in the interaction of high-energy nucleons with low-energy photons (this photocreation process is particularly significant in the ultra-high energy region). Hard radiation is also emitted following creation and subsequent decay of charged mesons, and in the production of delta-electrons; with regard to its properties, this radiation should be classified as bremsstrahlung. Finally, synchrotron and Compton radiation and bremsstrahlung are also produced by protons, but because of the large proton mass, the

corresponding component is generally negligible. We will give here only some simple final expressions for the principal emission mechanisms (for details, see /41–43/).

The volume luminosity $q(E_\gamma)$ is conveniently used in various applications. This quantity is defined as the number of photons emitted by unit volume in unit solid angle and unit energy interval. The emission intensity produced in a given direction over a path length L is

$$I(E_\gamma) = \int_0^L q(E_\gamma)\, d\tau, \tag{19}$$

and the radiation flux from a source of small angular size is

$$F(E_\gamma) = \int_{\Delta\Omega} I(E_\gamma)\, d\Omega = \frac{1}{R^2}\int_V q(E_\gamma)\, dV, \tag{20}$$

where V is the source volume. Alongside the luminosity $q(E_\gamma)$ and the intensity $I(E_\gamma)$, which express the photon flux in unit solid angle, one often uses the energy luminosity $e(E_\gamma)$ and the energy intensity $I(E_\gamma)$ referring to the energy flux. The two sets of physical quantities are clearly related by the equalities

$$\varepsilon(E_\gamma) = E_\gamma\, q(E_\gamma), \quad \mathcal{J}(E_\gamma) = E_\gamma\, I(E_\gamma) \tag{21}$$

Synchrotron radiation. The average energy of photons emitted by an electron of energy $E \gg mc^2$ moving at an angle θ to the magnetic field H can be found using the well-known spectrum of the radiation emitted by a particle in a magnetic field /42/:

$$\langle E_\gamma \rangle = \xi_s \hbar\omega_H \left(\frac{E}{mc^2}\right)^2 \sin\theta = 0.54\cdot 10^{-8} H_\perp \left(\frac{E}{mc^2}\right)^2 \text{ eV}, \tag{22}$$

where

$$\omega_H = 1.76\cdot 10^7 \text{ sec}^{-1} \text{ and } \xi_s = 4/(9\sqrt{3}) \simeq 0.462.$$

For an isotropic distribution of electrons with an energy spectrum

$$N(E)\,dE = K\left(\frac{E}{mc^2}\right)^{-\varkappa} \frac{dE}{mc^2} \text{ cm}^{-3}, \tag{23}$$

which move in a random magnetic field, the energy luminosity per unit volume is

$$4\pi\varepsilon_s(E_\gamma)\,dE_\gamma = f_s(\varkappa)\,\sigma_T c\,\frac{H^2}{8\pi} K\left(\frac{E_\gamma}{\hbar\omega_H}\right)^{-\frac{\varkappa-1}{2}} \frac{dE_\gamma}{\hbar\omega_H}, \tag{24}$$

where $f_s(\varkappa) = 4\left(\frac{3}{2}\right)^{\frac{\varkappa+1}{2}} a(\varkappa)$, and the value of the function $a(\varkappa)$ is given in /42/; $\hbar\omega_H = 1.85\cdot 10^{-20} H$ erg $= 1.16\cdot 10^{-8} H$ eV. A characteristic feature of synchrotron radiation is its high degree of polarization, which for a homogeneous magnetic field is given by

$$\Pi = \frac{\varkappa + 1}{\varkappa + 7/3}, \tag{25}$$

and the electric vector oscillates at right angles to the projection of the magnetic field onto the image plane.

Compton scattering. The mean energy of photons produced in Compton scattering of thermal photons by ultrarelativistic electrons is

$$\langle E_\gamma \rangle \simeq \frac{4}{3} E_T \left(\frac{E}{mc^2}\right)^2 = 3.6\,\mathrm{kT}\left(\frac{E}{mc^2}\right)^2, \tag{26}$$

where $E_T = 2.7\,\mathrm{kT}$ is the mean energy of the thermal photons for radiation of temperature T. Assuming the power spectrum (23), the energy luminosity per unit volume under isotropic conditions is

$$4\pi \mathcal{E}_c(E_\gamma)\,dE_\gamma = f_c(\varkappa)\sigma_T c w_{ph} K \left(\frac{E_\gamma}{E_T}\right)^{-\frac{\varkappa-1}{2}} \frac{dE_\gamma}{E_T}, \tag{27}$$

where the function $2(4/3)^{\frac{\varkappa-1}{2}} f_c(\varkappa)$ is listed in /43/; for the relict radiation with $T = 2.7°K$, $3.6\,\mathrm{kT} = 8.2 \cdot 10^{-4}$ eV. Compton radiation is unpolarized.

Bremsstrahlung. The emission of equilibrium plasma at temperature T in the absence of absorption is characterized by the volume luminosity

$$4\pi \epsilon(\nu) = \frac{7.7 \cdot 10^{-38}}{\sqrt{T}} n^2 e^{-\frac{h\nu}{kT}} \frac{\mathrm{erg}}{\mathrm{cm}^3 \cdot \mathrm{sec} \cdot \mathrm{Hz}}, \tag{28}$$

where n is the electron concentration. If, however, the "optical" thickness of the plasma is large, it emits as a blackbody: the spectral energy density emitted by unit surface area is described by Planck's equation

$$B_\nu = \frac{2h\nu^3}{c^2} \frac{1}{\exp(h\nu/kT - 1)}. \tag{29}$$

As we have seen, in most cases the emission spectrum of celestial objects in the X-ray region is distinctly nonthermal or at least displays a nonthermal "tail" for high-energy photons. In this relation, we should consider the bremsstrahlung of nonthermal electrons. For sufficiently fast ($v/c > e^2/\hbar c = 1/137$), and yet nonrelativistic, electrons in a hydrogen plasma (without screening), the electron energy distribution (23), with E interpreted as the kinetic energy, leads to the volume luminosity

$$4\pi \mathcal{E}_b(E_\gamma)\,dE_\gamma = \frac{\sqrt{2}}{\pi} I(\varkappa) n c \sigma_T \alpha K \left(\frac{E_\gamma}{mc^2}\right)^{-(\varkappa - \frac{1}{2})} dE_\gamma, \tag{30}$$

where the function $I(\varkappa) = \frac{1}{\varkappa - 1}$ has been defined in /44/, and $\alpha = e^2/\hbar c = 1/137$.

For ultrarelativistic electrons ($E \gg mc^2$)

$$4\pi \mathcal{E}_b(E_\gamma)\,dE_\gamma = f_b(\varkappa) n c \sigma_T \alpha K \left(\frac{E_\gamma}{mc^2}\right)^{-(\varkappa - 1)} dE_\gamma, \tag{31}$$

where the function $f_\ell(\varkappa)$ is defined in /44/. For anisotropic beams of non-thermal electrons, the bremsstrahlung may display marked polarization /45/.

Comparison of the three mechanisms. All the three emission mechanisms are associated with electrons, and therefore they should not be considered separately. Indeed, it may turn out that when one of these mechanisms is applied to account for the radiation flux in a particular frequency interval, the other two mechanisms combined will lead to excessively large radiation fluxes in other frequency intervals. Electrons of a given energy $E \gg mc^2$ emit photons of different energies by the three processes, and the ratio of the mean photon energies is

$$\langle E_\gamma \rangle_s : \langle E_\gamma \rangle_c : \langle E_\gamma \rangle_\ell = \frac{1.7 \cdot 10^{-5}\, H}{T} : 1 : \frac{4 \cdot 10^{14}}{T E(\mathrm{eV})}, \tag{32}$$

where we take $\langle E_\gamma \rangle_\ell = E/2$. The spectral intensities in the corresponding energy intervals from (32) relate as ($\varkappa \simeq 3$)

$$\varepsilon_s : \varepsilon_c : \varepsilon_\ell \approx 10^{19} \frac{H}{n_\varphi} : 1 : 10^{-3} \frac{n}{n_\varphi}, \tag{33}$$

where $n_\varphi = w_\varphi / E_T$ is the concentration of thermal photons. If we compare the intensities of Compton and synchrotron radiation photons associated with electrons of a given energy, we readily find

$$\frac{q_c}{q_s} \simeq \frac{w_\varphi}{H^2/8\pi} \frac{\langle E_\gamma \rangle_s^2}{\langle E_\gamma^2 \rangle_c}. \tag{34}$$

Hence it follows that for $w_\varphi \simeq H^2/8\pi$, the Compton radiation will be a continuous extension of the synchrotron radiation if the power index in (23) is $\varkappa = 3$ and the corresponding index of the photon spectrum $q \sim E_\gamma^{-\beta}$ is $\beta = \frac{\varkappa + 1}{2} = 2$. If $\varkappa > 3$, the Compton component prevailing in the hard part of the photon spectrum will extend above the continuation of the synchrotron spectrum, and if $x < 3$, the Compton component will extend below the continuation of the synchrotron spectrum.

Gamma-ray emission mechanisms. The three processes considered above may also act as sources of hard gamma rays. For photon energies $E_\gamma > 100$ MeV, an additional contribution is due to the creation and decay of neutral mesons in nuclear collisions with the participation of cosmic rays. To assess the effectiveness of this process, we may use the expression / 42/ :

$$q(E_\gamma) = 10^{-27}\, E^{-2.8} \frac{\text{photons}}{\mathrm{cm}^3 \cdot \mathrm{sec} \cdot \mathrm{sterad} \cdot \mathrm{GeV}}, \tag{35}$$

where n is the concentration of hydrogen atoms and the energy E_γ is measured in GeV. Expression (35) refers to cosmic ray intensities observed at the Earth and may be used to estimate the intensity of gamma rays produced by cosmic rays in the Galaxy.

MODERN HYPOTHESES REGARDING THE ORIGIN OF THE HARD COSMIC RADIATION

The theory of cosmic X rays and gamma rays is still far from perfect. Gamma- and X-ray astronomy is still in its embryonic stage, and we have to rely on very limited data. Another unfavorable factor is the insufficiency of astronomical and astrophysical information about such objects as supernovae and nonstationary stars, distribution of matter and radiation in the Galaxy and the Metagalaxy, etc. Thus gamma- and X-ray astronomy is in effect expected to supplement and refine the current astronomical knowledge, rather than draw upon it. The theoretical analysis is therefore often based on models of astronomical objects whose properties are in no way illuminated by optical and radio astronomy. This accounts for the great uncertainty and ambiguity of the results.

Models using the synchrotron and the bremsstrahlung mechanisms have been equally applied to the interpretation of discrete galactic X-ray sources /46/. The same applied to sources with distinctly nonthermal spectrum, such as the Crab Nebula (the bremsstrahlung mechanism of X-ray emission of the nebula is discussed in /47/), and to "thermal" sources of the type of Sco XR-1 (synchrotron radiation is assumed in /48, 49/).

Various hypotheses are also advanced regarding the origin of the diffuse X-ray background: it is variously described as the resultant emission of the discrete sources in all the galaxies /50/, Compton scattering of relativistic electrons in the intergalactic space /51, 52/, Compton scattering of electrons in radio galaxies /53/. A characteristic feature of these hypotheses is that they all assume a pronounced evolutionary effect for X-ray sources, i.e., it is assumed that the radiation mainly originated in the early stages of evolution of the Metagalaxy. Moreover, considerable difficulties are encountered in the interpretation of the X-ray spectra /54/.

The situation regarding gamma rays with photon energies $E_\gamma \gtrsim 100$ MeV is no clearer at this stage. The galactic origin of this radiation has been firmly established in /31/. However, the very likely mechanisms of gamma-ray generation in nuclear collisions of cosmic rays /42/ yields intensities which are approximately 1/20 of the observed intensity /31/. This divergence naturally exceeds the permissible margin of error and necessitates further analysis of other alternatives. In /55/ it has been suggested that the hard gamma rays are generated together with X rays in the nonthermal discrete galactic sources. The spatial distribution and the intensity of gamma rays can be accounted for if the X-ray spectrum is extended with the same slope into the gamma-ray region.

Our concepts regarding the origin of cosmic gamma rays and X rays are thus still in a state of high fluidity. There are no grounds for pessimism, however. On the contrary, gamma- and X-ray astronomy has yielded highly valuable results for a number of known objects (Crab Nebula, matter and cosmic rays in the Metagalaxy) and led to the discovery of new objects and processes in the Galaxy, primarily the powerful processes of fast electron generation. There is no doubt that we are now on the threshold of solving the great puzzle and elucidating the origin of these cosmic processes and their significance in the physics of the Universe.

Bibliography

1. Hudson, H.S., L.E. Peterson, and D.A. Schwartz.— Astrophys. J. 1969. (In press).
2. Hinteregger, H.E.— J. Geophys. Res., **66**:2367. 1961.
3. Giacconi, R., H. Gursky, F.R. Paolini, and B. Rossi.— Phys. Rev. Lett., **9**:439. 1962; **11**:530. 1963.
4. Rossi, B.B. Discrete Extrasolar X-Ray Sources.— Intern. Symp. on Contemporary Physics. Preprint. 1968.
5. Giacconi, R., P. Gorenstein, H. Gursky, E.M. Kellog, and H. Tananbaum. The X-ray Explorer Experiment.— Preprint ASE, Dec. 12, 1968.
6. Firedman, H., E.T. Byram, and T.A. Chubb.— Science, **156**: 374. 1967.
7. Johnson, H.M. Galactic X-Ray Statistics.— Preprint. 1968.
8. Peterson, L.E., A.S. Jacobson, R.M. Pelling, and D.A. Schwartz.— Canad. J. Phys., **46**:437. 1968.
9. Schwartz, D.A., H.S. Hudson, and L.E. Peterson.— Astrophys. J. Lett., **152**. 1968.
10. Buselli, G., M.C. Clancy, P.J.N. Davison, P.J. Edwards, K.G. McCraken, and R.M. Thomas.— Nature, **219**:5159. 1969.
11. Boldt, E., H. Doong, P. Serlemitsos, and G. Riegler.— Canad. J. Phys., **44**:S444. 1968.
12. Byram, E.T., T.A. Chubb, and H. Friedman.— Science, **152**. 1966.
13. Gursky, H., R. Giacconi, P. Gorenstein, J.R. Waters, M. Oda, H. Bradt, G. Garmire, and B.V. Sreekantan.— Astrophys. J., **144**:1249. 1966.
14. Sandage, A.R., P. Osmer, R. Giacconi, P. Gorenstein, H. Gursky, J. Waters, H. Bradt, G. Garmire, B.V. Sreekantan, M. Oda, K. Osawa, and J. Jugaku.— Astrophys. J., **146**:316. 1966.
15. Chodil, G., H. Mark, R. Rodrigues, F.D. Seward, C.D. Swift, I. Tariel, W.A. Hiltner, G. Wallerstein, and E.J. Mannery.— Astrophys. J., **154**:645. 1968.
16. Lewin, W.H.G., G.W. Clark, and W.B. Smith.— Astrophys. J., **152**:L55. 1968.
17. Ables, J.G. The Variation of the Radio Emission from Sco XR-1.— Univ. of Adelaide, Preprint. Nov. 1968.
18. Gorenstein, P., H. Gursky, and G. Garmire.— Astrophys. J., **153**:885. 1968.
19. Peterson, L.E. and A.S. Jacobson.— Astrophys. J., **145**:962. 1966.
20. Francey, R.J., A.G. Fenton, J.R. Harries, and K.G. McCraken. The Variability of Centaurus XR-2.— Univ. of Adelaide, Preprint. 1966; Nature, **217**:773. 1967.
21. Lewin, W.H.G., G.W. Clark, and W.B. Smith.— Astrophys. J. Lett., **152**:49, 55. 1968.
22. Syrovatskii, S.I.— Astronomicheskii Zhurnal, **43**:340. 1966; Trudy V Vsesoyuznoi ezhegodnoi zimnei shkoly po kosmofizike, p. 58, Apatity, Izd. Kol'skogo filiala AN SSSR. 1968.

23. Gorenstein, P., R. Giacconi, and H. Gursky.— Astrophys. J. Lett., 150:85. 1967.
24. Bradt, H., W. Mayer, S. Naranan, S. Rappaport, and G. Spada.— Astrophys. J. Lett., 150:199. 1967.
25. Shklovskii, I.S.— Astronomicheskii Zhurnal, 44:58. 1967.
26. Giacconi, R., R. Gorenstein, H. Gursky, and J.R. Waters.— Astrophys. J., 148:211. 1967.
27. Bleeker, G.A.M., J.J. Burger, A.J.M. Deerenberg, A. Scheepmarker, B.N. Swannenburg, Y. Tanaka, S. Hayakawa, F. Makino, and H. Ogawa.— Canad. J. Phys., 46:461. 1968.
28. Gorenstein, P., E.M. Kellog, and H. Gursky.— Astrophys. J., 156:315. 1969.
29. Bowyer, C.S., G.B. Field, and J.E. Mack.— Nature, 217:32. 1968.
30. Henry, R.C., G. Fritz, J.F. Meekins, H. Friedman, and E.T. Byram.— Astrophys. J., 153:L11. 1968.
31. Clark, G.W., G. Garmier, W.L. Kraushaar.— Astrophys. J., 153:L203. 1968.
32. Kidd, J.M.— Nuovo Cimento, 27:57. 1963; 29:315. 1963.
33. Duthie, J., P.H. Fowler, A. Kaddoura, D.H. Perkins, and K. Pinkau.— Nuovo Cimento, 24:122. 1962.
34. Firhowski, R., J. Gawin, A. Zawadski, and R. Maze.— Nuovo Cimento, 29:19. 1963; Proc. Ninth Intern. Conf. Cosmic Rays (London), 2:639. 1965.
35. Toyoda, Y., K. Suga, K. Murakami, H. Hasegawa, S. Shibata, V. Domingo, I. Escobar, K. Komata, H. Bradt, G. Clark, and M. La Pointe.— Proc. Ninth Conf. Cosmic Rays (London), 2:708. 1965.
36. Vernov, S.N., V.I. Solov'eva, B.A. Khrenov, and G.B. Khristiansen.— Izvestiya AN SSSR, Seriya Fizicheskaya, 29:1676. 1965.
37. Frye, G.M. and L.H. Smith.— Phys. Rev. Lett., 17:733. 1966.
38. Frye, G.M. and C.P. Wang.— Phys. Rev. Lett., 18:132. 1967.
39. Chudakov, A.E., V.L. Dadykin, V.I. Zatsepin, and N.M. Nesterova.— Trudy FIAN, 26:118. 1964.
40. Fruin, J.H., S.V. Jelley, C.D. Long, N.A. Porter, and T.C. Weekes.— Phys. Lett., 10:176. 1964; Proc. Conf. Cosmic Rays (London), 1:318. 1965.
41. Fazio, G.G.— Ann. Rev. Astron. Astrophys., 5:481. 1967.
42. Ginzburg, V.L. and S.I. Syrovatskii.— UFN, 84:201. 1964.
43. Ginzburg, V.L. and S.I. Syrovatskii.— UFN, 87:65. 1965.
44. Korchak, A.A.— Astronomicheskii Zhurnal, 44:328. 1967; Geomagnetizm i Aeronomiya, 5:32. 1965.
45. Korchak, A.A.— DAN SSSR, 173:291. 1967.
46. Burbidge, G. Discrete X-Ray Sources.— Preprint. 1969.
47. Sartori, L. and P. Morrison.— Astrophys. J., 150:385. 1967.
48. Manley, O.P.— Astrophys. J., 144:1253. 1966.
49. Manley, O.P. and S. Olbert. Preprint. 1968.
50. Hayakawa, S., M. Matsuoka, and K. Yamashita.— Proc. Conf. Cosmic Rays (London), 1:119. 1965.

51. Felten, S.E. and P. Morrison.— Astrophys. J., 146:686. 1966.
52. Brecher, K. and P. Morrison.— Astrophys. J., 150:L61. 1967.
53. Bergamini, R., P. Londrillo, and G. Setti.— Nuovo Cimento, 52B:495. 1967.
54. Longair, M.S. and R.A. Sunyaev. Preprint. 1969.
55. Ögelman, H.— Nature, 221:753. 1969.
56. Fritz, G., J.F. Meekins, R.C. Henry, E.T. Byram, and H. Friedman.— Astrophys. J. Lett., 153:199. 1968.

LOW-ENERGY GAMMA RAYS (0.1 – 10 MeV) IN THE ATMOSPHERE AND IN OUTER SPACE

A. M. Romanov

X-rays and gamma rays from outer space carry valuable information on the distribution of matter and fields in the interstellar and intergalactic medium and on cosmic-ray composition and fluxes in the Galaxy and the Metagalaxy. Because of the straight-line propagation and the vanishingly small absorption of gamma rays, this information reaches the Earth in undistorted form. Theoretical analysis of processes responsible for the production of cosmic gamma rays will be found in the paper by V. L. Ginzburg and S. I. Syrovatskii /1/.

The current state of the experimental studies of cosmic gamma rays with $E_\gamma > 50$ MeV is reviewed in /2 – 5/ and in papers /6 – 8/ delivered at the International Conference on Cosmic Ray Physics in Canada. A review of the results pertaining to cosmic X rays will be found, e.g., in /9, 10/. The present paper reviews the experimental studies of low-energy gamma rays (0.1 – 10 MeV) in the atmosphere and in outer space.

PRODUCTION OF LOW-ENERGY GAMMA RAYS IN THE INTERSTELLAR MEDIUM AND IN STELLAR ATMOSPHERES

Intensity estimates of galactic and metagalactic low-energy gamma rays

The principal generation processes of X rays and soft gamma rays with a continuous spectrum are bremsstrahlung, synchrotron radiation, and Compton scattering of fast electrons. Line gamma spectra are generated when slowed-down positrons annihilate or excited nuclei get rid of some of their excitation energy. The gamma ray intensity is a function of the cosmic-ray intensity in the source region and also depends on the mass and the radiation energy density per unit area along the line of sight. According to /1/, the intensity of the galactic gamma rays with $E_\gamma > 0.5$ MeV produced as a result of Compton effect is about 10^{-4} photons $\cdot$ cm^{-2} $\cdot$ sec^{-1} $\cdot$ sterad^{-1} when averaged over all directions. The intensity in the direction to the anticenter should be $^1/_5$ of the centerward intensity. According to the same authors /1/, the expected intensity of galactic gamma rays in line spectra is $^1/_{100}$ – $^1/_{1000}$ of the continuous radiation intensity.

The intensity of the metagalactic gamma rays significantly depends on the values of ξ_{cr} and ξ_e which characterize the intensity ratio of the cosmic rays and the electron component in the Metagalaxy and the Galaxy. According to /1/, the intensity of the metagalactic gamma rays with $E_\gamma > 0.5$ MeV produced by Compton scattering of light photons is $0.1\xi_e$, whereas the intensity in the 0.5 MeV line is $5 \cdot 10^{-4}\xi_{cr}$.

Intensity estimates of the gamma rays of the quiet Sun

Virtually the entire gamma radiation emitted by the quiet Sun is attributable to the interaction of the galactic cosmic rays with the solar photosphere. The intensity of the solar gamma rays can be computed from measurement data of the spectral distribution of gamma rays in the upper layers of the Earth's atmosphere (see Figure 9). These computations should take into consideration atmospheric absorption, latitudinal dependence, and the ratio of the solid angles for the detection of atmospheric and solar radiation.

An additional source of weak gamma rays from the quiet Sun is provided by the decay of radioactive nuclei in the solar atmosphere (K^{40}, Th^{228}, etc.).

Gamma rays of solar flares

The intensity of gamma rays generated by solar flares is estimated in /12, 13/. These estimates are based on idealized solar flare models, which incorporate certain assumptions regarding the depth and the area of the flare region and the concentration of nuclei and electrons in the spectrum of accelerated particles.

The bulk of solar gamma rays between 0.1 and 10 MeV is associated with electron bremsstrahlung. According to /12/, the flare area is on the average 10^{19} cm^2, and the flare depth is 10^9 cm; the concentration of protons and electrons is about $3 \cdot 10^{13}$ cm^{-3}, i.e., the thickness of the generating layer is of the order of 0.1 g/cm^2. The flare duration is from 10 to 1000 sec, and the number of protons N accelerated by the flare ranges between 10^{31} and 10^{35} sec^{-1}. The spectrum of the accelerated protons is expressed by the exponential function

$$N(P) = N_0 \exp(-P/P_0), \qquad (1)$$

where P is the proton magnetic rigidity, P_0 is the characteristic rigidity of the flare.

For $P_0 = 70$ MV and $N = 10^{32}$ sec^{-1}, the solar bremsstrahlung fluxes at the Earth according to /12/ are F_γ (> 0.1 MeV) = 100 cm^{-2}sec^{-1}, F_γ (> 1 MeV) $\approx$ 60 cm^{-2}sec^{-1}, F_γ (> 10 MeV) = 20 cm^{-2}sec^{-1}. The fluxes markedly diminish as P_0 decreases.

The protons accelerated by the flare are scattered inelastically by the nuclei C^{12}, N^{14}, O^{16}, and Ne^{20}. This scattering gives rise to line

gamma-ray emission with line energies of 4.43 MeV (C^{12}), 1.63 and 2.31 MeV (N^{14}), 6.14 and 7.12 MeV (O^{16}), and 1.63 MeV (Ne^{20}). Moreover, solar flares generate gamma rays with energies of 0.51 MeV (positron annihilation) and 2.22 MeV (the reaction $H^1(n, \gamma) D^2$). Gamma rays with energies above 50 MeV and with a continuous spectrum of energies are produced by neutral pion decay. Figure 1 plots the computed Earth-orbit fluxes of solar gamma rays generated during the accelerating phase of the flare in a layer 1 g/cm^2 thick for various values of P_0. Figure 2 lists the same data for the deceleration phase (it is assumed that a fraction of the accelerated particles is retained by the Sun and slows down in a time comparable with the acceleration time t_1).

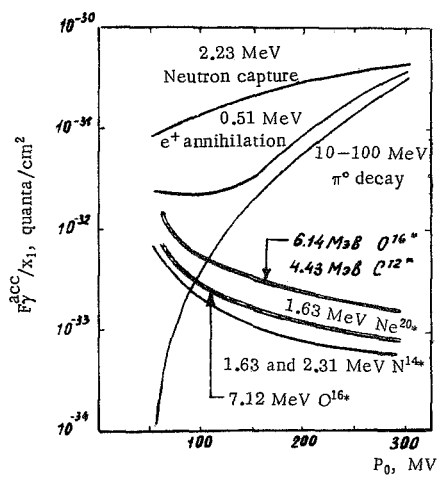

FIGURE 1. Computed gamma ray fluxes generated during the accelerating phase of a solar flare.

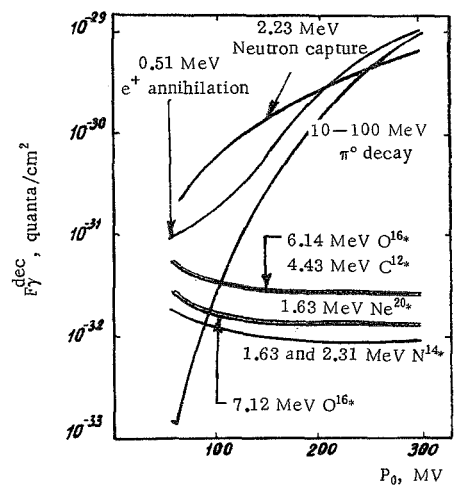

FIGURE 2. Computed gamma ray fluxes generated during the decelerating phase of a solar flare.

If a flare with P_0 = 150 MV generates 10^{34} protons with energies of over 30 MeV in $t_1 = 10^3$ sec, the mean fluxes of 2.23 and 0.51 MeV gamma rays at Earth orbit, according to Figure 1, will be 2 and 0.3 photons/cm^2 · sec. It is assumed that the number of protons emitted by the Sun is equal to the total number of protons generated during the flare. If half of the total number is retained and decelerated on the Sun, Figures 1 and 2 shows that the Earth-orbit fluxes of 2.23 and 0.51 MeV gamma rays will be 16 and 6 photons/cm^2 · sec, respectively.

EQUIPMENT FOR MEASURING THE SPATIAL AND SPECTRAL DISTRIBUTION OF LOW-ENERGY GAMMA RAYS

The equipment for gamma ray measurements should ensure selective recording of low gamma-ray fluxes in a chosen energy range. The results of experiments in the upper atmosphere and in the Earth space should be

corrected for the background of gamma quanta and neutrons generated in the atmosphere and also for those generated in the detector or the surrounding materials (the local background). For measurements far from Earth, the local background is the most significant distorting factor.

The search for weak point sources necessitates accurate correction for the isotropic "background" of X rays and gamma rays. The instrument used in these measurements should ensure a low local background level and it should be highly directional and possess a high energy resolution.

Effective background corrections also require measurements with differently oriented directional detectors. This setup will record sources with intensities of the order of $^1/_{10}$ of the background intensity.

Measurements of the isotropic gamma-ray intensity

In the early stages /14 – 18/, the isotropic gamma-ray intensity in the atmosphere was measured with Geiger counters. In /15/, the flux of atmospheric gamma rays was found from the anticoincidence count of the central (main) counter and the double ring of shielding Geiger counters. The efficiency of Geiger counters for gamma rays is low (about 1%) and it is roughly a linear function of the quantum energy. The Geiger counters essentially measure the energy flux of gamma rays, and not the photon flux. The coincidence count of the central counter with the shielding counters will give the isotropic intensity of charged particles in the same geometry. Arrays of Geiger counters were also used in separate detection of gamma quanta and charged particles in outer space /19 – 20/.

In /21 – 27/, the low-energy gamma-ray fluxes were measured with scintillation counters without active shielding from charged particles. The "background" of charged particles was estimated using the large difference in the detection efficiencies of Geiger and scintillation counters for charged particles and gamma rays /23, 27/. Gamma rays with energies between 0.3 and 5 MeV in the atmosphere and in outer space are commonly recorded with so-called "phoswich" scintillation detectors, using a "sandwhich" phosphor /28 – 39/.

Gamma rays are efficiently recorded by a central NaI(Tl) or CaI(Tl) crystal. This crystal is completely enclosed in a thin screen of plastic scintillators whose luminescence time is approximately $^1/_{100}$ of the luminescence time of the central crystal. The phoswich is generally monitored by a single photomultiplier. The large difference in the luminescence times of the central crystal and the shield permits separate recording of gamma quanta and charged particles by special electronic circuits. The main shortcoming of the phoswich detectors is their low energy resolution. Typical resolutions reach about 18% (for CsI crystals in the screen) and 12% (NaI) at 660 keV. Semiconductor Ge(Li) detectors are promising in this respect, as they ensure energy resolutions one order of magnitude higher /40/.

Directional intensity detectors

We distinguish between directional intensity detectors with passive and active collimation. Thus the OSO-1 satellite recorded directional

gamma-ray intensities at 50 – 150 keV using a scintillation counter at the bottom of a tall lead beaker. Jones /41/ placed a phoswich detector inside a lead screen, and the entrance window was periodically closed and opened.

An active collimator was proposed by Frost and Rothe /42/ and actually applied in /43 – 51/. Figure 3 is a diagram of a directional detector for measuring solar gamma rays with energies between 160 and 800 keV /44/. The gamma rays are detected by a sodium iodide crystal 1. It is placed in a small well in the "active" collimator 2 – a cesium iodide crystal coupled by an anti-coincidence circuit to the central crystal 1. The collimator markedly suppresses the "background" of charged particles and atmospheric photons. For the actual dimensions indicated in Figure 3, the geometrical factor of the shielding crystal for isotropic radiation is $S_2 = 360$ cm^2, and that of the central crystal is $S_1 = 19.2$ cm^2; the geometrical factor of the telescope is $G = 10$ cm$^2 \cdot$ sterad, the detector angular aperture is 30°. In /45/, the entrance window of the shielding crystal was covered with a CsI(Na) scintillator 60 mm thick with 48 holes. The angular aperture was thus brought down to 8.4°.

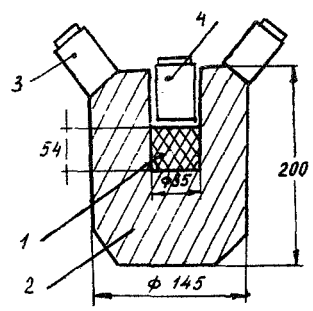

FIGURE 3. A directional detector with an "active" collimator.

A detector for point sources with $E_\gamma \leqslant 1$ MeV /46, 49, 50/ is shown in Figure 4. A central detector 1 is placed inside a large collimating crystal 2 (both crystals are NaI(Tl)). The entrance aperture is covered by a thin plastic scintillator 3. The central crystal is thus screened from charged particles on all sides. Additional collimation of gamma rays is accomplished by three plastic scintillator rings 4. Scintillators 2, 3, and 4 are coupled into an anticoincidence circuit with the central counter 1. The resolving power of counter 1 was 27% at 50 keV and 9.2% at 511 keV. To improve the resolving power /40/, a Ge(Li) detector of 22 cm^3 volume was used as the central crystal.

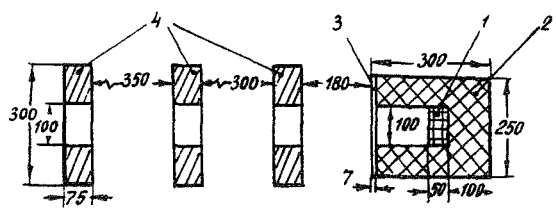

FIGURE 4. A directional detector with an "active" shielding and an arrangement of collimating disks.

A gamma spectrometer with twelve cylindrical Ge(Li) detectors of 40 cm^3 each is described in /52/. The detectors are divided into four groups and immersed in a liquid-nitrogen cryostat. The detectors are

surrounded by a collimating shield. The working surface area of all the detectors is 200 cm^2, the energy resolution is 7 keV, the range of measurement is between 50 keV and 2.4 MeV.

ATMOSPHERIC GAMMA RAYS

Balloon measurements in the upper atmosphere or orbital satellite measurements record a substantial fraction of atmospheric gamma rays. It is therefore highly important to have independent data on the spatial and the spectral distribution of atmospheric gamma rays. The study of atmospheric gamma rays is also of independent interest in connection with the processes of interaction of primary and secondary cosmic rays with the Earth atmosphere, the atmospheres of other planets, and the surface of celestial objects, such as the Moon and the Sun.

Altitude and latitude variation of atmospheric gamma ray fluxes

The distribution of atmospheric gamma rays with altitude is shown in Figure 5. The measurements were carried out in 1966—1967 at geomagnetic latitude λ_m = 47°N with a phoswich detector from balloons /34, 35/. Near the Earth, the gamma ray intensity is seen to increase with increasing altitude. The minimum intensity is observed at altitudes of 2—3 km. The peak intensities are reached in the transitional maximum at altitudes of 16—18 km (atmospheric thickness x = 80—100 g/cm^2). In May 1966, the isotropic intensity of 0.3—3 MeV gamma rays in the transitional maximum at a depth of x_0 = 100 g/cm^2 reached F_0 = 5.5±0.8 photons/cm^2sec, and that of 1—3 MeV gamma rays, F_0 = 1.9±0.3 photons/cm^2sec.

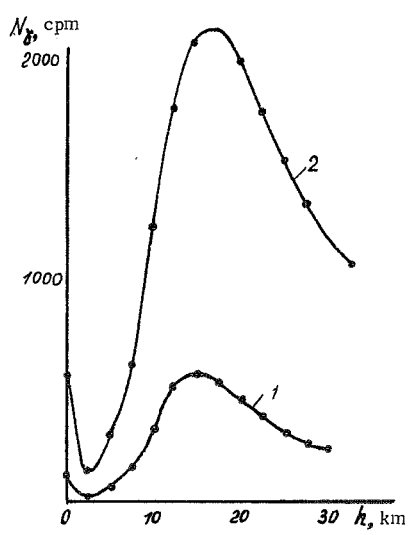

FIGURE 5. The flux of atmospheric gamma rays with energies of 1—3 MeV (curve 1) and 0.3—3 MeV (curve 2) as a function of altitude /34, 35/.

Between 200 and 600 g/cm^2 (equilibrium atmosphere), the gamma-ray intensity varies as exp(−x/L) where L is the mean absorption length. For the curves of Figure 5, L ≈ 180 g/cm^2. It is shown in /25, 26/ that the gamma-ray flux with E_γ = 70—800 keV increases at higher geomagnetic latitudes. In the transitional maximum (x_0 ≈ 90 g/cm^2), the flux reaches 7±0.6 (λ_m = 30°N, 1963), 12.5 (47°, 1965), and 17.5 (65°, 1966) photons/cm^2sec. At λ_m = 7°

and 6 g/cm^2 depth, the flux of gamma rays with energies between 1 and 5 MeV is 1 photon/cm^{2}sec /47/, and the absorption length in the equilibrium region (400 – 700 g/cm^2) is L = 247±25 g/cm^2. The flux of 0.51 MeV photons in the transitional maximum in 1965 – 1966 reached 0.98 and 1.33 photons/cm^{2}sec at 47 and 65°N respectively. According to /33/, the flux of 0.51 MeV gamma rays at a depth of 4 g/cm^2 at λ_m = 41°N was 0.29±0.04 photons/cm^{2}sec in 1966.

The soft gamma-ray fluxes at high altitudes are approximately one order of magnitude higher than the intensity of charged particles. Thus, in the Northern Hemisphere, for x_0 = 90 g/cm^2, F_0(0.03 – 0.3 MeV) = = 22 photons/cm^{2}sec, whereas the flux of charged particles is 1.9 cm^{-2} · sec^{-1} /27/. According to /24, 25, 27, 32/, the soft gamma rays in the atmosphere are genetically related to the electromagnetic component of the secondary cosmic rays. It is remarkable that the angular distribution of gamma quanta with E_γ < 10 MeV in the upper atmosphere is definitely anisotropic /32/. The results of measurements of the atmospheric neutrons with scintillation counters, including phoswich detectors, should be corrected by allowing for the interaction of neutrons with the crystal nuclei /24, 32, 33, 43, 44/.

The atmospheric gamma-ray albedo

The albedo is determined either by extrapolating the measurements in the upper atmosphere to zero air density, or by direct measurements from rockets and satellites. The corresponding experimental data are summarized in Table 1.

TABLE 1. Experimental values of the atmospheric gamma-ray albedo

Measurements	Gamma energy, MeV	Intensity j, photons/cm^{2}sec · sterad or flux F, photons/cm^{2}sec
1960 /28/	2.22	F < 0.5
λ_m = 41°, 1959	0.51	j = 0.000 ± 0.034
x = 6 g/cm^2 /41/		
λ_m = 78°, 1960 /27/	0.03	F = 8 (extrapol.)
λ_m = 41°, 1961 /24/	0.025 – 1.06	F = 5.7 (extrapol.)
λ_m = 55°, 1962 /43/	0.51	j = 0.05
h = 260 – 780 km, 1963 /19/	0.1 – 3	F = 9 – 22
λ_m = 55°, 1963 /31/	0.51	j = 0.025 ± 0.002
λ_m = 47°, 1963 /25/	0.1 – 1.5	F = 5
	0.51	F = 0.35 ± 0.08
λ_m = 30°, 1963 } /26/	0.07 – 0.8	F = 1.3 ± 0.2
λ_m = 47°, 1965 } /26/	0.07 – 0.8	F = 3.8
λ_m = 65°, 1966 } /26/	0.07 – 0.8	F = 7.5
λ_m = 41°, 1966 /33/	0.51	F = 0.29 ± 0.04
x = 4 g/cm^2		
λ_m = 7°, 1966 – 1968 } /38/	0.51	F = 0.16 ± 0.02 (Dec. 1966)
x = 3.7 g/cm^2 } /38/		F = 0.21 ± 0.02 (April 1968)
1966 – 67	0.4 – 2.5	F = 2.3 (P = 1.3 GV)
h = 250 – 650 km /37/		F = 0.55 (P = 16 GV)
		F = 0.1 (P = 5 GV)
1966 – 67	0.51	F = 0.07 (P = 16 GV)
h = 250 – 650 km /37/		

The measurements of KOSMOS-135 /37/ established that in the epochs of the Gemenids and Ursids (13–18 Dec. and 22 Dec. 1966) the 0.51 MeV intensity was approximately 1.5 times as high as the mean intensity for December 1966 and January 1967. The intensity of gamma rays at other energies from the 0.4–2.5 MeV range and the charged particle fluxes remains constant during the observations (together with the level of solar and geomagnetic activity). It is noted in /33/ that the intensity of 0.51 MeV gamma rays in 1966 was double the intensity in 1961 in a similar experiment. It is also noted /39/ that the 0.51 MeV intensity changed by 25% between December 1966 and April 1968. OSO-3 measurements give an albedo of (0.10±0.03) photon/cm^{2}sec for atmospheric gamma quanta with $E_\gamma > 50$ MeV.

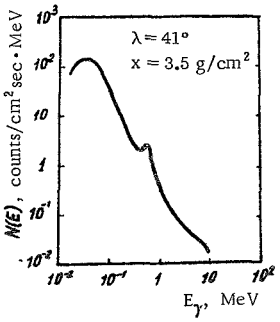

FIGURE 6. Gamma spectrum at a depth x = 3.5 g/cm^2 and λ_m = 41° N.

The energy spectrum of atmospheric gamma quanta

Figure 6 is the spectrum of atmospheric gamma quanta measured at a depth of 3.5 g/cm^2 (h = 39 km) and 41°N latitude /11/. Between 1 and 10 MeV, the spectrum can be fitted with a power function /32/:

$$F(E_\gamma) = AE_\gamma^{-\alpha} \qquad (2)$$

with α = 1.55.

For $E_\gamma < 1$ MeV, the spectrum index α is a function of the depth in the atmosphere and the exact energy range. The dependence is fairly complex in this case. The experimental data on the subject are quite contradictory /24–27, 32, 43/.

EXPERIMENTAL INVESTIGATION OF LOW-ENERGY GAMMA RAYS FROM OUTER SPACE

The following basic results were obtained in measurements of gamma rays from outer space:

1. The isotropic X-ray and gamma-ray background radiation was discovered and studied /8, 9, 22, 25, 53–58/.
2. Discrete gamma-ray sources were discovered in the constellations of Taurus (the Crab Nebula), Centaurus, and Sagittarius /45, 49, 50/. Prior to that, these objects had been identified as powerful X-ray sources.
3. Attempts were made to detect gamma-ray emission from quasars and pulsars, including the low-energy gamma-ray component /48/.
4. The gamma-ray emission of the quiet Sun and of solar flares was studied /14, 32, 38, 39, 43/. The upper bound flux values were determined for gamma rays of 0.5 and 2.2 MeV emitted by solar flares /30, 38, 39/.

5. Studies have begun of lunar gamma rays, produced by the bombardment of the lunar surface with cosmic rays or by the decay of radioactive nuclei in lunar rocks /59, 60/.

We will only consider the results listed under 1 through 4 above. The subject of lunar gamma rays requires a separate analysis.

Diffuse X-ray and gamma-ray background from outer space

The first measurements of the hard electromagnetic radiation in the interplanetary space were carried out in 1959 by Vernov and Chudakov /23/ using a scintillation counter on board LUNA-1. In 1962—1963, proof was obtained of the existence of the isotropic, or diffuse, X-ray and gamma-ray background. A phoswich scintillation detector /30/ on board RANGER-III and RANGER-V measured the intensity of gamma rays between 0.07 and 4.4 MeV. The spectral intensities of the diffuse gamma-ray background between 0.07 and 1 MeV computed from the RANGER data are marked by light circles in Figure 7. In these computations the energy spectrum was expressed by relation (2) with $\alpha = 2$. The measurement results /30/ for $E_\gamma > 1$ MeV contain a significant error according to /9, 32/, and were therefore ignored in the construction of Figure 7.

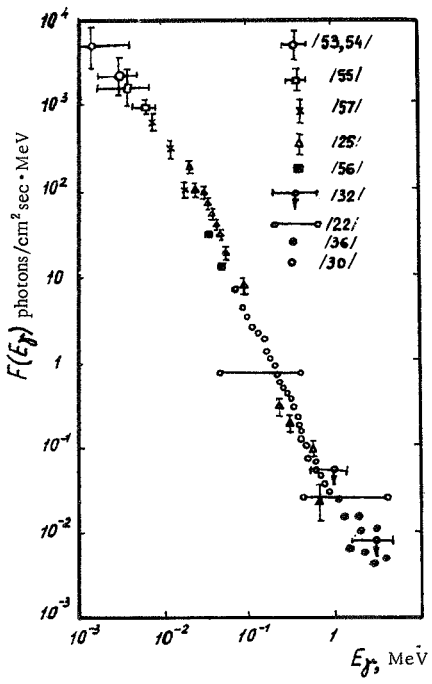

FIGURE 7. The spectrum of the diffuse background of cosmic gamma rays.

An experiment carried out on board the OSO-1 satellite /32/ established the upper limits of the radiation fluxes from outer space between the energies of 0.05—0.15, 0.5—1.5, and 1.5—4.5 MeV. Phoswich detectors with pulse analyzers were used to measure the differential fluxes between 20—900 keV /25/ and 1.2—3.1 MeV /36/. The results of /25, 32, 36/ are plotted in Figure 7 assuming isotropic fluxes. Figure 7 also contains the experimental data on the intensity of the isotropic X-ray background radiation obtained with proportional gas and scintillation counters on board rockets /53—55/ and balloons /26, 36, 56/.

The spectral distribution of the diffuse X-ray and gamma-ray background from around 1 keV to 10 MeV is adequately described by the power function (2) with $\alpha = 2.3 \pm 0.2$. Between 20 and 180 keV, according to /56/, the

numerical values of the constants in (2) are A = 135, $\alpha = 2.4 \pm 0.2$, with energies expressed in keV. For $E_\gamma < 10$ keV, the spectrum is "flattened."

The isotropic gamma-ray background is also observed for $E_\gamma > 100$ MeV. According to the latest data from OSO-3 /8/, the radiation intensity in this range is j_γ (> 100 MeV) = $(1.1 \pm 0.2) \cdot 10^{-4}$ cm^{-2}sec^{-1}sterad^{-1}.

Extrapolation of the low-energy spectrum (Figure 7) using $\alpha = 2.3$ in (2) gives for j_γ (> 100 MeV) one quarter of the measured value /8/.

The background intensity in all the energy ranges is higher than the computed average for the Galaxy (see above). The isotropy of the background radiation is a consequence of the extragalactic origin of this radiation. The power spectrum is an indication of its nonthermal character.

The bulk of the diffuse X-ray and gamma-ray background with $E_\gamma < 1$ MeV is produced by Compton scattering of fast electrons by the photons of the relict thermal radiation in the intergalactic space /9, 10, 61/. The density of stellar light quanta is insufficient to account for the observed background intensity. The electrons are injected into the intergalactic space by radio galaxies or are produced as secondary particles /9, 10/. In /10/ it is proved that a certain part of the low-energy background ($E \leqslant 1$ keV) is associated with the bremsstrahlung of the heated intergalactic gas.

X-ray and gamma-ray emission of the Crab Nebula

The first experiment of Haymes' group /46/ using the detector shown in Figure 4 established the exponential form of the spectrum of the Crab Nebula between 30 and 74 keV. This contradicted the observations of Peterson's group /45/, according to which the differential spectrum between 20 and 100 keV is a power function (2) with an index of -1.91 ± 0.10 (the differential intensity at 20 keV, according to Peterson, is about 10^{-2} photons/cm^{2}sec · keV). Repeated measurements of Haymes' group /49/ covered the energies from 35 to 560 keV. Normalization and introduction of appropriate corrections yielded the results which are marked by dots in Figure 8. The spectrum in this energy range has the form

$$dN/dE = (7.1 \pm 2.8)\, E^{-2.19 \pm 0.08} \text{ counts/cm}^2\text{sec} \cdot \text{keV},$$

i.e., it adequately fits the data of Peterson (marked by crosses in Figure 8), and also the results of Grader /58/, who established a power index with $\alpha = 2.3 \pm 0.2$ for the Crab Nebula between 1 and 30 keV. The upper bound values of the gamma-ray fluxes from the Crab Nebula according to 1962

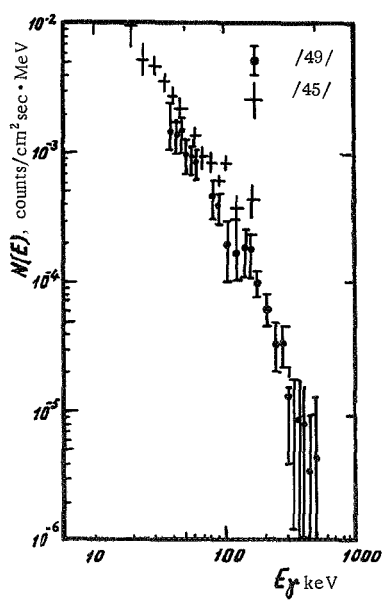

FIGURE 8. The gamma spectrum of the Crab Nebula.

balloon measurements are also listed in /9, 11, 43/: F_γ (0.16 – 0.32) < $9 \cdot 10^{-5}$, F_γ (0.32 – 0.49) < $7.5 \cdot 10^{-5}$, F_γ (0.49 – 0.65) < $7 \cdot 10^{-5}$, F_γ (0.65 – 0.77) < < $4.5 \cdot 10^{-5}$ photons/cm^2 · sec · keV. (The energy intervals in MeV are given in parentheses.)

The power spectrum of the Crab Nebula points to the synchrotron origin of the X-ray and gamma-ray emission. Moreover, since the optical and the radio spectrum constitute a smooth continuation of the X-ray and gamma-ray spectrum of the nebula /49/, there are reasons to believe that the entire range of frequencies emitted by the Crab Nebula (10^8 to 10^{20} Hz) is of synchrotron origin. To explain the peculiar features of the spectrum, magnetic fields of the order of 10^{-4} Oe and 10^{14} eV electrons have to be assumed in the nebula. The results of /49/ also helped to establish the upper limit of the fluxes produced by positron annihilation in the nebula: $F_{0.51}$ < < $8.4 \cdot 10^{-4}$ photons/cm^2 sec.

Solar gamma rays

In 1961 – 1966, Peterson's group carried out systematic observations /32, 44, 45/ of the solar gamma-ray emission (E_γ = 0.05 – 10 MeV). They either used directional detectors of the type shown in Figures 3 and 4 or employed the "day – night" effect in measurements with isotropic phoswich detectors. Figure 9 gives the experimental /43, 45/ upper bound values of the gamma-ray fluxes of the quiet Sun between 20 keV and 10 MeV (they are approximately $^1/_{30}$ of the corresponding upper bound values of the fluxes measured by OSO-1 /32/). The absolute upper bound value of the flux from the quiet Sun between 0.16 and 0.8 MeV is 0.05 photons/cm^{2}sec /43/ and F_γ (> 0.8 MeV) < 0.02 photons/cm^{2}sec. The dashed curve in the same figure shows the spectrum of solar gamma quanta produced by the interaction of cosmic rays with the surface of the Sun. The spectrum of the solar albedo gamma rays was computed from the experimental spectrum of the atmospheric gamma quanta (see Figure 6).

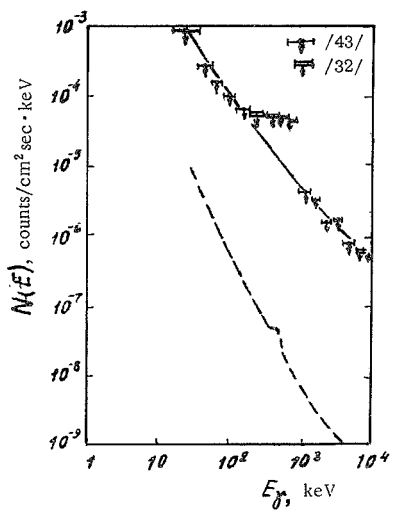

FIGURE 9. Experimental upper bound values of the gamma-ray fluxes from the Sun (dots) and the computed spectrum of the solar albedo gamma rays (dashed curve).

Repeated attempts were made to measure the fluxes of solar gamma rays in the 0.5 and 2.2 MeV lines. Table 2 lists the upper bound estimates obtained in various experiments.

Some cases of enhanced gamma-ray intensity associated with solar flares were noted. Peterson and Wincler /14/ in 1958 discovered a gamma-ray enhancement at 0.2 – 0.5 MeV during the maximum of an

optical flare. The "burst" continued for 18 sec, so that the integral radiation flux reached $3.6 \cdot 10^{-4}$ erg/cm^2. According to the authors, the gamma-ray emission of the flare was associated with electron bremsstrahlung. During the flare of 7 July 1966, the gamma-ray intensity at 80 keV – 1 MeV exceeded 300 photons/cm^{2}sec at the maximum /62/.

TABLE 2. Upper bound values of the line intensities of solar gamma radiation

Measurements	Equipment	Gamma-ray flux, photons/cm^{2}sec
1962–1963, RANGER, $7 \cdot 10^4 - 4 \cdot 10^5$ km from the Earth	Phoswich (CsI + plastic)	$F_{0.5} < 0.014$ $F_{2.22} < 0.005$
June 1962, $\lambda_m = 40°$N, $x = 3.5$ g/cm^2 /43/	Directional detector with active collimator	$F_{0.5} < 0.013$
May–June 1967, balloon, $\lambda_m = 41°$N, $x = 3.8$ g/cm^2 /38/	Phoswich (CsI + plastic)	$F_{2.22} < 0.005$
December 1966–April 1968, balloon, $\lambda_m = 41°$N, $x = 3.7$ g/cm^2 /39/	Ditto	$F_{0.5} < 0.04$

In conclusion, let us list some new experimental data on the upper bound values of the fluxes of hard solar radiation ($E_\gamma > 50$ MeV). According to the latest measurements of Kraushaar et al. /8/, for the quiet sun $F_\gamma(>50\,\text{MeV}) = (1 \pm 1) \cdot 10^{-4}$ photons/cm^{2}sec. This is consistent with the result F_γ (> 100 MeV) $< 7.4 \cdot 10^{-5}$ photons/cm^{2}sec obtained for the quiet Sun by Fazio et al. /7/. For flares of class 2+, according to Fazio, F_γ (> 100 MeV) $< 6 \cdot 10^{-3}$ photons/cm^{2}sec.

Gamma-ray emission of other discrete sources

The upper bound value of the gamma-ray flux at 25 – 100 keV from Centaurus A, according to /50/, reaches $1.9 \cdot 10^{-2}$ photons/cm^{2}sec. A report of gamma-ray emission from discrete sources M 87 and Cygnus A was published in /51/. The flux of photons with energies between 40 and 107 keV from the galaxy M 87 (in Virgo) is $(8.2 \pm 3.5) \cdot 10^{-2}$ photons/cm^{2}sec, i.e., the radiation power in this range is 100 times the radio power. The upper bound values for the line emission of the quasar 3C 286 were established in /48/: F_γ(0.5 MeV) < 0.04 photons/cm^{2}sec and F_γ (2.2 MeV) < 0.13 photons/cm^{2}sec. It was shown /50, 51/ that Sagittarius A and Cygnus A have a power gamma spectrum. The spectrum index of Sagittarius A between 25 and 550 keV is $\alpha = 2.1 \pm 0.3$, for Cygnus A between 35 and 125 keV, $\alpha = 1.80 \pm 0.04$ and between 152 and 450 keV, $\alpha = 2.80$, i.e., a break in the spectrum is observed at $E \approx 150$ keV.

PROBLEMS AND FUTURE PROSPECTS

1. Measurement of the anisotropy of the diffuse (background) radiation from outer space.

2. Determination of the absolute gamma-ray fluxes from point sources — the Sun, quasars, pulsars, etc.

3. Measurement of the line intensities of rays, especially in the 0.51 MeV line.

4. Measurement of the degree of polarization of the radiation from point sources.

To solve these problems, we will need instruments with angular apertures of less than 1°, energy resolution of about 0.5 – 0.7% (at $E_\gamma \sim 1$ MeV), and geometrical factor $G \sim 10 - 100$ cm^2 sterad.

Bibliography

1. Ginzburg, V.L. and S.I. Syrovatskii.— UFN, 84:202. 1964.
2. Fazio, G.G.— Ann. Rev. Astron. and Astrophys., 5:481. 1967.
3. Gal'per, A.M. and B.I. Luchkov.— In: "Elementarnye chastitsy i kosmicheskie luchi," p. 101. Moskva, Atomizdat. 1967.
4. Chuikin, E.I.—Trudy V Vsesoyuznoi ezhegodnoi zimnei shkoly po kosmofizike, p. 146. Apatity, Izd. Kol'skogo filiala AN SSSR. 1968.
5. Duthie, I.G.— Canad. J. Physics, 46:401. 1968.
6. Delvaille, I.R., P. Albats, K.I. Greisen, and H.B. Ogelman.— Canad. J. Physics, 46:425. 1968.
7. Fazio, C.G.— Canad. J. Physics, 46:427. 1968.
8. Kraushaar, W.L., G.W. Clark, and G. Carmire.— Canad. J. Physics, 46:414. 1968; Clark, G.W. and G.P. Carmire, and W.L. Kraushaar.— Astrophys. J. Lett., 153:L203. 1968.
9. Could, R.I.— Amer. J. Physics, 35:376. 1967.
10. Friedman, H.— Nature, 220:862. 1968.
11. Peterson, L., R. Jerde, and A. Jacobson. Balloon X-Ray Astronomy. — AIAA Journal, 5(11):1921. 1967.
12. Dolan, I.F. and G.G. Fazio. — Rev. Geophys., 3:319. 1965.
13. Lingenfelter, R.E. and P. Ramaty. High-Energy Nuclear Reaction in Solar Flares. — Preprint. 1967.
14. Peterson, L.E. and I.R. Wincler. —J. Geophys. Res., 64:697. 1959.
15. Rest, F.G., L. Reiffel, and C.A. Stone.— Phys. Rev., 81:894. 1951.
16. Perlow, G.I. and C.W. Kissinger.— Phys. Rev., 84:572. 1951.
17. Perlow, G.I. and C.W. Kissinger.— Phys. Rev., 81:552. 1951.
18. Danielson, R.E.— J. Geophys. Res., 65:2055. 1960.
19. Avdyushkin, S.I., N.K. Pereyaslova, and N.E. Petrenko.— In: "Issledovaniya kosmicheskogo prostranstva," p. 510. Moskva, Izdatel'stvo "Nauka." 1965.
20. Fan, S.I., R. Meier, and I.A. Simpson.— In: "Van Allen Radiation Belt." [Russian translation. 1962.]
21. Reiffel, L., C.A. Stone, and F.C. Rest.— Phys. Rev., 82:120. 1951.

22. Vernov, S.N., A.E. Chudakov, Yu.I. Logachov, P.V. Vakulov.— Planet Space Sci., 1:86. 1959.
23. Vernov, S.N. and A.E. Chudakov.— UFN, 70(4). 1960.
24. Vette, I.E.— J. Geophys. Res., 67:1731. 1962.
25. Rocchia, R., F. Rothenflug, D. Bocklet, G. Dugros, and I. Labeyrie.— Space Res., 7/2:1327. 1967.
26. Bocklet, D.— Report CEA-R 3177. 1967.
27. Anderson, K.A.— Phys. Rev., 123:1435. 1961.
28. Northrop, I.A. and R.L. Hastetler.— Bull. Amer. Phys. Soc., 6:52. 1961.
29. van Dilla, M.A., E.C. Anderson, A.E. Metzger, and R.L. Schuch.— IEEE Trans., NS-9:405. 1962.
30. Arnold, I.R., A.E. Metzger, E.C. Anderson, and M.A. van Dilla.— J. Geophys. Res., 67:4878. 1962; Metzger, A.E., E.C. Anderson, M.A. van Dilla, and I.R. Arnold.— Nature, 204:766. 1964.
31. Peterson, L.E.— J. Geophys. Res., 68:979. 1963.
32. Schwartz, D. and L.E. Peterson.— Trans. Amer. Geophys. Union, 46:129. 1965; Space Res., 6:53. 1966.
33. Chupp, E.L., A.A. Sarkady, and H.P. Gilman.— Planet. Space Sci., 15:882. 1967.
34. Lenin, A.S., A.M. Romanov, and E.I. Chuikin.— Geomagnetizm i Aeronomiya, 9:152. 1969.
35. Lenin, A.S., A.M. Romanov, and E.I. Chuikin.— Konferentsiya po fizike kosmicheskikh luchei. Tashkent. 1968. (In press).
36. Okudaira, K. and Y. Hirasima.— Canad. J. Physics, 46:494. 1968.
37. Konstantinov, B.P., R.L. Aptekar', M.M. Beglov, S.V. Golenetskii, Yu.A. Gur'yan, V.N. Il'inskii, E.P. Mazets, and V.N. Panov.— Konferentsiya po fizike kosmicheskikh luchei. Tashkent. 1968. (In press).
38. Chupp, E.L., P.I. Lavakare, and A.A. Sarkady.— Phys. Rev., 166:1299. 1968.
39. Chupp, E.L., D.I. Forrest, R.I. Lavakare, and A.A. Sarkady.— Bull. Amer. Phys. Soc., 13:1398. 1968.
40. Womack, E.A. and I.W. Overbeck.— Bull. Amer. Phys. Soc., 13:1398. 1968.
41. Jones, F.C.— J. Geophys. Res., 66:2029. 1961.
42. Frost, K.I. and E.D. Rothe.— IEEE Trans., NS-9:381. 1962.
43. Frost, K.I., E.D. Rothe, and L.E. Peterson.— J. Geophys. Res., 71:4079. 1966.
44. Peterson, L.E., D.A. Schwartz, R.M. Pelling, and D. McKenzil.— J. Geophys. Res., 71:5778. 1966.
45. Peterson, L.E., A.S. Jacobson, R.M. Pelling, and D.A. Schwartz.— Canad. J. Physics, 46:437. 1968.
46. Haymes, R.C. and W. Craddock.— J. Geophys. Res., 71:3261. 1966.
47. Apparao, M.V.K., R.R. Daniel, G. Joseph, G.S. Cokhale, P.J. Lavarare, and R. Sunderrayan.— Canad. J. Physics, 46:1030. 1968.

48. Adams, D.I., R.R. Hiller, and A.F. Janes.— Nature, 207:396. 1965.
49. Haymes, R.C., D.V. Ellis, C.J. Fishman, J.D. Kurfess, and W.H. Tucker.— Astrophys. J., 151:L10. 1968.
50. Haymes, R.C., G.J. Fishman, S.W. Glenn, and J.D. Kurfess.— Bull. Am. Phys. Soc., 13:1458. 1968.
51. Haymes, R.C., D.V. Ellis, G.J. Fishman, and J.D.Kurfess.— Astrophys. J., 151:125, 131. 1968.
52. Marshall, J.N. and G. Halpern.— IEEE Trans., NS-15:242. 1968.
53. Bowyer, S., E.T. Byram, T.A. Chubb, and H. Friedman.— Science, 147:394. 1965; Nature, 201:1307. 1964.
54. Giacconi, R., H. Gursky, J.R. Waters, B. Rossi, G. Clark, G. Carmire, M. Oda, and M. Wada.— Proc. Intern. School of Physics E. Fermi, Course XXXV. New York, Academic Press. 1966.
55. Fisher, P.C., H.M. Johnson, W.C. Jordan, A.J.Meyerhoff, and L.W. Acton.— Astrophys. J., 143:203. 1966.
56. Blecker, I.A.M.— Phys. Rev. Lett., 21:301. 1966; Canad. J. Physics, 46:461. 1968.
57. Hayakawa, S., M. Matsuoka, and K. Yamashita.— 6th Intern. Space Symp. Buenos Aires. 1966.
58. Grader, R., R. Hill, F. Seward, and A. Toor.— Science, 152:1499. 1966.
59. Vinogradov, A.P., Yu.A. Surkov, and L.P. Moskaleva.— Moon and Planets, p.71. Amsterdam. 1967.
60. Elizarov, B.G., B.N.Kononov, S.S. Kurochkin, Yu.A. Surkov, and N.A. Shekhortsev.— Kosmicheskie Issledovaniya, 6:265. 1968.
61. Vainshtein, L.A., V.G. Kurt, S.L. Mandel'shtam, A.P. Presnyakov, S.I. Syrovatskii, R.A. Syunyaev, and I.P. Tindo.— Kosmicheskie Issledovaniya, 6:242. 1968; Vainshtein, L.A. and R.A. Syunyaev.— Ibid., p.635.
62. Cline, T.L., S.S. Holt, and E.W. Hones.— J. Geophys. Res., 73:434. 1968.

X-RAY AND GAMMA-RAY OBSERVATIONS FROM ARTIFICIAL EARTH SATELLITES

M. M. Anisimov, L. S. Bratolyubova-Tsulukidze, N. L. Grigorov, L. F. Kalinkin, A. S. Melioranskii, E. A. Pryakhin, I. A. Savenko, and V. Ya. Yufarkin

The investigations of the short-wave electromagnetic radiation with wavelengths $\lambda \leq 100$ Å (or photon energies of over 0.1 keV) from outer space have been developing vigorously in recent years. This range of energies is generally divided into three subranges: 0.1 – 100 keV (X-ray radiation), 100 keV – 10 MeV (soft gamma rays), and over 10 MeV (hard gamma rays). The largest progress has been attained in the X-ray range, mainly because of the high intensities at these energies. Most experiments were carried out with guided probes outside the atmosphere /1 – 6/. Measurement data are available for the intensity and the energy spectrum of the X-ray background radiation with energies $E_X \gtrsim 0.28$ keV, and a few dozen local sources have been discovered with X-ray fluxes $I_X \gtrsim 2.5 \cdot 10^{-2}$ $(cm^2 sec)^{-1}$. The energy spectra of some local sources have been measured, and intensity variations have been noted in certain cases. Most of these sources lie inside the Galaxy. Presumably only few weak local sources with fluxes $I_X < 10^{-1}$ $cm^{-2} sec^{-1}$ lie outside the Galaxy, e.g., Vir XR-1, Leo XR-1, and the source identified with the quasar 3C 273 /2 – 6/.

The principal results at these energies were obtained with high-efficiency proportional counters (detector area of up to 1000 cm^2) having a limited energy response. Moreover, the background intensity and the intensities of the local sources markedly diminish with the increase in energy, and the measurements limited to the duration of the probe rocket flight (a few minutes) do not provide a sufficiently representative statistical sample.

To increase the time of observation, the equipment was sometimes launched on high-altitude guided balloons, using scintillation spectrometers as X-ray and soft gamma-ray detectors /7 – 11/. The absorption in the residual atmosphere ($\gtrsim 4$ g/cm^2), however, precludes recording electromagnetic radiation with energies below 15 keV by these methods. For some of the stronger local sources, the energy spectrum was extended to around 150 keV, and the background X-ray and gamma-ray spectrum was measured to around 1 MeV. The high-energy limit is associated with difficulties of providing effective shielding from the secondary gamma-ray emission of the atmosphere. The most accurate gamma-ray background spectrum to $E_\gamma \simeq 2$ MeV was obtained with the equipment of the lunar probe /12/, when the atmospheric albedo gamma-ray fluxes were negligible at large distances from the Earth. The OSO-1 measurements

established the upper bound values of the gamma-ray intensities up to 4.5 MeV for the global radiation /13/.

Hard gamma rays ($E_\gamma > 10$ MeV) are measured with telescopes consisting of scintillation and Cherenkov detectors. In these experiments (as in most of the previously mentioned experiments), the shielding from the charged particle background is of the utmost significance, since its intensity is substantially higher than the intensity of the recorded component. Suitable shielding is generally provided by anticoincidence scintillators surrounding the telescope detectors. However, because of the high intensity of the secondary gamma rays of the residual atmosphere, balloon measurements only give the upper bound value of the intensity of the global gamma-ray emission, $I_\gamma \leq 10^{-3}$ (cm^2 sec sterad)$^{-1}$ for $E_\gamma > 100$ MeV. The inclusion of a spark chamber in the payload considerably improves the measurement of gamma-ray fluxes from local sources (the spark chamber will localize the direction of incidence of gamma rays with an accuracy of about 1°). However, these measurements again yield only upper bound values /14–20/. Further development of measurements in the entire X- and gamma-ray range may be accomplished using artificial satellites and space probes. We will review the X-ray and hard gamma-ray measurements carried out with satellites of the KOSMOS and PROTON series.

X-RAY MEASUREMENTS

KOSMOS-208 carried an instrument which sought local X-ray sources and measured their intensity at X-ray energies between 2 and 50 keV /21–22/. The instrument axis was aimed to the zenith. The instrument used four proportional counters with 125μ Be windows, coupled two by two. The effective area of each counter pair was 135 cm^2 (corrected for the collimator transmission). A brass slit collimator was used with a 32' × 18° aperture (width at half slit height level). The collimator slits were set at right angles to the satellite path; the collimators of one counter pair were displaced 2° along the slit in one direction from the zenith, and the collimators of the other pair were displaced in the opposite direction. This collimator geometry permits pinpointing the position of the local source relative to the zenith in the direction of the slits from the X-ray intensity ratio of the different counter pairs. To suppress the charged particle background, the proportional counters were shielded from the sides and from the bottom by scintillation counters whose pulses were delivered to an anticoincidence circuit connected with the proportional counters. The X-ray radiation was recorded by each pair of counters separately between 2 and 10 keV and by the four counters jointly for the energy ranges 4–7, 7–10, 10–15, 15–25, 25–35, and 35–50 keV. The table gives the instrument specifications and the experimental conditions on board the satellite for comparison with the specifications and measurement conditions applicable to the rocket payload used in measuring local sources. The smaller the angular velocity and the larger the effective detector area, the smaller is the detectable intensity of local sources. For comparison purposes, the table gives the value of the effective counter area S_{ef} multiplied by the time to traverse 1° (a hypothetical collimator with a

1° slit) at right angles to the slit ($t_{1°}$). We see from the table that the best results are ensured by high effective area counters /4/. A single scanning of a 12° sky area in the direction of flight was carried out in /4/. The KOSMOS-208 experiment scanned about 120° during one orbit circuit. Summing the measurements over a number of circuits, we may reach values of $S_{ef} t_{1°} n$ exceeding the figure of /4/. Satellite experiments, despite the smaller effective area, thus scan a larger portion of the celestial sphere and ensure a higher statistical reliability than rocket measurements. Figure 1 shows the count rate of the KOSMOS-208 instruments in various energy intervals: 2 – 10, 7 – 10, 10 – 15 keV. Figure 2 plots the X-ray intensity in the sky areas corresponding to some constellations, obtained by adding up the measurements over nine orbital circuits. Peaks 1, 2, and 4 apparently correspond to individual local sources. Peak 3 is associated either with an extended source or with a superposition of several unresolved sources. The measurement results are currently being processed.

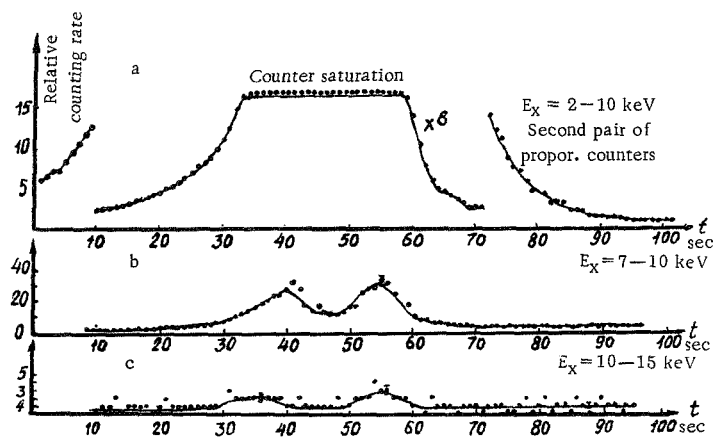

FIGURE 1. Solar X-ray emission:

a) for E_X = 2–10 keV, b) E_X = 7–10 keV, c) E_X = 10–15 keV.

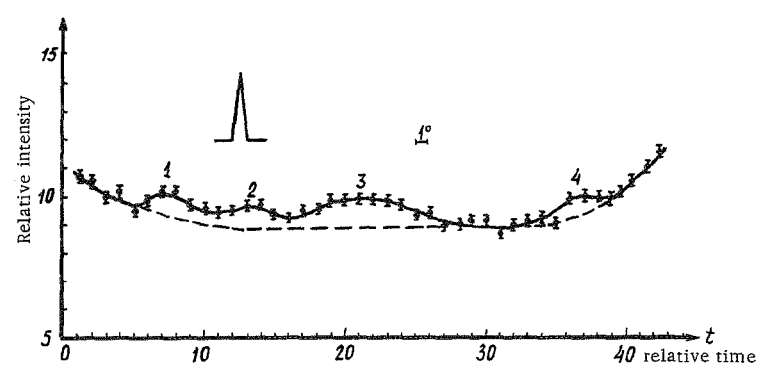

FIGURE 2. X-ray intensity in Corvus, Crater, Virgo, Coma Berenices, and Leo.

SATELLITE MEASUREMENTS OF HARD GAMMA RAYS

Hard gamma rays with energies $\geqslant 50$ MeV were measured on EXPLORER XI /23/, PROTON 1 and PROTON 2 /24–27/, OSO-1 /28/, OSO-3 /29/, KOSMOS-208 /30/, and KOSMOS-264 /31, 32/. KOSMOS-264 was also equipped with a shower spark chamber, similar to that used in /19/. The geometrical factor of the instrument was $G = 22\ cm^2$ sterad. The spark chamber measurements were $12 \times 12 \times 12$ cm. The particle direction on stereophotographs could be measured to within about 4°. The instrument recorded gamma rays with energies $E_\gamma \geqslant 100$ MeV. Over 10,000 stereophotographs were taken in orbit, and they ensure reliable separation of the gamma quanta from various background events and permit computation of the gamma-ray flux from outer space. A preliminary analysis revealed a dependence of the count rate on geographical latitude. The selection of events with electron showers in the spark chamber markedly reduces the recorded flux, without affecting the latitudinal dependence. The flux intensity of gamma rays near the equator (from −13 to +13°) is $I_\gamma (E_\gamma \geqslant 100\ \text{MeV}) = (1.3 \pm 0.3) \cdot 10^{-3} cm^{-2} sec^{-1} sterad^{-1}$. A substantial proportion of this flux is probably due to gamma quanta from the horizon. Analysis of gamma-ray directions from the configuration of spark-chamber tracks (selection of events corresponding to small zenith angles) will lead to a more reliable isolation of the gamma-ray flux from outer space. The observational material is being currently processed.

The measurement results of /23–29/ show that charged particles and the atmospheric gamma-ray albedo may imitate the primary gamma rays. The measurement equipment should therefore meet fairly exacting standards.

The counting efficiency of the charged-particle background should be not less than 0.9999. The number of gamma-quantum imitations by charged particles due to the anticoincidence circuit missing a count will then be of the same order of magnitude as the expected count from the primary gamma rays with energies $\geqslant 50$ MeV.

The quantity of matter within the angle of view of the instrument and also near the instrument (although outside the shielding scintillator) should be minimized. Cosmic-ray protons and nuclei interacting with this matter may produce neutral pions, which decay into two gamma quanta. Electrons produce bremsstrahlung gamma quanta. The unavoidable material components should therefore be placed as close as possible to the shielding scintillator. Then the charged particles which are usually formed simultaneously with the neutral pions will be picked up by the shielding scintillator.

The probability of detection of charged particles arriving from "below" and absorbed in the radiator should be reduced to a minimum. These charged particles, especially electrons, may trigger the telescope when their direction changes as a result of multiple scattering. The gamma-ray converter should be as thin as possible, so that the pairs created by gamma quanta arriving outside the geometrical angle of view of the instrument are not particularly likely to be scattered into the telescope solid angle.

KOSMOS-208 carried an instrument for recording and measuring the energy spectrum of the primary gamma rays with energies $\geqslant 50$ MeV.

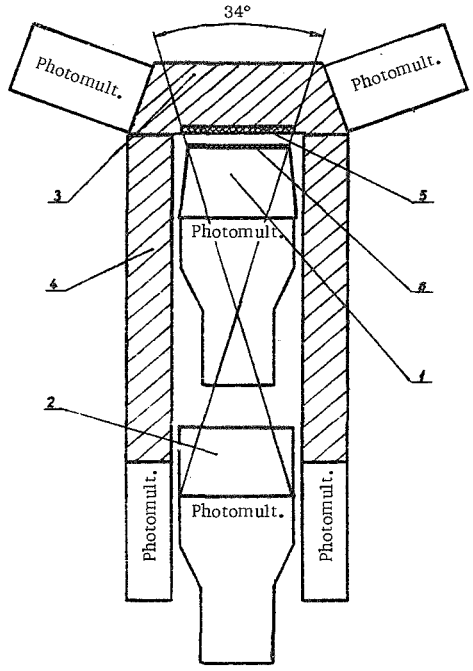

FIGURE 3. Block diagram of the instrument for measuring hard gamma rays:

1) Cherenkov counter with Plexiglas radiator, 2) Cherenkov counter with lead glass radiator, 3) top of shielding plastic scintillator, 4) cylindrical shielding plastic scintillator, 5) CsI(Tl) gamma-ray converter, 6) Pb gamma-ray converter.

This instrument was a modification of the equipment mounted on PROTON 1 and PROTON 2 /24/ (Figure 3). Two Cherenkov counters with a Plexiglas radiator 1 and a TF-5 lead glass radiator 2 form a telescope enclosed inside a plastic scintillator "hood" 3, 4 used as a shield from the charged particle background (the "hood" signals are computed in anticoincidence with the telescope pulses). The gamma-ray converters are CsI(Tl) scintillator plates 4 mm thick (0.21 t units) and lead plates 2 mm thick (0.35 t units) (5 and 6 in Figure 3, respectively). Both scintillators are monitored by the same photomultipliers. The signals from CsI(Tl) and the plastic scintillator are separated using the difference in the luminescence time. With gamma-ray conversion in CsI(Tl), the instrument recorded both the triple coincidences of pulses from CsI(Tl) and counters 1 and 2 and the double coincidences from counters 1 and 2. When the electron-positron pair formed as a result of the interaction of gamma rays with lead, only the double coincidences were counted. The lead glass radiator of the Cherenkov counter is 2.6 t units thick, so that this counter can be used as a gamma energy spectrometer. The use of the Cherenkov counter 1 as the second detector in the telescope in place of the previously used scintillation counter /24/ improved the directivity of charged particle detection. Ground tests show that the counting rate of the telescope for muons travelling in the "reverse" direction (from counter 2 to counter 1) does not exceed 0.5% of the counting rate of particles travelling in the "direct" direction. Moreover, the intensity of the low-energy gamma-ray background was reduced, and the number of accidental coincidences of signals from the telescope detectors decreased. Considerable attention was paid to increasing the efficiency of the anticoincidence detector ε_{ac}, especially for the top part of the "hood." A test carried out for muons at sea level gave $\varepsilon_{ac} > 0.9998 \pm 0.0002$. The longitudinal axis of the instrument mounted on the outer skin of the satellite hull was aimed at the zenith. The quantity of matter within the angle of view of the instrument did not exceed 0.15 g/cm^2. Below we give some preliminary results obtained using the following data processing procedure. Each orbital circuit was divided into 36 equal 10° segments, and the zero points was taken to coincide with the time of South — North passage of the

satellite across the equator. The count of gamma quanta and the measurement time for each segment were added up. The total measurement time reached 152 hr, and the total time for each segment was 4 hr (the time the satellite spent in the radiation belts was ignored). Figure 4 plots the measured counting rate in the different segments for γ quanta with energies $\geqslant 50$ keV. The observed latitudinal dependence is apparently mainly due to imitation of gamma quanta by charged particles. The increased counting rate in the Milky Way area (points 6 and 24) is probably associated with the gamma-ray emission of the Galaxy, as was noted in /29/. The absolute gamma-ray intensities were determined using the total instrument efficiency $\bar{\varepsilon}$ calculated by the Monte Carlo method. $\bar{\varepsilon}$ allows for the geometrical characteristics of the instrument, for the efficiency of gamma-ray conversion, for the distribution of energy between e and e^+, for particle scattering, etc. The values of $\bar{\varepsilon}$ computed assuming a power spectrum of the primary gamma quanta with an index $\gamma = -1$ and $\gamma = -2$ did not reveal a marked dependence on this index. Therefore, the average values of $\bar{\varepsilon}$ corresponding to $\bar{\gamma} = -1.5$ were used. These values were found to be 0.36, 0.54, 0.57, and 1.2 cm^2 sterad for the energy intervals 50 – 90, 90 – 146, 146 – 465, 465 – 2000, and 2000 – 16,000 MeV, respectively. In the equatorial belt (points 1 – 3, 16 – 21, 34 – 36), at energies between 50 – 90, 90 – 146, and 146 – 465 keV, 4.5 and 1 quanta were recorded during 52.5 hr. The table below gives the integrated intensities I_γ ($\geqslant E_\gamma$) in $(cm^2 \text{ sec sterad})^{-1}$ for the equatorial belt and for high latitudes:

E_γ, MeV	$\geqslant 50$	$\geqslant 90$	$\geqslant 146$	$\geqslant 465$	$\geqslant 2000$
Equator	$(1.0 \pm 0.4) \cdot 10^{-4}$	$(6.2 \pm 3.3) \cdot 10^{-5}$	$(1.0 \pm 1.3) \cdot 10^{-5}$		
High latitudes	$(5.9 \pm 1.4) \cdot 10^{-4}$	$(3.7 \pm 1.1) \cdot 10^{-4}$	$(2.0 \pm 0.7) \cdot 10^{-4}$	$(3.9 \pm 2.6) \cdot 10^{-5}$	$(1.5 \pm 1.5) \cdot 10^{-5}$

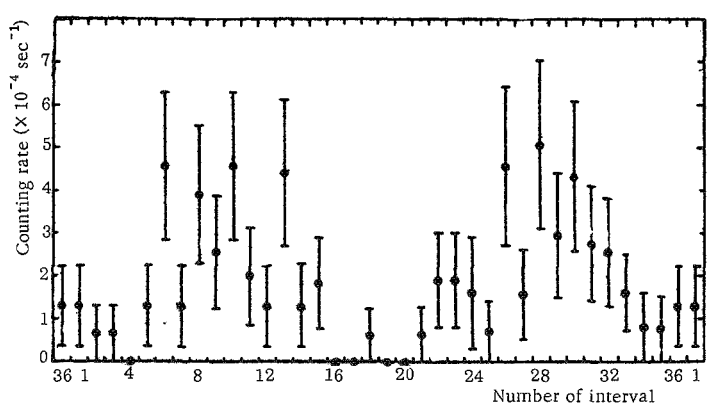

FIGURE 4. Counting rate as a function of the instrument position in orbit.

The errors in the table do not allow for the accuracy of the Monte Carlo method ($\sim$10%). Since the gamma-ray counting rate is influenced by charged-particle imitations, the intensity in the equatorial part of the orbit should be regarded as the upper bound value of the primary gamma rays.

Nevertheless, it seems that the integrated intensity I_γ ($\geq$90 MeV) = = $(6.2 \pm 3.3) \cdot 10^{-5}$ (cm^2 sec sterad)$^{-1}$ coincides within the margin of error with the isotropic gamma-ray background I_γ ($\geq$100 MeV) = $(1.1 \pm 0.2) \cdot 10^{-4}$ as measured by OSO-3 /29/.

Experimental conditions

Angular velocity, deg/sec	Scanning time in the direction of flight (1°), sec	Effective area S_{ef}, cm^2	Collimator solid angle aperture	$S_{eff} \cdot t_{1°}$, cm · sec	Exposure, $S_{ef} \cdot t_{slit}$*	Source
24	0.0417	900	8° (50 sq. deg)	38	7200	/2/
75	0.0132	1385	4° × 28° (112 sq. deg)	18	5540	/6/
0.38	2.63	350	2°×20° (40 sq. deg)	920	1840	/5/
0.077	13.0	525	1°× 8° (8.0 sq. deg)	6820	6820	/4/
0.067	14.8	135	32' × 18° (9.6 sq. deg)	2000	1000	Our data

* t_{slit} *is the slit traversing time (for slit width at half the slit height).*

Figure 5 plots the combined X-ray and gamma-ray spectrum. The results at energies between 2 keV and 1 MeV are borrowed from /33/.

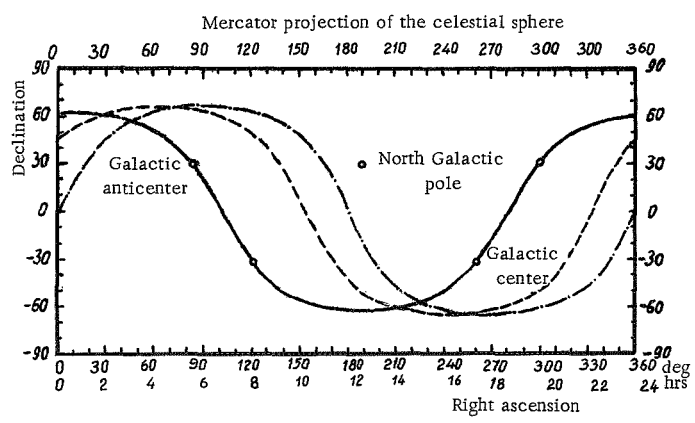

FIGURE 5. The global X-ray and gamma-ray spectrum.

The data for hard gamma rays are plotted according to the intensity measurements at various energies carried out by EXPLORER XI /23/, PROTON 2 /27/, OSO-3 /29/, and KOSMOS-208 /30/. Between 10 keV and 1 GeV, the spectrum may be fitted with a power function with $\gamma \approx 2.2$.

The KOSMOS-208 instrument was aimed to the galactic poles in the equatorial region. Therefore, the above integrated intensities constitute the upper bound values for the hard gamma fluxes in these directions.

Both the X-ray and the hard gamma-ray spectrum should be studied in greater detail, with special emphasis on the global background and the local sources.

Bibliography

1. Giacconi, R., H. Gursky, F.R. Paolini, and R. Rossi.— Phys. Rev. Lett., 9:439. 1962.
2. Byram, E.T., T.A. Chubb, and H. Friedman.— Science, 152:66. 1966.
3. Fisher, Ph.C., W.C. Jordan, A.J. Meyeroff, L.W. Acton, and D.T. Roetting.— Nature, 211:920. 1966.
4. Friedman, H. and E.T. Byram.— Science, 158:257. 1967.
5. Bradt, H., W. Mayer, S. Naranan, S. Rappaport, and G. Spada.— Astrophys. J. Lett., 150:1967. 1967.
6. Adams, A.J., B.A. Cooke, K. Evans, and K.A. Pounds.— Preprint. 1968.
7. Bleeker, J.A.A., J.J. Burger, A.J.M. Deerenberg, A. Scheepmaker, B. Swananburg, and J. Tanaka.— Astrophys. J., 147:391. 1967.
8. Peterson, L.E., A.S. Jacobson, and R.M. Pelling.— Phys. Rev. Lett., 16:142. 1966.
9. Haymes, R.C., D.V. Ellis, J. Fishman, S.W. Glenn, and J.D. Kurfuss.— Astrophys. J., 151:131. 1968.
10. Rocchia, R., R. Rotherflug, D. Boclet, and Ph. Durouchux.— Astron. and Astrophys., 1:48. 1969.
11. Peterson, L.E., R.L. Jerden, and A.S. Jacobson.— AIAAJ, 5:1921. 1967.
12. Metzger, A.E., E.L. Anderson, M.A. van Dilla, and J.R. Arnold.— Nature, 204:766. 1964.
13. Peterson, L.E.— Space Res., 6:53. 1965.
14. Duthie, J.J., R. Cobb, and J. Stewart.— Phys. Rev. Lett., 17:263. 1966.
15. Ogelman, H.B., J.P. Delvaill, and K.J. Greisen.— Phys. Rev. Lett., 16:491. 1966.
16. Frye, G.M. and C.P. Wang.— Phys. Rev. Lett., 18:132. 1967.
17. Fazio, G.G. and H. Helmken.— Canad. J. Phys., 46:5456. 1968.
18. Hafner, E.M. and G. Share.— Preprint. 1964.
19. Bezus, V.A., A.M. Gal'per, N.L. Grigorov, V.V.Dmitrenko, L.F. Kalinkin, V.G. Kirillov-Ugryumov, B.I. Luchkov, A.S. Melioranskii, Yu.V. Ozerov, I.L. Rozental', I.A. Savenko, and E.M. Shermanzon.— Izvestiya AN SSSR, Seriya Fizicheskaya, 32:1863. 1968.
20. Chuikin, E.A., A.M. Romanov, and A.S. Lepin.— Izvestiya AN SSSR, Seriya Fizicheskaya, 30:1791. 1966.

21. TASS Communiquee, "Pravda," 22 March 1968.
22. Grigorov, N.L., L.F. Kalinkin, A.S. Melioranskii, I.A. Savenko, and R.M. Tul'skii.— Materialy Vsesoyuznoi Konferentsii po fizike kosmicheskikh luchei. Tashkent. 1968. (In press).
23. Kraushaar, W., G.W. Clark, G. Garmire, H. Helmken, H. Higbie, and M. Agageno.— Astrophys. J., 141:845. 1965.
24. Grigorov, N.L., L.F. Kalinkin, A.S. Melioranskii, V.E. Nesterov, E.A. Pryakhin, I.A. Savenko, E.A. Sysoev, and I.V. Estulin.— Kosmicheskie Issledovaniya, 5(1):124. 1967.
25. Grigorov, N.L., L.F. Kalinkin, A.S. Melioranskii, V.E. Nesterov, E.A. Pryakhin, I.A. Savenko, and I.V. Estulin.— Izvestiya AN SSSR, Seriya Fizicheskaya, 30:1765. 1966.
26. Grigorov, N.L., L.F. Kalinkin, A.S. Melioranskii, E.A. Pryakhin, and I.A. Savenko.— Materialy Vsesoyuznoi Konferentsii po fizike kosmicheskikh luchei. Novosibirsk. 1967.
27. Bratolyubova-Tsulukidze, L.S., N.L. Grigorov, L.F. Kalinkin, A.S. Melioranskii, E.A. Pryakhin, and I.A. Savenko.— Materialy Vsesoyuznoi konferentsii po fizike kosmicheskikh luchei. Tashkent. 1968. (In print).
28. Fazio, G.G. and E.M. Hafner.— J. Geophys. Res., 72:2452. 1967.
29. Clark, G.W., G.P. Garmire, and W.L. Kraushaar.— Astrophys. J., 153:203. 1969.
30. Grigorov, N.L., L.F. Kalinkin, A.S. Melioranskii, E.A. Pryakhin, I.A. Savenko, and V.Ya. Yufarkin.— Kosmicheskie Issledovaniya. (In press).
31. Volobuev, S.A., A.M. Gal'per, N.L. Grigorov, L.F. Kalinkin, S.V. Dvoretskii, V.G. Kirillov-Ugryumov, B.I. Luchkov, A.S. Melioranskii, Yu.V. Ozerov, I.A. Savenko, E.M. Shermanzon, and I.D. Shashko.— Kosmicheskie Issledovaniya. (In press).
32. TASS Communiquee, "Pravda," 24 January 1969.
33. Fazio, G.G.— Ann. Astron. and Astrophys., 5:481. 1967.

VARIATIONS OF THE ELECTRON COSMIC-RAY COMPONENT WITH ENERGIES BETWEEN 100 AND 1500 MeV IN THE UPPER ATMOSPHERE

A. M. Gal'per and B. I. Luchkov

Considerable attention has been devoted to measurements of the primary electron component of cosmic rays between 10^2 and 10^3 MeV in view of its importance in space physics and Earth-space phenomena. The corresponding experimental work is carried out at high latitudes, where the virtually total lack of the geomagnetic cutoff permits study of the primary electrons at the relevant energies /1 – 12/. Similar measurements carried out at low altitudes are generally assumed to provide information only regarding the double electron albedo, i.e., the electron albedo returning to the atmosphere along the magnetic lines of force. This treatment, however, is much too simplified. A considerable proportion of the electrons hitting the boundary of the atmosphere at energies below the geomagnetic threshold are in fact different from the double electron albedo. This problem constitutes the subject of the present paper.

During 1967 – 1968, the Moscow Engineering-Physical Institute and the Space Research Institute carried out measurements of the intensity and the energy spectrum of the direct and the reverse electron flux at energies between 100 and 1500 MeV at altitudes up to 7 g/cm^2 of residual atmosphere. Preliminary results of these studies were published in /13 – 14/.

The experiments were carried out at geomagnetic latitude of 46°, where the geomagnetic threshold momentum is 3.5 GeV/c. The general flight data are summarized in the table below.

Date	Start (Moscow time, hr – min)	Instrument recording period (Moscow time, hr – min)	Maximum flight altitude, km	Measured flux
14 June 1967	5 – 22	5 – 22 – 7 – 20	24.8	Direct electron flux
6 July 1967	5 – 53	5 – 53 – 9 – 52	27.5	Ditto
27 Oct. 1967	6 – 28	6 – 28 – 8 – 33	26.5	"
31 Oct. 1967	4 – 47	4 – 47 – 12 – 02	28.0	Electron albedo
9 July 1968	6 – 16	6 – 16 – 10 – 48	32.2	Direct electron flux
9 July 1968	6 – 16	6 – 16 – 12 – 25	32.2	Electron albedo
8 Oct. 1968	5 – 54	5 – 54 – 9 – 58	33.0	Direct electron flux
19 Nov. 1968	7 – 11	7 – 11 – 11 – 10	31.0	Ditto

A block diagram of the recording instrument is shown in Figure 1. The instrument comprises a directional threshold Cherenkov counter (with a Plexiglas radiator), three scintillttion counters C_1, C_2, C_3, a multiplate spark chamber SC with total plate thickness of 3.7 lead rad. units; a lead absorber L (3 rad. units thick), and a stereophotographic camera P. The geometrical factor of the instrument was 14.5 cm^2 sterad. When an electron reaches the instrument and an electron shower is produced in the spark chamber (subsequently absorbed by the lead absorber), the instrument develops a master pulse $ChC_1C_2\overline{C}_3$ (here $\overline{C}_3$ signifies that the counter delivers no pulse) which triggers the spark chamber and causes the event to be photographed.

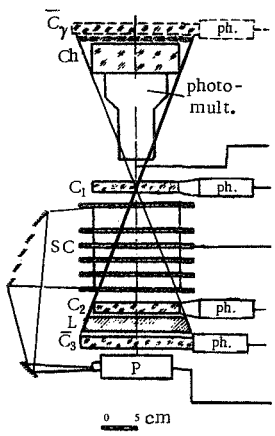

FIGURE 1. A block diagram of the recording instrument. The dashed elements represent the additional scintillation counter and the lead converter used for gamma-ray recording.

In flight, the instrument is sealed in a thermally insulated air-tight container. To record the electron albedo, the container with the instrument is turned through 180°. To elucidate the working characteristics of the instrument, the high-altitude balloon flights were preceded by calibration tests using electron beams of 100 – 1500 MeV. Figure 2 plots the electron counting efficiency vs. the electron energy obtained in these calibration tests. The instrument is seen to have a peak sensitivity between 250 and 1000 MeV. The calibration results also show that the spark chamber has a nearly 100% efficiency for the detection of electron showers, and the mean total number of sparks in the recorded showers is virtually a linear function of the electron energy. It is assumed that under natural conditions the differential electron energy spectrum is described by a power function $N(E) = AE^{-\alpha}$; the calibration data were applied to compute the dependence of the total average number of sparks in the observed showers on the index α between 1 and 3.

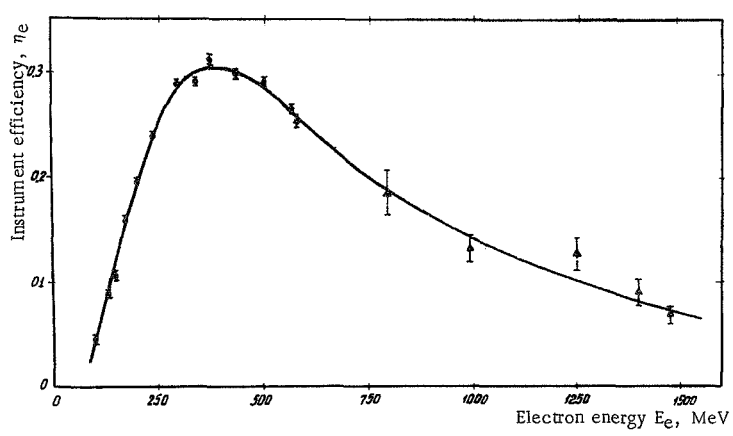

FIGURE 2. Instrument efficiency vs. electron energy:

the FIAN SSSR electron synchrotron, the FTI AN UkrSSR electron linear accelerator.

Protons with velocities exceeding the threshold velocity of the Plexiglas radiator clearly penetrate through the instrument and trigger the counter C_3. In some cases, however, not a single particle passes through C_3 because of the interaction in the chamber plates and in the absorber, and this event is registered as an electron event. To assess the spurious background, calibration measurements were carried out using a proton beam with 2 GeV/c momentum. The results show that only 0.5% of proton nuclear interactions can be mistaken for an electron event if a further selection based on the shower photograph in the spark chamber is instituted. Thus, double selection of events, first according to the master pulse and then according to the SC shower photograph, ensures reliable identification of electron events.

The experimental measurement data for the electron component of cosmic rays at high altitudes lead to the following conclusions:

1. The altitude variation of the electron component with energies between 100 and 1500 MeV was measured in six flights. The measurement results are shown in Figure 3. Note the marked difference between the recorded fluxes at high altitudes and the relative constancy of the fluxes at high altitudes. Thus, during the measurements of 14 June and 27 October 1967, the electron flux recorded at maximum altitude (16 g/cm^2 residual atmosphere) is 2.5 times as large as the electron flux recorded at the same altitude on other occasions. The intensity remained constant during the entire flight (2 hr) at the maximum altitude.

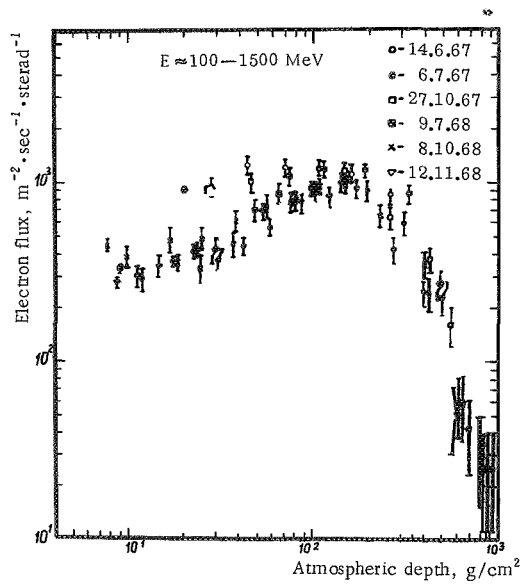

FIGURE 3. The 100—1500 MeV cosmic-ray electron component vs. altitude.

2. The statistical sample is sufficient for dividing the experimental results into two groups corresponding to "elevated" intensity (14 June and 27 October 1967) and "normal" intensity (all other days). Assuming

a power spectrum, we can find the spectrum index of the electrons. A harder spectrum is obtained for the days of "elevated" intensity ($\alpha = 2.3 \pm 0.1$, as compared to 3.0 ± 0.2 for the other days). This fact points to differences in the origin of the electrons on days of "normal" and "elevated" activity.

3. The altitude variation of the albedo electrons from two flights is given in Figure 4. Unlike the results of /9/, these data reveal a maximum at much higher altitudes, whereas the recorded albedo is lower. These differences are apparently attributable to the more reliable separation of the electron albedo in our measurements. The results of these albedo measurements show that the albedo does not account for the direct electron flux extrapolated to the top of the atmosphere, even in cases of normal intensity. It is assumed that the electron albedo at the top of the atmosphere (the maximum on Figure 4) all return into the atmosphere.

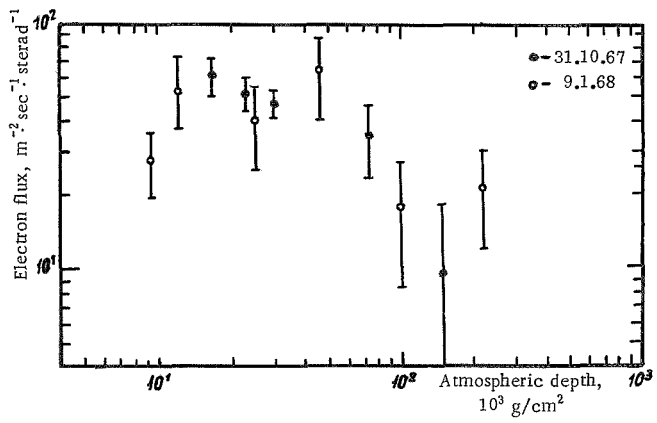

FIGURE 4. The electron albedo vs. altitude.

4. The experimental data show that the increase of the direct electron flux depends on the total value of the index Kp on days of measurement: the totals ΣKp for six days were respectively equal to 23, 14, 18, 9, 14, 12. The "elevated" intensity electron fluxes correspond to days with maximum values of ΣKp.

No correlation of the electron flux with other astrophysical or geophysical phenomena, such as the number of sunspots, changes in the readings of the neutron monitor, etc., was discovered. The direct electron flux variations are apparently associated with changes in the state of the magnetosphere near the Earth.

The increase of the electron flux cannot be accounted for by changes in the reflection of the albedo flux by the magnetic field. Apparently it cannot be accounted for by the increase in the flux of primary cosmic rays and the associated increase of the albedo electrons, either. On the relevant days, neither the neutron monitor nor the results of our measurements reveal any changes in the primary cosmic-ray flux. Our instrumentation, in addition to electrons, also recorded a certain number of muons and protons which penetrate through the spark chamber and are stopped in the absorber. The number of these particles is a

function of the primary cosmic-ray flux. However, the muon flux remained constant within the margin of experimental error on all the relevant days. The possible contribution from the diffusion of primary electrons with energies of 100 – 1500 MeV to geomagnetic latitude of 46° apparently can also be ignored, because of the low likelihood of the event. The only logical interpretation of the increase in the electron flux, in our opinion, is that additional electrons are injected from traps. This assumption necessitates a further elucidation of a number of effects associated with the kinematics and the dynamics of the region of trapped radiation. These include (a) the origin of these high-energy electrons and the probable acceleration mechanism, (b) the conditions of existence of electrons and their accumulation, (c) the factors responsible for injection from traps. The answer to these questions falls outside the scope of our paper, but it is clear that the identification of the electron flux variation with electron injection from traps is a highly important result.

No direct observations were made of electrons with energies higher than 100 MeV in the radiation belt. This is apparently due to the limitations of the experimental instruments. The only experiment using a gaseous Cherenkov counter for electron detection was undertaken on board PROTON 1. Electrons with energies of $\gtrsim 300$ MeV were detected, and their intensities markedly exceeded both the cosmic-ray albedo and the primary cosmic-ray flux. There is a definite possibility that PROTON 1 actually recorded the injection of electrons from traps /16/.

In conclusion, we would like to comment on one further aspect. The variable electron fluxes reaching the upper atmosphere may affect the altitudinal variation of the secondary gamma quanta recorded in the top layers of the atmosphere. Indeed, if we assume that the intensity of the secondary gamma quanta at high altitudes is determined by the double albedo electrons and by electrons injected from traps, as well as by the nuclear interactions of the primary cosmic rays, we conclude that an additional maximum should be observed at a depth of about 30 g/cm^2 residual atmosphere. Marked changes in the flux of the injected electrons may alter the amplitude of this additional maximum. This apparently explains the changes in the amplitude of the additional maximum, observed by Chukin et al. /17/.

Bibliography

1. Earl, J.– Phys. Rev. Lett., 6:125. 1961.
2. Meyer, P. and R.E. Vogt.– J. Geophys. Res., 66:3950. 1961.
3. Shong, J.A. de.– Phys. Rev. Lett., 12:3. 1964.
4. Cline, T.– Phys. Rev. Lett., 13:786. 1964.
5. L'Heureux, J. and P. Meyer.– Phys. Rev. Lett., 15:93. 1965.
6. Schmoker, J.W. and J. Earl.– Phys. Rev., 138:B-300. 1965.
7. Freier, P.S. and C.J. Waddington.– J. Geophys. Res., 70:5753. 1965.
8. L'Heureux, J.– Astrophys. J., 148:399. 1967.
9. Verma, C.D.– J. Geophys. Res., 72:915. 1967.
10. Webber, W.R. and C. Chotkowski.– J. Geophys. Res., 72:2783. 1967.

11. Simnett, G.M.— Planetary and Space Sci., 15:1787. 1967.
12. Bewerman, K.P.— Phys. Rev. Lett., 22:412. 1969.
13. Bezus, V.A., A.M. Gal'per, N.L. Grigorov, V.V. Dmitrienko, L.F. Kalinkin, V.G.Kirillov-Ugryumov, B.I. Luchkov, A.S. Melioranskii, Yu.V. Ozerov, I.L. Rozental', I.A. Savenko, E.M. Shermanzon.— Izvestiya AN SSSR, 32(11):1863. 1968.
14. Dmitrienko, V.V. and B.I. Luchkov.— Trudy V Vsesoyuznoi ezhegodnoi zimnei shkoly po kosmofizike, p.163. Apatity, Izd. Kol'skogo filiala AN SSSR, 1968.
15. Bezus, V.A., A.M. Gal'per, N.L. Grigorov, V.V. Dmitrienko, L.F. Kalinkin, V.G.Kirillov-Ugryumov, B.I. Luchkov, A.S. Melioranskii, Yu.V. Ozerov, I.L. Rozental', I.A. Savenko, and E.M. Shermanzon.— Tezisy dokladov Vsesoyuznoi konferentsii po fizike kosmicheskikh luchei, Part 2, p.24. 1968.
16. Grigorov, N.L., Yu.S. Klintsov, V.E. Nesterov, I.D. Rapoport, I.A. Savenko, and B.M. Yakovlev.— Izvestiya AN SSSR, 30:1773. 1966.
17. Chuikin, E.A., A.M. Romanov, and A.S. Lenin.— Geomagnetizm i Aeronomiya, 7:810. 1967.

THE NEUTRINO EMISSION OF THE SUN

G. E. Kocharov

The neutrino occupies a special place among all the currently known elementary particles. Unlike other particles, the neutrino only takes part in weak interactions whose probability is exceedingly low. It suffices to mention that the range or the free path of a neutrino of about 1 MeV in the Universe is 10^{31} light years, whereas the radius of the entire observed part of the Universe is a mere 10^{10} light years. Neutrinos thus have a virtually infinite lifetime in the Universe and they may retain in their "memory" the specific features of the cosmic processes responsible for their creation. Therefore, if we manage to catch a neutrino, it may reveal some of the secrets of the distant past and also shed light on the processes which take place in the stellar interiors. The neutrino proved an exceptionally intractable particle for the experimental physicist. It took several decades before the neutrino was actually registered with physical instruments. And yet, the very first experimental results vividly confirmed the original predictions of the theory. The neutrino thus ceased to be a myth: it evolved into a legitimate elementary particle.

The rapid development of experimental physics during the last twenty years provided adequate tools for neutrino detection under natural conditions: a whole new branch of science – neutrino astrophysics – was thus raised and discussed at the International Cosmic Ray Conferences in view of the tremendous interest aroused by this science and the steady influx of new theoretical and experimental information. The sensational results of Davis /1/ concerning solar neutrinos were discussed at last year's session of the Winter School. We saw that Davis' negative results could be explained without breaking the basic premises of the theory of the structure of the stellar interior and stellar evolution. A number of reports published during the last year were devoted to the interpretation of Davis' results. A special seminar held in Moscow (9 – 11 September 1968) with the participation of eminent Soviet and Western scientists dealt with various aspects of neutrino physics and astrophysics. We will try to review here the new additions to the pool of our knowledge which became available after the Fifth Winter School of Space Physics. For the sake of completeness, we will have to repeat some of the topics discussed in the previous session /2/.

DAVIS' SOLAR NEUTRINO EXPERIMENTS /1/

The tremendous penetrating power of the neutrino enables us to "peep" into the interior of the nearest star, the Sun. This extremely attractive

prospect, however, is offset by a fundamental difficulty: the neutrino is virtually intractable and is very difficult to detect. Because of this difficulty, experimental neutrino astrophysics has been often regarded as a purely fantastic proposition. The situation has changed, however. Experimental neutrino astrophysics is now a reality, although it has not yielded any positive results so far.

Davis tried to detect the neutrino using the reaction $Cl^{37}(\nu, e^-)A^{37}$, originally proposed back in 1946 by Pontecorvo /3/. The choice of this reaction is by no means accidental. We will now list the basic requirements to be met by the target material in radiochemical neutron-detection experiments.

1. A reliable method should be available for the isolation of the reaction products from the target. This is particularly significant since according to estimates solar neutrinos will produce a few tens or at most hundreds of product atoms in a detector weighing several tons. It is therefore not desirable to have the target and the product in the same state of aggregation, since phase separation in this case would be a difficult undertaking. The reaction $Cl^{37}(\nu, e^-)A^{37}$, on the other hand, may be triggered using a liquid target (e.g., a common cleaning fluid CCl_4), whereas the reaction product is gas, argon-37.

2. A highly sensitive atom-counting method should be available. Product atoms in tiny numbers (tens or hundreds of atoms) are naturally best detected if they are radioactive. The half-life of the product isotope should not be too long, so as to ensure an adequate specific activity, and yet it should not be too short, since isotopic separation and other processing take some time. A^{37} is a radioactive isotope with a half-life of 35 days. By capturing an orbital electron, argon-37 is transformed into chlorine -37 emitting Auger electrons and two X-ray lines (the 2.8 keV K-line and the 280 keV L-line, Figures 1, 2 /4/). A few tens of A^{37} atoms are difficult to detect and count. This task required the development of special low-background counting assemblies using miniature proportional counters /1, 4–8/.

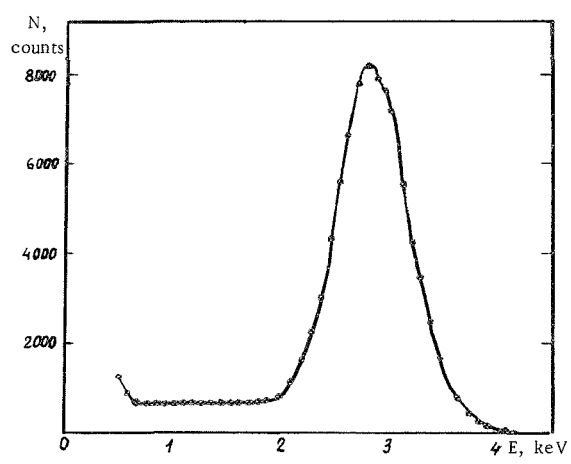

FIGURE 1. A^{37} K-line in a counter 24 mm long and 3 mm in diameter.

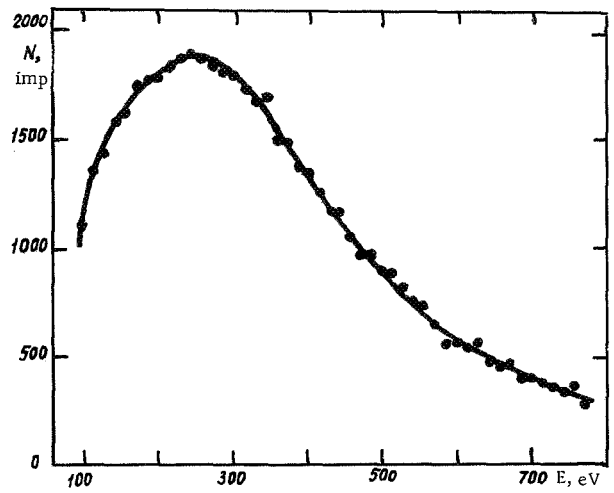

FIGURE 2. A^{37} L-line in a counter 12 mm long and 3 mm in diameter.

3. The target material should be cheap, since hundreds of tons of it are required.

4. The target should be pure from impurities liable to produce background reaction products.

5. The reaction cross section should be relatively large. The reaction $Cl^{37}(\nu, e^-)A^{37}$ with its threshold at 0.81 MeV is insensitive to the strongest group of solar neutrinos ($E_{max} \simeq 0.42$ MeV). The main contribution to this reaction is from neutrinos produced by the decay of B^8 ($E_{max} \simeq 14.06$ MeV) and by the reaction $Be^7(\nu, e^-)Li^7$ (E = 0.86 MeV). The reaction $Cl^{37}(\nu, e^-)A^{37}$ best meets these requirements.

Davis used in his experiments 390,000 liters of CCl_4 (this quantity of liquid would fill an olympic swimming pool). The target contained 520 tons of chlorine, 128 tons of which were Cl^{37} (the natural isotopic mixture of chlorine contains 24.6% of Cl^{37}). The target mass was chosen so as to ensure a countable quantity of A^{37} during the exposure time. The length of the experiment (2 – 3 months) was limited by the half-life of A^{37}. Background reactions triggered by cosmic rays and radioactive impurities in the target, the container, and the surrounding objects have a highly detrimental effect on the solar neutrino experiments. To reduce the background, the target was exposed at a depth of 1.5 km in a disused gold mine, in South Dakota, USA. According to the estimates of /1/, the yield of background reactions did not exceed 0.2 A^{37} atoms per day: half of this number was due to the muon background. According to the theoretical data which were available at that time, the solar neutrinos were expected to produce from 2 to 10 A^{37} atoms per day, the daily average being 4.

An important link in the entire experimental procedure is the effective separation of ultrasmall quantities of argon from the tremendous bulk of the target. Davis et al. attacked this problem in the following manner. A certain quantity of carrier was introduced into the liquid: about 1 cm^3 NTP

of the nonradioactive argon isotope A^{36}. The system was then scavenged with gaseous helium, which removed from the liquid the A^{36} carrier together with the A^{37} produced by the solar neutrinos. The gas mixture was then delivered to a trap at −40°C to freeze out the CCl_4 vapor; after the trap, the gases were passed through activated coal at 77°K. Argon was effectively sorbed by coal, and helium was recirculated in the working volume. The sorbent was heated to desorb the argon, which was then passed through the counting assembly. Observations showed that the working liquid invariably contained traces of atmospheric xenon and krypton: their content is comparable to or even greater than that of argon. A particularly dangerous isotope is Kr^{85}, with a half-life of 10.8 years. Argon therefore had to be separated from xenon and krypton before its delivery to the counting assembly. To reduce the krypton content to the harmless level of 10^{-8} parts per part of argon, two chromatographic separation stages were required.

To check the argon separation efficiency, several tests were run. After preliminary purification from atmospheric argon, a known quantity $V_0(A)$ of 99.9% pure A^{36} was injected into CCl_4. Argon was then separated by the method described above. The residual amount of argon in the liquid V(A) was measured as a function of the amount of helium V(He) passed through the system. The empirical relation $V(A)/V(He) = \exp(-7.21 \cdot 10^{-6} V(He))$, where the volume of helium is expressed in liters, shows that the separation efficiency reached 95% when 420,000 liters of helium had been passed through the system. In Davis' setup, 22 hrs were required to scavenge the system with this volume of gaseous helium. A second test was designed to produce a known quantity of A^{37} for separation. A radium—beryllium neutron source with an intensity of $7.38 \cdot 10^4$ neutrons per sec was introduced into the system. The total neutron irradiation time was 0.703 days. The neutrons transformed Cl^{35} (the natural chlorine mixture contains 75.4% Cl^{35}) into S^{35} and protons were emitted with energies exceeding the 1.6 MeV threshold of the reaction $Cl^{37}(p, n)A^{37}$, i.e., in the final analysis, A^{37} atoms were produced in the target, just as in the interaction with solar neutrinos. Addition of 1.118 cm^3 of A^{36} carrier was followed by argon separation in three stages: 350,000, 260,000, and 340,000 liters of gaseous helium were successively passed through the system. The measurement results are listed in Table 1. The rate of production of A^{37} can be determined from the table: it is equal to $(7.5 \pm 0.4) \cdot 10^{-7}$ argon atoms per neutron, in good agreement with the results obtained in previous tests with small quantity of CCl_4.

TABLE 1. Rate of argon separation from the liquid

Amount of helium, m^3	A^{36}, %	A^{37}, atoms
350	90.6	3200 ± 182
260	6.2	116 ± 56
340	0.7	35 ± 25

This shows that the argon yield virtually does not change when the liquid volume is increased. Another noteworthy feature is the similarity in the

decrease of the A^{36} and A^{37} content in the liquid from one cycle to the next. It now remains to establish that the A^{37} atoms produced in the reactions $Cl^{37}(p,n)A^{37}$ and $Cl^{37}(\nu,e^-)A^{37}$ are actually in the same state. The Cl^{37} atom in the initial state is bound in a CCl_4 molecule. The kinetic energy of the A^{37} atom produced by solar neutrinos is between 11 and 1000 eV, i.e., it is less than in the reaction $Cl^{37}(p,n)A^{37}$, and yet higher than the bond energy of A^{37} in the original molecule. On the basis of these considerations, Davis suggests that the conditions of formation of free A^{37}, its mixing with the nonradioactive A^{36} (present in amounts of around 10^{10} atoms/cm^3 in the target), and its separation in solar neutrino experiments are the same as in experiments with a neutron source.

The ultra-small quantities of argon-37 were counted using a special low-background assembly. The specific feature of the counting techniques for ultra-small quantities of radioactive gases were considered in /4–8/. We will only describe the fundamental parameters of Davis' system. A proportional counter 5 mm in dia. and 30 mm long was used as a detector (Figure 3). The detector was placed in a well in an NaI scintillation counter (12.5×12.5 cm). The entire system was surrounded by a ring of proportional counters 5 cm in diameter. The scintillation and the proportional counters were coupled into an anticoincidence circuit with the central detector.

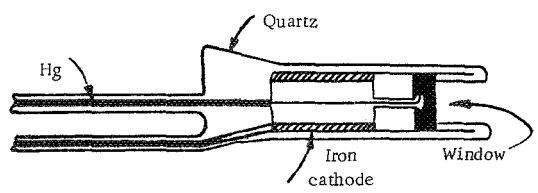

FIGURE 3. Davis' proportional counter /1/.

A 30-cm-thick iron shield is used as passive protection. The time of arrival, the amplitude, and the shape of each pulse in the central detector are determined. The half-width of the A^{37} K-line is 28%. The background counting rate in the 14 analyzer channels around the maximum of the A^{37} K-line (the 50th channel) is about 0.3 counts per day (Figure 4a). The A^{37} counting efficiency is 51%.

Two exposures, 48 and 110 days long, were made in 1967. After the first exposure, 22 pulses were counted in the main channel during 39 days. The background, however, was 31±10 counts. The effective count thus did not exceed the background value. Considering the A^{37} separation and counting efficiency, we obtain a rate of -1.1 ± 1.4 events per day for the reaction $Cl^{37}(\nu,e^-)A^{37}$. The results of the second exposure are shown in Figure 4b, 4c. During the first 35 days, 11±3 counts were detected, while the background was 12±4. The effective count again did not exceed the background. The results indicate that the rate of the $Cl^{37}(\nu,e^-)A^{37}$ reaction within the limit of one rms error does not exceed 0.5 events per day. This signifies that the rate of the reaction $Cl^{37}(\nu,e^-)A^{37}$ is $\xi_e < 3\cdot10^{-36}$ sec^{-1} per 1 Cl^{37} atom. Therefore, the upper bound value of the neutrino flux from B^8 decay works out to be $2\cdot10^6$ neutrinos/cm$^2\cdot$sec. Thus, despite theoretical

predictions, Davis' solar neutrino experiments gave negative results. The experimental upper bound value for the rate of the reaction $Cl^{37}(\nu, e^-)A^{37}$ worked out to be approximately one order of magnitude less than the theoretical figure. We will consider the probable reasons for this divergence between theory and experiment.

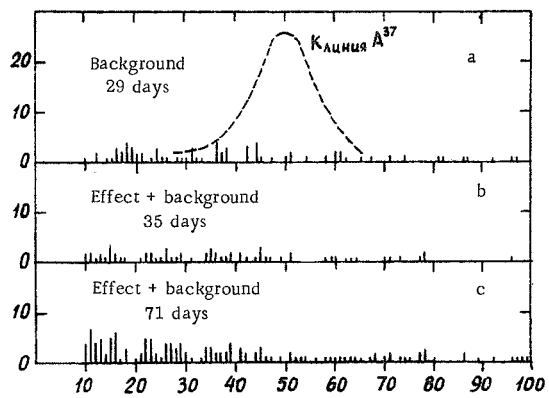

FIGURE 4. Counting rate vs. channel number:

a) counter background in 29 days, b) effect + background in 35 days, c) effect + background in 71 days.

INTERPRETATION OF DAVIS' RESULTS

The negative results of the solar neutrino detection experiment revealed some fundamental deficiencies in our conception of the processes in the stellar interior. The failure of the experiment stimulated a more critical approach to the theory of stellar structure and evolution and focused our attention on the need for new theoretical and experimental studies. This, in our opinion, is the main contribution of Davis' experiment. We will now review, in a condensed form, the basic premises which are generally used in the construction of theoretical models of the Sun.

1. Nuclear parameters, chemical composition of the initially homogeneous Sun, the age of the Sun

In Sun models it is generally assumed /9/ that some time $t_\odot$ ago (this is the age of the Sun), the Sun was a sphere of radially homogeneous chemical composition. The present-day chemical composition of the Sun's surface is regarded as fully corresponding to the initial composition of the entire Sun $t_\odot$ years ago. Successive evolutionary models are constructed step by step, by analyzing the variation in conditions in the solar interior due to the contribution from the thermonuclear reactions, and the model, after $t_\odot$ years of evolution, should fit the present-day characteristics of the Sun.

Nuclear reaction cross sections for the conditions of the solar interior and the chemical composition of the Sun's surface were considered in /2/. Here we only reproduce Table 2 borrowed from /10/, which summarizes the old (used for the construction of solar models prior to Davis' experiments) and the new (obtained recently) values of some of the basic theoretical parameters. In a number of cases, the new values are significantly different from the old values. Given the dependence of the neutrino flux on various parameters, we can easily find the change in the theoretical cross section of the reaction $Cl^{37}(\nu, e^-)A^{37}$ on the basis of the new data. The new flux value $I(B^8) \approx (4.5 - 6.5)$ neutrinos/cm^2 sec is clearly less than the old value, but it is still higher than the upper bound value of $2 \cdot 10^6$ cm^{-2} sec^{-1} obtained by Davis. If we further allow for errors in the values of the initial parameters, an adequate fit is observed in principle between theory and experiment /2, 10, 20, 21/. However, as we have seen /2/, this fit can be ensured only if the true values of the parameters listed in Table 2 correspond to those extreme values (with allowance for one rms error which yield the minimum value of the flux $I(B^8)$. Solar models based on the new values of the parameters were published only after Davis' experiments /20, 21/.

TABLE 2. Some parameters for the construction of Sun models

Parameters	Old value	New value	Dependence of $I(B^8)$ on parameter	$\frac{I(B^8)_{old}}{I(B^8)_{new}}$	$I(B^8)_{new} \cdot 10^6$ cm^{-2}sec^{-1}
Cross section parameter, keV · barn:					
$p+p \to D^2+e^++\nu$, $S_{11} \cdot 10^{-22}$	3.36 ± 0.40	3.78 ± 0.15 /11/	$S_{11}^{-2.5}$ /12/	1.3	
$He^3+He^3 \to He^4+2p$, S_{33}	1100	4130 ± 1220 /2, 13/ 5100 ± 600 /14/	$S_{33}^{-0.35}$ /2, 13/ $S_{33}^{-0.40}$ /12/	1.7	
$Be^7+p \to B^8+\gamma$, S_{71}	0.030 ± 0.010	0.035 ± 0.004 /15/	S_{71}	0.9	
	0.021 ± 0.008			0.6	
	0.043 ± 0.004			1.2	
Probability of reaction:					
$Be^7+e^- \to Li^7+\nu$	Capture of bound electrons ignored, λ_0	$\frac{\lambda}{\lambda_0} = 1.2$ /2/	$\frac{\lambda}{\lambda_0}$	1.2	
Initial chemical composition of the Sun					
hydrogen X	0.630 /16/	0.787 ± 0.028 /2/			
	0.708 /17/				
	0.680 /18/				
	0.739 /19/				
helium Y	0.336 /16/	0.198 ± 0.036 /2/			
	0.272 /17/				
	0.276 /18/				
	0.240 /19/				
heavy elements Z	0.034 /16/	0.015 ± 0.003 /2/	Z /2, 12/	2.3	
	0.020 /17/			1.3	
	0.044 /18/			2.9	
	0.021 /19/			1.4	
Neutrino flux $I(B^8)$, 10^6 cm^{-2}sec^{-1}	36 /16/			5.5	6.5
	19 /17/			3.1	6.1
	26 /18/			4.4	5.9
	9.5 /19/			2.1	4.5

Table 3 lists the results for the currently favored model (so-called model C, $t_\odot = 4.7 \cdot 10^9$ years, $X = 0.764$, $Y = 0.221$, $Z = 0.015$, $T_C = 14.9 \cdot 10^6$ °K, $\rho_C = 150$ g/cm^3) according to the data of /20/.

TABLE 3. Neutrino fluxes and rates of the reaction $Cl^{37}(\nu, e^-)A^{37}$

	$p(p, e^+\nu)D^2$	$p(pe^-, \nu)D^2$	$Be^7(e^-,\nu)Li^7$	$B^8(e^+\nu)Be^8$	$N^{13}(e^+\nu)C^{13}$	$O^{15}(e^+\nu)N^{15}$	Σ
I, neutrinos/cm^{2}sec	$6.4 \cdot 10^{10}$	$1.7 \cdot 10^8$	$2.9 \cdot 10^9$	$4.7 \cdot 10^{6*}$	$2 \cdot 10^8$	$2 \cdot 10^8$	$6.7 \cdot 10^{10}$
σ, 10^{-46} cm^2	0	17.0	3.0	$1.35 \cdot 10^4$	2.0	8.0	
$I\sigma$, 10^{-36} sec^{-1}	0	0.29	0.87	6.35	0.04	0.16	7.7*

* In /12/, $I(B^8) = 3.6 \cdot 10^6$ neutrinos/cm^{2}sec. Given this flux, $\xi_T = 6 \cdot 10^{-36}$ sec^{-1}.

Allowing for the uncertainty in S_{11} and Z, the authors of /20/ obtained the following relation:

$$\xi_T = (7.7 \pm 3) \cdot 10^{-36} \frac{S_{71}}{0.043 \text{ keV} \cdot \text{barn}} \text{ sec}^{-1}.$$

Thus if we take for S_{71} the last of the values listed $S_{71} = 0.035$ keV·barn /15/, the rate of the reaction $Cl^{37}(\nu, e^-)A^{37}$ comes out as $\xi_T \approx 6.3 \cdot 10^{-36}$ sec^{-1}, i.e., approximately double the experimental limit. Particular attention should be paid to the considerable variance in the values of the cross section parameter S_{71} according to various authors. The cross section parameter of the first reaction of the proton-proton cycle S_{11} should also be computed with a higher accuracy. The error in S_{11} is associated with the uncertainty in the values of the weak interaction constant and in the wave functions of the initial and the final state of the reacting particles. Further improvement of the measurement accuracy of the neutron half-life will lower the error in the determination of the weak interaction constant and consequently the error in S_{11}. As is known, the content of the heavy elements is determined from spectroscopic and solar cosmic-ray data. The steady increase in theoretical and experimental information regarding the state of the Sun's surface suggests that in the near future we will be able to determine the concentrations of the heavy elements with better accuracy. However, even if the surface concentration of all the elements is known with infinite accuracy, we are still faced with a considerable uncertainty which stems from the assumption that the chemical composition of the primordial Sun was identical with the present-day composition of the Sun's surface and the assumption of homogeneous radial distribution of the various elements in the initial stage (only homogeneous distribution of the heavy elements is assumed today). These two assumptions require a comprehensive and thorough analysis, especially in view of various processes which take place on the Sun's surface and which may conceivably lead to changes in its chemical composition in the course of evolution. Another source of uncertainty is the inaccuracy in the age of the Sun. It has been shown /12/ that the rate of the reaction $Cl^{37}(\nu, e^-)A^{37}$ increases with age as $t_\odot^{1.4}$. No direct methods are currently known for the determination of the Sun's age. The formation of the Sun is generally linked with the formation of the entire solar system: it is assumed that the Sun and the planets originated from the same matter and roughly at the same time. Under

this assumption, the age of the Sun is taken equal to the age of the Earth. According to current data, the age of the Earth ranges between 4.5 and 10 billion years. The recent Sun models assume $t_{\odot} = 4.7 \cdot 10^9$ years.

2. Nonsphericity of the Sun's surface, the rotation of the Sun, the neutrino fluxes

The negative results of the solar neutrino experiments, on the one hand, and the measurements of the nonsphericity of the Sun's surface by Dicke and Goldenberg /22/, on the other, stimulated a vigorous discussion of the possible mixing of matter in the solar interior /23—27/. The exceedingly strong dependence of the neutrino flux $I(B^8)$ on temperature, combined with Davis' data, naturally suggests that we should search for some mechanism "cooling" the solar interior. Right after Davis' experiments, Ezer and Cameron /23/ showed that the negative results of the solar neutrino experiment may be accounted for if intensive mixing processes in the nucleus of the Sun are assumed. We know /13, 28, 29/ that in ordinary models of the Sun, without mixing, the effective neutrino generation by the decay of N^{13}, O^{15}, B^8 and by the reaction $Be^7(\nu, e^-)Li^7$ is confined within a small region at the center of the Sun. Thus, 90% of all the neutrinos are generated within a sphere whose radius is 2.4% of the solar radius for N^{13} and O^{15}, 5.5% of the solar radius for B^8, and 9.0% of the solar radius for Be^7 /13/. Intensive mixing raises the hydrogen concentration and lowers the density and the temperature at the center of the Sun. As a result, the concentrations of the various isotopes (He^3, Be^7, B^8) change and the probability of neutrino-producing reactions is altered. At a given temperature $T \leqslant 15 \cdot 10^6$ °K, $I(B^8)$ decreases with the increase in hydrogen concentration /30, 31/. Thus, for $T = 12 \cdot 10^6$ °K, a change in X from 0.33 to 0.67 lowers $I(B^8)$ to one half /31/. As the temperature decreases, the flux of B^8 neutrinos also diminishes. Therefore, mixing should lower the rate of the reaction $Cl^{37}(\nu, e^-)A^{37}$. Figure 5, borrowed from /25/, illustrates the effect of mixing on the rate of the reaction $Cl^{37}(\nu, e^-)A^{37}$. We see that in the limiting case of intensive mixing throughout the Sun during the entire course of evolution, ξ may drop approximately to one quarter.

Very little is known about the mechanism of mixing in the solar interior. There are some suggestions that this process is reflected in the observed nonsphericity of the Sun /22/. Schwartzschild /9/ has shown that in a star whose figure is nonspherical because of rotation, the radiant flux alone is unable to sustain the conditions of the thermal equilibrium throughout the star and this leads to circulation directed into the equatorial plane and out along the spin axis. This circulation may lead to a definite mixing of the inner and outer layers of the star. It has been shown /9/ that the circulation velocity V_c is an increasing quadratic function of the equatorial velocity V_e, assuming the star to rotate as a rigid body. The Sun has $V_e = 2$ km/sec, which gives $V_c = 10^{-9}$ cm/sec /9/. Given this figure, some 10^{12} years will be required to mix the solar matter, and this is substantially longer than the total age of the Sun. Schwartzschild thus concludes /9/ that in the Sun, circulation associated with its rotation

does not lead to considerable mixing. However, the measurements of the flattening of the Sun necessitated a complete revision of our notions concerning the mixing of matter in the solar interior. According to /22/, the nonsphericity of the Sun is $(5 \pm 0.7) \cdot 10^{-5}$, which is 5 times the nonsphericity computed for rigid-body rotation. The observed nonsphericity may be attributed to a gravitational quadrupole moment, associated with the faster spin of the interior layers in the Sun /22/. The mixing in the solar interior may thus yet prove to be quite significant. We have seen /32/ that for $r < 0.1 R_{\odot}$,* the circulation velocity in the central region of the Sun may be sufficient for intensive mixing. Without going into a detailed discussion of the various hypotheses attempting to account for the observed nonsphericity of the Sun, we will only consider the question of the quadrupole moment of the Sun.

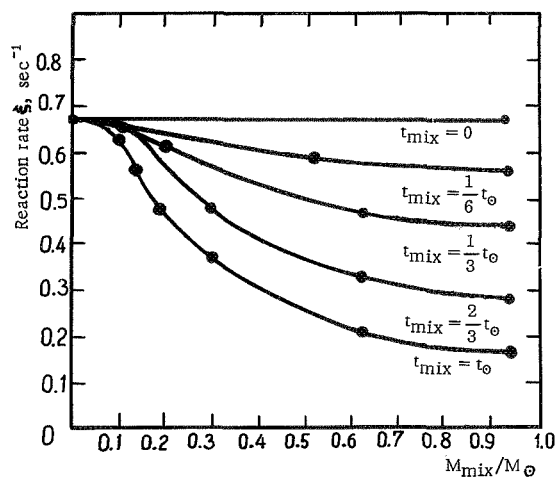

FIGURE 5. The rate of the reaction $Cl^{37}(\nu, e^-) A^{37}$ as a function of the mixing mass for various mixing times.

Einstein listed three effects as suitable for the experimental verification of the general relativity theory: the displacement of the planetary perihelia, the deflection of light near massive objects (the Sun), and the gravitational frequency shift of radiation. We will only consider the displacement of the perihelia,** as this aspect has a direct bearing on our problem.

As is known, planets move in ellipses with the Sun in one of the foci. The perturbing effect of other planets produces a slow rotation of the orbit in the orbital plane in the direction of orbital motion of the planet. As a result, the perihelion of the planet (i.e., the point of the orbit closest to the Sun) moves through a certain angle. The rotation of the planetary perihelion, however, is not entirely due to the perturbations from other planets: a certain contribution is associated with general relativity effects.

* Effective generation of neutrinos by N^{13}, O^{15}, and B^8 decays and by the reaction $Be^7(\nu, e^-) Li^7$ is observed in this region with $r < 0.1 R_{\odot}$ /13, 29/.

** A general review of the problem of experimental verification of the general relativity theory will be found in /33, 37/.

The following expression has been derived for the angle of rotation of the perihelion in one century due to relativistic effects /33, 34/:

$$\psi = \frac{3.34 \cdot 10^{33}}{a^{5/2}(1-\varepsilon^2)},$$

where a is the semimajor axis, $\varepsilon = \frac{\sqrt{a^2-b^2}}{a}$ is the eccentricity, b is the semiminor axis, ψ is expressed in angular seconds.

The values of ψ for Mercury, Venus, Earth, Mars, and Jupiter computed from this relation are the following: (43.03±0.03)" /34/, 8.63", 3.84", 1.35", 0.06", respectively. Experimental measurements give for Mercury (42.56±0.94)" /35, 36/. It has been noted in /37, p. 33/ that, using corrections corresponding to the latest data on planetary masses, Clemens gives for the observed relativistic perihelion rotation (42.9±0.2)". This fit between theoretical and experimental data constitutes the best confirmation of the general relativity theory.

In addition to planetary perturbations and general relativity effects, the rotation of the perihelion is also influenced by the gravitational quadrupole moment of the Sun, whose existence is inferred from the observed nonsphericity. According to /22, 38/, the displacement of the perihelion of Mercury due to the quadrupole moment of the Sun is 3.4" in 100 years, i.e., the general relativity effects account only for 39.5". This figure is 8% lower than the prediction of Einstein's theory of gravitation and it fits the results of the scalar-tensor gravitation theory /39, 40, 41/. This led Dicke and Goldenberg /22/ to prefer the scalar-tensor theory of gravitation. This preference is naturally influenced by subjective bias, as the scalar-tensor theory was developed by Dicke in cooperation with Brans /40/. The perihelion precession of Mercury reaches about 5600" in 100 years, i.e., 130 times the relativistic correction. Of these, 5026" are of purely geometrical origin, associated with the rotation of the coordinate axes, and the remaining 574" are of dynamic origin, being mainly due to the perturbations from other planets (the contribution from Venus is about 278"). The small relativistic effect is thus determined as a difference of large numbers, and this may naturally lead to large errors in the result for the relativistic effect, as Dicke agrees /37, p. 55/. Moreover, it is by no means certain that the entire nonsphericity of the Sun is due to the gravitational moment. Some authors tried to account for the observed flattening by certain processes in the outer layers of the Sun (turbulence, magnetic fields, etc.). Therefore, the only certain conclusion is that, in principle, the rate of the reaction $Cl^{37}(\nu, e^-)A^{37}$ may decrease due to mixing processes in the solar interior. The question of the actual mixing mechanism and the quantitative decrement of the neutrino fluxes require further study.

3. The hypothesis of the time-dependent gravitational constant and the solar neutrinos

Brans and Dicke /40, 41/ tried to further generalize the general relativity theory by including a scalar field Φ related to the gravitational

constant by the equality

$$G = \frac{4+2\omega}{3+2\omega} \cdot \frac{1}{\Phi},$$

where ω is a nondimensional interaction constant of the scalar field.

For $\omega \to \infty$, the Brans and Dicke theory reduces to the general relativity theory. In the Brans and Dicke theory, the gravitational constant is variable in time.* In one year, the gravitational constant should decrease by about $3 \cdot 10^{-11}$. This change is too small to be detectable under laboratory conditions, and yet it is sufficiently large to produce noticeable astronomical and geophysical effects. For example, the exceedingly strong dependence of the stellar luminosity on the gravitational constant (in proportion to G to the power of 7 – 8 /37, p. 851/) should lead to a change of 100% in the luminosity of the Sun in 4 – 5 billion years. This implies that the temperature of the Earth 4 – 5 billion years ago was 353 – 363°K, and the temperature of the Moon about 523°K. The gradual decrease in G should lead to a steady expansion of the Earth (the length of the equator increasing by 150 km in 10^9 years) and the Moon (its equator should increase by 1 km in the same period). Unfortunately, our knowledge of the expansion of the Earth and the Moon and their temperatures in the past are insufficient for either confirming or disproving the theory with $G = f(t)$. A very recent paper /43/ discusses the Brans and Dicke theory in relation to the isotopic abundance of D^2, He^3, and He^4. The abundances of these isotopes are given for various present-day matter densities p_0 and various values of ω. It is shown that for $p_0 > 10^{-30}$ g/cm^3, ω should not be less than 10, since otherwise the content of helium will be too high. At lower densities, the abundances of D^2, He^3, and He^4 are virtually constant for $\omega = \infty$ (general relativity) and $\omega = 5$. These results thus only fix an upper limit on the ratio $\dot{G}/G$ below which the theory with $G = f(t)$ does not conflict with the actual abundance of D^2, He^3, and He^4. The results of /43/ indicate that Einstein's theory should be preferred to the Brans and Dicke theory.

Let us now consider the relation of the Brans and Dicke theory to the solar neutrino flux. The existence of this relation emerges from the following qualitative considerations. If the gravitational constant was larger in the past, the temperature at the center of the Sun also should have been higher, other conditions being constant. Allowing for the extreme sensitivity of the neutrino flux $I(B^8)$ to temperature ($I(B^8) \sim T^{17}$ around $T \approx 14 \cdot 10^6$ °K), we conclude that for $G = f(t)$, $I(B^8)$ should have been higher than for a constant gravitational constant. Sequences of evolutionary models of the Sun with time-dependent gravitational constant were constructed by Ezer and Cameron /44/. In accordance with Dicke's suggestions, Ezer and Cameron used $\omega = 5$ for the interaction constant of the scalar field. The evolution of the Sun was assumed to have begun $4.5 \cdot 10^9$ years ago, when the age of the Universe was $2.5 \cdot 10^9$ years. As could have been expected, the time-dependence of G altered the central temperature and the content of hydrogen in the solar interior: T_c increased from $15.8 \cdot 10^6$ °K (for G = const) to $18.2 \cdot 10^6$ °K (for $G = f(t)$), and X dropped from 0.409 to 0.191. As a result, the flux of high-energy solar neutrinos increased approximately by a factor of 4. As we have noted

* A critical review of various cosmological trends, including the theory with variable gravitational constant, will be found in /42/.

before, Davis' results give for $I(B^8)$ an upper limit which is substantially lower than the theoretical value for G = const. For G = f(t) the divergence between theory and experiment is even larger, and this may be regarded as an argument against the Brans and Dicke theory (or definitely not as an argument for this theory). It should be stressed, however, that intensive mixing in the solar interior may be adjusted to reduce the flux $I(B^8)$ to such an extent as to offset entirely its increase due to G = f(t). In this sense, the divergence between the theory with G = f(t) and the experiment may be brought down to the same level as for the theory with G = const. It is clear, however, that the hypothesis G = f(t) does not contribute to a better fit between theory of experiment, and may only increase the discrepancy. If we further remember that Ezer and Cameron /44/ failed to recover the increased rate of lithium burning on the Sun predicted by Dicke for the G = f(t) model* and that there are altogether no reliable experimental data corroborating the Brans and Dicke theory, we come to the conclusion that the existing constellation is by no means favorable for the Brans and Dicke theory (at least, as far as the solar neutrino data are concerned).

4. Pontecorvo's oscillation hypothesis /46/ and the rate of the reaction $Cl^{37}(\nu, e^-)A^{37}$

When discussing various aspects of neutrino physics and astrophysics, it is generally assumed that the neutrino is not "lost" on its way from the source to the detector, except in those rare cases when the neutrino is absorbed in traversing a tremendous thickness of matter. This assumption is justified both by experimental data on the cross sections of nuclear reactions with the participations of neutrinos produced in reactors and accelerators and by the theory of weak interactions, which predicts a vanishingly low probability for the interaction of the neutrino with matter. This approach, however, ignores the probability of neutrino absorption by the vacuum. Pontecorvo /46/ advanced an oscillation hypothesis, according to which transitions between various states of the neutrino occur in the vacuum. The oscillation hypothesis is based on the assumption that only four neutrino states exist in nature and that the conservation of the leptonic charge is not exact. The four states of the neutrino $\bar{\nu}_{left}$, ν_{left}, $\bar{\nu}_{right}$, ν_{right} correspond in the conventional notation to $\nu_e, \nu_\mu, \bar{\nu}_\mu, \bar{\nu}_e$. The conservation of leptonic charge was proposed by Konopinski and Mahmoud /47/ to account for the conspicuous absence of some decay processes. Experiments confirmed this assumption. Our problem now is to establish the accuracy of the experimental data corroborating the conservation of the leptonic charge or, in other words, to determine the probability of its nonconservation. Analysis /46/ of the experimental data for the processes $\mu^+ \to e^+ + \gamma$, $\nu_\mu + p \to \mu + n$,

* The content of lithium in the Sun is lower than in meteorites /45/. This fact in the model with G = f(t) is qualitatively accounted for by the higher rate of lithium burning in the solar interior. However, detailed calculations /44/ fail to confirm this conclusion. It should also be noted that, contrary to expectations, the theory with G = f(t) did not lower the time of hydrogen burning in the solar interior. This is explained by Ezer and Cameron as being due to the increase in the total quantity of fuel due to the influx of hydrogen from regions far from the center.

$Ca^{48} \rightarrow Ti^{48} + e^- + e^-$ gives the following values for the upper bound value of the constant f of the interaction not conserving the leptonic charge: $5 \cdot 10^{-3}$ G, $1.5 \cdot 10^{-2}$ G, $2 \cdot 10^{-2}$ G, respectively (G is the weak interaction constant). We can thus speak of the nonconservation of the leptonic charge with the above values of the constant f. In this case, transitions between the various neutrino states are allowed: $\nu_\mu \rightleftarrows \nu_e$, $\tilde{\nu}_\mu \rightleftarrows \tilde{\nu}_e$. The oscillations are characterized by a period of length $t = l = \frac{1}{\mu} \cdot \frac{E}{m}$ /46/, where E is the neutrino energy, μ is the mass difference between the two neutrino states, m is the neutrino mass, h = c = 1. For the mass difference μ either $\mu \leqslant m$ or $\mu \ll m$. Since the experimental cross section of the reaction $\tilde{\nu}_e + p \rightarrow e^+ + n$ using reactor antineutrino fits the theory of the two-component neutrino, we may assume that there are virtually no $\tilde{\nu}_e \rightleftarrows \tilde{\nu}_\mu$ transitions on the way from the source to the detector, i.e., $l > 10$ m. If we were to take $l \ll 10$ m, the detector would receive half the number of electron antineutrinos and the experimentally measured cross section would be half the theoretical value. The oscillation length can be applied to determine the constant f: $f \leqslant 10^{-4}$ G. If $f < 10^{-5}$ G, we have $l > 100$ m, and no oscillations can be detected in accelerator and reactor experiments. Astrophysical research should be particularly helpful in this respect. In particular, detection of solar neutrinos would provide a possibility of verifying the oscillation hypothesis.

If the oscillation length is less than the size of the effective neutrino source region on the Sun, i.e., $l \ll 0.1 R_\odot = 139{,}000$ km, the observed neutrino flux should be half the total flux. Also note that the intensity of solar neutrinos on the ground may show variations because of changes in the Sun—Earth distance. If the oscillation length is of the order of $5 \cdot 10^6$ km (the difference in the semiaxes of the Earth's orbit), intensity fluctuations with a period of a few hundred days will be observed /46/. As the oscillation length decreases, the period of variation of the solar neutrino intensity correspondingly decreases. Thus, if there exist oscillations between electron and muon neutrinos, the observed effect in solar neutrino experiments should be half the expected value and even less. Davis' results thus may be explained within the framework of the oscillation hypothesis.

5. Variation of the rate of energy production in the solar interior

Sheldon /48/ recently suggested that the rate of energy production in the solar interior is variable in time. Within the framework of this assumption, Davis' results have a trivial explanation: some thermonuclear reactions were "switched off" during the relevant time. Note that the same assumption had been previously advanced by Zatsepin and Kuz'min in 1964 /49/. Davis' negative results indicated that our notions of stellar evolution, and in particular the specific properties of nuclear processes in the solar interior (at high pressures and temperatures) are deficient. The renewed consideration of the time-dependent properties of the solar energy sources /48/ is therefore quite timely, although as before /49, 50/, no specific reasons for this time-variation are suggested.

The energy released in thermonuclear reactions is carried away as electromagnetic radiation and neutrinos. The neutrinos escape from the Sun unimpeded, whereas the electromagnetic radiation undergoes a multitude of interactions before it emerges from the Sun after about 10^7 years /51/. The sunlight observed today thus originated in thermonuclear reactions which occurred in the distant past, whereas the solar neutrinos carry contemporary information. If the energy production in the Sun undergoes variations with a characteristic time much greater than 10^7 years, the luminosity of the Sun cannot provide any information about the time-dependent properties of the energy source. The situation is different as far as the neutrino is concerned. Any changes in the rate of energy production will be instantaneously reflected in the neutrino fluxes. If we assume that in the time of Davis' experiments, the intensity of the energy source was so low that $I(B^8)$ fell below the detection threshold, a time will come when $I(B^8)$ will become higher, in accordance with the results of the existing theoretical models of the Sun. There may be some relation between the neutrino fluxes and surface phenomena (solar flares, solar cosmic rays, etc.) /48 – 50/. If such a relation is noted, the neutrino may emerge as the best agent for solar activity predictions. The neutrino may yet enable us to develop long-range forecasts which are absolutely essential for the purposes of spaceflight.

CONCLUSIONS

1. The new values of nuclear parameters and concentrations of hydrogen, helium, and the heavy elements on the surface of the Sun give $\xi_T \approx \approx 6 \cdot 10^{-36}$ sec^{-1} for the rate of the reaction $Cl^{37}(\nu, e^-)A^{37}$. With allowance for the uncertainties in the initial parameters, the theoretical reaction rate ξ_T appears to fit satisfactorily the experimental rate $\xi_e \leqslant 3 \cdot 10^{-36}$ sec^{-1}.
2. If we assume intensive mixing in the solar interior, ξ_T can be reduced to about one quarter.
3. The Brans and Dicke hypothesis of a time-dependent gravitational constant raises the reaction rate ξ_T. In the absence of reliable data bearing out the hypothesis $G = f(t)$, Davis' negative results should be accepted as evidence against the Brans and Dicke theory.
4. Pontecorvo's oscillation hypothesis halves the value of ξ_T and predicts possible variations in the intensity of the solar neutrinos.
5. The assumption of time-dependent energy sources in the Sun may also account for Davis' negative results, as it leads to a variation of the rate of energy production and hence to a variation in the neutrino fluxes.
6. If variations in the intensity of the solar neutrinos are detected, measurements of the neutrino energy spectrum will prove of the greatest importance in elucidating the reasons for this variation. If, say, the variations are due to oscillations between different neutrino states, the variation periods will depend on the neutrino energy. The existence of different neutrino groups leads to different variation periods. Moreover, for a given oscillation length, the neutrino intensity recorded on the ground will depend on μ, m, L (where μ is the mass difference of the two

neutrino states, m is the neutrino mass, L is the source – detector distance). This signifies that the shape of the intensity variation curve will provide information about the source – detector distance, the size of the source region on the Sun, the neutrino mass, etc.

7. Thus, in principle, there is a way of explaining not only the experimental upper bound value of ξ_e, but also lower values.

8. As we have seen, the theory of stellar structure and evolution is plagued by numerous uncertainties and further research is needed. This fact, combined with the high sensitivity of $I(B^8)$, $I(Be^7)$, $I(N^{13})$, and $I(O^{15})$ to the particular physical conditions in the solar interior, leads to a considerable uncertainty in the estimates of the rate of the reaction $Cl^{37}(\nu, e^-)A^{37}$ The reader may thus form an impression that the theory may be twisted to explain any experimental result. In this connection we would like to stress that if the source of solar energy is the proton-proton cycle, the rate of the reaction $Cl^{37}(\nu, e^-)A^{37}$ cannot be less than $(2.8 \pm 0.2) \cdot 10^{-37}$ sec^{-1}, irrespective of the particular version of the p-p cycle operative in the Sun /12, 20/. The fact is that the first reaction of the p-p cycle $p(p, e^+\nu)D^2$ is invariably supplemented by the reaction $p + p + e^- \rightarrow D^2 + \nu$. The product neutrinos have energies of 1.44 MeV, and thus contribute to the reaction $Cl^{37}(\nu, e^-)A^{37}$. Irrespective of the further course of the p-p cycle, the Sun will generate 1.44 MeV neutrinos in a flux of $1.7 \cdot 10^8$ cm^{-2} sec^{-1}, thus ensuring the minimum reaction rate indicated above. Therefore, if the general hypothesis of thermonuclear stellar energy sources is valid, a ten-fold increase of the detection sensitivity ($\xi_{exp} \leqslant 3 \cdot 10^{-36}$ sec^{-1}) should lead to positive neutrino detection results.*

9. Davis' experiments suggest a number of conclusions concerning the structure of the Sun.

(a) The C – N cycle cannot be the main energy source in the Sun, since it prescribes for ξ_{exp} a value of $3.5 \cdot 10^{-35}$ sec^{-1}. Comparison of this figure with the experimental value $\xi_{exp} \leqslant 3 \cdot 10^{-36}$ sec^{-1} shows that the contribution of the C – N cycle to the Sun's luminosity does not exceed 9%. This is significantly the only experimental result which establishes the low probability of the C – N cycle in the solar interior.

(b) If the proton-proton cycle is operative in the Sun, the experimental data indicate that the central temperature of the Sun does not exceed $14.5 \cdot 10^6$ degrees.

(c) The weight concentration Z of elements heavier than helium is at most 2% in the central region of the Sun /12, 20/. This fits the results for the solar atmosphere, $Z = (1.5 \pm 0.3)\%$ /2/. This result provides an indirect corroboration of the assumption of homogeneous distribution of the heavy elements along the Sun's radius.

(d) The weight concentration of helium in the solar interior in the initial stages of its evolution is found to be about 0.22 ± 0.03 /12, 20/ and even 0.16 – 0.17 /52/, which is markedly lower than the content of helium in other objects in the Galaxy.

10. The neutrino detection sensitivity of Davis' experimental setup can be increased soon. The background of the proportional counter used in these experiments (0.5 cm^3 volume) is relatively high, 0.3 – 0.8 counts

* Positive results can be obtained in principle. Because of oscillations between the neutrino states or time-dependent properties of the energy source, we may end up with negative results even with sensitivities of $3 \cdot 10^{-37}$ sec^{-1}. However, persistent measurements over a sufficiently long period of time will inevitably lead to positive results. Also note that mixing in the solar interior virtually does not reduce /25/ the flux of the 1.44 MeV neutrinos.

per day, i.e., 10 times higher than the background achieved by Davis on an earlier occasion with a 0.08 cm^3 counter /53/. Enrichment of the argon separated from the working liquid (1 cm^3) with A^{37} and use of small counters will improve the counting sensitivity. Moreover, exposure of the liquid target at great depths and reduction of the fast neutron background by means of appropriate shielding will reduce the quantity of A^{37} produced by background reactions (0.2 atoms per day so far). Davis hopes to be able to increase the sensitivity five-fold in the nearest future, i.e., to attain the limit $\xi \approx 6 \cdot 10^{-37}$ sec^{-1}. Note that for this reaction rate, the equilibrium quantity of A^{37} in a 600 ton detector will be 5 atoms.

11. Davis' experiments led to a radical revision of the neutrino detection programs. In particular, it became clear that dynamic methods (direct detection of the electron produced by the reaction) and neutrino scattering by electrons are virtually unfeasible in the original form, as proposed prior to Davis' experiments.

12. On the theoretical level, Davis' experiments, as we have seen, stimulated further studies.

Bibliography

1. Davis, R., D.S. Harmer, and K.C. Hoffman.— Phys. Rev. Lett., **20**:1205. 1968.
2. Dergachev, V.A., G.E. Kocharov, and Yu.N. Starbunov.— Trudy V Vsesoyuznoi ezhegodnoi zimnei shkoly po kosmofizike, p.73. Apatity, Izd. Kol'skogo filiala AN SSSR. 1968.
3. Pontecorvo, B.— Nat. Res. Council, Canada Rept., P.D., p.205. 1946.
4. Kocharov, G.E. and V.O. Naidenov.— Preprint FTI AN SSSR, p.133. 1968.
5. Viktorov, S.V., G.E. Kocharov, and V.O. Naidenov.— ZhTF, **36**:1997. 1966.
6. Barabanov, I.R., V.B. Veshnikov, and A.A. Pomanskii.— PTE, No.2:109. 1967.
7. Kocharov, G.E. and V.O. Naidenov.— PTE, No.3:5. 1966.
8. Kocharov, G.E. and V.O. Naidenov.— Trudy V Vsesoyuznoi ezhegodnoi zimnei shkoly po kosmofizike, p.100. Apatity, Izd. Kol'skogo filiala AN SSSR. 1968.
9. Schwarzschild, M. Structure and Evolution of the Stars. — New York, Dover. 1958.
10. Dergachev, V.A., G.E. Kocharov, and Yu.N. Starbunov.— Seminar "Fizika neitrino i neitrinnaya astrofizika." Moskva, Izd. FIAN, 9—11.IX.1968. (In press).
11. Bahcall, J.N. and R.M. May.— Astrophys. J. Lett., **152**:17. 1968.
12. Bahcall, J.N. Seminar "Fizika neitrino i neitrinnaya astrofizika." Moskva, Izd. FIAN, 9—11.IX.1968. (In press).
13. Dergachev, V.A. and G.E. Kocharov.— Izvestiya AN SSSR, Seriya Fizicheskaya, **32**:1847. 1968.
14. Dwarakanath, M.R. and H.C. Winkler.— BAPS, **12**:1140. 1967.

15. Sears, R.L.— Astrophys. J., 153:181. 1968.
16. Bahcall, J.N., W.A. Fowler, I. Iben, and R.L. Sears.— Astrophys. J., 137:344. 1963.
17. Sears, R.L.— Astrophys. J., 140:477. 1964.
18. Pochoda, P. and H. Reeves.— Planet. Space Sci., 12:119. 1964.
19. Ezer, D. and A.G.W. Cameron.— Canad. J. Phys., 43:1497. 1965.
20. Bahcall, J.N., N.A. Bahcall, and G. Shaviv.— Phys. Rev. Lett., 20:1209. 1968.
21. Bahcall, J.N., N.A. Bahcall, W.A. Fowler, and G. Shaviv.— Phys. Rev. Lett., 26B:359. 1968.
22. Dicke, R.H. and H.M. Goldenberg.— Phys. Rev. Lett., 18:313. 1967.
23. Ezer, D. and A.G.W. Cameron.—Ap. Lett., 1:177. 1968.
24. Shaviv, G. and G. Beaudet.— Ap. Lett., 2:17. 1968.
25. Bahcall, J.N., N.A. Bahcall, and R.K. Ulrich.— Ap. Lett., 2:91. 1968.
26. Shaviv, G. and E.E. Salpeter.— Phys. Rev. Lett., 21:1602. 1968.
27. Iben, I.— Phys. Rev. Lett., 22:100. 1969.
28. Kuz'min, V.A.— Astronomicheskii Zhurnal, 42:1228. 1965.
29. Dergachov, V.A. and G.E. Kocharov.— Canad. J. Phys., 46:S491. 1968.
30. Kocharov, G.E.— Proc. X Int. Conf. Cosmic Rays (London), p.1020. 1965.
31. Dergachev, V.A. and G.E. Kocharov.— In: "Kosmicheskie luchi," 10:175. Moskva, Izdatel'stvo "Nauka." 1969.
32. Maidrykin, S.S. and Yu.N. Starbunov. Present collection, p.177.
33. Ginzburg, V.L.— In: "Einshtein i razvitie fiziko-matematicheskoi mysli," p.117. Moskva, Izdatel'stvo AN SSSR. 1962.
34. Synge, J. General Theory of Relativity. — New York, Interscience. 1960.
35. Clemence, G.M., Rev. Mod. Phys., 19:361. 1947.
36. McVittie, G.C. General Relativity and Cosmology. New York. 1956.
37. Chiu, H. and W. Hoffman (editors). Gravitation and Relativity.— New York, Benjamin. 1964.
38. Dicke, R.H.— Nature, 202:432. 1964.
39. Jordan, P.— Astronom. Nachr., 276:193. 1948.
40. Brans, C. and R.H. Dicke.— Phys. Rev., 124:925. 1961.
41. Dicke, R.H.— Phys. Rev., 125:2163. 1962.
42. Zel'dovich, Ya.B. and I.D. Novikov. Relyativistskaya astrofizika (Relativistic Astrophysics).— Moskva, Izdatel'stvo "Nauka." 1967.
43. Greenstein, G.S.— Ap. Lett., 1:139. 1968; Astrophysics and Space Science, 2:155. 1968.
44. Ezer, D. and A.G.W. Cameron.— Canad. J. Physics, 44:593. 1966.
45. Shima, M. and M. Honda.— J. Geophys. Res., 68:2849. 1963.
46. Pontecorvo, B.M.— Preprint DI-3242, OIYaI, 1967; Seminar: "Fizika neitrino i neitrinnaya astrofizika," Moskva, Izd. FIAN, 9—11.IX.1968. (In press).

47. Konopinski, E. and N.M. Mahmoud.— Phys. Rev., 93:1045. 1953.
48. Sheldon, W.R.— Nature, 221:650. 1969.
49. Zatsepin, G.T. and V.A. Kuz'min.— Vestnik AN SSSR, No.2:50. 1964.
50. Kocharov, G.E. and Yu.N. Starbunov.— Izvestiya AN SSSR, Seriya Fizicheskaya, 30:1090. 1966.
51. Salpeter, E.E.— Comments on Nuclear and Particle Physics, 2:97. 1968.
52. Iben, I.— Phys. Rev. Lett., 21:1208. 1968.
53. Davis, R. and D.S. Harmer.— BNL, p.9119. 1965.

DIFFERENTIAL ROTATION AND NONSPHERICITY OF THE SUN'S SURFACE

S. S. Mandrykin and Yu. N. Starbunov

Dicke and Goldenberg /1/, in their measurements of the nonsphericity of the Sun's surface, pointed to the possible existence of a gravitational quadrupole moment of the Sun. The flattening of the Sun can be attributed to the quadrupole moment /1/ if Zeipel's lemma /2/ is applicable to the surface layers of the star. The observed nonsphericity may be associated with various processes taking place in the outer layers of the Sun. We are aware of the existence of nonpotential forces in the surface layers of the Sun, and these forces may in fact invalidate Zeipel's lemma. The nonpotential surface forces include magnetic forces and also forces related to the shearing stresses produced by differential rotation and turbulence. The contribution of the magnetic field to the nonsphericity of a constant-density surface can be estimated from the equation of magnetohydrodynamics /3/ including the gravitational field:

$$(\vec{v}\nabla)\vec{v} = -\frac{1}{\rho}\nabla\left(p + \frac{H^2}{8\pi}\right) + \frac{1}{4\pi\rho}(\vec{H}\nabla)\vec{H} - \nabla\varphi. \qquad (1)$$

A magnetic field with slow radial variation $(\frac{\partial H}{\partial r} \sim \frac{H}{r})$ cannot lead to a significant distortion of a constant-density surface, since in this case estimates give for the Sun's surface $(\vec{H}\nabla)\vec{H}/4\pi\rho \ll (\vec{v}\nabla)\vec{v}$. Consider a magnetic field whose component H_r rapidly varies with depth.* Projecting equation (1) onto the unit vectors $\vec{e}_r$ and $\vec{e}_\theta$ and dropping the small terms, we obtain for the nonsphericity of a constant-density surface

$$\frac{\Delta r}{r} = \delta - \frac{3}{8\pi g_0 r\, d\rho_0/dr}\left\langle H_r \frac{\partial H_r}{\partial r}\right\rangle,$$

where δ is the nonsphericity due to centrifugal forces and forces of gravitational origin: g_0, ρ_0 are the acceleration and the density averaged over a surface of radius r,

$$\left\langle H_r \frac{\partial H_r}{\partial r}\right\rangle = \int_0^x H_r \frac{\partial H_r}{\partial r} P_2(\cos\theta)\, d\cos\theta \Big/ \int_0^x [P_2(\cos\theta)]^2 d\cos\theta,$$

where $P_2(X)$ is the second-order Legendre polynomial.

To account for the observed nonsphericity with $H_z \approx 10$ gauss, the vertical scale $l = H_r/\partial H_r/\partial r$ should be about 1 km,** and with $H_r \approx 1$ gauss, $l \sim 10$ m,

* Our derivation remains valid if other field components, as well as H_r, vary rapidly in the radial direction.

** A slightly different result has been obtained in /5/, where a less rigorous method has been used.

and this evidently does not fit our notions of the structure of the surface layers of the Sun. The effect discovered by Dicke and Goldenberg thus can hardly be attributed to the magnetic field.

The effect of the shearing stresses due to differential rotation has been analyzed in detail by Dicke and Goldenberg /4/. They considered the relation of nonsphericity to various models of surface rotation. The observed nonsphericity could be accounted for within the framework of the rotation model with a large negative radial derivative of the angular velocity $\partial\omega/\partial r$, but this rotation model, in the opinion of the authors /4/, does not fit the spectroscopic data on the broadening of absorption lines and the observed motion of sunspots. This rotation would lead to a temperature difference of several hundreds of degrees between the pole and the equator, in clear contradiction with actual observations /1/.

The nonsphericity of the Sun may be accounted for if the Sun is assumed to possess a substantial gravitational quadrupole moment. There are at least two different schools of thought regarding the origin of the quadrupole moment. Sturrock and Gilvary /5/ are of the opinion that a magnetic field may have remained locked in the nucleus since the time of formation of the Sun. Magnetic fields of $H \sim 10^6$ gauss in the Sun's nucleus are quite sufficient to account for the observed nonsphericity. We know, however, that in Hayashy's stage /6/ the Sun was completely convective. Convection should have randomized the primary magnetic field, which would decay when convection had stopped, so that in the present epoch only a very insignificant magnetic field can be expected /1/.

Another possible mechanism producing a quadrupole moment is a relatively fast rotation of the internal layers of the Sun /7/. The slow rotation of the outer layers may be attributed to the retarding effect /8/ of the solar wind, which applies a torque of the order of 10^{31} dyne $\cdot$ cm to the solar surface. This torque is sufficiently strong to slow down the rotation of the convective zone in a time of the order of 10^6 years. The slowing-down continues until the retarding solar-wind torque is balanced by the spinning action of the solar interior. Certain spectroscopic data /9–11/ indicate that main-sequence stars of late types showed faster rotation in the earlier stages of their evolution. Kraft /11/ has shown that the boundary between fast and slow spinning stars corresponds to types F4–F5. Stars of these and later types, according to modern concepts, carry a convective envelope. The relatively slow rotation of the late-type stars is thus apparently due to the slowing-down effect of the convective envelope, whereas the initial surface velocity for most main-sequence stars reaches a few tens of kilometers per second. Observation data enabled Kraft to estimate the time constant τ for the slowing-down of the surface layers for Sun-type stars and the surface velocity v_0 of stars past the Hayashy stage: $\tau = 4 \cdot 10^8$ years, and $v_0 = 75$ km/hr. There is thus a definite possibility that the solar interior is characterized by a faster spin than the surface.

REDISTRIBUTION OF ANGULAR VELOCITY IN A SPINNING STAR

If we assume that the young Sun rotated faster than the present-day rotation velocity of the Sun's surface, we have to determine the angular

velocity redistribution with time. We will consider the effect of ordinary viscosity and meridional circulation on the redistribution of angular rotation velocity in the radiant nucleus of the Sun.

The equation of motion of a viscous compressible fluid /12/ in a gravitational field is written in the form

$$\rho\left(\frac{\partial v_i}{\partial t}+v_k\frac{\partial v_i}{\partial x_k}\right)=-\frac{\partial p}{\partial x_i}+\frac{\partial}{\partial x_i}\left\{\eta\left(\frac{\partial v_i}{\partial x_k}+\frac{\partial v_k}{\partial x_i}-\frac{2}{3}\delta_{ik}\frac{\partial v_e}{\partial x_e}\right)\right\}+\frac{\partial}{\partial x_i}\left(\zeta\frac{\partial v_e}{\partial x_e}\right)-\rho\frac{\partial\varphi}{\partial x_i}, \qquad (2)$$

where ρ is density, v_i is the corresponding velocity component, p is pressure, η, ζ are the viscosity coefficients, φ is the gravitational potential. We will work in spherical coordinates (r, θ, α). Let u be the projection of the velocity vector $\vec{v}$ on $\vec{r}$, $\omega(r,t)$ the angular velocity of rotation, which is assumed independent of the angle θ. Assuming that all the variables in (2) are independent of the angle α and the problem is symmetrical about the plane $\theta = \pi/2$, we obtain from equation (2) for the equatorial plane

$$r\frac{\partial\omega}{\partial t}+u\left(r\frac{\partial\omega}{\partial r}+2\omega\right)=\nu r\frac{\partial^2\omega}{\partial r^2}+4(\nu+\mu)\frac{\partial\omega}{\partial r}, \qquad (3)$$

where $\nu = \eta/\rho$ is the kinematic viscosity, $\mu=\frac{r}{4\rho}\frac{\partial\eta}{\partial r}$. Let the initial distribution of the angular velocity (at the time t = 0) be $\Omega(r)$. The solution of equation (3) is sought in the form $\omega(r,t) = \Omega(r)\exp\{f(r,t)\}$. The function $f(r,t)$ is represented in series form $t/\tau^*(r)+t^2/\tau^{**}(r)+\ldots$ Inserting the expression for $\omega(r,t)$ in (3) and setting t = 0, we obtain the relaxation time

$$\tau^*(r)=\frac{\tau_\eta\cdot\tau_u}{\tau_\eta+\tau_u},\quad \tau_\eta=\frac{r\,\Omega}{\nu r\Omega''+4(\nu+\mu)\Omega'},\quad \tau_u=-\frac{r\,\Omega}{u(r\Omega'+2\Omega)},$$

where primes denote differentiation with respect to r.

Comparison of τ_η and τ_u shows which of the two processes — mixing or viscosity — makes the major contribution to angular velocity redistribution. If the angular velocity $\Omega(r)$ initially does not vary rapidly with the radius, $\Omega\sim r^\alpha$, where $|\alpha|$ is of the order of unity, we have $\Omega'\sim\Omega/r$, $\Omega''\sim\Omega/r^2$. The kinematic viscosity of the Sun is $\nu\sim 1$ cm^2/sec and it slowly varies with the radius, so that we may take $\nu\sim\mu$. This gives $\tau_\eta\sim 10^{19}$ sec = $= 3\cdot 10^{11}$ years; consequently, viscosity is unable to produce a substantial redistribution of angular velocity in the solar interior during the lifetime of the star ($\sim 5\cdot 10^9$ years).

If Ω is slowly variable along the radius, $\tau\sim\frac{r}{3u}$. Assuming rigid-body rotation, we have $u\sim 10^{-9}$ cm/sec /13/ and $\tau\sim 10^{11}$ years. The rate of meridional circulation increases approximately as Ω^2 /13/; if we assume that the Sun upon termination of the Hayashy stage rotated a factor of 30 — 40 faster than its present-day surface, we find $u\sim 10^{-6}$ cm/sec and $\tau\sim 10^8$ years; the angular velocity distribution in the interior of fast spinning Sun-type stars should markedly deviate from the law Ω = const and the angular velocity should increase toward the center due to meridional circulation, which is unavoidable in a spinning star. In the equatorial plane, the angular velocity under steady-state conditions varies as $1/r^2$ wherever the viscosity is negligible, and this motion is stable. In the convective envelope, the eddy viscosity is so high that the dependence $\omega\sim\frac{1}{r^2}$ is inapplicable. To elucidate the effect of viscosity

on the radial variation of the angular velocity, we will ignore the turbulent flow in the convective zone and consider irrotational motion of a fluid with high constant viscosity. In this model $\Delta\vec{v} = 0$; the solution of this equation is

$$v = \sum_{i=1}^{\infty} c_i r^i P_i^{(1)}(\cos\theta) + \sum_{k=1}^{\infty} D_k \frac{1}{r^{k+1}} P_k^{(1)}(\cos\theta),$$

where $P_j^{(1)}(x)$ is the associate Legendre polynomial of the first kind of order j and degree 1. This model of motion in the convective zone is very crude, but it will nevertheless enable us to demonstrate that in regions of high viscosity, both angular and radial differential rotation are significant.

NONSPHERICITY ASSOCIATED WITH DIFFERENTIAL ROTATION

Let us consider a method for the derivation of the surface nonsphericity of a star with a general radial dependence of the angular velocity. The conditions of hydrostatic equilibrium lead to the following equation in spherical coordinates (r, θ, α):

$$\frac{v^2}{r} = \frac{1}{\rho}\frac{\partial p}{\partial r} + \frac{\partial \varphi}{\partial r}, \quad v^2 \operatorname{ctg}\theta = \frac{1}{\rho}\frac{\partial p}{\partial \theta} + \frac{\partial \varphi}{\partial \theta}. \tag{4}$$

If the variables are independent of the angle α and the problem is symmetrical about the plane $\theta = \frac{\pi}{2}$, the density ρ, the pressure p, and the potential φ may be expanded in even-order Legendre polynomials. Retaining the first two terms in these expansions, we find

$$\rho(r) = \rho_0(r) + \rho_2(r) P_2(\cos\theta), \quad p(r) = p_0(r) + p_2(r) P_2(\cos\theta), \quad \varphi(r) = \varphi_0(r) + \varphi_2(r) P_2(\cos\theta). \tag{5}$$

For the case $v(r, \theta) = \omega(r)\, r \sin\theta$, substitution of (5) in (4) leads to the following expression for ρ_2:

$$\rho_2 = \frac{r^2}{3 g_0}\frac{d}{dr}(\rho_0 \omega^2) + \frac{\varphi_2}{g_0}\frac{d\rho_0}{dr}, \tag{6}$$

where $g_0 = d\varphi_0/dr$.

The nonsphericity of a constant-density surface is expressible in terms of ρ_2 by the following equality:

$$\frac{\Delta r}{r} = \frac{3}{2r}\frac{\rho_2}{d\rho_0/dr}. \tag{7}$$

If the differential rotation of the surface layers of the Sun is ignored, we obtain for the surface

$$\frac{\Delta r}{r} = \frac{1}{2}\frac{\omega^2 r}{g_0} + \frac{3}{2}\frac{\varphi_2}{g_0 r}. \tag{8}$$

φ_2 can be found from the differential equation

$$\Delta_2 \varphi_2 - \frac{6}{r^2}\varphi_2 = 4\pi G \rho_2$$

which follows from the Poisson equation $\Delta\varphi = 4\pi G\rho$, or from the equivalent

expression

$$\varphi_2(r) = -\frac{4\pi G}{5}\left\{\frac{1}{r^3}\int_0^r \rho_2(r')r'^4 dr' + r^2\int_r^\infty \frac{\rho_2(r)}{r'}dr'\right. \qquad (9)$$

Equalities (6) and (9) constitute an integral equation for φ_2. The latter can be found if the function $\omega(r)$ is known. We have seen above that in regions of negligible viscosity where the flow is stable, meridional circulation may lead to the establishment of the angular velocity distribution $\omega \sim \frac{1}{r^2}$ in the equatorial plane.

The stability was checked in terms of the Richardson number. To derive an expression for the Richardson number of a rotating fluid in a gravitational field, the usual arguments /14/ have to be supplemented by additional considerations of the invariance of the expression for Ri under transformation from the fixed axes to a coordinate system rotating around the polar axis. The final expression for the Richardson number has the form

$$\mathrm{Ri} = \frac{g - \omega^2 r \sin^2\theta\left\{\left(\frac{\partial\rho}{\partial r}\right)_{\mathrm{adiab}} - \left(\frac{\partial\rho}{\partial r}\right)_{\mathrm{real}}\right.}{\rho r^2 \sin^2\theta\left(\frac{\partial\omega}{\partial r}\right)^2}.$$

The Richardson numbers Ri were computed for the equatorial plane, where $\omega = \frac{A}{r^2}$; $r^* = 5 \cdot 10^{10}$ cm is the boundary of the convective zone in Ezer and Cameron's model, ω_s is the angular velocity on the surface of the Sun ($2.8 \cdot 10^{-6}$ sec^{-1}). The results of these computations are given in Figure 1,* which shows that in the radiant nucleus, from $0.03 - 0.04\,R_\odot$ to the bottom of the convective zone, the Richardson numbers are fairly high and the motion is stable. A characteristic feature of the function Ri(r) is the rapid increase of Ri at $r = 0.03 - 0.04\,R_\odot$; it seems that the lower boundary of stable flow is virtually independent of the particular choice of the Sun's model and the value of A.

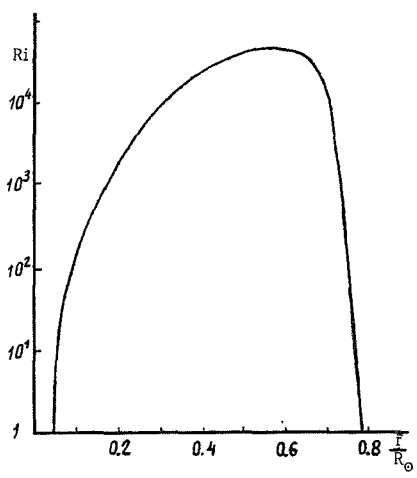

FIGURE 1. Richardson number Ri as a function of radius in the equatorial plane for differential rotation of the Sun.

One of our principal aims was to establish to what extent the rotation model with angular velocity distribution $\omega \sim \frac{1}{r^2}$ in the radiant core fits the measured nonsphericity of the Sun's surface. Weymann's fairly detailed model /16, 13/ was chosen as the basic model of the Sun. The convective envelope and the central nucleus with a radius of less than $0.04\,R_\odot$ were assumed to show "rigid-body" rotation with constant angular velocities. To account for the measured nonsphericity of the Sun's

* The density and pressure were used according to the model of Ezer and Cameron /15/.

surface /1/, we had to assume a gradient of 1.72 in the angular velocity across the boundary of the convective zone and the radiant nucleus. To determine the nonsphericity, we computed φ_2 by solving the integral equation by successive approximations. The results are listed in the table.

Corrections $\varphi_2^{(i)}$ to the gravitational potential obtained by successive approximations (i is the order of the approximation)

$X = \frac{r}{R}$	$\varphi_2^{(1)}(x)$ 10^{10} cm^2/sec^2	$\varphi_2^{(2)}(x)$ 10^{10} cm^2/sec^2	$\varphi_2^{(3)}(x)$ 10^{10} cm^2/sec^2	$\varphi_2^{(4)}(x)$ 10^{10} cm^2/sec	$\varphi_2^{(5)}(x)$ 10^{10} cm^2/sec
0.00	000	000	000	000	000
0.04	795	864	878	877	879
0.08	547	641	670	678	679
0.12	294	379	412	421	423
0.16	176	246	276	287	292
0.20	116	172	197	209	213
0.24	79.0	123	144	155	159
0.28	56.4	90.9	109	118	121
0.32	41.6	68.8	83.5	90.7	94.0
0.36	31.4	52.0	64.6	70.7	73.5
0.40	24.2	41.2	50.7	55.6	58.0
0.44	19.0	32.5	40.2	44.3	46.4
0.48	15.1	26.0	32.2	35.6	37.3
0.52	12.1	21.0	28.0	28.9	30.3
0.56	9.88	17.1	21.4	23.7	24.9
0.60	8.15	14.1	17.7	19.7	20.6
0.64	6.79	11.8	14.7	16.2	17.1
0.68	5.69	9.89	12.4	13.7	14.4
0.72	4.81	8.37	10.5	11.6	12.2
0.76	4.11	7.15	8.94	9.93	10.4
0.80	3.53	6.14	7.69	8.53	8.97
0.84	3.05	5.31	6.63	7.38	7.75
0.88	2.65	4.62	5.78	6.42	6.73
0.92	2.32	4.04	5.07	5.64	5.90
0.96	2.04	3.55	4.44	4.95	5.18
1.00	1.81	3.15	3.95	4.39	4.60

The nonsphericity obtained from (8) was found to be $4.6 \cdot 10^{-5}$.* Similar estimates indicate that for a reasonable dependence of the angular velocity on the angle θ, the contribution from the angular differential rotation to nonsphericity is one order of magnitude less than the contribution from the radial differential rotation.

THE RATE OF MERIDIONAL CIRCULATION

The divergence of the radiation flux $\vec{F}$ in a rotating star does not vanish even in regions without heat sources. This effect is associated with

* According to the measurements of Dicke and Goldenberg /1/, $\frac{\Delta r}{r} = (5 \pm 0.7) \cdot 10^{-5}$. If there is no angular velocity gradient, we find $\frac{\Delta r}{r} = 2.2 \cdot 10^{-5}$, and other mechanisms have to be considered in order to account for the observed nonsphericity.

meridional circulation flows intermixing the matter in the stellar interior. Using a model of a nonrotating Sun, we can find to first approximation the radial component of the mixing velocity u. To find u, we need only consider the radiant heat conduction in the process of energy transfer, so that /13/

$$\vec{F} = -\frac{4ac}{3\rho\varkappa} T^3 \Delta T, \tag{10}$$

where a is the Stefan—Boltzmann constant, c is the velocity of light, $\varkappa$ is the opacity coefficient of the stellar matter. To find the mixing velocity u, we require div $\vec{F}$. We will use expressions for $T, \rho, \varkappa$, analogous to (5). Since u is sought in the first approximation, we may assume the equality

$$\Delta T = 0. \tag{11}$$

For the radiation flux from a stationary star, we have

$$\int div\vec{F}\, d\sigma = 0, \tag{12}$$

where the integral is extended over the entire surface of a sphere of radius r. Using (11) and (12), we obtain from (10)

$$div\vec{F} = -\frac{4ac}{3\varkappa_0\rho_0} T_0^3 \frac{dT_0}{dr}\frac{d}{dr}\left\{\frac{3T_2}{T_0} - \frac{\rho_2}{\rho_0} - \frac{\varkappa}{\varkappa_0}\right\} P_2(\cos\theta) \tag{13}$$

The influx of radiant energy under steady-state conditions is offset by the work of expansion of the moving fluid and the convective heat transfer; we thus have

$$div\vec{F} = \frac{dE}{dt}. \tag{14}$$

The rate of change of energy per unit volume is described by the equality /15/

$$-\frac{dE}{dt} = \left(1 - \frac{2.5}{n+1}\right)\rho g u, \tag{15}$$

where n is the polytropic index. Equalities (13), (14), and (15) lead to the following expression for u:

$$u = -\frac{1}{\rho g}\frac{n+1}{n+1-2.5}\frac{L_r}{4\pi r^2}\frac{d}{dr}\left\{\frac{3T_2}{T_0} - \frac{\rho_2}{\rho_0} - \frac{\varkappa_2}{\varkappa_0}\right\} P_2(\cos\theta), \tag{16}$$

where L_r is the radiant energy flux through a sphere of radius r.

When computing u, $\varkappa$ and T are eliminated from (16) using the Kramers relation ($\varkappa \sim \rho T^{-3.5}$) and the equation of state of ideal gas. The variation of chemical composition along the radius was ignored. The values of u were obtained from the angular velocity distribution $\omega \sim \frac{1}{r^2}$ in the radiant nucleus, as this distribution adequately accounts for the observed nonsphericity. For φ_2 we used the values of $\varphi_2^{(5)}$ from the table. The computed circulation velocities are shown in Figure 2. We see that the resulting mixing velocities are sufficiently high to ensure an effective mechanism of momentum transfer and to sustain the angular velocity distribution $\omega \sim \frac{1}{r^2}$. In the central region with $r < 0.1 R_\odot$, the rapidly increasing circulation velocity leads to vigorous intermixing and equalizes the chemical

composition of the solar interior. This should affect both the temperature and the rate of nuclear reactions at the center of the Sun, reducing the neutrino output of B^8 decay /17/.

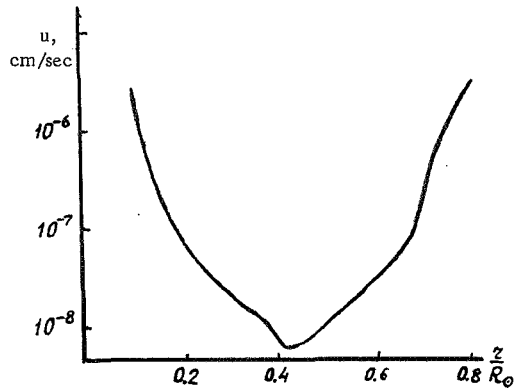

FIGURE 2. The meridional component of the circulation velocity u as a function of the radius in the equatorial plane for a model of the Sun with differential rotation.

We would like to acknowledge the help of G. E. Kocharov and to thank him for constant attention and valuable comments.

Bibliography

1. Dicke, R.H. and H.M. Goldenberg.— Phys. Rev. Lett., 18:313. 1967.
2. Eddington, A.S. The Internal Constitution of the Stars, p.282.— New York, Dover Publ. 1959.
3. Landau, L.D. and E.M. Lifshits. Elektrodinamika sploshnykh sred (Electrodynamics of Continuous Media).— Moskva, Fizmatgiz. 1959.
4. Dicke, R.H. and H.M. Goldenberg.— Nature, 214:1294. 1967.
5. Sturrock, P.A. and J.J. Gilvary.— Nature, 216:1280. 1967.
6. Hayashy, C.— Pub. Astron. Soc. Japan, 13:450. 1961.
7. Dicke, R.H.— Nature, 202:432. 1964.
8. Weber, E.J. and L.J. Davis.— Astrophys. J., 148:217. 1967.
9. Wilson, O.C.— Astrophys. J., 144:695. 1966.
10. Wilson, O.C.— Science, 151:1487. 1966.
11. Kraft, R.P.— Astrophys. J., 150:551. 1967.
12. Landau, L.D. and E.M. Lifshits. Mekhanika sploshnykh sred (Continuum Mechanics).— Moskva, Gostekhizdat. 1954.

13. Schwarzschild, M. Structure and Evolution of the Stars. — New York, Dover. 1958.
14. Prandtl, L. Hydro- und Aeromechanik. — Berlin, J. Springer. 1929.
15. Ezer, D. and A.G.M. Cameron.— Canad. J. Physics, **44**:593. 1966.
16. Weymann, R.— Astrophys. J., **126**:208. 1957.
17. Iben, I.— Phys. Rev. Lett., **22**:100. 1969.

NEUTRINO EXPERIMENTS ON ACCELERATORS

V. S. Kaftanov

The history of neutrino experiments on accelerators is very brief so far. In 1959, at the Kiev International Conference, Pontecorvo /1/ first suggested the idea of a neutrino experiment on a particle accelerator in order to establish the identity of ν_e and ν_μ. Later, the same problem was considered by Schwarz /2/. An analysis of the proposed experiments /3, 4/ showed that they could be staged on the then projected giant proton accelerators at CERN (28 GeV) and Brookhaven (32 GeV). The first experiment was carried out in Brookhaven in 1962 /5, 6/.

Two factors played a decisive role in this experiment: first, the high intensity of the accelerator beam, which was about $3 \cdot 10^{11}$ protons/sec at the time of the experiment, and second, the development of the spark chamber — a detector which, considering its relative simplicity, had quite a satisfactory spatial resolution and could be used with targets of much larger masses than before. The last factor was particularly significant for neutrino experiments.

The Brookhaven experiment was followed by the CERN experiment (1963 — 1964), which provided a study in depth of a number of problems, and then by the second Brookhaven experiment (1964) /7/, the Argonne National Laboratory experiment /8, 9/, and another CERN experiment in 1967 — 1968 /10/. We will briefly review the main experiments and the principal results.

THE FIRST NEUTRINO EXPERIMENT, BROOKHAVEN 1962

The general experimental setup is shown in Figure 1. The main parameters of the Brookhaven experiment (1962) were as follows:

Proton energy at the end of acceleration	15 GeV
Beam intensity at the end of acceleration	$2 - 4 \cdot 10^{11}$ protons/cycle
Frequency of acceleration cycles	50 cycles/min
Pulse length	$20 - 30\ \mu$sec
Beryllium target thickness	7.6 cm
Total number of protons passing through target	$3.48 \cdot 10^{17}$
Length of linear accelerator section	3 m
Mean angle of beam to proton orbit	7.5°
Meson decay path length	21 m

Iron shield thickness	13.5 m
Spark chamber — 10 modules each weighing	1 ton
Module composition — 9 plates measuring	$112 \times 112 \times 2.5\ cm^3$
Spark chamber electrode gap	9.5 mm

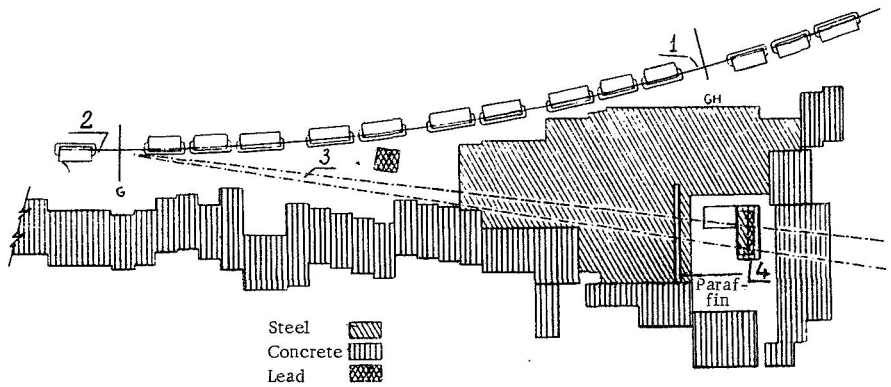

FIGURE 1. Schematic diagram of the 1962 Brookhaven neutrino experiment:

1) accelerator ring, 2) target, 3) meson beam, 4) spark chambers.

Neutrinos (and antineutrinos) were produced by high-energy pions and kaons generated in collisions of accelerated protons with the internal target:

$$\pi^+ \to \mu^+ + \nu_{\mu\pi} \qquad \pi^- \to \mu^- + \tilde{\nu}_{\mu\pi}, \tag{1}$$

$$K^+ \to \mu^+ + \nu_{\mu K} \qquad K^- \to \mu^- + \tilde{\nu}_{\mu K}. \tag{2}$$

Pions and kaons thus constituted the principal sources of muonic neutrinos. The impurity of electron neutrinos ($\sim 10^{-2}$) is mainly due to the decays

$$K^+ \to e^+ + \nu_e + \pi^0, \quad K^- \to e^- + \tilde{\nu}_e + \pi^0; \tag{3}$$

$$K_2^0 \to e^\pm + \nu_e + \pi^\mp. \tag{4}$$

To produce a pure neutrino beam, a 13.5 m iron shield was provided before the spark chambers, absorbing all particles except neutrinos (including the highest energy muons).

A total of 113 events associated with the neutral component were recorded in the effective volume of the spark chamber. Of these, 29 events were classified as individual muons with momenta higher than 300 MeV/c.

If $\nu_e \equiv \nu_\mu$, the neutrino should trigger the following reactions:

$$\nu_\mu + n \to p + e^-, \tag{5}$$

$$\tilde{\nu}_\mu + p \to n + e^+, \tag{6}$$

$$\nu_\mu + n \to p + \mu^-, \tag{7}$$

$$\tilde{\nu}_\mu + p \to n + \mu^+. \tag{8}$$

The corresponding reaction cross sections were computed in /11 — 16/. It follows from these considerations that if $\nu_e \equiv \nu_\mu$, reactions (5), (6) and (7), (8) should occur with approximately equal probabilities, and at momenta

higher than 300 MeV/c, 22 electron showers should have been recorded for the 29 muons detected (with allowance for the system efficiency). And yet, among the 113 events, the authors identified only 6 which could be classified as electron showers; of these 6 events, 1 or 2 are showers which may be due to electron neutrinos produced in decays (3, 4) and there is also a certain contribution from the neutron background. However, even if we assume that all the six events are truly electron showers produced by muonic neutrino, the experimental results do not allow the conclusion that ν_e and ν_μ are identical particles.

THE CERN NEUTRINO EXPERIMENT, 1963–1964 /17–19/

The neutrino beam

The general schematic diagram of the experimental setup and the arrangement of the various components are shown in Figure 2. Protons accelerated to 25 GeV were extracted with pulsed magnets and focused onto the target, a copper cylinder 4 mm in diameter and 250 mm long /30–33/.

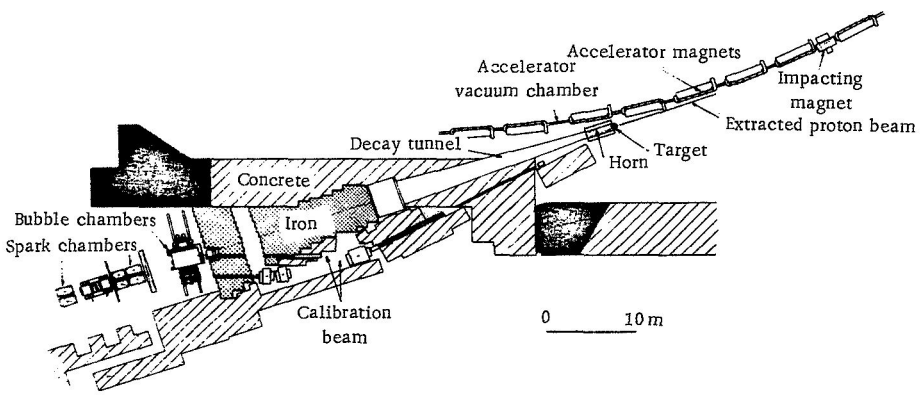

FIGURE 2. Schematic diagram of the 1963–1964 CERN neutrino experiment.

The target was placed in the narrow cavity of the so-called magnetic horn – a special device with a pulsed magnetic field intended to focus particles of the same sign toward the detector /34–36/. The horn stepped up the intensity of the neutrino beam by a factor of 5–10. Another important property of the horn is that by focusing particles of the same sign, it produces a preferentially neutrino or antineutrino beam. Most of the experiment was concerned with neutrino beams, so that the horn focused positive particles. The antineutrino impurity in the beam was about 2%. Figure 3 shows the neutrino spectrum at the detector site, computed for various horn currents (the working horn current was 300 kA).

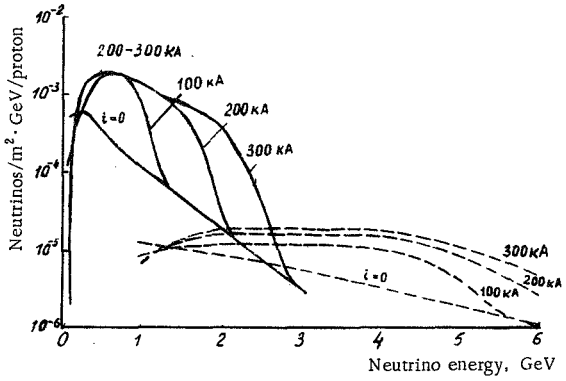

FIGURE 3. The neutrino spectrum:

solid curve — neutrinos produced by the reaction $\pi^+ \to \mu^+ + \nu$;
dashed curve — neutrinos produced by the reaction $K^+ \to \mu^+ + \nu$.

Rapid proton extraction, the use of the magnetic horn, and a stepped-up accelerator current made it possible to increase the neutrino beam more than 100-fold compared to the Brookhaven beam.

Detectors

The first beam detector was a bubble chamber filled with Freon CF_3Br. The chamber was a cylinder 115 cm in diameter and 50 cm tall (about 500 liter volume), immersed in a 27 kgauss constant magnetic field. The overall volume of the chamber in 1965 was increased to 1000 liter by doubling the depth of the chamber.

The next beam detector was a system of spark chambers. The main component element of the system was a three-electrode module in the form of an individual spark chamber measuring 1000×1600 mm^2. The electrode thickness was 5 mm and the interelectrode gap was 10 mm. Chambers of two types were used: brass or aluminum chambers. The experimental geometry was slightly changed in 1963 – 1964: in 1964 most of the measurements were carried out with the spark chamber arrangement shown in Figure 4. An important element of the system is component 2, a chamber with magnetized iron filters, permitting (rough) measurements of the charge sign and the momentum of muons penetrating through this part of the setup. Large scintillation counters fully covering the spark modules were provided to trigger the spark chambers. There were a total of 11 counters set along the entire length of the system. A master signal was triggered by a coincidence between any two adjacent scintillation counters. More detailed technical information about the spark chambers will be found in /37, 38/.

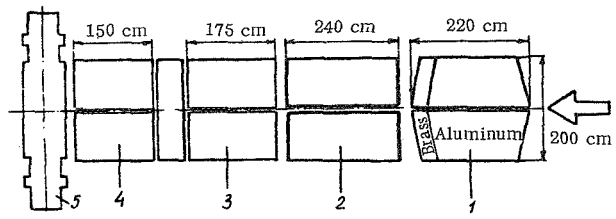

FIGURE 4. The arrangement of spark chambers (1964):

1) thin-wall chamber, 4.4 tons aluminum, 3.2 tons brass. A total of 80 three-electrode modules and 4 counters;
2) magnetized iron chamber, 5 cm plates, weight 25 ton, B = 18 kG. Total 38 modules;
3) iron chamber, 5 cm plates, weight 20 ton. Total 32 modules. In 2 and 3, eight counters;
4) lead chamber, 5 to 10 cm plates, weight 15 ton. Total 18 modules and 2 counters;
5) two magnetized iron plates, 15 cm each, B = 18 kG. Total 10 modules.

Measurements

About 10^6 accelerator pulses with mean intensity of $7 \cdot 10^{11}$ protons/pulse were used in the experiments, i.e., a total of about $7 \cdot 10^{17}$ protons passed through the target. About 800 events produced by neutral particles were recorded during this time in the total volume of the bubble chamber. Only events from an effective volume of 220 liters (330 kg of Freon) were selected for analysis. In this volume, 454 events contain a track of a negative particle which had not interacted in the chamber. This particle could be a muon. Five events contained an electron of over 500 MeV energy. The expected number of creation events of electrons of this energy due to the ν_{eK} impurity is $N_{\nu_e} \simeq 3.3$.

Basic results

1. A check of the identity of ν_e and ν_μ

Selection of spark chamber events classifiable as (5) and (7) gave

$$R = N_e/N_\mu = (1.7 \pm 0.5) \cdot 10^{-2}. \qquad (9)$$

Seeing that R should be of the order of 0.01 due to the admixture of electron neutrinos from decays (3) and (4), we conclude that ν_e and ν_μ are two different particles. If the muonic neutrinos do indeed produce electrons, the fraction of these electrons does not exceed 1% of the created muons. This result is in excellent agreement with the result obtained with the bubble chamber, which recorded 236 events classifiable as (7) and only 2 events classifiable as (5).

2. A check of the leptonic charge conservation

If the leptonic charge is conserved in neutrino interactions, the reaction $\nu_\mu + n \to p + \mu^-$ is allowed, whereas $\nu_\mu + p \to n + \mu^+$ is forbidden. Since the neutrino beam contains only a low antineutrino impurity ($\lesssim 3\%$), by analyzing the sign of the muon electric charge we can establish whether the leptonic charge is conserved, and if so to what accuracy.

The sign of the muon charge is best determined using the long tracks in magnetized-iron spark chambers, where the residual impurity of strongly interacting particles is truly negligible. To check the leptonic charge conservation, the sign of 924 particles with momenta exceeding 600 MeV/c was measured in this part of the chamber. The results gave

$$R^+/_- = N_+/N_- = (2.7 \pm 0.6) \cdot 10^{-2}. \qquad (10)$$

Seeing that the fraction of the positive muons contributed by the antineutrino impurity is about $(1-2) \cdot 10^{-2}$, we conclude that the leptonic charge is conserved in these reactions with an accuracy of about 2%.

3. Form factors

An analysis of the kinematics of the reaction $\nu + n \to \mu^- + p$ yields some information about the form factors entering the matrix element of this process. There are three such form factors: the vector form factor $F_1(q^2)$, the magnetic form factor $F_2(q^2)$, and the axial form factor $F_A(q^2)$. Within the framework of the hypothesis of the vector current conservation $F_1(q^2) = F_2(q^2) = F_V(q^2)$, where $F_V(q^2)$ is the electromagnetic form factor, which is available from electron–proton scattering: $F_V = 1/(1 + \frac{q^2}{M_V^2})^2$, where $M_V = 0.84$ GeV. In this case, the only unknown factor is $F_A(q^2)$, and it can be found from the experimental distribution over q^2 of the events $\nu + n \to p + \mu^-$.

Since $F_A(q^2)$ is not known in advance, we may assume for it the same form as for F_V, namely $F_A = 1/(1 + q^2/M_A^2)^2$, the parameter M_A to be determined experimentally.

This analysis, despite the complex processing, was actually carried out and it was found that the bubble chamber data were best fitted with $M_A = (0.81 {}^{+0.13}_{-0.20})$ GeV /29/, whereas the spark chamber data gave $M_A = (0.65 {}^{+0.45}_{-0.40})$ GeV /23/. Given the experimental accuracy, we thus conclude that the axial form factor is close to the electromagnetic form factor.

4. A search for the vector boson /39–47/

If the vector boson exists, it should be created from a neutrino beam in the electromagnetic field of the nucleus according to the reaction, say

$\nu + Z \rightarrow \mu^- + W^+ + Z^*$, subsequently decaying in about 10^{-18} sec along the following channels (with allowance for the particle signs):

$$W^+ \rightarrow \mu^+ + \nu\,, \tag{11}$$
$$W^+ \rightarrow e^+ + \nu\,, \tag{12}$$
$$W^+ \rightarrow n\pi + mK, \text{ etc.} \tag{13}$$

Because of the $\mu - e$ universality, the probabilities of (11) and (12) are approximately equal. The relative probability of the nonleptonic decays is poorly known, and the relative probability of decay of W into leptons is generally taken to be

$$B = \frac{W \rightarrow \text{leptons}}{\text{total probability of W decay}} = 0.5.$$

If W decays along channel (11), the entire event appears like the production of a pair of positive and negative muons:

$$\nu + Z \rightarrow Z^* + W^+ + \mu^- \qquad W^+ \rightarrow \mu^+ + \nu \tag{14}$$

Similarly, for the decay of W according to (12), the event should appear like the creation of a μ^-, e^+ pair. The best instrument for studying reaction (14) is the spark chamber, since it easily separates a high-energy muon from a pion, and the effective weight of the spark chamber is much higher than the effective weight of the bubble chamber.

Analysis of events in a magnetized iron chamber showed that the CERN experiment failed to record any events that could be interpreted as corresponding to reaction (14), and the experimental data only provided the lower limit of the mass of the W meson, $M_W \geqslant 2.1$ GeV/c^2 (99% likelihood, B = 0.5). At the same time, the Brookhaven group /7/ also searched for the W meson in neutrino interactions. In this experiment, no W meson was detected either, and the lower mass limit was found to be $M_W \geqslant 1.9$ GeV (with 90% likelihood). The smaller mass value compared to the CERN data is attributable to the fact that the Brookhaven setup did not contain a pion and kaon focusing system, so that the neutrino flux was substantially lower.

The main difficulty of the CERN experiment was the uncertainty of the absolute neutrino spectrum, which could be determined to within ± 50% only. Another difficulty in analysis was caused by the fact that the neutrino interacted not with stationary nucleons, but with nuclei in which the nucleons possess a Fermi motion, and secondary interactions inside the nuclei only complicated the overall picture of the events. In the next CERN experiment in 1967 – 1968, special emphasis was therefore placed on these two aspects.

THE 1967 – 1968 CERN EXPERIMENT

An entirely new neutrino beam was formed in this experiment /10/. The magnetic horn was replaced by a three-component focusing system

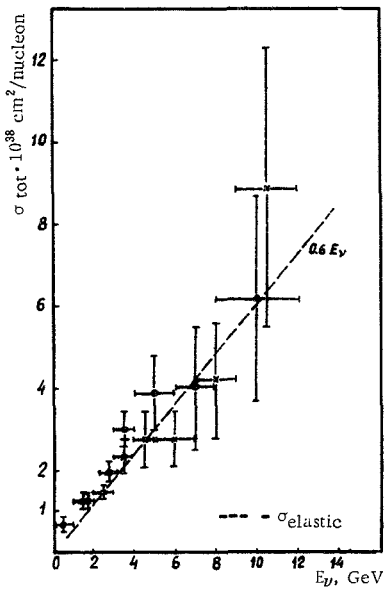

FIGURE 5. Total neutrino interaction cross section:

x – Freon (1963–1964), o – propane (1967).

which increased the neutrino beam intensity by a factor of 2–3. The detector in this new experiment was a propane-filled bubble chamber. The pion production reaction thus could be investigated in pure form:

$$\nu_\mu + p \rightarrow p + \mu^- + \pi^+ . \qquad (15)$$

The analysis of the experimental material has not been completed yet, but some results are already known.

1. The improved neutrino beam gave a new limit for (10): $R = N_e/N_\mu \leqslant 4.6 \cdot 10^{-3}$ with 95% likelihood, i.e., the leptonic charge is conserved with high accuracy.

2. Figure 5 plots the total neutrino cross section as a function of energy. Up to energies of about 5 GeV, this dependence is adequately fitted by the straight line $\sigma_{tot} \cdot 10^{38}\ cm^2 = 0.6\, E_\nu GeV$. The plot incorporates the bubble chamber results of the two experiments.

3. A study of the reaction $\nu_\mu + p \rightarrow p + \mu^- + \pi^+$ showed that isobar production followed by decay into p and positive pions predominates in this process. If we assume that all the events corresponding to this reaction proceed through the isobar, the corresponding cross section is

$$\sigma_{is} = (1.3 \pm 0.5) \cdot 10^{-38}\ cm^2\ /10/.$$

PLANNED NEUTRINO EXPERIMENTS FOR THE NEAREST FUTURE

Five organizations will be carrying out neutrino experiments on accelerators soon: Institute of High-Energy Physics, Serpukhovo, USSR; CERN, Geneva; Argonne National Laboratory, USA; Brookhaven, USA; Batavia, USA. The main data on the planned neutrino experiments in these laboratories are summarized in Table 1.

The neutrino experiment at the Institute of High-Energy Physics /47/ is planned to take place in a Freon–propane bubble chamber SKAT of 6 m^3 volume in a magnetic field of up to 27 kG and an assembly of spark chambers weighing some 400 tons. The higher proton energies, compared to those in Brookhaven and CERN, will enable the Serpukhovo experiment to cover a wider range of problems at neutrino energies of up to 25 GeV.

The immediate plans at CERN are based on the projected completion of the heavy-liquid Freon–propane bubble chamber scheduled for operation

in 1970. The total chamber volume will be 11 m^3 and the magnetic field will reach 27 kG. Some improvement of the neutrino beam will raise its intensity by an additional 20%.

TABLE 1. Basic data on neutrino experiments in various laboratories

Laboratory	Proton energy, GeV	Total volume of chamber with heavy liquid, m^3	Total volume of chamber with hydrogen or deuterium, m^3	Projected beginning of experiment	Range of neutrino energies, GeV
Inst. High-Energy Phys.	76	6	—	1972	20—25
CERN	28	11	—	1970	10
Argonne National Laboratory	12.5	—	25	1969	2
Brookhaven	32	—	9.5	1969	10
			25	1972	
Batavia	200	—	100	1974 (1973 with spark chambers)	50

At the Argonne National Laboratory /46/, a liquid hydrogen chamber with a total volume of 25 m^3 in a superconductive magnet of up to 20 kG has been assembled. At the end of 1969, the chamber will be filled with deuterium and exposed to a neutrino beam. The use of deuterium will permit observing the pure reaction $\nu + n \rightarrow p + \mu^-$ at neutrino energies of up to 2 GeV.

An experiment with a liquid-hydrogen bubble chamber of 9.5 m^3 volume in a superconductive magnet with a field of up to 30 kG was planned for 1969 in Brookhaven /46/. For the purposes of the experiment, the chamber will be filled with deuterium. A neutrino experiment planned for 1972 will be carried out using the Argonne hydrogen chamber.

A 200 GeV proton acclerator is under construction in Batavia /46/. According to schedule, the accelerator will be commissioned in the middle of 1972. Neutrino experiments using spark-chamber detectors may begin in 1973. For these purposes, a neutrino beam is being designed with an overall length of about 2.5 km, of which 1.8 km will constitute a decay channel with focusing systems, and 600 m will be allocated to natural soil shielding. The use of soil rather than iron for shielding purposes greatly reduced the overall cost, but it will lower the neutrino intensity at energies below 4 GeV. In 1974, a liquid-hydrogen bubble chamber will be ready for neutrino experiments, with a volume of 100 m^3 and a magnetic field of about 40 kG (superconductive magnet).

The expected number of events associated with various reactions in these experiments is listed in Table 2 /45, 47/. We see from the table that when the large bubble chambers are commissioned, the experiments will enter the stage of detailed studies of individual reactions. This stage of neutrino physics will parallel the stage that pion physics reached in the early 1950s.

TABLE 2. Expected number of events in neutrino experiments*

Process	CERN (Freon) $V_{ef}^{**} = 6\,m^3$	CERN (propane) free protons	Brookhaven, $9.5\,m^3$, $V_{ef} = 4\,m^3$		Argonne $25\,m^3$, $V_{ef} = 12\,m^3$		Serpukhovo (Freon)	
			H_2	D_2	H_2	D_2	C_3H_8	H_2
$\nu + n \rightarrow \mu^- + p$	15000			750		450	1400	280
$\tilde{\nu} + p \rightarrow \mu^+ + n$	1750	175	85		53			
$\tilde{\nu} + N \rightarrow \mu^+ + \Lambda, \Sigma$	~ 50	~5	~3		~2			
$\nu + p \rightarrow \mu^- + p + \pi^+$	22500	2250	1100		700		1100	220
$\nu + n \rightarrow \mu^- + n + \pi^+$ $\rightarrow \mu^- + p + \pi^0$	7500			1500			560	
$\nu + N \rightarrow \mu + N + n\pi$ $(n \geq 2)$	9000	900	450	900	≪ Brookhaven		2800	140
$\nu + N \rightarrow \mu^- + n\pi + Y + K$	750	75	37	75	≪ Brookhaven			

* All figures for 10^6 accelerator pulses.

** V_{ef} is the effective chamber volume.

The search for the W meson will continue in Serpukhovo and Batavia at masses of up to 6 and 8 GeV/c^2, respectively. A highly important topic is the production of lepton pairs in neutrino interactions in the nuclear Coulomb field without a W meson. The theory of the local four-fermion interaction predicts with fair certainty the cross sections of these processes, although not a single event of this kind has been detected so far. Detection or positive proof of absence of these processes are equally important for the theory.

Bibliography

1. Pontecorvo, B.M.— ZhETF, 37:1751. 1959.
2. Schwars, M.— Phys. Rev. Lett., 4:306. 1960.
3. Bernardini.— Proc. of Intern. Conf. on High-Energy Physics at Rochester, p.581. 1960.
4. Lederman.— Proc. of Int. Conf. on Instrumentation for High-Energy Physics. Berkeley. 1960.
5. Dandy, Gaillard, Goulianos, Lederman, Mistry, Schwars, Steinbarger.— Phys. Rev. Lett., 9:36. 1962; Proc. of Int. Conf. on High-Energy Physics at CERN, p.809. 1962.
6. Dandy, Gaillard, Goulianos, Lederman, Lee, Mistry, Schwars, and Steinberger.— Phys. Rev. Lett., 10:260. 1963.
7. Burns, Goulianos, Hyman, Lederman, Lee, Mistry, Rettberg, Schwars, and Sunderland.— Phys. Rev. Lett., 15:42. 1965.
8. Data of the Conference on Experimental Neutron Physics.— CERN 65—82, p.31. 1965.
9. Kuston, R.L., D.E. Lundquist, T.B. Novey, A. Yokosawa, and Chilton.— ANL. Preprint. 1969.

10. Thematic (Scientific) Conference on Physics of Weak Interaction.— CERN—Conseil européen de recherche nucléaire, 65—67. Genève. 1969.
11. Lee and Yang.—Phys. Rev. Lett., 4:307. 1960.
12. Yamaguchi.— Progr. Theoret. Phys. (Kyoto), 6:1117. 1960.
13. Gabbibo, and Gatto.— Nuovo Cimento, 15:304. 1960.
14. Lee and Yang.—Phys. Rev., 126:2239. 1962.
15. Bell.—CERN Report. CERN 63—37, p. 1. 1963.
16. Lovseth.—CERN Report. CERN 63—37, p. 203. 1963.
17. Bernardini, von Dardal, Egli, Faissner, Ferrero, Franzinetti, Fukui, Gaillard, Gerber, Hahn, Nillier, Kaftanov, Krienen, and Salmeron.— Proc. of Sienna Int. Conf., p. 571. Sienna, Italy. 1963.
18. Bernardini, Bienlain, Bohm, Von Dardel, Faissner, Ferrero, Gaillard, Gerber, Hahn, Kaftanov, Krienen, Reinharz, Salmeron, Soiler, Staude, Stein, and Stainer.— XII Mezhdunarodnaya konferentsiya po fizike vysokikh energii v Dubne. 1964 g. (12th High-Energy Physics Conference, Dubna, 1964), 2:16.— Moskva, Atomizdat. 1966. [English edition by IPST Cat. No. 5131, TT 68-50325/2.]
19. Bernardini, Bienlain, Von Dardel, Faissner, Ferrero, Gaillard, Gerber, Hahn, Kaftanov, Krienen, Manfredotti, Reinharz, and Salmeron.— XII Mezhdunarodnaya konferentsiya po fizike vysokikh energii v Dubne. 1964 g. (12th High-Energy Physics Conference, Dubna, 1964), 2:16. —Moskva, Atomizdat. 1966. [English edition by IPST, Cat. No. 5131, TT 68-50325/2.]
20. Bienlain, Bohm, Von Dardel, Faissner, Ferrero, Gaillard, Gerber, Hahn, Kaftanov, Krienen, Reinharz, Salmeron, Soiler, Staude, Stein, and Stainer.— Phys. Rev. Lett., 13:80. 1964.
21. Bernardini, Bienlain, Von Dardel, Faissner, Ferrero, Gaillard, Gerber, Hahn, Kaftanov, Manfredotti, Reinharz, and Salmeron.— Phys. Rev. Lett., 13:86. 1964.
22. Spark Chamber Group — Bubble Chamber Group.— Nuovo Cimento, 38:608.
23. Holder, M., A. Staude, A. Bohm, H. Faissner, H. Steiner, I. Bienlain, G. Von Dardel, F. Ferrero, I.M. Gaillard, H.I. Gerber, V. Kaftanov, F. Krienen, C. Manfredotti, M. Reinharz, and Salmeron.—Nuovo Cimento, 57A:338.
24. Voss.— Proc. of Int. Conf. on Fundamental Aspects of Weak Interactions, p. 114. Brookhaven. 1963.
25. Bingham, Burmeister, Cundy, Innocent, Lecourtais, Mollerud, Myatt, Paty, Perkines, Ramm, Schultze, Sletten, Soop, Voss, and Yeshiki.— Proc. of Int. Conf. on Elementary Particles, Sienna, p. 555. 1963.
26. Block, Burmeister, Cundy, Elben, Franzinetti, Keren, Mollerud, Soop, Stump, Venus, and Yoshiki.— Proc. of Int. Conf. on High-Energy Physics (Dubna). 1964.
27. Block, Burmeister, Cundy, Elben, Franzinetti, Keren, Mollerud, Schultze, Sirtten, Soop, Stump, Venus, and Yoshiki.— Phys. Rev. Lett., 12:281. 1964.

28. Paty.— CERN Report. CERN 65—12. 1965.
29. Young, E.— CERN Report. CERN 67—12. 1967.
30. Bertolotto, Van Breugel, Caris, Consigny, Dykhuizen, Goni, Hirshrunner, Kuiper, Milner, Pichler, and Blass.— Proc. of Int. Conf. on High-Energy Accelerations, NPA/Int, 63—15. Dubna. 1963.
31. Bertolotto, Van Breugel, Calis, Consigny, Dykhuizen, Goni, Hirshrunner, Kuiper, Lange-Seth, Milner, Pichler, Pladd, Pluym, Wachsmuth, and Zanasco.— Proc. of Int. Conf. on Elementary Particles, Sienna, Italy. 1963.
32. Kuiper, Plass.— CERN Report. CERN 59—30. 1959.
33. Langseth.— CERN Report. CERN 64—35. 1964.
34. Giesch, Van der Meer, Pluym, and Vahlbruch.— Proc. of Int. Conf. on Co Elementary Particles, p.536, Sienna, Italy. 1963.
35. Van der Meer.— CERN Report 61—7. 1961; CERN Report 62—16. 1962.
36. Glesch, Van der Meer, Pluym, and Vahlbruch.— Nucl. Inatr. and Methods, 20. 1963; 58. 1963.
37. Faissner, Ferrero, Ghani, Herr, Krienen, Muratori, Novey, Reinharz, and Salmeron.— Nucl. Inatr. and Methods, 20:213. 1963.
38. Faissner, Ferrero, Fukui, Gaillard, Gerber, Hahn, Krienen, Muratori, Reinharz, and Salmeron.— Proc. of Sienna Int. Conf., Sienna, Italy. 1963.
39. Lee, Markstein, and Yang.— Phys. Rev. Lett., 7:429. 1961.
40. Bell and Veltman.— Phys. Rev. Lett., 5:94. 1963.
41. Veltman.— CERN Report. CERN 63—27, p.179. 1963.
42. Veltman.— Physica, 29:161. 1963.
43. Wu, Yang, Fuchel, and Heller.— Phys. Rev. Lett., 12:57. 1964.
44. Gargamelle.— User's Meeting CERN/NPA. 8.1.1969.
45. CERN Courier, No.1:13, No.2:42. 1969.
46. Bolotov, Gerdyukov, Gershtein, Gorichev, Danil'nichenko, Devisheva, Devishev, Denisov, Kistenev, Kuznetsov, Lebedev, Makeev, Parshikura, Samoilov, Titov, Folomeshkin, and Yampol'skii. Vozmozhnosto provedeniya neitrinnykh eksperimentov na uskoritele IFVE (Neutrino Experiments on the Serpukhov Accelerator).— Preprint IFVE, 68—56 K. 1968.

Section III

PHYSICS OF THE SOLAR ACTIVITY AND DYNAMIC PROCESSES IN THE INTER-PLANETARY SPACE AND IN THE EARTH'S MAGNETOSPHERE

Edited by S. N. Vernov, V. A. Dergachev, S. I. Isaev, and G. E. Kocharov

STRUCTURE OF THE INTERPLANETARY SPACE FROM OBSERVATIONS OF LOW-ENERGY COSMIC RAYS IN 1965—1967

S.N. Vernov, G.P. Lyubimov, and N.V. Pereslegina

The probing of the interplanetary space with cosmic rays, which propagate over tremendous distances while interacting with the interplanetary medium, constitutes an important branch of space physics. Cosmic rays carry information about large-scale magnetic fields and solar plasma. The most effective approach calls for a simultaneous study of various characteristics of the solar cosmic rays (SCR) and the galactic cosmic rays (GCR) with an attempt to establish a correlation between cosmic-ray effects and solar activity.

Let us first consider the results of analysis of 15 SCR showers ($1 < E_p < 5$ MeV) associated with chromospheric flares on the visible side of the Sun. Most of these events were accompanied by Forbush decreases of the GCL in space ($E_p > 30$ MeV) and on Earth ($E_p > 1$ BeV). The cosmic ray intensity was studied in the following periods: 4—7 Oct. 1965, 29 Dec. 1965—3 Jan. 1966, 19—22 Jan. 1966, 24—28 June 1967, 1—5 Aug. 1967, 9—12 Aug. 1967, 17—22 Sept. 1967 /1, 2/.

Solar flares at longitudes of 30 to 90°W cause direct SCR showers. The length of the Archimedes spiral from the Sun to the Earth for plasma velocities of 300 km/sec is about $200 \cdot 10^6$ km. Protons with $1 < E_p < 5$ MeV and a pitch angle of 0° will traverse this spiral in from 2 to 4 hr. The initial distribution over pitch angles may increase the length of this time, but apparently by no more than a factor of 2. For flares in a weakly disturbed medium, the time of arrival of the SCR is indeed 2—4 hr. Inhomogeneities may increase this period up to about 10 hr for other flares. Thus, within the margin of measurement error (±2 hr) the time of direct arrival of the SCR from flares at longitudes of from 30 to 90°W approximately corresponds to the time of motion of the particles with velocities determined by their kinetic energy. Hence it follows that if the transverse diffusion coefficient is small for particles of these energies, the SCR in some unknown way (possibly because of the high energy density at the time of the flare) occupy a whole bundle of magnetic field lines emerging from the flare area. Thus, the angular distribution of the SCR particles is fixed during the solar flare. It determines the variation of the intensity across the bundle of magnetic field lines. The intensity increases from the leading (lateral) front toward the central channel and then decreases. The distribution should depend on the field geometry and may slowly vary with time owing to velocity variance, diffusion, and drift during the motion from the Sun. The particles generated by the

flare may be retained in substantial numbers for at least 3 days behind the shock-wave front /3/, thus creating a source which replenishes the particle flux downstream from the shock. As a result, we can ignore the variation of the particle flux with time and assume that the drop in intensity is associated with the SCR distribution across the beam as generated at the time of the flare. In this case, the delay time of the direct SCR maximum corresponds to the time required for the principal flux channel to turn with the Sun from its original position at the time of the flare to a position of coincidence with the detector. In all cases, the Archimedian spirals derived from delay measurements have a somewhat greater pitch than the spirals determined from the corresponding active regions and the solar wind velocity. This difference we call the "veering" of particles from the line of force. "Veering" can be caused by drift, directional collective pressure, and shock waves. "Veering" causes differences in the propagation of SCR westward and eastward from the optimal trajectory, i.e., from the spiral "aimed" from the active region to the detector. Figure 1 is an instantaneous directivity chart of the SCR flux based on maximum anisotropy data for six SCR flares. The chart clearly illustrates the westward "veering" from the field line.

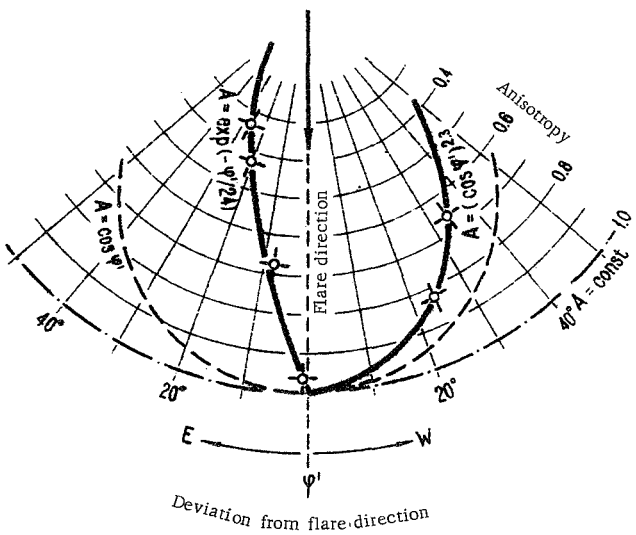

FIGURE 1. Distribution of the maximum SCR anisotropy (thick line) relative to the optimal longitude of the solar flare (about 60°W for 1 a.u.).

Let us consider the characteristics of SCR bursts observed simultaneously with Forbush decreases of the GCR. These events are observed either independently or at the time of the second maximum after the direct arrival of the SCR. For these SCR showers, the delay time of the maximum relative to the time of the solar flare reaches as much as 20 to 80 hr, which corresponds to a mean radial velocity of from 500 to 1500 km/sec, i.e., the velocity of propagation of shock waves from solar flares. The maximum

anisotropy varies from 16 to 37%. These SCR showers are particles generated during the solar flare which are localized between the shock-wave front and the plasma front produced by the same flare. Figure 2a schematically shows the Forbush decrease and the three space regions corresponding to 1) undisturbed medium downstream from the shock-wave front, 2) the enhanced compressed magnetic field between the shock-wave front and the plasma (the GCL decrease phase), 3) the region between the two fronts and the Sun (the GCL recovery phase). Figure 2b shows the same regions for the magnetic fields in the plane of the ecliptic, as viewed from the North Pole. The sections of the spiral lines correspond to the magnetic lines of force, and the dashed arcs are the shock-wave front and the plasma front. The figure is based on Parker's model of a shock wave propagating from a solar flare /4/.

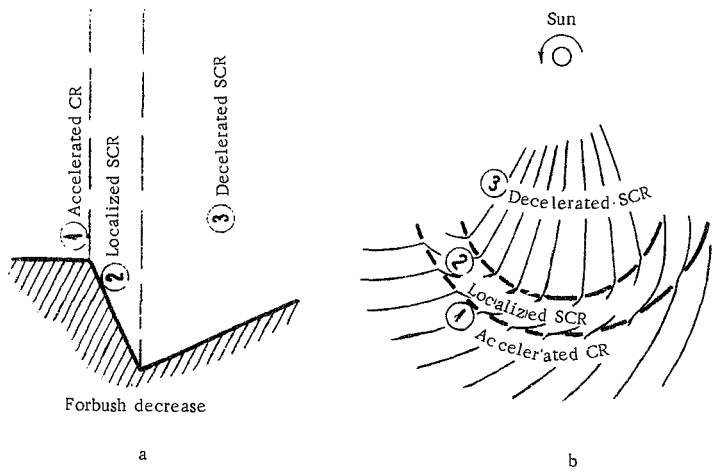

FIGURE 2. Localization of SCR.

The first region contains GCR and SCR particles — leftovers of previous showers or of quiet quasistationary streams — accelerated by the leading shock-wave front. These accelerated particles may produce a maximum before the onset of the Forbush decrease /5/.

The second region contains localized SCR generated by the flare and held up by the shock wave and the hot plasma front. These SCR propagate together with the second layer with the same velocity as the shock wave and the plasma. The SCR moving along the break in magnetic field lines may partially leak out from the localization layer feeding the first region. The anisotropy of the SCR in this layer may thus be fairly high along the field and small in the transversal direction.

The third layer contains particles which left the localized layer, were injected by a later flare, or originated in the active region during a lull between flares. The first two sources should be characterized by a bidirectional anisotropy owing to the motion of the particles between the layer and the Sun. SCR leaving the active region during a lull between

successive flares have a positive anisotropy because of the steady and continued activity of the source.

The above analysis of SCR propagation shows that protons with $1 < E_p < 5$ MeV generated by a solar flare propagate in the interplanetary space mainly by direct motion along the magnetic field lines with velocities corresponding to their kinetic energy and by being transported with the shock wave and the plasma envelope ejected by the flare. The particles are delivered to any point in space by either one of these mechanisms or by a combination of both. Whether or not they reach a certain point is mainly determined by the longitude of the solar flare relative to the detector. For "eastern" and "central" flares the transport mechanism is the dominant factor: direct motion along the lines of force is ruled out because the magnetic field is coiled eastward. For "western" flares the direct motion mechanism predominates, and it may be supplemented by transport as long as the flare is not too close to the limb. The experimental results on hand are insufficient to assess the contribution of the diffusion component to propagation of cosmic rays. The rate of transverse diffusion is apparently less than the transport velocity, and the rate of longitudinal diffusion is also substantially smaller than the direct velocity. The lines of forces in some cases are exceedingly smooth, and "mirror" condensations are observed only at large distances from the Sun ($\geqslant 1.5$ a.u. /3/). In other cases, a whole string of "distributed semitransparent mirrors" may be scattered along the field lines, so that our instruments simultaneously (to within ± 2 hr) detect streams of particles moving in opposite directions at the observation point.

Let us describe a model of propagation of low-energy SCR, injected by a solar flare, to a distance of 1 a.u. from the Sun. Figure 3a shows the position of the beam from three magnetic tubes relative to the detector (point 1) at the time t_0 corresponding to the beginning of a solar flare at a longitude $30° < \varphi < 60°$. At the time t_1, the most energetic particles having zero pitch angle reach the detector, moving along a tube of length l with a velocity corresponding to their kinetic energy. A time Δt after t_1 is required for all the particles injected into this tube with a flux $I < I_{max}$ (including particles of lower energies and particles with nonzero pitch angle) to reach the detector. Further growth of intensity is associated with the rotation of the bundle of tubes together with the Sun and the approach of the central channel with maximum particle density toward the detector. The tube density is fixed at a time close to the flare time t_0 and it is maintained constant by the SCR localized behind the shock wave. At the time t_2, the detector sees a tube carrying the flux I_{max}. The subsequent decrease in intensity is associated with the recession of the central channel from the detector.

Figure 3b corresponds to a situation when the central channel is aimed at the detector (point 2) at the time of the solar flare t_0 ($\varphi = 60°$W). In this case, the intensity reaches its maximum value I_{max} in a time Δt, i.e., the phase of intensity growth due to source rotation is not observed in this case, but all the other features remain as before.

In Figure 3c the flare developed at a time t_0 ($60° < \varphi < 90°$W), when a tube lying eastward of the central channel and carrying a SCR flux $I < I_{max}$ was aimed at the detector (point 3). The time t_1, the delay Δt, and the

dependence of the detected intensity on magnetic tube rotation in this case are exactly the same as before. At a time $t_1 + \Delta t$ the detector will see the intensity I which will steadily decrease thereafter.

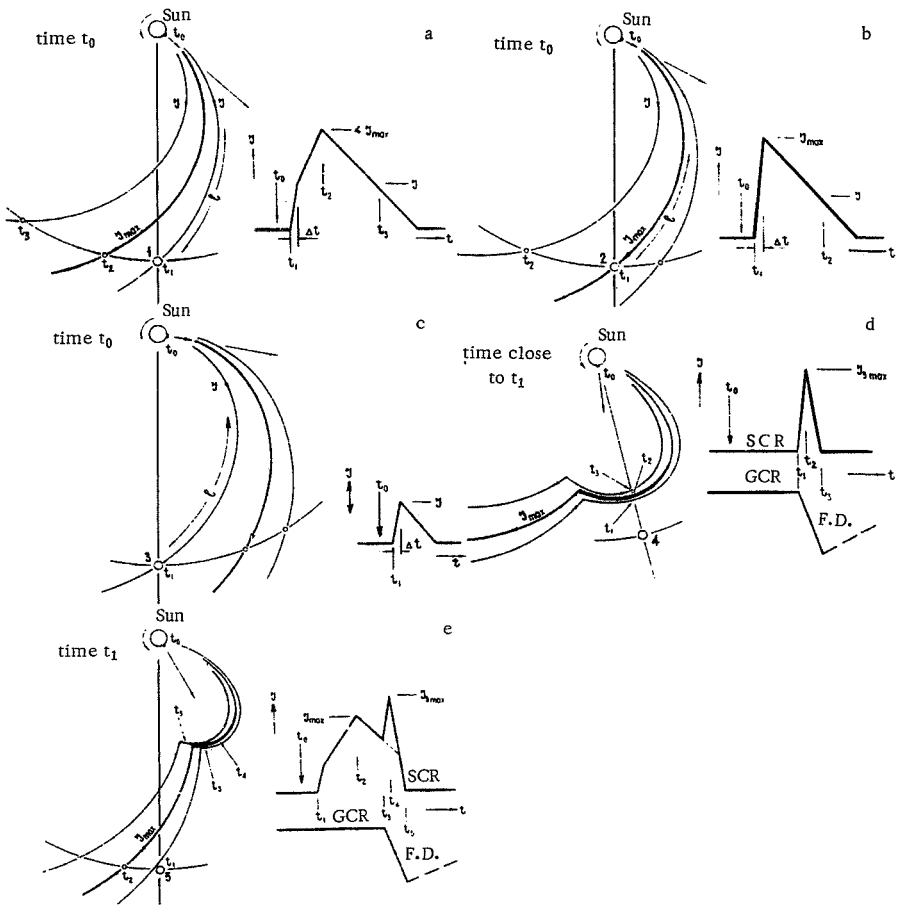

FIGURE 3. Schematic diagrams illustrating the distribution of SCR from a flare.

In Figure 3d, the flare which burst at the time t_0 lies in the eastern part of the Sun disk. The time required for the SCR-filled tubes to turn toward the detector (point 4) is greater in this case than the time for the shock wave to cover the distance from the Sun to the detector. The SCR intensity will therefore start increasing only at the time t_1 corresponding to the arrival of the shock wave and the beginning of the GCR Forbush decrease. This time is determined by the velocity of the shock wave in a given direction and the distance to the detector. The time t_2 will correspond to the maximum flux of localized SCR I_{3max}, i.e., the flux in the tube with maximum population, broken and compressed between the

leading and the trailing shock-wave fronts. This time approximately coincides with the middle phase of the GCR Forbush decrease. The time t_3 corresponds to the passage of the trailing front and signifies the beginning of the GCR recovery phase.

The intermediate case shown in Figure 3e corresponds to a solar flare which at the time t_0 lay approximately between the central meridian and 30°W. The development is determined by the relationship between the time needed for the central channel to turn toward the detector (point 5, time t_2) and the time t_3 for the shock wave to reach subsequently the same point. It should be emphasized that all these cases only constitute different facets of the same process of SCR propagation from the flare, as observed at a certain point in space.

Let us consider some results pertaining to the GCR Forbush decrease associated with solar flares. For type II flares accompanied by a Forbush decrease, the mean radial velocities of the shock waves were determined from the known Sun – detector distance and the known time when the decrease began. In seven cases, when the spacecraft and the Earth were at a sufficient distance from each other on the same radius from the Sun, two values of the mean radial velocity were determined: $\overline{V}_1$ to the detector closer to the Sun and $\overline{V}_2$ to the more distant detector. The mean velocity $\overline{V}_3$ in the space between the two detectors was also found /6/. The values obtained for $\overline{V}_1$, $\overline{V}_2$, and $\overline{V}_3$ show that the velocity decreases with distance and time, i.e., the shock waves are decelerated (Figure 4). Assuming that the mean velocity linearly decreases with time, we found for each flare the initial velocities $\overline{V}_0$, the decelerations a, and the distances S_0 at which the shock waves decay completely. The decelerations were found to range from about 140 to 4000 cm · sec^{-2}. The shock waves stop approximately at the same distance from the Sun (between the Earth and the Mars orbits) and the decelerations are $a \sim V_0^2$.

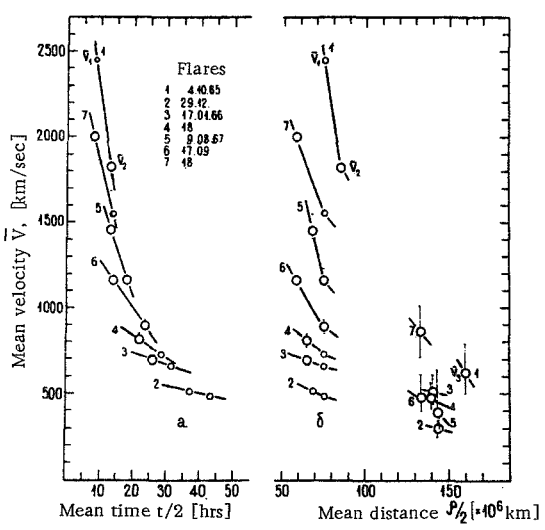

FIGURE 4. The mean shock-wave velocity vs. time (a) and distance (b).

The deceleration of shock waves should lead to a gradual reduction of the Forbush decrease, because of the decrease in the propagation velocity. At a certain distance from the Sun, no Forbush decrease will thus be observed. The solar cosmic rays localized behind the shock-wave front gradually leak out and accumulate near the boundary of the modulation region as the shock waves decay. These effects are corroborated by experimental findings. Over the simultaneous trajectory of VENUS-2 and ZOND-3 in December 1965 and January 1966, the Forbush decreases caused by the flares of 29—30 December 1965 and 17—18 January 1966 and observed by VENUS-2 had all but disappeared at distances of from 1.29 to 1.31 a.u. according to ZOND-3 measurements, although the SCR enhancements were observed on ZOND-3 (Figure 5).

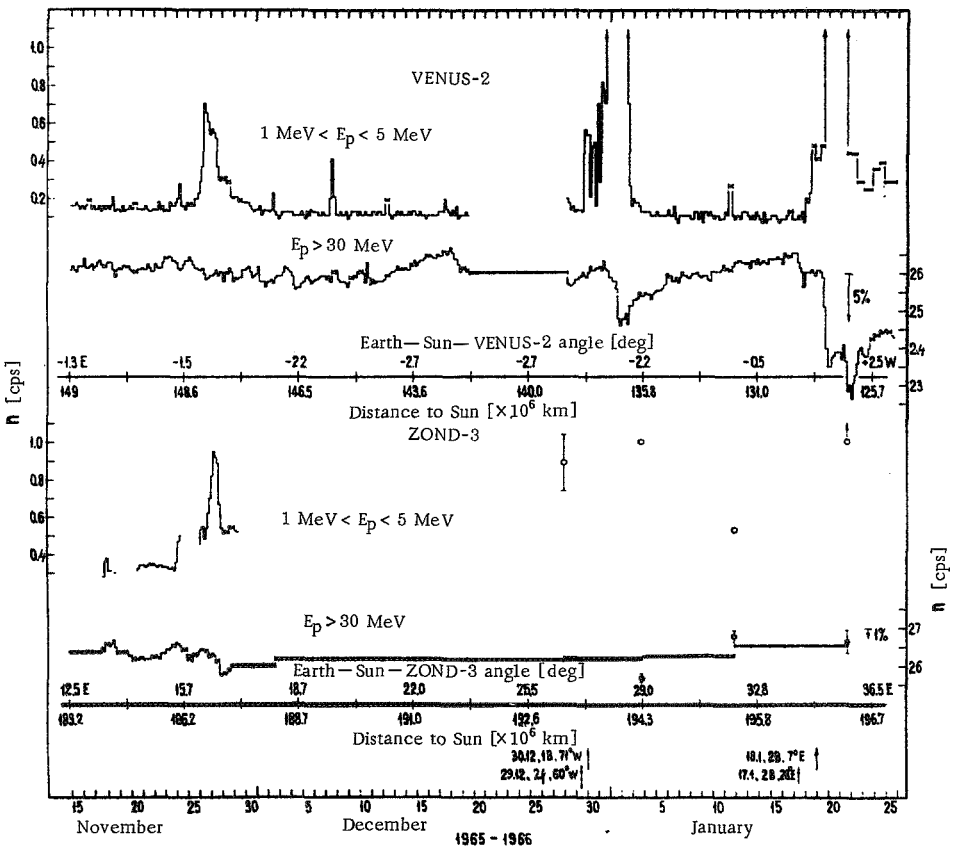

FIGURE 5. SCR and GCR intensity over simultaneous flight trajectories of VENUS-2 and ZOND-3. The arrows indicate solar flares.

The analysis of the depth and the steepness of the Forbush decrease shows a tendency toward a shallower decrease as one moves away from the Sun and away from the flare direction. The steepness of the Forbush

decrease diminishes more rapidly than its depth; this is associated with the longer duration of the decrease phase, i.e., with the noticeable spreading of the region between the leading and the trail shock-wave fronts during the motion of the shock wave from the Sun.

Observations of the Forbush decreases in a weakly disturbed medium reveal a break in the phase of the intensity drop corresponding to an increase in steepness. At high energies (>1 BeV), the increase in steepness is insignificant (approximately by a factor of two), and at low energies (> 30 MeV) it is quite substantial (by a factor of about 6 — 8). This fall in the GCR intensity may be qualitatively interpreted by assuming a semitransparent mirror moving from the Sun toward the detector. This mirror will screen off the GCR flux reaching the detector. When the mirror has reached the detector, the fall of intensity occurs inside the mirror. For low-energy cosmic rays the transparency factor is clearly smaller than for high-energy cosmic rays. The intensity of the low-energy cosmic rays will therefore fall more gently and gradually before the mirror and more steeply behind the mirror than the intensity of the high-energy cosmic rays.

Let us consider the results of the analysis of GCR variations, i.e., the shallow intensity decreases of the GCR caused by the magnetic fields of quasistationary corpuscular streams from active regions which turn together with the Sun.

At a distance of 1 a.u. from the Sun, the structure of the interplanetary magnetic field proposed by Parker /4/ for the solar wind and by Mustel /7, 8/ for corpuscular streams appears to be made up of discrete magnetic tubes with various field strengths, oriented on the average along the Archimedes spiral in the plane of the ecliptic. The rotation of the interplanetary magnetic field relative to the detector together with the Sun causes a modulation of the GCR flux which is recorded by the detector as a time-modulation of intensity.

During the flight of ZOND-3 and VENUS-2, i.e., during approximately 6 months, about 30 GCR intensity decreases were recorded ($E_p > 30$ MeV) with depths ranging from about 0.5 to 5% and duration (length of decrease phase) of from about 15 to 65 hr /9/. Each decrease was correlated with a definite active region, viz., with a bright calcium flocculus. Comparison of the successive transits of the active region across the central meridian of the Sun (regardless of the latitude of the active region) with the time of the beginning of the GCR intensity decrease (making allowance for the mean time shift of 5 days for the propagation of the corpuscular stream) reveals a strong correlation between these effects (correlation coefficient $K = 0.955 \pm 0.004$). This comparison confirms that the active regions were properly identified, that the plasma moves quasiradially in the equatorial plane from the active region, and that the magnetic fields of active regions from all latitudes apparently "focus" in the equatorial plane.

The mean radial velocities of the corpuscular streams V_p were determined from the known heliocentric orbits of the spacecraft at the time of observations of the GCR intensity decrease and from the delay of the observed decrease time relative to the transit of the active region across the central meridian. For active regions existing for the duration of more than a single axial rotation of the Sun, the velocity V_p was found to depend

on the phase of development of the active region. High velocities V_p correspond to maximum development of the active region. Observations of some cases of rapid development of active regions outside the central meridian show that these cases are also associated with GCR decreases with a steeper intensity drop. The active regions in these cases apparently eject a high-velocity corpuscular stream which does not move in the radial direction, i.e., the initial phase of this event corresponds to a flare.

Comparison of the "strength" of the active regions, i.e., the product of its area and brightness, with the depth of the GCR decrease reveals a definite correlation between these parameters ($K = 0.83 \pm 0.01$). Some points deviate from this dependence, which is apparently due to latitude effects, presence of M-regions, and rapidly developing active regions. One case of a very bright active region was observed, which did not cause a GCR decrease. This active region apparently did not inject corpuscular streams because of its peculiar configuration and the strength of its magnetic field.

In conclusion, let us consider the propagation of SCR not associated with solar flares in the quasistationary magnetic fields of corpuscular streams. The GCR intensity variations ($E_p > 30$ MeV) measured during the simultaneous flight of VENUS-2 and ZOND-3 (from 17 to 29 November 1965, Figure 5), the two spacecraft traveling at a distance of about $40 \cdot 10^6$ km from each other on the same radius-vector from the Sun, made it possible to establish the structure of the magnetic fields between the orbits of these spacecraft.

The field geometry is initially assumed to be in the form of Archimedes spirals. Relevant features, e.g., maxima, minima, steps, etc., were visually identified on the curves of the GCR intensity variation recorded on VENUS-2 and ZOND-3. The recording time t of each feature was determined and the time delays Vt between the corresponding features on VENUS-2 and ZOND-3 were found. For each t, a certain hypothetical velocity V_c was calculated, which characterized the pitch of the Archimedes spiral. Note that V_c characterizes the position of the magnetic field front of the cropuscular stream, and may thus have values ranging from 0 to $\pm\infty$ in various sections of magnetic tubes bent in the shape of a zigzag or a loop. V_c is equal to the plasma velocity only in undisturbed sections in cases of regular ejection of plasma from the active region /9/.

SCR streams of other than flare origin were also observed over the simultaneous flight trajectory of VENUS-2 and ZOND-3. Figure 5 shows that the position of the individual SCR maxima on ZOND-3 relative to the GCR variations is different from that on VENUS-2: the shift Vt between the SCR maxima is smaller than the shift between the GCR details at the same points. The velocity V_c can be calculated from the shift Vt between the SCR streams. The V_c for the SCR streams is invariably greater than the corresponding velocities of the corpuscular streams, i.e., the SCR propagate along a spiral with a greater pitch. Thus, SCR of other than flare origin show a definite westward "veering" from the helical magnetic fields, like the SCR generated by flares. The same effect was observed on the simultaneous flight trajectory of IMP III, ZOND-3, and MARINER IV /2/.

The probing of the interplanetary space by low-energy cosmic rays thus discloses the quasihelical structure of the interplanetary magnetic fields originating in the active solar regions and turning together with the Sun. These magnetic fields are disturbed by the traveling shock waves originating during solar flares. The shock waves rapidly decay, breaking up between the Earth and the Mars orbits. Solar cosmic rays propagating in helical magnetic fields "veer" westward. Low-energy solar cosmic rays are effectively transported from solar flares behind shock-wave fronts.

Bibliography

1. Vernov, S.N., A.E. Chudakov, P.V. Vakulov, Yu.I. Logachev, G.P. Lyubimov, A.G. Nikolaev, and N.V. Pereslegina.— Izvestiya AN SSSR, 31(8):1296. 1967.
2. Vernov, S.N., A.E. Chudakov, P.V. Vakulov, E.V. Gorchakov, N.N. Kontor, S.N. Kuznetsov, Yu.I. Logachev, G.P. Lyubimov, A.G. Nikolaev, N.V. Pereslegina, and B.A. Tverskoi.— Trudy V Vsesoyuznoi ezhegodnoi zimnei shkoly po kosmofizike, Apatity, p.5, Izd. Kol'skogo filiala AN SSSR. 1968.
3. Vernov, S.N., N.N. Kontor, S.N. Kuznetsov, Yu.I. Logachev, G.P. Lyubimov, and N.V. Pereslegina.— Doklad na Vsesoyuznoi konferentsii po fizike kosmicheskikh luchei, Tashkent. 1968.
4. Parker, E.N. Interplanetary Dynamic Processes.—New York, Wiley. 1963.
5. Rao, U.R., K.G. McCracken, and R.P. Bukata.— J. Geophys. Res., **72**:4325. 1967.
6. Lyubimov, G.P.— Astronomicheskii tsirkulyar, AN SSSR, No. 488:4. 1968.
7. Mustel', E.R.— Astronomicheskii zhurnal, **37**:403. 1960.
8. Mustel', E.R.— Astronomicheskii zhurnal, **39**:619. 1962.
9. Vernov, S.N., Yu.I. Logachev, G.P. Lyubimov, and N.V. Pereslegina.— Doklad na Vsesoyuznoi Konferentsii po fizike kosmicheskikh luchei. Tashkent. 1968.

PROPAGATION OF 1.5 MeV SOLAR PROTONS IN THE INTERPLANETARY SPACE

S.N. Vernov, E.V. Gorchakov, and G.A. Timofeev

Observations from interplanetary automatic stations and ground installations provided extensive experimental data concerning bursts of protons of solar origin /1 – 3/. In this connection, the problem of the proton transport from the source in the solar flare is of considerable significance.

Charged particles generated on the Sun propagate in the interplanetary magnetic field, which is made up of two components: the regular magnetic field of the Sun and the randomized magnetic field of the inhomogeneities. At the relevant distances $R \sim 1$ a.u., the protons should move almost parallel to the field lines because of the conservation of the magnetic moment in the Sun's regular field. However, the magnetic field inhomogeneities scatter the charged particles, thus essentially affecting their trajectory and distribution in time and in space. We will consider the propagation of 1.5 MeV protons in the interplanetary field. The regular field of the Sun is taken to vary as $1/R^2$. The interaction of a proton with the magnetic field inhomogeneities is given if we know the mean free path between the inhomogeneities and the mean angle of scattering by inhomogeneities, σ. An important parameter characterizing the transport process is the transport length Λ. In our case, the transport length, which is understood as the free path corresponding to the mean scattering angle $\pi/2$, is given by the equation

$$\Lambda = \ell \left(\frac{\pi}{2\sigma}\right)^2.$$

We assumed that the free path l, the mean scattering angle σ, and hence the transport length Λ are all independent of the heliocentric distance. The motion of a proton between inhomogeneities is governed by considerations of magnetic moment conservation.

The problem was solved by the Monte Carlo technique. The proton is injected into the interstellar field at a distance of 10^{-2} a.u. from the Sun at 30° to the field line. The first stage deals with the selection of the motion of the proton prior to collision with the first inhomogeneity. The heliocentric distance to the interaction point is calculated from the free path, and the pitch angle of the proton before the interaction is determined from the heliocentric distance. The next stage is concerned with the calculation of the scattering angle of the proton, and the pitch angle after the interaction is found. The procedure is repeated until the proton leaves the relevant region of space ($R \approx 10^{-2} - 2.0$ a.u.). Having analyzed

a sufficient number of protons in this way, we find the angular and the time dependence of the proton intensity at a distance of 1 a.u. from the Sun. We ignored the transverse diffusion of protons. In terms of starting assumptions, this corresponds, e.g., to uniform injection of protons into a field tube whose width is large compared to the Larmor radius.

We analyzed the motion of protons in the interplanetary field for three values of the transport length, Λ = 1.0, 0.3, and 0.1 a.u. Calculations show that the fundamental characteristic features of the time dependence of the proton bursts are determined by the transport length Λ, irrespective of the particular choice of the free path length l and the mean scattering angle σ. At first, instantaneous injection of protons was assumed. (The results of some calculations carried out assuming instantaneous injection were published in /4/.) Figure 1 shows histograms of the proton distribution angles for Λ = 1.0 a.u. The vertical axis gives the number of protons crossing a field line at a point with heliocentric distance R = 1.0 a.u. in a range of angles $\Delta\theta$ = 30°. We see from Figure 1 that in the high-intensity phase of the burst, the bulk of the protons at a distance of 1 a.u. cross the field line with pitch angles between 30 and 60°. (Our distribution refers to pitch angle intervals. If we change over to solid angles, the maximum of the distribution shifts, as expected, to 0 – 30°.) Eventually the protons fill uniformly the front hemisphere, and an isotropic distribution is finally established.

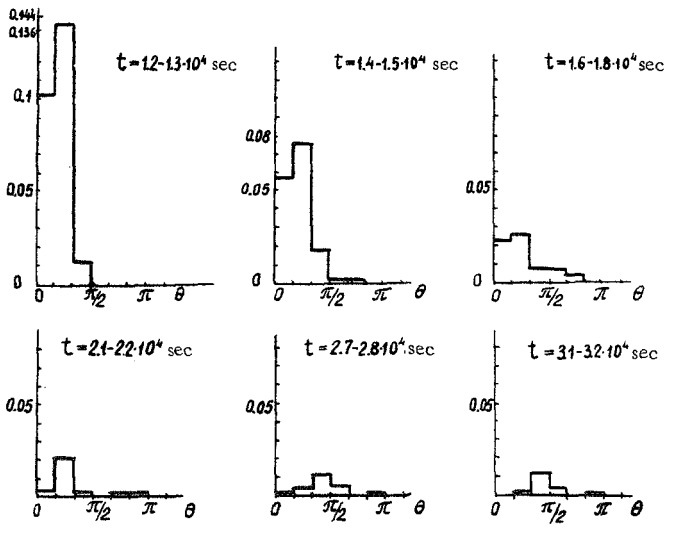

FIGURE 1. Angular distribution of 1.5 MeV protons at various times. Instantaneous injection.

Our calculations give the conditions of applicability of the diffusion theory to proton transport. Figure 2 is the time curve of the proton intensity at a distance of 1.0 a.u. for transport lengths Λ = 1.0 and 0.1 a.u. (for Λ = 1.0,

the results were obtained from two independent series of tests, designated by dots and circles). The solid curves correspond to the diffusion theory. Figure 2b shows that for $\Lambda = 0.1$ a.u. the diffusion theory gives a fair approximation to the results of our calculations. For $\Lambda = 1.0$ a.u. (Figure 2a), proton transport cannot be described in terms of the diffusion theory. In this case, our results considerably deviate from the diffusion-theoretical curve. Moreover, according to the diffusion theory, the intensity maximum is attained before the direct arrival of protons (10^4 sec). Note that calculations made with $\Lambda = 0.3$ a.u. do not fit the diffusion theory either.

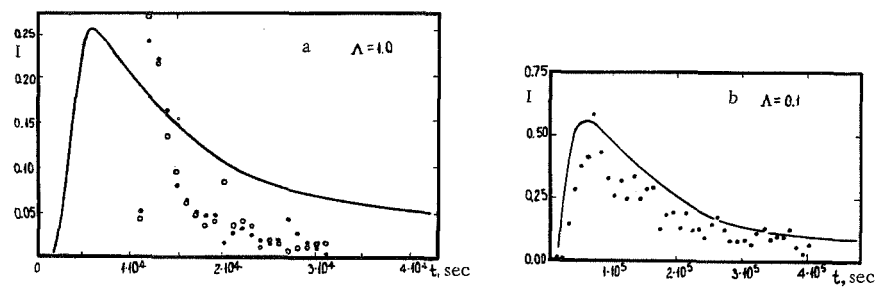

FIGURE 2. Time curves of intensity for different transport lengths:

a) $\Lambda = 1.0$ a.u., b) $\Lambda = 0.1$ a.u.

Anisotropy is an important characteristic of the proton distribution. Figure 3 plots the calculated time curve of the ratio of the intensity of the particles moving away from the source I_+ to the intensity of the particles moving toward the source I_- at a heliocentric distance R = 1.0 a.u.

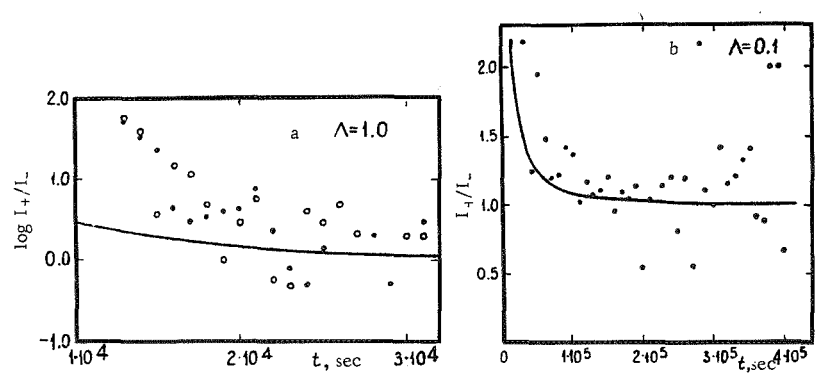

FIGURE 3. The ratio of the number of protons moving away from the Sun I_+ to the number of protons moving toward the Sun I_- for different transport lengths. Instantaneous injection.

a) $\Lambda = 1.0$ a.u., b) $\Lambda = 0.1$ a.u.

For transport lengths $\Lambda = 0.1$ a.u. (Figure 3b), which are small compared to the heliocentric distance, the distribution is nearly isotropic during the entire burst, except for the initial phase. This result is in good agreement with the diffusion theory (solid curves). For $\Lambda = 1.0$ a.u. (Figure 3a), the anisotropy is very high ($I_+/I_- = 10$) during the entire burst.

Bursts of cosmic rays of solar origin experimentally detected at distances of about 1 a.u. from the Sun show great variety. The duration of the burst and the anisotropy of the proton distribution greatly vary in different particular cases. Of particular interest are the highly anisotropic proton bursts with $A \sim 50-80\%$ ($A = (I_+ - I_-)/(I_+ + I_-)$) which persist for a few days. According to our calculations carried out assuming a constant transport length, a burst with a considerable anisotropy should be observed for transport lengths comparable with the heliocentric distance, i.e., $\Lambda \approx 1$ a.u. However, if the protons are injected instantaneously, the burst duration is short, about 10^4 sec. To obtain a burst duration of a few days, different injection conditions should be assumed, or alternatively the transport length should be taken as a function of the distance. Retaining a constant transport length, we considered the case of extended injection of protons, which continued at a uniform rate for $5 \cdot 10^4$ sec. In this problem, the dependences obtained under the assumption of instantaneous injection are functions of the source. Figure 4 plots the results of calculations for $\Lambda = 1.0$, 0.1 a.u.

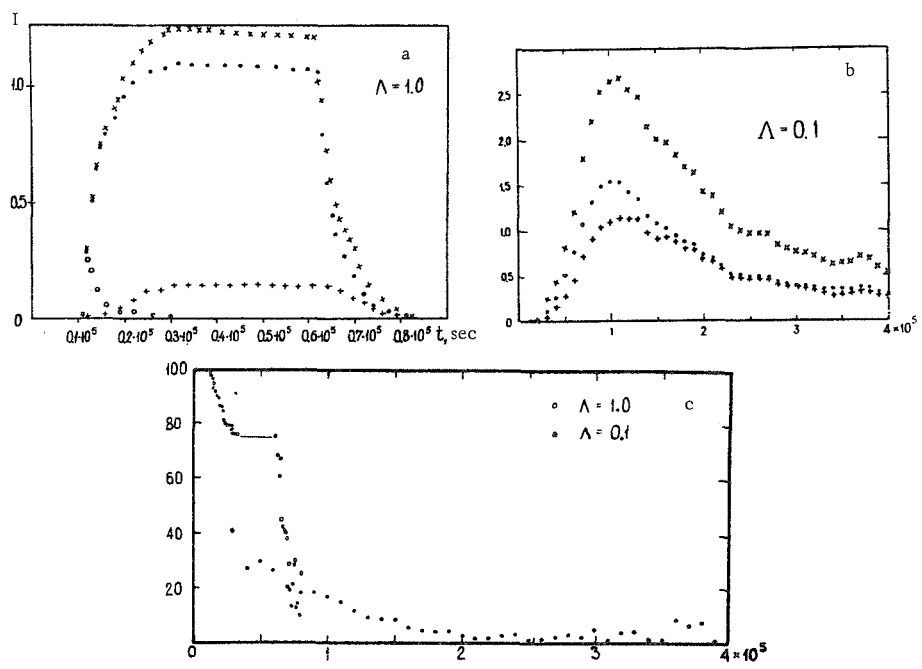

FIGURE 4. Time curves of I, I_+, I_- (a, b) and anisotropy $A = (I_+ - I_-)/(I_+ + I_-)$ (c). Uniform injection for $5 \cdot 10^4$ sec.

x — total intensity of protons, o — intensity of protons moving away from the Sun, + — intensity of protons moving toward the Sun.

As could be expected, the characteristic features of a proton burst from an instantaneous source are transferred to the case of continued injection: transport lengths $\Lambda = 0.1$ a.u. which are small compared to the heliocentric distance R = 1.0 a.u. correspond to long bursts of low anisotropy (Figure 4b), whereas transport lengths $\Lambda = 1.0$ a.u. give short bursts of high anisotropy (Figure 4a). Note that for $\Lambda = 1.0$ a.u. the anisotropy is high during that phase of the burst when the proton intensity is high (Figure 4c). It seems that the observed highly anisotropic proton bursts which persist for a few days /3/ can be attributed to prolonged injection of protons followed by propagation in a medium with $\Lambda = 1.0$ a.u. As the recorded proton bursts show a great variety of intensity time curves, the duration of injection should be determined for each particular case separately.

Bibliography

1. Vernov, S.N., A.E. Chudakov, P.V. Vakulov, Yu.I. Logachev, G.P. Lyubimov, and N.V. Pereslegina.— Izvestiya AN SSSR, Ser.fiz., 31(8):1255. 1967.
2. Charakhch'yan, A.N. and T.N. Charakhch'yan.— Geomagnetizm i aeronomiya, 6(3):406. 1966.
3. Vernov, S.N., A.E. Chudakov, P.V. Vakulov, E.V. Gorchakov, N.N. Kontor, S.N. Kuznetsov, Yu.I. Logachev, G.P. Lyubimov, A.G. Nikolaev, N.V. Pereslegina, and B.A. Tverskoi.— Trudy V Vsesoyuznoi ezhegodnoi zimnei shkoly po kosmofizike, Apatity, p.5, Izd. Kol'skogo filiala AN SSSR. 1968.
4. Getselev, I.V., E.V. Gorchakov, and G.A. Timofeev.— Trudy Mezhdunarodnogo simpoziuma sotsialisticheskikh stran po solnechno-zemnym svyazyam, Izd. KrAO. 1968.

INVESTIGATION OF PROTON FLUXES IN THE 1.50—50 MeV RANGE WITH ZOND-4 AND ZOND-5 AUTOMATIC INTERPLANETARY STATIONS

M. M. Bredov, A. A. Kolchin, V. V. Lebedev, and G. P. Skrebtsov

Investigation of low-energy cosmic rays has yielded valuable data on the structure of the interplanetary magnetic field and the mechanism of solar modulation. However, a comprehensive study of the corresponding phenomena in the interstellar space is impossible without periodic measurements of the solar activity. The bulk of reports published on the subject were based on data collected in periods of minimum solar activity /1, 2, 3/. Later findings are reported in one source only /4/.

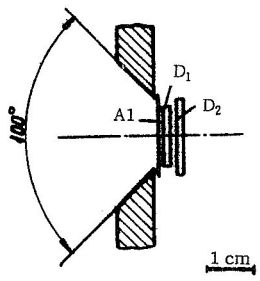

FIGURE 1. Schematic diagram of the PS-1 instrument.

The ZOND-4 and ZOND-5 interplanetary stations were launched on 2 March and 15 September 1968, respectively. Each remained in orbit for about 7 days. The payload included equipment for measuring proton fluxes between 1.5 and 50 MeV. One of the instruments, PS-1 device (Figure 1), was a sandwich of two Li-drifted silicon detectors. One of the two detectors (D2) was connected with the other detector D1 by an anticoincidence circuit. D1 had an area of 1.5 cm^2, D2 an area of 2.5 cm^2; the thickness of these detectors was 2.3 and 1.5 mm, respectively. The detectors were screened from light by aluminum foil. An electronic circuit isolated pulses corresponding to detection of protons between 1.5 — 10 and 10 — 20 MeV by D1. The geometrical factor of the instrument was 3.9 cm^2 sterad.

The other instrument (Figure 2) was a telescope (PT) comprising two identical Li-drifted silicon detectors D3 and D4, 1.2 mm thick and 2.5 cm^2 in area each. The opening angle of the sensitive cone was 100°. A1, A2, and A3 are aluminum absorbers. An appropriate choice of the absorber thickness and the height of the discrimination thresholds made it possible to record protons of 30 — 35 MeV and 45 — 50 MeV.

Figure 3 shows the proton detection efficiency of the telescope vs. the kinetic energy of the proton. Note that the discrimination thresholds in this telescope were so chosen that the instrument responded to protons only, and not to any other particles.

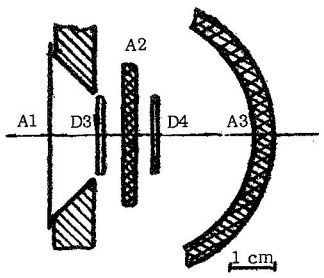

FIGURE 2. Schematic diagram of the PT instrument.

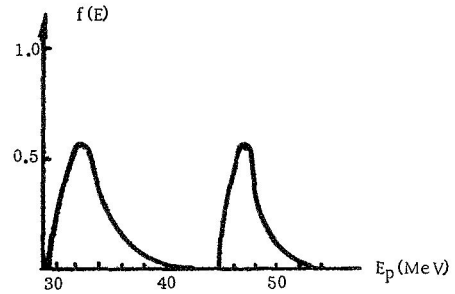

FIGURE 3. Proton counting efficiency vs. the kinetic energy.

The proton measuring equipment was oriented so that the instruments in the spinning interplanetary station scanned mainly in a plane perpendicular to the plane of the ecliptic. Over certain sections of the trajectory, however, midcourse maneuvers were carried out and the orientation changed. In the present report, we mainly consider the results obtained with ZOND-5.

The proton measuring equipment was turned on after the boost stage, when the station was on its course to the Moon. The first data were obtained at a distance of 22,000 km from the Earth, when the station was crossing the outer radiation belt. The PS-1 channel (1.5 – 10 MeV) recorded a high counting rate which fluctuated (increasing and decreasing) as the station was moving away from the Earth, and then gradually settled to the level measured outside the magnetosphere. The PT-1 and PT-2 channels (30 – 35 MeV and 45 – 50 MeV, respectively) did not register an increased count rate in the radiation belt. Brief "bursts" of the counting rate, which did not last more than a minute, were picked up in the PS-1 channel all the way to a distance of about 100,000 km from the Earth. Measurements carried out from this distance to the time when the equipment was turned off at a distance of about 80,000 km from the Earth on the way back are described in the following. The measurement data apparently characterize the conditions in the "free" interplanetary space between the Earth and the Moon which prevailed between 16 and 21 Sept. 1968. Figure 4 plots the time variation of the count rate as recorded on 19 Sept. 1968 from 03^h20^m to 04^h05^m in three channels at a distance of about 350,000 km from the Earth. The variation of the count rate observed during this period was typical of the entire trip. The rms error is indicated for the maximum and the minimum PS-1 reading. The statistics of the events in the PT-1 and PT-2 channels are insufficient for drawing any quantitative conclusions over times of the order of one or several minutes.

Figure 5 summarizes the data on the counting rates in the various channels for the entire period from 11^h16^m on 15 Sept. 1968 to 13^h30^m on 21 Sept. 1968. The points on this plot were obtained by averaging the readings taken over periods ranging from 45 to 140 min.

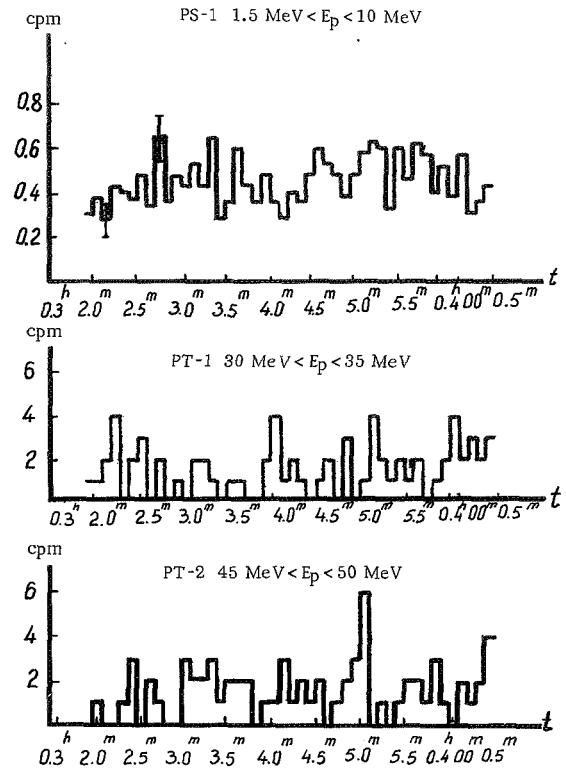

FIGURE 4. Variation of the count rate with time.

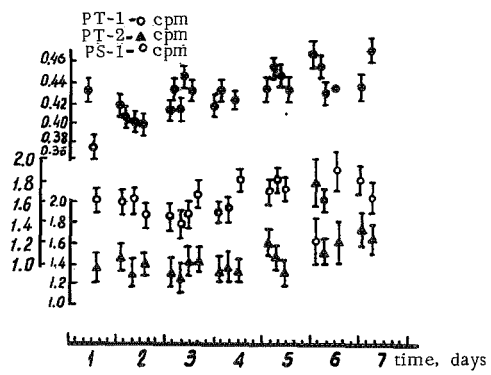

FIGURE 5. Count rate data for the period from 15 to 21 Sept. 1968.

Daily averaging brings out more clearly the slight increase in the count rate in the PS-1 channel from 0.39 to 0.46 sec^{-1} during the relevant period with a rms error of less than 0.01 sec^{-1}. The count rates in the PT-1 and PT-2 channels also showed a slight increase. On the whole, however, the instruments did not detect any significant change in the count rate between 15 Sept. and 21 Sept. 1968 which could have been attributed to a radical change in the physical conditions in the Earth—Moon space.

The relatively short duration of the proton stream records (ZOND-5 landed on 21 Sept. 1968) makes it impossible to decide what the instruments measured exactly, whether the "quiet" background between flares or perhaps a gradual increase in the intensity of solar protons. Since ZOND-5 was launched in a year of maximum solar activity, the latter assumption seems quite probable.

As we have already noted, ZOND-5 sometimes changed its orientation in space as a result of midcourse maneuvers. The count rate in all the channels nevertheless remained fairly constant, and we may thus introduce for our purposes a "mean intensity" of the proton stream, which is directly related (through the geometrical factor of the instrument) to the mean count rate. This approach is essentially equivalent to the assumption of an isotropic proton flux during the averaging period.

We give here the mean proton intensities obtained in our experiments:

1.5—10 MeV	—	$I = 0.9 \cdot 10^3\ m^{-2}\ sterad^{-1}\ sec^{-1}$
10—20	—	$I = 40$
30—35	—	$dI/dE = 35\ m^{-2}\ sterad^{-1}\ sec^{-1}\ MeV^{-1}$
45—50	—	$dI/dE = 50$

The intensities recorded by ZOND-4 in March 1968 fall somewhat below these values.

Bibliography

1. Vernov, S.N., A.E. Chudakov, P.V. Vakulov, Yu.I. Logachev, G.P. Lyubimov, A.G. Nikolaev, and N.V. Pereslegina.— DAN SSSR, 171:847. 1966.
2. van Allen, J.A., L.A. Frank, S.M. Krimigis, and H.K. Hills.— Science, 149:1228. 1965.
3. Fan, C.Y., M. Pick, K.R. Pyle, J.A. Simpson, and D.R. Smith.— J. Geophys. Res., 73:1555. 1968.
4. Grigorov, N.L., V.G. Kurt, V.N. Lutsenko, V.L. Madyev, N.F. Pisarevskii, and I.A. Savenko.— Kosmicheskie Issledovaniya, 7:137. 1969.

DYNAMIC ALIGNMENT OF ATOMIC AND MOLECULAR SPINS AS A NEW METHOD OF DETERMINATION OF THE INTERPLANETARY MAGNETIC FIELD

D. A. Varshalovich

The state of atoms, molecules, and ions in various astrophysical systems is generally characterized by their concentration, velocity distribution, and degree of ionization or excitation, but no information is given concerning the spin state of the particles. The spins are assumed to be randomly distributed, without interacting with any other systems. This assumption, however, is valid in isolated cases only.

STATIC AND DYNAMIC SPIN ALIGNMENT

A rarefied medium in thermodynamic equilibrium in the absence of external fields is isotropic. All directions in this medium are equivalent, so that the particle energy cannot depend on the orientation of the particle spins in space. Particles differing only in the projection M of the spin $\vec{I}$ on the quantization axis have the same energy

$$\varepsilon_M = \varepsilon_{M'} \tag{1}$$

for any allowed M and M' (I, I − 1, I − 2, . . . , −I). As a result, from Boltzmann's equation,

$$\frac{R_M}{R_{M'}} = e^{-\frac{\varepsilon_M - \varepsilon_{M'}}{kT}}, \tag{2}$$

the population R_M of all the (2I + 1) states corresponding to different spin orientations is constant, i.e., all the possible values of the spin projection M are equiprobable. In other words, the spins are entirely randomized and the medium as a whole is isotropic. This situation obtains, e.g., in the dense atmospheric layers, where the population of the various energy levels is determined by collisions of the particles with the equilibrium gas.

The spins of the particles in a medium in thermodynamic equilibrium can be aligned by a sufficiently strong external field, such that the magnetic energy is greater than or comparable with the thermal energy:

$$\mu H \gtrsim kT. \tag{3}$$

In this case, the energy levels of the particles are split into (2I + 1) sublevels characterized by different M values, and in accordance with the

Boltzmann equation (2) the populations of these sublevels are all different. The maximum population is characteristic of the lowermost sublevel, the one with $M = 1$ if the magnetic moment of the particle is positive $\mu>0$, or $M = -1$ if $\mu< 0$. This implies that the particle spins are preferably aligned along the field $\vec{H}$ (or against the field). This is known as the case of static alignment. The necessary condition of static alignment, (3), is hardly ever satisfied in the known astrophysical systems. For example, in the interstellar medium, for $H\sim 10^{-6}$ Oe and $T\sim 100°K$, $\mu H\sim 10^{-26}$ erg, whereas $kT\sim 10^{-14}$ erg. Even in magnetic stars, with $H\sim 10^{3}$ Oe and $T\sim 10^{4}$ °K, $\mu H\sim 10^{-17}$ erg and $kT\sim 10^{-12}$ erg. Therefore, static spin alignment associated with strong external fields is impossible in outer space.

In non-equilibrium media, however, an entirely different alignment mechanism is possible — the so-called dynamic spin alignment, whereby the particle spins are aligned through interaction with a directional beam of radiation or a stream of fast particles passing through the medium /1/. Thus, the optical emission and the radio waves from stars and nebulae, as well as beamed corpuscular streams piercing the interstellar medium, interact with the interstellar particles changing their momentum distribution and also aligning their spins. The momentum effects (radiation pressure and solar wind) are freely discussed in astrophysical literature, whereas the problem of the dynamic alignment of atomic and molecular spins in the interstellar medium has been ignored so far. And yet, both effects are closely interrelated, since both linear momentum and angular momentum are transferred in collisions. Angular momentum transfer is even more effective in the sense that the incident beam first aligns the medium particles and only then drags them along.

The fundamental reason for the dynamic spin alignment is to be sought in the spin-spin and spin-orbit interaction of the particles with the incident stream (photons, protons, electrons, etc., either polarized or nonpolarized). This interaction, however, may lead to spin alignment only if the angular distribution of the incident particles is anisotropic. Thus, a directed beam of unpolarized light scattered by a random medium will produce spin alignment even if the angular scattering function is spherically symmetric. The resonance scattering of photons is the most effective for spin alignment, since the resonance scattering cross section is exceptionally high and also because the photon spin $s = 1\hbar$ is always directed along (or against) the direction of wave propagation (transversality of electromagnetic waves). The angular distribution of particles is generally isotropic, whereas radiation fluxes are mostly anisotropic.

NECESSARY CONDITIONS AND THE MECHANISM OF OPTICAL SPIN ALIGNMENT

The analysis of conditions in various astrophysical systems has shown that resonance scattering of directional fluxes of unpolarized radiation constitutes the main process of spin alignment in outer space /2/. The necessary conditions for this optical dynamic spin alignment are encountered in numerous astrophysical systems, such as the interstellar

and interplanetary medium, nebulae, outer layers of stellar and planetary atmospheres, comets, etc. The main distinctive feature of all these systems is that their density is low and the collisions are ignorable,

$$W_{col} < W_{rad}, \tag{4}$$

whereas the radiant fluxes are very powerful and essentially anisotropic,

$$\frac{\Delta\Omega}{4\pi} \ll 1, \tag{5}$$

since the optical thickness is low,

$$\tau < 1. \tag{6}$$

Under these conditions resonance scattering will inevitably lead to spin alignment. We may therefore maintain that, unlike the static spin alignment, the dynamic alignment is an exceedingly widespread natural phenomenon. In laboratories, dynamic spin alignment is very difficult to create and it can be sustained even for very brief periods of time only by means of special experimental setups /3/. The spin system rapidly relaxes to an isotropic equilibrium state. On the other hand, the necessary conditions for optical spin alignment are always observed in tremendous regions of outer space. Nature itself constantly maintains the alignment. The mechanism of optical resonance spin alignment is illustrated by the simple and vivid example of a two-level atom with spin I = 1 in the ground state and spin I' = 0 in the excited state (Figure 1).

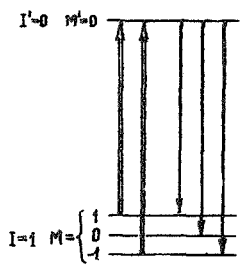

FIGURE 1. Level diagram illustrating the mechanism of optical spin alignment. I = 1 and I' = 0 are the particle spins in the ground and the excited state, respectively. M is the projection of the spin on the direction of the incident photon beam.

If the incident light is unpolarized, the beam contains right- and left-polarized photons in equal proportions. These photons are characterized by different projections of their angular momentum on the quantization axis, $m_\gamma = 1$ and $m_\gamma = -1$. There are no photons with $m_\gamma = 0$, because of the transversality of the electromagnetic field.

In virtue of angular momentum conservation, a resonance photon with $m_\gamma = \pm 1$ can be absorbed only by an atom with $M = \pm 1$, bringing it to an excited state with $M' = M + m_\gamma$; atoms in substate $M = 0$ cannot be excited by this mechanism. Therefore, atoms occupying the substate $M = 0$ can be excited to a state with a different M value only by collisions among themselves. On the other hand, excited atoms may drop with equal probability to all the M substates, since I = 0 and all the physical properties of a spin-zero system are independent of its spatial orientation; in particular, the matrix elements which determine the transition probabilities are independent of the projections m_γ and M. Thus, each scattering event increases the population of the $M = 0$ level and consequently the population of the $M = \pm 1$ levels is steadily depleted. If the system is subjected for a sufficient length of time to a beam of resonance photons, virtually all the atoms will be converted to a substate with $M = 0$, irrespective of their

initial spin alignment, and the medium will become transparent to the resonance radiation. Complete transparency of the medium is of course attainable only if there are no interatomic collisions. It is moreover assumed that the resonance radiation is directed in a narrow solid angle along the quantization axis. Note that the loss of opacity in this case is entirely different from the phenomenon observed in intense radiation fluxes, when the populations of the upper and the lower levels become equal; here the medium becomes transparent following the alignment of spins of the atoms in the lower level, an effect observable even in low-intensity radiation. Spin alignment does not necessarily result in complete transparency of the medium. Depending on the spins I and I' and on the angular distribution and polarization of the aligning radiation, we end up with partial loss of opacity or, conversely, partial suppression of transparency to resonance radiation. Moreover, if the ground state has a fine structure, the different magnetic sublevels of the upper state may undergo a population inversion relative to the corresponding lower sublevels as a result of spin alignment, i.e., there is a possibility of coherent amplification of the resonance radiation transmitted through the medium. This effect is possible, e.g., in the case of HI /2/ and OH /4/. Since spin alignment may substantially influence the transmission of resonance radiation, it must not be ignored in the analysis of astrophysical observations, since almost the entire body of our data on the interstellar medium (chemical composition, degree of ionization and excitation, etc.) is derived from observations of transmitted resonance radiation.

DESCRIPTION OF SPIN ALIGNMENT AND TRANSITION PROBABILITIES

Unlike static orientation, which is entirely described by a single parameter $\mu H/kT$, dynamic spin alignment is a complex function of several parameters. The spin state of particles is not always a statistical mixture of states with various M: it may also prove to be a coherent superposition. In the latter case, the spin alignment can be described only in terms of the polarization density matrix, and it is not enough to give the populations of the sublevels with different M. Under astrophysical conditions, however, we are often dealing with systems immersed in a magnetic field such that $kT \gg \mu H \gg \hbar (W_{rad} + W_{col})$, and the spin aligning radiation is a stochastic factor (without regular modulation). The polarization density matrix of atoms and molecules in this case is diagonal in M (with H taken as the quantization axis), and the atomic spin alignment can therefore be described in terms of the population of the magnetic sublevels R_{IM} in a coordinate system with the quantization axis pointing along H. These level populations are determined by the usual system of balance equations:

$$\sum_{I'M'} R_{I'M'} W_{I'M' \to IM} = R_{IM} \sum_{I'M'} W_{IM \to I'M'} , \qquad (7)$$

where $W_{IM \to I'M'}$ are the transition probabilities $IM \to I'M'$.

In every real case, we should consider the actual level diagram and the actual transition probabilities associated with all conceivable factors.

To bring out more clearly the dependence of the resonance spin alignment on the atomic spin characteristics and on the properties of resonance radiation, we will first analyze spin alignment of a system of two-level atoms without hyperfine structure. Let I be the ground-state spin, and I' the excited state spin. The probability of electric or magnetic dipole transitions under the above conditions is entirely determined by three parameters $\rho_\mu(\nu)$ — the diagonal elements of the radiation density matrix at the resonance frequency ν in a representation characterized by the μ-projection of the angular momentum of the photon on the quantization axis:

$$\begin{cases} W_{IM \to I'M'} = \gamma_0 \left(C^{IM}_{I'M'\,1\mu}\right)^2 (1+\rho_\mu) \\ W_{I'M' \to IM} = \gamma_0 \left(C^{IM}_{I'M'\,1\mu}\right)^2 \rho_\mu \end{cases} \qquad \mathcal{E}_{IM} > \mathcal{E}_{I'M'}, \tag{8}$$

where γ_0 is the spontaneous transition probability and $C^{IM}_{I'M'1\mu}$ are the Clebsch—Gordan coefficients. It should be stressed that the transition probabilities $W_{IM-I'M'}$ and hence the populations R_{IM} are independent of the fine features of the angular distribution and the polarization of radiation; substantially different angular and polarization states may have the same parameters ρ_μ. For isotropic unpolarized radiation

$$\rho_1(\nu) = \rho_0(\nu) = \rho_{-1}(\nu) = \frac{I_\nu \lambda^2}{h\nu}, \tag{9}$$

where I_ν is the radiation intensity (erg $\cdot$ cm^{-2} $\cdot$ sec^{-1} $\cdot$ Hz^{-1} $\cdot$ sterad^{-1}).

For a directional beam of polarized radiation

$$\begin{cases} \rho_{\pm 1}(\nu) = \frac{3}{2}\left(\frac{\Delta\Omega}{4\pi}\right)\left(\frac{\lambda^2 I_\nu(\vartheta)}{h\nu}\right)\left[1 \pm \eta\cos\vartheta - \frac{\sin^2\vartheta}{2}\left(1-(-)^\tau \xi \cos 2\alpha\right)\right] \\ \rho_0(\nu) = \frac{3}{2}\left(\frac{\Delta\Omega}{4\pi}\right)\left(\frac{\lambda^2 I_\nu(\vartheta)}{h\nu}\right)\sin^2\vartheta\left(1-(-)^\tau \xi \cos 2\alpha\right) \end{cases}, \tag{10}$$

where η and ξ are the degree of circular and linear polarization; ϑ is the angle between the direction of $\vec{H}$ and the beam; α is the position angle characterizing the linear polarization; $\tau = 1$ for electric dipole transitions and $\tau = 0$ for magnetic dipole transitions.

POPULATION OF MAGNETIC SUBLEVELS

Stationary populations of the magnetic sublevels R_{IM} with any I established by optical pumping through all the possible resonance sublevels, i.e., levels with I' = I — 1, I' = I, and I' = I + 1, were calculated /2/ for arbitrary angular distribution and polarization of the incident radiation. The solutions of the balance equations are shown graphically in Figure 2.

Figure 2 plots the populations of the ground-state sublevels R_{IM} for the principal astrophysical cases of spin alignment by low-intensity unpolarized radiation ($\rho_\mu << 1$). The values of R_{IM} are plotted in polar coordinates as a function of the angle θ between the spin aligning beam and the field vector H for various spin values I and I'. The circle marks

the equilibrium populations R_{IM} for any M which are established in an isotropic medium in the absence of directional radiation beams and particulate fluxes. Figure 2 clearly illustrates the changes in the character and the degree of spin alignment with increasing I for integer and half-integer values for various combinations of I and I'. It is also seen that the populations R_{IM} for $I \geqslant 1$ differ from the equilibrium values for any direction of the aligning beam, except $\vartheta \approx 55°$, when $\sin^2 \vartheta = 2/3$ and $\rho_1 = \rho_0 = \rho_{-1}$. In the case $I' = I - 1$ and $\vartheta = 0$, the maximum population is characteristic of the sublevels with the minimum $|M|$ (0 or $1/2$), whereas for $\vartheta = \pi/2$, conversely, the levels with $|M| = 1$ have the largest population. In particular, for $I = 1$ and $\vartheta = 0$, all the atoms are concentrated on the $M = 0$ sublevel.

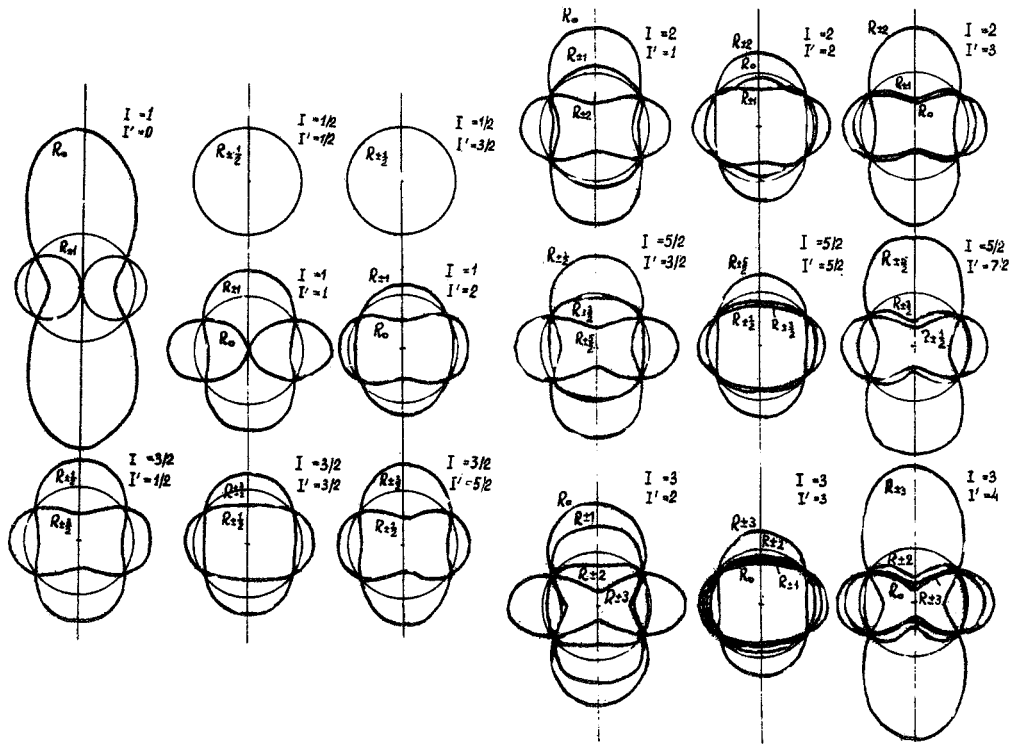

FIGURE 2. The population of the ground-state sublevels R_{IM} established by optical pumping in a beam of unpolarized radiation directed at an angle θ to the magnetic field (polar coordinates; I and I' are the spins of the ground state and the excited state, respectively).

It is also significant that for $I \gg 1$ and $I' \geqslant I + 1$, $\theta = 0$, virtually all the atoms are concentrated in the state with $|M| = 1$. This case is significant for the problem of optical spin alignment by molecules with a rotational structure of energy levels. Figure 2 makes it possible to find the populations R_{IM} in a more general case, when the radiation has an arbitrary angular distribution and an arbitrary degree of linear polarization, since then the entire dependence is determined by a single parameter, the ratio

of $\rho_+ = \rho_-$ to ρ_0 corresponding to a well-defined value of the angle θ:

$$\rho_+/\rho_- = \frac{1}{2}(\sec^2\theta - 1). \tag{11}$$

The results of calculations shown in Figure 2 permit assessment of populations of the magnetic sublevels of the ground state R_{IM} in a multilevel system under optical pumping by a continuous-spectrum radiation, without solving the balance equations. If the resonance levels with equal I' play the main role, the resulting populations R_{IM} are the same as for a single resonance level with I', irrespective of the actual number of the resonance levels. In a general case, on the other hand, the relative contributions from all the resonance levels with I' = I − 1, I' = I, and I' = I + 1 should be known.

The preceding results also make it possible to evaluate the spin alignment of atoms and molecules as a result of their interaction with a directed beam of fast electrons or protons, since the field of a fast charged particle is largely equivalent to the field of a transverse electromagnetic wave.

A METHOD FOR DETERMINING THE DIRECTION OF $\vec{H}$

Allowance for spin alignment of atoms and molecules in the interstellar medium introduces significant corrections in the determination of partial density, degree of excitation, etc. It also provides, however, qualitatively new information on the anisotropy of physical conditions in a given astrophysical system and primarily on the anisotropy of the radiation field. The dependence of the populations R_{IM} of the magnetic sublevels established by optical pumping on the direction of the magnetic field $\vec{H}$ enables us to apply this effect to the determination of the direction of $\vec{H}$ in a given region of space. This method is applicable to the case of weak fields, when all other optical methods fail. Let us consider a particular example.

The D_1 (λ = 5896 Å) and D_2 (λ = 5890 Å) lines in the spectrum of comets are produced by single scattering of the solar radiation by the Na I atoms in the cometary atmospheres. The intensity ratio of these lines clearly depends on the scattering angle, i.e., it is determined by the differential scattering cross sections. The D_1 line is unpolarized, and its angular distribution function is spherically symmetric, irrespective of the direction of the field $\vec{H}$ or the occupancy of the magnetic sublevels R_{FM}. The situation is different for the D_2 line: this line shows partial linear polarization. The degree of polarization and the angular distribution function of D_2 are significantly anisotropic and both depend on the occupancy R_{FM} of the hyperfine-structure magnetic sublevels F = 1 and F = 2($3S_{1/2}$) of the Na I ground state. The spins of the Na I atoms in the cometary atmosphere are aligned through the scattering of the resonance solar radiation.

We calculated the occupancies R_{FM} of the magnetic sublevels F = 1 and F = 2($3S_{1/2}$). All the resonance levels of Na I were taken into consideration and allowance was made for the interference effects associated with the partial overlap of the hyperfine structure sublevels of the excited states. The table lists resulting R_{FM} values for the two extreme cases: with $\vec{H}$ directed along the comet—Sun radius-vector ($\theta = 0°$ or $\theta = 180°$) and at right angles to this radius-vector ($\theta = 90°$). For $0 < \theta < 90°$ (or $180° > \theta > 90°$), R_{FM} varies monotonically between its extreme values, reaching $R_{FM} = 1.000$ at

$\theta \simeq 55°$. We see from the table that natural optical pumping may shift the occupancies R_{FM} of the individual sublevels by as much as 30% from the corresponding equilibrium values. The R_{FM} values are uniquely related to the angular distribution of the two linearly polarized components of the D_2 line. Measuring the D_1/D_2 intensity ratio and the degree of polarization of D_2, we can find the two angles characterizing the effective direction of $\vec{H}$ in the part of the interplanetary space where the head of the comet moves at the given time. In this case, the Doppler line width $\nu_0(\nu_T/c) \sim 10^8 - 10^9$ Hz is much greater than the Zeeman splitting $\mu H/h \sim 10^2$ Hz. Therefore, the usual optical method of measuring $\vec{H}$ from the degree of circular polarization at the line wings is inapplicable in practice. The magnitude of $\vec{H}$ can be found by measuring the rotation of the plane of polarization; in the absence of $\vec{H}$ the scattered radiation is polarized at right angles to the scattering plane, whereas in the presence of $\vec{H}$ the plane of polarization is turned through an angle $\Delta\alpha \sim \mu H_1 \tau/\hbar$, where H_1 is the component of $\vec{H}$ in the direction of observation, and τ is the lifetime of the atom in the excited state. Lines with large lifetimes τ should be used in this case.

It is hoped that continuous measurements of relative line intensities and line polarizations in the spectra of comets at various points of their orbit will eventually establish the exact extent of the regular magnetic field around the Sun. Note that direct measurements from space vehicles are practicable only inside a fairly small region near the Earth's orbit, whereas comets provide us with a much simpler and cheaper probe for studying the magnetic field geometry over distances from about 0.3 a.u. to about 3 – 5 a.u., both inside and outside the plane of the ecliptic.

R_{FM} values for $\theta = 0°$ and $\theta = 90°$

F, M	R_{FM} (θ = 0°)	R_{FM} (θ = 90°)
2, ±2	1.306	0.878
2, ±1	0.845	1.037
2, 0	0.787	1.139
1, ±1	0.999	1.011
1, 0	0.913	1.020

Bibliography

1. Kastler, A.— J. Phys. et radium, 11:255. 1950.
2. Varshalovich, D.A.— Astronomicheskii Zhurnal, 42:557. 1965; ZhETF, 52:242. 1967; Astrofizika, 4:519. 1968; ZhETF, 59:535. 1969.
3. Bernheim, R. Optical Pumping. New York. 1965.
4. Perkins, F., J. Gold, and E. Salpeter.— Astrophys. J., 145:361. 1967.

RADIATION TRANSFER IN SPACE PHYSICS

Yu. N. Gnedin and A. Z. Dolginov

I. Space physics is one of the most rapidly developing areas of modern science, using a wide range of theoretical and experimental methods. One of the principal subdivisions of space physics deals with the problems of interaction of radiation with matter in the interplanetary space, where the term "radiation" covers both optical and corpuscular radiation, such as hard gamma quanta, electrons, neutrons, protons, etc. The problem of interaction of radiation with matter is one of the traditional subjects in physics, known as the theory of radiation transfer. We distinguish between three classical directions in the theory of radiation transfer. One of these, which has received its maximum development in astrophysics, is concerned with the transmission of visible light (the optical range of wavelengths) through the atmospheres of stars, planets, and nebulae /1, 2/. Another direction, more closely related to the physics of nuclear reactors, deals with the moderation and thermalization of neutrons in solid and gas targets /3–5/. Finally, the third direction investigates multiple scattering of electrons in thick targets /6/. Each of these directions operates with its own tools, which are only seldom applicable to the other directions.

The problem of radiation transfer in space physics differs from the classical theory of radiation transfer not only in terms of the specific physical conditions but also in the more general formulation of the problem and the application of more general methods. This is so primarily because in space physics we are dealing with a wide range of various radiations covering a wide spectrum of energies (the classical methods of the theory of radiation transfer are always adapted to one particular type of radiation in a definite range of energies). Another reason is provided by the specific conditions prevailing in outer space: the interplanetary magnetic field and the interplanetary plasma are highly significant factors.

The characteristic features of radiation transfer in space physics emerge most vividly in the following problems:

1. The problem of propagation of galactic and solar cosmic rays through the interplanetary magnetic field. A detailed analysis of this problem was given in /7–10/.

2. The study of the generation mechanisms of various plasma waves and their propagation through the solar and the interplanetary plasma. A number of topics related to this problem were considered in /11, 12/. Some topics associated with the transmission of solar radiation through planetary atmospheres and the construction of models of planetary atmospheres are treated in /13, 14/.

3. The investigation of physical processes in cometary atmospheres, which is closely linked with the general problem of interaction of radiation with an expanding gas in a vacuum. The solution of this problem for comets was given in /15/.

We will consider in detail the following two problems.

The determination of the composition of planets and other celestial bodies is one of the most important tasks of space physics. The necessary information is obtained by measuring the total flux and the energy spectrum of radiation leaving the surface of the celestial body. The outgoing radiation may originate either from the decay of radioactive elements entering the composition of the planets or from the interaction of the planetary material with hard solar radiation and cosmic rays. The cosmic rays hitting the planet trigger certain nuclear reactions whose products are neutrons and hard gamma radiation. Significant information can be obtained by measurements of the neutrons produced in the surface layer. The validity of the method of measurement of surface radiations for obtaining information on the chemical composition of planets, in particular lunar rocks, was indicated in a number of published studies /16–20/ and in the paper by S.V. Viktorov, G.V. Kir'yan, and G.E. Kocharov at the Fifth All-Union School of Space Physics in Apatity (1968).

Orbiting stations and space vehicles have by now measured the X-ray and the gamma-ray spectrum of the lunar surface. The results of these measurements were published in /21, 22/.

Neutron measurements probe the composition of surface rocks to a much greater depth than the analysis of other radiations does. Neutrons are moreover highly sensitive to the presence of hydrogenous material. Observations of the neutron flux from planets shrouded in thick atmospheres, carried out outside the Earth's atmosphere, will provide valuable information on the composition of the planetary atmospheres. The problem thus reduces to the determination of the spectrum and the angular distribution of the neutrons emitted by the planetary surface.

The second important problem is concerned with the interaction of protons with the Earth's atmosphere. Protons penetrating into the atmosphere cause Balmer emission in the polar aurorae. Observations established that the H_α, H_β, and H_γ lines had wide contours which could be interpreted as Doppler broadening of the spectral lines of atomic hydrogen produced as a result of charge exchange processes between the protons and the atmospheric atoms and molecules. Extensive literature has been published /23, 24/ in which the energy and the angular distributions of the incoming protons is derived from the observed profiles of hydrogen emission lines. The reliability of the proton energy distributions recovered in this way is highly questionable, however: on the one hand, our knowledge of the effective cross sections of a number of processes which play an important role in the generation of moving excited hydrogen atoms is deficient and, on the other hand, the entire problem of distribution of protons and neutral hydrogen atoms in multiple charge exchange processes has not been solved. The difficulty is that protons interacting with the atmospheric gases capture electrons from the gas atoms and are thus converted to hydrogen atoms. The hydrogen atoms formed in this way change the direction of their linear momentum and lose energy while interacting with the target atoms, become ionized again, and so on.

Since at energies below 30 keV the charge exchange cross section for protons with the atoms of various gases is several times greater than the ionization cross section of atomic hydrogen, the proton spends a substantial proportion of its life as a neutral hydrogen atom, colliding several times with the target atoms. Multiple scattering of neutral hydrogen atoms therefore significantly influences the energy and the angular distribution of protons in the medium. The determination of the energy spectrum of protons penetrating into the upper atmosphere near the poles is of great importance in the physics of the atmosphere and nearby space. Once this spectrum is determined, we will be able to assess the effect of the auroral protons in the heating up and ionization of the polar upper atmosphere.

Finally, another important problem in the physics of interplanetary space is concerned with the interaction of ultraviolet radiation of the Sun ($L_y-\alpha$) with the interplanetary neutral hydrogen. Observations of the scattered $L_y-\alpha$ radiation so far provide the only source of information concerning the neutral hydrogen in the space around the Sun. Some topics pertaining to this problem were considered in /25/. Thus, even a partial listing of the main problems of space physics immediately reveals the significance of multiple scattering, or radiation transfer.

II. Multiple scattering is generally described by the so-called transfer equation, which is derived from considerations of particle flux balance:

$$\vec{n}_1 \nabla I_i(\vec{r},\vec{P}_1) = -N_0\sigma_{0i}(P_1)I_i(\vec{r},\vec{P}_1) + \sum_{\kappa}\int d\vec{p}\, W_{i\kappa}(\vec{P}_1,\vec{p})\, I_\kappa(\vec{r},\vec{p}) + Q_i(r,\vec{P}_1). \qquad (1)$$

Here $I_i(\vec{r},\vec{P}_1)$ is the intensity of the scattered particles. It gives the number of particles (photons, electrons, atoms) in a given state i with momentum $\vec{P}_1$ passing in unit time through a unit area at point $\vec{r}$ at an angle ϑ_1 to the given direction $\vec{n}_0$;

$$W_{i\kappa}(\vec{P}_1,\vec{p}) = \frac{N_0(1+\gamma)^2}{mP_1}\sigma_{i\kappa}(\vec{P}_1,\vec{p})\,\delta\left[\frac{P_1^2}{2m} - \frac{p^2}{2m} + \frac{(\vec{P}_1-\vec{p})^2}{2M} + \varepsilon_i - \varepsilon_\kappa\right], \qquad (2)$$

where $W_{i\kappa}$ is the transition probability of the incident particle from state κ with momentum $\vec{p}$ to state i with momentum P_1; δ is a function which ensures the conservation of energy in single scattering; $\sigma_{i\kappa}$ is the differential cross section for the transition of the particle from state κ with momentum $\vec{p}$ to state i with momentum $\vec{P}_1$. It is related in the usual way to the quantum-mechanical transition amplitude A of the particle:

$$\sigma_{i\kappa}(\vec{P}_1,\vec{p}) = \sum_n A^+_{in}(\vec{P}_1,\vec{p})\, A_{n\kappa}(\vec{P}_1,\vec{p}), \qquad (3)$$

where m is the mass of the incident particles, M is the mass of the target atom.

The factor $(1+\gamma)^2(m\vec{P}_1)^{-1}$ arises from the normalization of $W(\vec{P}_1,\vec{p})$ to a quantity equal to the reciprocal of the range of the incident particle:

$$\sum_i \int d\vec{P}_1\, W(\vec{P}_1,\vec{p}) = N_0\sigma_0(P), \qquad (4)$$

where N_0 is the concentration of the scattering atoms in the medium.

The first term in the right-hand side of equation (1) describes the loss of particles in state i with momentum $\vec{P}_i$ as a result of collisions with target atoms, and the second term describes the addition of particles to this state. The third term $Q_i(\vec{r}, \vec{P}_i)$ describes the flux of incident particles undergoing multiple scattering (the particle source).

What are the physical quantities characterizing the transfer equation? First it follows from the transfer equation (1) that the scattering intensities add up at any point in the scattering medium (the balance of particle fluxes) and no effects are observed associated with the wave nature of the incident particles. Further, the transfer equation includes the cross sections of elementary processes. It is readily seen that if the characteristics of the medium depend only on the one coordinate x, the transfer equation is qualified by a single nondimensional combination $L(x) = \int_0^x N_0(x)\sigma_0 dx$ which is known as the optical thickness (or optical depth) in the theory of light scattering.

On the other hand, from the point of view of quantum mechanics, the interaction of a beam of particles with target atoms is a wave-mechanical effect, described as wave functions, wave packets, phases of the wave function, interference, etc. The transfer equation thus only provides an approximate description of multiple scattering, and the conditions of its applicability must be clearly formulated. Certain attempts have been made to "canonize" the transfer equations and thus use it in problems where the strict applicability conditions are not satisfied (we should be particularly careful in plasma physics). Other authors — especially astrophysicists — often try to solve the transfer equation with an excessive accuracy which does not fit within the restricted framework of its applicability.

III. We will start with the principal condition of applicability of the transfer equation: the wavelength λ of the incident radiation should be much less than the total range Λ of the particle in the medium ($\lambda \ll \Lambda$). When this condition is satisfied, waves scattered by different force centers do not interfere. Indeed, the attenuation of the incident coherent beam is caused, on the one hand, by true absorption in collisions and, on the other hand, by large-angle scattering of particles (i.e., large momentum transfer). The coherence is broken in this process, i.e., waves scattered by different force centers cannot interfere and are lost from the coherent beam. We can estimate the scattering angles for which the coherence is not broken. The angle should be such that the momentum transfer $P\vartheta$ falls inside the quantum-mechanical uncertainty in the momentum, ΔP. Although a plane monochromatic wave ($\Delta P = 0$) hits the target, the uncertainty inside the scattering volume is other than zero. The spatial position of the particle is pinpointed by the scattering events, and it therefore cannot have a definite momentum. The mean distance between scattering events is of the order of Λ, so that $\Delta P\Lambda \sim 1$ (the uncertainty relation). Hence $\Delta P \sim \Lambda^{-1}$, i.e., $P\vartheta \sim \Lambda^{-1}$ or $\vartheta \sim \lambda/\Lambda$. If $\lambda \ll \Lambda$, interference effects can be ignored virtually in the entire range of angles and we may use the transfer equation. The applicability conditions of the transfer equation were studied in detail in /26, 27/.

IV. Although the transfer equation was originally derived about 50 years ago, the analytical solution was obtained in very few cases only. The classical problem of the theory of radiation transfer is the problem of a point source in an infinite medium. If a finite medium is to be considered (even in the case of scattering without energy losses), substantial mathematical difficulties arise and no analytical solution can be found. Although

the application of numerical techniques is very helpful, they obscure the qualitative picture of the phenomenon. We will therefore proceed with a qualitative treatment of multiple scattering of a particle (or a quantum) in a medium. For simplicity, we start with the case of scattering which does not involve substantial energy losses ($\gamma \ll 1$).

First let us introduce the physical parameters describing multiple scattering. Let $\sigma_s = \int d\vec{n}\,\sigma(\vec{n}\vec{n}_0)$ be the total scattering cross section of a particle in a single collision, σ_0 the total collision cross section, including true absorption, $\varepsilon = \sigma_s \sigma_0^{-1}$ a parameter characterizing the scattering probability in a single collision, $1-\varepsilon$ a quantity characterizing the probability of true absorption in a single interaction event. For a medium without absorption, ε is equal to unity. In general, ε is a function of energy, radically influencing the energy and the position distribution of the particles in the medium.

Let us now introduce a parameter describing the angular distribution of particles in the medium. This angular scattering function is defined as $\varkappa(\vec{n}_1\vec{n}_0) = \sigma(\vec{n}_1\vec{n}_0)\sigma_0^{-1}$. If the scattering cross section is isotropic, the angular scattering function is a constant number, equal to $(4\pi)^{-1}$. A particle may move from one point in the medium to another either by direct flight, without scattering, or as a result of multiple collisions ("diffusion").

The radiation density at a point 2 is expressed by the equality $n(x) = (\varepsilon/4\pi)\int I(\vec{n}_1\vec{n}_0; x)\,d\vec{n}_1$ which can be developed to the form

$$n(x) = e^{-x} + C(\varepsilon)\exp(-\beta x). \tag{6}$$

The distance x is measured in units of the total range of the particle in the medium. $C(\varepsilon)$ is a constant which depends on ε. $\beta = \beta(\varepsilon)$ is the reciprocal of diffusion. For simplicity, the radiation density at point 1 is taken equal to unity (again an infinite medium is considered). β is a highly important physical quantity in the theory of radiation transfer: it describes the process of multiple scattering. Whereas the total range of the particle in the medium, Λ, gives the mean distance covered by the particle to its first collision, irrespective of whether this is scattering or true absorption of the particle, the diffusion length determines the mean distance traversed by the particle to the first true absorption event. The total range thus corresponds to the loss of the particle from the beam following a collision event (scattering or true absorption), whereas the diffusion length specifies the mean distance that the particle covers before it is annihilated by true absorption. It is clear from physical considerations that the diffusion length depends on the probability of true absorption of a particle. If the true absorption is low, $1-\varepsilon \to 0$, the diffusion length increases indefinitely, $\beta \to 0$. If the elastic scattering cross section is small and all the processes in the medium are determined by true absorption, $\varepsilon \ll 1$, the diffusion length is equal to the total range of the particle in the medium, since in this case true absorption provides the only mechanism for knocking particles out of the beam. Calculation of the reciprocal diffusion length for the case of low true absorption, $1-\varepsilon \ll 1$, gives

$$\beta = \left[\frac{3(1-\varepsilon)}{\varepsilon}\left(1 - \frac{\varepsilon}{3}\varkappa_1\right)\right]^{\frac{1}{2}}, \tag{7}$$

where $\varkappa_1$ is the coefficient in the expansion of the angular scattering function in Legendre polynomials $\mathcal{P}_\ell(\vec{n}_1\vec{n}_0)$ with $\ell = 1$:

$$\varkappa(\vec{n}_1\vec{n}_0) = \frac{1}{4\pi}\sum_\ell \varkappa_\ell \mathcal{P}_\ell(\vec{n}_1\vec{n}_0). \tag{8}$$

We thus have the following expression for the diffusion length squared Λ_d^2:

$$\Lambda_d^2 = \frac{1}{3(1-\varepsilon)}\Lambda\Lambda_T\ , \tag{9}$$

where Λ_T is the transport length, defined as the mean range of the particle for large-angle scattering ($\vartheta_1>0$):

$$\Lambda_T = \varepsilon\Lambda\left[\int d\vec{n}_1(1-\vec{n}_1\vec{n}_0)\,\varkappa(\vec{n}_1\vec{n}_0)\right]^{-1}. \tag{10}$$

The diffusion length is thus directly proportional to the square root of the product of the mean free path and the transport length. Given the diffusion length, we can assess the contribution from pure scattering and true absorption to multiple scattering without solving the transfer equation. Consider a plane target of thickness x_0. Then if $x_0\Lambda_d^{-1} \equiv \beta\,(x_0/\Lambda) \gg 1$, the particles are lost from the beam mainly on account of true absorption. If $x_0\Lambda_d^{-1} \ll 1$, pure scattering is the main factor in multiple scattering events.

Let us now consider the variation of radiation density (see (6)) at large distances from the radiation source ($x\to\infty$) if $1-\varepsilon \ll 1$, i.e., when the true absorption in a single collision is unlikely. It is readily seen that for $x\to\infty$ and $1-\varepsilon \ll 1$,

$$n(x) \to C(\varepsilon)\exp(-\beta x),$$

i.e., in an infinite medium particles diffuse over large distances from the source. Regarding the angular distribution of scattered particles, simple physical considerations show that diffusion leads to definite isotropization of the angular distribution irrespective of the particular angular scattering function of each individual force center. Deep inside the medium, the scattering intensity $I(\vec{n}_1\vec{n}_0;x)$ has the form

$$I(\vec{n}_1\vec{n}_0;x) = I_0(x) + I_1(x)\vec{n}_1\vec{n}_0, \tag{11}$$

where $I_1(x) \ll I_0(x)$.

If the medium is characterized by pure scattering, i.e., $1-\varepsilon \ll 1$, and the optical thickness is high $x_0\Lambda^{-1} \gg 1$, the angular distribution of the transmitted radiation is nearly isotropic; it is adequately described by the formula $1 + {}^3/_2\cos\vartheta_1$. The approximate expression $1 + 1.5\cos\vartheta_1$ describes with fair accuracy the angular distribution of the outgoing radiation at angles between 60° and 90°. The largest error (~14%) is observed at angles close to 0°. The angular distribution function $1 + {}^3/_2\cos\vartheta_1$ has a simple physical meaning. Calculation of the particle flux reaching the target surface $x = x_0$ in case of this angular distribution gives zero: $\int_0^1 d\cos\vartheta_1\left(1-\frac{3}{2}\cos\vartheta_1\right)\cos\vartheta_1 = 0$. This result is often used as a boundary condition in the calculation of physical processes in nuclear reactors (the so-called Marshak boundary condition).

In a high-absorption medium ($\varepsilon \ll 1$), the intensity of scattered radiation at angles $0 \leq \vartheta_1 \leq \pi/2$ is determined by the direct transmitted beam, decreasing exponentially with the diameter of the scattering system: $\exp(-x_0 \Lambda^{-1})$. This result corresponds to the case of low diffusion, when scattering is entirely determined by "fly-through" particles. As the absorption decreases, the contribution from diffusion becomes more significant, and the intensity of scattered radiation starts decreasing more slowly with the increase in system diameter: $\exp(-x_0 \Lambda_d^{-1})$, where $\Lambda_d > \Lambda$. Finally, in a pure scattering medium ($1-\varepsilon \ll 1$) without absorption, diffusion makes the scattered intensity inversely proportional to the thickness of the scattering volume, provided it is greater than the mean free path of the particle in the medium to start with. The intensity of reflected radiation in this case is equal to the intensity of reflection from a semi-infinite space plus terms of the order Λx_0^{-1}.

V. Let us consider the multiple scattering of particles in a plane material layer with allowance for the slowing down caused by collisions. We will concentrate on particles which lose a considerable part of their energy in these collisions, so that the energy E_1 is much less than the initial energy E_0. The physical parameter characterizing the slowing-down properties of the medium is the so-called moderation length $\tau\Lambda$, where $\tau^2 = (6\gamma)^{-1} \ln(E_0/E_1)$. This is the analog of the diffusion length in monoenergetic transport of particles. We recall that $\gamma = m M^{-1}$ is the ratio of the incident particle mass to the mass of a scattering atom. In what follows, we invariably take the incident particle to be much less massive than the target atom.

Note that the angular distribution of particles which have lost a substantial proportion of their initial energy is independent of energy in a fairly wide range. This is so because the angular distribution is mainly shaped at distances of the order of the total free path from the layer boundary, whereas the slowing down mainly occurs in the process of diffusion, which only "smoothes out" the angular distribution. The angular distribution of the outgoing radiation is adequately described by the function $1 + 1.5 \cos \vartheta_1$; the radiation emerging through $x = 0$ and $x = x_0$ has the same angular distribution. This is so because the two interfaces are virtually equivalent with regard to the highly moderated particles which form deep inside the scattering medium and diffuse in all directions. The anisotropy in the angular distribution, which develops near the layer boundaries, is therefore virtually equal for the radiation emerging through the interfaces $x = 0$ and $x = x_0$.

The number of particles of a given energy emerging through $x = x_0$ depends on the thickness of the layer, reaching a maximum for $x_0 \simeq \Lambda\tau$. The energy spectrum of these particles is described by

$$\frac{dn(E_1, x_0)}{dE_1} \sim \left(\frac{x_0}{\Lambda}\right)^2 \frac{1}{E_1 \tau^5} \exp\left[-\frac{x_0^2}{4\Lambda^2\tau^2} - \frac{1-\varepsilon}{2\gamma\varepsilon} \ln \frac{E_0}{E_1}\right]. \qquad (12)$$

For layer thicknesses less than $\tau\Lambda$, the particles are not slowed down to the energy E_1, and in thicker layers they are slowed down to lower energies. For $\Lambda\tau \ll x_0$ we have particles which, for a given energy loss, propagate very far from the boundary of the region where the radiation sources are contained. It follows from (2) that the smaller the scattering angle, the

smaller are the energy losses in collision. Therefore, for $x_0 \gg \tau\Lambda$, the particles emerging from the plane layer have mainly lost a small fraction of their initial energy and their angular distribution is prominently stretched in the forward direction.

The intensity of the radiation emerging through the interface $x = 0$ significantly depends on the relationship between the characteristic dimension L of the region containing the radiation sources and the moderation length of the particles in the medium. Thus, if the moderation length $\tau\Lambda$ is much greater than L, the energy spectrum of the radiation is given by

$$\frac{dn(E_1,0)}{dE_1} \sim \frac{1}{E_1\tau^3} \exp\left(-\frac{1-\varepsilon}{2\gamma\varepsilon} \ln \frac{E_0}{E_1}\right). \tag{13}$$

If the moderation length is much smaller than the characteristic dimension of the source region, the energy spectrum of the radiation emerging through the $x = 0$ interface is given by

$$\frac{dn(E_1,0)}{dE_1} \sim \frac{1}{E_1\tau} \exp\left(-\frac{1-\varepsilon}{2\gamma\varepsilon} \ln \frac{E_0}{E_1}\right). \tag{14}$$

Note that the dependence of the number of scattered particles on the reciprocal value of the mean atomic weight of the entire medium is also determined by the relationship between the moderation length $\tau\Lambda$ and the size of the source region (the generation length) L. Specifically, $n(E_1, x=0) \sim \sqrt{\gamma}$ if $L \ll \tau\Lambda$ and $n(E_1, x=0) \sim \gamma^{-1/2}$ if $L \gg \Lambda\tau$. A detailed theory of the slowing down of particles in matter is presented in /3, 28/.

VI. Let us now consider the determination of the energy spectrum and the neutron flux produced by the interaction of cosmic radiation with the surface of celestial bodies. The energy spectrum of the galactic cosmic protons is peaked at 1 BeV. The interaction of high-energy particles (protons, neutrons, pions) with the nuclei of elements is currently the subject of theoretical and experimental studies /29, 30/, and very few details are available at present. Experimental investigations show that the interaction of a high-energy particle with a nucleus proceeds in two stages. During the first stage, the incident particle creates a cascade inside the nucleus. The cascade releases several nucleons from the nucleus with energies substantially higher than 10 MeV and with an anisotropic angular distribution. At the same reaction stage neutral and charged pions are created, which interact with the nuclei and trigger other nuclear reactions releasing fast nucleons. At the second stage of the reaction, the nucleus remaining after the ejection of the fast nucleons "relieves" itself of the excitation by a characteristic evaporation mechanism. In the course of evaporation, the nucleus emits neutrons with an isotropic angular distribution and an energy spectrum $E_0^{\ell-1}\theta^{-\ell}\exp(-E_0\theta^{-1})$ /30/, where E_0 is the energy of the evaporating neutrons, $\theta \sim 1$ MeV (evaporation temperature), $\ell = 16/11$. The cascade nucleons created during the first stage of the nuclear reaction produce in their turn evaporating neutrons through (n,n') and (p,n') reactions. The source function in our problem thus describes isotropically distributed evaporating neutrons. In what follows, we will require some detailed information regarding this source. We will be dealing with neutrons whose energy E_1 is substantially less than the initial

energy E_0. These neutrons do not originate in the source: they are produced as a result of multiple scattering and slowing down in the medium.

The following three problems associated with neutron radiation attract considerable attention at this stage. The first problem deals with the determination of neutron radiation generated in terrestrial rocks by the action of secondary nucleons which are produced in the atmosphere and then reach the Earth /31/. This problem is of considerable significance for the purposes of neutron logging on the Earth, since the natural neutron background has to be determined with high accuracy. The second problem is concerned with the determination of the spectrum of epithermal neutrons produced by the cosmic rays in the Earth's atmosphere. The third problem aims at a determination of the composition of lunar rocks from the neutron radiation emitted from the surface of the Moon. This problem was studied in some detail by the present authors in collaboration with A.I. Tsygan /32/, and also in /20/. As an illustration, let us estimate the flux of neutrons with energies from 1 eV to several MeV leaving the surface of the Moon. Using the equations of the previous section, we write

$$n(E_1, E_2) = 2j\kappa L^{-1}(\tau_1 - \tau_2), \tag{15}$$

where j is the flux of incident cosmic protons, κ is the number of 10 MeV neutrons generated by a single proton and then slowed down in the medium (the source neutrons), L is the generation length of these neutrons (the characteristic dimension of the source region). The most difficult point in flux determination is the calculation of κ and L, which essentially depend on the particular interaction of the proton with the nucleus. We will not consider this problem, although it is definitely solvable /30/. Using (15) and the SURVEYOR-5 data on the composition of the lunar surface /33/, we can estimate the neutron flux emerging from the surface of the Moon. In accordance with the SURVEYOR-5 data, the predominant elements in the composition of the lunar surface at the mooning site were oxygen (58±5)% and silicon (18.5±3)%. We will therefore carry out the numerical calculations for the compound SiO_2, which in all probability is a component part of the lunar rocks. Taking the peak energy in the spectrum of evaporating neutrons as the initial neutron energy ($E_0 \sim 4$ MeV) and using $E_1 \sim 4$ eV for the final energy, we find $n = 0.62\ j\kappa = 10\ \mathrm{cm}^{-2}\mathrm{sec}^{-1}$. Let us evaluate the effect of hydrogen impurity on the outgoing neutron flux. The mean reciprocal mass number of a mixture of elements is given by

$$\bar{\gamma} = \frac{1}{2} C_H + \sum_i \gamma_i C_i, \quad C_i = \frac{N_0 \sigma_{0i}}{\sum_i N_{0i} \sigma_{0i}}, \tag{16}$$

where N_{0H} is the hydrogen concentration, N_{0i} is the concentration of the i-th element.

Consider a mixture of Si with 0.6% H. Then from (16) $\bar{\gamma} = 1/14$, whereas for pure Si, $\gamma = 1/28$. We thus see that even a small hydrogen impurity substantially influences the neutron flux, reducing it approximately by a factor of 1.5 – 2. This reduction of neutron flux at energies between 4 eV and 4 MeV occurs because of the high elastic scattering cross section of hydrogen for neutrons. As a result, hydrogen acts as a highly effective neutron moderator, slowing down the neutrons to energies below 4 eV.

Note that a mixture containing 99.4% Si and 0.6% H has the same slowing down properties as pure nitrogen.

Heavy element impurities increase the neutron flux. This flux increase is associated with the fact that the mean number of evaporating neutrons per heavy nucleus is approximately one order of magnitude higher than for the light nuclei. For example, a 10% lead impurity in SiO_2 roughly doubles the neutron flux.

VII. A complete solution of the problem of interaction of cosmic protons with the Earth's atmosphere requires knowledge of the distribution function of protons and neutron hydrogen atoms in the atmosphere. Strictly speaking, we have to solve a set of two couplet rate equations for the distribution function, allowing for the possible transition of the proton into the neutron hydrogen state as a result of charge exchange and for a reverse transition as a result of ionization. Detailed analysis of the physical features of the process, however, will substantially simplify our solution.

The main components of the upper atmosphere at altitudes of 150 – 500 km are atomic oxygen, molecular oxygen, and molecular nitrogen. Now, the charge exchange cross sections of protons in these gases with the production of an excited hydrogen atom is much lower than the cross section for charge exchange producing a ground-state hydrogen atom. It therefore seems that neutral hydrogen is produced in the ground state and is then excited by inelastic collisions with the atmospheric gases. We can also ignore the difference in the translational energy of the excited hydrogen atoms produced by various inelastic collisions and radioactive transitions. This approximation is quite justified since the energy of protons and hydrogen atoms in the Balmer emission region is two orders of magnitude higher than the excitation energy. Finally, the most important factor is that the mean free path of a neutral hydrogen atom in the atmosphere is much longer than the mean free path of a proton. This result clearly emerges from the table, borrowed from /34/. Let us compare the energy losses over the mean free path of a neutral hydrogen atom and a proton, respectively. The energy lost by a neutral hydrogen atom over its mean free path is obtained using (31) from the equality $2\tau = 1$:

$$\tau = \sqrt{\frac{1}{6\gamma} \ln \frac{E_0}{E_1}} = \sqrt{\frac{1}{6\gamma}} \sqrt{\ln \left(1 + \frac{\Delta E}{E_1}\right)}.$$

Mean free path of a proton and a neutral hydrogen atom in the Earth's atmosphere, km

Height, km	$H^+ \to H$	$H \to H^+$
700	9900	
600	4300	
500	490	10,000
400	98	2000
300	19	300
200	4	30
180	2	
150	1	5
120	0.2	

The condition $4\tau^2 = 1$ gives $\Delta E/E_1 \approx {}^3/_2\,\gamma \sim 1/9$ for the atmosphere. Thus, a neutral hydrogen atom loses about $^1/_9$ of its initial energy over the free mean path. The energy losses of protons can be found from the results of /35/: a proton with energies between 1 and 30 keV loses to ionization events about 100 eV in each collision. We see that the main energy losses are associated with the neutral hydrogen atoms, so that the angular and the energy distribution of protons in the medium is determined by the scattering and the slowing-down of the neutral hydrogen atoms produced in charge exchange reactions.

The angular and the energy distribution of protons and neutral hydrogen atoms thus can be determined directly from equations (12) and (13). Using these equations, we can also determine the intensity of Balmer emission and the energy spectrum of the original proton beam. In accordance with the preceding theory, the angular distribution of the neutral hydrogen atoms is described by $1 + \alpha \cos \vartheta_1$, $\alpha \leq {}^3/_2$. Some authors /23, 24, 36/ determined the angular distribution of protons from the angular distribution of the Balmer emission. The experimental data lead to an angular distribution of the form $1 + \alpha \cos \vartheta_1$, $0 \leq \alpha \leq 2$, but the data are insufficient for an exact determination of the coefficient α. It is hoped that satellite and rocket measurements in the very near future will provide direct data on the distribution function of penetrating protons, which can be used as a basis of comparison with the theory.

Bibliography

1. Chandrasekhar, S. Radiative Transfer.— New York-Denver. 1960.
2. Sobolev, V.V. Perenos luchistoi energii v atmosferakh zvezd i planet (Radiant Energy Transfer in Stellar and Planetary Atmospheres).— Moskva, Gostekhizdat. 1956.
3. Davison, B. Neutron Transport Theory.— Clarendon Press, Oxford. 1957.
4. Weinberg, A.M. and E.P. Wigner. The Physical Theory of Nuclear Chain Reactors.— Chicago, Univ. of Chicago Press. 1958.
5. Galanin, A.D. Teoriya yadernykh reaktorov na teplovykh neitronakh (Theory of Thermal-Neutron Nuclear Reactors).— Moskva, Atomizdat. 1959.
6. Scott, W.T.— Rev. of Mod. Phys., 35:231. 1963.
7. Dolginov, A.Z. and I.N. Toptygin.— ZhETF, 51-1771. 1966.
8. Dolginov, A.Z. and I.N. Toptygin.— Geomagnetizm i Aeronomiya, 7:967. 1967.
9. Parker, E.N.— Phys. Rev., 110:1445. 1958.
10. Dorman, L.I. and L.I. Miroshnichenko. Solnechnye Kosmicheskie Luchi (Solar Cosmic Rays).— Moskva, Izd. "Nauka." 1968.
11. Kaplan, S.A. and V.N. Tsytovich.— UFN, 97:77. 1969.
12. Tsytovich, V.N. and A.S. Chikhachev.— Radiofizika, 12:26. 1969.
13. Sagan, C. The Origin and Evolution of Atmospheres and Oceans. New York. 1964.

14. Sagan, C. and I.B. Pollack.— J. Geophys. Res., **72**:469. 1967.
15. Gnedin, Yu.N. and A.Z. Dolginov.— Astronomicheskii Zhurnal, **18**:181. 1966.
16. Konstantinov, B.P., M.M. Bredov, S.V. Viktorov, G.V. Kir'yan, G.E. Kocharov, and B.O. Naidenov.— DAN SSSR, **181**:55. 1968.
17. Berkner, L.V. and H. Odishaw (Editors). — Science in Space. New York, McGraw-Hill. 1961.
18. Hayakawa, S.— Space Res., **3**. 1962.
19. Kranev, H.W., G.L. Schroedev, G. Davidson, and I.W. Carpenter.— Nature, **152**:3726. 1966.
20. Lingenfelter, R.E., E.H. Canfield, and W.N. Hess.— J. Geophys. Res., **66**:2665. 1961.
21. Mandel'shtam, S.L., I.P. Tindo, G.S. Cheremukhin, L.S. Sorokin, and A.B. Dmitriev.— Kosmicheskie Issledovaniya, **6**:119. 1968.
22. Vinogradov, A.P., Yu.A. Surkov, G.M. Chernov, F.F. Kirnozov, and G.B. Nazarkina.—Kosmicheskie Issledovaniya, 5(6):874. 1967.
23. Gal'perin, Yu.I. In: "Polyarnye Siyaniya i Svechenie Nochnogo Neba." No. 1:70. Moskva, Izdatel'stvo AN SSSR. 1963.
24. Gal'perin, Yu.I., I.A. Polyektov, and I.I. Sobel'man.— Geomagnetizm i Aeronomiya, **6**:633. 1966.
25. Kurt, V.G. and T.A. Germogenova.— Astronomicheskii Zhurnal, **44**:352. 1967.
26. Gnedin, Yu.N. and A.Z. Dolginov.— ZhETF, **45**:1136. 1963.
27. Gnedin, Yu.N. and A.Z. Dolginov.— Astronomicheskii Zhurnal, **18**:800. 1966.
28. Tsygan, A.I. Thesis.— Leningrad, FTI AN. 1969.
29. Metropolis, N., R. Bivins, and M. Storm.— Phys. Rev., **110**: 185 and 204. 1958.
30. Koshin, V.A. and E.S. Matusevich.— Atomic Energy Rev., **6**. 1968.
31. Gorshkov, G.V. and O.S. Tsvetkov.— Atomnaya Energiya, **26**:27. 1969.
32. Gnedin, Yu.N., A.Z. Dolginov, and A.I. Tsygan.— Kosmicheskie Issledovaniya (in press).
33. Turkevich, A.L., E.J. Franzgrote, and I.H. Patterson.— Science, **158**:635. 1967.
34. Davidson, G.T.— J. Geophys. Res., **70**:1061. 1965.
35. Dalgarno, A. and G. Griffing.— Proc. Roy. Soc., **A248**:415, London. 1958.
36. Vaisberg, O.L.— In: "Polyarnye Siyaniya i Svechenie Nochnogo Neba," **9**:24, Moskva, Izdatel'stvo AN SSSR. 1962.

SPACE-PHYSICAL INVESTIGATIONS IN THE LABORATORY

I. M. Podgornyi

Shock waves constitute one of the most interesting phenomena which take place in the interplanetary plasma and in the solar corona. Since the solar wind is a kind of supersonic plasma stream, its interaction with the objects in the interplanetary space and the interaction between plasma clouds moving with different velocities will inevitably generate shock waves. The main distinction between these plasma shock waves and the shock waves in the Earth's atmosphere involves the particular mechanism of energy dissipation of the plasma streaming motion. When a shock wave is formed in a dense gas, e.g., in front of a supersonic aircraft, the energy is dissipated through molecular collisions between the gas particles. The width of the shock in this case is therefore of the order of $\lambda = 1/n\sigma$, where σ is the effective cross section for the interaction of molecules and n is the concentration of molecules.

In the interplanetary space, the particle concentration is approximately 10^{-19} of the concentration in the ground air, and the characteristic free paths of electrons and ions are substantially greater than the measured shock width. A similar situation is observed under laboratory conditions, when the shock wave in a thin plasma is produced by a so-called magnetic piston.

Let us consider in some detail one particular case, namely the case of a shock parallel to the magnetic field lines frozen into the plasma. The formal hydrodynamic treatment of the plasma behavior in a magnetic field is applicable to low-density plasma when the free path is substantially greater than the Larmor radius. If the wave amplitude in a low-pressure plasma is sufficiently small, the state behind the shock is independent of the particular dissipation mechanism. The pressure gradient in this case is mainly determined by the magnetic pressure and the starting equations are considerably simplified (the equation of energy flux conservation may be omitted). Sagdeev /1/ has shown that this treatment in the case of small amplitudes leads to a distinct oscillatory structure of the shock with an oscillation scale c/ω_0, where $\omega_0 = \sqrt{\frac{4\pi ne^2}{m}}$ is the Langmuir frequency, n, e, m are the electron concentration, the electron charge, and the electron mass, c is the velocity of light. Among the various damping mechanisms which are not related to Coulomb collisions, we should first mention reflection from the magnetic field maxima of particles with velocities close to the shock wave velocity. Dissipation may occur due to particle scattering by microfluctuations which are associated with the onset of instabilities.

A different behavior is observed for an oblique wave, i.e., a wave whose front forms a finite angle with the direction of the magnetic field lines. If $\theta > \sqrt{\frac{m}{M}}$ (M is the ion mass), the oscillatory structure of the shock is substantially different. The oscillations overtake the shock and their characteristic scale is $\frac{c}{\Omega_0}\theta$, where $\Omega_0 = \sqrt{\frac{4\pi e^2 n}{m}}$ is the ion Langmuir frequency.

The oscillatory structure is observed for Mach numbers smaller than some critical value. The critical value of the Mach number for a straight wave is about 3. For Mach numbers greater than M_{cr}, the shock topples over, just like the crest of a sea wave in shallow water. This "surf" gives rise to countercurrents. When the velocity of countercurrents exceeds the velocity of ionic sound $\sqrt{T_e/M}$, ionic sound instability develops. The scattering of particles by microfluctuations increases the effective scattering length, i.e., it leads to effective dissipation of streaming energy. The shock width in this case is $\sim c/\Omega_0$.

A typical experimental setup for the study of a collision-free shock wave propagating across the field is shown in Figure 1 /2 – 6/. The plasma is produced by a preliminary discharge in the solenoid magnetic field. A one-loop coil with low-inductance feeders is inserted into the solenoid. The discharge of a condenser bank produces a sharp increase of the magnetic field, so that a magnetic wall is created between the coil and the plasma, compressing the plasma in the axial direction with a super-Alfven velocity. The magnetic wall (piston) generates a shock wave, and if the coil is sufficiently large the shock may develop to steady-state conditions.

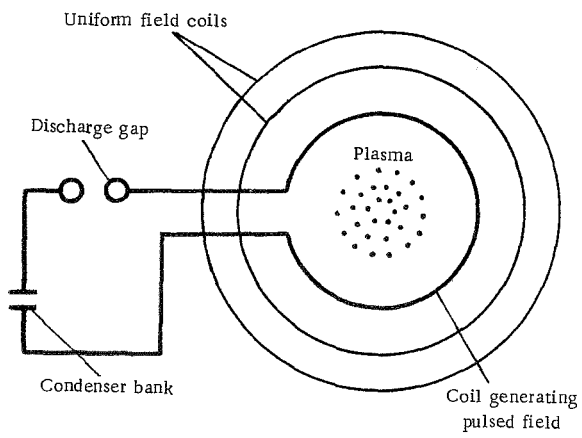

FIGURE 1. Experimental setup for studying a collisionless shock wave.

In accordance with the theoretical predictions, a distinct oscillatory structure with a scale of $\sim c/\omega_0$ is observed for $M < M_{cr}$. For supercritical Mach numbers, no oscillations are observed and the shock width

is of the order of c/Ω_0. These experiments demonstrate the generation of collision-free shock waves, but the results are not entirely suitable for comparison with measurements in outer space. It is clear from the above examples that, even for the same initial conditions, the shock wave is substantially different for Mach numbers below and above the critical value. These two extreme cases, however, by no means cover the entire range of various shock waves generated in a collision-free plasma. Therefore, simulation of the interaction of the solar wind with various objects in the interplanetary space is impossible without correct reproduction of the space conditions in the laboratory.

The experimental findings provided by satellites and rockets are sufficient for an approximate classification of the interaction effects of the solar wind with three objects — the Earth, the Moon, and Venus. Analysis of these effects will enable us to come up with a proper formulation of the simulation conditions for some phenomena associated with the solar-wind interaction. Each of the three cases above has its own characteristic features. Shock waves were discovered around Earth and Venus, but the generation mechanism is essentially different in these two cases. The interaction of the solar wind with the Moon does not produce a shock wave. Let us consider the simulation problem for each of these cases separately.

EARTH

The space around the Earth is the best studied part of the interplanetary space. There is a wealth of material for detailed comparison with various theoretical assumptions. On the other hand, only partial information can be obtained by direct measurements in outer space, and simulation experiments are essential for filling in the blanks.

The flow of the solar wind past the geomagnetic field creates a magnetosphere free from the solar wind plasma, and the interface acts as a magnetic piston. To create a magnetosphere in laboratory experiments, the skin-layer thickness should be less than the magnetosphere dimension, i.e., we should have

$$Re_m = \frac{4\pi\sigma L \bar{v}}{c^2} \gg 1, \qquad (1)$$

where Re_m is the magnetic Reynolds numbers, σ is the plasma conductivity, L is the characteristic dimension of the magnetosphere, $\bar{v}$ is the streaming velocity. Calculating the conductivity from Coulomb collisions

$$\sigma = 12\, T_e^{3/2}\,(\mathrm{eV})\,\mathrm{ohm}^{-1}\,\mathrm{cm}^{-1}, \qquad (2)$$

we obtain for the interaction of the solar wind with the geomagnetic field $Re_m \sim 10^{12}$. When choosing the laboratory conditions, we should remember that the collective processes in plasma increase the effective frequency of collisions. As a result, the plasma conductivity calculated from equation (2) may differ in its order of magnitude from the true plasma conductivity. Hence, the electron temperature of the plasma and the velocity should be chosen so that the condition $Re_m \gg 1$ is satisfied with an adequate margin

(of several orders of magnitude). In the experiments carried out at the Institute of Space Research, Re_m was taken of the order of 10^4 for $\bar{v} = 3 \cdot 10^7$ cm/sec and $T_e \sim 15$ eV.

We know from the theory of collisionless shock waves that the type of the shock wave, and in particular, the shock width and structure, are determined by the following nondimensional parameters:

1. The Mach number $M = \bar{v} / \sqrt{\frac{T_e}{M}}$.

2. The Mach number relative to the Alfven velocity $M_A = \frac{\bar{v}}{H/4\pi\rho}$, where $\rho = Mn$ is the plasma density.

3. The ratio of the gas-kinetic plasma pressure to the magnetic pressure $\beta = \frac{nk(T_e + T_i)}{H^2/8\pi}$.

4. The ratio of the electron Larmor frequency $\omega_H = \frac{eH}{mc}$ to the Langmuir frequency $\omega_0 = \sqrt{\frac{4\pi ne^2}{m}}$. A nondimensional parameter $\alpha = (\omega_H/\omega_0)^2$ is generally introduced.

5. The ratio of the electron temperature to the ion temperature.

In addition to the above conditions, simulation of a collisionless shock wave also requires that the free path length in an undisturbed stream be large compared to the characteristic scale of the experiment (dipole size, shock width).

If the phenomenon is a continuous function of the nondimensional parameters, there is no need to maintain exactly constant values of these parameters, which anyhow greatly differ from unity. It is only essential that the nondimensional parameters for the laboratory plasma be much greater (or much smaller, as the case may be) than unity, as in the interplanetary space, but it is not necessary to strive to attain the correct orders of magnitude. This principle was actually adopted in the model experiments carried out at the Institute of Space Research /7–9/. The table below lists the experimental conditions required for the simulation of the magnetosphere and the collisionless shock wave generated by the interaction of the solar wind with the geomagnetic field. Solar wind conditions are given for comparison purposes.

	Electron temperature, eV	Ion temperature, eV	Concentration, cm^{-3}	Velocity, cm/sec	Magnetic field in plasma, Oe
Space	20–50	10	$5 \cdot 10$	$3-5 \cdot 10^7$	10^{-4}
Experiment	15	5	10^{13}	$3 \cdot 10^7$	40

MOON

The Moon has no magnetic field, so that no shock wave can form in its interaction with the solar wind. However, as long as there are no detailed measurements of the magnetic field around the Moon, we cannot rule out the possibility of formation of a shock wave due to condensation of the magnetic field lines frozen into the plasma as the plasma stream flows

around a high-conductivity body. For low-conductivity bodies or for bodies with a nonconducting shell, there are two configurations of the induced magnetic field which may produce a shock wave.

1. The average conductivity of the planet is high and the skin-layer depth $\delta = \frac{c^2}{4\pi\sigma\overline{v}}$ is small compared to the planetary radius. The field lines do not penetrate into the interior, and an "induced" magnetosphere is formed at the surface. In other words, the conditions favor the formation of a shock wave in a supersonic plasma stream. The condition for shock formation in this case has the form

$$\frac{8\pi\sigma_{Moon} R_{Moon} \overline{v}}{c^2} >> 1.$$

Insertion of numerical values gives $\sigma_{Moon} >> 10^4$ CGSE, or 10^{-8} ohm^{-1} cm^{-1}, which corresponds to the conductivity of slate. The conductivity of paper, Na glass, and porcelain is four orders of magnitude lower. The average conductivity of the Moon is so far unknown, not even to orders of magnitude and no simulation experiments could therefore be carried out.

2. The other hypothesis of shock wave formation near the Moon is associated with the assumption of a conducting core at the center of the planet (Figure 2).

With this geometry, the incident plasma is absorbed by the lunar surface, and the magnetic field lines of the solar wind freely penetrate into the low-conductivity region until they are stopped by the conducting core. The field lines bypass the core, forming an induced magnetosphere. If the low-conductivity layer is sufficiently thick, this induced magnetosphere does not emerge on the day side of the planet. In this case, a shock wave around the Moon could form only far from the Moon – Sun center line.

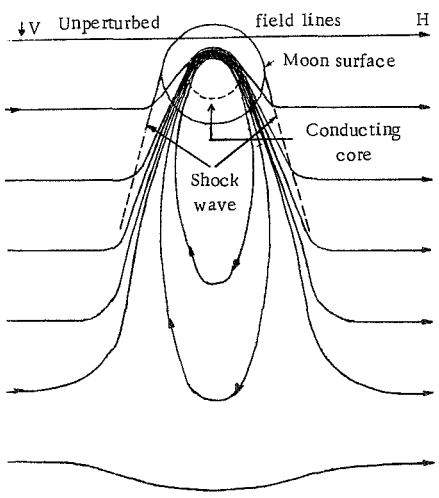

FIGURE 2. Formation of a shock wave around the Moon.

Until recently, the question of the formation of a shock wave near the Moon remained within the framework of pure hypothesis, and only the measurements of the magnetic field geometry by the three Explorers (33, 34, and 35) provided adequate factual data for analysis. One of the Explorers remained in a lunar orbit and carried out measurements on the night side of the Moon /10/. It was established that no shock wave formed around the Moon and no field distortion or concentration was observed on the day side, i.e., the Moon absorbs the incident plasma and the field lines freely pierce the bulk of the planet. A shadow trail with a markedly reduced plasma

concentration is observed on the night side of the Moon. The magnetic field in the trail is somewhat higher than in the nearby solar wind.

The Explorer measurements traced the propagation of the spatial magnetic field fluctuations through the bulk of the Moon. Fluctuations of about 5 sec duration were found to propagate through the Moon without noticeable distortion, which points to an average conductivity of $10^{-8} - 10^{-7}$ ohm^{-1} cm^{-1}.

VENUS

The measurements carried out from VENUS-4 /11/ show that at a distance of about 19,000 km from the surface of Venus the plasma concentration and the magnetic field strength increase markedly. This effect can be interpreted as formation of a shock wave. The existence of a shock wave around Venus cannot be attributed to the same physical factors that we use to explain the shock wave around the Earth. The main difference is that Venus has no magnetic field which could provide the magnetic piston. Under these conditions, a shock wave can form only around high-conductivity objects, when the time for the plasma to traverse one diameter is less than the spin time. We should again distinguish between two possible types of distortion of the frozen magnetic field in the solar plasma.

1. Venus has a high-conductivity core. The magnetic field lines encircling the planet and forming the induced magnetosphere will lie outside the bulk of the planet if the thickness of the low-conductivity envelope is less than 300 km /11/, i.e., $1/10$ of the Earth's mantle. Otherwise, the induced magnetosphere is retained inside the planet on the day side and a shock wave will form only far from the point of attack.

2. The upper atmospheric layers act as a conducting sphere. The requisite ionization is caused by the absorption of solar radiation. Particle traps recorded charged particle concentrations of about 10^3 near Venus, so that the second assumption seems justified.

Let us consider the conditions for the simulation of the solar-wind interaction with Venus. Our problem is to investigate the effects associated with the formation of a shock wave at the interface between the plasma envelope of the planet and the undisturbed stream of solar plasma. The absence of a magnetic field around Venus signifies that the interaction in fact takes place between a stream with a frozen magnetic field and a stream initially free from any fields. The allowed parameters of the artificial solar wind in simulation experiments were considered in connection with the shock wave around the Earth. We will now have to choose the conditions for the plasmoid simulating the Venusian ionosphere. The main conditions can be stated in the following form.

1. Plasmoid skin-layer thin compared to the shock width, i.e., $\frac{4\pi\sigma\bar{v}\delta}{c^2} >> 1$. Here δ is the shock width. Taking $\delta = 5$ cm, which corresponds to the experimental value, we get $\sigma >> 5 \cdot 10^{11}$.

2. For a steady-state shock wave to form, the stream pressure $\rho\bar{v}^2$ should be equal to the plasmoid pressure, i.e., $\rho\bar{v}^2 \sim n_2kT_2$. Inserting the ρ and $\bar{v}$ values of the artificial solar wind, we get $n_2kT_2 = 4 \cdot 10^{15}$ eV/cm^3.

3. To avoid destruction of the fast ions in the transitional layer through charge exchange with the neutral gas and thus maintain the pressure balance at the interface, we should have $\lambda_{tr} >> \delta$. For the given hydrogen plasma velocity $\overline{v} = 3 \cdot 10^7$ cm/sec, this condition can be written in the form $n_0 < 10^{14}$ cm^{-3}.

A nonmagnetized hydrogen plasma with $n_2 = 2 \cdot 10^{14}$ cm^{-3} and electron temperature $T_2 = 20$ eV meets these requirements. The neutral gas under these conditions burns out in less than one microsecond.

A plasma with T = 20 eV and $n = 10^{14}$ cm^{-3} can be produced without difficulty in an external magnetic field, but it is very difficult to avoid frozen-in fields. These difficulties, however, are of a technical nature only, so that in principle the interaction of the solar wind with Venus can be simultated in the laboratory.

LABORATORY EXPERIMENT

The experiments carried out at the Institute of Space Research /7, 9/ studied the interaction of an artificial solar wind with the parameters listed in the table with a two-dimensional magnetic dipole simulating the Earth. The aim was to reproduce the main effects taking place near the Earth's magnetosphere. The field of the two-dimensional dipole was set up by two parallel conductors with current flowing in opposite directions. The distance between the conductors was 2 cm. This geometry permitted measurement of the plasma concentration directly, without introducing any distortions into the system. In actual measurements, the beam from a laser interferometer /13, 14/ was directed parallel to the conductors, i.e., it propagated along a line of constant plasma concentration (apart from edge effects). In a three-dimensional dipole, the conversion from the average concentrations along the beam to local concentrations involves very tedious calculations and does not give accurate results. The magnetic field distribution was measured with probes.

The results of the magnetic measurements show that the plasma stream displaces the dipole field on the "day" side from the region where the magnetic pressure $H^2/8\pi$ is less than the stream pressure $\rho\overline{v}^2$. Near the dipole the magnetic field intensity increases, forming a plasma-free space — a magnetosphere. The extent of the magnetosphere in these experiments was about 10 cm. Near the magnetosphere boundary, a collisionless shock wave separates. The magnetic field strength and the concentration increase by a factor of 3—4 at the shock. The shock is 5 cm wide, which corresponds to the ratio c/Ω_0, where c is the velocity of light and $\Omega_0 = \sqrt{\frac{4\pi e^2 n}{M}}$ is the ion plasma frequency. Measurements carried out from artificial Earth satellites also give the value of c/Ω_0 for the shock width near the Earth.

Among the various modes of streaming energy dissipation, we should primarily mention particle scattering by ionic-sound oscillations and instability of magnetohydrodynamic waves as a result of pressure anisotropy (Alfven and magnetic sound instability). Both these mechanisms are effective in the interplanetary plasma and in the laboratory for $T_e > T_i$

and $\beta \gtrsim 1$. Since the excitation of ionic-sound oscillations has been previously studied in magnetic piston experiments /3/, our experiments were mainly concerned with energy dissipation through Alfven instability /16/.

The Alfven instability develops when $nkT_{\parallel} > nkT_{\perp} + \frac{H^2}{4\pi}$. Its characteristic length is of the order of the ion Larmor radius and its frequency is Ω_0. Experiments carried out by the present author jointly with E.M. Dubinin and G.G. Managadze (these experiments included correlation measurements) showed that the magnetic field fluctuations at the shock are consistent with the assumption of Alfven instability.

In addition to simulation experiments with a collisionless shock wave, the night side of the magnetosphere was also studied. Laboratory experiments /7—9/ established the formation of a geomagnetic tail with a neutral layer, produced by the anomalous diffusion of plasma through the boundary of the magnetosphere and subsequent entrainment of the magnetic field by the plasma stream. The results of the laboratory experiment fit the measurements of aritificial Earth satellites.

All the results of laboratory measurements show that certain effects associated with the interaction of the solar wind with the geomagnetic field can be effectively simulated in the laboratory. The observation of these effects in the laboratory is naturally immeasurably simpler than in outer space. The advantages of simulation experiments are particularly obvious in cases of correlation measurements which have to be carried out simultaneously at different points in space.

Bibliography

1. Sagdeev, R.Z.— In: "Voprosy Teorii Plazmy," 4:20, Moskva, Atomizdat. 1963.
2. Zagorodnikov, S.P., G.E. Smolkin, and G.V. Sholin.— Conference on Ionized Gases. Belgrad. 1965.
3. Alikhanov, S.G.— MAGATE Conference on Thermonuclear Fusion. Novosibirsk. 1968.
4. Paul, J.W.M., G.C. Goldenbaum, A. Iivoshi, L.S. Holmes, and R.A. Hardcastle.— Nature, 216:363. 1967.
5. Khintts, E.— MAGATE Conference on Thermonuclear Fusion. Novosibirsk. 1968.
6. Robson, A.E. and Dzh. Sheffil'd.— MAGATE Conference on Thermonuclear Fusion. Novosibirsk. 1968.
7. Managadze, G.G. and I.M. Podgornyi.— DAN SSSR, 180:1333. 1968.
8. Podgornyi, I.M. and G.G. Managadze.— Vestnik AN SSSR, No.7:38. 1968.
9. Managadze, G.G. and I.M. Podgornyi.— Geomagnetizm i Aeronomiya, 8:612. 1968.
10. Ness, N.F.— Conference on the Physics of the Moon and Planets, Kiev. 1968.
11. Gringauz, K.I., V.V. Bezrukikh, L.S. Musanov, and T.K. Breus.— Kosmicheskie Issledovaniya, 6:411. 1968.

12. Dolginov, Sh.Sh., E.G. Eroshenko, and L.N. Zhuzgov.— Kosmicheskie Issledovaniya, 6:561. 1968.
13. Managadze, G.G., I.M. Podgornyi, and V.D. Rusanov.— Geomagnetizm i Aeronomiya, 8:545. 1968.
14. Managadze, G.G., I.M. Podgornyi, and V.D. Rusanov.— In: "Voprosy Teorii Plazmy," Part 2, Moskva, Atomizdat. 1963.
15. Kaufman, R.L.— J. Geophys. Res., 72:2323. 1967.
16. Kenel, C. and R.Z. Sagdeev.— J. Geophys. Res., 72:3303. 1967.
17. Ness, N.F.— J. Geophys. Res., 70:2989. 1965.

THE TRAPPING OF CHARGED PARTICLES BY THE MAGNETIC FIELD WITH ALLOWANCE FOR IONIZATION LOSSES

D. Kh. Morozov

Several mechanisms have been proposed for the trapping of charged particles by the geomagnetic field /1/. We shall consider here still another possible mechanism of trapping high-energy protons by the magnetic field. A method is developed for analyzing the trapping of protons at energies when the drift approximation is inapplicable. The simplified model calculations used in this paper can only provide a qualitative description of the effect, but the method as such can be extended to cover more sophisticated models.

Consider the following model: a magnetic dipole μ at the center of a spherically symmetric concentration of matter of density $\rho = \rho_0 R(r)$ is irradiated with a beam of protons of energy E_0. At $r \to \infty$ the proton beam is homogeneous and isotropic. We will consider the motion of particles in the equatorial plane of the dipole only. For $\rho_0 = 0$ (unperturbed motion), the behavior of the protons is described by Störmer's theory. The integrals of motion are

$$M_0 = \frac{m r^2 \dot{\varphi}}{\sqrt{1-\frac{v^2}{c^2}}} + \frac{e\mu}{cr} \quad \text{and} \quad E_0, \tag{1}$$

and the particle Hamiltonian is written in the form

$$H_0 = \sqrt{\left[\left(\frac{M}{r} - \frac{e\mu}{cr^2}\right)^2 + p_r^2\right]c^2 + m^2c^4}\,. \tag{2}$$

The particles arriving from infinity at a given point in space may have momenta ranging inside the cone of allowed directions. The interaction with matter (scattering, ionization losses) alters the particle momenta and the cone itself, and as a result particles are trapped by the magnetic field. If the perturbation caused by the material medium is small, only particles near the surface of the cone can be trapped. Scattering may cause both a change from infinite to finite motion and a change in the opposite direction. Ionization losses, on the other hand, only convert infinite motion to finite. We will consider the role of ionization losses, ignoring scattering effects. The equations of motion of the particle take the form

$$\dot{M} = -\rho\left|\frac{dE}{dl}\right|\frac{r^2\dot{\varphi}}{v}\,, \quad \dot{p}_r = -\frac{\partial H_0}{\partial r} - \rho\left|\frac{dE}{dl}\right|\frac{\dot{r}}{v}\,, \tag{3}$$

where dE/dl are the ionization losses per 1 g/cm^2.

We assume that the ionization losses for motion along an unperturbed path are much less than the energy E_0. Then $Q = \frac{1}{v} \left| \frac{dE}{dl} \right| \rho_0$ may be regarded as a small parameter, and we should take its value for $v = v_0$. The motion of ionization losses can thus be described as motion with a new Hamiltonian,

$$H = H_0 + Q H_1 , \; H_1 = R(r) \cdot \varphi\left(M - \frac{e\mu}{cr}\right) \frac{\sqrt{1 - \frac{v^2}{c^2}}}{m} + f(M, p_r, r) \tag{4}$$

and a new retarding force

$$\mathcal{F}_r = - Q \left\{ R(r) i - \frac{\partial}{\partial r} \left[R(r) \left(M - \frac{e\mu}{cr}\right) \frac{\sqrt{1 - \frac{v^2}{c^2}}}{m} - f \right] \right\}.$$

Applying the ordinary theory of perturbations, as it crystallized in celestial mechanics, we make the substitution of variables /2/

$$\begin{aligned} M &= M' + Q \frac{\partial S}{\partial \varphi} , \quad p_r = p_r' + Q \frac{\partial S}{\partial r} , \\ \varphi' &= \varphi + Q \frac{\partial S}{\partial M} , \quad r' = r + Q \frac{\partial S}{\partial p_r} . \end{aligned} \tag{5}$$

The function S is defined so that to first approximation in Q, the Hamiltonian H is independent of φ'. Then M' is an integral of motion in the first approximation of the perturbation theory. To meet this condition, S should satisfy the equation

$$\frac{\partial H_0}{\partial M} \frac{\partial S}{\partial \varphi} + \frac{\partial H_0}{\partial p_r} \frac{\partial S}{\partial r} - \frac{\partial H_0}{\partial r} \frac{\partial S}{\partial p_r} = - H_1 . \tag{6}$$

This equation separates into two different equations for $p_r > 0$ and $p_r < 0$.

A particular solution of the equation for $p_r < 0$ is

$$S_1 = \varphi \int_{\infty}^{r} \frac{\left(M_0 - \frac{e\mu}{cr}\right) R(r)\, dr}{\sqrt{p_0^2 - \left(\frac{M_0}{r} - \frac{em}{cr^2}\right)^2}} , \tag{7}$$

and for $p_r > 0$

$$S_2 = \varphi \left[\int_{r}^{\infty} \frac{\left(M_0 - \frac{e\mu}{cr}\right) R(r)\, dr}{\sqrt{p_0^2 - \left(\frac{M_0}{r} - \frac{e\mu}{cr^2}\right)^2}} - 2 \int_{r_{min}}^{\infty} \frac{\left(M_0 - \frac{e\mu}{cr}\right) R(r)\, dr}{\sqrt{p_0^2 - \left(\frac{M_0}{r} - \frac{e\mu}{cr^2}\right)^2}} \right], \tag{7'}$$

where p_0 is the unperturbed momentum of the particle, $r_{min} = (\sqrt{2} - 1) \sqrt{\frac{lM}{cp_0}}$ is calculated from the unperturbed equation. These solutions where chosen so that for $r = r_{min}$, $S_1 = S_2$ and for $r \to \infty$, $S_1 \to 0$.

If R(r) falls off sufficiently fast, the particle angular momentum M after emergence from the material medium is

$$M = M_0 - 2Q \int_{r_{min}}^{\infty} \frac{\left(M_0 - \frac{e\mu}{cr}\right) R(r)\, dr}{\sqrt{p_0^2 - \left(\frac{M_0}{r} - \frac{e\mu}{cr^2}\right)^2}} , \tag{8}$$

where M_0 is the initial angular momentum of the particle.

The change in linear momentum for motion along an unperturbed path can also be calculated without difficulty. Upon emerging from the material medium

$$p = p_0\left[1 - 2Q\int_{r_{min}}^{\infty}\frac{R(r)\,dr}{\sqrt{p_0^2 - \left(\frac{M_0}{r} - \frac{eM}{cr^2}\right)^2}}\right]. \tag{9}$$

Note that a small perturbation may only trap particles with $M > 0$, since the linear momenta of particles with $M < 0$ lie near the axis of the cone of allowed directions. The trapping condition thus requires real positive solutions of the equation

$$\frac{p_\varphi}{p} = \frac{\frac{M}{r} - \frac{eM}{cr^2}}{p(r)} = 1. \tag{10}$$

Inserting (8) and (9) in (10) and retaining only terms of first order in Q, we obtain the equation

$$r^2 - r\frac{M^*}{p_0} + \frac{eM^*}{cp_0} = 0, \tag{11}$$

where $M^* = M_0(1 + 2QA) - 2QB$, $\mu^* = \mu(1 + 2QA)$,

$$A = \int_{r_{min}}^{\infty}\frac{R(r)\,dr}{\sqrt{p_0^2 - \left(\frac{M_0}{r} - \frac{eM}{cr^2}\right)^2}}, \tag{12}$$

$$B = \int_{r_{min}}^{\infty}\frac{R(r)\left(M_0 - \frac{eM}{cr}\right)dr}{\sqrt{p_0^2 - \left(\frac{M_0}{r} - \frac{eM}{cr^2}\right)^2}}. \tag{13}$$

Equation (11) is solvable if

$$\frac{M^{*2}}{p_0^2} - \frac{4eM^*}{cp_0} \geq 0. \tag{14}$$

In the zero approximation, this condition corresponds to the inequality

$$M \geq M_{cr}^0 = 2\sqrt{\frac{eMp_0}{c}}.$$

However, under our assumptions a particle is trapped whenever it reaches the material medium, so that M must be less than M_{cr}^0. The initial angular momenta of the trapped particles should therefore fall between the limits $[M_{cr}^0;\ M_{cr}^0 + \Delta M]$, where ΔM is defined by the equation

$$M_{cr}\Delta M + 2Q\left[A\left(M_{cr}^0 - \frac{2Mep_0}{c}\right) - BM_{cr}^0\right] = 0.$$

If R falls off sufficiently fast, A and B can be calculated as follows:

$$A = \psi_1(r_{min})\int_{r_{min}}^{\infty}\frac{R(r)\,dr}{\sqrt{r - r_{min}}},\quad B = \psi_2(r_{min})\int_{r_{min}}^{\infty}\frac{R(r)\,dr}{\sqrt{r - r_{min}}}.$$

This gives

$$B = -\frac{\sqrt{2} - 1}{2}AM_{cr}^0. \tag{15}$$

Then

$$\Delta M = (\sqrt{2} - 2) Q c A M^{\circ}_{cr}. \tag{16}$$

To calculate A, we should assume a particular form for R(r). Let $R(r) = e^{-\alpha(r - r_{min})}$, then

$$\Delta M \approx -0.31 (Q/\sqrt{\alpha}) (M^{\circ}_{cr}/p_{\circ})^{3/2}.$$

All particles with momenta between $M^0_{cr} + \Delta M$ and M^0_{cr} are thus trapped by the magnetic field. Their paths are limited by the lines $r = r_{min}$ and $r = r_{max}$, where r_{max} is the first root of equation (11), which because of the smallness of the perturbation does not differ much from the corresponding magnitude in the unperturbed case. It is readily seen that even a slight change in energy is sufficient to stop the subsequent circuits of the path of the trapped particles from penetrating into the dense atmospheric layers. Indeed from equation (11) we have

$$r_{min} = -\frac{M^*}{2p_{\circ}} + \sqrt{\left(\frac{M^*}{2p_{\circ}}\right)^2 + \frac{e M^*}{c p}} \tag{17}$$

After tracing n half-circuits,

$$M^* = M_{\circ}(1 + nQA) - nQB, \; \mu^* = \mu(1 + nQA), \; \Delta p = -nQAp_{\circ}. \tag{18}$$

Inserting (18) in (17) and expanding in powers of Q, we find

$$r_{min} = r^{\circ}_{min} \left(1 - 2.4 \frac{\Delta p}{p_{\circ}}\right), \tag{19}$$

where r^0_{min} is the minimum distance from the center along the first circuit.

Thus, as the momentum drops by only 5%, r_{min} increases approximately by 800 km. As a result, the particle lifetime is sufficiently long.

Bibliography

1. Tverskoi, B.A. Dinamika radiatsionnykh poyasov Zemli (The Dynamics of the Radiation Belts of the Earth).— Moskva, "Nauka." 1968.
2. Arnol'd, V.I. — UMN, 18(6): 91. 1963.

A CONTRIBUTION TO THE THEORY OF PARTICLE ACCELERATION IN INTERPLANETARY PLASMA

M. E. Kats and A. K. Yukhimuk

The spectral density of the ionic-sound oscillations in the interplanetary space is calculated in the quasilinear approximation and the integrated intensity spectrum of the particles accelerated by these oscillations is determined. Anisotropy in the velocity distribution of the plasma particles is regarded as the reason for the development of ionic-sound oscillations /1/. The existence of this anisotropy in the solar wind plasma has been confirmed by direct measurements /2/.

The calculated intensity spectrum of the accelerated particles has the form $I(>v) = A \exp(-v/v_0)$, where A = const, v is the velocity of accelerated particles, v_0 is a characteristic constant of the spectrum. The results show that the acceleration by ionic-sound oscillations may indeed be responsible for the observed spectrum of solar cosmic rays /3/.

Bibliography

1. Timofeev, A.V. and V.N. Pistunovich.— In: "Voprosy teorii plazmy," No.5. Moskva, Atomizdat. 1967.
2. Wolfe, I.H., R.W. Silva, and M.A. Myers.— J. Geophys. Res., 71(5):1319. 1966.
3. Freier, P.S. and W.R. Webber.— J. Geophys. Res., 68(6):1605. 1963.

A MECHANISM OF ACCELERATION OF THE SOLAR WIND PLASMA

M. V. Konyukov

Data on the temperature of the solar corona, the ions, and the electrons near the Earth's orbit reveal changes of the total proton energies from -1 keV in the corona to $+1$ keV in the interplanetary plasma. This change points to the existence of a definite plasma acceleration process in the solar corona. This acceleration mechanism was studied within the framework of a steady-state spherically symmetric model of plasma ejection with steady-state almost laminar flow, and the hydrodynamic approximation was applied, at least near the starting level.* The extended energy source accelerating the solar wind plasma is distributed beyond the maximum temperature level in the solar corona (the energy flux due to thermal conductivity at this level is zero), and it is physically identical with the heat source heating the solar corona. This heat source directed away from the Sun generates an energy flux via heat conduction by the electrons, and a positive net energy flow is observed at the level corresponding to the formation of a nearly laminar plasma outflow, despite the considerable negative energy associated with the attraction of the Sun. Since the total energy flow is conserved, the proposed acceleration mechanism is essentially a mechanism transforming the energy flow associated with the electron heat conduction into a flow of hydrodynamic ion energy. This energy conversion mechanism is attributed to the presence of an ambipolar electric field and collisional energy transfer from electrons to ions.

The proposed acceleration mechanism was analyzed using the equations of steady-state spherically symmetric plasma ejection in the two-fluid approximation. The nondimensional parameters of the problem /1/ were calculated from the experimentally observed total mass flow in the solar wind, the temperature in the solar corona, and the position of the level where the nearly laminar flow conditions originated, as derived from the observed density distribution. The resulting values of the reciprocal Reynolds number are such that the asymptotic methods are not applicable, and the analysis of the solutions of the starting system of equations therefore had to be carried out numerically. Certain caution should be exercised in the application of the numerical methods to the analysis of the model equations. After all, the model equations are valid only when the

* If generation of solar wind through ejection into interplanetary space of plasma jets accelerated to considerable energies is ignored, plasma acceleration is possible only in the region of frequent collisions since it is there that the attainable energy fluxes are substantially higher than the hydrodynamic ion energy flux at the starting level. The case when the turbulent motion energy is considerably higher than the thermal energy seems to be unlikely under the conditions of the solar corona and the interplanetary plasma.

hydrodynamic approximation applies. Thus, the Cauchy problem can be formulated for the starting level, since it is chosen in the region where the hydrodynamic approximation is valid, or a boundary-value problem can be formulated choosing the levels of known velocity in the region where this approximation applies. The second level must not be chosen near the Earth's orbit, since the results of observation indicate that the hydrodynamic approximation is inapplicable in this region. Analysis of a large number of alternatives has shown that 1) the hydrodynamic ion energy flux increases due to contribution from the electron heat conduction, 2) the hydrodynamic approximation for the electrons breaks down before the electron heat conduction flux is fully transformed into the hydrodynamic energy flux. Since in the collisionless region, the energy flow by heat conduction is ruled out, a transition layer should exist between the hydrodynamic region and the collisionless region, and it is in this layer that the final acceleration of the ionic plasma component occurs.*

The acceleration mechanism of the solar wind plasma should not only raise the plasma ions to the required energy but also account for the following experimental factors: a) $T_i > T_e$ in the heat source region and $T_i < T_e$ in the interplanetary plasma, b) the temperature falls off monotonically with distance from the starting level, c) collisionless flow conditions develop. The proposed acceleration mechanism, unlike Parker's hydrodynamic acceleration mechanism and its modifications /2, 3, 4/, naturally leads to these properties of the outflowing plasma /1/.

The frozen-in magnetic fields, with small transverse components, markedly suppress the transport coefficients under the conditions of the solar corona, so that the problem becomes essentially inviscid with zero thermal conductivity. The reciprocal Reynolds and Peclet numbers calculated from these coefficients are so small that the variation of velocity and temperature can be studied using asymptotic series in powers of the reciprocal Reynolds number /5/. The equations obtained under these conditions are only compatible with Parker-type solutions, which do not meet conditions (b) and (c) above, as formulated in /6/. This implies that the contribution of magnetic fields at the source of the heat-conduction energy flow and at the site of plasma acceleration is insignificant.

Bibliography

1. Konyukov, M.V. O mekhanizme uskoreniya plazmy, vytekayushchei iz Solntsa (Acceleration of Plasma Ejected from the Sun).— Preprint FIAN, No. 149. 1967.
2. Parker, E.N. Dynamic Processes in the Interplanetary Plasma. 1965.
3. Sturrock, P.A. and R.A. Hartle.— Phys. Rev. Lett., 16:628. 1966.
4. Konyukov, M.V.— Trudy FIAN, 38:132. 1967.
5. Konyukov, M.V.— Tezisy dokladov na IV Konferentsii po kometam. Kiev, Izdatel'stvo "Naukova Dumka." 1968.
6. Konyukov, M.V. K teorii istecheniya plazmy iz Solntsa (Theory of Solar Plasma Ejection).— Preprint FIAN, No. 123. 1968.

* Difficulties associated with the solution of the rate equations in the transition layer from the hydrodynamic to the collisionless region render virtually impossible any rigorous analysis of the transition layer, even by numerical methods.

QUASIEQUILIBRIUM STRUCTURES IN THE IONIZED ATMOSPHERES OF STARS AND PLANETS

V. M. Fadeev

The interplanetary space and stellar and planetary atmospheres contain regions of completely ionized gas with particle density $n(\vec{r}, t)$ which either conduct high current densities $\vec{j}(\vec{r}, t)$ or are immersed in external magnetic fields $\vec{H}(\vec{r}, t)$. Both these factors are often combined, and the bulk of the plasma is concentrated in filaments or sheaths. Analysis of the structure of physical objects (plasma formations in this case) reduces to the study of the following three aspects: 1) existence of indivisible system components—elements, 2) interaction and transformation of elements, 3) indestructibility of the object as a system of elements. The choice of the theoretical model is governed by considerations of simplicity, without impairing the principal properties of the objects. We will use the equations describing the macroscopic properties of a singly ionized nonrelativistic ideal gas consisting of n_i ions and n_e electrons. The Maxwell tensor is approximated by the scalar pressure. Quasineutrality is furthermore assumed ($n_i \approx n_e \approx n$) and dissipative effects are ignored.

The plasma in this model is described by the following functions:

$$\rho = n_i m_i + n_e m_e = n m, \tag{1}$$

$$\vec{v} = \frac{1}{\rho}(n_i m_i \vec{v}_i + n_e m_e \vec{v}_e), \tag{2}$$

$$\vec{j} = e\,(n_i \vec{v}_i - n_e \vec{v}_e) \tag{3}$$

and

$$p = p_i + p_e,$$

where ρ, $\vec{v}$, $\vec{j}$, p are the density, the mean velocity, the current, and the plasma pressure, respectively.

Among the equations for these quantities, the first is the equation for the conservation of the mean momentum of the plasma as one system:

$$\frac{\partial \vec{v}}{\partial t} + (\vec{v}\nabla)\vec{v} = \frac{\vec{j}}{\rho} \times \vec{B} - \frac{\nabla p}{\rho} - \frac{m_i m_e}{e^2}\left(\frac{\vec{j}}{\rho}\nabla\right)\frac{\vec{j}}{\rho}. \tag{4}$$

The second equation is the conservation of momentum for the relative motion of the electron and the ion gas, which is interpreted as a generalization of Ohm's law:

$$\begin{aligned} m_i m_e(\partial/\partial t + \vec{v}\nabla)\frac{\vec{j}}{\rho} &= \vec{E} + \vec{v}\times\vec{B} - \frac{m_i m_e}{e^2}\left(\frac{\vec{j}}{\rho}\nabla\right)\vec{v} + \\ &+ \frac{m_i m_e (m_i - m_e)}{e^3}\left(\frac{\vec{j}}{\rho}\nabla\right)\frac{\vec{j}}{\rho} - \frac{m_i - m_e}{e}\left(\frac{\vec{j}}{\rho}\times\vec{B}\right) + \frac{1}{e\rho}(m_i \nabla p_e - m_e \nabla p_i) = \\ &= \vec{E} + \vec{v}\times\vec{B} - \frac{m_i m_e}{e^2}\left(\frac{\vec{j}}{\rho}\nabla\right)\vec{v} + \frac{1}{e\rho}(m_e \nabla p_e - m_i \nabla p_i) - \frac{m_i - m_e}{e}\frac{d\vec{v}}{dt}. \end{aligned} \tag{5}$$

The third equation is an expression of the conservation of mass:

$$\frac{\partial \rho}{\partial t} + (\vec{v}\nabla)\rho = -\rho \, div \, \vec{v}. \tag{6}$$

Maxwell's equations are also added to the set:

$$rot \, \vec{B} = \mu_0 \vec{j} + \varepsilon_0 \mu_0 \frac{\partial \vec{E}}{\partial t}, \tag{7}$$

$$div \, \vec{E} = \frac{e(n_i - n_e)}{\varepsilon_0}, \tag{8}$$

$$rot \, \vec{E} = -\frac{\partial \vec{B}}{\partial t}, \tag{9}$$

where μ_0 and ε_0 are the magnetic permeability and the dielectric constant of vacuum.

The main distinctive feature of equations (4) and (5) is that, unlike the usual practice in physics, the electron inertia terms are included. Generally /1/, the electron inertia effects are assumed to be negligible, which is not always true for a collisionless plasma ($\nu \to 0$). Electron inertia may prove significant in the region where oppositely directed magnetic fields or currents cross, as it results in a relative motion of the plasma and the field, just as collisions do.

Proceeding from the above equations, we will consider the entire question of the existence of elements in plasma systems. For an element to exist, local equilibrium conditions must be maintained, although the system as a whole may change in space and time. Therefore, let us first consider the stationary equilibrium solutions of the equations. It will be seen in the following that the most widespread structural elements are the theta-pinch, the z-pinch, and the skin pinch (a plasmoid contained in a thin skin layer).

A quasistationary ($\vec{v}(\vec{r}, t) = 0$, $\rho = \rho(\vec{r})$, $\vec{j} = \vec{j}(\vec{r})$) theta-pinch is described by the following equations:

$$\frac{\vec{j}_\varphi}{\rho} \frac{1}{r} \frac{d}{dr}(r A_\varphi) - \frac{u_s^2}{\rho} \frac{d\rho}{dr} + \frac{m_i m_e}{e^2} \left(\frac{j_\varphi}{\rho} \right)^2 \frac{1}{r} = 0, \tag{10}$$

$$-\frac{d}{dr}\left[\frac{1}{r} \frac{d}{dr}(r A_\varphi) \right] = \mu_0 j_\varphi, \tag{11}$$

$$\frac{j_\varphi}{\rho} = \frac{e}{m_i + m_e} \omega r, \tag{12}$$

$$E_r = \frac{m_e^2 u_{se}^2 - m_i^2 u_{si}^2}{e} \frac{1}{\rho} \frac{d\rho}{dr}, \tag{13}$$

$$\frac{dE_r}{dr} = \frac{e(n_i - n_e)}{\varepsilon_0}, \tag{14}$$

where ω = const is the angular drift velocity of the electrons in an inhomogeneous magnetic field; equation (12) is the partial solution of equation (5) for the φ-component. Equation (13) corresponds to the r-component of Ohm's law and can be applied to determine the space charge field. Eliminating j_φ between (10) and (11) and inserting the integral of (10) in (11), we find

$$d^2 \Psi / d\rho^2 + G_H'^2 e^{\Psi} = 0. \tag{15}$$

where

$$\rho = r^2, \quad G_H'^2 = \mu_0 e^2 \omega^2 \rho_0 / 4 (m_i + m_e)^2 u_s^2,$$

$$\psi = \frac{m_i m_e}{2 u_s^2 (m_i + m_e)} r^2 + \frac{e\omega}{u_s^2 (m_i + m_e)} r A_\varphi .$$

The solution of equation (15) studied in /2/ is a theta-pinch of the characteristic size

$$\delta_H = \left[\frac{u_s^2}{\left(\omega_B \omega - \frac{m_i m_e}{(m_i + m_e)^2} \omega^2\right)} \right]^{1/2} , \tag{16}$$

where $\omega_B = eH_0/m_i + m_e$. For $\omega \geq eH_0/(m_i + m_e)/m_i m_e$ the structural element loses its identity. The distribution of the magnetic field B_z, the plasma density ρ, and the current density j_φ, is shown in Figure 1.

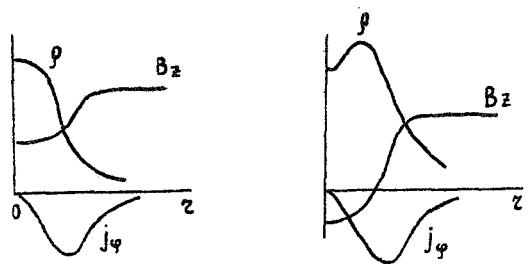

FIGURE 1. Qualitative distribution of the magnetic field B_z, plasma density ρ, and current j_φ for a theta-pinch plasmoid.

Note that, depending on the relationship of the parameters characterizing the gas-kinetic and the magnetic pressure, we have two different density distributions: a bell-shaped distribution and a pipe-shaped distribution. In the case of a pipe-shaped distribution, the inner magnetic field of the plasma is even greater than the external magnetic field, and the field reverses its polarity at the center of the plasmoid.

The existence of a z-pinch follows from the equations

$$\frac{j_z}{\rho} \frac{dA_z}{dr} - \frac{u_s^2}{\rho} \frac{d\rho}{dr} = 0, \tag{17}$$

$$-\frac{1}{r} \frac{d}{dr} \left(r \frac{dA_z}{dr} \right) = \mu_0 j_z , \tag{18}$$

$$\frac{j_z}{\rho} = \frac{e}{m_i + m_e} v_{0z} , \tag{19}$$

$$E_r = \frac{m_e^2 u_{se}^2 - m_i^2 u_{si}^2}{e} \frac{1}{\rho} \frac{d\rho}{dr} , \tag{20}$$

$$\frac{dE_r}{dr} = \frac{e(n_i - n_e)}{\varepsilon_0} , \tag{21}$$

where v_{0z} = const is the drift velocity of electrons in an inhomogeneous magnetic field. Equation (19) is a particular solution of equation (5) for the z-component, and equation (20) is the solution for the r-component.

Using (19) to eliminate j_z from (17) and (18), integrating (17), and inserting the result in (18), we get

$$\frac{1}{r}\frac{d}{dr}\left(r\frac{d\psi}{dr}\right) + G_E^2 e^{-\psi} = 0, \tag{22}$$

where $G_E^2 = \mu_0 e^2 \rho_0 v_{0z}^2 / (m_i + m_e)^2 u_s^2 = \mu_0 j_0^2 / p_0$, ρ_0 is the density at a fixed point, $\psi = -\frac{e v_{0z}}{(m_i + m_e) u_s^2} A_z$.

The solution of equation (22) describes a z-pinch /3/ with a characteristic transverse dimension

$$\delta_E = \left[\frac{(m_i + m_e)^2 u_s^2}{\mu_0 e^2 \rho_0 v_{0z}^2}\right]^{1/2} = \left(\frac{p_0}{\mu_0 j_0^2}\right)^{1/2} \tag{23}$$

The distribution of the magnetic field B_φ, the plasma density ρ, and the current j_z is shown in Figure 2.

To establish the existence of a quasistationary skin layer, we use equations (4)—(9). In connection with Ohm's law (5), we take

$$\vec{j} \perp \vec{v}, \tag{24}$$

$$\mathrm{rot}\, \vec{v} = 0. \tag{25}$$

Decomposing $\vec{E}$ into two components $\vec{j} \parallel \vec{E}_\parallel$ and $\vec{j} \perp \vec{E}_\perp$ and using (4), we replace (5) with two equations:

$$\frac{m_i m_e}{e^2}\left(\frac{\partial}{\partial t} + \vec{v}\nabla\right)\frac{\vec{j}}{\rho} = \vec{E}_\parallel + \vec{v} \times \vec{B} - \frac{m_i m_e}{e^2}\left(\frac{\vec{j}}{\rho}\nabla\right)\vec{v}, \tag{26}$$

$$\vec{E}_\perp = \frac{1}{e\rho}\left(m_e \nabla p_e - m_i \nabla p_i\right) - \frac{m_i - m_e}{e}\frac{d\vec{v}}{dt}. \tag{27}$$

Vector identities and conditions (24), (25) help to reduce equation (26) to the form

$$\frac{m_i m_e}{e^2}\frac{\partial}{\partial t}\left(\frac{\vec{j}}{\rho}\right) - \vec{E}_\parallel = \vec{v} \times \left(\frac{m_i m_e}{e^2}\,\mathrm{rot}\,\frac{\vec{j}}{\rho} + \vec{B}\right). \tag{28}$$

Equation (28) is an identity if

$$\frac{m_i m_e}{e^2}\frac{\partial}{\partial t}\left(\frac{\vec{j}}{\rho}\right) = \vec{E}_\parallel, \quad \frac{m_i m_e}{e^2}\,\mathrm{rot}\left(\frac{\vec{j}}{\rho}\right) = -\vec{B}. \tag{29}$$

For $\rho = \rho_0 =$ const, equations (29) are the ad hoc relationship introduced by London /4/ to explain superconductivity in metals at ultralow temperatures. We see now that these equations are in fact a consequence of Ohm's law when dissipative effects are ignored. Changing over to the potential $\vec{A}(\vec{r}, t)$, we get from (29)

$$\frac{\vec{j}}{\rho} + \frac{e^2}{m_i m_e}\vec{A} = \vec{C}. \tag{30}$$

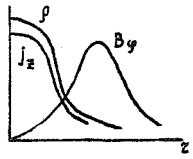

FIGURE 2. Distribution of B_φ, ρ and j_z in a z-pinch.

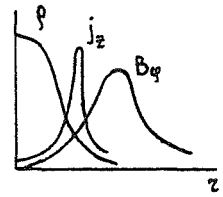

FIGURE 3. Distribution of B_φ, ρ, and j_z according to Weibel /5/.

Analogous solutions can be expected following the application of (30) to equations (4)—(9). Indeed, for the steady-state case $\vec{A} = \vec{A}(\vec{r})$, Weibel /5/ obtained a computer solution of the form shown in Figure 3. In the one-dimensional plane case $\partial/\partial z = \partial/\partial y = 0$, $\vec{A} = \hat{z}A$, the problem reduces to the equation

$$d^2\psi/d\xi^2 - \psi e^{-\psi^2} = 0, \tag{31}$$

which is readily solved in quadratures:

$$\xi = \int \frac{d\psi}{\sqrt{C - e^{-\psi^2}}} + C_1, \tag{32}$$

where

$$\psi = e/\sqrt{m_i m_e}\, u_s, \quad \xi = e\sqrt{\mu_0 \rho_0 / m_i m_e}\, x.$$

Unfortunately, further integration is impossible, and only qualitative analysis or machine solution should be attempted. The characteristic thickness of the skin layer is

$$\delta_j = (m_i m_e / \mu_0 \rho_0 e^2)^{1/2}. \tag{33}$$

Combination of two or three structural elements may lead to more complex configurations, some of which have been studied in /6—8/.

Cylindrical waves propagating in a cold thin plasma transversally to a strong magnetic field were studied in /6/. A set of equations similar to our equations (4)—(9) were solved by numerical integration. Figure 4a shows the typical time and space pattern of the magnetic field B_z directed along the plasma cylinder. The profiles of the density ρ (Figure 4b) and the current j_φ (Figure 4c) were obtained by an appropriate reduction of the magnetic field profile.

Comparison of the ρ, j_φ, and B_z in Figure 4 with the corresponding profiles in Figure 3 shows that the curves are completely analogous. Note that although the problem is time-dependent, equation (33) is nevertheless valid for the characteristic size of the current sheath. The formation of a bundle of plasma sheaths observed as the amplitude of the tube of force lines of the initial magnetic field H_{0z} increases can be apparently interpreted as a result of particle trapping by the magnetic field associated with electron inertia.

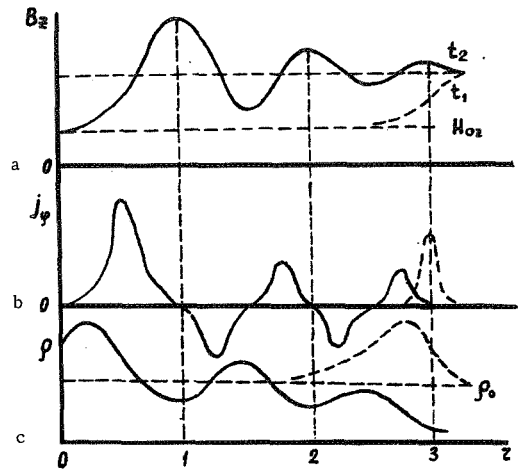

FIGURE 4. Time and space profiles:

a) magnetic field B_z, b) current j_φ, c) plasma density ρ.

A solution corresponding to a plasma sheath contained by the magnetic field of the plasma own current showing a space-periodic structure was derived in /7/. The characteristic sheath thickness is equal to the characteristic filament thickness, where each filament is a local Bennett pinch with δ_E expressed by (23). The inhomogeneous state was proved to be energetically advantageous for the case of a cylindrical current sheath with a z-pinch space-periodic structure /8/. It was moreover established that the number of filaments in a plasma sheath is of the order of magnitude of $I^2/NkTc^2$, where I and N are the total current and the linear number of particles in the current sheath, k is Boltzmann's constant, c is the velocity of light.

The peculiar feature of a self-pinched current sheath is the presence of a neutral plane where the antiparallel magnetic fields cross, so that the conversion of the homogeneous layer into a filamental layer is essentially a topological process. We can thus naturally expect a solution analogous to that derived in /7, 8/ to exist for the case of a plasma sheath focused in a homogeneous magnetic field by the diamagnetic effect of antiparallel plasma currents. The antiparallel currents cross at the neutral plane during the topological readjustment of the sheath. The corresponding topological structure is diagrammed in Figure 5.

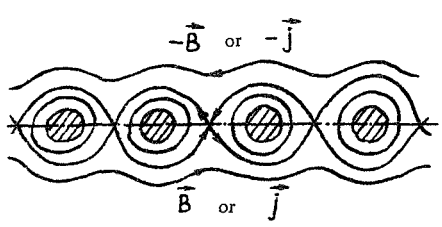

FIGURE 5. Topological conversion of a homogeneous layer into a filamental layer.

The z-pinch and the theta-pinch may form a combined pinch, which will display self-focusing under certain conditions, even without an external field and despite the defocusing effect of the internal field B_z. The necessary condition is that the kinetic pressure and the magnetic pressure of the

longitudinal field be balanced by the pressure of the azimuthal focusing field B_φ.

In auroral regions, the electrons spilling out of traps form high currents with densities of $\vec{j} = 10^{-10} - 10^{-11}$ A/cm^2. Typical temperatures and fields are $T_e = 5 - 10$ keV and $B = 5 \cdot 10^{-1} - 10^{-3}$ gauss. For these parameters, δ_E and δ_j range from a few kilometers to hundreds of kilometers, δ_H is of the order of hundred meters. The magnetosphere tail may have a filamental current structure /7/. For $n < 10$ cm^{-3}, $\varepsilon_p = 0.5 - 1$ keV, $B \sim 2 \cdot 10^{-4}$ gauss, $V_{e0} \sim 2 \cdot 10^6$ cm/sec, the characteristic filament size is $3 \cdot 10^3$ km. The characteristic size of the inhomogeneities for the case studied on PIONEER-6 with the parameters $\varepsilon_p = 13$ MeV, $B = 3 \cdot 10^{-4}$ gauss is

$$\delta_H = 1.4 \cdot 10^4 \text{ km for } \omega = \omega_B \; ; \quad \delta_H = 10^6 \text{ km for } \omega = 10^{-3} \omega_B .$$

If we assume that the fine structure of the galactic arms is determined by the balance between the gas-kinetic and the magnetic pressure and take $B = 10^{-6}$ gauss and $\varepsilon_p = 10^9 - 10^{11}$ eV, we find $\delta_H = 3 \cdot (10^{15} - 10^{16})$ cm for $\omega = \omega_B$ and $\delta_H = 10^{18}$ cm for $\omega \sim 10^{-3} \omega_B$. The fit between the observed and the calculated inhomogeneity sizes is really striking for such a crude model.

Further development of the theory should take into account the entire range of experimental factors, including dynamic and dissipative effects. As an example, let us consider the development of polar aurorae of layered and ray structure. Our results suggest the following mechanism of auroral development. Near the geomagnetic pole (the auroral oval), the geomagnetic field lines form a quasicylindrical bundle. The bundle is pinched and then expands following the interaction with the solar wind on the day side and the field lines in the wake of the magnetosphere tail. As a result, an induced field is formed (simultaneously or with a certain time lag):

$$E \sim \delta H / \tau c .$$

Taking $\delta \sim 4 \cdot 10^7$ cm, $H = 10^{-1}$ gauss, $\tau = 10^3$ sec, we get $E \sim \frac{4 \cdot 10^7 \cdot 10^{-1}}{10^3 \cdot 3 \cdot 10^{10}} 300 = 4 \cdot 10^{-5}$ V/cm, which is close to the usual mean field value in polar aurorae. This field is directed along the "oval" in the westward direction for increasing $\vec{H}_0$ and in the eastward direction for a decreasing field; it is distinctly rotational. Since the pinching is asymmetric, the maximum density of field lines is observed on the side where the incoming particles are incident (the day side) or where the external field lines touch (the night side). According to /6/, sheaths of increased density and increased current move to the pole. Streams of high-energy particles penetrating into the current sheaths from the direction of the magnetosphere tail create a system of longitudinal currents which, because of possible inhomogeneities or instabilities, will break into filaments preferentially directed along the magnetic field $\vec{H}_0$ (combined z-theta filaments). This mechanism does not clash with Piddington's theory, and yet it explains the fine structure of the layered and ray aurorae.

Equations (4) — (9) can be applied to consider the crossing of the magnetic field lines in the magnetosphere tail, which is topologically permissible. The dissipation mechanism of the magnetic field in the region where the field lines cross is not clear, however, although dissipation may definitely

take place for $\nu \to 0$. It is shown in /9/, for example, that the electron inertia remains analogous to the collision effects in the sense that it causes effective relative motion of the plasma and the field even for $\nu \to 0$. The problem reduces to the solution of the equations

$$\frac{\partial \vec{v}}{\partial t} = \operatorname{grad}\left[\frac{m_i m_e}{2 e^2}\left(\vec{c} - \frac{e^2}{m_i m_e}\vec{A}\right)^2 - u_s^2 \ln\rho - \vec{v}^2/2\right],$$

$$\Delta\vec{A} - \varepsilon_0\mu_0 \frac{\partial^2\vec{A}}{\partial t^2} + \mu_0\rho\left(\vec{c} - \frac{e^2}{m_i m_e}\vec{A}\right) = 0,$$

$$\partial\rho/\partial t + (\vec{v}\nabla)\rho = -\rho \operatorname{div}\vec{v},$$

which are derived from (4)—(9) under conditions (24)—(25).

Bibliography

1. Physics of Plasma and Magnetohydrodynamics.— Moskva, IL. 1961. [Russian translations.]
2. Komarov, N.N. and V.M. Fadeev.— ZhETF, 41(2/8):528. 1961.
3. Komarov, N.N. and V.M. Fadeev.— ZhTF, 32(2):133. 1962.
4. de Gennes, P.G. Superconductivity of Metals and Alloys. Translated by P.A. Pincus. — New York, Benjamin. 1966.
5. Weibel, E.S.— Phys. Fluids, 2(1):52. 1959.
6. Berezin, Yu.A.— PMTF, 1:107. 1966.
7. Fadeev, V.M., I.F. Kvartskhava, and N.N. Komarov.— Yadernyi sintez, 5:202. 1965.
8. Komarov, N.N., I.F. Kvartskhava, and B.M. Fadeev.— Yadernyi Sintez, 5:192. 1965; Tezisy dokladov na V Vsesoyuznoi ezhegodnoi zimnei shkoly po kosmofizike. Apatity, Izd. Kol'skogo filiala AN SSSR. 1968.
9. Furth, H.P. Nuclear Fusion, Suppl., Part 1, p.169. 1962.

RADAR ASTRONOMY OF THE SUN

I.M. Gordon

The basic aspects of the radar astronomy of the Sun were first formulated by N.D. Papaleksi in 1946. Following his suggestion, Ginzburg computed the absorption of radio waves in the solar corona /1/. The theory of formation of a reflected signal /2 – 5/ amounts to the following. The ray penetrating into the corona is refracted and, on reaching the point nearest the Sun's center, where the refractive index is close to zero, it is scattered by the electron density inhomogeneities. This scattering is either isotropic or Lambertian. Integrating over the power scattered in the direction of the receiving antenna and allowing for absorption due to Coulomb collisions along the direct and the return paths in the corona, we find the expected power of the reflected signal which is received by the observer. Note that the particular choice of the scattering function does not significantly change the expected result. The receiver power is generally comparable with the power of the signal reflected by an isotropic reflector of area $\pi R_{\odot}^2$. The effective cross section within the framework of the existing theory is essentially determined by the absorption in the corona, i.e., by the global distribution of electron concentration and temperature in the corona. It should be stressed that these parameters are highly stable. Even their variations in the course of the 11-year cycle lead to only insignificant changes in the effective diameter. There is naturally a possibility that the local values of these parameters, e.g., above active regions, may change between wide limits, but since the area of these formations constitutes an insignificant fraction of the Sun's surface, no substantial change (e.g., by one order of magnitude) will be observed in the estimated value of the effective cross section. The higher the frequency, the deeper it penetrates into the corona. Since the collision frequency increases with depth, signal damping is more pronounced at higher frequencies and the effective scattering diameter decreases. The low-frequency range is thus more promising for solar radar astronomy. However, the size of antennas needed to attain satisfactory beam widths imposes a technical limit on the expansion toward longer wavelengths.

The first successful attempt of radar probing of the Sun at 25.6 MHz did not yield any detailed information about the solar corona, since both the antenna size and the transmitter power were low /6/. Systematic experiments aimed at bouncing radar waves of 38 MHz frequency off the Sun were begun in 1964, using a special MIT antenna at El Campo /4, 5/. The knife-edge beam measuring $0.75° \times 6.5°$ permitted making one experiment daily, when the Sun was crossing the meridian. The transmission of the coded signal was 16 min long, and after that the

reception of the bounced signal would begin. Unfortunately, the low resolving power precluded probing separate parts of the solar corona, and the long averaging period made it impossible to study the structure of the reflected signal during a single session. Nevertheless, prolonged systematic experiments revealed highly significant and unexpected data concerning the structure of the reflected signal and the effective cross sections.

The effective cross section was found to vary between unusually wide limits — from a few hundredths to several tens of $\pi R_{\odot}^2$. These changes are particularly surprising, since within the framework of the current theory they entail enormous changes in the global values of the parameters n_e and T_e, which are definitely unacceptable. The variation of the effective cross section by as much as three orders of magnitude is in striking contrast to the observed stability of the mean values of the parameters of the quiet corona, where the reflected signal forms according to current notions. The structure of the signal reveals similarly surprising features. Together with the "violet" components, corresponding to ascending motions, the signal also contains "red" components, which should correspond to descending motions. The quasi-symmetric distribution of the reflected signal over the frequency shifts should be interpreted, within the framework of the theory of signal reflection from moving inhomogeneities, as an indication of the equiprobable occurrence of ascending and descending motions. This result is at variance with the theory of the solar wind.

Another remarkable feature of the reflected signal structure is the presence of extremely high reflections, up to $3R_{\odot}$ and higher, whereas the altitude of the layer with $n = 0$ corresponds to the stationary corona $\sim 1.4 R_{\odot}$. Reflection at the $3R_{\odot}$ altitude requires an electron density exceeding hundred-fold the density of the undisturbed corona.

These puzzling results indicate that the radar observations of the Sun cannot be interpreted within the framework of the existing theories. In particular, the existence of effective cross sections $\sim 100 \pi R_{\odot}^2$ requires high directivity of the bounced signal, since the Sun's image will be much greater than the antenna beam width. The directivity requirements become even more exacting if we remember that, according to /4/, there are periods of high correlation with the area of the flocculi in the central part of the disk (up to +0.95). Hence the conclusion that at least in these periods, most of the components of the reflected signal originated in the corona above the flocculi. Now, since the area of the flocculi is a mere 1% of the visible disk area, and the effective cross sections reached a few $\pi R_{\odot}^2$ units, it is clear that the reflection should be extremely directional /7 — 10/.

The assumption that most of the reflected signal components form in the corona above the flocculi is borne out by the fact that the spectra of the type-A reflected signal (whose principal components form in a thin layer of the corona at distances between 1.3 and $1.6 R_{\odot}$ from the center in the direction to the observer) appeared only when a flocculus was observed at the center of the disk. Besides a characteristic structure which proved totally incompatible with the assumption of signal formation by reflection from the global corona, type-A spectra were found to correspond to high effective cross sections. With noncentral flocculi, the effective cross section diminishes and the signal forms at substantially greater depths (type B).

Once type-A signals have been identified with the coronal regions above flocculi, we can find the solar wind velocity gradient above the active regions of the corona. Assuming that the mean frequency shift of a given coronal layer corresponds to the velocity of the plasma in which the signal originates (this is a straightforward conclusion from the scattering mechanisms considered below), we note that a rapid increase of velocity with altitude is sometimes observed above the active corona. This velocity gradient considerably exceeds that predicted by Parker's theory.

The fundamental difficulties encountered in the interpretation of the radar observations of the Sun within the framework of the existing theories indicate /7 – 10/ that the formation of the reflected signal is mainly governed by induced processes of interaction of electromagnetic waves with various wave modes excited in the turbulent coronal plasma /11 – 12/. An example of processes of this kind is provided by the Raman scattering of electromagnetic waves by Langmuir, magnetic-sound, and ionic-sound waves, "whistlers," etc. The limited applicability of computations which ignore the interactions with plasma turbulences was commented on in /3/.

These mechanisms may in principle account for all the observed properties of the reflected signal: the quasi-symmetry in the distribution of the frequency shifts is a result of the frequency change in Raman scattering, $\nu \to \nu + \nu^p$; the high effective cross sections are the result of predominant back scattering; finally, the high reflections are the result of strong plasma turbulence in the high coronal layers /7 – 10/.

Momentum conservation considerations lead to the following necessary condition for back scattering: $K^p \sim 2K^t$, where K^p and K^t are, respectively, the wave numbers of the wave in plasma and of the electromagnetic wave. In other words, a necessary condition of back scattering is $\lambda^p = \frac{\lambda^t}{2}$.

Let us now consider what wave modes in plasma will produce, through Raman scattering, reflected signal components with the observed frequency shifts ± 60 – 80 kHz. The scattering by Langmuir waves clearly cannot be responsible for the components observed in radar experiments, since it should lead to excessively large frequency shifts. Scattering by magnetic-sound and Alfven waves will not produce back scattering, since it is impossible to satisfy simultaneously the condition of back scattering and the condition which requires that the frequency shifts be equal to the frequency of the scattering waves. The physics of this effect is quite simple. To achieve frequencies of up to 60 – 80 kHz, a sufficiently strong magnetic field is needed. However, for these magnetic field strengths, the velocity and thus also the wavelength are substantially greater than the velocity and the wavelength of the signal. As a result, the signal will undergo small-angle scattering, whereas we are interested in scattering at angles close to 180°. Scattering by "whistlers" cannot produce back-scattering either, since the required characteristics are such that the waves will experience strong Cherenkov damping. Scattering by ionic-sound waves for various values of the electron temperatures and various levels of the ionic-sound turbulence may account for the formation of components with large frequency shifts /7 – 10/.

Excitation of weakly damped ionic-sound waves is possible only in a nonisothermal corona when $T_e \gg T_i$. The radar observations of the Sun at 38 MHz thus apparently indicate the possible formation of extensive

coronal regions with "hot" electrons and "cold" ions above the flocculi. Signal components with small frequency shifts are apparently associated with induced scattering on thermal ions. We have noted above that the fairly narrow angular distribution of the back scattered signal, determined by the k-spectrum of the scattering waves, accounts for the exceptionally large effective cross sections. The increase of the effective cross section may also be associated with the amplification of the signal during its propagation in coronal plasma.*

The "plasma" mechanism of signal reflection naturally explains why the cases of large effective cross sections invariably coincided with enhanced level of solar radio emission and strong fluctuations of its intensity. This distinct correlation is attributable to the fact that the scattering of electromagnetic waves by ionic-sound waves produces the reflected signal components, whereas the scattering of Langmuir waves by the ionic-sound waves in the same volume of turbulent plasma constitutes the source of solar radio emission. The above model can be checked experimentally. The amplification of the reflected signal from any level in the corona is naturally expected to be accompanied by an enhancement of the solar radio emission at the first and second multiples of the electron plasma frequency. Since the altitudes from 1.4 to $3R_{\odot}$ correspond to Langmuir frequencies from 38 to about 5 MHz, the emission of the turbulent plasma can be detected in the frequency band between 5 and 78 MHz. The attempts to discover signal components scattered by Langmuir waves also deserve attention.

It follows from the preceding that when radar observations are carried out with adequate resolution, the radar picture of the Sun will not be unlike the standard X-ray photographs of the Sun, where the flocculi appear as bright spots against the dark background of the quiet corona /9, 10/. The reason for this likeness is quite obvious. The source of solar X rays is the dissipation of plasma turbulence, while the reflected signal is in fact formed by scattering off the waves in the plasma in somewhat higher layers of the corona /9, 10/. It should be noted, however, that the obvious program which calls for an increase of the resolving power and a reduction of the signal averaging time encounters a number of serious difficulties: the powerful beam of electromagnetic waves proves to be unstable, since induced decay processes may lead to an avalanche growth of Langmuir waves and exponential extinction of the signal. The physical nature of the plasma thus sets an obvious limit to resolving power and time resolution which can be attained in radar observations.

One of the significant results of radar observations indicates that the signal power reflected by a "quiet" corona is either very low or zero. This conclusion primarily follows from the fact that in a number of cases the effective reflection cross section was less than a few hundredths of $\pi R_{\odot}^2$. Therefore, at least on these days, the "quiet" corona did not reflect at all, or in any event its reflectance was substantially less than the theoretically predicted figure. In view of the stability of the mean characteristics of the "quiet" corona, its contribution to the reflected power is probably low in other cases too. This conclusion is borne out by an analysis of type-A spectra, where the main components originate in

* V.A. Kotel'nikov called our attention to this point during the discussion of I.M. Gordon's paper at the November, 1968, session of the Department of General Physics and Astronomy of the USSR Academy of Sciences.

coronal regions above flocculi, and the total power of the diffuse components whose origin is still uncertain is low. There is no doubt that the interpretation of this fact may yield valuable information about physical processes in the "quiet" corona.

In conclusion let us consider the prospects of radar observations at other, in particular higher, frequencies. Note that the very existence of high reflections and the theory of scattering by plasma waves suggest that high-frequency radar observations of the Sun will probably prove much more fruitful than previously thought. It can be shown that the expected frequency shift in back scattering by ionic-sound waves and by particles is proportional to the frequency of the signal. Thus in high-frequency radar observations, the receiver pass band should be increased. Parker's theory predicted small expansion velocities deep inside the corona and we could thus expect substantially smaller frequency shifts for signal reflection from moving inhomogeneities. This was probably the reason for the failure of the radar observations of the Sun at 430 MHz. Another reason for the failure of these observations could be the low solar activity in the relevant period. It should be emphasized that the extremely valuable information about physical processes in the solar corona which can be obtained from radar observations at various frequencies provides more than sufficient justification for performing these observations in the nearest future.

Bibliography

1. Ginzburg, V.L.— DAN SSSR, 52:487. 1946.
2. Herr, E.— Proc. IRE, 40:660. 1952.
3. Bass, F.G. and S.Ya. Braude.— Ukrainskii Fizicheskii Zhurnal, 2:149. 1957.
4. James, J.C.— IEEE Trans. Antenna and Prop., A-12:876. 1964.
5. James, J.C.— Astrophys. J., 146:356. 1966.
6. Eshleman, V., R. Barthle, and P. Gallagher.— Science, 131:329. 1960.
7. Gordon, I.M.— Astronomicheskii Zhurnal, 45:1002. 1968; ATs, No.447, 30 October 1967.
8. Gordon, I.M.— Astrophys. Lett., 2:49. 1968.
9. Gordon, I.M.— Astrophys. Lett., 3. 1969. (In press).
10. Gordon, I.M.— ATs, No.487. 29 October 1968.
11. Tsytovich, V.N.— UFN, 90:435. 1966.
12. Tsytovich, V.N. Nelineinye protsessy v plazme (Nonlinear Processes in Plasma). Moskva. 1967.

PENETRATION OF AURORAL PARTICLES INTO THE EARTH'S ATMOSPHERE

L. L. Lazutin

During worldwide and polar magnetic storms, complex dynamic processes take place in the Earth's magnetosphere, involving interaction between charged particles, electric and magnetic fields, plasma and electromagnetic waves. These interaction processes accelerate the particles and cause their injection into the Earth's atmosphere at high latitudes. The present review summarizes the characteristics of the injected auroral particles; the atmospheric consequences of this injection (polar aurorae, geomagnetic storms, etc.) and the prehistory of auroral fluxes, i.e., the magnetospheric processes, are considered only in broad outline. The currently available characteristics of the injected particles were mainly derived from observations of aurorae /1, 2/, the absorption of radio noise from outer space /3, 4/, measurements from stratospheric balloons, rockets /5/, and polar-orbit satellites /6/. Each of these methods has its own advantages and shortcomings, and the main points are summarized in the table below.

A significant portion of the characteristics of auroral fluxes discussed in this review were obtained from stratospheric observations. The main advantage of the stratospheric methods is that they provide continuous data over a long period and measure the spectrum and the distribution of the time and space characteristics of the fluxes; the shortcomings of these methods include the limited spectrum range (> 20 keV) and the limited variety of determinable particle species (electrons only).

The second most extensive source of information — polar aurorae — is produced mainly by electron fluxes with energies from 1 to 10 keV.* Hence the origin of the distinction between soft and hard electron fluxes, which is used in what follows. It should be stressed that there is more to the concept of soft and hard electrons than a mere difference in methods of observation.**

In studying particle injection at high latitudes — admittedly a complex phenomenon — there can be several alternative approaches to the analysis of experimental data. The first (the simplest and the oldest) method aims at elucidating the space, time, and energy statistical characteristics of all the particle showers in general. This averaging obliterates numerous important characteristics, but brings out the general pattern of the process, a certain model which may occasionally prove to be aesthetically attractive

* The proton fluxes on the average are one order of magnitude smaller and show a substantially more homogeneous distribution in time and in space. We will therefore deal mainly with electron fluxes. Moreover, the number of direct measurements of auroral protons is unfortunately small.

** The methods and the instruments for X-ray measurements in the stratosphere are described by I. A. Kuz'min in his paper "Instrumentation for the Measurement of X-ray Bremsstrahlung in the Stratosphere in the Zone of Aurora Borealis" in Part 2 of the Proceedings.

(e.g., the Khorosheva – Feldstein ring – oval). The second approach calls for the identification of individual shower types with common energy and dynamic characteristics which are confined to some closed region in space. If a certain type of particle shower has been identified with fair certainty, we can say that the different disturbances are governed by the same acceleration mechanism and that the particle fluxes have the same history in the interval (both space and time) between acceleration and injection into the atmosphere.

Evaluation of various methods of observation as a source of information on the characteristics of auroral particles

Form of observation	Energy range, eV	Flux, spectrum	Angular distribution	Spatial distribution, motion	Variations	Observation time
Polar aurorae	10^2–10^4	Indirectly, from glow altitude and intensity	-	Excellent within limits of instrumental resolution		~10 hrs
Riometers	10^4–10^5	Very roughly from frequency dependence	-	Roughly, using the riometer network	Satisfactory for periods greater than 1 min	Continuously
Radiosondes	$2 \cdot 10^4$–10^6	Adequately, from the X-ray spectrum	-	Roughly from several instrument launchings in different locations, more precisely from combined measurements of narrow-beam detectors	Satisfactory within the limits of instrumental resolution	~10 hrs
Rockets	10^2–10^6	Satisfactory	+		Rapid variations	A few minutes
Satellites	10^2–10^6	Satisfactory, with some time and space averaging	+	Averaged characteristics, hard to separate from time variations	Rapid variations	A few minutes

The third approach calls for a comprehensive analysis of the development of a particular electromagnetic disturbance (a magnetospheric substorm). We are fairly close to perfecting a general model of the magnetospheric substorm, but individual disturbances greatly differ from one another and generalizations based on insufficient material must be avoided. This is a much more difficult approach, since it requires simultaneous measurements by a wide range of ground and airborne instruments. Therefore, it is only recently that publications of this class appeared in the literature /8, 9, 10/. We will not consider this approach in our review.

A general theory probably will be developed only after some progress has been made in the third stage of experimental research, but this is by no means a universal opinion, and the attempts to create a comprehensive theory of polar aurorae are not a passing fashion /11/.

The statistical features of the injection of auroral particles, which have been firmly established by now, amount to the following:

A. The particle injection is highly nonuniform in space and in time; the electron flux may vary by a factor of 10^6 (from 10^2 to 10^7 $(cm^2 sec\ sterad)^{-1}$ for E > 40 keV /6/); the rate of change may reach about one order of magnitude in 5 msec /12/ and the corresponding spatial scale is a few hundreds, and possibly tens, of meters at the boundary of the atmosphere /13/.

B. The particle injection zones form a fairly definite configuration, which hardly changes with time or with the level of magnetic activity. This configuration is fixed relative to the Earth—Sun direction, and the Earth (with the entire network of geophysical stations) spins under it.

C. In the midnight sector, the injection of both soft and hard auroral particles occupies a fairly narrow (5—10°) belt around geomagnetic latitude 65°.

D. The injection belt is split into two around noon; the hard electrons enter the atmosphere approximately at the same latitude as at night, whereas the soft electrons are injected in a narrow belt around 75°.

E. The particle showers near the pole show a greater stability in time; the particle fluxes and the energies are substantially lower than in the auroral zone.

F. In the afternoon sector, the average electron flux reaches a minimum.

These are the basic firm data on the spatial distribution of particle injection. Some less certain, but more detailed models will be considered below.

The data regarding the energy characteristics of the auroral electrons are less certain. The data on polar aurorae (altitude, relation to auroral absorption of radio noise from outer space) show that the average electron energy is substantially softened along the inner oval, from night side to day side /1/. In the outer ring, a reverse situation is observed: the hardest electron fluxes are observed in the morning /14/. Stratospheric data reveal a more complex variation of the energy of hard electrons during the day /15, 16/ (Figure 1).

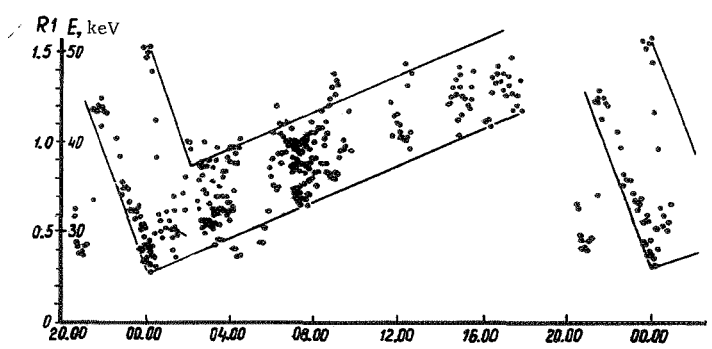

FIGURE 1. The diurnal variation of the spectral changes of the X-ray flux.

There are very few direct measurements of particles in the daytime inner injection zone; detailed studies based on the measurements of polar aurorae were carried out by Starkov and Fel'dshtein /17, 18/, and we will therefore consider the outer injection ring.

EVENING AND MIDNIGHT SHOWER TYPES

The injection of auroral particles reaches its most complex and dynamic character around midnight. Although numerous authors analyzed ground and stratospheric measurements of the midnight particle showers, the nature of the process can be described only in rough outline, with much less precision than for other shower types.

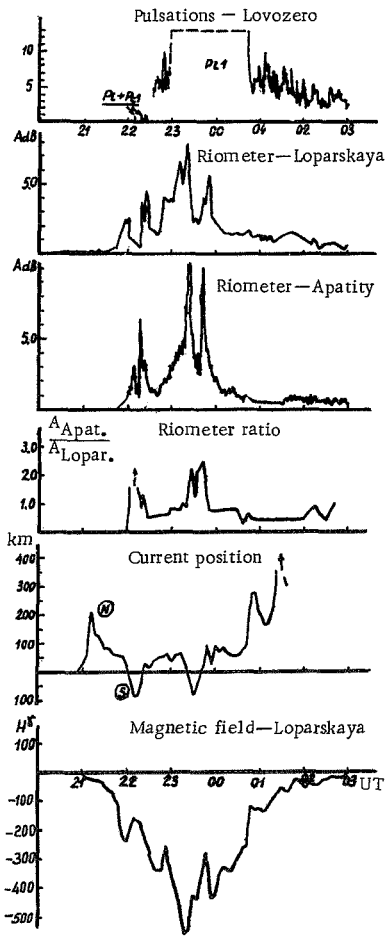

FIGURE 2. The time curve of the midnight electron injection according to /10/.

In the evening (20 — 24 LT), the showers are mostly quiet and structureless, covering an area with a characteristic dimension of D~200 km; the spectrum is at its hardest (E_0~30 — 50 keV)* /15, 19, 20/. On the other hand, satellite measurements /21/ indicate that the electron spectrum early in the evening is softer than at any other time. A similar conclusion emerges from auroral observations /22/; the polar aurorae occur in a homogeneous wide arc in the evening. Pudovkin /22/ attributes this discrepancy in results to the lack of excess X-ray radiation in the stratosphere during the relevant time interval. The measurements thus only give a weak background of hard electrons, which are detectable during the day irrespective of the disturbance level. This conclusion does not follow from the observations of particle fluxes in the stratosphere. Therefore, the most plausible assumption is that two independent fluxes of soft and hard electrons exist, and the different measurement methods respond to a limited spectrum range only. Moreover, the soft electrons may penetrate farther north than the hard electrons.

After the breakup of the polar aurorae, a new phase of particle penetration begins. The electron flux may increase by two orders of magnitude in about 10 msec /8/. As a rule, several bursts with duration from 20 msec /8, 13/ to several tens of minutes are observed. The dimensions of the injection regions are related to

* An exponential spectrum is generally assumed for the auroral electrons, $N(>E) = N_0 \exp(-E/E_0)$.

the burst duration: the shorter the burst, the more localized it is /10/. The instantaneous electron fluxes in these cases are larger than during any other time of the day; the flux of electrons with $E > 30$ keV may reach $5 \cdot 10^8$ $cm^{-2} sec^{-1}$ /23/. It is difficult to speak of regularities in the variation of the electron spectrum in this period, since the measurement data are often quite contradictory. The electron spectrum becomes markedly softer during the breakup /9/ or soon after /19/, hard and soft bursts may alternate, soft and hard electron fluxes may be observed simultaneously /19, 15/ and independently /24, 25/. It is hoped that careful analysis of the electron penetration regions during the bursts will shed some light on this problem. Indeed, the electron penetration regions in these cases are small and rapidly moving. Figure 2 shows that the brief electron bursts are injected to the south of the general penetration region; this is evident from the position of the ionospheric currents and from the ratio of the near riometers /10/. Moreover, a latitude separation of particles according to energies is observed, the soft electrons penetrating nearer the pole /26, 9, 27/. The measurement results thus significantly depend on whether the recorder is located in the northern or the southern part of the penetration region.

Breakup injections change into more prolonged injections, which are clearly associated with negative bay disturbances in the H-component of the magnetic field /28/. The corresponding electron spectrum is very soft ($E_0 \sim 10-15$ keV), and a satisfactory correlation is observed between the stratospheric X rays and polar aurorae /26, 29/ and Pi-1 micropulsations /10, 30, 31, 32/. In these cases, a latitude separation of particles of various energies is also possible.

SLOWLY VARYING ABSORPTION

In morning hours (06 – 13 LT), riometric and stratospheric data clearly bring out a special type of auroral particle injection, variously known in the literature as Brown-type absorption, slowly varying absorption (SVIA or SVA), or extended morning injections /14, 20, 22, 28, 34/.

The time curve of particle injection (consisting mainly or totally of electrons) is characterized by a rapid growth of intensity (20 – 30 min) and a slow quasi-exponential decrease, which takes 1 – 5 hrs. SVA is characterized by total absence of local geomagnetic disturbances, although a substorm is observed on the midnight meridian at the same time (particle injection, negative bays); the SVA onset lags 1 – 10 min /34/ or 20 – 30 min /33, 56/ relative to the breakup time.

Measurements of the X-ray energy spectrum in the stratosphere /15/ and energy estimates from riometric and photometric data /22/ indicate that the electron spectrum during the SVA is harder than at night during breakup or during negative bays; ground measurements give mean electron energies between 40 and 100 keV /22/, and E_0 according to stratospheric data varies between 15 and 40 keV /34, 19/.

Stratospheric measurements, and especially coordinated flights of several balloon probes launched at different latitudes and longitudes /37/, elucidated a number of new characteristics of SVA. In particular, it was

established that the penetration of electrons occurs simultaneously at points separated at least by as much as several hundred kilometers along the same geomagnetic parallel; the penetration begins to the north of L = 6.5, and then the equatorial boundary of the penetration region moves south with a velocity of some 500 m/sec, retaining its original orientation (Figure 3). The southward motion was observed down to L = 4.5. The decrease in the intensity of the penetrating electrons occurs synchronously over the entire area and begins during the phase of the southward motion.

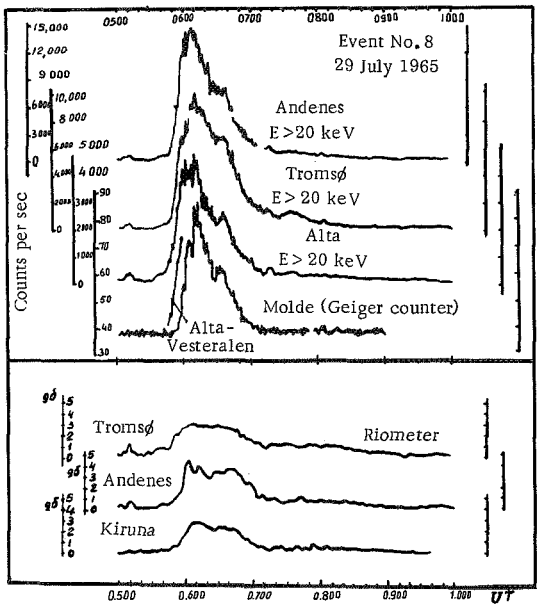

FIGURE 3. SVA curves from flights in Scandinavia.

The X-ray spectrum grows softer during the upward phase of the SVA intensity, and after that the energy increases /37, 19/; the softer spectrum is probably due to the approach of the penetration front to the balloon; the nearer the penetration region to the balloon, the smaller is the relative absorption of the low-energy photons in air. Comparison of the nighttime and daytime SVA shows that this absorption is due to electrons. Some authors, however, point to the possible injection of protons /34/, in particular in the last stage of SVA.

SLOW VARIATIONS (SV)

Slow variations of the electron flux with a period of 300 – 500 sec are often observed during the SVA. The dimensions of the region encompassed by the slow variation are comparable to the SVA dimensions: 200 – 500 km

in latitude and over 1000 km in longitude /38/. There are reports of synchronous variation across the entire injection region /38/ and of a fast motion of the wave from east to west with velocities of 2 — 2.5 km/sec /39/. The electron spectrum during a slow variation is apparently no different from the general background /19, 38/, although random changes in the spectrum were observed /40, 41/: in particular, the maximum was seen to grow softer /41/. The large spectral range of the slow variations is borne out by the cases of synchronous variation of X rays, polar aurorae, and riometer absorption /19, 34, 37/. A magnetic field variation (giant pulsations) /42, 43/ is often observed during the slow variation, both being of approximately the same period.

The slow variation in all probability is related to the modulation of the penetrating electron stream by magnetohydrodynamic waves /42/. The possible association of the slow variations with the variable electrical field produced in the ionosphere as a result of the gravitational oscillations of the air column was also considered /44/. Another important fact is that variations of the electron flux with a period of 100 — 200 sec are also observed in the plasma layer of the magnetosphere tail /45/. Variations of electrons with a period of 300 — 1000 sec were discovered by Lin and Anderson /46/ in the skirt, and the maximum of the observed cases falls in morning hours /46/.

FAST VARIATIONS (FV)

Starting with the breakup and up to the afternoon hours, fast variations with a period of 5 — 30 sec are sometimes superimposed on the smooth variations of the flux of auroral electrons. We should apparently distinguish between two types of FV — the faster type with a period of 5 — 20 sec, which are observed in early morning hours (02 — 10 LT) and the daytime type, which are observed around noon (10 — 15 LT), with a period of 20 — 30 sec /8/. The first type of FV has been studied in greater detail, and we will therefore mainly consider the characteristics of this type.

FV are generally observed against the background of the previously considered slower types of penetrations. They produce a modulation of the main flux, which is more like a pulse modulation than a sinusoidal modulation. The period may prove to be quite stable in a number of cases /8, 47/, bu mostly no distinct period is observed; the period of the daytime FV tends to decrease /37/.

The region corresponding to FV is significantly smaller than the region of the basic slow variations: it occupies 100 — 150 km for both the morning and the daytime types. In a number of cases this region may be larger. Thus, comparison of the data obtained at an altitude of 2350 km and with a radiosonde reveals a certain correlation of pulsations over a distance of up to 400 km in the east — west direction ($\Delta L \sim 0.9$) /48/. Not all the electron penetrations are subjected to FV, and the onset or disappearance of FV is often associated with alternation of the fundamental slow bursts (Figure 4). Measurements of the X-ray spectrum show that the electron flux is somewhat harder at the maximum (by 2 keV) /8/; in other words, the modulation coefficient increases with the increase in energy (from

1.7 to 40 keV to 2.3 – 2.4 for E > 80 keV /49/). The spectrum during the growth phase is harder than during the downward phase of the intensity curve /49/ (Figure 5).

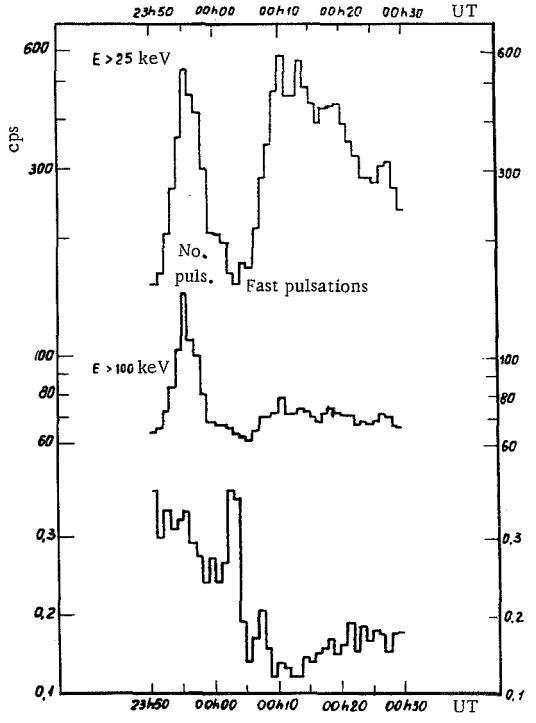

FIGURE 4. Appearance of fast variations with simultaneous change in the energy of the main electron penetrations.

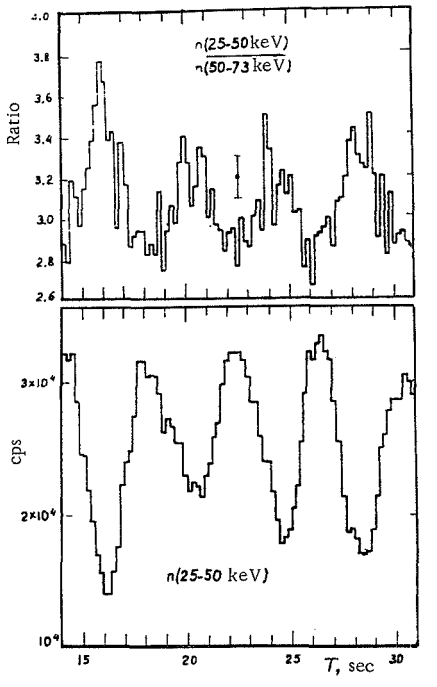

FIGURE 5. The spectrum of fast pulsations.

In some cases, FV have been observed during the spectrum of preferentially slow electrons /50/. The harder electron spectrum at the maximum indicates that this phenomenon cannot be attributed to the passage of inhomogeneous penetration regions above the radiosonde, since in this case a softer spectrum should have been observed /37/. Pulsations of similar periods are often observed in numerous geophysical effects associated with electron penetration. Pulsations with periods of 5 – 15 sec were observed in the auroral absorption of radio noise from space /37/; in the polar aurorae in morning hours /51 – 54/, the pulsations are generally associated with diffuse spots. Finally, Pi-1 pulsations are observed in the magnetic field at night and in morning hours, and in daytime the FV are accompanied by Pc-3 pulsations /31/.

Comparison of the various pulsation phenomena reveals a strict relationship between them. As a rule, the occurrence times coincide and there is no close correlation in the periods of the variations, although in certain cases the correlation is relatively close. Rosenberg et al. /55, 56/

launched a photometer on the same radiosonde, and since the angular characteristics of the detectors also coincided, closely correlated events were observed. Note that the emission in the 5577 Å line lagged behind the fast variation by approximately 1 sec for $\tau \sim 10$ sec, which may be interpreted as a result of relative nearness of the source of variations $(1-2\ R_E)$.

MICROBURSTS

Microbursts are generally observed against the background of quiet injection during the daytime hours, between 4 and 17.30 LT /57/; before noon, they are twice as frequent as in the afternoon hours, showing a central peak at 8.30 LT. The duration of microbursts is from a few minutes to 5 hrs; on the average, a single event comprises 10^3 individual bursts; two groups are generally observed daily for a few days after a magnetic storm. The characteristic duration of microbursts is about 0.2 sec, the recurrence period is about 0.6 sec, and the time between successive groups of bursts is about 10 sec /58/. The morning bursts are asymmetrical: they are described by the expression $1-\exp(-t/\tau_R)$, where $\tau_R \sim 30$ msec, and the downward phase is described by $\exp(-t/\tau_D)$, $\tau_D \sim 200$ msec. Later, after 9.30 LT, the bursts become symmetrical /59/. These symmetrical bursts are the most frequent ones (Figure 6).*

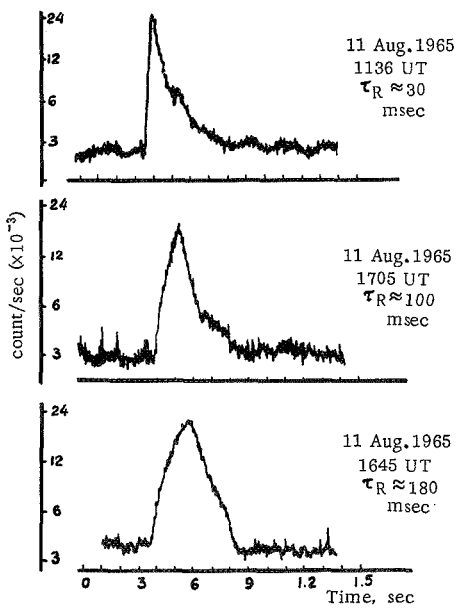

FIGURE 6. Three types of microbursts.

A characteristic particle flux at the maximum is 400–2000 $cm^{-2}sec^{-1}sterad^{-1}$ for $E > 30$ keV /58/; for $E > 60$ keV, the maximum flux is about 100 $cm^{-2}sec^{-1}$ /59/, or 0.2–15 $cm^{-2}sec^{-1}sterad^{-1}keV^{-1}$ /57/. Satellite measurements gave a flux of $3 \cdot 10^{-5}$ $cm^{-2}sec^{-1}sterad^{-1}$ for electrons with $E > 40$ keV, which corresponds to 20 $cm^{-2}sec^{-1}$ /60/. The observations exceeded the background readings by a factor of 20 /12/. Microbursts are observed in the auroral zone, more frequently at L = 6 than at L = 8 /57/, in strips elongated in the north–south direction which drift to the east with a velocity of 250–300 m/sec /58/. During 5% of the total time of observations, microbursts with velocities of up to 10–100 km/sec were observed. Comparison of satellite and balloon data shows that the region of simultaneous

* Very short bursts of 5–25 msec duration were occasionally observed /12/.

penetration extends over 400 km along the parallel and 250 km along the meridian /48, 60/ at L = 6 – 8.5. According to other data, the microburst region is smaller, as small as 40 km, or even 20 km /58/. The microburst spectrum coincides with the background spectrum; E_0 = = 20 – 25 keV /41, 57/, but according to other data the spectrum grows softer during the burst /58/. Rocket measurements record microburst electrons with E ~ 80 – 160 keV and 160 – 320 keV, and there are no electrons recorded between 5 and 20 keV (Figure 7).

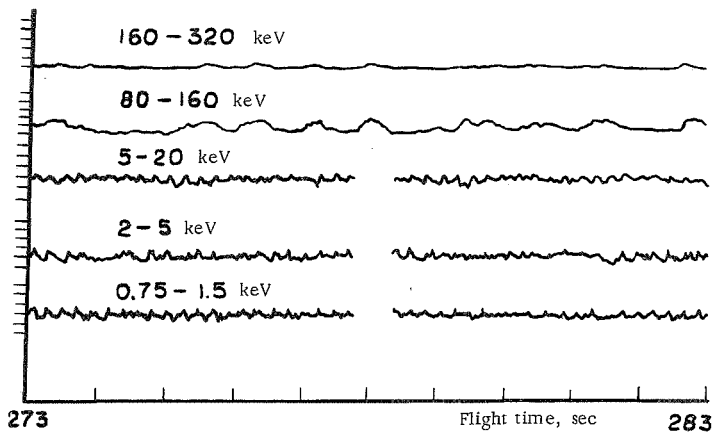

FIGURE 7. Spectral characteristics of microbursts according to rocket measurements.

Satellite observations of microbursts /60/ show that the flux of injected electrons (180°) during a microburst increases at double the rate characteristic of the trapped electrons (90°) (the background behaves in an exactly opposite manner), which does not correspond to the classical cases of penetration, when the fluxes are isotropic. Daytime rocket measurements /62/ revealed a 10-fold increase of the flux in 3 msec (the fastest variation so far recorded), and the high-energy particles preceded the soft particles (60 – 90 and 90 – 150 keV) by 0.01±0.01 sec, or by 0.1 – 0.26 sec in other cases; these figures give for the position of the sources distances ranging between 2.5 and 22 R_E. According to other data /59/, there is no dispersion (< 10 msec), which is either an indication of the nearness of the source or points to a significant interaction between the particles and also between the particles and the field.

In addition to the relation of microbursts to magnetic storms, there is a certain relation of the microbursts to magnetic pulses /30/ in a narrow time interval (11 – 13 LT) and to Pi-1 pulsations; the recurrence period of the microburst groups (10 sec) coincides with the periods of polar aurorae, discussed before.

DAYTIME MINUTE BURSTS (DMB)

Hard X-ray (electron) bursts with a duration of up to several minutes are observed in daytime /64/ (Figure 8). The extent of the DMB region in space is less than 230 km (one measurement /65/).

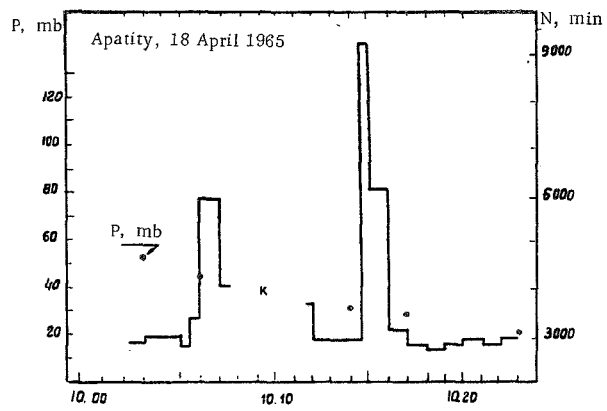

FIGURE 8. Daytime minute bursts.

According to our data /64/, DMB are observed in geomagnetically active periods, but they do not coincide with particular magnetic field or riometer disturbances. A case of DMB during a sudden impulse was described in /37/; the photon spectrum during the DMB (11.06 UT) was harder than before and after Si. According to spectral characteristics and time properties, daytime variations with a period of 95 — 110 sec are close to DMB /66/.

ROCKET MEASUREMENTS

Rocket measurements yield valuable information about the energy distribution of the injected particles in a wide range of energies, about the angular distribution, the composition of particles (in particular, the composition of the auroral protons), and some data about fast flux variations. Rocket measurements are so far fairly isolated and do not lead to any general conclusions in view of the tremendous variety of the space, time, and energy characteristics of the auroral radiation.

Spectrum measurements

Stratospheric measurements give an electron spectrum of the form $I = I_0 \exp(E/E_0)$, where E_0 varies from n to $n \cdot 10$ keV. Rocket measurements show, however, that this is not always so. In some cases, the spectrum is softer and almost monoenergetic /67 — 69/. Thus a monoenergetic spectrum with $E \simeq 6$ keV with a rapid drop in the high-energy region with $E_0 < 100$ eV was measured at 5577° Å /67/ (Figure 9). Soft spectra with $E_0 \simeq 4$ keV and 8 keV were measured /70/ in IBC-1 and IBC-2 emission. The variation of the (soft) electron flux was substantially

less than the variation of the auroral intensity. A soft non-monoenergetic spectrum consisting of several independent fluxes was measured by Reidy et al. /69/. In general, the fluxes of high-energy electrons cannot be regarded as a "tail" of the soft spectrum; some measurements /24, 71/ point to the possible existence of a second maximum (E ~400 keV), and in other cases the fluctuations in the high-energy region are much larger than in the low-energy region (the electron flux between 80 and 160 keV increased by two orders of magnitude in 50 sec, whereas between 5 and 20 keV it increased by one order of magnitude and between 2 and 5 keV the flux did not change /61/). According to measurements /13/, the maximum variation is observed for energies above 45 keV; for E > 100 keV the variation is smaller, but on the other hand the electron spectrum becomes softer during stable injections /24/. In one measurement, a steady growth of the electron energy from 10 to 15 keV was observed; it was due to the rocket having traveled 100 km in the southward direction (there is a latitude separation of the electrons according to energies /27, 33/, associated with local accelerations toward the pole in the field of about 55 mV/m).

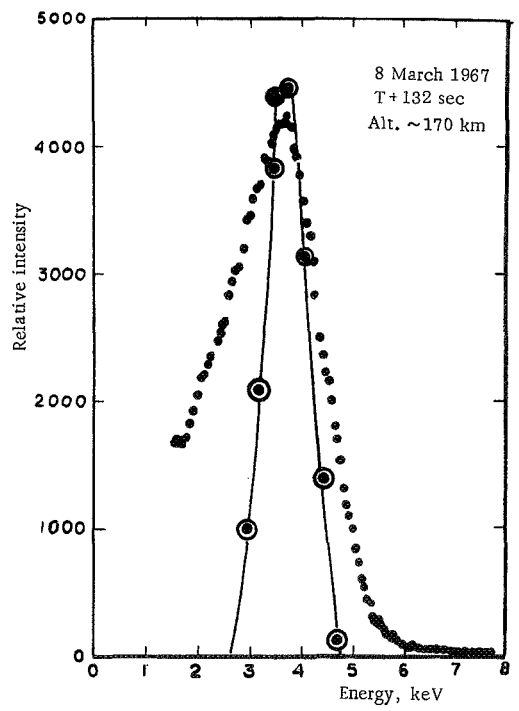

FIGURE 9. Monoenergetic spectrum of injected electrons measured from a rocket. The solid curve is the detector calibration.

Rocket measurements also permitted estimating the fluxes of electrons with energies below 1 keV. The measurements show that the electron spectrum extends beyond the 100 eV energy range, and the flux of these electrons is too high to be regarded as a flux of secondary particles; it may be accounted for by the local acceleration of particles in an electric

field directed along the magnetic lines of force /72, 73/. The same explanation applies to the residual upward electron flux, measured in /74, 75/.

We should stress one characteristic feature of the angular distribution of the particles: the electron flux in the undisturbed case is anisotropic, with a maximum at 90° to the line of force, whereas during penetration the flux is isotropized /24, 61, 74, 76/. The above-described cases of upward electron fluxes (> 40 keV) with intensities increasing the theoretical prediction constitute a deviation from this rule (they are observed for weak fluxes only; no such anomalies occur during high intensity penetrations). The explanation of this effect is to be sought in the modification of the pitch-angle distribution of the electrons by the ionospheric electric field /76/. In case of fast variations, the fluctuations in the loss cone may be one order of magnitude deeper than in a trapped flux /12/.

Measurements of the diurnal variation

Rocket measurements of the diurnal variation and of other statistical characteristics are less reliable than the stratospheric measurements, since the conclusions are based on isolated measurements. On the whole, the results are consistent with stratospheric data. They reveal, first, a greater variation of the spectrum and a higher average intensity of the electron flux at night than in daytime ($1.6 \cdot 10^8$ $cm^{-2} sec^{-1} sterad^{-1} keV^{-1}$ and $6 \cdot 10^7$ $cm^2 sec^{-1} sterad^{-1} keV^{-1}$ for E = 2 keV) /61/ and, second, a harder spectrum in daytime on the average.

Space and time characteristics

Rocket measurements of the space and time characteristics of the electron flux on the whole bear out the stratospheric measurements of the fast variations of the electron flux, as described before. Considerable importance is attached to measurements of small spatial inhomogeneities $D \sim 30$ m, which are observed from rockets /13, 24/, and time inhomogeneities (of the order of 1 msec); in particular, the existence of a time delay for electrons of various energies should be established. The results of the isolated measurements are still contradictory: in some cases the delay is observed /77/, while in others not /13/.

Rocket measurements of protons corroborate the results of indirect (ground-based) measurements indicating that the proton flux is one order of magnitude less than the electron flux /24, 78, 79/ and is constant in time /13/. The anticorrelation of protons and electrons during injection is particularly interesting /71/; as the electron flux increases and the angular distribution of electrons develops from anisotropic to isotropic, the flux of protons with E > 65 keV changes from isotropic to anisotropic with a maximum at 90° (a reduction by a factor of 5 in the loss cone) and the ascending proton flux exceeds the descending flux. The possible reason for this effect is to be sought in the existence of a local electric longitudinal field. The flux of alpha particles in auroral flow is even

smaller. The fluxes of electrons, protons, and alpha particles are 10^6, $1.4 \cdot 10^5$, and $2.6 \cdot 10^4$ particles/cm^{2}sec · sterad for energies greater than 20, 50, and 50 keV, respectively /79/.

CONCLUSION

The various characteristics of the auroral particles injected into the atmosphere present a fertile ground for the development and the verification of the mechanisms of particle acceleration and motion in the magnetosphere. This problem falls beyond the scope of our review, and we will only make a few general remarks on the subject.

Figure 10 shows a simplified block diagram of the history of auroral particles. It starts with an acceleration mechanism (or several acceleration mechanisms); the accelerated particles either penetrate directly into the Earth's atmosphere or experience certain additional interactions — drift motion, modulation by magnetohydrodynamic or plasma waves, etc. There is a further possibility of the accelerated particles becoming trapped in the radiation belt and later being injected into the atmosphere. Each of the possible acceleration—interaction—injection chains should correspond to a definite type of penetration, and vice versa. If a certain type of injection repeats itself in different cases, we conclude that these cases were characterized by the corresponding mechanisms of acceleration and additional interaction. The different penetration types thus provide the elementary cells from which the overall picture of the phenomenon can be constructed.

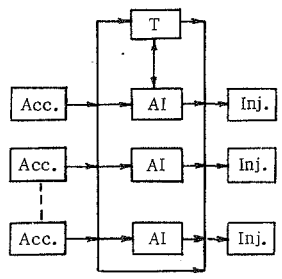

FIGURE 10. A block diagram illustrating the history of auroral particles (acceleration, additional interaction, trapping, injection).

Let us consider the existing models of the penetration zones of auroral particles. Figure 11 schematically shows some of the leading models: a) Khorosheva and Feldstein's zone /2, 17, 18/, b) two penetration zones according to Mishin /80/, c) the currently most popular penetration scheme of Hartz and Brice /81/. The various characteristics of the different penetration types considered above can be reduced to two groups. However, the models of particle penetration hardly improve our understanding of the processes which take place in the magnetosphere during disturbances. Indeed, this approach lumps different types of additional interactions and possibly even different acceleration mechanisms in a single ring zone. It is essential to consider separately the zones corresponding to each known type of particle penetration and also to examine the dynamic behavior of the entire process, e.g., during the development of a substorm. The dynamic approach has recently been worked on by Akasofu /82/; he also published a detailed analysis of the development of a substorm, but unfortunately his starting point was instrumental (a substorm in the X-ray spectrum, a substorm in riometric absorption, etc.), and no classification according to different types of penetration was attempted.

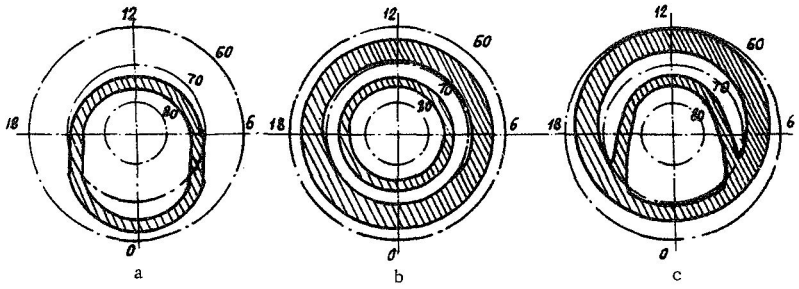

FIGURE 11. Penetration zones of auroral electrons:

a) according to Khorosheva and Feldstein /2,17/; b) according to Mishin and Saifudinova /80/; c) according to Hartz and Brice /81/.

We tried to classify the different penetrations of auroral particles into the Earth's atmosphere at high latitudes. In view of the great diversity and complexity of the phenomenon, the author tried to confine himself to sufficiently reliable experimental data. For this reason, many of the previously mentioned characteristics, which are based on individual measurements, were ignored, the important topic of the possible relation of the penetrating particles to auroral and trapped radiation in the Earth's magnetosphere was not considered, theoretical problems were not discussed. Limitations of space rule out a detailed discussion of the characteristics of auroral protons, auroral particles inside the polar cap, the dynamics of penetration during a substorm. These problems may constitute the subject of a separate paper.

I would like to acknowledge the help of my colleagues at the Cosmic-Ray Laboratory in the course of this project.

Bibliography

1. Isaev, S.I. Morfologiya polyarnykh siyanii (Morphology of Polar Aurorae).— Leningrad, Izdatel'stvo "Nauka." 1968.
2. Khorosheva, O.V.— In: "Polyarnye siyaniya," No. 16. Moskva, Izdatel'stvo "Nauka." 1967.
3. Driatskii, V.M.— Geomagnetizm i Aeronomiya, No. 6:1061. 1966.
4. Hiltquist, B.— Planet. Space Sci., 8:142. 1961.
5. Ivanov-Kholodnyi, G.S.— In: "Fizika magnitosfery i polyarnye buri," p. 171. Irkutsk, Izd. SO Izmiran. 1968.
6. O'Brien, B.J.— Review Presented at the IQSY/COSPAR Symposium. London, England. July, 1967.
7. Kuz'min, I.A. Present Collection, Part 2, p. 139.
8. Parks, G.K., F.V. Coroniti, R.L. Pherron, and K.A. Anderson.— J. Geophys. Res., **73**(5):1685. 1968.
9. Pilkington, G.R., C.D. Anger, and T.A. Clark.— Planet. Space Sci., **16**(6):1685. 1968.
10. Kuz'min, I.A., L.L. Lazutin, G.A. Loginov, M.I. Pudovkin, A.N. Charakhch'yan, and T.N. Charakhch'yan.

In: "Polyarnye siyaniya," No. 17, p. 98. Moskva, Izdatel'stvo "Nauka." 1968.
11. Lomonosov, M.V. Sochineniya (Collected Works), Vol. 3.— Moskva-Leningrad, Izdatel'stvo AN SSSR. 1952.
12. Parks, G.K., D.W. Milton, and K.A. Anderson.— J. Geophys. Res., 72(17):4587. 1967.
13. Mozer, F.S.— J. Geophys. Res., 73(3):999. 1968.
14. Ansari, Z.A.— J. Geophys. Res., 69(21):4493. 1964.
15. Bewersdorf, A., J. Dion, J.P. Legrand, E. Keppler, G. Kremser, and W. Riedler.— Space Res., 7/1:645. 1967.
16. Lazutin, L.L.— Trudy Alma-Atinskoi konferentsii po kosmicheskim lucham. 1966. (In press).
17. Feldstein, Y.I. and G.V. Starkov.—Planet. Space Sci., 15:209. 1967.
18. Starkov, G.V. and Ya.I. Fel'dshtein.— In: "Polyarnye siyaniya," No. 17:22. Moskva, Izdatel'stvo "Nauka." 1968.
19. Barcus, J.R. and T.J. Rosenberg.— J. Geophys. Res., 71(3):803. 1966.
20. Kremser, G. From Aurora and Airglow, p. 477. Chicago. 1967.
21. Fritz, T.A.— Trans. AGU, 47(1):130. 1966.
22. Pudovkin, M.I. Polyarnye magnitnye buri (Polar Magnetic Storms).— Leningrad, Izdatel'stvo "Nauka." (In press).
23. Barcus, J.R.— J. Geophys. Res., 70(5):1237. 1965.
24. Mozer, F.S. and P. Bruston.— J. Geophys. Res., 71(19):4451. 1966.
25. Reidy, W.P., E.R. Hegblom, and J.C. Ulwick.— J. Geophys. Res., 73(9):3072. 1968.
26. Lazutin, L.L. and V.K. Poldutin.— Izvestiya AN SSSR, Seriya Fizicheskaya, 30(11):1804. 1966.
27. Albert, R.D.— J. Geophys. Res., 72(23):5811. 1967.
28. Kremser, G. From "Introduction to Solar-Terrestrial Relations," p. 415. Holland. 1965.
29. Vinkler, D.P.— In: "Radiatsionnye poyasa i geofizicheskie yavleniya," p. 15. Moskva, Izdatel'stvo "Nauka." 1963.
30. Milton, D.W., R.L. McPherron, K.A. Anderson, and S.H. Ward.— J. Geophys. Res., 72(1):414. 1967.
31. McPherron, R.L., G.K. Parks, F.V. Coroniti, and S.H. Ward.— J. Geophys. Res., 73(5):1697. 1968.
32. Wilhelm, K.— J. Geophys. Res., 72(7):1995. 1967.
33. Albert, R.D.— Phys. Rev. Lett., 18(10):369. 1967.
34. Bewersdorf, A., G. Kremser, W. Riedler, and J.P. Legrand.— Arkiv. geophys., 5(2):115. 1967.
35. Pudovkin, M.I., O.I. Shumilov, and S.A. Zaitzeva.— Planet. Space Sci., 16:881. 1968.
36. Pudovkin, M.I. and O.I. Shumilov.— Uchenye Zapiski LGU, Voprosy Geofiziki, No. 17:241. 1967.
37. Bewersdorf, A., G. Kremser, J. Stadness, H. Trefall, and S. Ullaland.-- J. Atmos. Terr. Phys., 30(4):591. 1967.
38. Barcus, J.R. and T.J. Rosenberg.— J. Geophys. Res., 70(7):1707. 1965.
39. Brönstad, K. and H. Trefall.— J. Atmos. Terr. Phys., 30(2):205. 1968.
40. Trefall, H. and K. Bärdsen.— J. Geophys. Res., 68:4909. 1963.

41. Hudson, H.S.— Trans. AGU, 47(3):462. 1966.
42. Anger, C.D., J.R. Barcus, R.R. Brown, and D.S. Evans.— J. Geophys. Res., 68:3706. 1963.
43. Ullaland, S.L., H. Trefall, G. Kremser, and A. Bewersdorf.— J. Atmos. Terr. Phys., 29(4):395. 1967.
44. Parthasarathy, R. and V.P. Hessler.— J. Geophys. Res., 69:2867. 1964.
45. Bame, S.J., J.R. Asbridge, H.E. Felthauser, E.W. Hokes, and I.B. Strong.— J. Geophys. Res., 72(1):113. 1967.
46. Lin, R.P. and K.A. Anderson.— J. Geophys. Res., 71(7):1827. 1966.
47. Brown, R.R. and R.A. Weir.— J. Atmos. Terr. Phys., 29(12): 1611. 1967.
48. Milton, D.W. and M.N. Oliven.— J. Geophys. Res., 72(21):5357. 1967.
49. Brown, R.R. and R.A. Weir.— J. Geophys. Res., 72(21):5531. 1967.
50. Kangas, J.— Ann. Geophys., 24(1):147. 1968.
51. Campbell, W.H. and K. Matsuchita.— J. Geophys. Res., 67:555. 1964.
52. Poldugin, V.K.— Geomagnetizm i Aeronomiya, 7(3):74. 1967.
53. Pinter, S.— Informatsionnyi Byulleten' Sovetskoi Antarkticheskoi Ekspeditsii, No. 61:74. 1967.
54. Paulson, K.V. and G.G. Shepherd.— Canad. J. Phys., 44(4): 837. 1966.
55. Rosenberg, T.J., J. Bjordal, and G.J. Kvifte.— J. Geophys. Res., 72(13):3504. 1967.
56. Barcus, J.R.— J. Geophys. Res., 70(9):2135. 1965.
57. Anderson, K.A., L.M. Chase, H.S. Hudson, M. Lampton, D.W. Milton, and G.K. Parks.— J. Geophys. Res., 71(19):4617. 1966.
58. Parks, G.K.— J. Geophys. Res., 72(1):217. 1967.
59. Venkatesan, D., M.N. Oliven, P.J. Edwards, and K.G. McCracken.— J. Geophys. Res., 73(7):2333. 1968.
60. Oliven, M.N., D. Venkatesan, and K.G. McCracken.— J. Geophys. Res., 73(7):2345. 1968.
61. Chase, L.M.— J. Geophys. Res., 73(11):3469. 1968.
62. Lampton, M.— J. Geophys. Res., 72(3):8817. 1967.
63. Oliven, M.N. and D.A. Gurnett.— J. Geophys. Res., 73(7): 2355. 1968.
64. Lazutin, L.L.— In: "Kompleksnye issledovaniya polyarnoi ionosfery," Moskva, Izdatel'stvo "Nauka." 1969. (In press).
65. Fewersdorf, A., J. Dion, G. Kremser, E. Keppler, J.R. Legrand, and W. Riedler.— Ann. Geophys., 22(1):23. 1966.
66. Evans, D.S.— J. Geophys. Res., 68:1805. 1963.
67. Evans, D.S.— J. Geophys. Res., 72(17):4281. 1967.
68. Evans, D.S.— J. Geophys. Res., 73(7):2315. 1968.
69. Reidt, W.P., E.R. Hegblom, and J.G. Ulwick.— J. Geophys. Res., 73(9):3072. 1968.
70. Ulwick, J.C., W.P. Reidy, and K.D. Baker.— Space Res., 7/1:656. 1967.

71. Mozer, F.S. and P. Bruston.— J. Geophys. Res., **71**(19): 4461. 1966.
72. Mathews, D.L. and T.A. Clark.— Canad. J. Phys., **46**(3):201. 1968.
73. Ogilvie, K.W.— J. Geophys. Res., **73**:2325. 1968.
74. McDiarmid, I.B., E.E. Budzinski, B.A. Whalen, and N. Sikopke.— Canad. J. Phys., **45**(5):1755. 1967.
75. McDiarmid, I.B. and E.E. Budzinski.— Canad. J. Phys., **46**(8):911. 1968.
76. Cummings, W.D., R.E. LaQuey, and B.J. O'Brien.— J. Geophys. Res., **71**(5):1399. 1966.
77. Bryant, D.A., H.L. Collin, G.M. Courtier, and A.D. Johnstone.— Nature, **215**(5096):45. 1967.
78. Whalen, B.A., I.B. McDiarmid, and E.E. Budzinski.— Canad. J. Phys., **45**(10):3247. 1967.
79. Whalen, B.A. and I.B. McDiarmid.— J. Geophys. Res., **73**(7):2307. 1968.
80. Mishin, V.M. and T.I. Saifudinova (Vershinina).— In: "Fizika magnitosfery i polyarnye buri," p. 355. Irkutsk, Izd. SO IZMIRAN. 1968.
81. Hartz, T.R. and N.M. Brice.— Planet. Space Sci., **15**:301. 1967.
82. Akasofu, S.I. Polar and Magnetospheric Substorms.— D. Reindel Publ. Co., Dordrecht, Holland. 1968.

MAGNETOSPHERIC ELECTRIC FIELDS AND THE ROTATION OF THE EARTH

B. E. Bryunelli

We have previously mentioned one fundamental difficulty associated with the analysis of the electric field in the magnetosphere, namely that the field geometry emerging from our current concepts regarding the nature of the magnetospheric processes is incompatible with the results of the analysis of geomagnetic disturbances /1, 2/. Indeed, the penetration of charged particles into the Earth's atmosphere entails an influx of matter to the Earth. The motion of plasma to the Earth in the central parts of the magnetosphere tail is also part of the convection scheme proposed by Axford and Hines /3/; to ensure this Earthward motion, the electric field in the magnetosphere should have a high potential on the day side. On the other hand, a polar magnetic disturbance is characterized by one or two current streams flowing along the auroral zone in the westward direction above the morning and the night sectors and in the eastward direction above the day and the evening sectors. Both streams transport positive charges to the evening side of the Earth, and if the motivating force of the current system is localized in these streams, their existence should produce a field with a positive potential on the evening side of the Earth, i. e., the opposite of what emerges from Axford and Hines' convection scheme. I have tried /1, 2/ to treat the magnetospheric field (with a positive potential on the morning side) as the starting point and derive the current systems of the polar magnetic disturbance as a result of the magnetospheric field closing through the ionosphere.

A number of recent reports contain data which bear out or are at least consistent with the assumption of an electric field in the magnetosphere which has a high potential on the morning side. Freeman /4/ observed the motion of low-energy plasma in the magnetosphere which was consistent with Axford and Hines' scheme /3/. It was confirmed /5/ that the electron energy on the morning side of the magnetosphere tail is higher than that on the evening side. Vasyliunas /6/, equating the effect of convection and the Earth's rotation at the surface of the plasmosphere, estimated the strength of the magnetospheric field and derived the following expression (after inserting the numerical values of the constants):

$$E = 0.4\,(1 + \frac{K_p}{5})\ \text{V/km}. \qquad (1)$$

Piddington /7/ studied the effects of the asymmetry of the radiation belt, associated with the injection of fresh particles on the night side only.

He showed that the resulting electric field is opposed to the magnetospheric field and should make the plasma drift to the Earth.

The uncertainty regarding the electric field in the magnetosphere motivated a new research program at the Soviet Polar Geophysical Institute. The starting premise of this program was the assumption, advanced by V.B. Lyatskii, that the processes linked with the rotation of the Earth play a leading role in these phenomena. The following chain of effects can be reconstructed as possibly leading to generation of a large-scale electric field.

In the high latitudes, there are several regions where the geophysical effects display certain peculiar features. Thus, there is a zone of maximum recurrence frequency of the polar aurorae (the auroral zone, or the Fritz zone /8/), which corresponds roughtly to geomagnetic latitude 65°. Nikol'skii /9/ pointed to the possible existence of a second, inner auroral zone at geomagnetic latitude of about 75°, where the activity increases in daytime. Khorosheva /10/ and Feldstein /11/ introduced the concept of an instantaneous auroral zone, which is tangent to the Fritz zone on the night side and to the inner zone on the day side. Aurorae occur only along a certain oval, and the diurnal rotation of this oval is responsible for the inner and the outer zone acting as two envelopes. The oval is positioned at the site of injection of high-energy electrons /12/, and this led to the assumption that the oval represents a separating line between the lines of force which close through the parts of the magnetosphere near the Earth and the lines of force trailing off into the tail. In /13/ an enhancement of geomagnetic activity was detected on the day side of the Earth, which is associated with the formation of neutral points in the magnetosphere, with the solar wind blowing past these points. According to the calculations of Mead /14/ and Taylor and Hones /15/, the lines of force crossing the equatorial plane near the magnetospheric boundary enter the Earth at a latitude corresponding to a neutral point. It therefore seems that the geometry of the lines of force in the magnetosphere corresponds to that shown in Figure 1: lines of force forming the boundary of the magnetosphere emerge from the geomagnetic parallel corresponding to the inner auroral zone; they close both through the equatorial plane near the Earth and through the tail, which they reach along the outer part of the magnetopause. The daytime section of the inner zone corresponds to a neutral line on the surface of the magnetosphere. The lines of force emerging on the night side of this zone trail off into the tail, dividing it into parts filled with field lines emerging from the polar cap and from the region lying between the inner zone and the oval. We will refer to the latter region as the auroral region. The magnetic flux from these regions is approximately $6 \cdot 10^{16}$ and $3 \cdot 10^{6}$ maxwell, respectively. It is generally assumed that the north and the south halves of the tail are separated by a neutral layer, whose field (of the order of 1 gamma) is perpendicular to the interface /16/. At large distances from the Earth, a more complex picture is observed, the perpendicular field component often reverses its sign, but since on the whole the field was found to diminish /16/, we will take this component to point northward on the average (with the same magnitude as above). The existence of this perpendicular component should lead to a steady decrease of the magnetic flux in the tail, and it seems that the flux from the auroral region vanishes at a distance of 100—150 Earth radii.

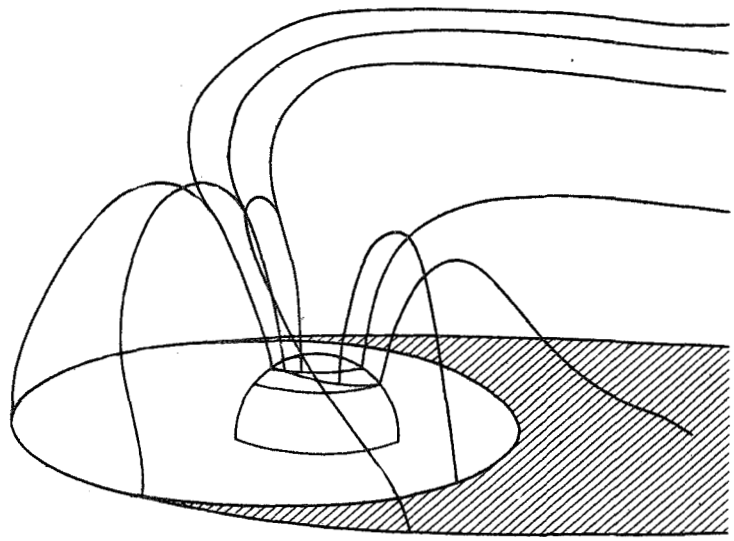

FIGURE 1. The geometry of magnetic lines from the high-latitude region. The lines from the inner zone are associated with the boundary of the magnetosphere, and the lines of the oval with the boundary of the plasma layer.

Studies of the distribution of low-energy plasma in the space around the Earth led to the conclusion that the Earth is surrounded by a relatively dense plasma — a plasmosphere, with a sharp boundary at a distance of 3 — 5 Earth radii; the plasma density drops markedly on crossing this boundary /17/. At large distances (about 10 Earth radii), Gringauz et al. /18/ discovered a region where the number of electrons with energies above 200 eV again increases. Vasyliunas /19/ in a recent report published a detailed review of the results pertaining to this part of the interplanetary space. The measurements were carried out in the evening sector of the magnetosphere; the lines of force emerging from the oval (in the form indicated by Feldstein and Starkov /20/) constitute the boundary of a plasma layer beyond which (farther from the Earth) high-intensity particle fluxes with energies above 1 keV are observed, and the mean energy density reaches 1 keV/cm^3. In the part of space inside this boundary, instruments with threshold sensitivity of 40 eV detected no measurable particle fluxes. The boundary of the plasma layer is sharp and distinct, its thickness not exceeding 0.4 Earth radii; the position of this boundary depends on the level of magnetic activity, varying in this sector from 11 — 12 radii in quiet times to 6 radii in stormy periods. The thickness of the layer at right angles to the equatorial plane is about 5 Earth radii. Figure 1 shows (greatly out of scale) a section through the magnetosphere obtained with the equatorial plane. The lines of force emerging from the oval, in accordance with Vasyliunas' results /19/, cross the equatorial plane at the boundary of the plasma layer; the lines of force corresponding to lower latitudes close through the parts of the magnetosphere near the Earth; the high-latitude lines trail off into the tail gradually closing through the neutral layer. The entire system

maintains a constant attitude relative to the Sun, and therefore rotates relative to the Earth. The Earth with its magnetic field rotates in the system of axes with fixed attitude to the Sun. This rotation must be taken into consideration if, in addition to the geomagnetic field, the Earth is also assigned an electric field

$$E = -\left[\frac{v}{c}, H\right]. \tag{2}$$

It is readily seen that, assuming a dipole geomagnetic field, the associated electric field can be represented as a gradient of the potential

$$\varphi = -\frac{\Omega M}{r} \sin^2\theta, \tag{3}$$

where M is the magnetic moment of the Earth, Ω is the angular velocity of the Earth.

Since the potential is determined apart from an additive constant, we can choose this constant so that the potential of the inner zone linked by lines of force with the magnetospheric boundary and the interplanetary space is zero. In this scheme, the pole is assigned a potential of +6 kV, the Fritz zone (ϕ = 65°) −10 kV, and the equator (in accordance with (3)) − 84 kV. If we assume that the lines of force are ideal conductors and are thus also lines of constant potential, the potential distribution and the electric field in the cross section through the magnetosphere tail should correspond to the pattern shown in Figure 2 (viewed from the Earth). The field vectors are directed from the centers of each segment of the magnetospheric "theta" through which passes the line of force of the geomagnetic pole, converging toward the middle of the neutral layer, through which pass the lines of force from the points of the oval closest to the equator in both hemispheres (these lines carry the most negative potential). The magnetic field in the upper (north) part of the tail is directed to the Earth; in crossed field in the northernmost part of the tail, the lines of force drift clockwise, synchronously with the diurnal rotation of the polar cap; in the inner part of the section, adjoining the neutral layer, the drift is directed from the evening to the morning side of the tail. The velocities invariably correspond to the diurnal rotation. Adjoining the neutral layer, the electric field is parallel to the layer and points to its middle. In the magnetic field of the layer, directed to the north part of the tail, the drift is away from the Earth on the evening side of the tail and to the Earth on the morning side (Figure 3). The

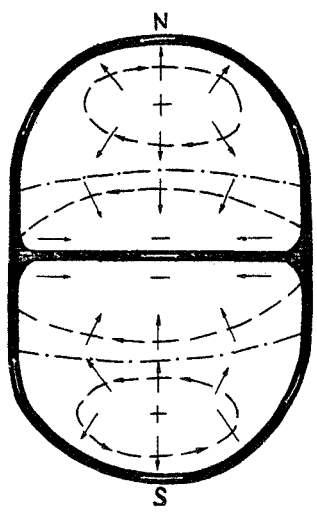

FIGURE 2. A section through the magnetosphere tail (viewed from the Earth). The directions of currents along the boundary, the electric field, and the drift of lines of force are shown. The dash-dotted line traces the boundary of the fluxes from the cap and from the auroral region. This boundary is also the zero-potential surface.

diurnal motion of a line of force thus consists of daytime rotation with the Earth, rapid trailing off into the tail in the evening, switch-over to the morning side of the tail during the night, and finally rapid return to the parts of the magnetosphere near the Earth in the morning hours. Let us consider this motion in more detail.

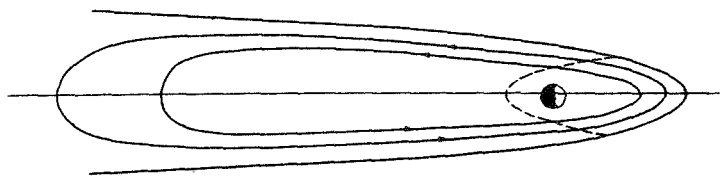

FIGURE 3. Plasma drift in the equatorial plane associated with the diurnal rotation of the Earth.

The daytime drift is produced by field (2) or (3). The transition to the evening drift mode, i.e., the lines trailing off into the tail, occurs at the time when the particular point on the Earth's surface approaches the oval and enters the part of space with a low magnetic field. The electric field associated with the Earth's rotation can be distorted by the boundary of the plasma layer; this distortion, apparently, compensates the field component normal to the boundary, while the tangential component crosses the boundary unaffected. The isopotential lines near the boundary are perpendicular to the boundary and the plasma therefore drifts at right angles to the boundary. Since the tangential component of the electric field remains constant, the marked drop of the magnetic field should produce a similarly pronounced increase in drift velocity. This may be attributed to the decrease in field strength, i.e., to the increase in the spacing between lines of force. The drift velocity is expected to continue increasing as the line of force moves through the plasma layer, provided this layer is exposed to solar wind pressure. Indeed, if we consider an isolated jet, its surface is isopotential and the electric field inside the jet should increase as it becomes thinner. The increase of the electric field, on the other hand, should increase the drift velocity, which in its turn should pinch the jet and increase the field. The motion inside the plasma layer can be classified as an instability — the transition from one stable state, with the lines of force closing through the near magnetosphere, to another stable state, with the lines of force closing through the tail.

When a drifting particle crosses the boundary where the magnetic field drops abruptly, its energy increases to

$$w = w_0 + m \cdot v_{dr}^2, \tag{4}$$

where w_0 is the energy of the particle when it reaches the boundary, v_{dr} is the drift velocity.

The physical reason for the increase in energy is that the particle is displaced along the electric field due to a change in the radius of curvature

(in general, this change in curvature is substantial in a small field). From equation (3), the electric field at the level of the boundary of the plasma layer should reach about 1 kV/Earth radius. If the magnetic field inside the plasma layer is taken equal to 1 gamma, the energy increment associated with the crossing over into a region of weaker magnetic field should be about 200 eV for a proton. The radius of curvature under these conditions is about $^1/_4$ of the Earth's radius, and the gyroperiod of a proton is about 1 min.

The very existence of the boundary of the plasma layer is apparently associated with this plasma drift phenomenon: in the space between the plasmosphere and the plasma layer, the density of the low-energy plasma is apparently higher than in the plasma layer, but its energy is below the sensitivity threshold of the instruments. Drifting in the field of the Earth's diurnal rotation, the low-energy plasma particles cross the boundary of the plasma layer. Due to the sudden increase of the gyroradius, the particle is displaced along the field. This displacement, accompanied by a certain acceleration of the particle, constitutes the current element which determines the magnetic field discontinuity across the boundary. The thinner the boundary, the easier is the transition from one radius to another and the easier is the generation of current along the boundary. Since current enhancement narrows the boundary, the entire process should produce a sharp boundary, as is actually observed. In the above analysis, we operated with protons only, whereas the measurements give the electron energy. There is probably an additional mechanism, in the form of local electric fields, equalizing the energies of electrons and protons.

Upon crossing the boundary, the drift approximation probably breaks down. Indeed, the thickness of the boundary layer is comparable to the radius of curvature, and the conditions of motion therefore change radically over a distance of the order of the radius. Fluctuations may cause a substantial change in the magnetic field during one revolution of the proton. Drifting inside the plasma layer, the particles enter a region where the thickness of the neutral plasma layer is comparable with the proton gyroradius. The drift approximation breaks down because both the gyroradius and the gyroperiod of a proton in a weak magnetic field are very large. The breakdown for the proton occurs earlier than that for the electron; the electrons drift with the line of force, whereas the protons may be lost by the line. The plasma moving with the line of force is therefore enriched in negative charges. The diurnal motion of the lines of force therefore leads to a buildup of negative charge on the evening side of the magnetosphere tail and positive charge on the morning side. The slow drift of the lines of force overnight does not require any further charge separation.

The above processes are associated with charge transfer from the boundary of the plasma layer into the tail interior and back. The charges induced near the outer surface of the layer apparently leak to the Earth, without causing any noticeable geophysical effects. Charge buildup inside the magnetosphere tail creates an additional electric field there, and the drift trajectories are altered. This effect can be allowed for by plotting the isopotential lines, which govern the particle drift. Initially, as in Figure 2, the potential inside the neutral layer had a minimum of -10 kV

in the middle part of the layer. The appearance of additional charges will alter the potential distribution: it will be lower on the morning side and higher on the evening side, as marked by the solid line in Figure 4b. The drift paths join the Earth only with those parts of the tail which are at the same potential as the Earth, i.e., between 0 and -10 kV. In Figure 4, these regions are marked by thick lines. The potential of the regions in between is either too low or too high, and they are therefore not joined with the Earth. Closed eddies form around these regions (Figure 4a) which essentially fit the Axford and Hines scheme /3/.

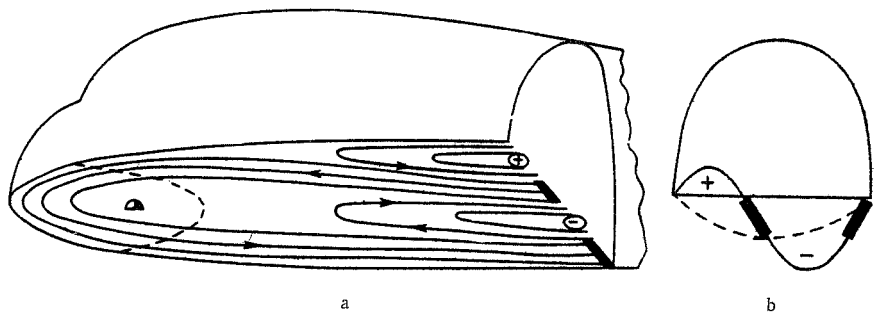

FIGURE 4. Formation of eddies in the neutral layer of the tail (a) and potential distribution in the neutral tail (b). The dashed line marks the situation produced by the diurnal rotation alone, and the solid line presents the distribution corresponding to charge transport. Thick segments identify the regions which are maintained at the same potential as the Earth.

The energy balance of this process can now be estimated. If we take tentatively 1 cm^{-3} for the density of protons in the neutral layer, 1 gamma as before for the magnetic field, and insert the electric field at the end of the process from equation (1), we obtain for the energy density

$$w = 2.5 \cdot 10^{-9} \left(1 + \frac{K_p}{5}\right) \text{ erg/cm}^3.$$

If the process is assumed to encompass a volume of 100 X 40 X 1 radii, i.e., approximately 10^{30} cm^3, the above expression gives a figure of the order of $2.5 \cdot 10^{21}$ erg for the total eddy motion energy in the tail plasma layer for a perfectly quiet field and 10^{22} for $K_p = 5$. The strength of the charge separation process can also be estimated. The tail and its plasma layer move relative to the Earth, trailing the Sun; the plasma layer exerts a certain pressure on the confining lines of force, i.e., on the lines of force of the oval. We tentatively assume the layer to be highly asymmetric, so that it exerts pressure only on the evening side of the Earth. This assumption is partly justified by the pronounced asymmetry of the plasmosphere, which is stretched above the evening meridian. If we take for the pressure $H^2/8\pi$, inserting for the field double the dipole field value (this doubling of the field is associated with the effect of the nearby boundary), the retarding effect produced by a strip of unit thickness stretched along the equator is then found to be $H_0{}^2 R_E{}^2/8\pi L^4$, where

$H_0 = 0.3$ is the field at the equator, L is the parameter of the line of force in the plasma layer which is closest to the equator, *i.e.*, the parameter of the Fritz zone (L = 6 according to the above). If the half thickness of the plasma layer near the Earth is 3 — 5 radii, we obtain for the layer power $5 \cdot 10^{16} - 10^{17}$ erg/sec. If the eddies and the associated electric field break up completely during a storm, some 24 hours will be required to restore the conditions corresponding to $K_p = 5$.

Charge separation is feasible only if charge leakage is substantially slower than charge buildup. Therefore, in a quiet magnetosphere, there is no potential transfer from the neutral layer to the Earth possibly because the neutral layer particles, with their large pitch angles, cannot escape from the deep magnetic field minimum in which they are trapped. If this isolation is broken at any time and the potential difference set up in the plasma layer is transmitted to the adjoining regions of the magnetosphere and onward along the lines of force to the Earth, a DP-2 disturbance is observed, as described by Obayashi and Nishida /21 — 23/: Hall current eddies are induced around high and low potential pockets in the ionosphere (Figure 5). The estimates in /22/ suggest that a potential difference of some 50 kV is needed to produce the variation; this figure is close to the result obtained from (1).

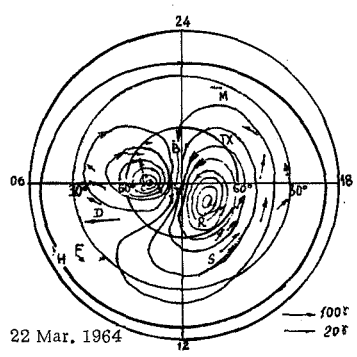

FIGURE 5. The current system of a DP-2 disturbance /23/.

A polar substorm is accompanied by a DP-1 magnetic field disturbance which is characterized by a current system in the shape of two jets flowing along the principal auroral zone in opposite directions (Figures 6a and 6b) or a closed current eddy embracing the oval (Figure 6c). The first two models were discussed in most of the earlier studies, and the last variant was first published in /24, 25/. As we have noted above, the assumption that the motivating force of the current system is localized in the current jet is inconsistent with our concepts of the electrical field in the magnetosphere. The current systems in Figure 6 are apparently produced by the general magnetospheric field interacting with the injected particle fluxes.

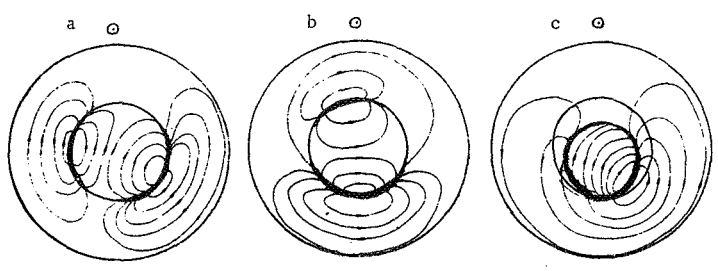

FIGURE 6. The current systems of a DP-1 disturbance /22/.

The particle fluxes injected in the ionosphere create a narrow conducting channel. Because of the existence of the boundary, the direct and the Hall conductivity in this channel change to Cowling conductivity, and the medium inside the channel is transformed into an excellent, relatively isotropic conductor. If a potential difference is applied between the evening and the morning side of the Earth (this potential difference may be transmitted from the magnetosphere along the lines of force) and the injecting particles have created a conducting channel short-circuiting this potential difference, electric current will flow in the closed circuit comprising the conducting regions in the ionosphere and the volume conductors — the lines of force. The magnetic field of this current is the same as that of the current system shown in Figure 6a and 6b: the field below the current jet is determined by the jet alone, and the field far from the jet is determined by the feeding conductors, whose field is indistinguishable from the field of the currents closing the jet. Thus, quiet conditions correspond to lack of any direct electric contact between the neutral layer of the tail and the Earth. When this contact is established and the potential is transmitted to the Earth, a DP-2 disturbance is observed. If the electric contact is further reinforced by particle injection, creating a conducting channel in the ionosphere, a DP-1 current system is formed. The high conductivity of the channel lowers the potential difference in the ionosphere and suppresses the DP-2 disturbance. The above model explains the principal features of the high-latitude geomagnetic disturbances. Certain discrepancies, however, nevertheless remain. Thus, the region of the largest potentials of the DP-2 variation (Figure 5) does not coincide with the ends of the current jets of the DP-1 system (Figures 6a and 6b). The existence of the current loop (Figure 6c) has not been explained either.

The transition from a DP-2 disturbance to a DP-1 disturbance is associated with particle injection. According to present-day concepts /26/, particle injection is linked with a sudden contraction of the lines of force previously stretched into the tail. The contraction is a rapid process, not unlike the breakdown of an instability, and it apparently involves partial loss of ions, like the diurnal motion of the lines of force. This, in its turn, will increase the electron content of the plasma transported Earthward by the contracting lines, whereas the distant parts of the tail are enriched with ions. As a result, the previously discussed field with a positive potential on the morning side of the magnetosphere and the ionosphere is supplemented by an additional field on the night side of the Earth, with a higher potential at higher latitudes. The centers of the charged regions are thus shifted in the required direction: the negatively charged region moves to lower latitudes, closer to the midnight meridian, and the positively charged region settles on the opposite meridian at higher latitudes (Figure 7).

There is one other factor to be considered: when the electric isolation of the neutral layer is broken, the weak electric field will be distorted (Figure 2) if the potential of the neutral layer is transmitted to that part of the magnetosphere where the field is directed to the Earth. Drift paths may form, linking the positive potential pockets in the neutral layer with the central part of the cross sections, where the lines from the near-polar region pass (Figure 8). The positively charged region

in this case extends from the neutral layer to the central part of the tail section, and when projected onto the Earth along the lines of force, the positive potential will spread over the entire near-polar region.

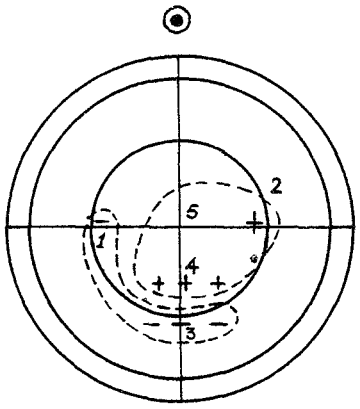

FIGURE 7. Potential distribution in the ionosphere during a DP-1 disturbance. The potential in regions 1, 2 is created by the principal magnetospheric field, that in regions 3, 4 by the field of injected particles, in region 5 by charge transfer to the central part of the tail.

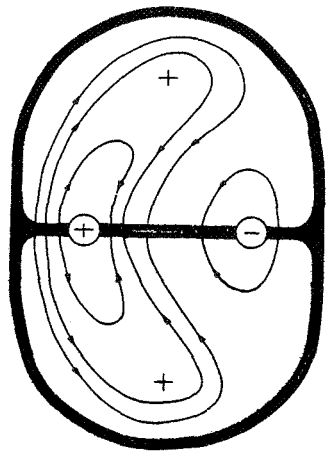

FIGURE 8. Possible drift paths in the tail when the isolation of the neutral layer has been broken.

The current system in Figure 6c differs from the other two current systems in that here a current jet extends in a direction almost opposite to the first two jets; the formation of this jet cannot be explained as the closing of an electric circuit between regions maintained at different potentials. Burdo /27/, in his search for general regularities governing the distribution of magnetic activity at high latitudes, proposed a chart of distribution of activity maxima which coincided with the chart of the maximum ionospheric current. At high latitudes, the activity maxima fell along three spirals, two of which extended from the day side of the inner zone, bypassing the pole on both sides, toward the night side of the principal zone; the third spiral stretched toward the evening side of the principal zone and along it. If these spirals are charted as on Figure 6, the first two will approximately coincide with the oval (Figure 6c), and the third with the daytime current (Figures 6a and 6b). It thus seems that the current systems (Figure 6) are made up of three basic jets: the morning jet, the night jet, and the evening jet. A combination of two jets — morning and evening — is responsible for the system shown in Figures 6a and 6b, whereas the current system in Figure 6c is produced by a combination of a morning and a night jet. The morning and the night jets have been previously associated with the shortcircuiting of different potentials. The night jet apparently can be identified with a Hall current flowing along the region of maximum electric field (maximum potential gradient) adjoining the boundary of the positive potential region. The difference in the origin

of these jets is also reflected in their shape: the night jet shows a much poorer focusing than the other two jets, and it has no sharp boundaries (which are produced by the injection region); the variation of the electric field and the Hall currents is furthermore more gradual. The blurred shape of this jet /24, 25/ is apparently one of the reasons why scientists concentrated on it at a much later date than on the other two.

It thus seems that the Earth's rotation produces a general magnetospheric electric field and a general circulation of the type described by Axford and Hines /3/. The generation of this field and the convection motion consume about 10^{22} erg, and the power of the charge separation mechanism is 10^{17} erg/sec. In quiet periods, the electric field arising in the neutral layer of the tail is not linked to the Earth and does not affect the geophysical processes. The penetration of this field in the magnetosphere and its propagation along the lines of force to the Earth produces a DP-2 disturbance. If this effect is further reinforced by particle injection, the field geometry is somewhat altered and the DP-2 variation changes to DP-1 disturbance, i.e., a polar substorm. The ionospheric current system of this disturbance in general is made up of three branches of different origin: two of the three branches are discharge currents flowing along the high-conductivity channel, and the third branch is a Hall current in the region of maximum electric field. The currents along the lines of force feeding the ends of the current jets also play an important role in the generation of the DP-1 magnetic field.

Bibliography

1. Bryunelli, B. E. — In: "Fizika magnitosfery i polyarnye buri," Trudy Letnei shkoly po kosmofizike, p. 3. Irkutsk, Izd. SO AN SSSR. 1968.
2. Bryunelli, B. E. — Trudy V Vsesoyuznoi ezhegodnoi zimnei skoly po kosmofizike, p. 212. Apatity, Izd. Kol'skogo filiala AN SSSR. 1968.
3. Axford, W. I. and C. O. Hines. — Canad. J. Phys., 39(10):1433. 1961.
4. Freeman, J. W. — J. Geophys. Res., 73(13):4151. 1968.
5. Montgomery, M. D. — J. Geophys. Res., 73(3):871. 1968.
6. Vasyliunas, V. M. — J. Geophys. Res., 73(7):2529. 1968.
7. Piddington, J. H. — Planet. Space Sci., 16(6):703. 1968.
8. Yanovskii, B. M. Zemnoi magnetizm (Geomagnetism). — Leningrad, Izd. LGU. 1963.
9. Nikol'skii, A. P. — In: "Fizika solnechnykh korpuskulyarnykh potokov i ikh vozdeistvie na verkhnyuyu atmosferu Zemli," p. 144. Moskva, Izdatel'stvo AN SSSR. 1957.
10. Khorosheva, O. V. — Geomagnetizm i Aeronomiya, 2(5):839. 1962.
11. Feldstein, Ya. I. — Geomagnetizm i Aeronomiya, 3(2):227. 1963.
12. Frank, L. A., J. A. van Allen, and J. D. Graven. — J. Geophys. Res., 69(15):3155. 1964.
13. Bobrov, M. S. — Astronomicheskii Zhurnal, 36(6):1028. 1959.

14. Mead, G. D. — J. Geophys. Res., 69(7):1181. 1964.
15. Taylor, H. E. and E. W. Hones. — J. Geophys. Res., No. 15:3605, 1965.
16. Mihalov, J. H., D. S. Colburn, R. G. Currie, and C. P. Sonett. — J. Geophys. Res., 73(3):943. 1968.
17. Carpenter, D. L. — Radio Science, 3(7):719. 1968.
18. Gringauz, K. I., V. G. Kurt, V. I. Moroz, and I. S. Shklovskii. — DAN SSSR, 132(5):1062. 1960.
19. Vasyliuvas, V. M. — J. Geophys. Res., 73(9):2339. 1968.
20. Feldstein, Y. I. and G. V. Starkov. — Planet. Space Sci., 15(2): 209. 1967.
21. Obayashi, T. — In: "Solnechno-zemnaya fizika," p. 172. Moskva, Izdatel'stvo "Mir." 1968.
22. Obayashi, T. and A. Nishida. — Space Sci. Rev., 8(1):3. 1968.
23. Nishida, A. — J. Geophys. Res., 73:1795, 5549. 1968.
24. Feldshtein, Ya. I. and A. N. Zaitsev. — Geomagnetizm i Aeronomiya, 5(6):1123. 1965.
25. Akasofu, S. I., S. Chapman, and C. I. Meng. — J. Atmos. Terr. Phys., 27(11/12):1275. 1965.
26. Piddington, J. H. — J. Atmos. Terr. Phys., 29(1):87. 1967.
27. Burdo, O. A. — In: "Fizika solnechnykh korpuskulyarnykh potokov i ikh vozdeistvie na verkhnyuyu atmosferu Zemli," p. 159. Moskva, Idatel'stvo AN SSSR. 1957.

MAGNETIC STORM DEVELOPMENT IN THE EARTH'S MAGNETOSPHERE

M. I. Pudovkin, S. I. Isaev, and S. A. Zaitseva

A magnetic storm is a highly complex agglomeration of various phenomena occurring in the Earth's ionosphere or magnetosphere. The sequence and the interrelation of the phenomena taking place in the ionosphere (polar aurorae, formation of enhanced ionization regions, electrical currents) have been studied in fair detail /1—3/. Our knowledge of the processes which develop during the magnetic storm in the magnetosphere is much less comprehensive, however.

It has been shown /4, 5/ that the study of polar storms reveals the dynamics of magnetospheric processes and thus provides us with a key to the understanding of the mechanism of storm generation as a whole. Moreover, the magnetospheric substorm (whose terrestrial counterpart is the polar storm) can be regarded as an elementary form of a general worldwide magnetic storm. We will therefore first concentrate on the development of an elementary polar storm. The exact choice of the commencement of the polar storm is a factor of great importance in these considerations. According to Akasofu /6/, the commencement of a polar substorm is generally identified with the commencement of the negative bay in the midnight region of the auroral zone. Khorosheva /7/ has shown, however, that at latitudes above the Fritz zone, the disturbance may commence long before the commencement of the bay in the zone proper. This conclusion is also confirmed by the findings of /8/.

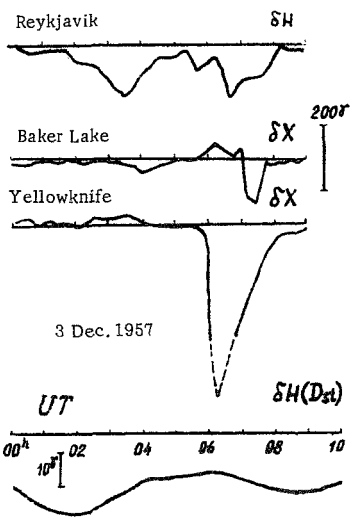

FIGURE 1. The development of a polar magnetic storm on 3 December 1957 at high latitudes and the $\delta H(D_{st})$ curve.

Figure 1 plots according to /9/ the variations δH in the bay of $06^h - 08^h$UT, 3 December 1957, as recorded at Yellowknife ($\phi = 69°.8$ N, $\Lambda = 295°$), Baker Lake ($\phi = 75°.1$ N, $\Lambda = 320°$), and Reykjavik ($\phi = 66°.6$ N, $\Lambda = 71°$). We see that at Yellowknife a sharp bay was observed against the background of an exceptionally quiet field, commencing distinctly at $05^h 50^m$UT. The δX curve at Baker Lake shows, however, that in accordance with the results of /7, 8/

the bay commencement at higher latitudes substantially preceded that at Yellowknife. A similar picture was observed at the Reykjavik observatory, which in the relevant period lay on the morning side (LT = $6^h - 8^h$) of the auroral zone. Here a substantial disturbance began about 4 hrs prior to the commencement of the Yellowknife bay.

Analysis of 30 geomagnetic bays carried out by Ivliev et al. /9/ shows that this is a typical situation, i.e., every magnetic bay is preceded by a peculiar disturbance. This preliminary disturbance differs from a typical geomagnetic storm in that its intensity is maximum not on the night side of the Earth, in the auroral zone, but rather on the morning side (Figure 2), at latitudes of 70 — 80°. It thus seems that the development of this disturbance is associated with the injection of plasma along the geomagnetic field lines passing through neutral points. This conclusion is confirmed by the results of /10/, according to which the auroral intensity on the day side of the auroral oval also increases considerably about 1 or 2 hrs prior to bay commencement on the night side of the auroral zone.

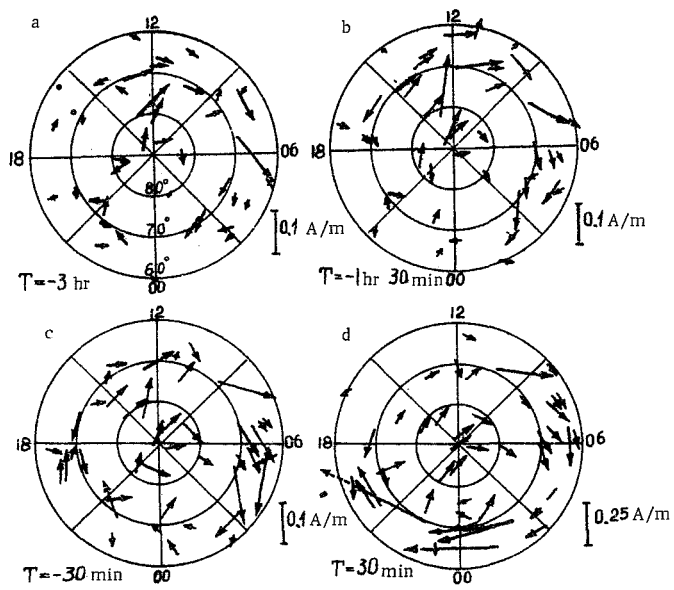

FIGURE 2. Space and time distribution of the disturbance currents in the polar cap (average for 30 storms) at various times after the commencement of the polar substorm.

What is the origin of this preliminary disturbance? According to /11, 12, 13/, every elementary magnetic storm on the night side is preceded by a small and yet sufficiently pronounced geomagnetic field disturbance on the equator (which occurs 1 — 3 hrs before the storm). This disturbance is apparently linked with an increase in solar wind pressure. The curves in Figure 1 show that an enhancement of the field H at low latitudes was observed in this case on 3 December 1957. The enhancement began simultaneously with the commencement of the preliminary disturbance in Reykjavik.

It thus seems that the preliminary disturbance in the polar cap, preceding the development of a polar bay, is directly associated with the increase in the solar wind pressure on the Earth's magnetosphere. The development of a geomagnetic bay is connected with the injection of auroral plasma from the magnetosphere tail /5, 11/. Since the plasma moves in a magnetic field, it apparently sets up an electric field in the Earth's magnetosphere during the storm; this field is directed from the morning to the evening side of the Earth.

In addition to the general drift toward the Earth, the particles also experience a gradient drift around the Earth, the protons drifting westward and the electrons eastward. This gradient drift can be observed in the westward displacement of positive bays of a certain kind along the auroral zone (proton drift) and in the eastward displacement of the absorption bays (electron drift) /5/. The following basic factors should be noted in this relation:

1. The region of corpuscular injection drifts along the Fritz zone, and not along the auroral oval. This implies that the drift envelope, touching the oval on the Earth's night side, does not coincide at any other point with the oval. As a result, the auroral oval can be identified with the outermost boundary of stably trapped radiation.

2. The particle energy increases in the course of the drift around the Earth.

The last conclusion is illustrated by Figure 3, which gives the diurnal variation of the energy of the electrons /14/ and protons /15/ injected into the upper atmosphere. The curves in Figure 3 show that the energy of auroral electrons is maximum at 07 hrs and minimum at 19 hrs local time, whereas the proton energy is conversely maximum at 18 hrs LT. This longitudinal distribution of particle energies points to the existence of an electric field in the magnetosphere. To judge from the figure, this field is equal to 10^{-5} V/cm and is directed from east to west on the Earth's night side. These results fit the conclusions derived from the analysis of the motion of polar arcs.

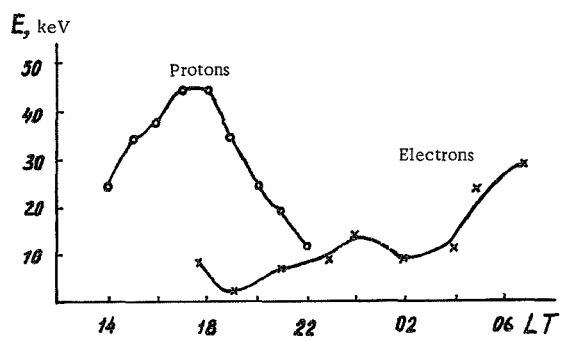

FIGURE 3. The diurnal variation of the energy of injected protons and electrons in the auroral zone.

How and when does the electric field form in the magnetosphere? Since the motion of the auroral arcs toward the equator begins almost simultaneously

with the enhancement of the field H on the equator /9/, it seems that the electric field is also generated at that time. This assumption is borne out by the fact that for $E=10^{-5}$ V/cm, a plasmoid will take about 1.5—2 hrs to move from the magnetosphere tail to the L corresponding to the auroral zone, and these are exactly the time intervals representing the delay of the magnetic storm commencement relative to the enhancement of the field H on the equator /11/. There is thus serious reason to believe that the development of the field E in the magnetosphere is associated with changes in some of the solar wind parameters. The electric field generation mechanism has been treated in detail in /16, 17/, where it is shown that the strength and the direction of the magnetospheric electric field are determined by the frozen magnetic field of the solar wind. Direct observations from satellites /18—20/ apparently confirm the theory of /14/.

The existence of an electric field in the Earth's magnetosphere explains the acceleration of the auroral plasma and also a number of other finer features in the development of polar storms, e.g., the shape of the electron and proton injection zones and their mutual position, the diurnal variation of the azimuths of the auroral arcs, the velocities of auroral glow inhomogeneities, etc. /16, 17/. The satisfactory fit between theory and experiment seems to suggest that the problem of development of an elementary polar storm in the magnetosphere has been solved in general lines.

Let us now consider the development of a universal magnetic storm. As is known, the main phase of the storm involves the formation (or enhancement) of a belt of DR currents, which in its turn is linked with an increase in the overall kinetic energy of the particles trapped by the geomagnetic field. The intensity of the DR field observed on the ground is related by the energy of the trapped particles by the equality $W=\frac{1}{2}M_E\cdot\delta H$ /21—23/, which for medium-strength storms ($\delta H=50\gamma$) gives $W=2\cdot10^{22}$ erg. The major part of the kinetic energy concentrated in the radiation belts is carried by low-energy particles with energies below 50 keV /24, 25/. This result is vividly illustrated by the table below /25/.

Total energy of protons and electrons ($200\,eV \le E \le 50\,keV$) in radiation belts

1966	Particles with $200\,eV \le E \le 50\,keV$	Total particle energy for $1 \le L \le 8$, erg	$\Delta B(0)$ calculated, gammas	$D_{st}(H)$ observed, gammas
23 June	Protons	$4.8\cdot10^{21}$	−12	*Quiet field*
25 June	"	$1.4\cdot10^{22}$	−36	−30 (± 10)
9 July	"	$2.1\cdot10^{22}$	−55	−50 (± 10)
	Electrons	$5.3\cdot10^{21}$	−14	

Thus, the nature of the DR currents has been elucidated. And yet the mechanism of formation of the DR belt is not quite clear. We have shown above that certain information on processes in the disturbed magnetosphere can be obtained from the analysis of polar storms. Therefore, before attempting to elucidate the formation mechanism of DR currents, we will consider the relation between DR and DP disturbances.

Already Chapman and Sugiura /26/ and Akasofu and Chapman /27/ showed that the development of the main phase of a magnetic storm is intimately

linked with polar disturbances. However, the causal relation between these factors remained unclear. This problem was considered in greater detail in /4/, where the authors came to the conclusion that the belt of DR currents forms simultaneously with the injection of the auroral plasma into the auroral zone. It is significant that the total energy of particles injected into the auroral zone is proportional to the energy injected into the DR current belt /4/. These data seem to indicate that the formation of the DR belt is not only simultaneous with but is also directly associated with the development of a polar storm in the Earth's magnetosphere.

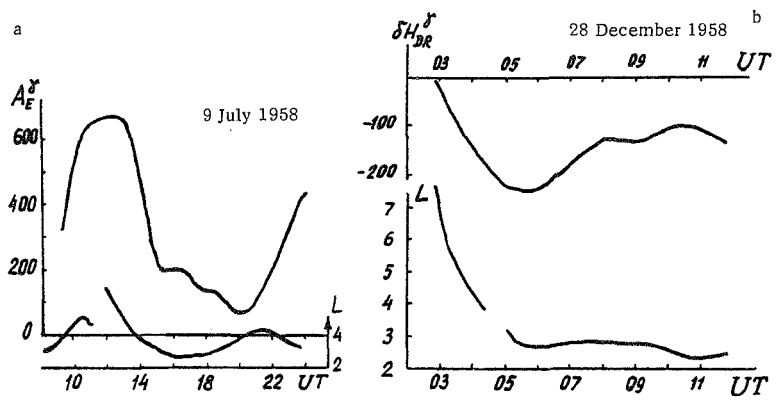

FIGURE 4. Variation in the position of the DR current belt during a polar storm: a — 9 July 1958 (magnetic data); b — 28 December 1958 (observation of a red stable arc).

Let us now try to establish how the DR belt exactly forms. To this end, we will consider some peculiar features observed for particular storms. Figure 4a plots, according to the data of /28/, the variation of the mean radius of DR currents (assuming that they are shaped as an equatorial current ring) during the recovery phase of the storm of 9 July 1958. Figure 4a also gives the intensity of the polar disturbances (the AE indices according to /29/). We see from the curves that around 10—11 hrs UT, the intensity of the polar disturbances markedly increases, reaching a maximum at 12 hrs UT. At the same time the radius of the DR currents increases (up to $7 R_E$), and this may be interpreted as due to the formation of a new DR belt at a greater distance from the Earth. As the polar storm develops, the radius of the DR belt decreases, reaching the minimum value of $\rho = 2.2 R_E$ toward the end of the polar storm. In the period free from strong polar disturbances (16—20 hrs UT), the radius of the DR currents slowly increases, and a renewed decrease begins simultaneously with the commencement of a new burst of polar disturbances. Analysis of several storms carried out in /28/ shows that this is a typical pattern, i.e., during strong polar storms, the radius of the DR belt generally decreases, only to increase in the quiet periods.

However, the determination of the radius of the DR belt from ground magnetic data involves a number of serious errors /28/, so that more reliable (though scantier) results are obtained from observations of middle-latitude red arcs, whose relation to the DR belt has been convincingly

demonstrated in /39—33, 28/. Figure 4b plots the position of the red arc from observations at Barrow ($\phi = 68°.6$ N), College ($\phi = 64°.7$ N), Fritz Peak ($\phi = 48°.7$ N) and the variation of $\delta H(D_{st})$ from the data of /34/. Again, as in the case of the storm of 9 July 1958, the arc, which is in fact a projection of the DR belt along the geomagnetic field lines onto the ionosphere, appeared near the auroral zone ($L = 7$) and moved toward lower latitudes to $L \approx 2.5$ as the storm developed. The data of ground observations of the DR current field and of middle-latitude red arcs thus show that the DR currents originate in the magnetosphere at distances corresponding to the auroral zone, and only later move deeper into the magnetosphere. This result is also borne out by satellite observations. Indeed, Figure 5b, borrowed from /24/, shows the equatorial distribution of the proton flux intensity with $E < 50$ keV during the storm of 7—13 July 1966 (Figure 5a). We see that both before and after the storm, a low-intensity low-energy radiation belt was observed at a distance of $6-7 R_E$ from the Earth. During the main phase of the storm, the particle flux intensity in the belt increased almost by one order of magnitude and the belt intensity maximum shifted to $L = 3.5$.

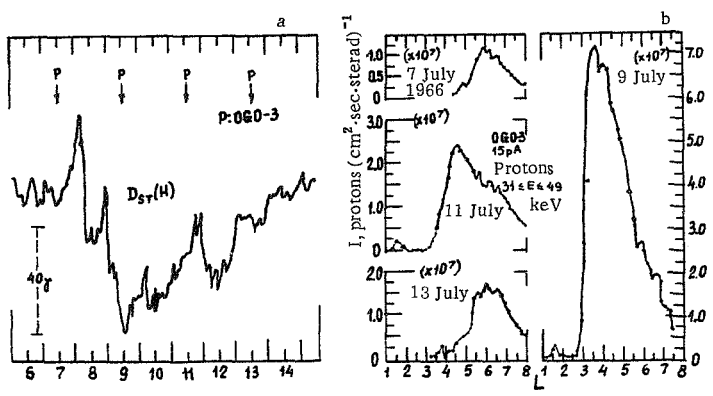

FIGURE 5. The variation of $\delta H(D_{st})$ during the storm of 7—13 July 1966 (a) and the equatorial distribution of the proton flux intensity for 31 keV $\leq E \leq$ 49 keV during this storm (b).

The plasma filling the DR belt during the storm thus penetrates into the inner magnetosphere from the peripheral regions. This penetration occurs simultaneously with the injection of the auroral plasma, also mainly on the night side /34/. It therefore seems that the auroral plasma moving during the storm from the magnetosphere tail acts as a source of both the polar storms and the DR currents /4/. The authors of /35—37/ reach the same conclusion.

The acceleration of charged particles in the Earth's magnetosphere during a polar storm was considered in detail on the basis of Alfven's theory in /38/. The results show that as the particles move from the magnetosphere tail to the L corresponding to the auroral zone, the particle energy increases by

1–2 orders of magnitude. A highly significant factor is that the existence of the electric field in the magnetosphere is apparently intermittent, and not continuous: it is turned on for about 1.5–2 hrs at a time /11, 38/, with a mean periodicity of about 4 hrs /2/. As a result, only part of the particle trajectory around the Earth lies in an electric field (otherwise, no significant change in energy would be registered), and the mean particle energy increases. If the time to complete one circuit around the Earth coincides with the recurrence period of the polar bays, the particle acceleration mechanism becomes highly effective. It can be shown that for a bay recurrence period of some 4 hrs at L=4–5, the acceleration is most effective for particles with energies of a few tens of keV. This result is apparently not inconsistent with the experimental findings /24, 25/.

We thus see that the polar substorm is an elementary form of the universal magnetic storm as a whole, and not only of the polar storm. However, the relation between the DP and DR disturbances is not limited to the above considerations, and the development of the DR currents in its turn affects the development of the polar storm.

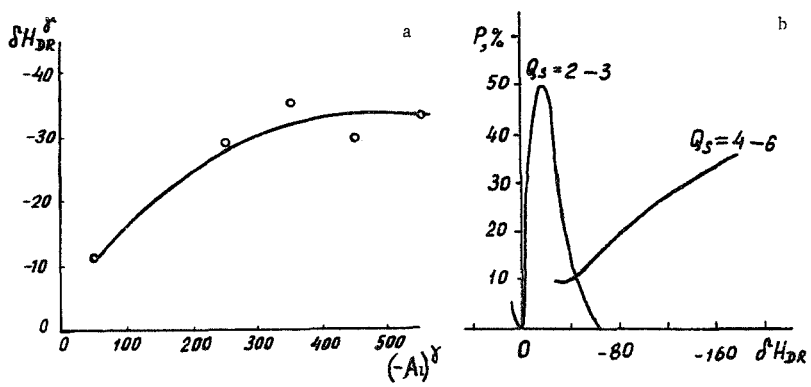

FIGURE 6. The field of DR currents and the intensity of polar disturbances (A_L index) at the time of splitting of the auroral zone ($\Delta l \geqslant 200$ km) (a) and the probability of auroral zone splitting vs. the intensity of the DR field for various magnetic activity levels (b).

Direct inspection of photographs reveals a distinct splitting of the auroral belt in certain cases: two widely spaced auroral zones are actually observed. This splitting at first may seem quite accidental, since it is observed both at high magnetic activity levels and under relatively quiet conditions. However, a more detailed examination of the splitting conditions reveals certain regular features in this phenomenon. Figure 6a plots (average data for 30 storms) the DR current field (δH_{DR}) and the intensity of the polar disturbances (A_L indices from /29/) corresponding to the time of splitting of the auroral zone. (Splitting is assumed to occur when the two auroral glow regions are spaced by more than 200 km). We see from Figure 6a that the points do not fall at random: they are distinctly clustered around a certain curve. Hence the conclusion that the splitting of the auroral zone is largely determined by these two factors, viz., the intensity of the DR currents and the intensity of the polar disturbances. It is moreover fairly clear that for small δH_{DR} the

zone splitting is observed only for small A_L, but as δH_{DR} increases, the polar storm intensity needed to initiate this splitting also becomes higher. This result is shown in a slightly different form in Figure 6b, which plots from the data of /39/ the probability of splitting of the auroral zone as a function of the DR field intensity for various magnetic activity levels. We see that for a fixed polar disturbance intensity, the probability of zone splitting first increases with the increase in the intensity of DR currents, reaching a maximum at $Q = 2-3$ for $\delta H_{DR} \approx -30\gamma$, and then steeply decreases. For $\delta H_{DR} = 0$, the splitting probability is very low. Hence it follows that the existence of a belt of DR currents is a necessary condition for the splitting of the auroral zone. Let us try to establish how the existence of DR currents may affect the configuration of the auroral zone.

It has been shown /38/ that the shape of the auroral zone can be derived by considering the adiabatic drift of particles in the magnetosphere in crossed electric and magnetic fields. However, the calculations of particle motion were carried out assuming a dipole magnetic field in the magnetosphere. In accordance with the above data, it is better to explain the auroral zone splitting by the peculiar features of electron motion in the geomagnetic field distorted by the field of DR currents. The electron trajectories in this field were computed in /40/ by numerical integration of the equation of motion of the particles:

$$\frac{d\vec{r}}{dt} = \frac{[\vec{E} \times \vec{B}]}{B^2} - \frac{\mu}{eB^2}[\nabla B \times \vec{B}].$$

The following parameters were used: $\mu = 0.7 \cdot 10^{-5}$ CGSM, $E = (0.3-3) \cdot 10^3$ CGSM.

The field of the DR currents was calculated using the Akasofu-Chapman model /41/. The center of the DR belt was taken at $\rho = 5 R_E$ and the ground value of δH_{DR} was taken to be $(-70)\gamma$ (Figure 7). Figure 8 shows the electron paths for $E = 3.3 \cdot 10^2$ CGSM. It is clear from the figure that the presence of DR currents significantly modifies the motion of particles in the magnetosphere. Indeed, outside the DR belt, the electron trajectories are equivalent to the Alfven trajectories, and the electrons drift eastward around the Earth. As a result, the particle energy and the plasma density increase. On crossing the outer boundary of the DR belt, the particles enter a region where the magnetic field gradient is reversed, and they are thus driven in the westward direction around the Earth. As a result, the electron energy and the plasma density decrease. Having traversed the region of maximum field depression, the electrons again enter a region where the magnetic field increases toward the Earth, and they again start drifting eastward, their energy increasing. The sections of the trajectories over which the electron energy $E \geqslant 5$ keV are shown by bold lines in Figure 8. The auroral zone, which was found to be continuous for a dipole field B, falls into two parallel zones in the presence of DR currents, with a significant depression of auroral intensity in the gap between the two zones. This conclusion is of the highest importance in the interpretation of the observed splitting of the auroral zone, which is responsible for the development of the middle-latitude auroral zone during strong magnetic storms /39, 42/.

A similar analysis of electron motion in a magnetic field has been carried out for various values of E. Some of the results are presented in Figure 9,

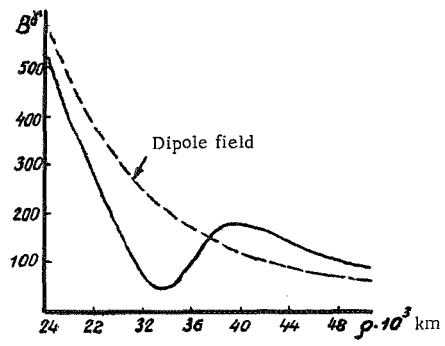

FIGURE 7. The geomagnetic field in the equatorial plane with allowance for the field of DR currents.

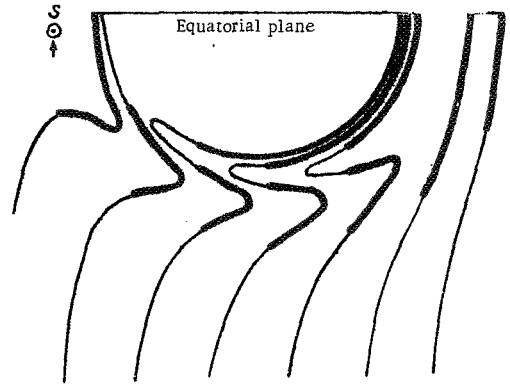

FIGURE 8. Electron trajectories ($\mu = 0.7 \cdot 10^{-5}$ CGSM) in the equatorial plane for $E = 3.3 \cdot 10^{2}$ CGSM.

which gives the position of the south boundary of the auroral zone as a function of the field strength E. The dashed line marks the latitude corresponding to the region of maximum B values, where following the change in the sign of VB the electrons reverse the direction of their motion and the auroral inhomogeneities start drifting in the opposite sense along the arc. The latitudes of zero or low-intensity auroral glow correspond to minimum fields B.

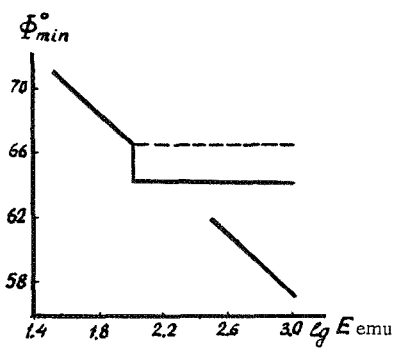

FIGURE 9. The position of the southern boundary of aurorae (calculated) vs. the electric field E.

The above analysis of the motion of charged particles in the Earth's magnetosphere thus explains the observed splitting of the auroral zone and also yields the mean values of the relevant characteristics by tying up the phenomenon with certain points of the DR field. Indeed, it has been shown in /39/ that the probability of observing polar aurorae at various magnetic activity levels differs in years of minimum and maximum solar activity. For low magnetic activity in years of active Sun, the latitudinal distribution of the aurorae has a single maximum at the Fritz zone latitudes. The main maximum of the frequency of auroral occurrence splits into two in days of high disturbance, and an additional maximum is observed at $\phi \approx 52°$. In the light of the above interpretation of the observed zone splitting, it would seem that these features of the latitudinal variation of the auroral frequency indicate that the DR belt in magnetically disturbed days in years of maximum solar activity is located at a distance of from 3 to 5.5 Earth's radii. This is clearly a very plausible conclusion.

The experimental and theoretical results accumulated during the last 2—3 years are on the whole sufficient for elucidating the physical nature of the processes which take place in the Earth's magnetosphere during a

magnetic storm. They enable us to reconstruct the general sequence of development of these processes, which mainly include the generation of the electric field in the magnetosphere, the drift of the auroral plasma in crossed electric and magnetic fields and adiabatic acceleration of the drifting particles, the partial trapping of the auroral plasma by the geomagnetic field, and the formation of the DR current belt. These processes, however, do not cover the entire range of effects accompanying a magnetic storm. In particular, we have so far disregarded such important processes as the onset of instabilities in the auroral plasma, which lead to a redistribution of the particles over the pitch angles and thus cause their penetration into the upper atmosphere /43/. The study of these effects constitutes a highly important independent problem, and we therefore chose to confine the present discussion to macroscopic processes in the magnetosphere.

Bibliography

1. Cole, K.D.— Space Sci. Rev., **5**(6):99. 1966.
2. Akasofu, S-I.— Space Sci. Rev., **6**(1):21. 1966.
3. Pudovkin, M.I.— In: "Fizika magnitosfery i polyarnye buri," p.100. Irkutsk. 1968.
4. Zaitseva, S.A., M.I. Pudovkin, and O.I. Shumilov.— Geomagnetizm i Aeronomiya, **8**(5):905. 1968.
5. Pudovkin, M.I., O.I. Shumikov, and S.A. Zaitzeva.— Planet. Space Sci., **16**:881. 1968.
6. Akasofu, S-I. and D.S. Kimball.— Annals of IGY, **38**. 1965.
7. Khorosheva, O.V.— Synopses of Reports at the International Symposium on Solar-Terrestrial Physics, p.18. Izd. KrAO.
8. Lijima, T. and T. Nagata.— Rept. Ion. Space Res. in Japan, **22**(1/2):1. 1968.
9. Ivliev, D.Ya., M.I. Pudovkin, and S.A. Zaitseva.— Geomagnetizm i Aeronomiya. 1969. (In press.)
10. Starkov, G.V. and Ya.I. Fel'dshtein.— Geomagnetizm i Aeronomiya, **10**(2):367. 1967.
11. Belyakova, S.I., S.A. Zaitseva, and M.I. Pudovkin.— Geomagnetizm i Aeronomiya, **8**(4):712. 1968.
12. Sano, Yu. and T. Ondon.— Memoirs of the Kakioka Magnetic Observatory, **12**(2):1. 1966.
13. Lijima, T. and T. Nagata.— Rep. Ion. Space Res. in Japan, **22**(3):16. 1966.
14. Zaitseva, S.A., D.Ya. Ivliev, and M.I. Pudovkin.— Geomagnetizm i Aeronomiya, **9**(1):108. 1969.
15. Loginov, G.A., V.A. Mitinev, and M.I. Pudovkin.— Geomagnetizm i Aeronomiya. 1969. (In press.)
16. Pudovkin, M.I. and O.I. Shumilov.— Ann. Geophys., **25**(1):555. 1969.
17. Pudovkin, M.I. Polyarnye magnitnye buri (Polar Magnetic Storms).— Leningrad, "Nauka." (In press.)
18. Fairefield, D.H. and L.J. Cahill.— J. Geophys. Res., **71**(1):195. 1966.

19. Wilcox, J.W., K.H. Shatten, and N.F. Ness.— J. Geophys. Res., **72**(1):19. 1967.
20. Rostoker, G. and C-G. Fälthammar.— J. Geophys. Res., **72**(23):5853. 1967.
21. Dessler, A.J. and E.N. Parker.— J. Geophys. Res., **64**(12):2239. 1959.
22. Bryunelli, B.E.— Geomagnetizm i Aeronomiya, **6**(6):1083. 1966.
23. Scopke, N.— J. Geophys. Res., **71**(13):3125. 1966.
24. Frank, L.A.— J. Geophys. Res., **72**(5):1905. 1967.
25. Frank, L.A.— J. Geophys. Res., **72**(15):3753. 1967.
26. Sugiura, M. and S. Chapman.— Abhandl. Akad. Wiss., Göttingen Math. Phys. Klasse, Sonderheft, 4. 1960.
27. Akasofu, S-I. and S. Chapman.— J. Geophys. Res., **68**(10):3155. 1963.
28. Zaitseva, S.A., M.I. Pudovkin, V.V. Dryakhlov, and V.N. D'yachenko.— Geomagnetizm i Aeronomiya. 1969. (In press.)
29. Echols, C., Yu.S. Wong, and T.N. Davis. Hourly Values of the Auroral Electrojet Activity Index for 1958.— Alaska, Geophys. Inst. Univ., UAG R-192. 1967.
30. Cole, K.D.— J. Geophys. Res., **70**:1689. 1965.
31. Roach, F.E. and J.R. Roach.— Planet Space Sci., **11**:523. 1963.
32. Rees, M.H. and S-I. Akasofu.— Planet Space Sci., **11**:105. 1963.
33. Truttse, Yu.L.— Planet Space Sci., **16**(8):981. 1968.
34. S-I Akasofu and C-I Meng.— J. Geophys. Res. **72**(19):4905. 1967.
35. Davis, T.N. and R. Parthasarathy.— J. Geophys. Res., **72**(23):5825. 1967.
36. Piddington, J.H.— J. Atm. Terr. Phys., **29**(1):87. 1967.
37. Piddington, J.H.— Planet Space Sci., **16**(6):703. 1968.
38. Pudovkin, M.I. and O.I. Shumilov.— Geomagnetizm i Aeronomiya, **8**(6):1072. 1968.
39. Isaev, S.I.— Geomagnetizm i Aeronomiya, **2**(5):861. 1962.
40. Isaev, S.I., M.I. Pudovkin, D.I. Shumilov, and S.A. Zaitzeva.— International Symposium on the Physics of the Magnetosphere. Washington, 9. 1968.
41. S-I Akasofu and S. Chapman. A Study of Magnetic Storms and Auroras.— Sci. Rept., No.7, NSF Grant No.4/22. 1961.
42. Isaev, S.I.— Geomagnetizm i Aeronomiya, **2**(4):663. 1962.
43. Tverskoi, B.A. Dinamika radiatsionnykh poyasov Zemli (Dynamics of Van Allen Radiation Belts).— Moskva, "Nauka." 1968.

APPLICATION OF THE METHODS OF MEASUREMENT OF SMALL AND ULTRASMALL QUANTITIES OF VARIOUS ISOTOPES TO ASTROPHYSICAL RESEARCH

V. O. Naidenov

Let us consider the principal astrophysical problems that are being solved and can be solved with the aid of the methods of measurement of small and ultrasmall amounts of various isotopes.

First we would like to stress the relative meaning of the term "small and ultrasmall" quantities of isotopes. The exact meaning of this term is determined by three factors: a) the present-day level of technical development, b) the particular experimental conditions, c) the individual properties of the isotope to be measured. Let us consider this problem in some detail.

The main way for increasing the detection sensitivity of radioactive isotopes is through the development of low-noise detectors. Analysis of the maximum attainable sensitivity with the existing methods has shown /1/ that a certain experimental setup will measure 10—50 A^{37} atoms and only 10^4 tritium atoms. The great variety of decay modes, decay energies, states of aggregation, etc., results in an enormous diversity in the technical performances of low-noise detectors /2, 3/. The measurement sensitivity of stable isotopes is increased by appropriate development of mass spectrometry and activation analysis. The application of these relatively new methods will determine 10^{11}—10^{12} atoms of the isotope in a sample /4—7/. In some cases (He^3, Li^6, A^{36}), the sensitivity can be increased to 10^7 atoms /1, 8/. In this context, we would like to stress two points.

a) The quantity of the isotope depends on its concentration in the sample and the mass of the sample. Often, the experimental conditions limit the sample to a very small mass. Therefore, even measurements of fairly high concentrations must rely on the techniques developed for the determination of small and ultrasmall quantities of the isotopes. For example, the content of Na, Sc, Cr, Mn, Co, Cu in meteorite chonders is between 10^{-3} and 10^{-1}%. However, the measurements of these elements in individual chonders required the application of activation analysis /9/.

b) The isotopic composition of a given element (e.g., the Pb isotopes in a meteorite) is determined by mass spectrometry and activation analysis. Therefore, in general, these measurements should also be classified as measurements of small and ultrasmall quantities of isotopes (especially as we are actually measuring small isotopic shifts in these cases).

Experience shows that to attain maximum sensitivity, we must take into consideration the specific properties of the isotope. As a result, narrow-purpose equipment is generally used, capable of determining at most 1 to 3 isotopes.

Dynamic methods and methods employing photographic emulsion are not classified among the conventional detector techniques. In astrophysical research, we are naturally interested in comparing the performance of different experimental techniques. The entire range of astrophysical problems can be divided into two parts: astrophysical processes which occur in the present or whose effects are observable in the present, and astrophysical processes which took place in the past. The processes of the first group can be dealt with by examining synthetic, artificial specimens. The development of satellite techniques will probably open new vistas in this direction. The second group must rely on natural specimens only. These include various terrestrial minerals, marine and glacial sediments, some biological objects, etc. Specimens of extraterrestrial origin occupy a position of special significance. These include meteorites and cosmic dust. In the near future, scientists will actually be able to examine rocks of lunar origin and specimens from other planets.

PAST PROCESSES

1. The origin of the solar system

Numerous studies have been published on the origin of the solar system and the early stages of its development /10—13/. However, the theory is still far from being complete. Any theory should explain the entire range of currently observable effects and phenomena. This primarily includes the various topics of nucleosynthesis and the related aspects of the abundance of the chemical elements in the Sun and the planets, as compared to the cosmic abundance of the elements in the Universe. This also includes various mineralogical and laboratory studies aimed at elucidating the conditions necessary for the formation of the isotopic, cosmic, mineralogical, and other compositions. Measurements of small and ultrasmall quantities of isotopes inevitably occupies a position of leading importance in this work. They are mainly applied to dating and determination of the isotope composition of various formations in meteorites, abyssal terrestrial rocks, and other natural specimens. Dating is done by measuring the mother to daughter isotope ratio (K—Ar, Rb—Sr, U—Pb methods) or by measuring the isotope ratio of the same element (Pb—Pb method). These dating techniques are naturally based on certain starting assumptions which are not immune to occasional criticism /14/. The isotope ratio of a given element, e.g., Pb or Xe, in principle may shed light on nucleosynthesis processes. Indeed, the quantity of the element being determined, Pb^{204} say, is assumed to have remained constant since the time of nucleogenesis, whereas the other isotopes may have built up gradually owing to the decay of the heavier radioactive elements ($U^{235} \rightarrow Pb^{207}$). The uncertainty in the interpretation of these measurements is fairly high, since the details of the r-process have been poorly developed, and various differentiation and diffusion processes have to be allowed for in the last stages. Some topics should be revised in connection with the probable existence of "stability islands" among the transuranides. Therefore, large-scale measurements are required of the isotopic composition of various meteorites, meteoritic inclusions (the individual chonders),

and various terrestrial rocks. The establishment of a time scale and the isotopic composition will apparently be the main problem when the first lunar specimens are obtained.

2. The history of cosmic rays

The celestial bodies in the solar system are subjected to the continuous impact of cosmic rays. The interaction of cosmic rays with the surface of meteorites, interplanetary dust, and the Earth's atmosphere has been considered in great detail /15—20/, and we will therefore only list the main astrophysical aspects with brief comments. At the earliest stages of evolution of the solar system the flux of cosmic rays was probably higher than it is today. This is uncertain, however, since the only sufficiently long-lived isotope produced by exposure to cosmic rays is K^{40} ($T_{1/2}=1.3 \cdot 10^9$ years). Comparison of the K^{40} and K^{41} abundance in various iron meteorites did not provide a conclusive solution to this problem /21/. The last 10^7 years, on the other hand, were studied in much greater detail. Several overlapping and mutually reinforcing methods are available for this period. We can analyze the quantity of stable and radioactive isotopes, or short-lived and long-lived isotopes produced in nuclear reactions with cosmic rays. So far, however, results confirm the constancy of the cosmic ray intensity during the relevant period apart from a factor of 2. This uncertainty is largely associated with various impurities in natural targets and with inaccuracies in the excitation function.

The problem of the cosmic ray intensity has been adequately covered only for the last $5 \cdot 10^4$ years. This is entirely due to the great advance in radiocarbon dating. The cosmic ray intensity was found to have remained constant within a few per cent. These topics are closely linked with the detection of short intensity bursts and modulation of cosmic rays in the past. Simultaneous measurement of the concentrations of radioactive isotopes with various halflives in principle should provide information regarding both these aspects /17/. The corresponding experiments, however, involve considerable difficulties and no adequate measurements have been carried out so far. One point should be stressed: the Earth's atmosphere provides a much more suitable target for these studies than the meteorites do. The radioactive isotopes forming in the Earth's atmosphere in reactions with cosmic rays naturally separate to settle in different sedimentary strata. Be^{10}, for example, makes it possible to identify a major burst even if it occurred a few million years ago. These studies require measurements in strata of known age. The situation in this respect is analogous to the currently developed idea of studying supernova bursts during the last millennium from the increased C^{14} content in the tree rings /22/.

3. The history of meteorites

The meteorite dating obtained by K—Ar and U—Pb methods does not agree with the results which take into consideration the yield of nuclear products in reactions triggered by cosmic rays (the so-called "cosmic age" of the meteorites). This discrepancy can be resolved by assuming that the meteorites, being minor objects in the solar planet, originated from a substantially larger body in whose interior the effect of cosmic rays was greatly suppressed.

Analysis of the stable to radioactive isotope ratios provided some insight into the preatmospheric shape of the meteorites and made it possible to estimate the collision frequencies and the erosion of meteorites in the interplanetary space. Typical quantities of some isotopes in stony meteorites produced by cosmic ray reactions are the following /23/: in 10^8 years, He^3, Ne^{21}, and A^{38} form in quantities of $2 \cdot 10^{14}$, $4 \cdot 10^{13}$, and $5 \cdot 10^{12}$ atoms per cm^3, respectively. Higher instrumental sensitivity is required for the analysis of individual inclusions in meteorites (chonders, magnetic or nonmagnetic fractions) or individual layers. The cosmic age of meteorites of various classes constitutes a highly important problem. A low cosmic age indicates that meteorites of the given type apparently formed near the Earth, possibly from the outer layers of the Moon. A high cosmic age (10^7 years) implies asteroidal origin.

4. Interplanetary dust

Zodiacal light and meteorite trails reveal the existence of macroscopic dust particles in the interplanetary space. The mass spectrum of these particles has been studied by various methods, but there is still no clear picture /24—26/. Interplanetary dust settles in layers in glacial and other sediments. The peculiar features of the dust particles as minute members of the solar system are reflected in the rate of formation of the various isotopes, which is mainly determined by the low-energy soft solar cosmic rays, and not the harder galactic cosmic rays affecting the meteorites. The dust therefore is expected to show a high level of activity for isotopes with low-threshold nuclear reactions and can be used to study the variation of solar cosmic rays /18, 20, 27/. Problems relating to the origin of interplanetary dust, its lifetime in the interplanetary space, and interaction with other objects of the solar system are solved by a combination of methods applicable to the determination of isotopic composition and dust mass spectrum.

* * *

In the nearest future we will be able to analyze directly the surface rocks of the Moon and Mars. This will provide a tool for studying various rare and little-probable events which can be detected only over large time intervals. For example, a slight excess of the induced radioactivity over the general background in individual patches of the lunar surface will supply an indication of antibodies having impacted against the Moon /28/. The presence of isotopes produced by cosmic ray reactions may be used as proof of the extraterrestrial origin of the specimen.

PRESENT PROCESSES

1. Spatial distribution of cosmic rays and modulation effects

Several methods are available for solving this problem. One of the methods is based on measuring the ratio of a short-lived (days, weeks) to a long-lived (years) isotope, forming in similar nuclear reactions (e.g.,

the A^{37}/A^{39} ratio). Another method involves dynamic measurements from spaceships. So far, however, detailed measurements have been carried out inside the Mars orbit, while the meteorites probe more distant parts of the solar system. The distribution of the light isotopes (H^3, He^3, He^4) in the interior of a meteorite /29/ sheds light on modulation effects.

2. The solar wind

The solar wind is studied by a great variety of methods. The combination of the results is adequately described by the theory /30/. However, further insight is required into the nature and the effects of the solar wind. Detailed studies of the isotopic composition of the solar wind may greatly help in this direction. Both natural and artificial specimens can be used. The solar wind particles penetrate into the outer skin layer (a few microns thick for a density of about $3\,g/cm^3$) of the meteorite or the lunar surface. The meteorites lose this skin-deep information on entering the Earth's atmosphere because of partial ablation. The lunar surface, on the other hand, reliably stores the information. In general, numerous ambiguities and uncertainties encountered in meteorite measurements are eliminated when we deal with the surface of the Moon. Moreover, lunar surface measurements will certainly provide a new angle for analyzing the extensive results of meteorite measurements. Artificial specimens avoid the uncertainties associated with the complex chemical composition of natural targets. A thin foil of high-purity material exposed on board a spaceship or by the astronauts on the Moon will readily separate the solar wind particles from high-energy particles and their secondary products. Estimates /31/ show that in 24 hours a $300\,cm^2$ target may acquire $2 \cdot 10^{14}$ He atoms, $5 \cdot 10^{12}$ Ne atoms, and $8 \cdot 10^{10}$ A atoms. A 40 kV potential applied to the target will increase the collection efficiency by a factor of 50. As a result, the fluxes of H^2, H^3, He^3, He^4, and other solar wind isotopes can be measured. Although this is not a dynamic method and the exposure takes a few days, this is a fairly short time for various purposes. Measurements carried out under various conditions, at various distances and in different phases of the solar activity, will reveal the dynamics of numerous phenomena associated with the solar wind. Comparison of the abundance of isotopes in the solar wind with the content of these isotopes in various meteorites (there are meteorites with anomalous content of the rare gases) and their abundance on the Sun will provide certain information relating to the origin of the solar system. These measurements will possibly supply an indication of whether or not the solar wind "blew stronger" in the past.

3. The composition of the galactic cosmic rays

Considerable attention is currently focused on the isotopic composition of the galactic cosmic rays in connection with problems of their origin, the probing of the interstellar medium, etc. The photographic emulsion and the dynamic methods are widely supplemented by techniques which call for the development of the traces of heavy metals in meteorites and special artificial specimens. The last method makes it possible to determine the preatmospheric shape of the meteorite and the mass lost in the atmosphere /32/. The high content of He^3, Li, Be, B in the galactic cosmic rays has been established long ago. A substantial percentage of deuterium nuclei has also been detected /33/. Assuming that these are secondary products, we can

estimate the mass traversed by the cosmic rays and their lifetime /34/. In principle, large high-purity targets will measure the tritium fluxes also. We can thus find the mass traversed by the cosmic rays in the neighborhood of the solar system (a few tens of light years). Estimates show that a 1 m^2 target exposed for 100 days will detect the tritium nuclei if their number exceeds 0.1—0.15 of the total number of He^3 nuclei.

4. Solar cosmic rays

Large solar flares may eject streams of relatively energetic particles. This explains the considerable attention focused on the mechanism of this phenomenon. Measurements of the isotopic composition of the solar cosmic rays and its comparison with the abundance of the elements on the Sun makes it possible to decide whether these isotopes are products of nuclear reactions in the solar flare or the entire solar composition is accelerated. By measuring the content, in the solar cosmic rays, of those isotopes whose abundance in the Sun is negligible, we can find the interplanetary mass traversed by the particles (as for the galactic cosmic rays) /35, 36/. The acceleration mechanism can be inferred from the ratio of isotopes with different charge to atomic weight ratio (H^1, H^2, H^3, He^3, He^4, C, A). Measurements of H^3 and He^3 were carried out during a large solar flare /37, 38/ and a relatively high content of these isotopes was discovered: the content of tritium was 0.4% of the number of protons, and the content of He^3 reached 10%. These experiments, however, suffered from uncertainties which interfered with unambiguous interpretation: no measurement data were available on the integral flux of H^1 and He^4; the measurements were made with random samples without preliminary isotopic purity control. It is highly desirable to proceed with further measurements of this kind. Interesting results will probably be obtained by exposing a stack of special purity plates. The sensitivity of the equipment for tritium (10^5—10^6 atoms) and He^3 (10^7—10^8 atoms) is sufficient for additional measurements of the energy spectrum of each isotope.

5. Accretion of matter by the Earth

The origin of He, A, Xe and similar gases in the Earth's atmosphere is often explained by reference to accretion of gases from the interplanetary space. Quantitative estimates of this effect, however, involve considerable difficulties. In particular, the magnetic field near the Earth and in the plasma apparently lowers the rate of accretion. Detailed calculations should therefore proceed from measurements of the isotopic composition of the solar wind and the low-energy component of the solar cosmic rays outside the Earth's magnetosphere.

6. The radiation belts of the Earth

The problems of stability, origin, and lifetime of particles in the radiation belts and the relation of these parameters to solar activity — this is only a partial list of topics of current interest. Protons and electrons are so far the only particles detected in any measurable quantities /39/. However, during large solar flares, the nuclei of solar cosmic rays may be trapped. Measurements of tritium in the metal of rockets and satellites made after a solar flare /37/ suggest that particles other than protons may be trapped;

these measurements even went further and provided the lifetime of H^3 in the radiation belt (a few months). However, as we have already noted, there are numerous uncertainties in the interpretation of these results /37/. Measurements in radiation belts should therefore be continued, using methods similar to those described for solar cosmic rays above.

7. Measurements of the neutrino flux from the Sun

The high penetrating power of the neutrino, although ideal for probing deep into the solar interior, constitutes a great disadvantage from the viewpoint of detection. The problems of neutrino astrophysics are widely discussed in this volume, and we will therefore mention only one point which has bearing on the methodology of A^{37} measurements. By using a low-noise proportional counter, we can raise the sensitivity to 10 A^{37} atoms. This record sensitivity is in no way inferior to the sensitivities of photoemulsions and dynamic methods.

CONCLUSION

Our survey is by no means complete and exhaustive. And yet, it gives some idea of the enormous scope of astrophysical problems that can be studied and solved by measuring small and ultrasmall quantities of various isotopes. Our discussion takes into consideration the availability of lunar rock samples and exposure of large artificial targets in outer space. This, however, by no means detracts from the importance of natural samples, such as meteorites, marine and glacial sediments, etc. The increased sensitivity of the measuring equipment will enable us to measure individual inclusions, formations, or strata.

It is only natural to strive to determine the maximum number of different isotopes in a single sample. This is a difficult task, however, since the high-sensitivity techniques, as we have noted above, are generally suitable for simultaneous measurements of from 1 to 3 isotopes. Cooperation between different laboratories or installation of different kinds of equipment for the determination of small and ultrasmall quantities of various isotopes in one institute is therefore inevitable.

I would like to acknowledge the help of G. E. Kocharov and Yu. N. Starbunov and their valuable critical comments.

Bibliography

1. Kocharov, G.E. and V.O. Naidenov.— Trudy V Vsesoyuznoi ezhegodnoi zimnei shkoly po kosmofizike, p. 100. Izdatel'stvo Kol'skogo Filiala AN SSSR, Apatity. 1968.
2. Watt, D.E. and D. Ramsden. High Sensitivity Counting Techniques.— Pergamon Press. 1964.
3. Kocharov, G.E. and V.O. Naidenov.— PTE, No.3:5. 1966.
4. Metody analiza veshchestv vysokoi chistoty (Methods of Analysis of High-Purity Materials). Edited by I.P. Alimarin.— Moskva, "Nauka." 1965.

5. Yoe, J.H. and H.J.Koch [Editors]. Trace analysis. New York, Wiley. 1957.
6. Taylor, D. Neutron Irradiation and Activation Analysis.— Princeton, Van Nostrand. 1964.
7. Kuznetsov, R.A. Aktivatsionnyi analiz (Activation Analysis).— Moskva, Atomizdat. 1967.
8. Alimova, I.A., B.S. Boltenkov, V.N. Gartmanov, B.A. Mamyrin, and B.N. Shustrov.— Geokhimiya, No.9:1044. 1966.
9. Schmitt, R.A., R.H. Schmitt, and G.G. Goles.— J. Geophys. Res., **70**:2419. 1965.
10. Fowler, W.A., J.L. Greenstein, and F. Hoyle.— Geophys. J., **6**:148. 1962.
11. Cameron, A.G.W.— Icarus, **1**:314, 339. 1962.
12. Marshall, R.R.— Icarus, **1**:95. 1962.
13. Kohman, T.R.— J. Chem. Educ., **38**, 73. 1961.
14. Rancitelly, L.A. and D.E. Fisher.— J. Geophys. Res., **73**:5429. 1968.
15. Anders, E.— Rev. Mod. Phys., **34**:287. 1962.
16. Arnold, J.R.— Ann. Rev. Nucl. Sci., **11**:349. 1961.
17. Geiss, H., H. Oeschger, and U. Schwarz.— Space Sci. Rev. **1**:197. 1962.
18. Lal, D. and B. Peters.— Prog. Element. Particle and Cosmic Ray Phys., **6**:3. 1962.
19. Arnold, J.R., M. Honda, and D. Lal.— J. Geophys. Res., **66**: 3519. 1961.
20. Wasson, J.T.— Icarus, **2**:54. 1963.
21. Voshage, H. and H. Hintenberger.— Z. Naturforsch., **14a**: 828. 1959.
22. Konstantinov, B.P. and G.E. Kocharov.— Doklady AN SSSR, **165**:63. 1965.
23. Eberhardt, P., O. Eugster, J. Geiss, and K. Marti.— Z. Naturforsch., **21a**:414. 1966.
24. Öpik.— Proc. Roy. Irish Acad., **54a**:165. 1951.
25. Nazarova, T.N.— KI, **4**:900. 1966.
26. Konstantinov, B.P., M.M. Bredov, and E.P. Mazets.— Doklady AN SSSR, **174**:580. 1967.
27. Alder, V., H. Oeschger, and J.T. Wasson.— In: "Radioactive Dating and Methods of Low-Level Counting," p.189. Vienna. 1967.
28. Vlasov, N.A. Antiveshchestvo (Antimatter).— Moscow, Atomizdat. 1968.
29. Shen, C.S. and R.K. White.— J. Geophys. Res., **73**:4273. 1968.
30. Parker, E.N.— Planet Space Sci., **13**:9. 1965.
31. Singer, P., P. Eberhardt, and J. Geiss.— J. Geophys. Res., **70**:2243. 1965.
32. Fleisher, R.L., P.B. Price, R.M. Walker, and M. Maurette.— J. Geophys. Res., **72**:331. 1967.
33. Fan, C.J., G. Gloeckler, and J.A. Simpson.— Phys. Rev. Lett., **17**:329. 1966.
34. Ramaty, R. and R.E. Lingenfelter.— Can. J. Phys., **46**:5627. 1966.
35. Biswas, S. and C.E. Fichtel.— NASA X-611-65-219. 1965.

36. Lingenfelter, R.E. and R. Ramaty.— Publ.593. Univ. of California, Los Angeles. 1967.
37. Tilles, D., J. Defelice, and E.L. Fireman.— Icarus, **2**:258. 1963.
38. Schaeffer, O.A. and J. Zähringer.— Phys. Rev. Lett., **8**:389. 1962.
39. Fenten, K.B.— J. Geophys. Res., **72**:3889. 1967.

PLASMA CONTAINMENT IN ADIABATIC TRAPS

B. B. Kadomtsev

Research into plasma containment in adiabatic traps was begun in connection with the purely applied problem of controlled thermonuclear fusion. In quite a short time, a wide range of interesting physical phenomena were discovered in a plasma contained in an adiabatic trap, and the discovery of the radiation belts of the Earth demonstrated that similar effects may occur under natural conditions also. Considerable progress has been achieved by now toward understanding the physical effects in traps and we are in a position to summarize the various results in this field. The various problems of containment of isolated particles, equilibrium and hydrodynamic stability of plasma have been clarified in general outline, and our understanding of the kinetic plasma instability has markedly improved.

Experimental studies of the containment of isolated particles have shown that the adiabatic invariant is conserved with exponential accuracy, and in very strong magnetic fields longer containment is observed. This is probably a hint at the permanent conservation of the adiabatic invariant in axisymmetric traps, theoretically predicted by Arnold.

An important stage in the investigation of plasma containment in adiabatic traps was marked by the experiments of M.S. Ioffe and co-workers, who showed that plasma in ordinary traps develops the theoretically predicted fluting hydrodynamic instability. The same experiments established the possibility of stabilizing the flute instability by means of additional current-carrying rods.

The main emphasis at present is on the kinetic instabilities, which are a manifestation of the maser effect of electromagnetic wave amplification by means of population inversion. In hot-ion plasma, this group of instabilities includes cyclotron pumping of Alfven waves ("pearls") and Langmuir waves (Harris instability), conical and drift-conical instability of dense plasma, modified negative-mass instability, and a number of more restricted and less significant instabilities. Conical and drift-conical instabilities are the only ones which have not been observed so far experimentally.

In hot-electron plasma, the principal instability is the cyclotron pumping of whistlers. This instability is observed in most laboratory experiments, and it is also highly effective in the radiation belts of the Earth.

Experiments show that the instabilities are in fact responsible for the collective processes in a plasma contained in adiabatic traps;

instabilities also play a decisive role in the formation of the radiation belts around the Earth.

A paper on plasma containment in adiabatic traps will be published in Uspekhi Fizicheskikh Nauk by B. B. Kadomtsev, and M. S. Ioffe. It will deal in detail with the various aspects of this problem.

DISTRIBUTION OF THE OUTER BELT PROTONS IN THE μ, L SPACE

Yu. I. Gubar' and V. P. Shabanskii

Comparison of the theory of charged particle transport across the drift envelopes with experimental findings is more meaningful in the space of adiabatic invariants.

The particle distribution in this space was derived from experimental data on low-energy proton fluxes. The results of intensity measurements provided by EXPLORER XII, EXPLORER XXVI, and ELEKTRON-series satellites were used to this end. The equatorial particles were first considered. Proton fluxes with energies above a given value are converted into fluxes with fixed minimum magnetic moment. The transformation is performed assuming an exponential energy spectrum and also directly, without any assumption concerning the spectrum.

With the exponential spectrum, magnetic moment conservation leads to a radial intensity profile which is independent of μ_{min} in a certain range. The fluxes $j(>\mu)$ rapidly increase as L rises from 2 to 3 – 3.5. For L values beyond the belt maximum, $j(>\mu)$ is a relatively weak function of L. This is particularly obvious for the section of the outer proton belt according to the EXPLORER XII 1961 data. A somewhat stronger (decreasing) dependence of the fluxes $j(>\mu)$ on L emerges from the measurements of EXPLORER XXVI early in 1965, at low magnetic disturbance levels. The transformation from energy to the magnetic moment thus revealed a definite time variation of intensity, which was apparently associated with significant changes in solar activity.

The radial variation of the equatorial fluxes for small μ fits the analogous computations of L. S. Chesalin for particles near the equator (EXPLORER XII). For large μ, a certain divergence is observed due to the latitudinal dependence of the fluxes. The proton distribution function in the μ, L space is obtained from the Nakada-Mead relation. The connection of this relation with Janosi's more general relation and with Dungee's expression for the phase space element in the variables μ, L is established. A dipole magnetic field is assumed.

The distribution function based on experimental data differs from the steady-state distribution without losses and sources beyond the belt maximum. The difference is particularly significant for 1961, when the solar activity was still fairly high. Instead of decreasing as L^{-2}, the distribution function increases with L. For some values of μ, the distribution function even increases as L^5. The results are in qualitative agreement with Hess' calculations for nonequatorial particles (from the data of EXPLORER XII).

The separability of the distribution function, established by Hess for nonequatorial particles, follows for equatorial particles from the exponential energy spectrum and the conservation of μ. Certain processes which may be responsible for the observed proton distribution are considered.

The pressure of protons with a given minimum magnetic moment is not particularly sensitive to L beyond the belt maximum. The protons are thus in a nearly equilibrium state, which may be the result of sufficiently rapid diffusion. Direct measurements of the fluxes $j(>\mu)$ are highly desirable.

SELF-SIMILAR FLOW IN RAREFIED PLASMA

M. A. Gintsburg

The problems of the self-similar evolution of a spherical plasmoid, a cylindrical plasma pinch, and a plane plasma sheath are considered. The corresponding differential equation is

$$\delta \cdot v + (\eta v)' = (1-\eta v)\left\{ \ln\left[e^{\int \frac{dv}{\eta}} e^{-\frac{v^2}{2}} \cdot \frac{1}{\eta^2} - (1-\eta v)\eta v'' + v'(\eta^2 v' - \delta) + \eta v' v (1+\delta) \right] \right\}', \qquad (1)$$

where v is the ion velocity,

$$\delta = \begin{cases} 0 \text{ for the cylinder,} \\ 1 \text{ for the plane sheath,} \\ -1 \text{ for the sphere.} \end{cases}$$

Prime denotes differentiation with respect to $\eta = t/r$.

Numerical solution of equation (1) on a computer leads to the following conclusions.

1. When the variation of the density n as a function of the time t is observed at a fixed point, n(t) is not a monotonic function (as for a flowing neutral fluid) but has a maximum for some $\eta < 1$ (a solution in the form of a unit density and velocity pulse). The plasma spreads out in sheaths.

2. A characteristic velocity inversion effect is observed: once the density and velocity pulse has passed through a given point, the ion velocities at that point are directed inward, to the center, i.e., besides the general outward flow of the plasmoid, there is also inward, centerward flow of ions.

3. The ions are accelerated in the course of their centerward motion. After the pulse has passed, the ion velocities do not go to the unperturbed value v = 0. In other words, ion acceleration is irreversible, a highly significant point for its efficiency.

4. The spherical (cylindrical, plane) pulse gradually spreads and becomes diffuse, and its amplitude decreases.

If the magnetic field is introduced, the self-similar equations of magnetic hydrodynamics take the following form in the plane case:

$$\vec{v}' = \frac{(1-v^2)^{\frac{1}{2}}}{1-\eta v_x}\left(\vec{E} - \vec{v}(\vec{E}\vec{v}) + [\vec{v}\vec{H}]\right),$$

$$H_y' = \frac{\eta}{1-\eta^2}\left(H_y + n_i v_{iz} - n_e v_{ez}\right) - \frac{E_z}{1-\eta^2}; \quad E_y' = \frac{1}{1-\eta^2}\left(\eta E_y + H_z + n_e v_{ey} - n_i v_{iy}\right), \text{ etc.}$$

In the cylindrical case,

$$v_z' = \frac{v_z^2}{1-\eta v_z} + \frac{(1-v^2)^{1/2}}{1-\eta v_z}\left(E_z - v_z(\vec{E}\vec{v}) + v_\varphi H_z - v_z H_\varphi\right), \text{ etc.}$$

We also derived a numerical solution of the two-dimensional steady-state problem of the transverse flow of a plasma beam as a result of the formation of runaway electrons along the or axis (the beam moves along the oz axis). Computations show that there are no electrons inside a certain cone directed along the oz axis with an opening angle $\pi - 2\theta_{max}$. Let K_1, K_2, K_4, K_5 be the density, the transverse velocity, the field, and the longitudinal velocity of the beam ions in the plane $z = 0$. Then to first approximation ($\tan\theta < 1$)

$$\tan\theta_{max} = 2K_5 \frac{\left[\left(\frac{K_4}{K_5} + K_2\right)^2 + 8 + A\right]^{1/2} - \left(K_2 + \frac{K_4}{K_5}\right)}{8 + A}, \qquad (2)$$

where $A = e^{K_3} - K_1 - 2\delta + (K_4/K_5)^2 + K_2 \cdot (K_4/K_5)$.

Equation (2) is the solution of the problem of flow around a cone ($\delta = 0$) or a wedge ($\delta = +1$) with an opening angle $\pi - 2\theta_{max}$. If the conical angle θ is larger than $\pi - 2\theta_{max}$, the drag is high, and for $\frac{\theta}{2} < \frac{\pi}{2} - \theta_{max}$ the drag is low.

PARTICLE ACCELERATION IN A PLASMA IN OUTER SPACE

M. A. Gintsburg

A mechanism of particle acceleration by the eddy electric fields of nonlinear waves was described in the author's publications (see below). For example, the energy increment of an ion in a hydromagnetic wave is given by

$$\Delta W = 4H_0^2/8\pi n_0,$$

where H_0 and n_0 are the average parameters of the unperturbed plasma, i.e., the particles absorb four times the energy of the initial magnetic field. Under the conditions of a strong chromospheric flare ($H_0 = 500$ gauss, $n_0 = 10^8$ cm^{-3}), we have $\Delta W = 250$ MeV, which is in fact the typical energy of solar cosmic rays. Electrons are also accelerated by the nonlinear wave, so that ion acceleration is invariably accompanied by X-ray bursts. The role of particles trapped in the potential well of relativistic electron waves is also analyzed.

Bibliography

Ginzburg, M.A. — J. Geophys. Res., **72**:2749. 1967. Gintsburg, M.A. — Astronom. Zh., **45**:610. 1968.

COMPARISON OF THE VARIATIONS OF HIGH-ENERGY ELECTRONS AND ULTRA-LOW-FREQUENCY RADIATION

A. B. Malyshev, P. M. Svidskii, V. A. Burov, I. G. Kleimenova, and V. A. Troitskaya

The results of simultaneous observations of the injected high-energy electron fluxes and ULF radiation ("hissing") are compared.

1. The electron fluxes were observed in the region of drift envelopes with L from 3 to 5.5 at altitudes between 220 and 1150 km. Electrons with energy above 0.2 MeV (scintillation counters) and above 1.5 MeV (Geiger counters) were recorded. The ULF radiation between 0.5 and 10 kHz was picked up by ground stations. The electron and the radiation fluxes were measured in the area of Kerguelen Isl.

2. During these observations (2 – 11 July 1965), significant variations in the high-energy electron fluxes were noted. Analysis of observation findings points to three types of electron injection: a) catastrophic, b) normal, c) slight. Each type of injection is associated with a certain spectrum of ULF radiation.

3. Assuming that the ULF wave propagates along a line of force, we can compute the upper cutoff frequency for each L envelope. The upper cutoff frequency in the spectrum of ULF radiation in the magnetosphere is determined by the electron cyclotron resonance absorption at the apex of the force line.

4. Comparison of the computations with the observed spectrum of ULF radiation during the high-energy electron injection indicates that the injection type is correlated with the ULF radiation spectrum. The interaction of the trapped electrons with the electromagnetic waves modifies the pitch-angle distribution and eventually leads to their injection into the atmosphere.

5. Interaction with ULF radiation is the only effective mechanism allowing electrons to escape from the outer radiation belt.

THE EFFECT OF SOLAR WIND VELOCITY INHOMOGENEITIES ON THE STRUCTURE OF THE INTERPLANETARY FIELD

I. I. Alekseev, A. P. Kropotkin, and A. R. Shister

Experimental data reveal a significant dependence of the solar wind velocity on the heliolatitude θ and the heliolongitude φ. We considered the structure of the interplanetary field in relation to this anisotropy of solar plasma ejection.

The streaming velocity V of the solar wind is known to be high compared to the velocity of sound c_s and the Alfven velocity c_A in the interplanetary space. Therefore, to first approximation, we may ignore the effect of the thermal and magnetic pressure gradients on the velocity field. The velocity field is therefore assumed given and independent of time; we take $v_r = \text{const}$, $v_\theta = v_\varphi = 0$. The magnetic field is frozen into this given, and in generally spherically asymmetric, plasma stream. The problem of the kinematic transport of the magnetic field from the space around the Sun into the interplanetary space was solved under these assumptions. The solution gives the following field components:

$$B_r = B_{r_0}\left(\frac{r_0}{r}\right)^2 + \frac{r_0}{rV}\left(1-\frac{r_0}{r}\right)\left[\frac{B_{\varphi_0}}{\sin\theta}\frac{\partial V}{\partial \varphi} + B_{\theta_0}\frac{\partial V}{\partial \theta}\right];$$

$$B_\theta = \frac{r_0}{r}B_{\theta_0}; \qquad B_\varphi = \frac{r_0}{r}B_{\varphi_0},$$

where $B_{r_0} = B_r(r_0, \theta, \varphi)$, $B_{\theta_0} = B_\theta(r_0, \theta, \varphi)$, $B_{\varphi_0} = B_\varphi(r_0, \theta, \varphi)$, the scale r_0 is conveniently taken of the order of a few Sun's radii. We thus see that B_r is essentially determined by the inhomogeneities of the solar wind velocity, and the corresponding effect increases with increasing distance r. Estimates show that velocity inhomogeneities of scale $\Delta\varphi \sim 1$ may produce significant changes in B_r at the Earth's orbit, and even reverse its sign, for $\Delta V/V \sim 10\%$. For smaller-scale $\Delta\varphi$, a similar effect is observed even for smaller velocity inhomogeneities.

We derived the shape of a force line which significantly differed from the ordinary Archimedes spiral, forming, in particular, characteristic loops of different sizes, not unlike those observed experimentally.

INTERACTION OF HIGH-ENERGY PARTICLES WITH THE NEUTRAL LAYER OF THE MAGNETOSPHERE TAIL

I. I. Alekseev and A. P. Kropotkin

Since the neutral layer in the magnetosphere tail, where the tangential magnetic field component reverses its sign, is relatively thin, $d \sim 0.1 R_E$ (where R_E is the Earth's radius), the motion of particles of sufficiently high energies with Larmor radii $r_L \gtrsim d$ in the field of the tail is no longer adiabatic in this layer. On the other hand, when $r_L \gg d$, the motion of particles near the neutral layer may be analyzed by treating this layer as an infinitesimally thin boundary between two regions with a homogeneous field. The tangential component of the magnetic field has opposite signs on the two sides of this plane boundary. Analysis of particle motion in this simple model leads to the following results.

1. For a given ratio of normal to horizontal field components $\frac{B_n}{B_t} = \tan\alpha$, the particle will either be transmitted through the boundary or reflected from the boundary, depending on the pitch angle β_0 and the phase of the Larmor rotation φ_0 which the particle has when it first crosses the boundary.

2. Before being transmitted or reflected, the particle will in general cross the boundary several times. The crossing multiplicity n also depends on β_0 and φ_0.

3. If the angle α is not too small, $\alpha \gtrsim 1$ (this case is observed during magnetic disturbances, when the Earth-ward edge of the current layer approaches to the Earth and $\frac{B_n}{B_t} \sim 1$). In this case, $n \sim 1$ almost for all values of β_0 and φ_0. The simple relations expressing the variation of β and φ when the particle moves near the boundary make it possible to compute for $\alpha \gtrsim 1$, the values of the parameters β_n, φ_n which the particle acquires when it moves away from the boundary (assuming that the "initial" parameters β_0, φ_0 are known). The evolution of the pitch angle distribution of the particles crossing the boundary and being reflected from the boundary was estimated, with allowance for the actually observed strong dispersion in pitch angles.

4. For small $\alpha \ll 1$, which is the case observed in the magnetosphere tail proper ($\alpha \sim 1/20$), the first adiabatic invariant is approximately satisfied, $\beta_n \simeq \beta_0$, although the motion is nonadiabatic, as before.

5. For $\alpha \ll 1$ the number of particles reflected from the boundary is equal to the number of transmitted particles.

6. For $\alpha \ll 1$ the total number of boundary crossings n was computed as a function of β_0 and the resultant displacement of a particle in the plane of the neutral layer across the magnetosphere was determined. Effects of particle leakage from the magnetosphere through the neutral layer and particle injection effects can be assessed on the basis of these findings.

LOCALIZATION OF ACTIVE SOLAR REGIONS RESPONSIBLE FOR THE GENERATION OF THE GEOEFFECTIVE AGENT

V. P. Nefed'ev

To determine the probable onset and duration of the generation of the agent responsible for the decrease of the cosmic ray intensity, we considered certain processes in active regions on the Sun at the level of the photosphere (variation of sunspot area); at the level of the chromosphere (chromospheric flares of strength 2B and higher); at the level of the corona (number and spectrum of events at meter wavelengths). We thus analyzed the solar activity during ten months in 1967 and for the months of August–September 1966. The solar activity varied quite markedly during this period.

Periods of solar activity sufficiently clearly localized in time were selected for analysis. The beginning of each active period was identified either with a marked increase in sunspot area or with a marked increase in flare activity (or both, if the increase in sunspot area and in flare activity were observed simultaneously). The end of the active period was identified with the decrease in flare activity or in sunspot area. A total of 13 active periods were identified.

Twelve active periods on the Sun corresponded to decreases of cosmic ray intensity of various amplitude and character. The tracings of cosmic ray intensity decrease showed three characteristic points: T_1 – the decrease begins, T_2 – the cosmic ray intensity starts increasing back to the initial level, T_3 – the cosmic ray intensity has fully recovered.

The time between T_1 and T_2 was found to be equal (to within one day) to the overall duration of the active period on the Sun. Short active periods on the Sun (of about 1 day) corresponded to intervals $T_1 - T_2 \simeq 1$ day. The longest of the observed active periods (7 – 8 days) corresponded to a cosmic ray intensity decrease with $T_1 - T_2$ also equal to 7 – 8 days.

The active regions on the Sun were observed between E50 and W40 (at the beginning of each active period), except for a single region at E90, which did not have a substantial effect on the cosmic ray intensity.

APPLICATION OF ELECTRICAL FIELDS IN INTERPLANETARY SPACE AS RADIATION SHIELDING AGAINST PROTONS AND ELECTRONS

T. Ya. Ryabova and K. A. Trukhanov

One of the basic problems encountered in connection with the feasibility of a prolonged stay in interplanetary space involves the radiation shielding of the scientific equipment, materials (photographic film, say), and naturally also spacecraft crew and other living organisms on board.

Since the weight of the conventional radiation shielding which attenuates the penetrating radiation in a suitable absorbing mass accounts for a substantial fraction of the total spacecraft weight (especially in long trips), it is highly desirable to ensure maximum shielding efficiency with minimum weight and maximum reliability in relation to the particular conditions of interplanetary travel.

One of the most attractive solutions of this problem is by deflection of charged particles from the spacecraft hull by strong electrical fields. Analysis shows than an electrostatic radiation shielding system is highly effective and its weight is one order of magnitude less than the weight of the equivalent absorbing shielding (the power requirements are quite low also). The main results pertaining to the electrostatic shielding against the protons of the inner radiation belts and the principal engineering difficulties making the electrostatic shielding unfeasible in the nearest future were analyzed. Effective electrostatic shielding can be provided at this stage under the conditions of natural and artificial electron radiation belts, ensuring adequate shielding of a small volume from solar flare protons.

Since the electron flux intensity in the radiation belts is fairly high ($\sim 10^7 - 10^8$ el/cm^{2}sec), the deflecting electric field of the electrostatic shielding may be set up by utilizing the charge induced by the electrons from the radiation belts, i.e., without resorting to any high-tension sources on board spacecraft.*

Another highly important problem is the shielding against electrons (it is relevant for long-lived orbital stations in 24-hour orbit, for spacecraft accelerated by low-thrust engines, for objects exposed to high electron fluxes from the beta decay of nuclear reaction products). In view of the high intensity of the electrons and the production of highly penetrating bremsstrahlung, the conventional shielding is generally very bulky.

The efficiency of the electrostatic shielding was assessed in terms of certain parameters which express the principal characteristics of

* Leakage currents from the surface of a high-voltage electrode are virtually suppressed by means of a thin (about 0.01 g/cm^2) system screening off the ultraviolet radiation of the Sun and interplanetary plasma ions.

shielding in general form for any given electron spectrum ($dN/d\varepsilon \sim \varepsilon^{-\gamma}$, $dN/d\varepsilon \sim \exp(-\frac{\varepsilon}{\varepsilon_0})$, $dN/d\varepsilon \sim \exp(-0.5758 - 0.0558^2)$. Using these characteristics, the weight of the electrostatic shielding was estimated: it was found to be $1/20 - 1/30$ of the corresponding weight of conventional absorbing shielding. The "self-charging" of the shielding makes it no less reliable than any conventional shielding.

The electrostatic shielding thus provides one of the most promising ways of ensuring radiation safety of spacecraft in the radiation belts of the Earth.